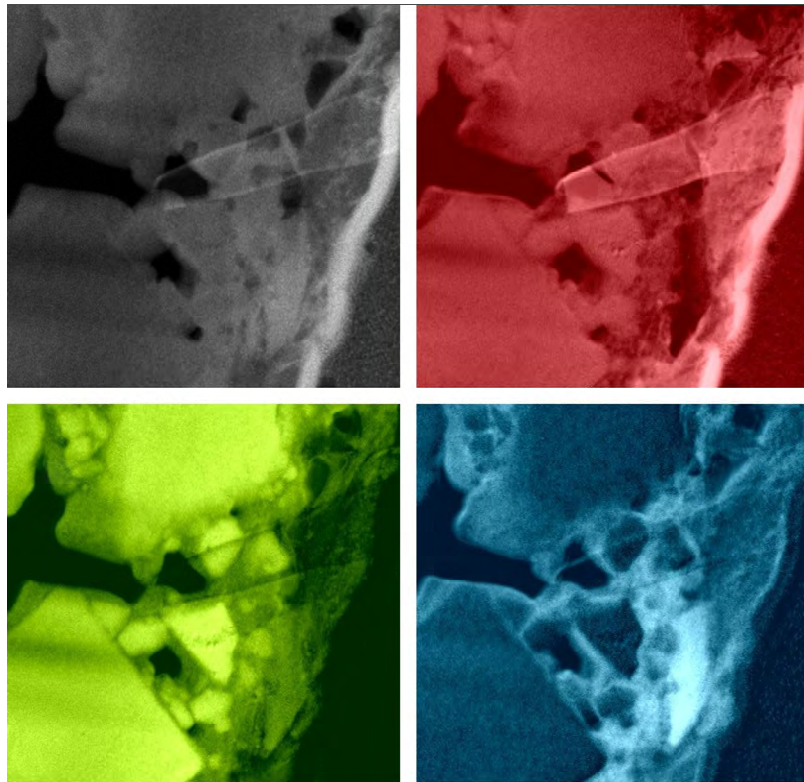


OXIDATION AND WET WEAR OF SILICON CARBIDE



Dissertation zur Erlangung des Grades eines
Doktors der Naturwissenschaften
der geowissenschaftlichen Fakultät
der Eberhard-Karls-Universität Tübingen

2009

vorgelegt von
Volker Presser
aus Immenstadt

OXIDATION AND WET WEAR OF SILICON CARBIDE

Dissertation

zur Erlangung des Grades eines Doktors der Naturwissenschaften

der Geowissenschaftlichen Fakultät
der Eberhard-Karls-Universität Tübingen

vorgelegt von
Volker Presser
aus Immenstadt

2009

Tag der mündlichen Prüfung: 17.06.2009

Dekan: Prof. Dr. Peter Grathwohl

1. Berichterstatter: Prof. Dr. Klaus G. Nickel

2. Berichterstatter: Dr. Christoph Berthold

3. Berichterstatter: Prof. Dr. Yury Gogotsi

***“I am among those who think that science has great beauty.
A scientist in his laboratory is not only a technician:
he is also child placed before natural phenomena
which impress him like a fairy tale.”***

Marie Skłodowska–Curie (1867 - 1934)

ACKNOWLEDGEMENTS:

This work was financially supported by the German Research Foundation DFG (grant number Ni299/12-1) and partially from my Bernd-Rendel-award prize money.

First of all I would like to thank my advisor and dear mentor Prof. Klaus Georg Nickel for giving me the chance to work on this interesting project and also for the possibility to participate on numerous conferences, collaborations and side projects - and of course for all of his kind help and support! Also, Dr. Christoph Berthold is gratefully thanked for his help. This work would not have been possible without his input and support - both work-related and work-unrelated. Thank you, Christoph!

Also, none of this work could have been carried out without sample material. For that, I would like to thank ESK ceramics GmbH (Kempten) and SiCrystal AG (Erlangen) for the kind supply of sintered SiC bodies (ESK) and SiC single crystals (SiCrystal), respectively. And of course special thanks to our master mechanics Norbert Walker and Barbara Maier and their team along with Indra Gill-Kopp for all their help and preparing such small sample volumes even specialized companies thought impossible. Our workshop was always the best address to turn to solve “unsolvable” problems and to get access to sample holders or tools “impossible to build”.

I owe special thanks to Dr. Richard Wirth who played a major role in the sub-micrometer scale characterization of tribolayers using FIB for sample preparation and HR-TEM / EDX / EELS for sample characterization. This technique along with his skillful practice opened a whole new dimension in triboscale analysis. Also, I like to express my gratitude also to the GeoForschungsZentrum Potsdam (now Helmholtz-Zentrum Potsdam) for letting me conduct my research free of charge.

Our department’s secretary, Dagmar Dimitrovice, is gratefully thanked for thoroughly dealing with all the organizational work and giving the very best example of how kind and friendly a bureaucrat can be.

For the introduction into HDAC operations I would like to thank Dr. Andreas Audétat (Bayerisches Geoinstitut Bayreuth) and of course Prof. Hans Keppeler for kindly putting his laboratory equipment in Tübingen at my disposal.

Dr. Christoph Glotzbach is thanked for introducing me to the field of age determination and his kind help and helpful input throughout our valued and successful collaboration.

Dipl.-Chem. Christoph Raisch is thanked for conducting XPS measurements and his help during the interpretation phase.

Thanks also to my colleagues at the Fraunhofer IWM in Freiburg - Dr. Andreas Kailer and Dipl.-Min. Oliver Krummhauer - for covering the simulation part and conducting tribometer experiments.

The helpful and greatly appreciated input of so many others for the individual papers presented in this cumulative thesis is acknowledged in detail in the corresponding sections.

ABSTRACT:

Silicon carbide (SiC) as both the most important non-oxide ceramic and promising semiconductor material grows stoichiometric SiO_2 as its native oxide during hot-gas corrosion (= passive oxidation). During SiC oxidation, there are many influencing parameters, for example, porosity, presence of sintering aids, impurities, crystallographic orientation, subsequent surface treatment, and atmospheric composition. Also, the initially vitreous silica scale undergoes structural transformation during crystallization as disc-like devitrification areas appear (radialites). These areas show significantly decreased oxidation rates due to decelerated gas diffusion. Impurities, for example, originating from the furnace atmosphere, accumulate over time on the silica scale and lead to a second morphological transition due to a melt-catalyzed recrystallization. In the end, small crystalline spheres (globulites) appear which are separated by a significant pore volume. The latter acts as pathway for accelerated gas diffusion causing higher oxidation rates. Therefore, the kinetics can be complex.

Nonetheless, a general linear-parabolic time-law can be found for most SiC materials for passive oxidation. The pronounced anisotropy of SiC expresses itself by quite different oxidation rates for the various crystallographic faces that vanish approximately at $1350^\circ - 1400^\circ\text{C}$. Manifold impact factors are reflected by oxidation rate-constants for silicon carbide that vary over orders of magnitude. The understanding of SiC oxidation and silica formation is still limited; therefore, different oxidation models are presented and evaluated in light of current knowledge.

Silicon carbide sustains chemical and mechanical deterioration during tribological exposure under water lubrication. Hydrothermal treatment alone only leads to active corrosion of SiC while tribochemical wear causes the formation of a thin (tens to hundreds of nanometer) layer composed of nanoscale SiC wear debris embedded in a silica-like matrix (SiO_xH_y) with possibly some minor oxycarbide content. The SiC wear particles are plastically deformed and rounded as a result of mechanical tribolapping. Below that layer, subsurface damage builds up in the form of dislocations, ruptures and shear cracks. As a result of plastic deformation (similar to indentation plasticity) SiC single crystals within that transition zone are transformed into mosaic crystals with smaller domains due to slip plane gliding.

A first qualitative wear model combines hydrothermal corrosion with mechanical wear. While mechanical contact yields pathways for water inflow and generally disrupts the structural integrity of SiC grains, hydrothermal reactions of trapped water and subsequent pressure relief leads to a mechanism of dissolution and reprecipitation. The latter produces the observed amount of SiO_xH_y which acts as an adhesive for the SiC wear debris.

As for analytical methods, tribologically influenced ceramic surfaces are usually only looked at in terms of the wear effects: surface topography, friction coefficient, loss rates. Current efforts go towards a deeper understanding of mechanisms and kinetics. To gain this, the effects of the wear of ceramics on the phases and microstructures have to be analyzed in detail. Because structural changes occur within the uppermost μm and tribochemical reaction layers are often restricted to the nm-range, appropriate analytical tools have to be used and those come only now available. This study shows how the currently developed techniques of X-ray microdiffraction combined with Raman spectroscopy can resolve many issues. Another recent improvement, transmission electron microscopy (TEM) on cross sections prepared via the focused ion beam technology (FIB), helps to verify the findings of the former techniques.

Zusammenfassung:

Siliziumkarbid (SiC) ist sowohl die wohl bedeutendste Nichtoxidkeramik aber auch als Halbleiter ein vielversprechendes Material. Gaskorrosion in Gegenwart von Sauerstoff führt dabei als einzige feste Phase zu Bildung von SiO₂ (passive Oxidation). Hierbei spielen jedoch viele Einflussfaktoren eine wichtige Rolle, wie zum Beispiel Porosität, Sinteradditive, Verunreinigungen, die kristallographische Orientierung, vorhergehende Oberflächenbehandlung und die chemische Zusammensetzung der oxidierenden Atmosphäre. Als Folge von Kristallisation verändert die zunächst glasartige SiO₂-Schicht ihre Struktur und es kommt zur Ausbildung von runden Kristallisationszentren (Radialite). Diese Bereiche zeigen eine geringere Oxidationsrate, was auf langsamere Gasdiffusion zurückzuführen ist. Verunreinigungen, wie sie beispielsweise in der Ofenatmosphäre vorkommen können, akkumulieren sich auf der Oberfläche der SiO₂-Schicht und es kommt zu einer schmelzkatalysierten Rekristallisation als zweiter morphologischer Umwandlung der Oxidschicht. Schließlich bilden sich kleine kristalline Kugeln (Globulite). Das dazwischen befindliche Porenvolumen führt zu erhöhten Oxidationsraten. Die Gesamtkinetik der Oxidation ist somit potentiell komplex.

Dennoch kann für die meisten SiC Materialvarianten ein allgemeines linear-parabolisch Zeitgesetz für den gesamten Oxidationsverlauf gefunden werden. Die ausgeprägte Anisotropie von SiC führt dazu, dass sich die Oxidationsraten auf unterschiedlichen kristallographischen Flächen stark unterscheiden, wobei dieser Unterschied ab circa 1350° - 1400°C verschwindet. Die Vielzahl an Einflussfaktoren zeigt sich auch darin, dass die berichteten Oxidationsratenkonstanten für SiC über mehrere Größenordnungen streuen. Auch heute ist unser Verständnis für die der SiC Oxidation zu Grunde liegenden Mechanismen beschränkt und deswegen werden in dieser Arbeit verschiedene Modelle in Hinblick auf neue Erkenntnisse kritisch diskutiert.

In wässriger Umgebung erleiden SiC Keramiken unter tribologischer Beanspruchung sowohl strukturelle als auch chemische Degradation. Unter hydrothermalen Bedingungen zeigt SiC indes nur aktive Korrosion während es bei tribologischer Beanspruchung zur Ausbildung einer tribochemischen Reaktionsschicht kommt. Deren Schichtdicke variiert zwischen n·10 - n·100 nm und besteht aus nanoskaligen Abrieb in einer sauerstoffreichen Matrix (SiO_xH_y). Bezüglich letzterer kann eine oxykarbidische Zusammensetzung nicht ausgeschlossen werden. SiC Abriebpartikel werden im Verlauf der Beanspruchung plastisch deformiert und kontinuierlich abgerundet (mechanisches Läppen). Unter dieser Reaktionsschicht kommt es zur mechanischen Zerrüttung der keramischen Matrix (Versetzungen, Risse, Scherrisse. Plastische Deformation ähnlich der Indentationsplastizität führt in diesem Bereich dazu, dass aus großen SiC Körnern in der Matrix durch Versetzungen Mosaikkristalle mit kleineren Domänengrößen entstehen.

Ein erstes qualitatives Verschleißmodell verbindet hydrothermale Korrosion mit mechanischem Verschleiß. Die mechanische Verschleißkomponente öffnet durch Risse eine Wegbarkeit für Wasser und führt generell zu einer Zerrüttung der Kristallstruktur der Körner der keramischen Matrix. Hydrothermale Reaktionen des zwischen Rauheitsspitzen und Oberflächenrissen eingeschlossenen Wassers (Lösen von SiO₂) mit anschließendem Druckabfall (Wiederausscheidung von SiO_xH_y) führt zur Bildung einer sauerstoffreichen Reaktionsphase. Diese Phase verbindet die eingebetteten SiC Abriebpartikel.

Die meisten Untersuchungen zu tribologischem Verschleiß konzentrierten sich bisher auf Veränderungen der Oberflächentopographie, dem Reibkoeffizient und Verschleißraten. Tiefergehendes Verständnis der Verschleißmechanismen erfordert es jedoch, mikrostrukturelle, phasenbezogene und chemische Veränderungen zu charakterisieren. Da diese Änderungen auf den oberflächennahen Bereich und z.T. im Submikrometerbereich ablaufen, müssen die analytischen Methoden hinreichend hoch auflösend sein. Diese Arbeit zeigt wie insbesondere aktuelle Entwicklungen im Bereich Röntgenmikrodiffraction und Raman-Spektroskopie hier zum Einsatz kommen können. Wichtige Informationen über chemische und strukturelle Aspekte von tribochemischen Verschleiß können mittel hochauflösender Transmissionselektronenmikroskopie an FIB-Proben (fokussierende Ionenstrahlpräparation) gewonnen werden.

CONTENT:

Acknowledgements	page i
Abstract	page ii
Zusammenfassung	page iii
Contents	page iv
List of publications	page vi
1. Introduction	page 1
2. Silica formation on silicon carbide under static conditions	page 37
V. Presser, K. G. Nickel: "Silica on silicon carbide". <i>Critical Reviews in Solid State and Material Sciences</i> 33 (1), 1 - 99 (2008).	
Own contribution: Idea: 75 %, Data generation: 90 %, Interpretation: 75 %, Writing: 75 %	
3. Structural defects in single crystal SiC: character and characterization	page 189
V. Presser, A. Loges, K. G. Nickel: "Scanning electron and polarization microscopy study of the variability and character of hollow macro-defects in silicon carbide wafers". <i>Philosophical magazine</i> 88 (11), 1639 - 1657 (2008).	
Own contribution: Idea: 60 %, Data generation: 60 %, Interpretation: 60 %, Writing: 80 %	
4. Gas corrosion of SiC: Microstructural evolution of silica on silicon carbide. Part 1. AFM/HF-etching method.	page 211
V. Presser, A. Loges, Y. Hemberger, K. G. Nickel: "Microstructural evolution of silica on single crystal silicon carbide. Part I: Devitrification and oxidation rates". <i>Journal of the American Ceramic Society</i> 92 (3), 724 - 731 (2009).	
Own contribution: Idea: 70 %, Data generation: 60 %, Interpretation: 75 %, Writing: 80 %	
5. Gas corrosion of SiC: Microstructural evolution of silica on silicon carbide. Part 2. Influence of impurities and defects.	page 231
V. Presser, A. Loges, R. Wirth, K. G. Nickel: "Microstructural evolution of silica on single crystal silicon carbide. Part II: Influence of impurities and defects". <i>Journal of the American Ceramic Society in press</i> , (2009).	
Own contribution: Idea: 70 %, Data generation: 60 %, Interpretation: 75 %, Writing: 80 %	

- 6. How to use Raman spectroscopy to characterize amorphization** page 253
Part 1. Profile line deconvolution method.
 V. Presser: "Metamictization in zircon: Raman investigation following a Rietveld approach. Part I: Profile line deconvolution technique". *Journal of Raman Spectroscopy* **40** (5), (2009).
Own contribution: Idea: 95 %, Data generation: 100 %, Interpretation: 100 %, Writing: 100 %
- 7. How to use Raman spectroscopy to characterize amorphization** page 269
Part 2. Application example: zircon.
 V. Presser, C. Glotzbach: "Metamictization in zircon: Raman investigation following a Rietveld approach. Part II: Sampling depth implication and experimental data". *Journal of Raman Spectroscopy* **40** (5), 499 - 508 (2009).
Own contribution: Idea: 80 %, Data generation: 80 %, Interpretation: 60 %, Writing: 80 %
- 8. How to conduct static hydrothermal experiments using HDAC** page 287
 V. Presser, M. Hei, K. G. Nickel: "EOS calculations for hydrothermal diamond anvil cell operation". *Review of Scientific Instruments* **78** (8), 085104-1 - 085104-9 (2008).
Own contribution: Idea: 90 %, Data generation: 90 %, Interpretation: 75 %, Writing: 90 %
- 9. How to characterize sub-micrometer tribolayers** page 307
 V. Presser, C. Berthold, R. Wirth, K. G. Nickel: "Structural characterization of tribologically influenced silicon carbide ceramic surfaces". *Current Opinion in Solid State & Materials Science in press* (invited paper), (2009).
Own contribution: Idea: 75 %, Data generation: 80 %, Interpretation: 60 %, Writing: 80 %
- 10. Comparison of the hydrothermal and tribological behavior of silicon carbide** page 323
 V. Presser, O. Krummhauser, K. G. Nickel, A. Kailer, C. Berthold, C. Raisch: "Tribological and hydrothermal behaviour of silicon carbide under water lubrication". *Wear* **266** (7 - 8), 771 - 781 (2009).
Own contribution: Idea: 60 %, Data generation: 60 %, Interpretation: 60 %, Writing: 75 %
- 11. A Model for Wet Silicon Carbide Tribo-Corrosion** page 341
 V. Presser, K. G. Nickel, O. Krummhauser, A. Kailer: "A Model for Wet Silicon Carbide Tribo-Corrosion". *Wear in press*, (2009).
Own contribution: Idea: 60 %, Data generation: 60 %, Interpretation: 60 %, Writing: 75 %
- 12. Summary & Outlook** page 361

LIST OF PUBLICATIONS:

Peer review (printed / in press / submitted):

- Presser, V.; Klouzkova, A.; Mrazova, M.; Kohoutkova, M.; Berthold, C. (2008): Micro-Raman spectroscopy on analcime and pollucite in comparison to X-ray diffraction. *Journal of Raman Spectroscopy* **39** (5): 587 - 592.
- Presser, V.; Nickel, K. G. (2008): Silica on silicon carbide. *Critical Reviews in Solid State and Material Sciences* **33** (1): 1 - 99 (invited review).
- Presser, V.; Loges, A.; Nickel, K. G. (2008): Variability and character of hollow macro-defects in silicon carbide wafers: evidence from scanning electron and polarization microscopy. *Philosophical Magazine* **88** (11): 1639 - 1657.
- Presser, V.; Heiß, M.; Nickel, K. G. (2008): EOS calculations for hydrothermal diamond anvil cell operation. *Review of Scientific Instruments* **78** (8): 085104-1 - 085104-9.
- Presser, V.; Berthold, C.; Wirth, R.; Nickel, K. G. (2008): Structural characterization of tribologically influenced silicon carbide ceramic surfaces. *Current Opinion in Solid State & Materials Science* **12** (5 - 6): 73 - 80.
- Presser, V.; Krummhauer, O.; Nickel, K. G.; Kailer, A.; Berthold, C.; Raisch, C. (2009): Tribological and hydrothermal behaviour of silicon carbide under water lubrication. *Wear* **266** (7 - 8): 771 - 781.
- Presser, V. (2009): Metamictization in zircon: Raman investigation following a Rietveld approach. Part I: Profile line deconvolution technique. *Journal of Raman Spectroscopy* **40** (5): 491 - 498.
- Presser, V.; Glotzbach, C. (2009): Metamictization in zircon: Raman investigation following a Rietveld approach. Part II: Sampling depth implication and experimental data. *Journal of Raman Spectroscopy* **40** (5): 499 - 508.
- Presser, V.; Loges, A.; Hemberger, Y.; Nickel, K. G. (2009): Microstructural evolution of silica on single crystal silicon carbide. Part I: Devitrification and oxidation rates. *Journal of the American Ceramic Society* **92** (3): 724 - 731.
- Künle, M.; Janz, S.; Eibl, O.; Berthold, C.; Presser, V.; Nickel, K. G. (2009): Thermal annealing of SiC thin films with varying stoichiometry. *Materials Science and Engineering B* **159 - 160**: 355 - 360.
- Presser, V.; Nickel, K. G.; Krummhauer, O.; Kailer, A. (2009): A Model for Wet Silicon Carbide Tribo-Corrosion. *Wear* **in press**.
- Presser, V.; Loges, A.; Wirth, R.; Y.; Nickel, K. G. (2009): Microstructural evolution of silica on single crystal silicon carbide. Part II: Influence of impurities and defects. *Journal of the American Ceramic Society* **in press**.
- Presser, V.; Schuster, B.-E.; Casu, M. B.; Heinemeyer, U.; Schreiber, F.; Nickel, K. G.; Chassé, T. (2009): Raman polarization studies of highly oriented organic thin films. *Journal of Raman Spectroscopy* **in press**.

- Nickel, K. G.; Presser, V.; Schultheiß, S.; Berthold, C. (2009): Vorbild Seeigel - Meeresfrucht mit Köpfchen. **Labor & More submitted.**
- Presser, V.; Schultheiß, S.; Berthold, C.; Nickel, K. G. (2009): Sea urchin spines as a model-system for permeable, light-weight ceramics with graceful failure behavior. Part I. Mechanical behavior of sea urchin spines under compression. **Journal of Bionic Engineering submitted.**
- Presser, V.; Keuper, M.; Berthold, C.; Nickel, K. G. (2009): Experimental determination of the Raman sampling depth in zirconia ceramics. **Applied Spectroscopy submitted.**
- Zhang, H.; Wu, X.; Nickel, K. G.; Chen, J.; Presser, V. (2009): High-pressure powder x-ray diffraction experiments and *ab initio* calculation of Ti_3AlC_2 . **Journal of Applied Physics submitted.**

Conference proceedings (printed / in press):

- Krummhauer, O.; Presser, V.; Kailer, A.; Nickel, K. G. (2007): Comparison of tribological and corrosive behaviour of silicon carbide under water lubrication. **48. Tribologie Fachtagung.** Reibung, Schmierung und Verschleiß. Forschung und praktische Anwendungen. Band 1. Göttingen, Gesellschaft für Tribologie. 1: 13/1 - 13/15.
- Presser, V.; Nickel, K. G. (2007): Hydrothermal Oxidation of Silicon Carbide Single Crystals Using a Modified Diamond Anvil Cell. **10th International Conference of the European Ceramic Society,** Berlin, Göttinger Verlag GmbH.
- Nickel, K. G.; Presser, V.; Krummhauer, O.; Kailer, A.; Wirth, R. (2008): Hydrothermal Oxidation of Silicon Carbide and its Bearing on Wet Wear Mechanisms. **Ceramic Engineering Science Proceedings 29:** 143 - 154.
- Krummhauer, O.; Presser, V.; Kailer, A.; Nickel, K. G.; Hollstein, T. (2008): Corrosion behavior of silicon carbide in aqueous media lubricated sliding applications. **International Symposium on Friction, Wear and Wear Protection, Aachen in press.**
- Presser, V.; Krummhauer, O.; Nickel, K. G.; Kailer, A.; Wirth, R. (2009): On the p-T Conditions of Wet Silicon Carbide Tribo-Corrosion. **International Symposium on Friction, Wear and Wear Protection, Aachen in press.**
- Nickel, K. G.; Presser, V.; Schultheiß, S.; Berthold, C.; Kohler, C.; Nebelsick, J. H.; Grossmann, N.; Stegmaier, T.; Vohrer, A. (2009): Seeigelstachel als Modell für stoffdurchlässige Einschlagschutzsysteme. **Bionik-Kongress "Patente aus der Natur" 2008,** Bremen **in press.**

Experimental reports:

- Presser, V.; Kaliwoda, M.; Aliouane, N. K. (2008): Boron coordination in synthetic sodalites, **BENSC annual user reports 2008:** 104.
- Presser, V.; Aliouane, N.; Eichele, K. (2008): Boron coordination in synthetic and natural sodalites, **BENSC annual user reports 2008:** 105.

SiC semper erat, et SiC semper erit

Chapter 01

Chapter 02

Chapter 03

Chapter 04

Chapter 05

Chapter 06

Chapter 07

Chapter 08

Chapter 09

Chapter 10

Chapter 11

Chapter 12

INTRODUCTION

TABLE OF CONTENTS

1. INTRODUCTION	4
1.1 Aim of this study	4
1.2 Structure of this study	6
1.3 SiC under hydrothermal conditions.....	7
1.4 SiC in tribological systems.....	10
2. EXPERIMENTAL METHODS	12
2.1 Hydrothermal Diamond Anvil Cell (HDAC)	12
2.2 Tribometer	16
3. ANALYTICAL METHODS	18
3.1 Raman spectroscopy.....	19
3.2 X-Ray micro-diffraction (μ -XRD).....	24
3.3 Focused Ion Beam (FIB) preparation & Transmission Electron Microscopy (TEM).....	29

1. INTRODUCTION

1.1 Aim of this study

The aim of this study was to improve the understanding of the tribological behavior of silicon carbide (SiC) under water lubrication. Although being commonly used as face seals (Fig. 1) since the 1970s, our knowledge of the basic tribochemical aspects (reaction products, kinetics) of SiC in aqueous media is still quite limited. This applies especially for the interface region as high-resolution techniques down to the nm-scale - that also allow area-selective preparation - have only been available for several years.

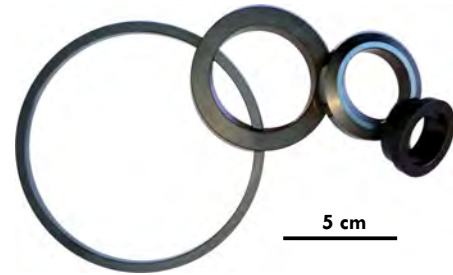


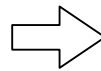
Fig. 1. SiC mechanical seals.

Because of the diversity of silicon carbide's crystal structure and the complexity of chemical, morphological and structural changes caused by tribological exposure, preliminary studies dedicated to individual aspects were carried out before being able to gain a more comprehensive understanding. For that, we started with simple systems and characterization methods and gradually extended these to cope with more complex demands (which are posed by the industrial application). In general, this study was developed in three directions (Fig. 2):

(1) Material



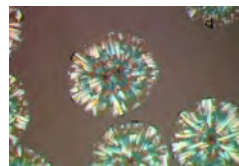
Single-crystal SiC



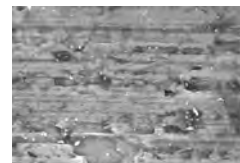
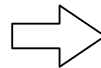
Sintered SiC
(coarse / fine)

(2) Environment

Passive oxidation



Hot gas



Active oxidation

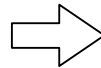
Hydrothermal

(3) Hydrothermal exposure mode

Isostatic



Diamond anvil cell



Sliding contact

Tribometer

Fig. 2. Material- / instrument-related parameters. For discussion see text.

(1) **Material** *from single-crystal SiC to sintered SiC ceramics*

Due to SiC's structural variety, we started with single-crystal silicon carbide and suitable characterization techniques. Using methods like Raman spectroscopy and polarization microscopy, defects were analyzed and their influence on, for example, the oxidation behavior critically evaluated. Only for high-purity materials such as single-crystals influencing factors during oxidation like impurities present in furnace atmospheres (sodium, potassium, water etc.) can be addressed. For example, the oxidation rate increases significantly in the presence of impurities and the morphology changes drastically due to devitrification and melt-catalyzed recrystallization.

Later, we expanded the scope of our experiments to sintered silicon carbide ceramics where several SiC modifications and grain orientations are present along with sintering aids (like boron carbide). Due to SiC's pronounced optical, structural and chemical anisotropy, significant differences were observed as far as oxidation rates are concerned. Also, sintering aids are very common impurity sources and known to cause bubble-formation, disrupting the oxide scale. Sintered SiC ceramics are employed as face seals in industrial applications, and are, therefore, the actual system on which tribological studies must focus.

(2) **Environment** *from hot gas corrosion to hydrothermal conditions*

Thermal oxidation (i.e., exposure to an oxygen-containing atmosphere at high temperatures; here $> 1300^{\circ}\text{C}$) of silicon carbide causes the formation of a solid silica layer. It is commonly assumed that this process is mainly diffusion controlled; however, limitations and implications to this are critically discussed as our knowledge even of basic SiC oxidation is limited. For example, it is still a matter of debate whether it is CO out-diffusion or O₂ in-diffusion that is truly rate-limiting for the oxidation kinetics. Also, the overall observation of a parabolic time-law is contrasted by different oxidation-rates on the various SiC faces (anisotropy). This raises questions on further influencing factors as diffusion through silica alone would be independent of the crystal orientation.

We then expanded our work to hydrothermal conditions similar to face seal working conditions where SiC is exposed to hot water instead of hot air. For this exposure environment, dissolution of reaction products must be considered. In fact, active corrosion of SiC as observed under hydrothermal conditions is the result of fast silica dissolution. Only in saturated media or after depressurization, reprecipitation of silica can be observed.

(3) **Hydrothermal exposure mode** *from isostatic compression to tribological exposure*

Experiments to study the static hydrothermal behavior of silicon carbide were applied using a Hydrothermal Diamond Anvil Cell (HDAC) and pure water as pressure mediating substance. *In-situ* monitoring via optical microscopy evidenced the roughening of the SiC surface due to active corrosion. Also, using Equations Of State (EOS) of water, it was possible to calculate at which specific p-T conditions the experiments were carried out. *Ex-situ*, the samples were thoroughly studied by means of optical microscopy, interferometry, vibrational spectroscopy, electron microscopy and chemical analyses (EDX, EELS).

Using a tribometer, tribological exposure of sintered silicon carbide ceramics was carried out under controlled conditions (lubricant pressure, sliding velocity, external cooling / no external cooling, static / dynamic load mode). Two different SiC ceramics were studied: one with a fine, monomodal grain-size distribution and another with a bimodal grain-size distribution (which is, in general, coarser). *In-situ*, the friction coefficient and the sub-surface temperature (3 mm below surface) were monitored and, *ex-situ*, the surface morphology and chemical / structural changes were studied.

1.2 Structure of this study

As outline before, this thesis is thematically divided into several sections:

(1) *Properties of silicon carbide (chapter 2, 3).*

This section gives a review mainly on the structural and chemical properties of silicon carbide and summarizes important aspects of SiC oxidation (in hot gas / humidified air / hydrothermal systems). Especially the structural variability of SiC with a myriad of different polytypes and structural defects (voids, pipes) must be evaluated critically when examining single-crystal SiC. Therefore, we have examined closely the character of hollow-core defects in PVT-grown SiC wafers. Without exact knowledge of the real structure of SiC samples and suitable ways to characterize them, no systematic study of tribochemically induced changes to silicon carbide would be possible.

(2) *Gas corrosion of SiC and microstructural evolution of the silica layer (chapter 4, 5).*

This section provides a systematic study of the microstructural evolution of the silica layer thermally grown on silicon carbide. This preliminary study covers kinetic aspects during hot gas corrosion of SiC and critically discusses factors influencing the oxide layer's microstructure. At the temperatures studied ($> 1300^{\circ}\text{C}$), vitreous silica readily devitrifies and, therefore, drastic changes in the microstructure arise. AFM-scanning in combination with HF-etching is shown to be a most suitable tool to characterize the oxide scale's morphology on a sub-micrometer scale which allows to derive information on the oxidation rate and crystallization speed.

(3) *Raman profile line deconvolution: characterization of amorphization (chapter 6, 7).*

This section describes and explains how profile line deconvolution of Raman spectra is a powerful tool to characterize amorphization of otherwise crystalline materials. As a preliminary study for severe kinds of amorphization as a result of tribological exposure, we chose the natural mineral zircon (ZrSiO_4) which shows radiation-induced amorphization (so-called "metamictization") to various degrees depending on (1) the uranium and thorium concentration and (2) the age of the mineral grain. Therefore, all necessary steps for a quantitative characterization of amorphization-induced profile line broadening are given that also take the instrument's function contribution into account.

(4) *Hydrothermal experiments using a hydrothermal diamond anvil cell (chapter 8).*

This section summarizes important aspects of hydrothermal diamond anvil cell (HDAC) operation and critically discusses problems like overcoming nucleation to correctly determine homogenization temperatures. Therefore, this section describes the methodological basis for all HDAC experiments that were conducted in the course of this thesis.

(5) *Tribological experiments in comparison with static hydrothermal behavior (chapter 9 – 11).*

This section shows suitable ways to characterize sub-micrometer tribolayers and critically discusses findings on the tribological and hydrothermal behavior of silicon carbide in water. Based on the observation of a thin tribochemically altered oxygen-rich layer (sub-micrometer) above a mechanically deteriorated zone ($1 - 2 \mu\text{m}$) a qualitative model for the tribocorrosion of silicon carbide under water lubrication is presented.

1.3 SiC under hydrothermal conditions

Silicon carbide is not stable under hydrothermal conditions (i.e., “hot high-pressure water”; not to be mistaken with hot high-pressure water vapor) and, consequently, chemical reactions will occur. Fig. 3 provides an overview over possible reaction situations.




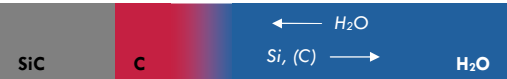
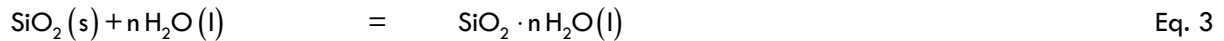
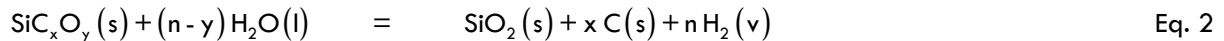
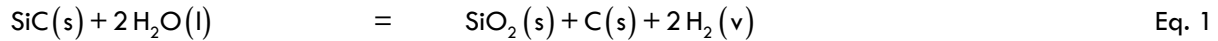
		Possible reaction products		
		Solid	Liquid	Gaseous
a) Initial state		-	-	-
b) Active oxidation		-	SiO ₂ ·nH ₂ O H ₄ SiO ₄	CH ₄ , CO, CO ₂
c) Silica formation		SiO ₂	SiO ₂ ·nH ₂ O H ₄ SiO ₄	CH ₄ , CO, CO ₂
d) Carbon formation		C	SiO ₂ ·nH ₂ O H ₄ SiO ₄	CH ₄ , CO, CO ₂

Fig. 3. Possible reactions for hydrothermal oxidation of silicon carbide (after Ref. 1,2).

In detail, the following reaction equations (Eq. 1 – 3) were used to describe the hydrothermal degradation of silicon carbide²⁻⁷ (where l denotes liquid, s solid and v gaseous phases):



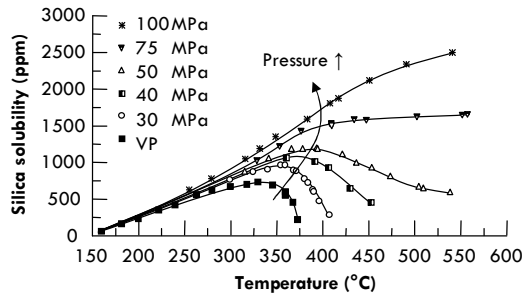
Systematic studies showed that the water-to-sample ratio ζ greatly affects which reaction phases will be produced.³ Eq. 4 – 6 list possible reaction equations as a function of the sample-to-water ratio.²⁻⁷



As a result, it was found that silica would be stable within a range of $0 \leq \zeta \leq 5$ but carbon is to become unstable above $\zeta = 2$. Adjusting ζ , either active oxidation or carbon / silica formation will occur.^{3,7} Graphitization of silicon carbide as a result of hydrothermal treatment and possible ways to synthesize sp^3 hybridized carbon (diamond) was subject of several recent studies.^{6,8-12}

An important complication is that hydrothermal fluids (and water in particular) show a high solubility for silica. Therefore, even with silica as the only stable reaction product, net active oxidation occurs when the SiO_2 solution rate exceeds the kinetic formation rate.^{3,7} The silica solubility itself is also a function of temperature, pressure and the pH-value. For instance, the solubility rate under ambient pressure and constant pH-value increases from 0.8 μm per year (30°C) and 0.2 μm per day (100°C) to 0.1 μm per second at 500°C .¹³ Fig. 4 depicts the p-T- and pH-dependency of silica dissolution rates.

a) Temperature and pressure dependency



b) pH-dependency

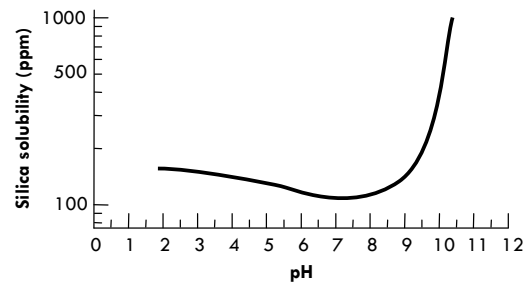


Fig. 4. Schematic illustrations showing the influence of (a) temperature and pressure (VP = vapor pressure; Ref. ¹⁴) and (b) pH (Ref. ¹⁵) on the solubility of silica in pure water substance.

Also, the sample-to-water ratio ζ plays a key role: once the solubility limit has been reached, a process of dissolution and reprecipitation will occur.^{11,16} The latter, however, is not known to produce passivating layers of dense silica.¹⁶ Typical examples of non-dense silica layers as found after hydrothermal treatment of SiC fibers are given in Fig. 5. Similar scales were also found on the inner surface of the gold capsules, in which the hydrothermal experiments were carried out evidencing a redeposition mechanism.

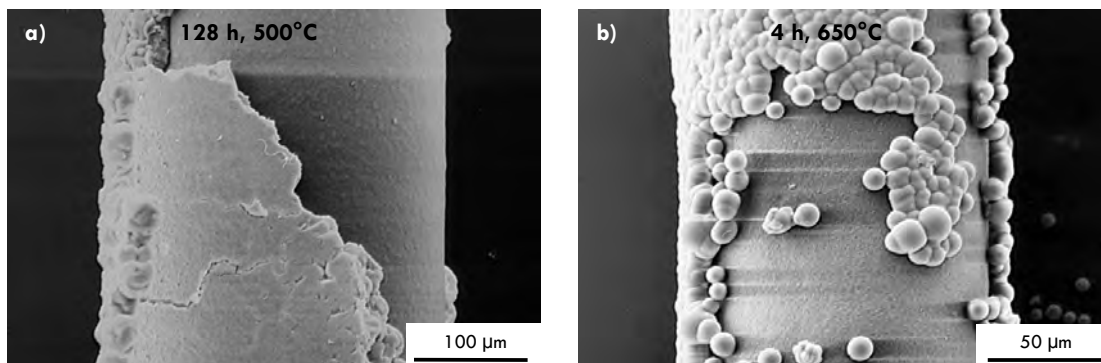


Fig. 5. Examples of non-protective silica layers on SiC CVD fibers as redeposited after hydrothermal treatment (Ref. ¹⁶).

Apart from silica, the formation of solid carbon as a result of selective oxidative extraction of silica was observed under certain hydrothermal conditions on SiC fibers.^{6,10,12,17-19} An example of local carbon layer formation is shown in Fig. 6. Unlike silica scales, dense carbon scales were reported to act as a protective layer towards hydrothermal corrosion.¹⁶ However, delamination and non-uniform carbon coverage inhibits an effective corrosion passivation of the whole fiber.

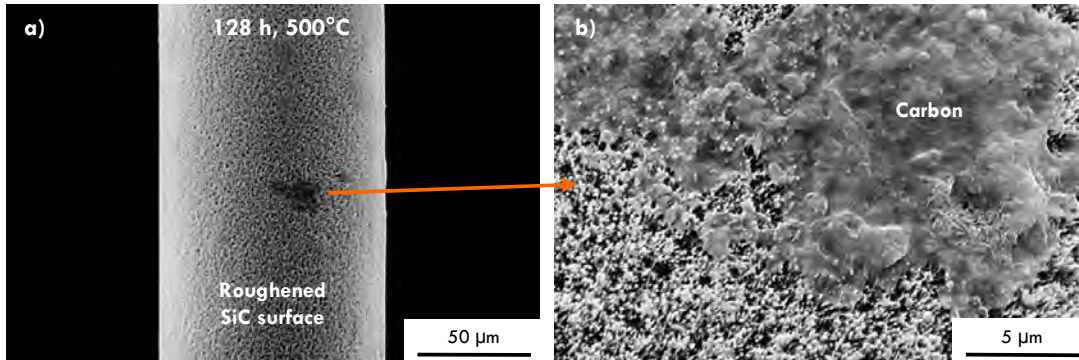


Fig. 6. Examples of carbon formation on a SiC CVD fiber (Ref. 16).

As seen, although static hydrothermal exposure lacks the mechanical component present in tribological systems, there are many influencing parameters to the hydrothermal behavior of SiC. These factors can be divided into three main groups:

(1) Material-related properties of SiC

There are great differences in the hydrothermal behavior between different varieties of silicon carbide. Grain boundaries and sintering aids are sites of preferential chemical degradation and, therefore, single-crystals or SiC varieties with a low amount of grain boundary phases show superior chemical stability under hydrothermal conditions.²⁰⁻²² Also, silicon carbide single-crystals show a pronounced anisotropy with respect to oxidation and corrosion rates.^{23,24}

(2) Chemical properties of the fluid phase

Important factors influencing hydrothermal reactions are, for example, the pH-value and the overall chemical composition of the fluid phase.^{25,26} Especially the influence of the pH-value on silica solubility is important when SiO₂ is the expected reaction product of tribochemical degradation.^{15,27,28}

(3) Pressure and temperature conditions

First corrosive attacks on sintered silicon carbide ceramics were reported above 120°C, which, however, were limited to grain boundary corrosion.^{20,29} First hydrothermal reactions on bulk SiC were reported for temperatures > 200°C.²⁵ An increase in temperature accelerates hydrothermal reactions and strongly influences the appearance of the SiC surface (e.g., increased surface roughness) and formation of redeposited films (e.g., large crystals or fine-grained scales).^{16,18} The influence of pressure, however, has not been analyzed in a systematic manner, yet.

1.4 SiC in tribological systems

Tribology (Greek: τριβο = “to rub”, λόγος = “meaning”) is the science of interacting surfaces in relative motion; ergo, tribology can be called science of friction, lubrication, and wear.³⁰ As such, it comprises more than just bulk physical wear and resulting changes in surface morphology. Changes in chemistry, phase content and structure are important factors for materials in sliding contact, too.³¹⁻³³ Fig. 7 provides an overview of four main factors in tribological wear.

(1) *Tribochemical reactions*

Tribochemical reactions are believed to be the main reason for the low friction coefficient of silicon carbide friction couples under water lubrication. Chemical reactions between the environment (in our case: hydrothermal water) and the rubbing surfaces will, therefore, affect the ceramic and, depending on several parameters, a tribolayer will form.^{31,34,35} The formation and properties of the latter are very sensitive to the actual p-T conditions and chemical aspects such as pH-value or the overall chemical composition of the lubricating medium.^{32,33} Tribochemical reactions are desirable phenomena as long as they lead to the formation of a solid-state lubricant or to surface passivation. However, delamination of tribochemical reaction layers may also occur; the latter leaves an unprotected surface behind, which is once more attacked by chemical agents and chemically degraded.

(2) *Surface fatigue*

A dominant wear mechanism of SiC in sliding contact is surface fatigue in form of crack formation and flaking.^{32,36} Brittle materials such as ceramic bodies are very susceptible to surface fatigue especially under cyclic load.³⁵ Shear crack formation is often observed below the surface as the critical shear stress reaches its maximum there.³² Shattering of the surface finally leads to bulk volume loss (mechanical wear) and surface roughening (which itself increases the friction coefficient). Also, cracks can act as pathways, for example, for water ingress and, therefore, accelerate the tribochemical degradation of the ceramic matrix.

(3) *Abrasion*

Abrasion is usually connected to either the presence of a hard particle on the interface or the combination of a hard and a soft material acting as a friction couple.³² Contributing to abrasive processes are plastic deformation and ductile fracture. As for hard and brittle materials like silicon carbide, plastic deformation occurs in form of indentation plasticity, that is, plastic deformation due to the extreme p-T conditions when two asperity peaks collide.^{37,38} The resulting pressures, assuming a Hertzian-contact as a first approximation, exceeds tens of GPa.³⁹ Abrasion is also important for tribosystems which undergo tribochemical reactions: in this case, abrasive wear of the soft lubricating tribolayer may occur.

(4) *Adhesion*

Adhesion describes molecular-atomistic interactions between sliding surfaces.³² Important factors are the net area in direct contact, the chemical properties of the friction couple, and the load mode. Typical examples for adhesive wear of metals are cold-weld junctions. As for ceramics, mainly, van-der-Waals and electrostatic bonds contribute to adhesion. The latter, however, cannot be a dominant wear mechanism for tribosystems involving ceramics.

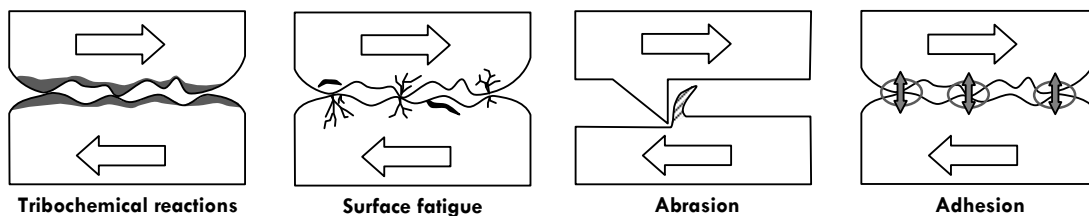


Fig. 7. Schematic illustration of main wear mechanisms (after Ref. ³²).

Sintered silicon carbide and, in general, SiC-based ceramics have been widely employed in tribological systems for decades. The widespread application of silicon carbide is due to its high chemical and structural stability. While under dry running conditions high friction coefficients above 0.6 can be observed, silicon carbide face seals show low friction coefficients of ≤ 0.1 under water lubrication.^{40,41} The dry-run behavior of SiC can significantly be improved and the lifetime of sintered ceramic bodies prolonged. Yet, water lubrication yields lower friction coefficients and longer device lifetimes. The latter was explained in terms of tribochemical changes on the surfaces of the friction couple which itself acts as a self-produced lubricant during device employment.^{30,33}

Still, also for water-lubricated systems there is no perfect hydrodynamic behavior and due to a small, yet significant, friction coefficient some wear is observed – that is, bulk volume loss and chemical / structural degradation.³² Depending on the exposure conditions (rotational speed, interface temperature and so on) different wear rates and degrees of tribochemical alteration of the ceramic surface will result and device lifetimes vary greatly. For the industrial application it would be highly desirable to gain a better understanding of the actual mechanical / chemical processes that happen on the friction couple interface and, eventually, to be able to calculate more reliable lifetime expectancies under certain application conditions.

There are many influencing parameters on the tribochemical alteration of SiC – for example, it is known that the chemical composition / pH-value of the lubrication medium strongly affects the friction behavior. Also, the overall surface roughness⁴² and the texture of the sintered body (grain size, grain distribution and so on)³⁶ are relevant. Finally, the experimental conditions (sliding speed etc.) greatly influence the observed wear rates^{41,43}. Therefore, tribological wear rates are complex **system-related** factors³² which are strongly affected by both (1) material-related properties and (2) experimental setup. As for this study, we chose two SiC ceramic varieties with different grain size distribution and similar phase composition and deionised water was applied as lubricant.

Most models for chemical + mechanical = tribological wear of materials are based on the work of Quinn⁴⁴⁻⁴⁷, in which he focused on metals. Most important is that sliding bodies are not in direct contact over the whole surface area but only where two asperity peaks meet. There, however, severe p-T conditions are met and temperature augmentation reaches up to 1000°C at these “hot spots”.³⁶ Using simulations, values for the temperature and pressure can be calculated following a micro-asperity based approach and localized temperature maps can be obtained. Input data originate, for example, from atomic force microscopy (AFM) or stylus profilometry.

2. EXPERIMENTAL METHODS

2.1 Hydrothermal Diamond Anvil Cell (HDAC)

Since its development in the 1950s, the diamond anvil cell (DAC) is probably the most commonly used device for high-pressure experiments on small sample volumes ($< 0.1 \text{ mm}^3$).⁴⁸⁻⁵² Wide-spread application of the DAC took place after Forman et al.^{53,54} introduced the ruby-fluorescence-method which allowed *in-situ* measurements of applied pressures. Although the used diamond anvils are highly transparent and ideally free of inclusions, special low-fluorescence diamonds need to be selected when performing systematic Raman-, IR-, or Brillouin-studies. In fact, less than 2% of all diamonds show a sufficiently low fluorescence background⁴⁹ and it is important to carefully select diamond anvils that are suitable for the wavelength range of interest.

Fig. 8a displays the overall setup of a diamond anvil cell. The sample is put in a hole which was drilled into a metal foil (gasket; usually rhenium or stainless steel) and the rest of the sample chamber is filled with a pressure mediating fluid (e.g., a 4:1 methanol-ethanol-mixture or water). Vertically, the sample chamber is enclosed by two diamond anvils. In contrast to jewellery diamonds, these DAC anvils have two parallel flat faces; the larger one is called table and the smaller face culet (Fig. 8b). Commonly, the anvil shape uses the Drukker-Dubbledee standard geometry⁵⁵ shown in Fig. 8 with an octagonal outline. To reduce forces acting on the anvil corners when both anvils are not perfectly aligned, diamond anvils with more than 8 faces have shown to be preferable.⁵⁶ In our study, we used $\frac{1}{4}$ ct. diamond anvils with a round culet face.

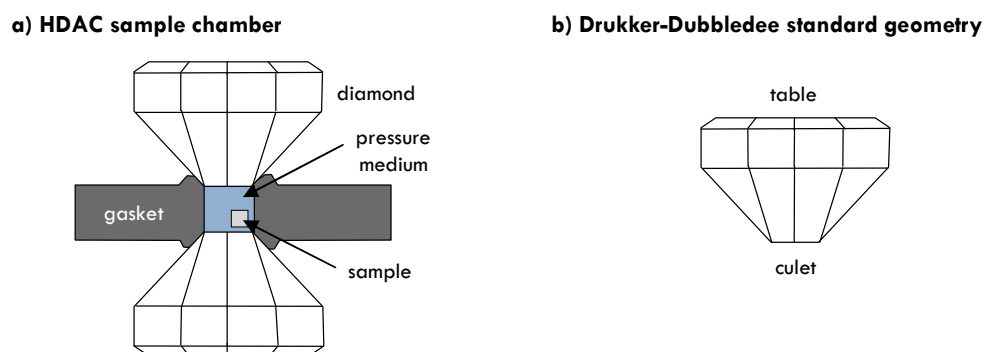


Fig. 8. Schematic illustration of the DAC sample chamber and anvil design.

In a traditional DAC, external force is applied on the diamond anvils and pressure acts on the sample via a pressure mediating fluid present in the sample chamber. In this study, we used a modified Bassett-type hydrothermal diamond anvil cell (HDAC; cf. Fig. 9). Here, the pressure is not applied externally but by heating the isochoric sample chamber. Therefore, only discrete p-T paths can be studied which depend on the density of the fluid phase. The latter can be modified, for example, by introducing an air bubble into the sample chamber to lower the total density of the fluid phase after homogenization at elevated temperatures. Also, the use of an air bubble is most useful to calculate the p-T path as described later and, in more detail, in section 8. In general, significantly lower pressures are studied in the HDAC (usually up to 2 GPa) compared to other DAC setups (> 10 GPa).

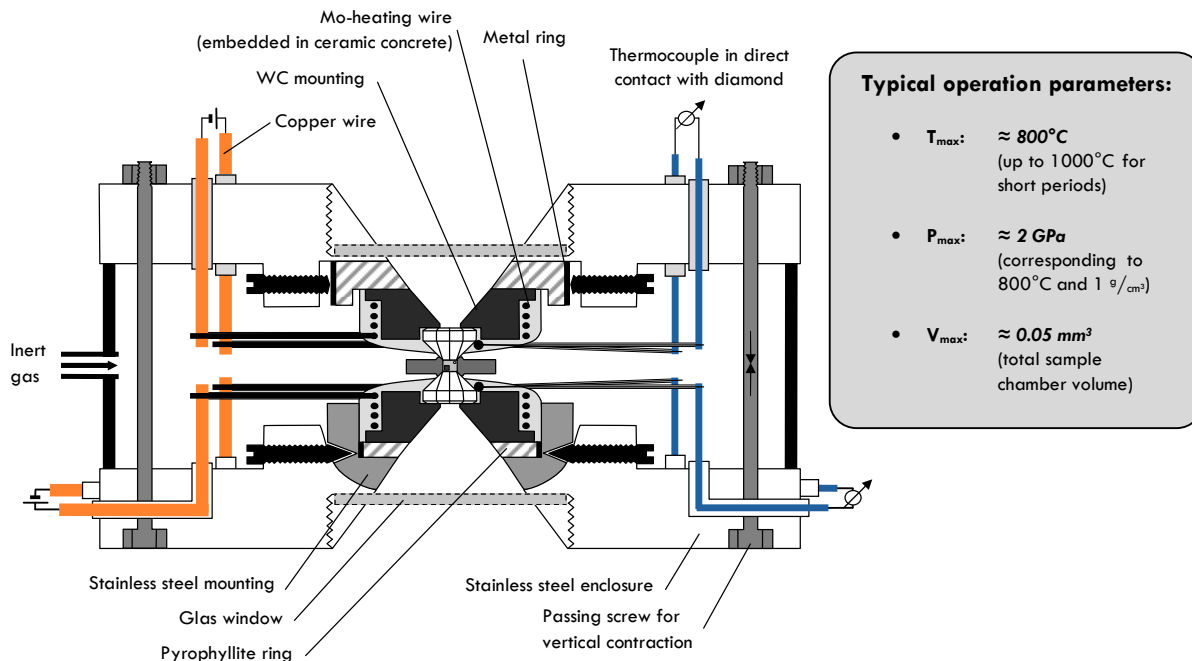


Fig. 8. Schematic assembly and operation specifications of a HDAC (after Ref. ⁵⁷).

In a Bassett-type HDAC, both diamond anvils are seated on a tungsten carbide mounting that is surrounded by a molybdenum heating wire ($\varnothing = 0.25$ mm). All these parts are embedded in insulating ceramic cement and placed on preheated pyrophyllite rings. Two thermocouples, both in contact with a diamond anvil, allow temperature measurements of the individual anvils. We used programmable DIC controllers to monitor the temperatures of both anvils and to define constant heating rates (e.g. 10 K/min). During the dwell time, T_{\max} was held for several hours within $\pm 1^\circ\text{C}$.

Applying an inert gas (e.g., argon with trace amounts of hydrogen) prevents the diamonds from oxidation. The x-y alignment is possible by adjusting screws on the upper plate while a pan-like stainless steel mounting on the lower plate allows a tilt correction. However, we made some modifications to the traditional Bassett-type geometry for the setup of our low-pressure hydrothermal diamond anvil cell (LYDIA).

Any tripod based setup tends notoriously to become stuck when assembling the two platings. Therefore, a constantly distributed and upwards directed force pushing up the upper plating could prevent misalignment from happening. Springs placed around the tripod holder were carefully adjusted in length and placed within polytetrafluorethene insulating to match the diameter of the holding nuts. As a side-effect of this modification it is now impossible for the two diamond anvils to become damaged when the upper plating is dropped.

In order to make the HDAC device small enough to fit under regular microscopes (e.g., for *in-situ* Raman microprobe measurements), a water-cooled base was completely removed. Heat-dissipation was ensured by designing a specific water-cooled microscopy table capable of micro-adjustment for the fully assembled HDAC device under the microscope. A constant flow of compressed air was directed between the microscope's objective and the upper plating to cool the upper window without condensation of water.

Essential for a fast and reproducible assemblage is a modular concept of the HDAC's components. This especially concerns the heating elements surrounding the tungsten carbide mountings. Usually, these heating elements consist of molybdenum wire coiled around the cement embedded WC mounting. With a total height of 4 mm only a few loops can be realized as the single pathways must not touch each other leading to a rather small total length of the conductor path. Moreover, embedding the WC mounting so that no conductive contact occurs and enclosing the molybdenum wire with ceramic concrete is time-consuming and yields the problem of reproducibility as both anvils should be heated with the very same number of Mo-filament loops. Both problems can be avoided by using a wire twisted to form a spring put into a shell made out of alumina or heat-treated pyrophyllite. The spring itself must be coiled in such a manner that the single loops are evenly spaced even when forming a sling put around the inner shell. Latter is formed by a solid ring with a milled-in notch capable of accommodating the spring.

The non-twisted part (feed lines) is fortified by a second molybdenum wire wrapped around the original wire which is both separated and shielded by an alumina capillary. To enclose these heating elements, the molybdenum wire is embedded in ceramic cement within the outer shell. To form small loops at the end of the feed lines the wire is compressed between two flat washers by internal screws around a 2 mm diameter copper wire. On the outer ends of this copper feed line the electric voltage is applied to heat the furnace.

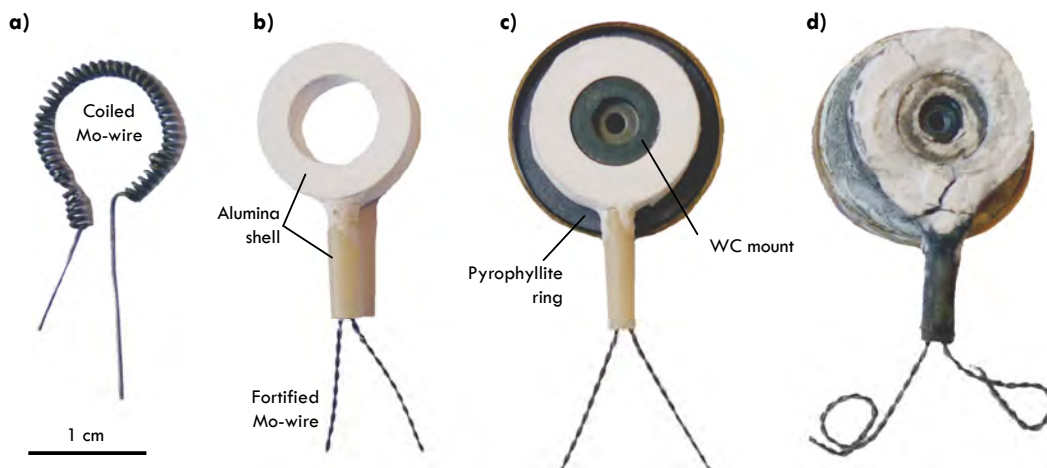
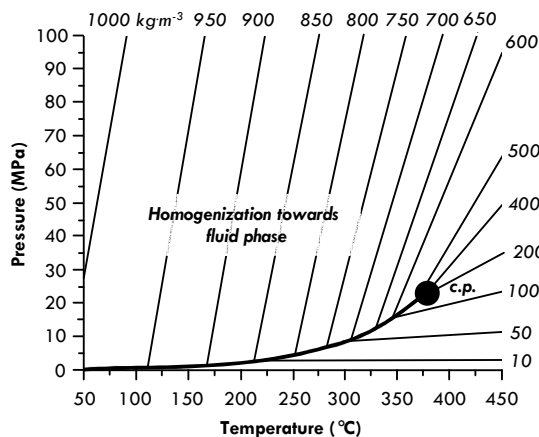


Fig. 9. Modular heating concept. a) coiled heating wire, b) heating wire embedded in alumina shell, c) WC mount placed into the modular heating element and put onto pyrophyllite ring, d) heating system after use.

As stated before, hydrostatic pressure is applied by increasing temperatures. There is a direct proportionality between the mean density ρ_{mean} of the homogenized fluid and the corresponding pressure $p(\rho)$ at a discrete temperature T . Depending on the mean density ρ_{mean} this fluid phase will become unstable at temperatures below the homogenization temperature T_{hom} and two different phases will appear (one fluid phase with a higher density than ρ_{mean} and a vapor phase with a lower density than ρ_{mean}). It is possible to access different pressure ranges by changing the volume of the gas bubble and, therefore, adjusting ρ_{mean} . Fig. 10a shows the phase diagram of pure water with the boiling curve ending at the critical point (c.p.). For different ρ_{mean} different isochors will result at different homogenization temperatures T_{hom} . Isochors do not only arise from the boiling curve but also from the melting curve.

a) Phase diagram of water



b) p-T path with decreasing sample chamber volume

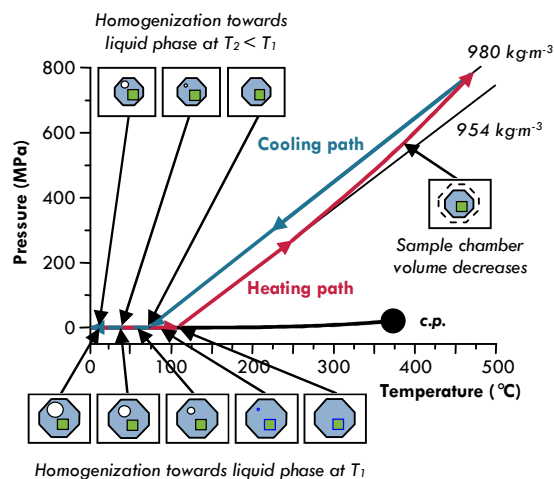


Fig. 10. Phase diagram and isochors of pure water (c.p.: critical point; after Ref. 58).

However, the assumption of an isochoric system with a constant sample chamber volume does not take into account the compressibility of both the rhenium gasket and the sample chamber's content. While the solid sample may be considered to be of constant volume, the liquid phase cannot.^{58,59} By decreasing the sample chamber volume as gasket material will flow in (when plastic deformation and thermal extension take place) the mean density ρ_{mean} will increase (Fig. 4). In some cases, due to the outward directed pressure and plastic flow of the heated gasket, the sample chamber volume can also slightly increase which leads to a decreased mean density ρ_{mean} . Therefore, it is essential to determine the pressure that was actually applied during the hydrothermal experiment by measuring T_{hom} during cooling down of the HDAC. It should be kept in mind that if the sample itself reacts with water and hereby changes its volume, more corrections need to be done. The mean density ρ_{mean} can even be determined if it is impossible to measure the homogenization temperature T_{hom} . In such a case, for example, when ρ_{mean} is greater or equal to 1000 kg/m³, the sample will be cooled down until ice formation. By heating the HDAC up again the melting point can be determined. The melting temperature T_{melt} corresponds to a melting pressure^{60,61} which can be used directly to calculate the mean density ρ_{mean} at the melting point^{62,63}.

Due to its meaning as the most important substance in life, an enormous number of physical and chemical measurements have been carried out on the basic properties of water (often referred as ordinary water substance). For a continuous description of the thermodynamic behavior of water, reliable equations of state are necessary. International research regarding the thermodynamic properties of H₂O has been coordinated by the International Association for the Properties of Water and Steam (IAPWS) since the 1970s. This organization is responsible for international standards of several thermodynamic properties like density, entropy or enthalpy. These standards as well as recommendations are published in form of releases and guidelines. Probably the most important standard is the equation of state for the thermodynamic properties of ordinary water substance as needed for both general and scientific use.

Although there are numerous correlations for the thermodynamic properties of water, most of them cover only a small range of the fluid region or do not meet present demands for accuracy. The first standard for the thermodynamic properties of water and steam was the equation package of the IFC-68. In 1984, a Helmholtz-free-energy equation was adopted (IAPS-84) as a new international standard covering now consistently large pressure and temperature ranges. IAPWS-95 is now based on the International Temperature Scale of 1990 (ITS-90) and on updated data sets and shows an improved representation in the critical region even when extrapolated to high pressures and high temperatures⁶³ (see section 8 for a more detailed discussion of the application of IAPWS-95 for HDAC experiments).

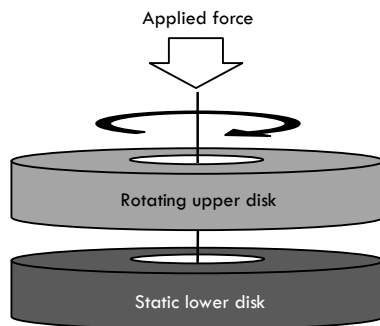
Experiments using a HDAC were chosen to study the static hydrothermal behavior of silicon carbide without the contribution of mechanical wear. During tribological exposure, water between asperity peaks becomes separated from the remaining rest of the water reservoir and can be considered to be isochoric for a short period of time. As the collision of asperities on real surfaces of silicon carbide ceramics results in severe temperature augmentation, the conditions are, in principle, comparable to the p-T paths accessible via hydrothermal diamond anvil cell experiments. However, these extreme p-T conditions are only valid for a very short period of time and only for localized areas (e.g., when asperity peaks are in direct physical contact). This is why tribological wear causes the formation of a tribochemical reaction layer instead of bulk active corrosion as expected from static hydrothermal experiments.

2.2 Tribometer

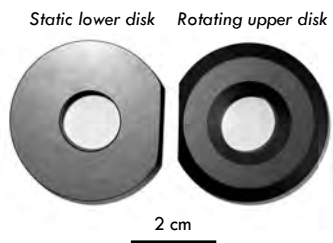
Tribometer experiments were conducted at the Fraunhofer Institute for Mechanics of Materials IWM in Freiburg on a modified Instron 1380 (Instron Deutschland GmbH, Pfungstadt, Germany). The tribometer test bench used for this study was developed by Dr. M. Zimmermann during his PhD thesis and was used to study disk-on-disk friction couples (Fig. 11a, b).

The experimental setup for tribological tests is outlined in Figure 10c. A static slide ring is attached to a torque meter. The applied load and the sliding velocity can be varied over a wide range. As lubricant deionized water was used and the electrical conductivity was both monitored and kept below 0.09 S/m . During the experiment, the lubricant was applied with a pressure of 0.1 MPa between the friction couple. Also, the test apparatus offers the possibility for external cooling and, therefore, experiments with (mild wear regime) and without (severe wear regime) were conducted. As a modification to the setup of Zimmermann, a thermocouple was introduced 3 mm below the surface of the static lower disk via a horizontal bore hole to monitor the temperature during the experiment.

a) Disk-on-disk geometry



b) Used sliding rings



c) Setup of the used tribometer

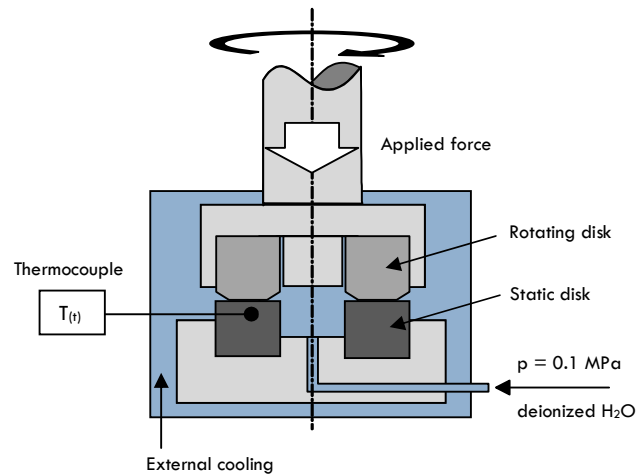
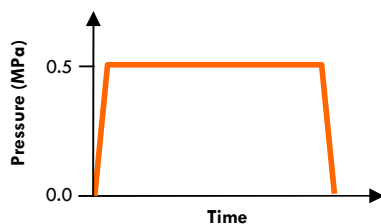


Fig. 11. Schematic illustrations showing the setup of the tribometer and the used slide rings.

Two different tribological regimes were chosen: (1) a static mode and (2) a dynamic mode (Fig. 12). In order to determine the general running behavior, static pressure conditions at 0.5 MPa, external cooling and a sliding velocity of 6 m/s were chosen. Some experiments in dynamic conditions were carried out in absence of external cooling and with a sliding velocity of 6 m/s . The abort criterion in case of scuffing was a measured torque of $2 \text{ N}\cdot\text{m}$.

a) Static load mode



b) Dynamic load mode

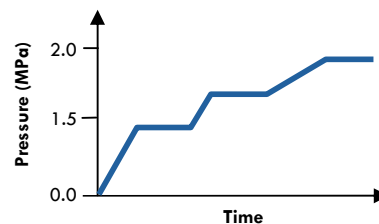


Fig. 12. Load modes selected for tribometer experiments.

During the tribometer experiments, the friction coefficient of the disk-on-disk friction couple can be monitored. In tribology, the evolution of the friction coefficient over time is an important factor. This is especially true since it is accessible via *in-situ* measurements while other system characteristics (e.g., chemical or phase-related changes) are only accessible after the experiment has been carried out (i.e., *ex-situ*). The friction coefficient is a result of several influencing factors such as (1) surface smoothing, (2) surface amorphization, and (3) tribochemical reactions. Also, the friction coefficient is strongly influenced by the experimental parameters chosen (e.g.: external cooling? what kind of lubricant? surface pressure?). This is why we monitored the friction coefficient on the one hand, but on the other hand used more process-sensitive (*ex-situ*) characterization methods.

In contrast to HDAC experiments, the p-T conditions during tribometer experiments on the contact surface cannot be determined using direct methods. Performing simulations using a micro-asperity based model, p-T values can be calculated.³⁶ Fig. 13 depicts simulated p-T conditions for a typical tribometer experiment (using coarse sintered SiC, 2 MPa applied pressure and a sliding speed of 6 m/s. Also, the p-T range accessible via the hydrothermal diamond anvil cell is shown. While tribologically influenced surfaces are subject to higher pressures, the temperature range is comparable. However, the severe conditions as calculated for sliding surfaces are restricted to very localized areas (small asperity peaks) and, therefore, do not act on the entire surface. For water trapped in-between such asperities, the EOS of water are applicable and, thus, HDAC experiments are still a suitable tool to study static corrosive aspects. As pointed out before, the p-T conditions acting on the entire surface are less extreme than those observed in HDAC experiments and this is why a tribochemical reaction layer can be formed as a process of solution and reprecipitation.

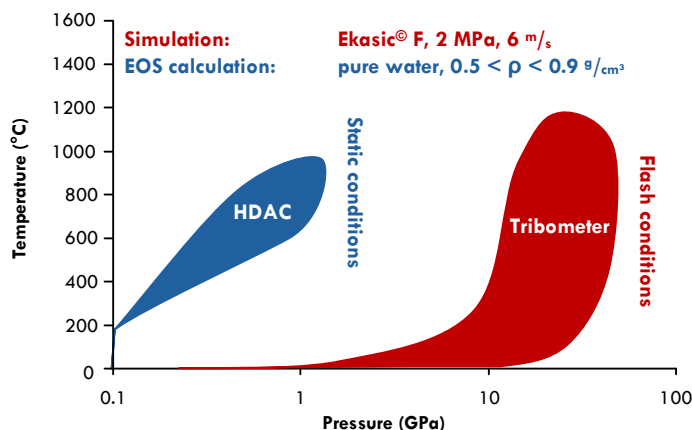


Fig. 13. p-T paths for HDAC and tribometer experiments.

3. ANALYTICAL METHODS

The challenges for analysis of sub-micrometer reaction layers were met by using (1) fast, spatially resolving characterization methods (optical microscopy / conoscopic imaging, μ XRD, μ Raman) in advance to (2) high-resolution techniques (mainly HR-TEM on FIB-prepared samples). High-resolution studies substantiated findings by lower-resolving but less time-consuming methods and complemented information about chemical changes on the nm-scale. In this section only the most important analytical methods (i.e., Raman spectroscopy, X-ray micro-diffraction, FIB preparation and TEM analysis) will be presented and discussed in the context of characterization of tribologically influenced SiC surfaces. A later section (section 9) will provide a more thorough examination of selected analytical methods.

3.1 Raman spectroscopy

Raman spectroscopy is a non-destructive method to characterize, in general, gaseous, liquid and solid media and is based on the so-called Raman effect. The latter was theoretically predicted by A. G. Smekal in 1923⁶⁴ and experimentally observed a few years later by C. V. Raman⁶⁵ (hence the term “Raman effect”). The Raman-effect describes the interaction of light with elemental excitations such as, for example, phonons, magnons, excitons, and plasmons via inelastic scattering. In comparison to the incident monochromatic light, scattered light shows additional frequencies after interaction with the sample.

For vibration spectroscopy of liquid or solid bodies, the energy difference between the frequency of the incident monochromatic light and the additional frequencies found in scattered light correspond to the nuclear motions. For gaseous media, also rotational states must be considered. Any vibrational state observed may be either excited to a higher state (Stokes), or, when the system is already in an excited state, Raman scattering may cause it to return to its ground state (Anti-Stokes). In case of the latter, the scattered photon has a higher frequency than the incident light. Most of the incident photons, however, are elastically scattered causing the so-called Rayleigh line. In particular, the Raman-effect is by a factor of 10^{-6} to 10^{-8} smaller than Rayleigh scattering and, therefore, only accessible by the use of a laser in combination with a highly sensitive CCD (which is usually cooled to -60°C by Peltier elements). Rayleigh scattering itself is by a factor of $\approx 10^{-4}$ weaker than the incident radiation's intensity. Thus, it is imperative to blank the high-intensity Rayleigh scattering from the obtained Raman spectrum by the use of edge or notch filters.

Fig. 14 provides an overview of Rayleigh, Stokes, and anti-Stokes scattering and the energy of the scattered radiation.

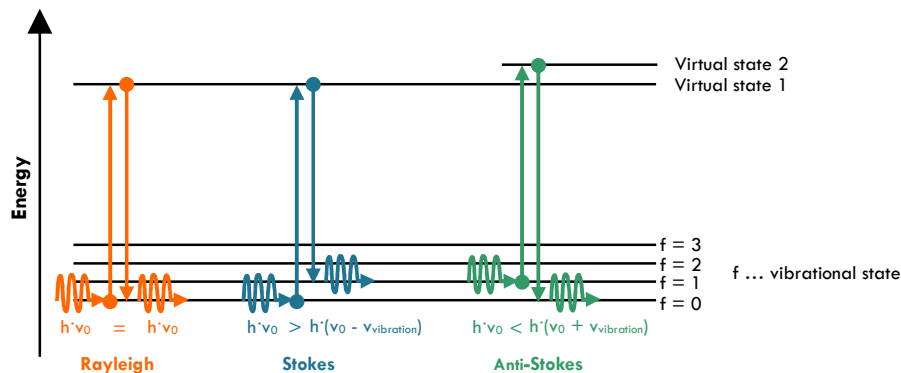


Fig. 14. Rayleigh, Stokes, and anti-Stokes scattering (after Ref. ⁶⁶).

The ratio between Stokes and Anti-Stokes scattering is a function of sample temperature: the higher the temperature, the more populated will the excited vibrational states be and, therefore, the anti-Stokes signal will become more intense. Also, compared to Stokes scattering, anti-Stokes scattering will become weaker as the frequency of the vibration increases, due to the decreased population of high-energy vibrational states. Eq. 7 shows the functional relation between Stokes and anti-Stokes scattering intensity.

$$\frac{I_{\text{Anti-Stokes}}}{I_{\text{Stokes}}} \propto \left(\frac{\nu_0 + \nu_{\text{vibration}}}{\nu_0 - \nu_{\text{vibration}}} \right)^4 \cdot e^{-\frac{h \cdot \nu_{\text{vibration}}}{k \cdot T}} \quad \text{Eq. 7}$$

From Eq. 7 it becomes also clear that the measured intensity of either Stokes or anti-Stokes scattering is a function of the incident radiation's frequency (Eq. 8):

$$I_{\text{Raman scattering}} \propto (\nu_0 \pm \nu_{\text{vibration}})^4 \quad \text{Eq. 8}$$

This is why bands associated with weak Raman scatterers, like water, can best be studied using high-frequency light (e.g., 488.0 nm using an argon ion laser).⁶⁷

In Raman spectroscopy, the energy difference between incident and scattered radiation contains the information on the vibrational mode energy; consequently, the Raman shift ν_{RS} is defined as (Eq. 9):

$$\nu_{\text{RS}} = \nu_0 \pm \nu_{\text{vibration}} \quad \text{Eq. 9}$$

Fig. 15 depicts a typical Raman spectrum of carbon tetrachloride showing the Stokes, anti-Stokes, and Rayleigh domain along with a historic microphotograph of the CCl_4 -spectrum obtained by Raman 1929 (Ref. ⁶⁸).

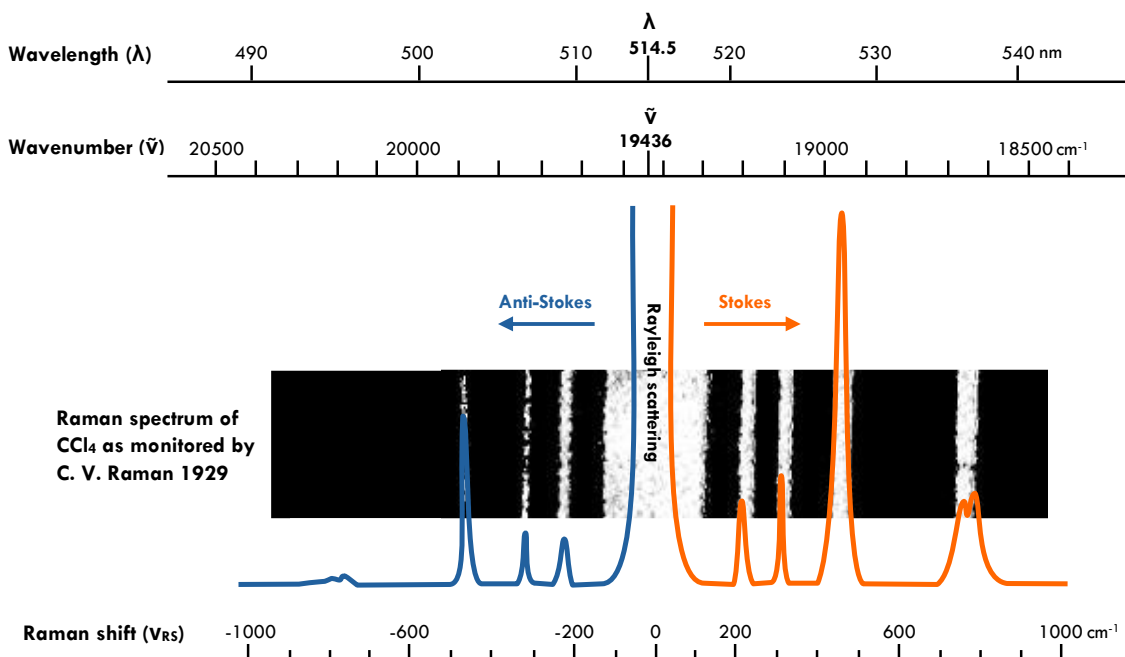


Fig. 15. Rayleigh, Stokes, and anti-Stokes domain of a Raman spectrum of CCl_4 (after Ref. ^{68,69}).

Due to the higher intensities in the Stokes-domain, Raman spectra are usually recorded on the low-energy side. Sometimes, however, studies are carried out on the low-intensity high-energy domain (anti-Stokes). The reason for this is that Raman modes in the Stokes-domain are often superimposed by fluorescence interference. As Raman spectroscopy is usually carried out using visible light for excitation, fluorescence is a significantly more relevant problem than for UV or NIR spectroscopy.

Prerequisite for a vibration to be Raman active is a change in polarizability. In contrast, a vibration is IR-active when there is a change in the dipole moment. Unless a molecule is centrosymmetric, vibrational modes may be either only Raman-active, only IR-active, or both. The electron cloud model is a suitable tool to illustrate the change of polarizability and of the dipole moment, respectively. Fig. 16 depicts a linear triatomic molecule (CO_2), where a Raman-active (symmetrical stretch) and an IR-active vibration (deformation mode) are shown. Vibration of the molecule will alter the electron density distribution (electron cloud) in a way, that either affects the dipole moment (change of charge center) or the polarizability.

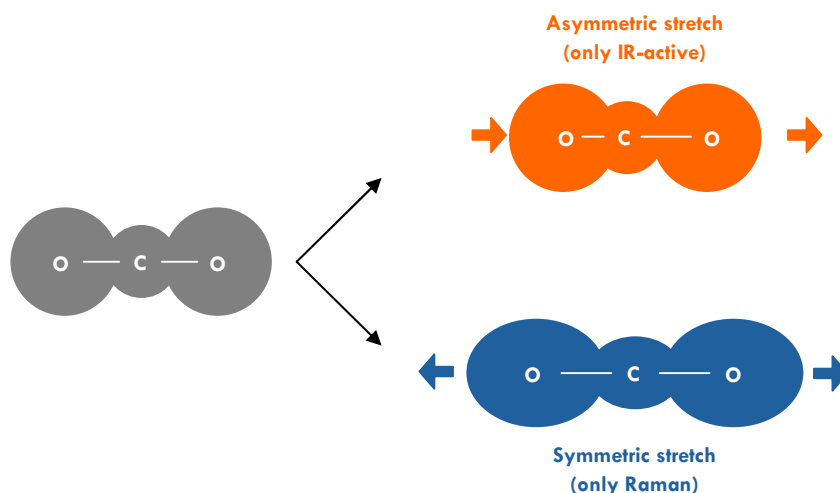


Fig. 16. Electron cloud model for CO_2 (after Ref. 70).

The spectral position of a Raman active mode assigned to a vibrating molecule can be calculated, in first approximation, using a harmonic oscillator as a model (more complex than this, however, is the description of lattice vibrations). As for a diatomic molecule with the atomic masses m_1 and m_2 , we can write for the vibration frequency ν (Eq. 10):

$$\nu = \frac{1}{2\pi} \cdot \sqrt{\frac{k}{\frac{m_1 \cdot m_2}{m_1 + m_2}}} \quad \text{Eq. 10}$$

where k denotes the force constant. This simple model can be used to explain why the frequency shift is towards lower wavenumbers when...

- (1) the bond becomes weaker (e.g., ionic instead of covalent bond or elongated bond distance)
- (2) the atoms are heavier atoms (e.g., by substituting caesium for sodium)

In case of tribological exposure, the crystal structure of the sample is deteriorated. With increased structural damage to the crystal lattice, both position and shape of Raman-active modes changes in four ways: (1) they shift in their spectral position, (2) they decrease in total Raman intensity, (3) the bands become broader and (4) they become asymmetric when amorphisation reaches a critical level.⁷¹⁻⁷³ In case of amorphisation due to mechanical contact Raman-active modes of tribologically influenced SiC will shift towards higher wavenumbers, because mechanical exposure leads to densification.⁷⁴ Radiation-induced amorphisation, instead, is known to cause a down-shift of Raman modes.^{72,73}

Profile line analysis of Raman spectra requires careful separation of the instrument's contribution to the total linewidth so that sample-related line broadening can be quantified. Otherwise it is impossible to get values for the Raman linewidth which are independent from the specific experimental setup of the instrument used. In particular, each change of the spectrometer configuration (i.e., emission profile, slit width etc.) will affect the resulting profile form.

Measured Raman intensities, in theory, can be used for a quantitative analysis – for example, to calculate a scale thickness or concentrations. Quantification, however, is very problematic as it is influenced by many factors (surface roughness, scattering cross-section etc.) and can only be performed when the system is calibrated by another method like Rietveld-analysis of XRD data.

The measured Raman intensity is also depending on the crystal orientation and polarization of the incident laser beam according to Eq. 11 (Ref. ⁶⁶):

$$I_{\text{Raman}} \propto |\mathbf{e}_i \cdot \mathfrak{R} \cdot \mathbf{e}_s|^2 \quad \text{Eq. 11}$$

Where \mathbf{e} denotes the polarization direction of the electric field of the incident (\mathbf{e}_i) and scattered (\mathbf{e}_s) beam and \mathfrak{R} is the Raman tensor. The latter reflects the symmetry of the crystal; for example, the A-mode of $\delta\text{H-SiC}$ (C_{6v}^4) has the form (Eq. 12; Ref. ⁷⁵):

$$\mathfrak{R}_A = \begin{bmatrix} a & 0 & 0 \\ 0 & b & 0 \\ 0 & 0 & c \end{bmatrix} \quad \text{Eq. 12}$$

When rotating the (0001)-face of a $\delta\text{H-SiC}$ single-crystal around its c-axis ($\vartheta =$ rotation angle), the Raman tensor \mathfrak{R} transforms to \mathfrak{R}_{xyz} (Eq. 13). For both the polarizer and the analyzer being parallel towards the a-axis – that is, (100) - the measured intensity of the A-mode will periodically change following Eq. 14.

$$\mathfrak{R}(A)_{xyz} = \Phi_{xyz} \cdot R(A) \cdot \overline{\Phi}_{xyz} = \begin{bmatrix} \cos\vartheta & -\sin\vartheta & 0 \\ \sin\vartheta & \cos\vartheta & 0 \\ 0 & 0 & 1 \end{bmatrix} \cdot \begin{bmatrix} a & 0 & 0 \\ 0 & b & 0 \\ 0 & 0 & c \end{bmatrix} \cdot \begin{bmatrix} \cos\vartheta & \sin\vartheta & 0 \\ -\sin\vartheta & \cos\vartheta & 0 \\ 0 & 0 & 1 \end{bmatrix} \quad \text{Eq. 13}$$

$$I_{\text{Raman}} \propto |\mathbf{e}_i \cdot \mathfrak{R}_{xyz} \cdot \mathbf{e}_s|^2 = a \cdot (\cos^2\vartheta + \sin^2\vartheta) \quad \text{Eq. 14}$$

As seen, for orientation studies it is imperative to choose a suitable coordinate system with respect to the crystal coordinate system.

In general, several pieces of information can be gained from the analysis of Raman spectra (Fig. 17).

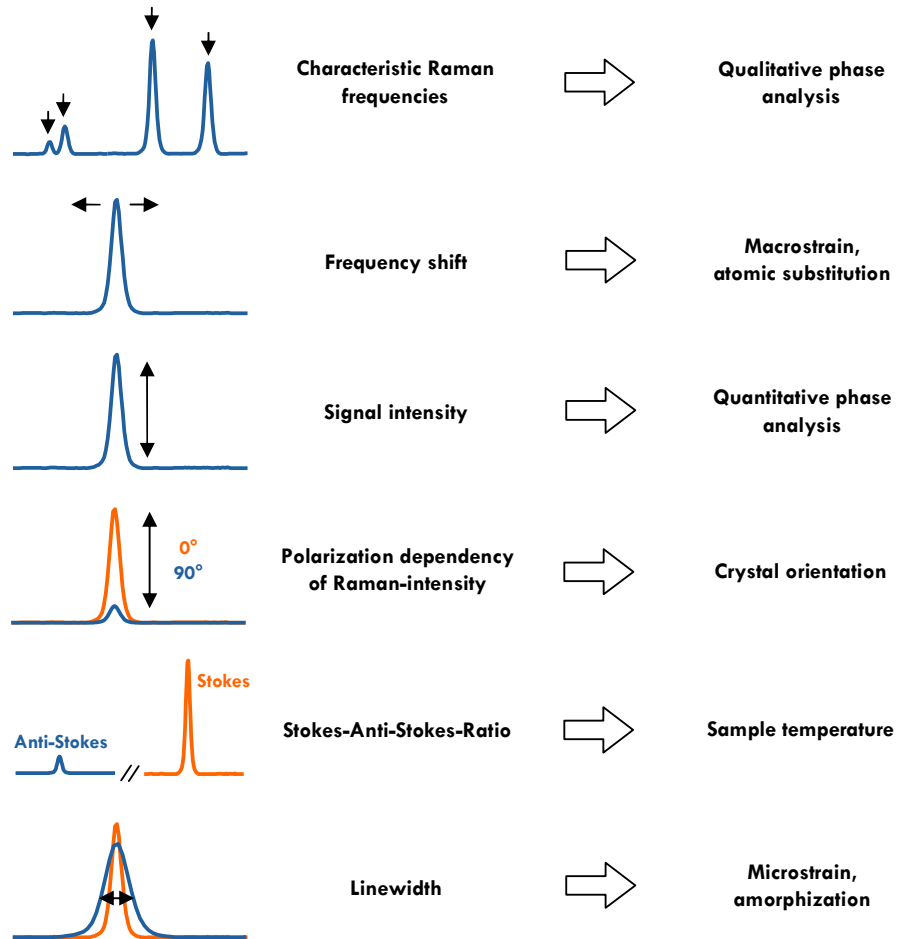


Fig. 17. Some information accessible via Raman spectroscopy (after Ref. ⁷⁶).

Raman spectroscopy allows probing samples on the micrometer-scale. Regarding the focus point, the lateral resolution is limited by the numeric aperture of the objective lens used and the applied laser radiation wavelength. The axial sampling depth, however, is a complex quantity and strongly affected by the optical transparency of the sample material. For transparent materials like ZrO_2 the axial sampling depth is in the range of tens of micrometers.⁷⁷ This is in agreement with new theoretical calculations for confocal Raman spectrometers.^{78,79} For non-confocal Raman systems, the axial sampling depth is significantly larger than this. It should be kept in mind that the lateral resolution decreases in out-of-focus areas which, however, significantly contribute to the measured total Raman signal (Fig. 18a). The resulting shape of the Raman-excited volume is, in first approximation, cone-like.^{76,79} There are, however, significant limitations to that approximation due to the Gaussian intensity profile of the laser beam (Fig. 18b).

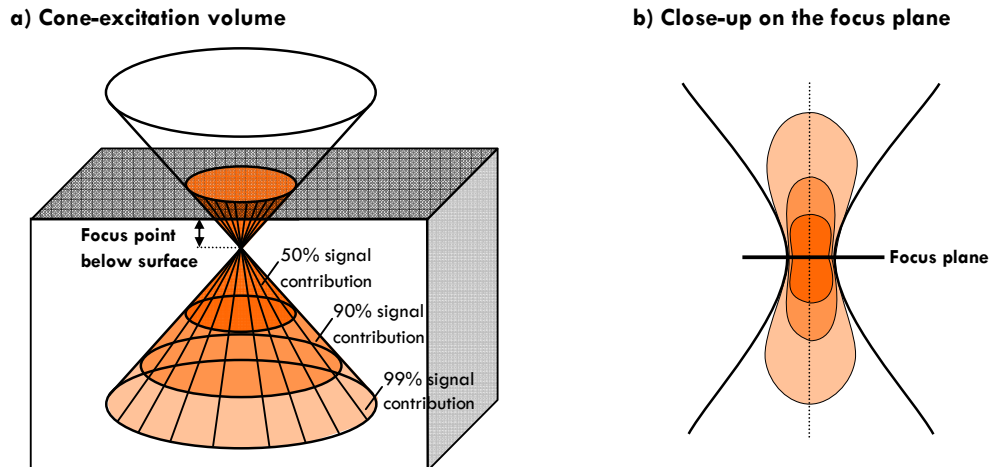


Fig. 18. Schematic representation of the excited Raman volume (after Ref. ⁷⁸⁻⁸¹).

3.2 X-Ray micro-diffraction (μ -XRD)

Ever since X-radiation was discovered by W. C. Röntgen in 1895 and first applied to study the structure of crystalline media a few years later by von Laue, Friedrich and Knipping, X-ray diffraction (XRD) has evolved into a standard characterization technique and it is difficult to image an analysis laboratory without it. The basis for XRD experiments is the Bragg-law (Eq. 15) which defines certain angles under which X-ray diffraction occurs for a crystalline body (i.e., constructive interference).

$$2d \cdot \sin\theta = n \cdot \lambda \quad \text{Eq. 15}$$

where d denotes the lattice plane distance, θ is the diffraction angle, n an integer ($n = 1, 2, 3, \dots$) and λ is the wavelength of the used monochromatic X-ray radiation.

This section will not discuss the physical basics of XRD but concentrates on new developments in the field of X-ray instrumentation which were essential in analyzing tribologically influenced SiC surfaces - that is, micro-diffraction and area-sensitive detectors. Fig. 19 illustrates the wide field of structural information which can be gained from XRD experiments.

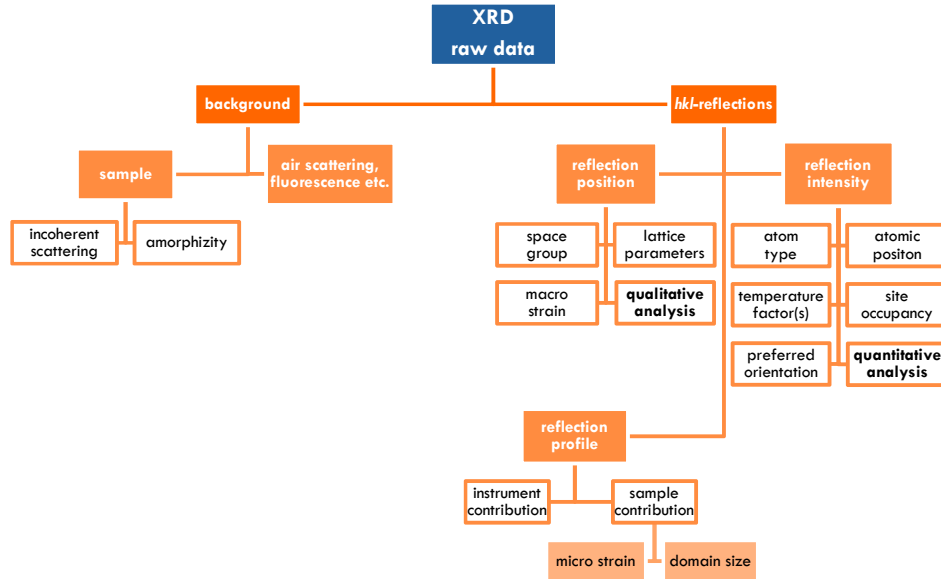
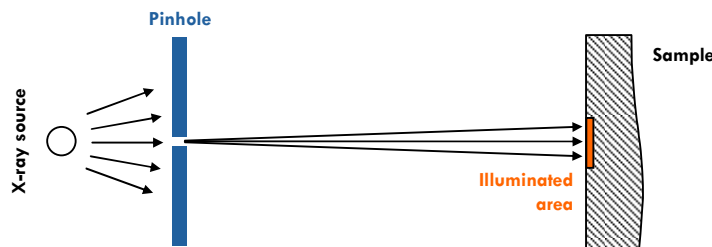


Fig. 19. Some information accessible via X-ray diffraction (after Ref. ⁸²).

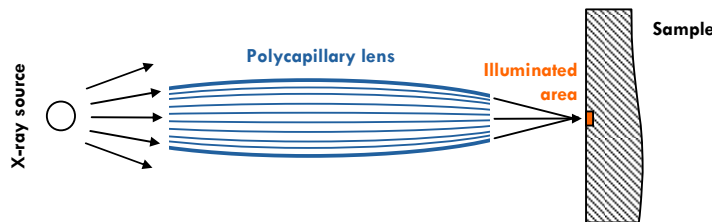
During the generation of X-ray radiation, more than 99% of power input is turned into heat energy – less than 1%, therefore, can be used for the XRD experiments. Improving the spatial resolution by decreasing the probed area on the sample requires a smaller diameter of the X-ray beam. Conventionally, this was done by introducing pinholes with the desired diameter blocking off the rest of the incident beam (Fig. 20a) resulting in a drastic decrease in measured total intensity. Introducing further optical elements like Soller slits, the divergence shown in Fig. 20a can be contained at a huge cost of total intensity.

Instead of blocking large parts of the incident radiation, capillary optics made of glass (Fig. 20b) collect X-ray beams over a certain angle and focus them onto a specific spot (full lens). In principle, capillary optics work like glass fibers: due to total internal reflection, the collected beam can be guided. Using not only one capillary (monocapillary optics) but many capillaries (polycapillary optics), it is possible to arrange them into an array like as shown in Fig. 20b which allows focusing the exiting X-ray beams onto a specific area. X-ray capillaries are, in contrast to glass fibers, hollow cores within a glass matrix as air is optically denser than glass for X-ray radiation. Instead of air, however, it is more convenient to use the noble gas helium to avoid radiation of the glass matrix from ozone formation. Also, X-ray absorption is decreased inside the lens due the smaller scattering of He in contrast to nitrogen, oxygen and argon. Thin beryllium windows are usually used to seal the noble gas filling and to keep off dust particles from entering the capillaries.

a) Pinhole configuration



b) Polycapillary optics

Fig. 20. Concepts for micro-diffraction (after Ref. ⁸³).

Using focusing X-ray lenses, beam diameters defined by the Gaussian beam halfwidth of $\leq 20 \mu\text{m}$ are attainable for short working distances.⁸⁴⁻⁹⁰ For synchrotron radiation beam diameters of less than 100 nm have been reported.⁹¹ Alternatively, focusing mirrors have been applied successfully for studies carried out on the grain scale (i.e., $\geq 1 \mu\text{m}$).⁹² This is why X-ray microdiffraction is sometimes referred to μ -XRD.

As a positive side-effect of the use of capillary optics, the high-energy bremsstrahlung is suppressed when the X-ray radiation exits the lens. The reason for this is that above a certain photon energy the critical angle for reflection will be smaller than the maximum incident angle and X rays will no longer be efficiently guided along the capillary tubes. Thus, for low-resolution diffraction applications, the energy filtration provided by the optic allows to replace the monochromator with a simple filter for the low-energy radiation.

Although there is an enormous gain in total signal intensity (several orders of magnitude; Ref. ⁹³) this happens at the cost of an increase in the profile width of the Bragg reflections. The latter can easily be explained: in contrast to a setup using (almost) parallel X-ray beams, polycapillary optics suffer from a large convergence angle (several degrees). As the X-rays incident on the sample surface encompass a small range of diffraction angles, crystal domains which would not ideally fulfill the reflection condition (Bragg law) for a parallel beam contribute to the total pattern signal and the resulting measured Bragg reflection is smeared in theta. It is important not to mistake this phenomenon with a distribution in d-values as a result from stress / strain or finite domain size. These would also cause an increase in the measured width of Bragg reflections.

Increasing the throughput is a practicable way to increase the measurable diffracted signal intensity and, hence, realize both, high spatial resolution and/or short measuring times. Besides creating a more efficient way of radiation guidance and focusing on a small spot, it is important to collect as much of the diffracted signal as possible. Conventional 1D detectors that are incrementally moved along the diffraction sphere are not up to this task. More suitable are 2D-detectors which collect diffracted signals over a certain theta- and chi-range (Fig. 21).

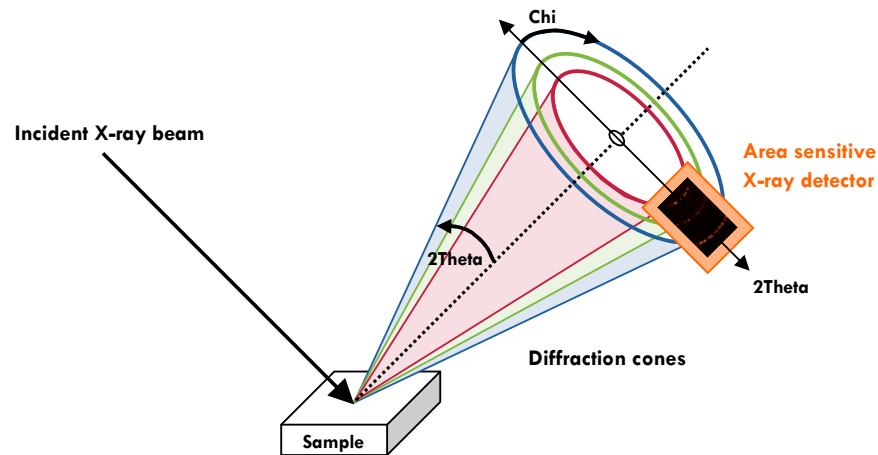


Fig. 21. Schematic diffraction cones produced from polycrystalline sample showing the geometrical meaning of theta and chi.

A striking advantage of 2D detectors (because of which XRD is sometimes referred to as XRD²) is that besides the information on d-values, also information on the orientation of the crystal domains within the probed volume can be gained (chi). This textural information is crucial for the understanding of preferred orientation or, as a special case of preferred orientation, for the characterization of mosaicity. Also, spotty Debye-Scherrer-rings (= 2D cuts of diffraction cones) indicate a poor crystallite statistics (for example when the powder contains too large grains which contribute strong single-crystal like reflections). An example of this is shown in Fig. 22. In the early times of X-ray diffraction, the use of Debye-Scherrer film techniques enabled both, d- and chi-dependent analysis of diffraction patterns. However, it took the electronic development several decades to catch up realizing fast and efficient area-sensitive detectors which allow (almost) real-time measurements.

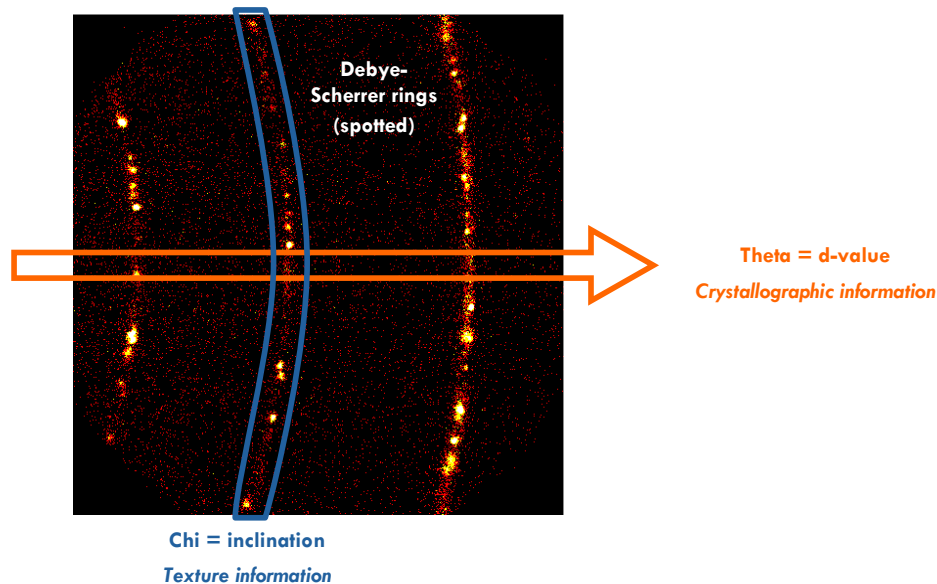


Fig. 22. Diffraction frame for SiC ceramic body with very large crystallites (2θ range: $10 - 30^\circ$ [Co-K α], Chi-range: $270 - 310^\circ$).

Today, there exist several technical solutions for 2D detectors ranging from image plates and X-ray sensitive charge-coupled devices (CCD) to area-sensitive multi-wire proportional chambers. The latter system was used for this study and has the distinct advantage that real-time observation of the diffraction cone segments is possible. This way, information on both, crystal structure and textural aspects can be gained in a fast and comprehensive way.

The overall excitation volume of XRD experiments is rather pan-like (in contrast to the cone-like sampling volume for Raman experiments). While the lateral resolution is limited by the X-ray beam diameter (in case of micro-diffraction: $\ll 1$ mm) is the axial sampling depth a function of the used wavelength, the materials effective absorption coefficient (which is influenced by atomic number and density) and incident angle. For a X-ray beam ($\varnothing = 100 \mu\text{m}$) which perpendicularly incidents on a dense SiC ceramic body, the laterally illuminated area of $\approx 8000 \mu\text{m}^2$ is opposed by a very low axial sampling depth of a few micrometers. The depth-related signal intensity follows, to be more precise, a Lambert-Beer-law. That is why for the case presented (i.e., SiC & 90° incident beam), 50% of the measured signal comes from a depth-segment which is $\approx 11 \mu\text{m}$ thick while the first $\approx 38 \mu\text{m}$ of the sample beneath the very surface contribute to 90% of the total signal intensity.

XRD is made more surface-sensitive when decreasing the incident angle. By enhanced surface-sensitivity, systematic studies by means of xy-mapping and varying incident angles are possible and the well-known effect of superficial amorphisation causing linewidth broadening of hkl -reflections^{82,94} after mechanic contact of sliding surfaces can now be characterized on a μm -scale via μ -XRD. For SiC, the depth-segment contributing to 90% of the measured signal intensity is decreased from $\approx 23 \mu\text{m}$ at 90° incident angle to $\approx 5 \mu\text{m}$ at 10° and even to $\gg 1 \mu\text{m}$ at 1° . It should be kept in mind, however, that the beam spot on the surface becomes elongated and will be relatively large when using small incident angles (like 0.5 or 1.0°) – that is, the strongly decreased axial sampling depth is only achievable on cost of lateral resolution (Fig. 23). A technical solution for this problem is the introduction of beam knives which cut-off parts of the divergent beam (what, of course, results in decreased count-rates).

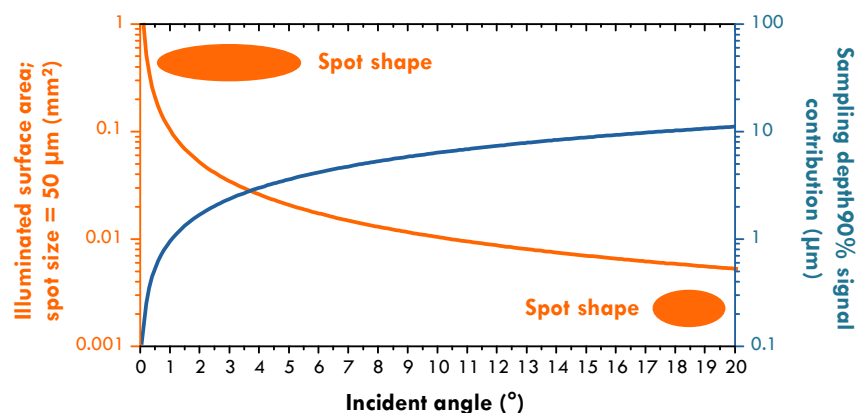


Fig. 23. Illuminated surface area versus sampling depth as a function of incident angle. No sample rotation is considered.

3.3 Focused Ion Beam (FIB) preparation & Transmission Electron Microscopy (TEM)

Transmission electron microscopy (TEM) is, just like XRD, a standard analysis method for scientific studies related to materials sciences as well as to biology, chemistry and medicine and many others. This section does not intend to provide an in-depth discussion of *state-of-the-art* developments or electron optics in general, but gives a short introduction into TEM analysis and sample preparation via the focused ion beam (FIB) technology.

The origins of TEM date back even longer than scanning electron microscopy: in 1931, Ernst Ruska and his colleague Max Knoll designed the first transmission electron microscope.^{95,96} A few years later, the first recognizable efforts were made to construct a scanning electron microscope (SEM) and a working prototype was presented by Zworykin et al. (Ref. 97) in 1942. In general, a SEM requires a less-complex setup in comparison to TEM: the electron beam is focused on surface of a solid sample and the resulting secondary or back-scattered electrons are used for high-resolution imaging. This way, a maximum lateral resolution of approximately 1 – 20 nm can be achieved depending on the instrument's specifications. Also the sample preparation is quite easy: solid samples need only to be conductive or can be made so by sputter-coating them via carbon or metal (e.g., platinum). This is why SEM instruments are more widespread in analytical laboratories than TEM.

Transmission electron microscopy is more complex than scanning electron microscopy - beginning with the requirements put to sample materials. In particular, the sample must be sufficiently thin so that transmission of electrons is possible (that is, thinner than 100 nm). This was also the major historical limitation to this technology until the diamond knife and ultra-microtome sections were available since the 1950s. Also, the general setup of a TEM instrument is highly sophisticated comprising several electron lenses and apertures using very acceleration currents (> 100 kV instead of < 30 kV in case of SEM). In addition to its high resolution (down to the atomic scale for high-resolution techniques), TEM offers also the possibility to access crystallographic information of the sample by analyzing electron diffraction pattern. Fig. 24 shows schematically the ray path for TEM diffraction and imaging mode. In the focal plane, all rays emerging from the transmissible sample under the very same angle converge (diffraction pattern) while on the image plane, a magnified representation of the actual sample can be observed (image). The latter, however, is not so straight-forward to interpret as SEM images as dislocations, a non-uniform thickness and other factors give raise to diffraction contrast.

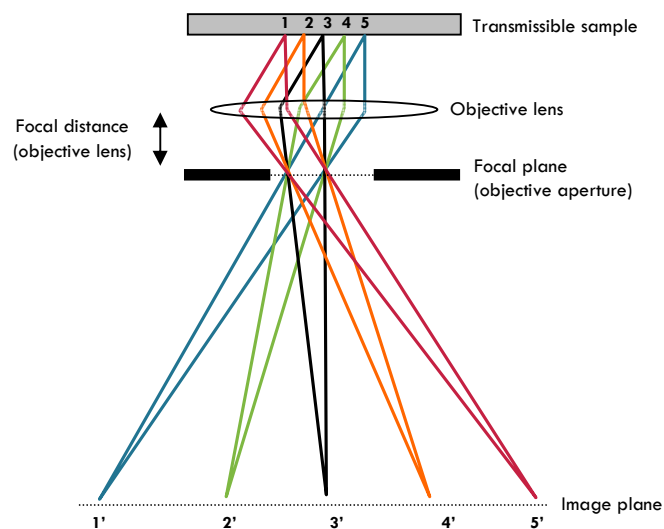


Fig. 24. TEM image versus diffraction mode (after Ref. 98). For discussion see text.

Conventional TEM sample preparation encompasses several steps. For hard ceramic bodies, microtome cutting is no suitable method. One possible preparation method is to thin the sample a few micrometers thickness and subsequently use ion beam etching (usually using gentle Ar^+ -milling avoid amorphization effects) to introduce a small hole. At the edges of the hole the sample is sufficiently thin for electron transmission. This way, only non-area selective samples can be obtained, that is, the analyzable sample section cannot be chosen within the sub-millimeter scale. More difficult is the preparation of cross-sections. Here, the so called sandwich method⁹⁹ has been proven to be a suitable yet time-consuming approach. The latter requires cutting of selective sample segments and glue them together with the interface region of interest being now localized in the middle of the array. This way, conventional ion beam etching can be applied. However, hard sample materials or hard-soft-composites are extremely difficult to prepare using conventional methods.

For analysis of heterogeneous scales, an easy-to-perform preparation technique would be highly desirable that allows specifying a certain sample region for TEM studies. Focused ion beam (FIB) preparation is such a tool that enables selection of superficial depth profiles within a sub-micrometer precision. A FIB as such is nothing else but a beam of ions (usually gallium) which is focused on a sample for area-selective ion beam etching. Only the most important preparation steps of FIB are presented below (Fig. 25).

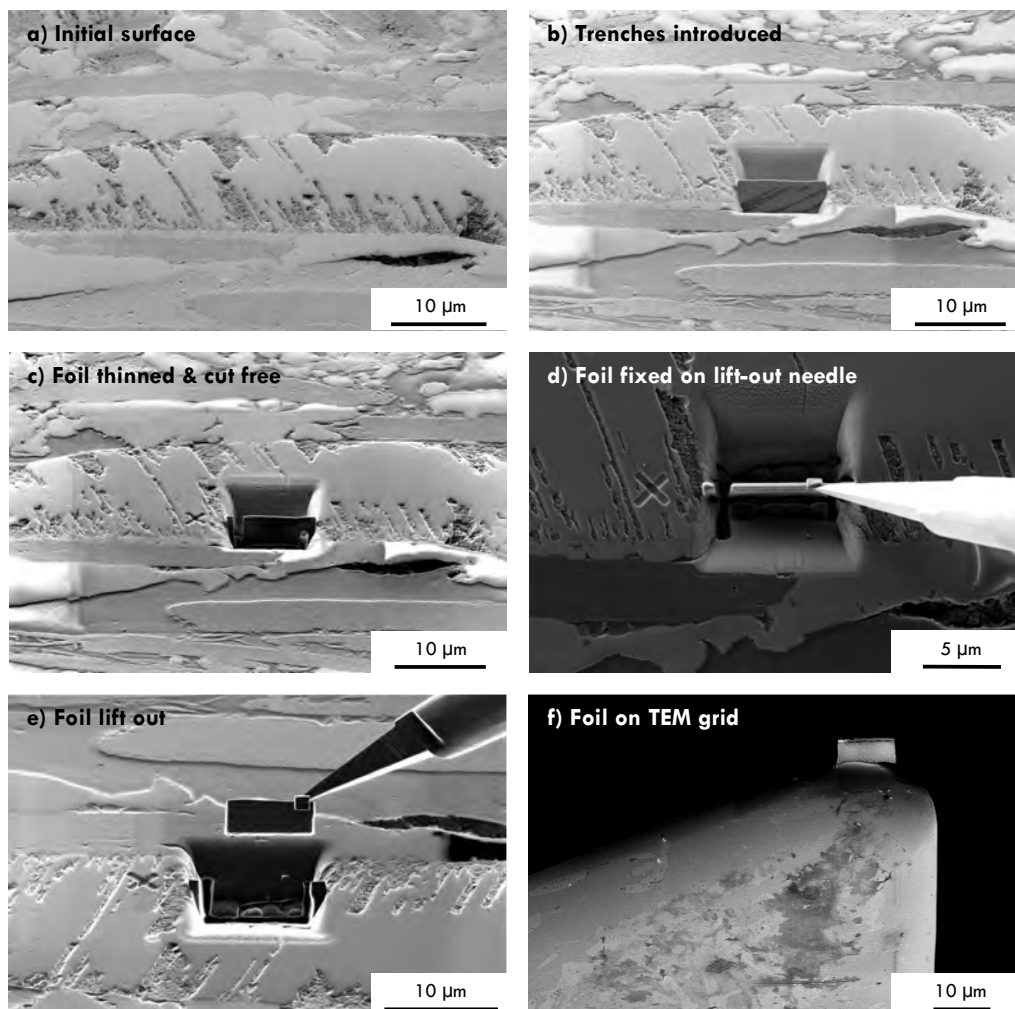


Fig. 25. Some steps of TEM foil preparation via FIB. The sample is a graphitized SiC grain.

First, a suitable sample area is selected using either ion imaging or, in case the FIB is integrated into a SEM, electron imaging (Fig. 25a). To protect the topmost surface scale from ion implantation and amorphization, a thin coating is applied and usually a small Pt strip is deposited by gas injection. After that, two trenches are cut in front of and behind the selected area (Fig. 25b). Typical sample dimensions are 10 – 20 μm width x 5 – 15 μm height x 100 – 200 nm thickness. For electron transmission, the foil can subsequently be further thinned down to or less than 50 nm (Fig. 25c). By tilting, the FIB foil then can be cut free from the surrounding material and a needle can be used to lift-out the sample (Fig. 25c - 25e). Finally, the sample foil will be fixed on a TEM grid (e.g., by deposition of Pt; Fig. 25f) and is ready for TEM analysis. More detailed information on the method can be found in Ref. ^{90,100-107}.

Although being a routine method for lithographical application, the focused ion beam technology suffers from some disadvantages. For example, gallium implantation and even amorphization of the sample can occur during FIB treatment. Hopefully, new approaches like the triple-beam-technology where subsequent to bulk ion etching gentle argon-ion bombardment (with very low ablation rate) is applied will bring improvement to this problem.

FIB has become much more than just a TEM foil preparation method over the last decade. Being integrated into conventional SEM instruments, cutting into the sample and extracting depth profiles for the first few micrometers of the surface is now possible. This way, the beneath-surface volume can be analyzed, for example, using chemical analysis (e.g., energy-dispersive X-ray spectroscopy EDX) or electron imaging. This short introduction cannot give a *state-of-the-art* overview over the many applications of FIB in materials sciences apart from TEM preparation but one important application is FIB tomography. For this, a trench is cut into the sample and, while cutting continuously into the sample, electron images are obtained. Combining these steps enables to create a 3D representation of the analyzed sample segment (Fig. 26). In contrast to X-ray tomography, however, FIB tomography is a destructive method.

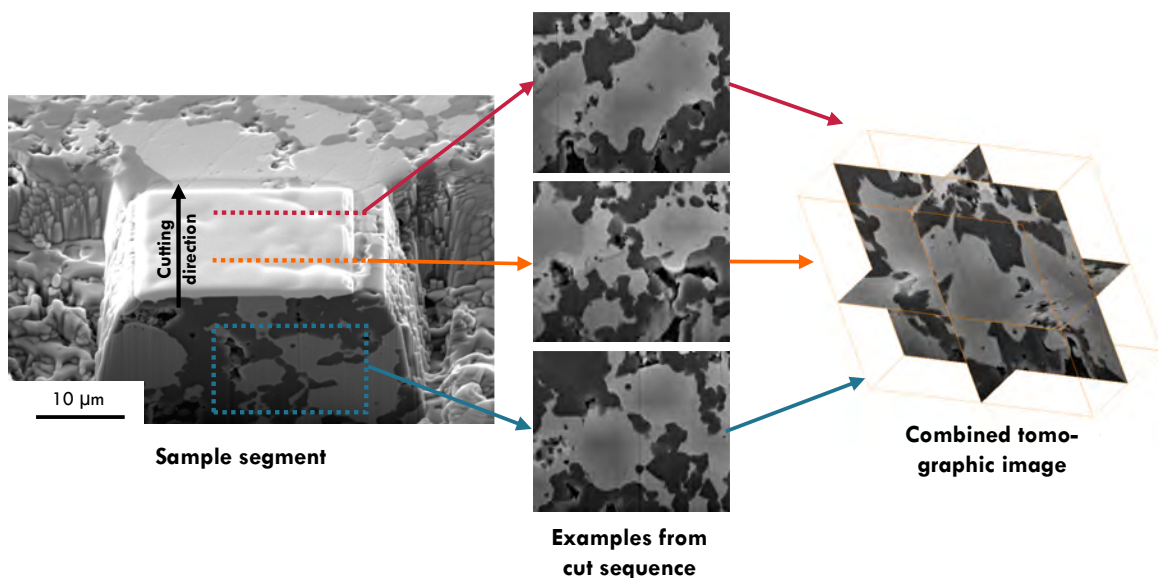


Fig. 26. Example of FIB tomography. The sample is a SiC-ZrB₂-ZrSi₂ ceramic.

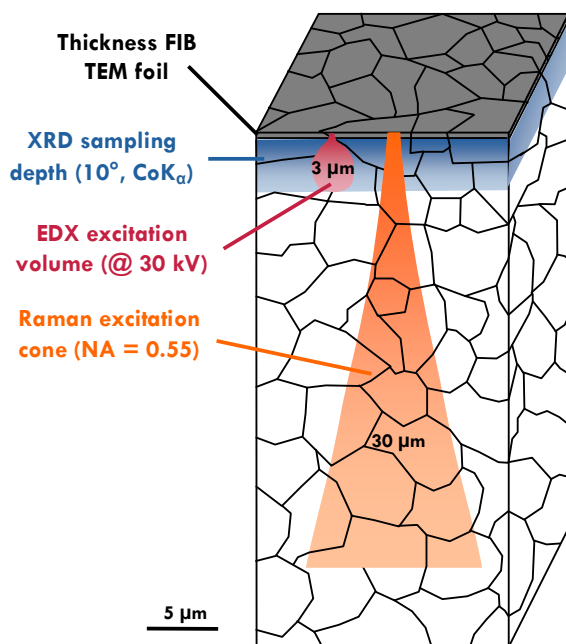


Fig. 27. Comparison of excitation volumes for EDX on bulk samples / FIB TEM foils and Raman spectroscopy. As theoretical sample material, ZrO_2 is considered.

As discussed, FIB TEM foil preparation is an area-selective method which requires besides the instrumental prerequisites no further sample pretreatment (except coating the surface with a conductive layer). FIB-prepared foils, however, also have the distinct advantage of increasing the spatial resolution for chemical analysis. Usually, the electron beam interacts with the solid sample and the resulting excited volume used for chemical analysis via EDX is quite large. Depending on the mean atomic number of the sample and used acceleration current, the diameter of the pyriform excited volume lies in the range of a few micrometers. The advantage of the analysis of thin FIB prepared TEM foils in contrast to bulk sample EDX (as performed using a SEM) is understandable when looking at Fig. 27. The mere thinness of the TEM foil limits the axial spread of the excited volume segment. This is why FIB preparing of foils would be interesting way to decrease the large axial sampling depth in Raman spectroscopy.

For the chemical analysis, EDX and EELS were used. Both spectroscopic techniques use the interactions between the sample material and the electron beam for chemical characterization. EDX (energy dispersive X-ray spectroscopy) uses the characteristic X-rays which are emitted when inner shell electrons are ejected and an outer shell electron fills the induced hole. EELS (electron energy loss spectroscopy) analyzes the energy loss of the electron beam when being transmitted through a solid sample. Energy can be lost due to inelastic scattering, for example, plasmon or phonon excitation or shell ionization. The latter can be used for chemical analysis of the sample.^{95,108-110}

EDX and EELS are often considered to be complementary methods. The first, EDX, can show a lower detection limit for heavy atoms and its technological adaptation is quite easy (e.g., EDX is a standard tool in SEM instruments). EELS, although technological more demanding, allows besides probing the chemical composition also characterizing the chemical bonding and even surface properties. While EELS is limited to energies below ca. 3 keV energy ELSS (with an energy resolution of ≤ 1 eV, EDX analysis encompasses a larger energy range (several 10 keV) with a poorer energy resolution (tens of eV).^{95,108,111}

REFERENCES

1. Nickel, K.G. & Gogotsi, Y.G. Approaches to Standardisation: High Temperature Oxidation and Hydrothermal Corrosion of Silica Forming Ceramics. *Key Engineering Materials* **113**, 15 - 29 (1996).
2. Gogotsi, Y.G. & Yoshimura, M. Water Effects on Corrosion Behaviour of Structural Ceramics. *MRS Bulletin*, 39 - 45 (1994).
3. Nickel, K.G. & Gogotsi, Y.G. Hydrothermal Synthesis of Diamond. in *Handbook of Ceramic Hard Materials*, Vol. 1 (ed. Riedel, R.) 374 - 389 (Wiley-VCH Verlag, Weinheim, 2000).
4. Gogotsi, Y.G. & Yoshimura, M. Formation of carbon films on carbides under hydrothermal conditions. *Letters to nature* **367**, 628 - 630 (1994).
5. Gogotsi, Y.G. & Yoshimura, M. Degradation of SiC-based fibres in high-temperature, high-pressure water. *Journal of Materials Science Letters* **13**, 395 - 399 (1994).
6. Kraft, T. & Nickel, K.G. Carbon formed by hydrothermal treatment of α -SiC crystals. *Journal of Materials Chemistry* **10**, 671 - 680 (2000).
7. Jacobson, N.S., Gogotsi, Y.G. & Yoshimura, M. Thermodynamic and Experimental Study of Carbon Formation on Carbides under Hydrothermal Conditions. *Journal of Materials Chemistry* **5**, 595 - 601 (1995).
8. Kraft, T. & Nickel, K.G. Kohlenstoffmikrokugeln und Verfahren zur Herstellung eben solcher Kohlenstoffmikrokugeln. in *Offenlegungsschrift* Vol. DE 199 35 447 A1 (2001).
9. Gogotsi, Y.G., In-Deok, J. & McNallan, M.J. Carbon Coatings on Silicon Carbide by Reaction with Chlorine-Containing Gases. *Journal of Materials Chemistry* **7**, 1841 - 1848 (1997).
10. Gogotsi, Y.G., Kofstad, P., Yoshimura, M. & Nickel, K.G. Formation of sp^3 -bonded carbon upon hydrothermal treatment of SiC. *Diamond and Related Materials* **5**, 151 - 162 (1996).
11. Gogotsi, Y.G. et al. Structure of carbon produced by hydrothermal treatment of β -SiC powder. *Journal of Materials Chemistry* **6**, 595 - 604 (1996).
12. Gogotsi, Y.G., Nickel, K.G. & Kofstad, P. Hydrothermal Synthesis of Diamond from Diamond-seeded β -SiC Powder. *Journal of Materials Chemistry* **5**, 2313 - 2314 (1995).
13. Perera, G., Doremus, R.H. & Lanford, W. Dissolution Rates of Silicate Glasses in Water at pH 7. *Journal of the American Ceramic Society* **74**, 1269-1274 (1991).
14. Kennedy, G.C. A portion of the system silica-water. *Economic geology* **45**, 629 - 653 (1950).
15. Iler, R.K. *The chemistry of silica*, 896 (John Wiley & Sons, New York, 1979).
16. Kraft, T., Nickel, K.G. & Gogotsi, Y.G. Hydrothermal degradation of chemical vapour deposited SiC fibres. *Journal of Materials Science* **33**, 4357 - 4364 (1998).
17. Gogotsi, Y.G. et al. Formation of Carbon Coatings on SiC Fibres by Selective Etching in Halogens and Supercritical Water. *Ceramic Engineering & Science Proceedings* **19**, 87 - 94 (1998).
18. Kraft, T. & Nickel, K.G. Solvothermal Formation of sp^2 - and sp^3 -Carbon From Carbides. in *Eurocarbon '98* Vol. 2 881 - 882 (Strasbourg, 1998).
19. Kraft, T. & Nickel, K.G. Hydrothermal Carbon Coatings of α -SiC Crystals. in *Surface Engineering - EURO-MAT 99*, Vol. 11 (ed. Dimigen, H.) 306 - 311 (Wiley-VCH, 1999).
20. Schwetz, K.A. & Hassler, J. Zur Beständigkeit von Hochleistungskeramiken gegen Flüssigkeitskorrosion. *Ceramic Forum International* **79**, D9 - D19 (2002).
21. Kim, W.-J., Hwang, H.S. & Park, J.Y. Corrosion behavior of reaction-bonded silicon carbide ceramics in high-temperature water. *Journal of Materials Science Letters* **21**, 733 - 735 (2002).
22. Kim, W.-J., Hwang, H.S., Park, J.Y. & Ryu, W.-S. Corrosion behaviors of sintered and chemically vapor deposited silicon carbide ceramics in water at 360°C. *Journal of Materials Science Letters* **22**, 581-584 (2003).
23. Christiansen, K. & Helbig, R. Anisotropic oxidation of 6H-SiC. *Journal of Applied Physics* **79**, 3276 - 3281 (1996).
24. Shenoy, J.N., Das, M.K., Cooper, J.A., Jr., Melloch, M.R. & Palmour, J.W. Effect of substrate orientation and crystal anisotropy on the thermally oxidized SiO₂/SiC interface. *Journal of Applied Physics* **79**, 3042 - 3045 (1996).
25. Herrmann, M., Michael, G., Schubert, C. & Hermel, W. Korrosionsverhalten von Hochleistungskeramiken in wässrigen Medien. in *Werkstoffwoche '98*, Vol. 3 (eds. Kranzmann, A. & Gramberg, U.) 281-286 (Wiley-VCH, Weinheim, 1998).
26. Wendland, K., Hollstein, T., Pfeiffer, W., Heinrich, J. & Zeus, D. Das Festigkeitsverhalten von SiSiC in flüssigen korrosiven Medien. in *Korrosion und Verschleiß von keramischen Werkstoffen* (eds. Telle, R. & Quirnbach, P.) 107 - 113 (Deutsche Keramische Gesellschaft e.V. (DKG), Aachen, 1994).
27. Alexander, G.B., Heston, W.M. & Iler, R.K. The Solubility of Amorphous Silica in Water. *Journal of Physical Chemistry* **58**, 453 - 455 (1954).
28. Cherkinskii, Y.S. & Knyaz'kova, I.S. Silica concentration dependence on pH in the presence of solid silica. *Doklady Akademii Nauk SSSR* **198**, 358 - 360 (1971).

29. Schwetz, K.A. Silicon Carbide Based Hard Materials. in *Handbook of Ceramic Hard Materials*, Vol. 2 (ed. Riedel, R.) 683 - 748 (Wiley-VCH Verlag GmbH, Weinheim, 2000).
30. Fischer, T.E. & Mullins, W.M. Chemical Aspects of Ceramic Tribology. *Journal of Physical Chemistry* **96**, 5690 - 5701 (1992).
31. Hsu, S.M., Zhang, J. & Yin, Z. The nature and origin of tribochemistry. *Tribology Letters* **13**, 131 - 139 (2002).
32. Zum Gahr, K.-H. *Microstructure and Wear of Materials*, 560 (Elsevier, Amsterdam, 1987).
33. zum Gahr, K.-H., Blattner, R., Hwang, D.-H. & Pöhlmann, K. Micro- and macro-tribological properties of SiC ceramics in sliding contact. *Wear* **250**, 299 - 310 (2001).
34. Chen, M., Kato, K. & Adachi, K. Friction and wear of self-mated SiC and Si₃N₄ sliding in water. *Wear* **250 - 251**, 246 - 255 (2001).
35. Erickson, L.C., Blomberg, A., Hogmark, S. & Bratthall, J. Tribological characterization of alumina and silicon carbide under lubricated sliding. *Tribology International* **26**, 83 - 92 (1993).
36. Zimmermann, M. *Experimentelle Untersuchung und numerische Modellierung des Gleitkontaktverhaltens von gesintertem Siliciumcarbid (SSiC)*, 102 (Universität Karlsruhe, Karlsruhe, 1998).
37. Lankford, J. & Davidson, D.L. Indentation plasticity and microfracture in silicon carbide. *Journal of Materials Science* **14**, 1669 - 1675 (1979).
38. Wereszczak, A.A. & Johanns, K.E. Spherical indentation of SiC. *Ceramic Engineering and Science Proceedings* **27**, 43 - 57 (2007).
39. Jahanmir, S. Wear transitions and tribochemical reactions in ceramics. *Proc Instn Mech Engrs Part J: Engineering Tribology* **216**, 371-385 (2002).
40. Hollstein, T. & Westerheide, R. Zur Korrosion von Hochleistungskeramiken in wässrigen Lösungen. in *Handbuch der Technischen Keramischen Werkstoffe* (ed. Kriegesmann, J.) Chapter 5.4.1.2.2: 1 - 27 (Deutscher Wirtschaftsdienst, Köln, 2000).
41. Kitaoka, S., Tsuji, T., Katoh, T., Yamaguchi, Y. & Kashiwagi, K. Tribological Characteristics of SiC Ceramics in High-Temperature and High-Pressure Water. *Journal of the American Ceramic Society* **77**, 1851 - 1856 (1994).
42. Andersson, P., Juhanko, J., Nikkila, A.-P. & Lintula, P. Influence of topography on the running-in of water-lubricated silicon carbide journal bearings. *Wear* **201**, 1 - 9 (1995).
43. Tomizawa, H. & Fischer, T.E. Friction and wear of silicon nitride and silicon carbide in water: hydrodynamic lubrication at low sliding speed obtained by tribochemical wear. *ASLE Transactions* **30**, 41 - 46 (1987).
44. Quinn, T.F.J. Oxidational Wear. *Wear* **18**, 413 - 419 (1971).
45. Quinn, T.F.J. Oxidational wear modelling: I. *Wear* **153**, 179 - 200 (1992).
46. Quinn, T.F.J. Oxidational wear modelling: Part II. The general theory of oxidational wear. *Wear* **175**, 199 - 208 (1994).
47. Quinn, T.F.J. Computational methods applied to oxidational wear. *Wear* **199**, 169 - 180 (1996).
48. Besson, J.M. Pressure generation. in *High-pressure techniques in chemistry and physics* (eds. Holzapfel, W.B. & Isaacs, N.S.) 1 - 45 (Oxford university press, Oxford, 1997).
49. Weir, C.E., Lippincott, E.R., van Valkenburg, A. & Bunting, E.N. Infrared Studies in the 1- to 15Micron Region to 30,000 Atmospheres. *Journal of Research of the National Bureau of Standards* **63A**, 55 - 62 (1959).
50. Lawson, A.W. & Tang, T.-Y. Diamond bomb for obtaining powder pictures at high pressures. *Review of Scientific Instruments* **21**, 815 (1950).
51. Jamieson, J.C. X-ray diffraction data on KNO₃ IV, a high-pressure phase. *Zeitschrift für Kristallographie* **107**, 65 - 71 (1956).
52. Jamieson, J.C. Introductory studies of high-pressure polymorphism to 24,000 bars by x-ray diffraction with some comments on calcite II. *Journal of Geology* **65**, 334 - 342 (1957).
53. Piermarini, G.J., Block, S., Barnett, J.D. & Forman, R.A. Calibration of the pressure dependence of the R1 ruby fluorescence line to 195 kbar. *Journal of Applied Physics* **46**, 2774 - 2780 (1975).
54. Forman, R.A., Piermarini, G.J., Barnett, J.D. & Block, S. Pressure Measurement Made by the Utilization of Ruby Sharp-Line Luminescence. *Science* **176**, 284 - 285 (1972).
55. Dunstan, D.J. & Spain, I.L. The technology of diamond anvil high-pressure cells: I. Principles, design and construction. *Journal of Physics E* **22**, 913 - 923 (1989).
56. Spain, I.L. & Dunstan, D.J. The technology of diamond anvil high-pressure cells: II. Operation and use. *Journal of Physics E* **22**, 923 - 933 (1989).
57. Presser, V., Heiß, M. & Nickel, K.G. EOS calculations for hydrothermal diamond anvil cell operation. *Review of Scientific Instruments* **78**, 085104-1 - 085104-9 (2008).
58. Shen, A.H., Bassett, W.A. & Chou, I.-M. Hydrothermal Studies in a Diamond Anvil Cell: Pressure Determination Using the Equation of State of H₂O. in *High-Pressure Research: Application to Earth and Planetary Sciences* (eds. Syono, Y. & Manghnani, M.H.) 61 - 68 (American Geophysical Union, Washington D.C., 1992).
59. Bassett, W.A., Shen, A.H., Bucknum, M. & Chou, I.-M. Hydrothermal Studies in a New Diamond Anvil Cell up to 10 GPa and from -190°C to 1200°C. *PAGEOPH* **141**, 487 - 495 (1993).
60. Holzapfel, I. & Holzapfel, W.B. *High Pressure Techniques in Chemistry and Physics: A Practical Approach*, (Oxford University Press, Oxford, 1997).

61. Haselton, H.T., Chou, I.-M., Jr., Shen, A.H. & Bassett, W.A. Techniques for determining pressure in the hydrothermal diamond-anvil cell: Behaviour and identification of ice polymorphs (I, II, V, VI). *American Mineralogist* **80**, 1302 - 1306 (1995).
62. Tanaka, H. Simple physical model of liquid water. *Journal of Chemical Physics* **112**, 799 - 809 (2000).
63. Wagner, W. & Pruss, A. The IAPWS Formulation 1995 for the Thermodynamic Properties of Ordinary Water Substance for General and Scientific Use. *Journal of Physical and Chemical Reference Data* **31**, 387 - 535 (2002).
64. Smekal, A. The quantum theory of dispersion. *Naturwissenschaften* **11**, 873 - 875 (1923).
65. Raman, C.V. & Krishnan, K.S. A new type of secondary radiation. *Nature* **121**, 501 - 502 (1928).
66. Long, D.A. *The Raman Effect: A Unified Treatment of the Theory of Raman Scattering by Molecules*, 597 (John Wiley & Sons Ltd., Chichester, 2001).
67. Presser, V., Klouzkova, A., Mrazova, M., Kohoutkova, M. & Berthold, C. Micro-Raman spectroscopy on analcime and pollucite in comparison to X-ray diffraction. *Journal of Raman Spectroscopy* **39**, 587 - 592 (2008).
68. Raman, C.V. & Krishnan, K.S. The production of new radiations by light scattering. I. *Proceedings of the Royal Society of London, Series A* **122**, 23 - 35 (1929).
69. van den Kerkhof, A.M. Vrije Universiteit (1988).
70. Smith, E. & Dent, G. *Modern Raman Spectroscopy: A Practical Approach* 222 (John Wiley and Sons Ltd., New York, 2005).
71. Kailer, A., Gogotsi, Y.G. & Nickel, K.G. Micro-Raman spectroscopy of indentation-induced phase-transformations. *Materials, Functionality & Design, Proceedings of the European Conference on Advanced Materials and Processes and Applications* **5**, 171 - 174 (1997).
72. Nasdala, L., Irmer, G. & Wolf, D. The degree of metamictization in zircon: a Raman spectroscopic study. *European journal of mineralogy* **7**, 471 - 478 (1995).
73. Nasdala, L. et al. Metamictization of natural zircon: accumulation versus thermal annealing of radioactivity-induced damage. *Contributions to Mineralogy and Petrology* **141**, 125 - 144 (2001).
74. Kailer, A., Nickel, K.G. & Gogotsi, Y.G. Raman microspectroscopy of nanocrystalline and amorphous phases in hardness indentations. *Journal of Raman Spectroscopy* **30**, 939 - 946 (1999).
75. Clark, R.J.H. & Hester, R.E. *Advances in Infrared and Raman Spectroscopy*, 372 (Heyden & Son Ltd., London, 1980).
76. Lewis, I.R., Lewis, L. & Edwards, H.G.M. *Handbook of Raman Spectroscopy: From the Research Laboratory to the Process Line*, 1080 (CRC Press, New York, 2001).
77. Dorn, M. Ph.D., Eberhard-Karls-Universität Tübingen (2004).
78. MacDonald, A.M. & Vaughan, A.S. Numerical simulations of confocal Raman spectroscopic depth profiles of materials: a photon scattering approach. *Journal of Raman Spectroscopy* **38**, 584 - 592 (2007).
79. Overall, N. The Influence of Out-of-Focus Sample Regions on the Surface Specificity of Confocal Raman Microscopy *Applied Spectroscopy* **62**, 591 - 598 (2008).
80. Lipkin, D.M. & Clarke, D.R. Sample-probe interactions in spectroscopy: Sampling microscopic property gradients. *Journal of Applied Physics* **77**, 1855 - 1863 (1995).
81. Presser, V. & Glotzbach, C. Metamictisation in zircon: Raman investigation following a Rietveld approach. Part II: Sampling depth implication and experimental data. *Journal of Raman Spectroscopy* **40**, in press (2009).
82. Dinnebier, R.E. & Billinge, S.J.L. *Powder Diffraction: Theory and Practice*, (Royal Society of Chemistry, Cambridge, 2008).
83. Beckhoff, B., Kanngießer, B., Langhoff, N., Wedell, R. & Wolff, H. *Handbook of Practical X-Ray Fluorescence Analysis* 863 (Springer Verlag, Berlin, 2006).
84. Langhoff, N., Bjeoumikhov, A., Bjeoumikhova, S., Langhoff, N. & Wolff, H. Capillary optics for real time X-ray diffractometry. *Journal of X-Ray Science and Technology* **13**, 185 - 190 (2005).
85. Bjeoumikhov, A., Wedell, R. & Bjeoumikhova, S. Mono- and polycapillary optics-state of the art and applications. *Guangxue Jingmi Gongcheng* **15**, 1932 - 1945 (2007).
86. Schell, N., Eichhorn, F., Bjeoumikhov, A., Prinz, H. & Ollinger, C. Parabolic capillary optics with less than 50 µm focus and large focal distance for synchrotron radiation scattering. *AIP Conference Proceedings* **879**, 975 - 980 (2007).
87. Wroblewski, T., Bjeoumikhov, A. & Hasse, B. Micro diffraction imaging of bulk polycrystalline materials. *Materials Science Forum* **524 - 525**, 273 - 278 (2006).
88. Bjeoumikhov, A. et al. New generation of polycapillary lenses: Manufacture and applications. *X-Ray Spectrometry* **32**, 172 - 178 (2003).
89. Mayer, J., Giannuzzi, L.A., Kamino, T. & Michael, J. TEM sample preparation and FIB-induced damage. *MRS Bulletin* **32**, 400 - 407 (2007).
90. Wirth, R. Focused ion beam (FIB): a novel technology for advanced application of micro- and nanoanalysis in geosciences and applied mineralogy. *European Journal of Mineralogy* **16**, 863 - 876 (2004).
91. Hignette, O., Cloetens, P., Rostaing, G., Bernard, P. & Morawe, C. Efficient sub 100 nm focusing of hard x rays. *Review of Scientific Instruments* **76**, 063709-1 - 063709-5 (2005).

92. Chang, C.H., MacDowell, A.A., Thompson, A.C., Padmore, H.A. & Patel, J.R. Grain orientation mapping of passivated aluminum interconnect lines by X-ray micro-diffraction. *AIP Conference Proceedings* **449**, 424 - 426 (1998).
93. Berthold, C., Bjeoumikhov, A. & Brügemann, L. Fast XRD² Microdiffraction with Focusing X-Ray Microlenses. *Particle & Particle Systems Characterization* **accepted**(2008).
94. Klug, H.P. & Alexander, L.A. *X-ray Diffraction Procedures for Polycrystalline and Amorphous Materials*, 716 (John Wiley & Sons Inc., New York, 1954).
95. Goldstein, J. et al. *Scanning Electron Microscopy and X-Ray Microanalysis*, 689 (Springer Science + Business Media, Inc., New York, 2003).
96. Ruska, E. & Knoll, M. Die magnetische Sammelspule für schnelle Elektronenstrahlen. *Zeitschrift für technische Physik* **12**, 389 - 400 (1931).
97. Zworykin, V.K., Hillier, J. & Snyder, R.L. A scanning electron microscope. *Proceedings of the Institute of Radio Engineers* **30**, 255 (1942).
98. Fultz, B. & Howe, J.M. *Transmission Electron Microscopy and Diffractometry of Materials* 758 (Springer Verlag, Berlin, 2007).
99. Kienzer, M., Nisch, W. & Joensson, C. Cross-sectional preparation of metal-insulator-metal thin-layer cathode systems for high-resolution transmission electron microscopic imaging. *Optik* **77**, 62 - 66 (1987).
100. Wirth, R., Langer, K. & Platonov, A.N. TEM study of a chromium-bearing kyanite from a mantle xenolith: Evidence for an alumina-rich exsolution precursor phase *European Journal of Mineralogy* **13**, 311 - 318 (2001).
101. Wirth, R. Focused Ion Beam (FIB) combined with SEM and TEM: Advanced analytical tools for studies of chemical composition, microstructure and crystal structure in geomaterials on a nanometre scale. *Chemical Geology* **in press**(2008).
102. Giannuzzi, L.A. & Stevie, F.A. *Introduction to Focused Ion Beams: Instrumentation, Theory, Techniques and Practice*, 358 (Springer Verlag, Berlin, 2005).
103. Lozano-Perez, S. A guide on FIB preparation of samples containing stress corrosion crack tips for TEM and atom-probe analysis. *Micron* **39**, 320 - 328 (2008).
104. Presser, N. & Hilton, M.R. Applications of focused ion beam machining to the characterization of carbide, nitride and oxide films. *Thin Solid Films* **308 - 309**, 369 - 374 (1997).
105. Volkert, C.A., Heiland, B. & Kauffmann, F. Preparation of hard-to-make TEM samples using the FIB microscope. *Praktische Metallographie* **40**, 193 - 208 (2003).
106. Volkert, C.A. & Minor, A.M. Focused ion beam microscopy and micromachining. *MRS Bulletin* **32**, 389 - 399 (2007).
107. Yao, N. *Focused Ion Beam Systems: Basics and Applications*, (Cambridge University Press, Cambridge, 2007).
108. Ahn, C.C. *Transmission Electron Energy Loss Spectrometry in Materials Science and the EELS Atlas*, 472 (Wiley-VCH, Weinheim, 2004).
109. Goodhew, P.J., Humphreys, J. & Beanland, R. *Electron Microscopy and Analysis*, 251 (Taylor & Francis, London, 2001).
110. Reed, S.J.B. *Electron Microprobe Analysis and Scanning Electron Microscopy in Geology*, 206 (Cambridge University Press, Cambridge, 2005).
111. Schneider, R. Electron Energy-loss Spectroscopy (EELS). in *Surface and Thin Film Analysis: Principles, Instrumentation, Applications* (eds. Bubert, H. & Jenett, H.) 50 -70 (Wiley-VCH Verlag GmbH, Weinheim, 2002).

Chapter 01

Chapter 02

Chapter 03

Chapter 04

Chapter 05

Chapter 06

Chapter 07

Chapter 08

Chapter 09

Chapter 10

Chapter 11

Chapter 12

SILICA ON SILICON CARBIDE

V. Presser⁽¹⁾, K. G. Nickel⁽¹⁾

⁽¹⁾ Institut für Geowissenschaften, Universität Tübingen

ABSTRACT:

Silicon carbide (SiC) as both the most important non-oxide ceramic and promising semiconductor material grows stoichiometric SiO₂ as its native oxide. During passive oxidation, a surface transformation of SiC into silica takes place causing bulk volume and bulk mass increase. This review summarizes *state-of-the-art* information about the structural aspects of silicon carbide, silica and SiC-SiO₂ interfaces and discusses physicochemical properties and kinetics of the processes involved. A special section describes the electronic properties of carbide-oxide-interfaces, which are inferior compared to Si-SiO₂ interfaces, limiting the use of SiC-based electronics. In the oxidation of SiC there is a variety of parameters (e.g., porosity, presence of sintering aids, impurities, crystallographic orientation, surface treatment, and atmospheric composition) influencing the process. Therefore, the kinetics can be complex and will be discussed in detail. Nonetheless, a general linear-parabolic time-law can be found for most SiC materials for passive oxidation, thus indicating a mainly diffusion-controlled mechanism. The pronounced anisotropy of SiC expresses itself by quite different oxidation rates for the various crystallographic faces. Manifold impact factors are reflected by oxidation rate-constants for silicon carbide that vary over orders of magnitude. The understanding of SiC oxidation and silica formation is still limited; therefore, different oxidation models are presented and evaluated in light of current knowledge.

TABLE OF CONTENTS

1. INTRODUCTION AND HISTORIC ASPECTS	42
2. STRUCTURAL ASPECTS	43
2.1 Silicon carbide and its polytypes.....	43
2.1.1 Crystallographic aspects	43
2.1.2 Nomenclature.....	47
2.1.3 General properties of polytypes	48
2.1.4 Origin of polytype formation.....	50
2.1.5 Defects in silicon carbide single-crystals	52
2.1.5.1 General remarks	52
2.1.5.2 Techniques for defect characterization.....	54
2.1.5.3 Micropipes and macropipes.....	54
2.1.5.3.1 Origin and basic features.....	54
2.1.5.3.2 Defect density and quality control in SiC	58
2.1.5.3.3 Analyzing micropipes	58
2.1.5.4 Low-angle boundaries.....	61
2.1.5.5 Stacking faults.....	62
2.1.5.6 Voids.....	62
2.1.5.7 Polytypic inclusions	63
2.1.5.8 Graphitization and silicon droplets	63
2.2 Silica and its polytypes.....	64
2.2.1 Crystallographic aspects	64
2.2.2 Amorphous silica.....	66
2.2.3 Cristobalite	67
2.2.4 Tridymite.....	68
2.3 Surface structures.....	71
2.3.1 Surface structures of silicon carbide.....	71
2.3.1.1 Non-reconstructed (natural) surfaces.....	71
2.3.1.2 Reconstructed surfaces	73
2.3.1.2.1 Introduction.....	73
2.3.1.2.2 (3x3)-SiC(0001) / (3x3)-SiC(111)	74
2.3.1.2.3 ($\sqrt{3}\times\sqrt{3}$)R30°-SiC(0001)	75
2.3.2 Surface structures of silica	77
2.3.2.1 Amorphous silica	77
2.3.2.2 Crystalline silica	77
2.3.2.3 Impurities and silica surfaces.....	78
2.4 SiC/SiO ₂ interfaces.....	79
2.4.1 Introduction	79
2.4.1.1 Basic structural aspects.....	79
2.4.1.2 p- and n-type SiC.....	79
2.4.1.3 Differences between SiC and Si interface abruptness	79
2.4.1.4 Surface influence	81
2.4.2 Interface states	81
2.4.2.1 General aspects	81

2.4.2.2	Polytypic influence and interface states distribution.....	82
2.4.2.3	Dangling bonds.....	84
2.4.2.4	Carbon clusters.....	86
2.4.2.4.1	General aspects.....	86
2.4.2.4.2	Cleaning procedure influence on carbon cluster.....	86
2.4.2.4.3	Carbon cluster formation and removal.....	87
2.4.2.4.4	Hydrogen passivation and carbon cluster.....	88
2.4.2.4.5	Carbon cluster interface states.....	88
2.4.2.5	Oxide traps.....	89
2.4.2.6	Polytypic inclusions.....	90
2.4.3	Dry and wet oxidation.....	90
3.	EXPERIMENTAL AND ANALYTICAL ASPECTS	92
3.1	Introduction and historic aspects.....	92
3.1.1	Oxidation types.....	92
3.1.2	Furnaces and impurities.....	92
3.2	Analytical aspects and methods.....	93
3.2.1	Gravimetry.....	93
3.2.2	Microscopy.....	95
3.2.3	IR and Raman spectroscopy.....	95
3.2.4	Ellipsometry.....	96
3.2.5	X-ray diffraction.....	96
3.2.6	Outlook.....	97
4.	THE KINETICS OF SILICA GROWTH	97
4.1	Dry thermal oxidation.....	97
4.1.1	Introduction.....	97
4.1.2	Growth laws.....	99
4.1.2.1	Deal-and-grove model.....	99
4.1.2.2	Application of the Deal-and-grove model to sic oxidation.....	101
4.1.2.3	Conversion of gravimetric data.....	103
4.1.2.4	Differences between silicon and silicon carbide oxidation.....	105
4.1.2.5	Alternative models.....	107
4.1.2.6	Initial oxidation.....	109
4.1.3	Gas diffusion.....	112
4.1.3.1	Preliminary aspects.....	112
4.1.3.2	Activation energies.....	113
4.1.3.3	Diffusion of oxygen.....	115
4.1.3.4	Diffusion of CO.....	116
4.1.3.5	Diffusion of SiO.....	116
4.1.3.6	Special case of ultrathin oxide layers.....	117
4.1.4	Influencing parameters.....	117
4.1.4.1	Introduction.....	117
4.1.4.2	Hexagonality.....	118
4.1.4.3	Crystal orientation and interlayer model.....	120
4.1.4.4	Crystallization of amorphous silica.....	124
4.1.4.4.1	General aspects.....	124
4.1.4.4.2	Cyclic oxidation.....	125

4.1.4.4.3	Time-law	127
4.1.4.4.4	Structural aspects	127
4.1.4.5	Extrinsic impurities	137
4.1.4.6	Intrinsic factors	139
4.1.4.6.1	General aspects	139
4.1.4.6.2	Pores	139
4.1.4.6.3	Intrinsic impurities and bubble formation	142
4.1.4.6.4	Polycrystalline, polymorphic texture	145
4.1.4.7	Atmosphere composition	146
4.1.5	Activation energy and temperature influence.....	147
4.1.6	Passive oxidation at very low oxygen partial pressures	151
4.2	Wet oxidation	153
4.2.1	Introduction	153
4.2.2	Diffusion of water	153
4.2.3	Crystalline silica	155
4.2.4	Oxidation kinetics	155
4.2.5	Structural aspects	156
4.3	Hydrothermal oxidation	157
4.3.1	Introduction	157
4.3.2	Chemical reactions	158
4.3.3	Solubility of silica in water	159
4.3.4	Silica formation	161
4.4	Active oxidation	162
5.	CONCLUSIONS	165

1. INTRODUCTION AND HISTORIC ASPECTS

What was true in 1980 still applies today: “Silicon carbide (SiC) presents a special case, since it has shown so much promise for so long.”¹ Its history dates back to the 19th century, as Jöns Jakob Berzelius, today acknowledged as the founder of modern chemistry, published in 1824 findings about a new compound named “Kohlensilicium” (carbon silicon) with a stoichiometry of Si:C = 1:1.² Later, it was synthesized by C. M. Despretz (1849), P. Schützenberger (1881), and Henry Moissan (1891),³ who was the first to discover natural silicon carbide, which is now named in his honor “moissanite”. By a quirk of history, “moissanite” was discovered with the aid of a SiC impregnated drill - just a few years after this new ceramic material was commercially available.

But it was a scientist originally trying to manufacture synthetic diamonds by recrystallizing graphite in an aluminium silicate melt who must be considered the patriarch of modern ceramic silicon carbide: Edward Goodrich Acheson.^{2,3} He was the first scientist to discover the true importance of SiC; and he established a large-scale synthesis procedure using an electric smelting-furnace newly developed in 1885.⁴ In 1893 already 60.000 grinding discs were manufactured via carbothermal reduction.^{5,6} Acheson was also the first person to call the mainly covalent compound of silica and carbon “Carborundum” (today still present as a trademark). The strange name can be explained by Acheson’s first impression to have found a compound of carbon and alumina as both of these substances were present in the synthesis process.³

However, it took until the 1990s for large, high-quality single-crystals (of just one specific SiC crystal structure) to be processed, enabling more fields of application than the bulk non-oxide ceramic market would provide. Due to this development, silicon carbide was no longer restricted to abrasives use or heat-resistant ceramics. Blue light-emitting diodes, high-frequency devices⁷ or even artificial gemstones⁸ (like the natural phase referred to as “moissanite”) are only three out of many examples for new applications direction.

As far as the use of SiC in electronic devices is concerned, it should be noted that as early as in 1907 the first light-emission of SiC single-crystals was observed.⁹ Once again, SiC obtains a unique position because it was the first material on which this phenomenon (thence called “electroluminescence”) was discovered - 55 years before the first widespread, commercially available (red) LEDs were produced. It is not surprising that SiC today has the merited rank of both being the single most important non-oxide ceramic material and the most promising semi-conductor material to replace silicon-based devices.

Early reports of silicon carbide oxidation date back beyond the 1950s, but it was in the 1980s and especially the 1990s that the oxidation behavior of silicon carbide came on the agenda of scientific research. The development of SiC-SiO₂-compounds, directly applicable as electronic devices (Metal-Oxide-Semiconductor: MOS), has increased the research efforts in this area. Silica can directly be grown by a reaction of silicon carbide within oxygen containing environments. However, unlike silicon oxidation, SiC oxidation behavior is rather complex and still not entirely understood. Not limited to the semiconductor sector, the classic ceramic sector is also interested in SiC oxidation. The chemical inertness of SiC is connected to the formation of a protective SiO₂ layer and the development of this oxide scale – or example whether it develops cracks or shows bubble formation - can limit the fields of application for certain SiC-based devices.

We intend to give a short summary about the current knowledge of structural aspects, silicon carbide oxidation, silica formation, and kinetic aspects. We feel that a review of the silicon carbide/silica-assembly needs to include an overview about the structures and defects in the individual materials, because several features thereof do influence the kinetics of silica growth. It should also be noted that in light of several hundred publications only concerning SiC/SiO₂ interfaces, this article cannot refer to every single aspect but concentrates on some most commonly discussed issues. For more specific information, the interested reader will find a substantial list of references. Time will hopefully bring more insight and understanding of basic aspects of the SiO₂-SiC transition and oxidation kinetics - for the moment many issues remain a matter of current and often vivid dispute.

2. STRUCTURAL ASPECTS

2.1 Silicon carbide and its polytypes

2.1.1 Crystallographic aspects

Silicon carbide is a remarkably structural versatile substance: more than 200 different crystal modifications - called polytypes - are known today.¹⁰⁻¹² Polytypism as a special two-dimensional case of polymorphism is a well-known phenomenon and is particularly present in layer-like structures like graphite (C), molybdenite (MoS₂) or cadmium iodide (CdI₂).^{10,11} Different polytypes differ only in the number of distinct basic units and the way these are connected with each other, while the chemical composition stays the same. Baumhauer described polytypism as early as in 1912 when he studied silicon carbide crystals - hence SiC can be seen the paradigmatic material for polytypism itself.¹²

Silicon carbide is a highly covalent compound of sp³-hybridized silicon and carbon in a stoichiometric ratio of 1 : 1.¹³ As seen in Fig. 1, SiC is the only solid binary compound within the system carbon - silicon.¹⁴⁻¹⁶ The pronounced covalent character can be estimated to be ≈ 88 % and with a ≈ 12 % ionic part from Pauling's formula. Latter can be seen in X-ray emission spectra of Si in form of a small shift of the K_α doublet due to the small positive charge.¹⁴

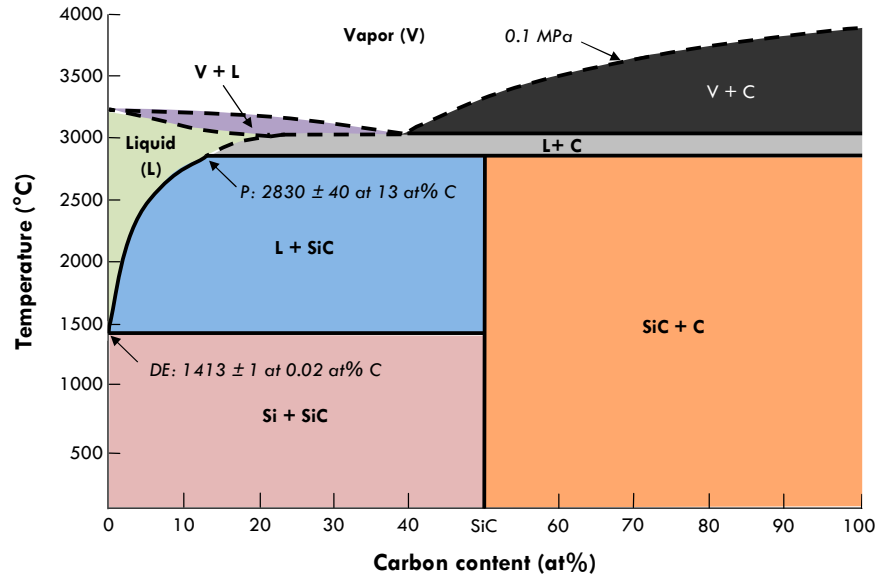


Fig. 1. Binary phase diagram of silicon and carbon showing silicon carbide as the only solid compound phase (after Ref. ¹⁵). At $2830^{\circ} \pm 40^{\circ}\text{C}$ SiC melts peritectically at 0.1 MPa (P). A degenerated eutectic point (DE) can be found at $1413^{\circ} \pm 1^{\circ}\text{C}$ at a carbon content of 0.02 at%. At higher pressures, the sublimation temperature of graphite (3826°C) will shift towards higher temperatures.

The smallest structural units are Si_4C or C_4Si tetrahedra (depending on frame of reference) forming hexagonal Si-C-bilayers subsequent to each other in a discrete stacking order with three distinct sites to occupy (Fig. 2). As shown in Fig. 3, there exist two different kinds of subsequent Si-C-tetrahedra constellation: one resulting in a hexagonal site (Fig. 3a; further denoted as “h”) and one resulting in a cubic site (Fig. 3b; further denoted as “c”) - both just differing in a 60° twist of the upper tetrahedra.

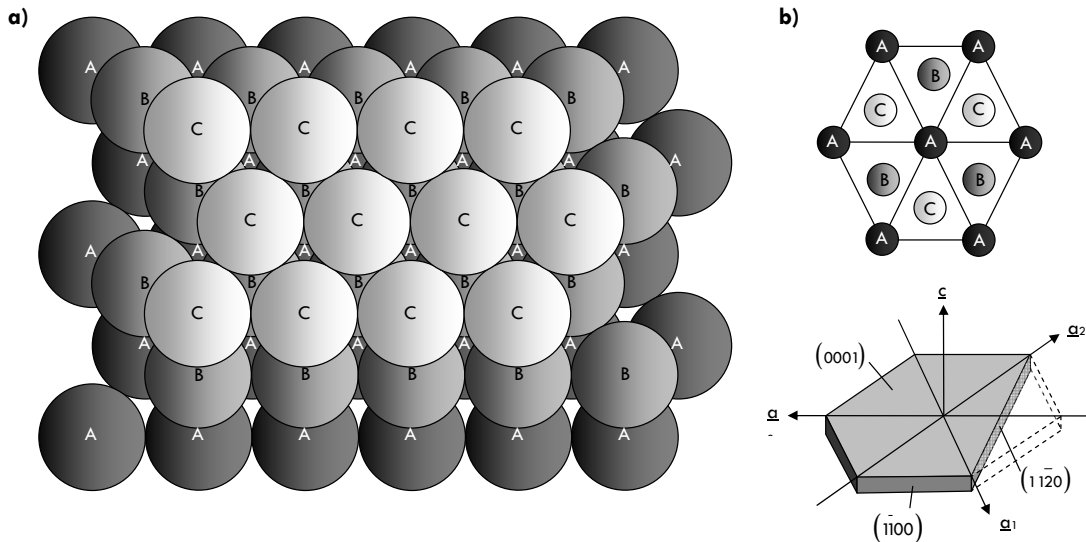


Fig. 2. a) Close-packed sphere model showing three distinct layers (A, B, C). In case of silicon carbide, the stacking order of such close-packed layers determines the resulting polytype. A simple stacking order like the one in the above shown scheme (ABC) would result in a wurtzite structure (3C-SiC) polytype (Ref. ¹⁶). b) Two-dimensional projection representation of the three distinct hexagonal close-packed sphere model sites. c) Low index faces of hexagonal silicon carbide crystals.

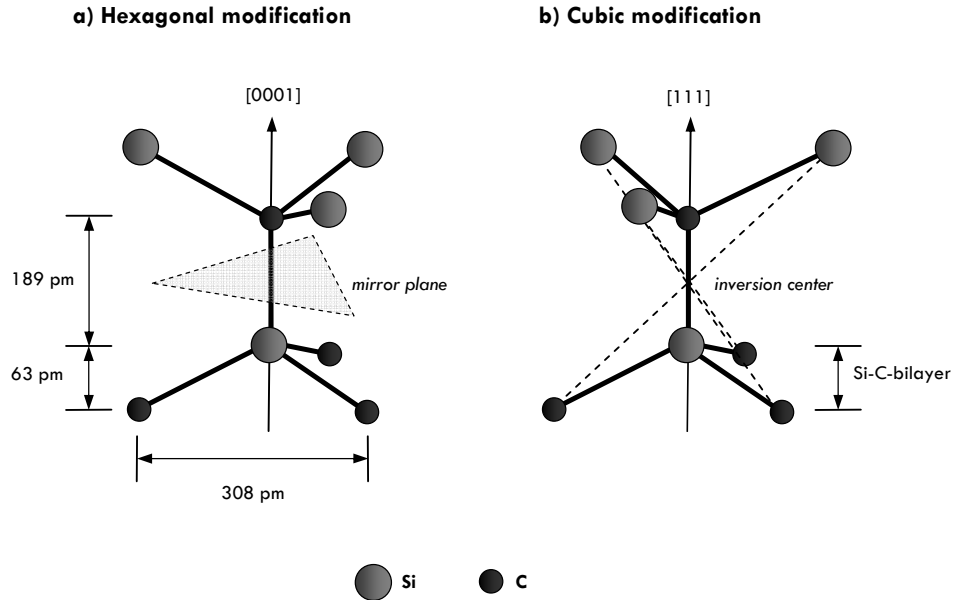


Fig. 3. The basic units of the SiC crystal structure are two interconnected $\text{Si}_4\text{C}/\text{C}_4\text{Si}$ tetrahedra. While the first configuration will lead to a hexagonal modification (a), a twist of the second bilayer by 60° will result in a cubic site within the close-packing sphere model (data from Ref. ^{11,17}).

Depending on this stacking order, different polytypes with different crystal modification will result - like a cubic zincblende-type structure for the sequence ABC or a hexagonal wurtzite-structure in case of AB (Fig. 4). More complex periods will show different crystal structures while the stoichiometric ratio will remain unchanged. Along this stacking order, different terminated surfaces appear. While the (0001) face on hexagonal silicon carbide shows an atomic silicon termination, the opposite $(000\bar{1})$ side of a bulk, truncated crystal will show a C-termination (cf. Fig. 5). Respectively, the (111) face on cubic silicon carbide is silicon terminated and the opposing $(\bar{1}\bar{1}\bar{1})$ side is carbon terminated. This anisotropy - often referred to as polarity - can be distorted depending on temperature and surface treatment as reconstructive processes may take place (as discussed in more detail in section 2.3).

SiC anisotropy is of particular importance because some basic properties, like dissolution or oxidation rate or even interface quality, do depend on which face of the truncated crystal is present.¹⁸⁻²² Also, compression along the c-axis will lead to the formation of opposite electric charges on the opposing Si- and C-terminated faces (piezoelectric effect).¹⁷ As shown by Muehlhoff et al.¹⁷ the crystal structure's "memory" of the present termination can be observed even when disordering the original surface by Ar^+ ion sputtering.

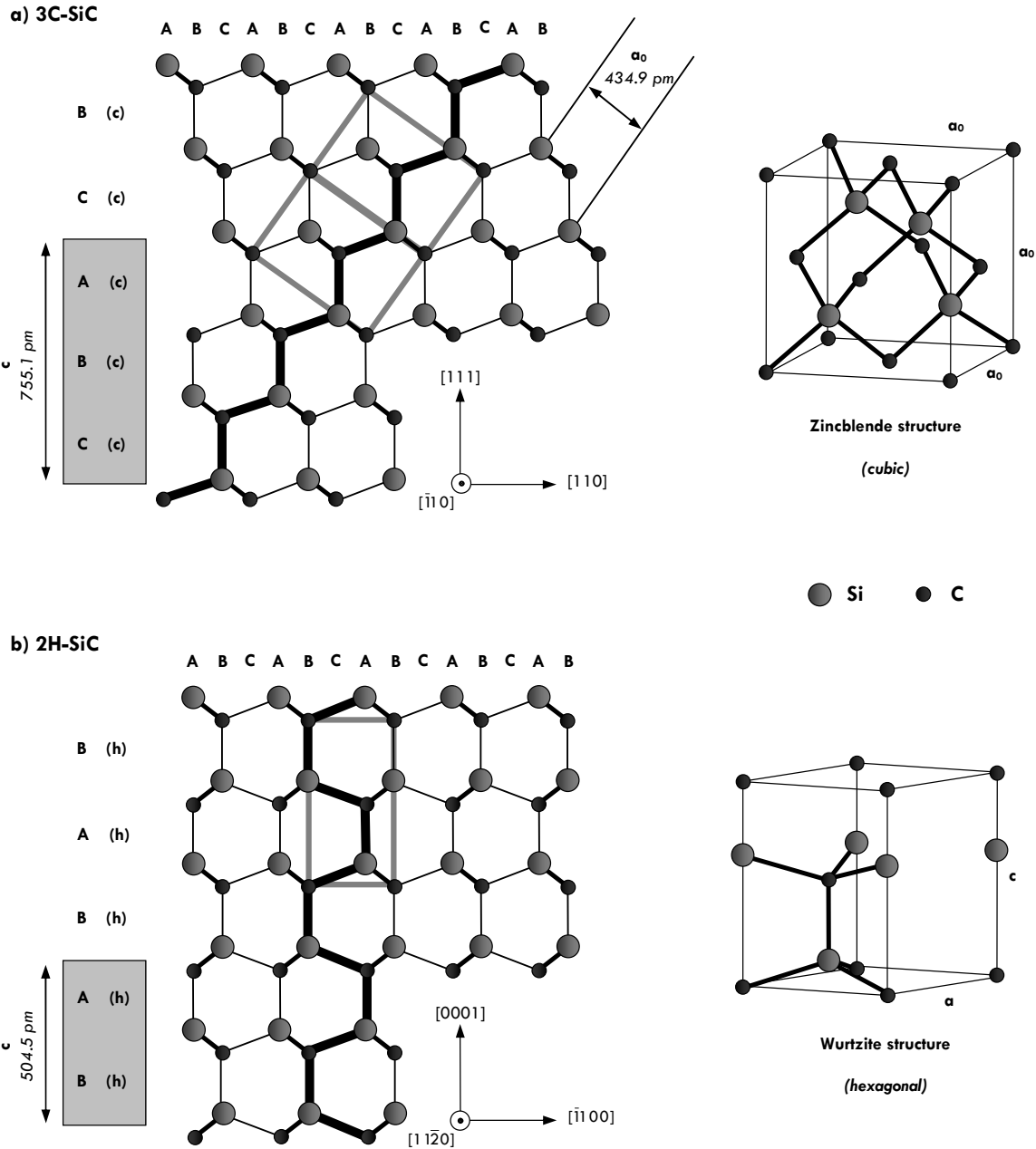


Fig. 4. Two simple crystal structures resulting from hexagonal and cubic close-packed stacking orders. a) 3C-SiC is the very only 100 % cubic polytype exhibiting a strict wurtzite-type structure while b) 2H-SiC represents the only 100 % hexagonal polytype of silicon carbide (zincblende-type structure). Within the zigzag pattern, the outlines of the two unit cells have been marked. The small insets showing crystallographic orientations do apply for the stacking-order model. (h) and (c) denote hexagonal and cubic sites within the stacking order (i.e., whether two Si-C-bilayers form a hexagonal or cubic modification). The structure data is taken from Ref. ¹⁸.

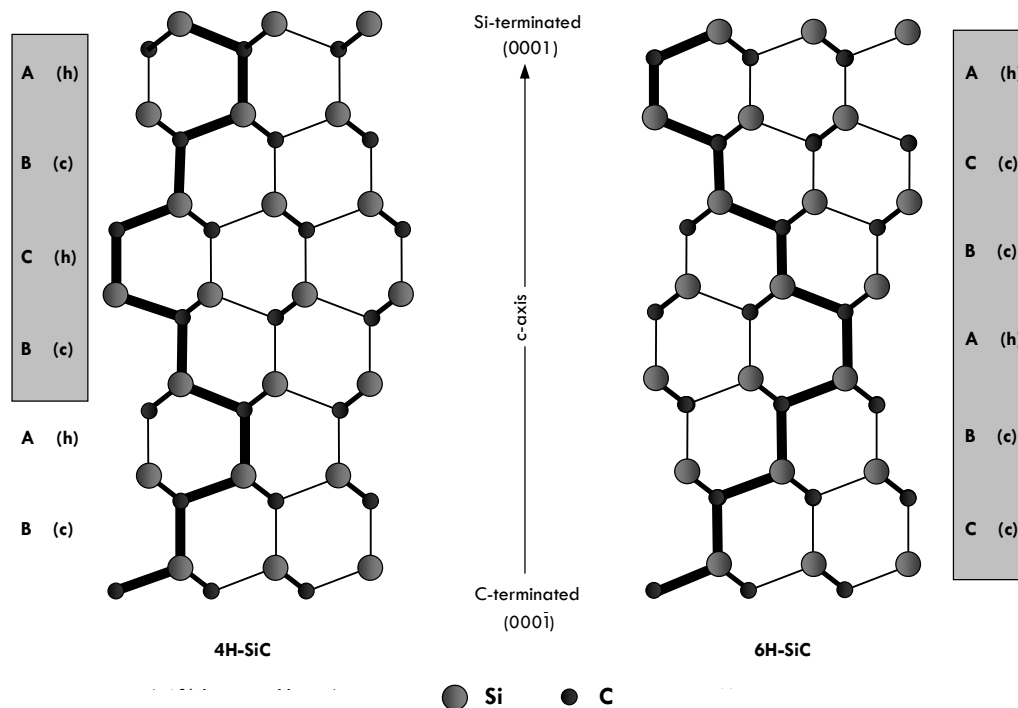


Fig. 5. The crystal structures of the two most important SiC polytypes 4H- and 6H-SiC. As seen in this schematic model, along the *c*-axis two different terminated faces can be found: one silicon and one carbon terminated side. It becomes evident that hexagonal sites are always located at the edges of the zigzag pattern while cubic sites are always within straightforward directed rows.

2.1.2 Nomenclature

It is a wide-spread convention to name the (meta-stable) cubic polytype of SiC (3C-SiC) “ β -SiC” and to accumulate all other polytypes under the term “ α -SiC”.^{14,16,19} This is misleading as it provokes the wrong assumption of a division between low- and high-temperature (or pressure) phases. For clarity, one should specify the SiC polytype at hand in a more accurate and less general manner. The most commonly used notation for the different polytypes - mainly due to its formal shortness - was introduced by Ramsdell in 1947.²⁰ This notation consists out of a digit *n* and letter *S*. The digit *n* denotes the smallest periodicity of the stacking order along the *c*-axis (for uniaxial crystals) or along [111] (for cubic silicon carbide) and the letter *S* the holoedry (C... cubic; H... hexagonal, R... rhombohedral). Holoedry names the point group of highest symmetry of a specific crystal system.¹⁰ In this nomenclature, a hexagonal crystal with the stacking order “abcacb” is designated as 6H-SiC.

The name “moissanite” should only be used for specimens of natural origin - hence moissanite-6H would not be appropriate for a 6H-SiC sample of anthropogenic origin.

Alternative denotations, like the Jagodzinski notation,^{21,22} provide the information of hexagonality by naming the subsequent layers hexagonal (h) or cubic (c). 3C-SiC would, therefore, be called (c) and 15R-SiC (hkhkk)₃ with three succeeding “hkhkk” layers.

Another notation was suggested by Zhdanov (sometimes referred to as “Zhdanov”)¹⁹, who described close-packed structures by determining the zigzag-pattern (forward and backward) along the stacking-order.²³ Rhombohedral polytypes are marked with an indexed “3” and 3C - the only polytype without a change of direction within the zigzag-pattern - becomes the infinity symbol (∞).

In this article, we will adhere to using the Ramsdell notation.

2.1.3 General properties of polytypes

Although most physicochemical (solubility, chemical reactivity ...) and mechanical properties (density, hardness ...) of SiC polytypes are quite similar, some important ones, namely their electrical structures (e.g., band gap width, dielectric constant ...) do differ (cf. Tab. 1, 2). This concerns, in particular, the width of the band gap E_g , which is directly proportional to the degree of hexagonality (i.e., percentage of hexagonal layers in the bulk stacking order) of the polytype. This makes SiC once more exceptional.²⁴ All known ZnS polytypes, for instance, only show a band gap width variation within ± 0.1 eV due to its different electronic structure.²⁵

R	Stacking order	J	ZH	Hex.	SG	Z	CB _{min}	E _g [eV]
3C	abc	(k)	(∞)	0.00	F $\bar{4}3m$	2	X	2.390
6H	abcacb	(hkk) ₂	(33)	0.33	P $\bar{6}3mc$	12	U	3.023
15R	abacbcacbabcbac	(hkhkk) ₃	(32) ₃	0.40	R $3m$	10	X	2.986
4H	abcb	(hk) ₂	(22)	0.50	P $\bar{6}3mc$	8	M	3.265
2H	abab	(h) ₂	(11)	1.00	P $\bar{6}3mc$	4	K	3.330

Tab. 1. Some basic properties of selected SiC polytypes. R denotes the Ramsdell noted polytype (Ref. ²⁰), J the Jagodzinski notation (Ref. ²⁶) and ZH the notation after Zhdanov (Ref. ²³), Hex. the hexagonality, SG the space group, Z the number of atoms within the unit cell, CB_{min} the position of the conduction band minimum within the Brillouin zone and E_g the band gap width (at 2K after Ref. ^{18,27}). It should be kept in mind, that the cubic or rhombohedral X points equal the hexagonal M point. M denotes a point on the L-M line.

	Lattice parameters [pm]			Hexagonality
	a	c	c/n	
3C	308.269	755.124	251.708	0.00
6H	308.086	1511.74	251.957	0.33
15R	308.043	3780.14	252.009	0.40
4H	307.997	1008.30	252.075	0.50
2H	307.860	504.470	252.235	1.00

Tab. 2. Selected structural properties of various SiC polytypes (data taken from Ref. ^{18,19,28,29}). a and c denote lattice parameters while c/n denotes the reduced c-lattice parameter (i.e., reduced by the Ramsdell periodicity). The cell parameters of the cubic phase 3C-SiC have been recalculated to a hexagonal coordination system with the diagonal along [111] to be the c-axis ($a = a_0 / \sqrt{2}$ and $c = a_0 \sqrt{3}$).

The differences within inner energy of different polytypes are very small¹⁹ due to the same character of bonding to the nearest and next-nearest neighbors. This enables different polytypes to coexist next to each other within the same environment without forcing the system to undergo a reconstructive or displacive phase transformation.^{11,19,30,31} A complete transformation of polytypes would require a partial recrystallization, which would be energetically quite disadvantageous for a three-dimensional crystal. This is why such a reconfiguration has only been seen in thin films. However, the ambient conditions during crystal growth seem greatly to determine which polytype will be expressed.^{29,31,32}

From a thermodynamics point of view, the quite low stacking-fault energy (≈ 3 eV per atom) makes almost every periodic stacking-order possible.³³ Only succeeding equal layers - like AA or CC - are forbidden as the criterion of close-packed structures would be violated and the structure itself would become unstable. This explicit periodicity makes a strictly stacking-fault related cause to polytypism unlikely.

Due to its basic structure consisting of Si-C-bilayers, no inversion centers or mirror planes perpendicular to the c-axis are possible. Therefore, only the following space groups can be observed: P $\bar{6}3mc$ (wurtzite structure = 2H-, 4H-, 6H-, 8H-SiC), P $3m1$ (all other hexagonal polytypes), R $3m$ (all rhombohedral structures) and F $\bar{4}3m$ (zincblende structure = 3C-SiC).¹⁶

More than 180 - 250 polytypes are known today^{19,34} and include even some ultra-long periods like 594R-SiC.^{35,36} Of this multitude only few are of particular interest - namely 3C-, 4H- and 6H-SiC. In the optoelectronics industry, the latter two are used almost exclusively.

As pointed out earlier the band gap width E_g of SiC polytypes varies from 2.39 eV (3C-SiC, 0 % hexagonal) to 3.33 eV (2H-SiC, 100 % hexagonal),^{11,19} with a clear dependence between E_g and hexagonality (cf. Tab. 1). On the other hand, all polytypes have almost no difference in the valence band offset (e.g. 0.04 - 0.1 eV at the 3C-6H-SiC transition).³⁷⁻³⁹ These ESR (Electron Spin Resonance) findings are in accordance with results derived from internal photoemission of holes by Afanas'ev et al., who did not find any significant difference at all within a ± 0.1 eV range of error.^{40,41}

The differences in E_g also determine the different colors of the various SiC modifications. Doped SiC crystals will change the "native" color - for example from colorless (undoped SiC) to red (4H-SiC when doped with vanadium). Heavy doping ($> 10^{18} \text{ cm}^{-3}$) results in almost black color while all undoped SiC polytypes are all colorless-transparent. In case of *n*-type SiC:N specimens with same doping-level, 3C-SiC shows a light yellow color, while 6H-SiC is green and 4H- and 15R-SiC are both rather brownish.⁴² Nitrogen is the reason why high-purity SiC samples derived from the Acheson process have their typical green coloration. Doping SiC, for example, with boron or aluminium (*p*-type SiC) yields bluish coloration (cf. Ref. ^{43,44}). Bulk SiC samples synthesized via carbothermal reduction using the Acheson method show a dark black color with strong metallic luster due to Al (maximum solubility 2 wt%), B (maximum solubility 5 wt%) and related impurities.⁵

Also, some small variations of the lattice parameters (like the reduced c-axis parameter) of silicon carbide polytypes have been found (Tab. 2).⁴⁵ With increasing hexagonality, the unit cell will be contorted and it will show both a larger reduced cell parameter c/n (*n* denoting the periodicity of the stacking order) and a smaller lattice parameter a .^{31,45,46}

The correlation between hexagonality and both lattice parameters or band gap widths (correlating with experimental minimum band gap widths) is only linear between 0 % and 50 % hexagonality (i.e., between 3C- and 4H-SiC) while there are only minor changes at a higher hexagonality values (i.e., 2H-SiC; cf. Fig. 6). This behavior is well known as the Choyke-Hamilton-Patrick rule.^{28,39,43,47} Theoretical calculations of band gap minima (being located around the M point or between the M and L point for hexagonal polytypes and at the X point in the case of 3C-SiC) seem to prove this observation.^{24,48,49}

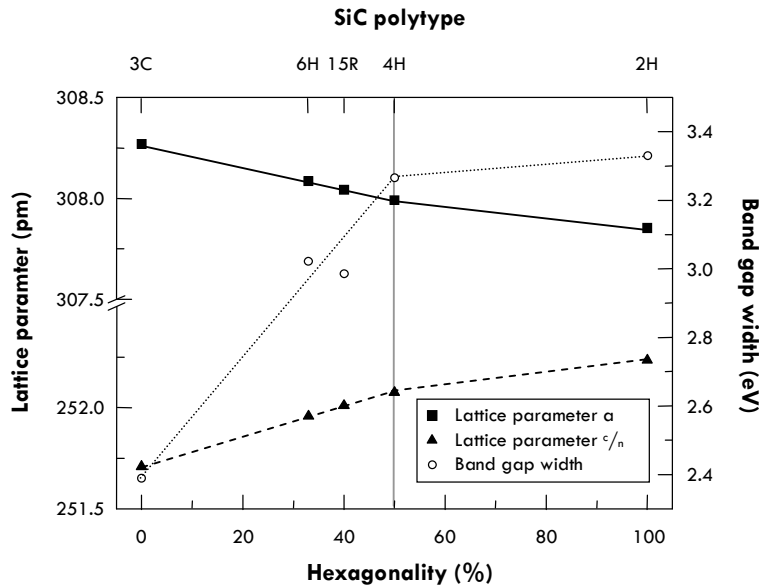


Fig. 6. Graphical illustration of the correlation between hexagonality and lattice parameters/band gap width.^{24,29,50} Between 0 % and 50 % (grey intersect) hexagonality, an almost linear correlation can be observed for experimental values (for further discussion of minimum and k-specific gaps in SiC polytypes see Ref. ²⁴).

2.1.4 Origin of polytype formation

Since polytypism of SiC was first described by Baumhauer,¹² scientists struggle to explain its origin. Still today, the origin of polytype formation is a matter of vivid dispute as our basic understanding of this phenomenon is quite limited.^{19,31} A simple impurity derived cause for polytype formation, as proposed by Lundquist,⁵¹ can be ruled out. However, the bulk crystal growth ambient parameters (amongst which impurities are one essential factor)⁵² greatly influence polytype growth and formation. Generally, there are two categories frequently used to explain polytypism: growth conditions (involving screw dislocations) and thermodynamic considerations⁴⁶ - but until now, no satisfactory model containing both theoretical approaches has yet been accomplished which would explain the complex polytypic transformations at elevated temperatures.

A model proposed by Frank et al. explains polytype growth and formation in terms of screw dislocations.⁵³ During crystal growth a polytype can be considered to grow stable, when the Burger's vector of the screw dislocation and the unit cell (or an integer multiple of latter) are equal. Otherwise (for non-integer Burger's vectors) a new polytype will form and grow.^{16,54} Long-period polytypes would, therefore, be created out of simple basic structures and spiral growth mechanism. Later, Pandey et al. expanded Frank's screw dislocation model by explaining structural anomalies by the concept of a "faulted matrix".⁵⁵ Their concept suggests that not only basic stacking orders (like 2H- or 3C-SiC) but also faulted matrices should be used to deduce long-period polytypes. Unfortunately, screw dislocation models fail to satisfactorily explain the occurrence of long-period polytypes and the explanation of this being the result of a radial impurity gradient does not satisfy.⁵⁶ Also, bulk crystal growth of a three-dimensional crystal cannot be satisfactorily explained in terms of growing screws theory.³¹

As for the second category - thermodynamic considerations - almost every SiC polytype has the very same inner energy (as stated earlier). Jagodzinski introduced a model estimating that 12 % disordered Si-C-bilayers would be sufficient to lead to the energetically most advantageous configuration due to calculations of the vibrational and configurational entropy.²⁶ More recently conducted studies (Ref. ^{46,57}) show small differences in energies between the various polytypes in the range of some meV (Ref. ⁵⁷) or even below (Ref. ⁴⁶), hence suggesting the existence of different thermodynamically stable polytypes for certain p-T-ranges. Yet, until now, no direct phase transformation of the two most frequently found phases, 4H- and 6H-SiC, has ever been observed – suggesting these phases to not be true thermodynamically distinguishable phases (as proposed by Verma et al.).¹⁶ It should be kept in mind, that during sublimation growth (e.g., within the modified-Lely-method; Ref. ^{58,59}) these small energetic differences are opposed by thermal energy that is several orders of magnitude larger. Especially for the production of large-scale single-crystal SiC specimens, the basic understanding of polytype formation limits the success of controlling single-polytype growth. The monitoring of all possibly influencing factors, like the growth temperature,^{60,61} derivations from the ideal stoichiometry/impurities ^{29,62} or the seeds face-polarity ⁶³ make SiC single-crystal growth a technically challenging procedure.⁶⁴

Due to their most frequent occurrence as significant phases, 4H-, 6H-, and 15R-SiC seem to be energetically advantageous phases at elevated temperatures while the cubic SiC phase and 2H-SiC undergo irreversible phase transformations. All other phases (like 21R-, 33R- and 8H-SiC) only occur in minor amounts. Long-period polytypes sometimes are explained to be the result of screw-dislocations (with non-integer Burger's vectors) derived from basic structures like 4H-, 6H- or 15R-SiC. However, doping level, growth rate/temperature and other growth related parameters also greatly influence polytype formation, stabilization, transformation and growth.

An alternative, but not widely accepted, model is the existence of a superstructure or superlattice.^{43,65,66} This model suggests that all polytypes can be derived from a disordered 3C-SiC structure as a result of a superperiodic potential creating ordered long-period polytypes. However, no real experimental evidence for this mechanism was yet supplied.

2.1.5 Defects in silicon carbide single-crystals

2.1.5.1 GENERAL REMARKS

Defects in SiC single-crystals greatly limit fields of application and influence physicochemical as well as electrical properties. Therefore, significant efforts were undertaken over the last decade to achieve the low present-day defect concentration in commercially available silicon carbide wafers. All these developments show that SiC single-crystal growth technology grows out of its infancy.

The manufacturing process determines largely the observed defects of the product. SiC crystals cannot be grown using a melt method (like the methods developed by Verneuil⁶⁷ or Czochralski⁶⁸) under easily achievable conditions, because temperatures above 3200°C and pressures above 10 GPa would be needed to melt stoichiometric SiC.^{69,70} Therefore, silicon carbide wafers are usually grown using a vapor growth technique. Most standard wafers are grown by Physical Vapor Transport (PVT) and epitaxial SiC layers or thin films by Chemical Vapor Deposition (CVD). In both procedures a significant influence by the properties of the substrate and eventually occurring structural misfits can be observed.⁷¹ Also, the orientation of the crystal, that is, the growth direction, has a great influence on the occurrence of defect structures.

The defects occurring in SiC from PVT are (1) micropipes (and related screw-dislocations), (2) low-angle boundaries (as a source of further dislocations), (3) stacking faults, (4) (polygonized) voids, (5) polytypic inclusion and (6) graphitization/silicon droplet (Fig. 7). Out of those, the first two defect types are the most important and most limiting ones, but all defect types may be present in silicon carbide to various extent and should be critically evaluated when conducting studies of SiC structural properties, the chemical behavior or the electronic structure of SiC/SiO₂ interfaces (cf. section 2.4.).

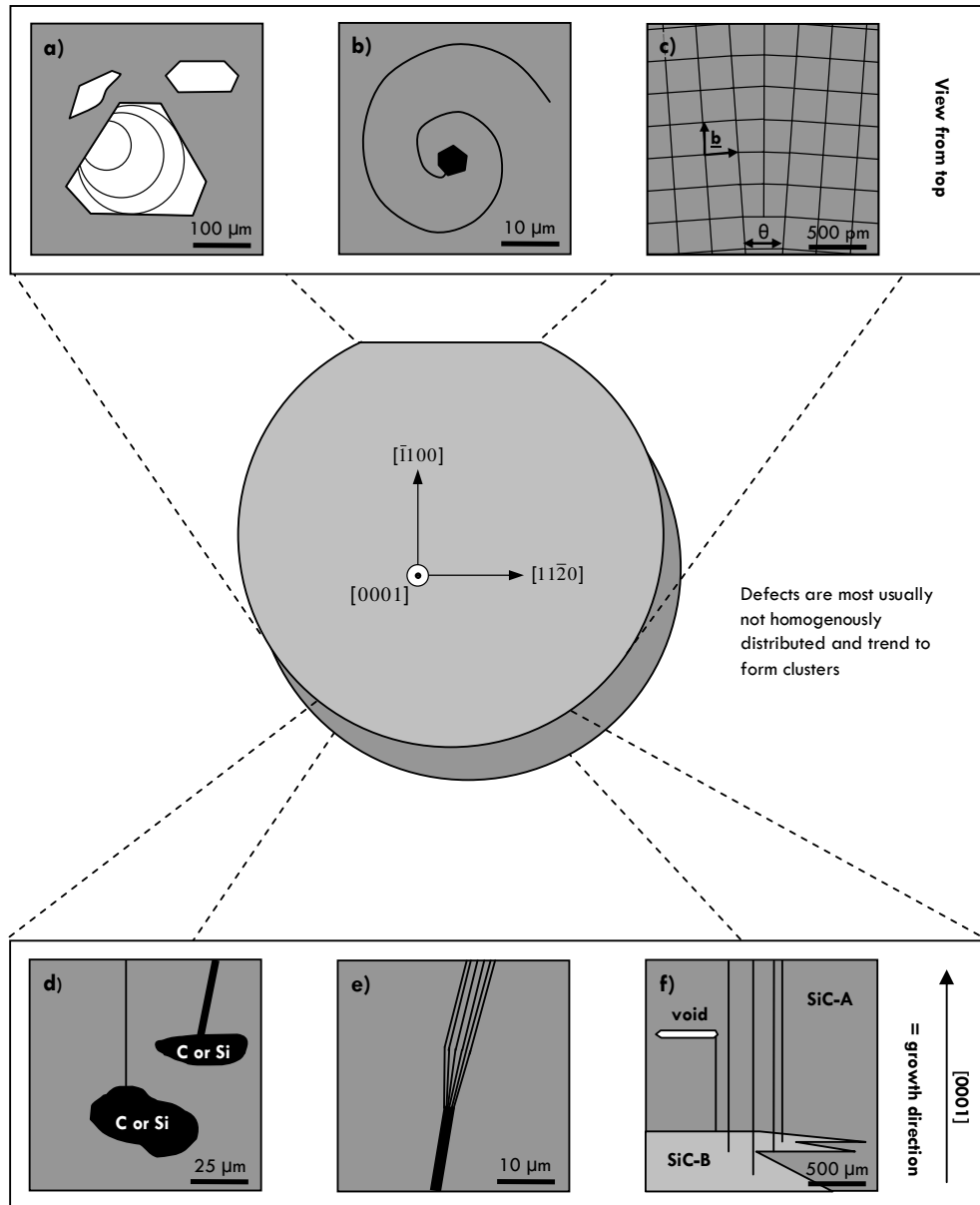


Fig. 7. Some commonly observed defect types found in SiC single-crystals grown by PVT perpendicular to the c -axis (a - c) or parallel c (d - f). a) Hexagonal or hexagonalized voids (rather two-dimensional defect type with visible macrosteps), b) macropipe as a central structure within a growth spiral, c) low-angle grain boundary leading to the well known domain structure ("mosaicity"; θ = angle of misalignment; \underline{b} = Burger's vector) of silicon carbide, d) micro- and macropipe formation (mostly along the growth direction, i.e., mainly along c -axis) correlated with local impurities (graphitization and silicon droplets as two possibilities), e) one single macropipe dissociating into several smaller superscrew dislocations (micropipes), f) hollow-core screw dislocation and void formation accompanying polytypic inclusion formation (polytypes SiC-A and SiC-B).

2.1.5.2 TECHNIQUES FOR DEFECT CHARACTERIZATION

Naturally, defects can be observed and characterized by high resolution methods such as Scanning or Transmission Electron Microscopy (SEM or TEM respectively), Atomic Force Microscopy (AFM) and detailed information about crystallographic misalignment is obtained via Synchrotron White Beam X-ray Topography (SWBXT) and High-Resolution X-Ray Diffraction (HRXRD).⁷²⁻⁷⁷

The coarsest method to make some defects evident is a visual inspection using optical microscopy (e.g., Nomarski Differential Interference Contrast NDIC) after salt melt corrosion (cf. section 2.1.5.3.3).

A particularly easy method to characterize defects in SiC is Polarization Microscopy (PLM). It is recommended for the first inspection. With transmitted light microscopy and crossed polarizers, a conoscopic image of the crystal can, first of all, tell about the actual orientation. For instance, the optical uniaxial crystal 6H-SiC will show a movement of the isogyres on the (0001)-face during sample rotation when it is not cut perfectly perpendicular to the c-axis. On the other hand, no movement will confirm a true (0001)-face, that is, a cut perpendicular c.

Undulatory extinction will be seen in strained areas of silicon carbide crystals (e.g., when using thin section techniques or transparent crystals). This useful feature will be easily shown in transmitted light mode with crossed polarizers e.g. micropipes (cf. section 2.1.5.3.3). Correspondingly, the isogyres of a strained section will show an anomalous biaxial figure (i.e., a small opening of the central cross = melatope).

Another relatively easy method is Raman spectroscopy. It allows to detect polytypic inclusions or inclusions of graphite or silicon.^{78,79} Secondly stacking faults can be examined, because they lead to a break-down of the wave vector selection rule.^{80,81} Furthermore Raman-mapping is an interesting method for micropipe detection,⁸¹ because carrier trapping centers are densely present around micropipes and cause a well known shift in the position and an increase of the width (Full Width at Half Maximum FWHM) of the LO-phonon mode by phonon-plasmon coupling (LOPC).⁷⁸ However, this is only significant when investigating *n*-type (0001)- α -SiC.^{82,83}

Hexagonal voids can also be examined using Raman-mapping as the edges of the single voids are not perfect perpendicular to the growth direction hence different faces will attribute to the total Raman signal and different relative band intensities will occur.

2.1.5.3 MICROPIPS AND MACROPIPES

2.1.5.3.1 Origin and basic features

Hollow tube-shaped defects, called micropipes, are long known to be present in SiC (Ref. ^{84,85}) but occur also in other crystalline materials like CdI₂⁸⁶ or ZnS⁸⁷.

The commonly observed, preferential direction of these defect structures for hexagonal silicon carbide is parallel to the c-axis⁵⁰ with very little aberration to it. The deviation seems to be related to faceted growth: micropipes on areas, where faceted growth occurs, are almost ideal orientated along the c-axis, micropipes grown on non-faceted areas can occur with a certain angle in respect to the c-axis itself.^{31,88} However, also randomly orientated, short range micropipes have been observed.⁶¹

Varying the growth direction to another orientation will lead to decreased micropipe formation or even micropipe-free wafers.^{89,90} However, other growth directions yield an increased formation of stacking faults.^{91,92}

Typical diameters of micropipes range from a few nm up to more than 5 μm . Latter are sometimes referred to as “macropipes”⁹³ (and more rarely as “channels”⁶³, “pin-holes”⁹⁴ or “microchimnies”⁹⁵) but a clear differentiation between the two is not made (especially since macropipes can split into a bundle of several micropipes). Further confusion in terminology is related to articles by Pirouz, who used the expressions “nanopipes” and “micropipes” for the categories “micropipes” and “macropipes” of this review.⁹⁶

Macropipe formation is still not entirely understood. It was speculated that sublimation processes may explain macropipe formation on surfaces and defect structures.^{63,97}

A more generally accepted line of discussion about the origin of micropipes is associated with Frank's theory⁵³, in which a micropipe would be associated with a screw dislocation characterized by a Burger's vector with a length several times (n) of the unit cell length in growth direction¹⁶ (“superscrew dislocations”). As discussed by Pirouz,⁹⁶ open-core dislocations of nc length are capable of attracting m (conventional) closed-core dislocations ($1n$) c and incorporating them by increasing their diameter and becoming a $(m+n)c$ superscrew dislocation.

It is possible to describe the micropipes' diameter by means of Frank's equation⁵³ as a function of the Burger's vector, the shear modulus and the specific surface energy (later, this model was expanded for kinetic considerations).⁹⁸⁻¹⁰⁰ The relationship between screw dislocation site nucleation (i.e., including micropipes) and contaminations by foreign materials (like graphite or silicon particles/droplets or even voids)¹⁰¹ is very likely but still a matter of current research (for further reading see Ref. 58).

The circumstance of growth spirals that originate at micropipe centers shows a clear correlation between Frank's theory and observed micropipes. Important influences in micropipe formation can be seen during single-crystal growth in dislocation formation, vapor phase composition (thermodynamic factors), process instabilities, contaminations, seed preparation (technological factors), and nucleation processes, constitutional supercooling, growth face morphology (kinetic factors). Critical control of these factors and high-quality seed material can even yield to (almost) micropipe-free wafer fabrication.^{89,102} Defects in low-quality seed materials for epitaxial growth will trace to the growing adlayer and different kinds of defects can possible lead to micropipe formation (like inclusions¹⁰¹, stacking-related defects^{100,103} and grain boundaries⁹⁶). For further reading on this topic, e.g. possible correlation between growth pits and micropipes, see Ref. 50,58,102,104.

It is a matter of dispute how long the Burger's vector has to be in order to lead to micropipe formation. Si et al. (Ref. 105) found no micropipes shorter than ≈ 1.5 nm (i.e., approximately the length of the unit cell along the c -axis of 6H-SiC), which is understandable in terms of the need of a screw dislocation being longer than just one unit cell length. It seems that a value above 3 nm (i.e., a minimum of two times the c -axis length of 6H-SiC and three times that of 4H-SiC) would be a good starting point for estimating the limiting shortness of micropipe forming Burger's vectors.^{105,106}

However, also hollow-core screw dislocations were found for Burger's vectors as small as 1.5 nm for 6H-SiC .⁹⁹ This different minimum Burger's vector lengths may be explicable in terms of different growth conditions and/or the necessity to include an edge component in the evaluation of screw dislocation components.¹⁰⁰ However, the existence of such an edge component is questioned by different authors in more recently published studies but corroborated by polarization microscopy results.^{73,74,95,107}

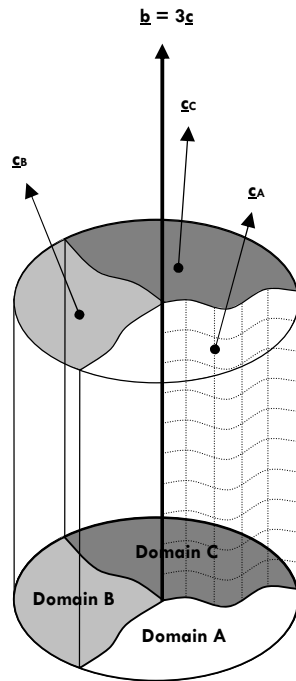
Promoted by a high level of mechanically induced stress, it becomes energetically more advantageous to form rather a hollow-core than a closed-core dislocation during single-crystal growth, as more elastic stress-related energy can be saved than surface energy must be spent. In this context, micropipes can be seen as hollow-core screw dislocations (in contrast to closed-core screw dislocations - another type of defects well present in SiC single-crystals). Mainly, micropipes occur along the c-axis, which is also the polytype propagation direction (i.e., stacking order direction) and which is most often chosen to be the growth direction.⁷³

As for the native origin of a micropipe, a mosaicity related origin (i.e., related to the domain structure of PVT grown SiC wafers as discussed in section 2.1.5.4) was proposed.⁹⁶ This could be accommodated by considering three distinct domains within the SiC crystal structure. All three domains are characterized by small twist dislocations in respect to each other (cf. Fig. 8). In the case of small grain boundary angles, the twist between the domains can be accommodated by a set of conventional, closed core screw dislocations with a Burger's vector of $\underline{b} = \underline{c}$. Vertical grain-boundary dislocations are characterized by line directions parallel to the c-axis, whilst horizontal grain-boundary dislocations lie perpendicular to the c-axis. In the case of tilt and twist between two domains, a mixture of both edge and screw dislocation components will be found perpendicular to the c-axis for horizontal grain-boundary dislocations.⁹⁶ At the triple-point (t.p.) - in case all screw dislocations are in the same sense - a Burger's vector $\underline{b}_{tp} = 3\underline{c}$ will be found, creating a hollow-core superscrew dislocation. With an attractive force to conventional screw dislocations lying close to the triple junction, increasing the diameter of the open-core screw dislocation simultaneously increases its attractive force. Latter was postulated to exist as a dislocation near a surface, that is, near the newly created open-core surface, being less constrained than within a solid crystal.⁹⁶

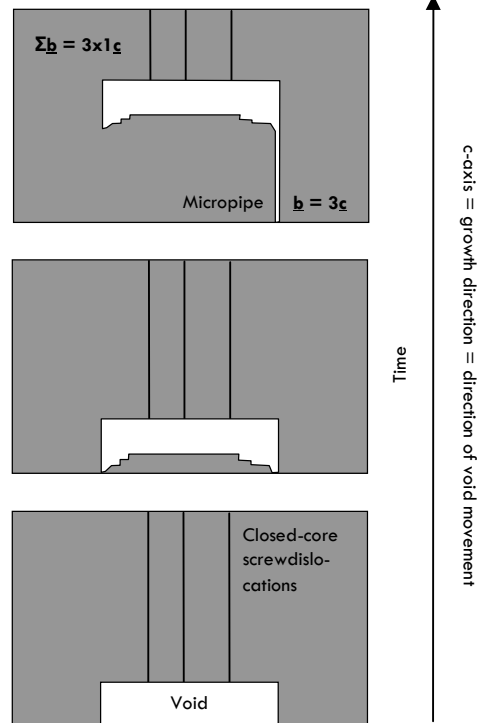
Overgrowth (Fig. 8b) and the movement of hexagonal voids are other possible ways to form micro- or macropipes (Fig. 8c). In the overgrowth model, it is assumed that two macrosteps approach each other after overgrowing an obstacle (like foreign material in form of a void, an inclusion or some sort of impurity). Due to their different height and the faster feed of the overlapping edges, an overhanging ledge is formed, that on its behalf is susceptible to deformation. Depending on the kind of overgrowing material, a depression (for voids) or elevation (for solid material) of the overhanging ledge can be assumed. A Burger's vector with a magnitude of the step height difference will, therefore, compensate for the misalignment.¹⁰¹

The model of the movement of polygonized voids along growth direction was motivated by the observation of micropipes sometimes to be terminated by voids.⁷⁰ As deduced by Kuhr et al.,¹⁰⁸ this phenomenon can be explained by voids moving along the growth direction (i.e., through a process comparable to PVT growth itself). These voids will terminate closed-core dislocations (1c) and on their top and beneath the void micropipes may originate opposing the growth direction in order to preserve the same Burger's vector (cf. Fig. 8).¹⁰⁸ Typically, these void terminated macropipes are not strictly limited to directions along the c-axis, but often show a convoluted geometry.¹⁰⁹

a) Domain-related origin



b) Void-movement-related origin



c) Overgrowth-related origin

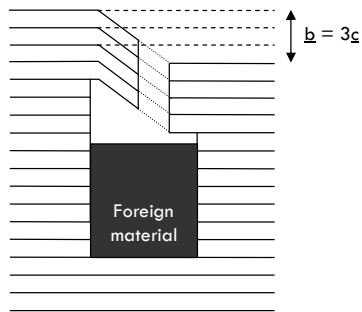


Fig. 7. Different models for formation of a $b = 3\epsilon_c$ micropipe. a) Domain-related origin (after Ref. ⁹⁶), b) void-movement-related origin (after Ref. ¹⁰⁸), c) overgrowth-related origin (after Ref. ¹⁰¹). The overgrowing material could be anything from voids, impurities or inclusions.

2.1.5.3.2 Defect density and quality control in SiC

Sometimes micropipes were referred to as “device killers” or “killer defects” for the electronic use of a SiC based device¹¹⁰. As pointed out by Davis et al.¹¹¹ and Powell⁵⁰, a MicroPipe Density MPD below 15 cm^{-2} is critical for the application to the majority of device structures.

Today commercial PVT grown SiC 2” wafers with a MPD $< 30 \text{ cm}^{-2}$ are available, state-of-the-art 3” wafer can reach a MPD as low as $\leq 5 \text{ cm}^{-2}$ and MPDs of $\approx 1 \text{ cm}^{-2}$ are technologically possible for 4H-SiC 2” wafers.¹¹² Furthermore, micropipe-free SiC single-crystals have been grown by the modified Lely method.⁵⁸

Liquid Phase Epitaxial (LPE) growth has proven to be a method to remove micropipes with an efficiency up to 90 % - depending on thickness of the LPE layer¹¹³ - by capillary action during liquid phase growth near the solid-liquid-contact and higher supersaturation for growth from concave shaped liquids near the seed interface (as the capillary forces form menisci).¹⁰⁹

Besides the possibility to alter the growth direction or carefully control the growth conditions, another method to decrease MPD shall be mentioned briefly. While on CVD materials a lattice misfit induced transformation of hollow-core to several closed-core micropipes has been observed depending on process conditions (like the C/Si ratio),^{114,115} PVT grown materials inherit the elimination of superscrew-dislocations by an overgrowth mechanism.⁷¹ As suggested by Yakimova, different closing mechanism of micropipes or different kinds of hollow-core screw dislocations may be present for different growing procedures.⁶⁴

Another mechanism, the dissociation of micropipes into several 1c closed-core screw dislocations (occurring mainly in the initial stages of CVD growth), and other possible influencing factors are still topics of present-day research.^{114,116}

Further improvement of crystal growth conditions will certainly lead to decreased MPD values for even larger SiC single-crystals and ultrahigh-quality or even micropipe-free wafers are in the grasp of feasibility.^{93,102,117-119}

However, it should be borne in mind that the density of closed-core screw dislocations is unlikely higher (in a range of 100 cm^{-2}).⁷⁴

2.1.5.3.3 Analyzing micropipes

Under the optical microscope, micro- and macropipes can be seen as small, dark tubes. They are seen more easily after etching with, for example, molten potassium hydroxide (KOH) at $> 450^\circ\text{C}$,^{70,120} because areas of increased structural strain around screw dislocations of all kinds will lead to a preferential etching of these areas^{70,94} and so the opening of the pipe on the crystal face surface will be easier to be identified.³¹ An alternative, non-destructive way for defect decoration has been described by Yakimova et al.¹²¹ by using electrolytic dissolution. It should be kept in mind that micropipes and related screw dislocation defect structures are not homogeneously dispersed within a single-crystal but often tend to form clusters.

As discussed in detail by Kato et al.,^{1,22} an improved way to make micropipes visible under the light microscope is by using the crossed polarizers condition. Thus, a unique interference pattern will be created by the distribution of internal stress. These “bright star patterns” will change by rotating the sample; and due to their larger diameter in comparison to that of the originating micropipes, they indicate very precisely the position even of smaller micropipes (Fig. 9). The origin of these halo like patterns is strain acting perpendicular to the c-axis as normally no birefringence can be seen on the (0001)-face on uniaxial crystals like hexagonal silicon carbide (since the c-axis and the optical axis converge).^{1,22}

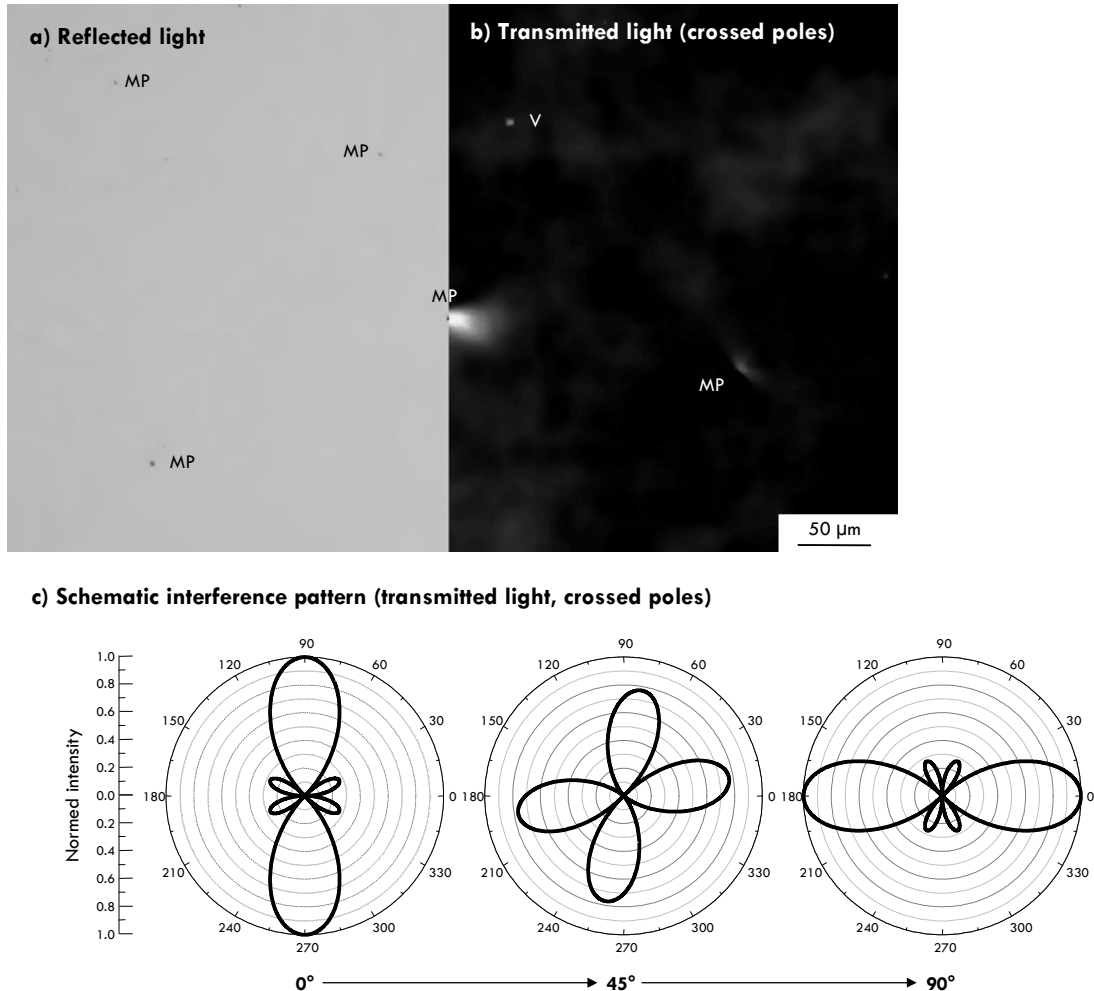


Fig. 7. Comparison of reflected light (left part, a) vs. transmitted light with crossed polarizers (right part, b) pictures of a 6H-SiC:N wafer cut perpendicular the c-axis. As seen in the middle, the central micropipe (MP) with an approximated diameter of 3 μm is much better visible with crossed polarizers since the interference pattern (halo) has a lateral width of $\approx 50 \mu\text{m}$. For the effect of strained areas on the conoscopic image, see Fig. 10. Also, a single, small-sized polygonized void can be seen (V). With an inserted red I compensator (λ -plate: 551 nm), the interference pattern will show different colors indicating the distribution of internal stress. c) Schematic interference pattern showing contours of same intensity when rotating the sample under crossed polarizers using 45° steps.

This behavior, well known from natural, deformed quartz grains, is referred to as undulatory extinction due to a locally anomalous biaxial optical character (cf. Fig. 9).¹²³ It is clear that simple polarization microscopy is, therefore, capable of characterizing strained regions in SiC in general and especially around micropipes (as long as the stress field is large enough for optical resolution) as well as off-axis orientations (by conoscopic imaging; cf. Fig. 10).

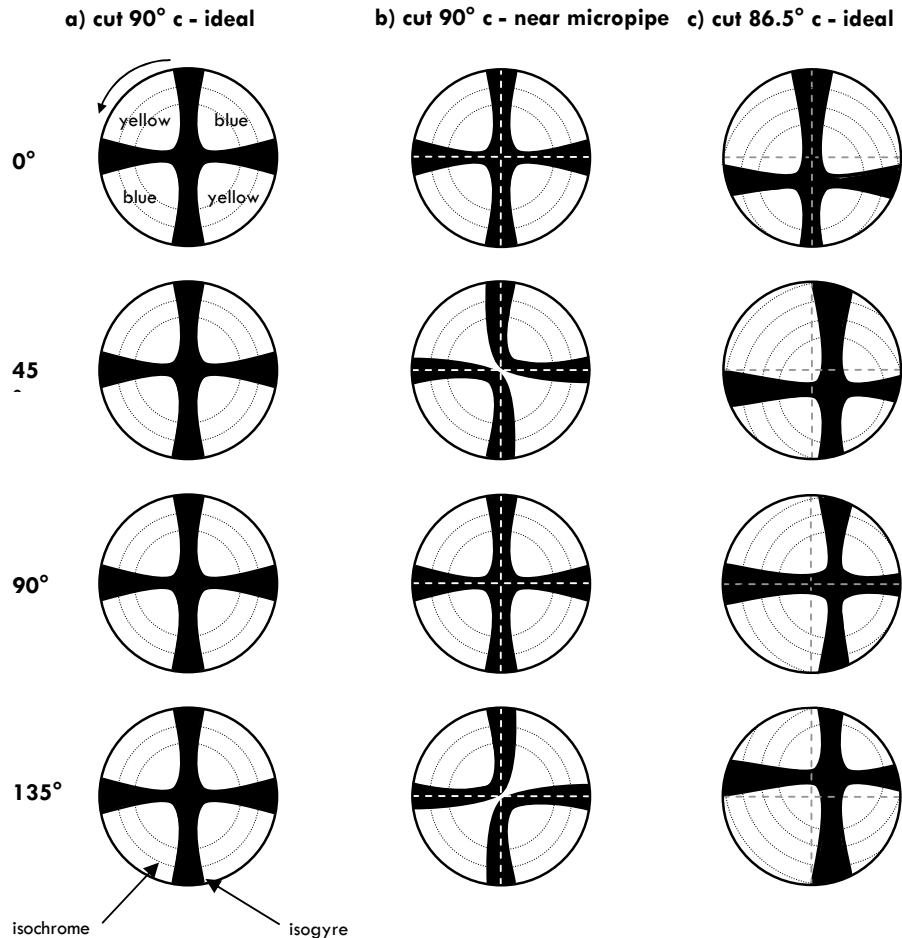


Fig. 10. Schematic conoscopic images of a 6H-SiC:N-wafer cut perpendicular c (a, b) and with a 3.5° inclination towards the c-axis (c). The rotation was conducted anticlockwise. As shown in the first figure, the colors denote the birefringence colors when the red λ -plate (551 nm) is inserted. The observed pattern shows the positive optical uniaxial character of 6H-SiC. a) Usually, the conoscopic image only shows centered, closed isogyres. b) Due to strained areas around e.g. micropipes, the optical uniaxial crystal becomes locally anomalous biaxial and the isogyres will slightly open. c) In comparison, a wafer cut with an offset towards the c-axis will ideally show closed isogyres that are not centered.

2.1.5.4 LOW-ANGLE BOUNDARIES

A prominent feature of PVT-grown SiC is the tendency to form a pronounced mosaicity (domain structure) with domain-boundaries characterized by a high level of dislocations.^{94,124,125} Low-angle boundaries that extend radially inward from the crystal's periphery¹²⁶ are especially seen on large-diameter SiC wafers and can be drastically reduced by thoroughly controlling the growth conditions.¹²⁷ As indicated by X-ray topography, these domain-like structures show quite small misorientation angles (60 - 540 arcsec; increasing towards the center and radially decreasing towards the edges)^{126,128} and almost no further defects within.^{94,126} For a complete analysis of orientational variations both "on-growth-axis" and "off-growth-axis" reflections have to be considered for triple-axis X-ray diffraction. In case of 6H-SiC grown along the c-axis, (1) (00l) and (2) (hkl) diffraction peaks yield information about (1) lattice planes parallel to the basal plane or (2) planes tilted towards the basal plane.⁹⁴

At least some low-angle grain boundaries seem to be composed out of edge dislocations heading along the growth direction¹²⁹ originating from non-basal plastic deformation. Basal deformation on its behalf would lead to basal plane dislocations, as observed in 4H- or 6H-SiC, because basal planes are the primary slip plane of these structures. Due to thermoelastic stress during PVT growth, the basal (0001) $[1\bar{1}20]$ glide system is quite easily activated.¹³⁰ In the case of pure tilt low-angle grain boundaries, these threading edge dislocations are believed to align by polygonization during post-growth cooling to reduce the total strain energy.¹²⁹ Arrays like these can often be observed after KOH etching, that is, making dislocations visible for light microscope analysis. As expected from the discussed statements made before no significant strain associated with such low angle-grain boundaries was measured and these interfaces are considered to be in a relaxed state.⁹⁴

A second type of domain structures, as pointed out by Kuhr et al.¹²⁶ and Ha et al.¹²⁹, shows a combination of tilt and twist components. Both types are distinguishable by means of High-Resolution X-Ray Diffraction (HRXRD) mapping with various orientations and reflections.¹²⁹

There are also differences between various sublimation deposition processes: The typical domain-structure of silicon carbide wafers (mosaicity) is quite pronounced for single-crystals grown by the seeded or modified Lely method¹³¹, while classical Lely platelets¹³² do not show this feature to this extent.⁷⁰ This was explained by a larger amount of nucleation sites for growth centers and the possibility of those to be misorientated in respect to each other⁹⁴ in the case of the modified Lely method, as lower temperatures and higher super-saturation environments are applied there.⁷⁰ The spiral growth mechanism is supposed to be a dominant process, thus the initiation of independent growth centers (nucleation) during growth seems very plausible. Low-angle grain boundaries may, therefore, be caused by the interaction of two growth spirals. Growing and encountering growth centers will inevitably lead to domain walls, that are characterized by a very high density of structural defects (and defective boundaries are once more a problem for high-quality, high-performance applications).⁶⁴ This model of mosaicity origin is not to be mistaken with the aforementioned one in which prismatic slip during post-growth cooling initiates polygonization of threading edge dislocations creating domains.¹²⁹

Because of the experimentally deduced activation of the prismatic slip system $\langle 1\bar{1}20 \rangle [1\bar{1}00]$ in hexagonal SiC during post-growth cooling¹³³ - in contradiction of the basic assumption made by Pirouz⁹⁶ - the mosaicity formation is no longer limited to growth-related misorientation and makes stress-relaxation an alternative mechanism. However, as aforementioned, more than just one origin of domain structures is likely and implications of mosaicity and polytypic inclusions were already shown.¹²⁴

Critical control of the growth process on its behalf can lead to a minimization of SiC's mosaicity⁹¹ although the origin of mosaicity is still not completely understood.

2.1.5.5 STACKING FAULTS

Stacking faults (SF) mainly - but not always - occur in the basal plane along the $[1\bar{1}20]$ direction in hexagonal silicon carbide.⁶⁴ With small formation energies,^{33,134} stacking faults may frequently be found in bulk SiC wafers in the basal plane itself, especially when induced by local stresses.¹³⁵ In the context of stress-related origin of stacking faults, this defect type can be found near micropipes.⁶⁴

The mechanism of stacking fault formation is not limited to the initial stages of SiC single-crystal growth as only few SF's are generated at the seed/crystal interface (with a SF low [0001] seed used).⁹¹ However, SF formation strongly depends on the used polytype material and the growth direction. For example, the SF density of $[1\bar{1}20]$ grown 6H-SiC specimens were 100 times higher than the corresponding values of [0001] grown samples.⁹¹

Since micropipe formation seems to become controllable, e.g. by growth perpendicular to the c-axis, much emphasis is put on hindering stacking faults from occurring. As mentioned earlier, choosing an orientation different from [0001] can provide low MPD values but increase SF densities.^{64,91}

It should be noted that stacking faults on their behalf can also lead to polytypic inclusions. One example studied by Iwata et al.³⁹ shows the existence of localized 3C-SiC formation within a 4H-SiC single-crystal by multiple stacking faults during growth. Also, stacking faults may cause localized electronic states by inducing a quantum-well-like structure.^{39,136}

2.1.5.6 VOIDS

One of the most striking and very evident macroscopic defect types are hexagonal voids parallel to (0001), already mentioned by Gabor in 1965.⁸⁵ Current data verifies that these planar defects with anisotropic edge faces are hollow structures.¹⁰⁸ For hexagonal SiC, these voids are mostly hexagonal parallelepipeds within the (0001)-layer^{31,137} and can reach ranges from a few μm up to above 500 μm . There are speculations about the influence of contaminations¹³⁸ and the polarity of the growing crystal¹³⁹ on hexagonal void formation.³¹

The formation of voids in crystals grown by the modified Lely method may be due to imperfections at the interface of the seed holder and the SiC seed (see also Fig. 8b).^{108,109} Such cavities in the seed attachment layer will start moving along the growth direction during the mass transfer processes at the temperature conditions of PVT. Inside the voids, a local PVT process will result in void movement towards higher temperatures. Differences in the heat transfer distribution around such cavities along with different kinetics of the sublimation face (bottom) and the growth face (ceiling) might explain the polygonization of such defects (parallelepiped geometry).¹⁰⁹ As discussed by Hofmann et al.¹⁰⁹, only voids of a critical size are kinetically favored to move along the growth direction (analogous to the thermal migration of liquid droplets through silicon).¹⁴⁰ Applying this migration model, movement speeds of 40 - 225 $\mu\text{m}\cdot\text{h}^{-1}$ were observed.¹⁰⁹ This model suggests a method to reduce polygonized void formation by improving the seed/seed holder interface.¹⁴¹

2.1.5.7 POLYTYPIC INCLUSIONS

Due to the small stacking fault energy³³, different polytypes may occur during SiC growth for small variations within kinetic and thermodynamic parameters have an important influence. As more than only one polytype can exist at a certain temperature¹⁴², critical control of all environmental conditions becomes one of the most challenging obstacles to overcome, especially when growing large-scale silicon carbide single-crystals.^{58,70} Wafer edges in particular will be affected by polytypic inclusions when critical parameters, such as seed polarity, are not properly controlled. Inclusions like these can act as nucleation sites for superscrew dislocations and, therefore, induce micropipe formation when these inclusions are overgrown.

The polytypic transformation of, for example, 4H-SiC into 3C-SiC within small layers of the original phase has been described.³⁹ This phenomenon was observed to occur in highly N-doped 4H-SiC at 1150°C under oxidizing conditions,¹⁴³ in the case of H₂ etching at higher temperatures (1575°C)¹⁴⁴ or under vacuum conditions at $\approx 1800^\circ - 2000^\circ\text{C}$ in 6H-SiC:N samples with high nitrogen doping levels and excess silicon in the atmosphere.¹⁴⁵

These special cases, however, cannot be seen as a general trend of heat treated α -SiC to transform to β -SiC (in sintered SiC rather the opposite is the case).¹⁴⁵ This polytypic transformation may be the result of the interaction of stacking-faults in neighboring gliding planes.³⁹ The motion of a partial dislocation could create stacking faults in such a way that a different polytype is created (e.g., slightly varying the 6H-SiC stacking order abcacb-abcacb-abcacb... to abcacb-abcabc-abcacb... yields three layers of 3C-SiC).^{146,147}

2.1.5.8 GRAPHITIZATION AND SILICON DROPLETS

Graphitization denotes the presence of excess carbon which originates from the gas phase during SiC PVT growth,⁵⁸ for example, caused by a higher vapor pressure of silicon.⁷⁰ Alternatively, non-stoichiometric C can be present within the source material or the seed surface.

In addition to carbon, silicon droplets may occur also, depending on the Si-to-C-ratio within the gas phase during PVT synthesis and process related instabilities like constitutional supercooling.^{70,148} While carbon precipitation often is characterized by particles of uneven, rough outline, silicon contaminations are droplet-like and can reach diameters in the range of 1 μm .¹⁴⁹ As pointed out by Bickermann³¹, until now no thoroughly conducted study of the droplet structure's chemical composition has yet been published.

Both, carbon inclusions and silicon droplets must be seen as native sources of nucleation sites of micropipes (analogous to polytypic inclusions; contaminations such as metallic inclusions shall not be discussed here). During crystal growth, the mesa-like surface will enclose these local contaminations, because they cannot be incorporated into the crystal structure itself.¹³⁸ A second sublimation process can result in the formation of hollow-core screw dislocations (most likely macropipes) and/or hexagonal voids.

2.2 Silica and its polytypes

2.2.1 Crystallographic aspects

This review concentrates on just three forms of solid silica, because mainly amorphous SiO_2 , tridymite or cristobalite were observed on oxidized SiC samples (except Guinel and Norton¹⁵⁰ under dry thermal conditions and Kraft et al. (Ref. ¹⁵¹) under hydrothermal conditions detected also quartz, cf. section 4.3).¹⁵² At room temperature and standard pressure conditions all these three crystalline silica phases can be found because the conversion of tridymite/cristobalite to α -quartz below $\approx 870^\circ\text{C}$ is a very sluggish phase transformation.¹⁵² Fig. 11 and 12 show a phase diagram and a schematic plot of thermodynamically expected and observed phase transitions. For more detailed insights of phase transformations, see section 2.2.

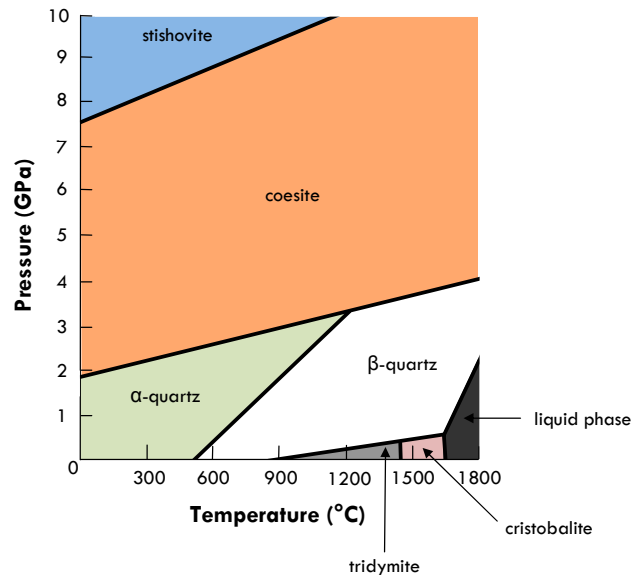


Fig. 11. Phase diagram of the unary system SiO_2 (data taken from Ref. ¹⁵³). Additionally to the shown phase stability fields, sub-fields of α - and β -forms of tridymite and cristobalite along with different phases of tridymite must be considered. For discussion, see text.

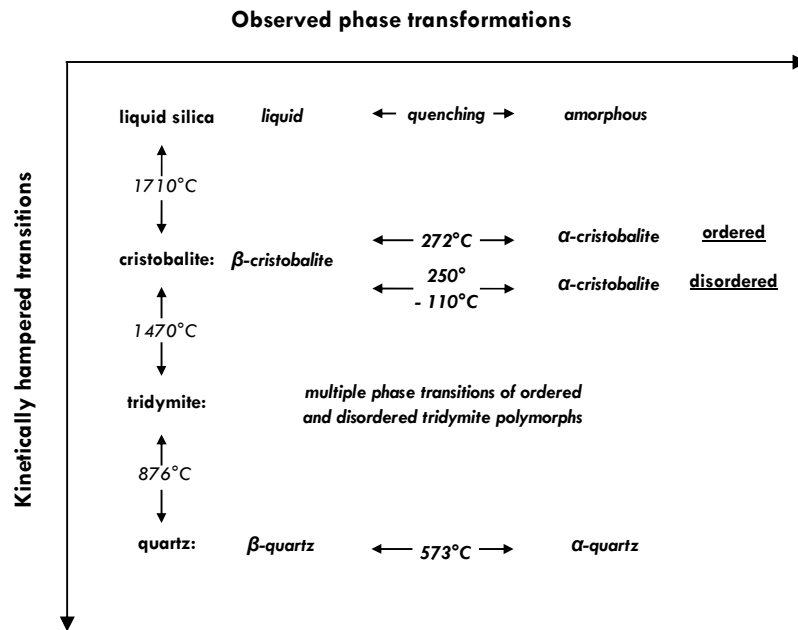


Fig. 12. Schematic illustration of selected phase transitions within the unary system SiO_2 with decreasing temperature (data taken from Ref. ^{152,154,155}).

As SiC_4 tetrahedra are the basic units to build up the SiC structures, SiO_4 tetrahedra are the basic units for crystalline silica. These tetrahedra show a mean O-Si-O angle of 109° (range: $106^\circ - 111^\circ$), and mean bond-lengths for O-O of 258 pm (range: 253 - 261 pm), Si-O of 160 pm (range: 155 - 165 pm) and Si-Si of 308 pm (range: 304 - 310 pm).^{152,156-158} Different ways of interconnecting the basic units by just one joint oxygen atom on one corner build the different structures of silica.

In general, α - β -transitions of cristobalite and tridymite are fast, reversible displacive transformations while the transitions between cristobalite, tridymite and quartz are slow reconstructive transformations,^{152,159} hence metastable preservation during cooling is commonly found.

Oxidation of SiC is extremely slow at $T \leq 900^\circ\text{C}$ and few experiments are conducted in the low-temperature region, where quartz would be expected to be the stable silica form. Thus, the silica phases usually observed at 298 K are amorphous silica, α -cristobalite and α -tridymite.

Both cristobalite and tridymite are structurally related and polytypic (Fig. 13): while β -cristobalite shows only trans-connected pairs of tetrahedra (i.e., the basal plane oxygen atoms are rotated by 60° , minimizing repulsive forces)¹⁶⁰ the β -tridymite structure shows both trans- and cis-configuration (i.e., the oxygen atoms within the basal plane lie directly on top of each other, maximizing repulsive forces).¹⁶⁰ It is obvious that this stacking order related property destabilizes the ideal β -tridymite structure.¹⁶¹ In contrast to β -cristobalite, whose stacking sequence requires a three-layer repetition (ABC), β -tridymite is comprised by the repeat of only two kinds of layers (AB). Consequently, the 6-membered rings do not superimpose in β -cristobalite and no typical tunnel structures as seen in β -tridymite are observed.

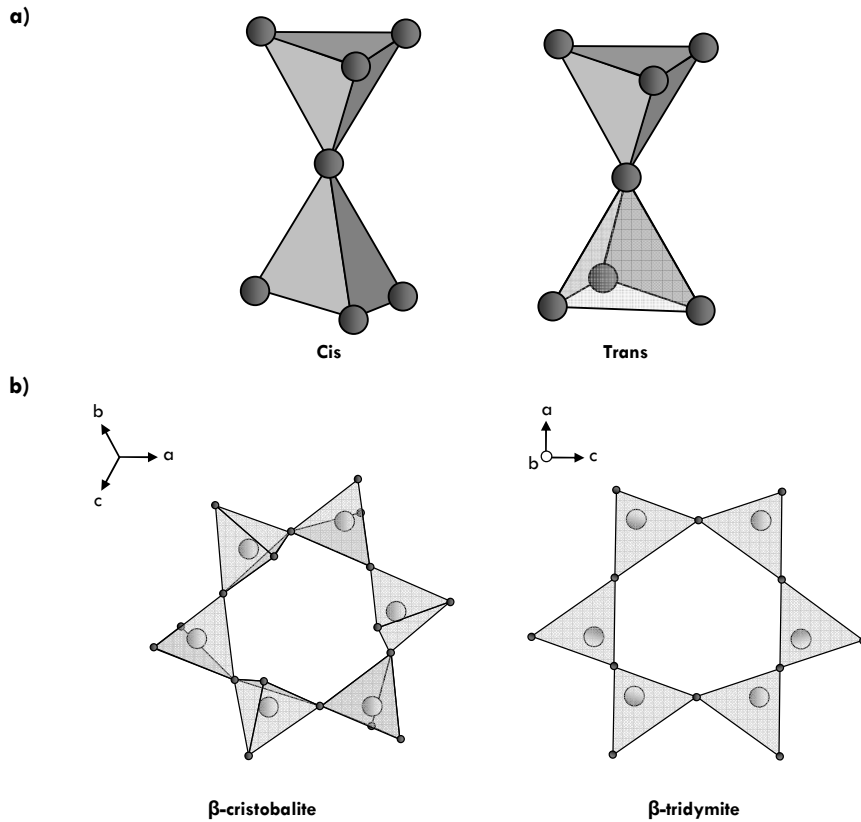


Fig. 13. (a) cis- and trans-configuration (after ¹⁶¹) of SiO_4 -tetrahedra (drawn without central silicon atom) in β -cristobalite (only trans) and β -tridymite (cis and trans) and (b) resulting 6-membered ring-structure.

2.2.2 Amorphous silica

Fig. 14 shows the network of SiO_4 tetrahedra as the structure of amorphous silica. Its density ranges from 2000 - 2200 $\text{kg}\cdot\text{m}^{-3}$ as a function of tetrahedra arrangement.¹⁵³ Compared to β -cristobalite (48.4 % void space per unit cell) or β -tridymite (51.7 %), shows amorphous silica an estimated void space of 57 % per unit cell volume.¹⁵² It is trivial to assume gas transport to be faster in amorphous silica relative to corresponding crystalline phases. However, due to its disordered structure, vitreous silica will show an inhomogeneous distribution and locally increased/decreased densities and consequently locally altered physical properties.¹⁶²

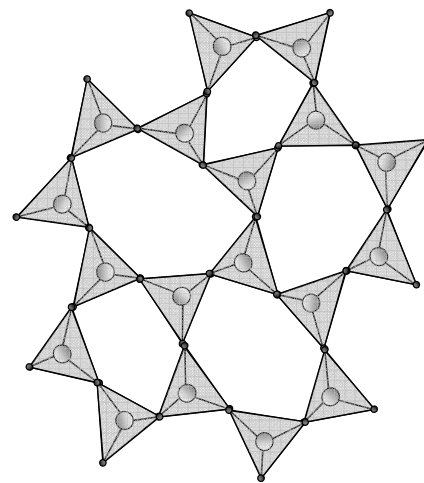


Fig. 14. SiO_4 -tetrahedra arrangement in amorphous silica creating a mean density of 2000 - 2200 $\text{kg}\cdot\text{m}^{-3}$ (depending of the real structure).

Amorphous silica has been the topic of intensive research for many decades.^{152,163} The variation in the Si-O-Si-bonding angles (120° - 180°) supports a random network hypothesis¹⁶³⁻¹⁶⁵, which allows other forms of coordination (like 5 or 7) next to the common 6-membered rings in amorphous SiO_2 (Fig. 14).

Alternatively, the microcrystalline theory states that vitreous silica consists of microcrystallites of various crystalline silica modifications or domains out of fractions of unit cells. The latter model is motivated by the observation that amorphous silica preserves much of the short and/or intermediate range scale order. In the case of small domain sizes both models coincide.¹⁶⁵

To be discussed later in more detail, crystallization (= devitrification) of vitreous silica is essential for the understanding of high-temperature silicon carbide oxidation. Usually, the first devitrification product at elevated temperatures will be β -cristobalite even though the tridymite stability field ranges from 867° - 1470°C .^{152,166} When looking at vitreous silica as an extremely distorted form of cristobalite related phases and taking the small differences in density into account (β -cristobalite: $2200 \text{ kg}\cdot\text{m}^{-3}$ vs. vitreous silica: $2000 - 2200 \text{ kg}\cdot\text{m}^{-3}$)¹⁵³, the pronounced tendency of forming β -cristobalite as the dominating crystalline oxidation product of SiC oxidation does seem reasonable. However, when impurities are present (like K^+ , Li^+ or Na^+), a significant tridymite formation out of the amorphous precursor is possible.

As long as oxidation temperatures for silicon carbide samples do not significantly exceed 1200°C and the oxidizing environment is characterized by low to ultra-low impurity levels (especially as far as water and sodium/aluminium contents are concerned) amorphous silica is the dominant solid oxidation product.

2.2.3 Cristobalite

Cristobalite (Fig. 15; density of α -form: $2320 \text{ kg}/\text{m}^3$, β -form: $2000 \text{ kg}/\text{m}^3$) is the high-temperature modification of silica and stable between 1470° and the melting point at 1710°C .^{153,167} Below a critical temperature of $\approx 270^\circ\text{C}$, the β -form ($\overline{\text{Fd}3\text{m}}$) undergoes a rapid, reversible first order phase transition to α -cristobalite ($\text{P}4_12_12$). This phase transition is accompanied by a significant decrease in volume (6.2 vol%) which induces crack formation and/or tensile stress within dense silica layers.^{159,164,167-169} Cristobalite is in almost all cases the crystalline silica phase found on oxidized silicon carbide samples as a devitrification product derived from amorphous SiO_2 (cf. section 4.).

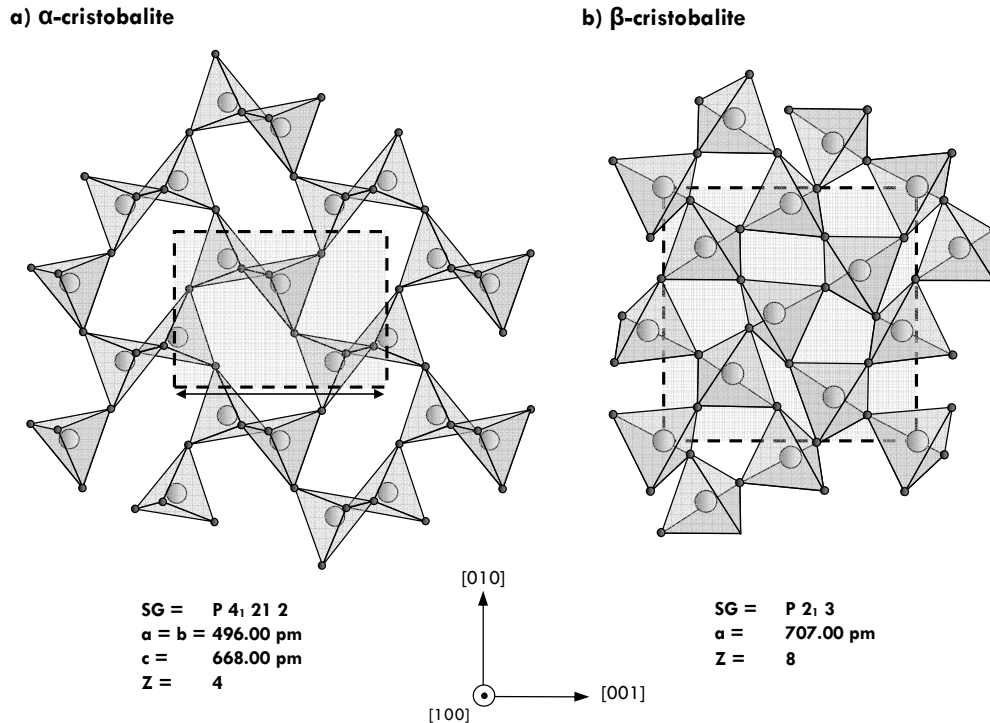


Fig. 15. Crystal structure of alpha- (a) and beta-cristobalite (b) (data taken from Ref. ¹⁵⁶). SG denotes the space group; a and c denote lattice parameters and Z denotes the number of atoms within each unit cell. Alpha cristobalite is significantly less dense ($2200 \text{ kg}\cdot\text{m}^{-3}$) than the beta modification ($2320 \text{ kg}\cdot\text{m}^{-3}$).

2.2.4 Tridymite

The tridymite structure (Fig. 16; density of α -form: $2270 \text{ kg}/\text{m}^3$, β -form: $2260 \text{ kg}/\text{m}^3$) shows sheets formed by 6-membered-rings parallel to (0001).^{153-155,170} Within these rings the tetrahedra's corner vary within their orientation (alternating between $+c$ and $-c$).¹⁵⁹ Rather large cavities within both β - and α -tridymite (cf. Fig. 16) can take up sodium into the crystal lattice by the substitution of Si by Na.¹⁰ Charge balancing requires one aluminium atom for each sodium substituted silicon atom.^{10,171} Up to 9 mol% sodium may be incorporated within the lattice ^{166,171}, while β -cristobalite incorporates only up to 4 mol% sodium. It is this affinity of tridymite to sodium and alumina - two impurities typical for many furnace related environments - that makes the occurrence of this crystalline silica phase a pronounced indicator for impurities.

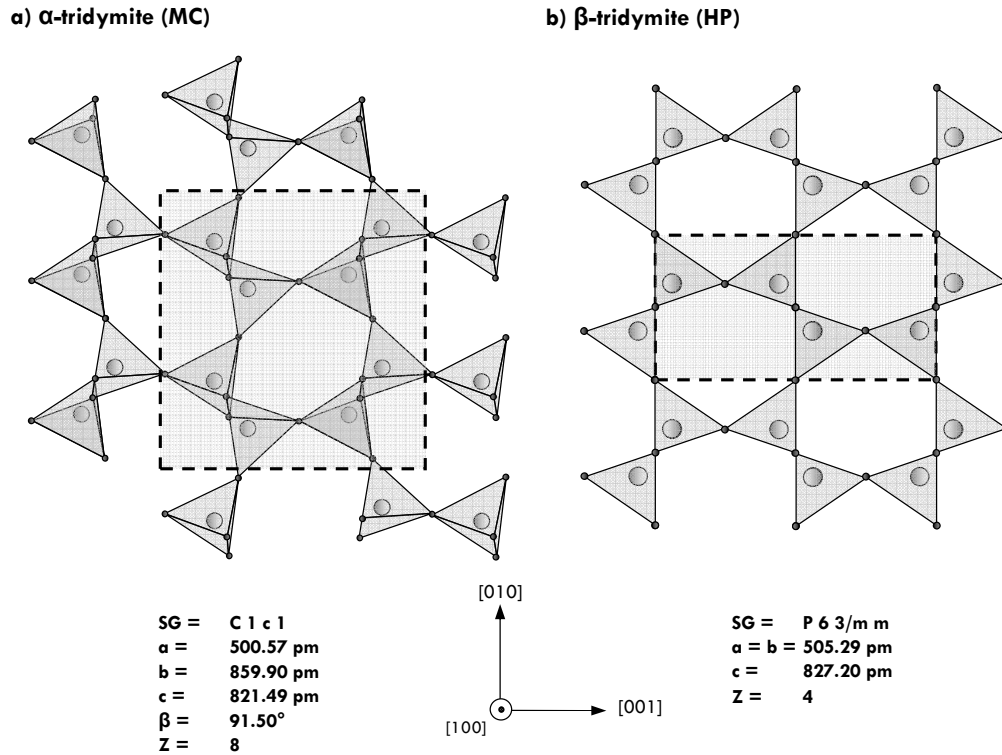


Fig. 16. Crystal structure of alpha- (a) and beta-tridymite (b) (data taken from Ref. ^{158,172}). SG denotes the space group; a and c denote lattice parameters and Z denotes the number of atoms within each unit cell. MC (monocline, c-centered) and HP (hexagonal, primitive unit cell) refers to the nomenclature after Nukui et alii.¹⁷³ Unlike cristobalite the tridymite polymorphs HP ($2270 \text{ kg}\cdot\text{m}^{-3}$) and MC ($2260 \text{ kg}\cdot\text{m}^{-3}$) not differ greatly in density.

Tridymite is a rather complex structure which shows polymorphism.¹⁶¹ At 298 K and 0.1 MPa at least three (meta)stable polymorphs of the low-temperature phase α -tridymite exist: MC (Ref. ^{174,175}), MX-1 (Ref. ^{172,176}) and PO- n (Ref. ¹⁷³). While MC occurs in meteorites and synthetic materials, MX-1 can be found in quenched MC-phases. PO- n (with n as a factor showing the multiplicity along the c -axis compared to β -tridymite) can be found in terrestrial minerals or by synthesis.

There was a long debate whether tridymite is a pure phase of its own or just an impurity derived structure, because sodium and aluminium stabilize the crystal structure of tridymite ¹⁶¹ and all samples contained these elements. Synthesis of tridymite out of ultra-pure raw material using H_2O und D_2O as fluxes led most scientists to the assumption of tridymite being an indigenous, stable phase of silica.¹⁷⁷ Crystallographic examination of tridymite is aggravated by its microcrystallinity, its tendency of forming twins and intergrowth with cristobalite - along with the fact of tridymite often showing a high degree of disorder.¹⁷¹ Twinning or interior tensions can quite easily lead to slip planes and, therefore, suggest a wrong space group.

To characterize the different phases within the complex system, various “tridymite” nomenclatures have been introduced. The two-letter notation proposed by Nukui et al.¹⁷³ denotes (first) the polymorph’s crystal system and (second) the unit cell type – for example, MC signifies a monoclinic crystal structure with a c-centered unit cell. Another way of nomenclature is the formalism proposed by Löns et al.¹⁷⁸ differing between high (H) and low (L) temperature modification with an ordered (o) or disordered (d) structure. For example, L2-T_D would denote a disordered, low-temperature phase with the running number 2 in order to distinguish between different kinds of low-temperature forms. Alternatively, L2-T_D would be designated PO_{5/10} according to Nukui et al. (the index 5/10 signifies the multiplicity of c compared to the high-temperature modification).

Table 3 lists some known tridymite phases along with the phase transformation temperature and various pieces of crystallographic information. For a detailed description of the various tridymite polymorphs see, for example, Ref.¹⁶¹.

Phase	T (K)	Space group	Lattice parameters (Å) and angles (°)	Ref.
MX-1 / L3-T _o	298	C1 Phase with incommensurate modulation	a = 5.01 b = 8.60 c = 8.22 β = 91.51	178
PO-n / L2-T _d	298	Disordered, pseudo-orthorhombic structure	a = 17.22 b = 9.93 c = n·C _{hex}	173
MC / L1-T _o	298	Cc	a = 18.54 b = 5.00 c = 23.80 β = 105.7	174
- / H5-T _o	368	Metrically orthorhombic	a = 26.17 b = 4.99 c = 8.20	170
OP / H4-T _o	428	P2 ₁ 2 ₁ 2 ₁	a = 26.17 b = 4.99 c = 8.20	170
OS / H3-T _o	423 - 463	C112 ₁ Phase with incommensurate modulation	a = 65.00 – 95.00 b = 5.02 c = 8.18	154,157
OC / H2-T _o	493	C222 ₁	a = 8.74 b = 5.04 c = 8.24	174
HP / H1-T _o	733	P6 ₃ /mmc	a = 5.51 c = 8.27	157

Tab. 3. Various modifications of tridymite (α- and β-modification) and corresponding lattice parameters. As far as possible, all phases were denoted with both nomenclatures introduced in the text. At room temperature, at least three distinct metastable α-tridymite polymorphs exist.

2.3 Surface structures

2.3.1 Surface structures of silicon carbide

2.3.1.1 NON-RECONSTRUCTED (NATURAL) SURFACES

As discussed in section 2.1.1 and shown in Figs. 4 and 5 silicon carbide shows an atomic termination of silicon or carbon along the c -axis (α -SiC) or along (111) (β -SiC). When truncating a bulk crystal this termination will be conserved leaving one dangling bond per unit cell on the surface. Hence, when considering a bulk truncated 6H-SiC single-crystal cut perpendicular to the (0001)-face (as most wafers are), two different polar faces are found. Different polytypes will show different stacking orders but the very same principle of a Si-terminated (0001)-face and an opposing C-face will be preserved.

As shown by Starke et al.¹⁷⁹ further differentiation of surface structures must be applied even for one distinct polytype and one distinct polar face for a bulk truncated surface. Six possible surface layer stacking terminations could be present in the case of 6H-SiC (ABCACB). Shown in Fig. 17 are three of those surfaces with A (S3), B (S2) or C (S1) layer termination on a (0001)-face. The other three surface configurations - called S1*, S2* and S3* - can be obtained by a 180° rotation of S1, S2 or S3 accompanied by a translation along the c -axis with $c/2$.¹⁸⁰ The S_n nomenclature introduced by Starke et al. denotes different kinds of configurations indicating the total number of identically orientated bilayers within the concept of a zigzag-pattern configurations like (ACBABC)A and (ABCACB)A show the very same structure due to a glide plane symmetry in hexagonal polytypes (leading to a nomenclature discriminating only between S_n and S_n^*).

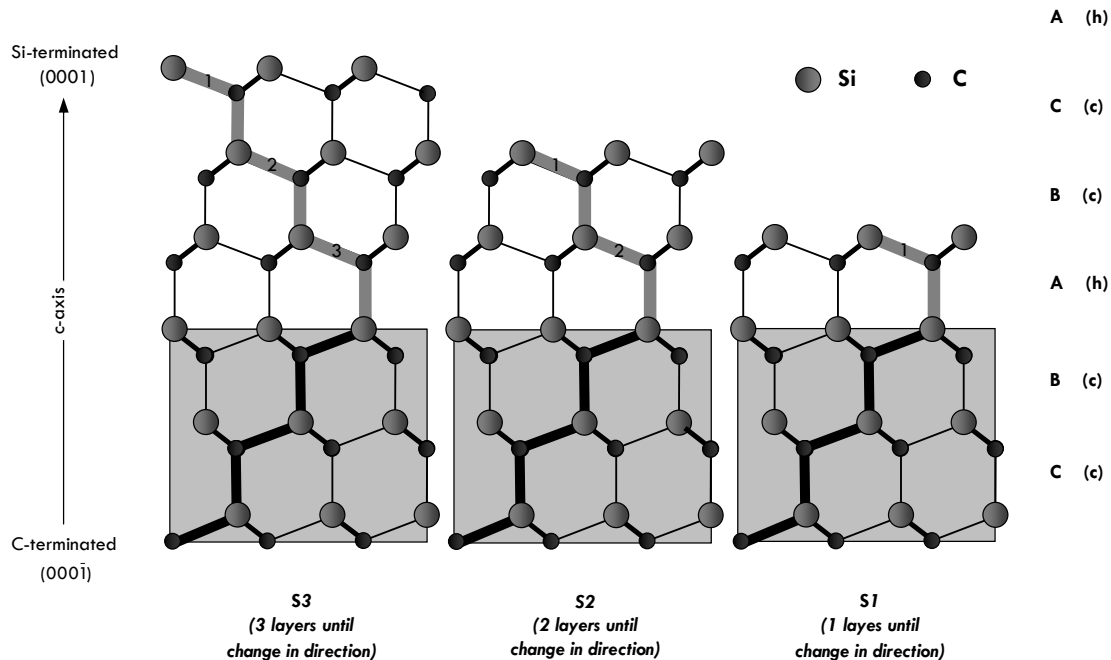


Fig. 17. For 6H-SiC, six distinct surface termination layer sequences can be found: S1, S1*, S2, S2*, S3 and S3*. As S_n^* can be transformed into S_n , only three termination modifications must be considered.

On comparison, 4H-SiC will show two and 3C-SiC one distinct surface configuration for the Si-face. This makes the interpretation of LEED patterns for, for example, (111)-3C-SiC much easier than for (0001)-6H-SiC (with several domains of different surface stacking layers all having to be taken into account when examining real surfaces).¹⁸¹

Real surfaces do only sometimes correspond to a $S1:S2:S3 = 1:1:1$ configuration¹⁸¹ (i.e., an equally dispersed areal density of all possible surface configurations).¹⁸⁰ The observed deviation from this statistical value in real surfaces was explained to have been resulted from step bunching. The latter is a common phenomenon on off-axis grown SiC single-crystals with step heights depending on face-polarity (Si-C bilayers for the C-face and half or full unit-cell steps for the Si-face).¹⁸²⁻¹⁸⁵ The six-fold symmetry of LEED-patterns is explainable by a balance of S_n and S_n^* stacking sequences.¹⁸¹

Only few non-basal plane surfaces have yet attracted scientific interest. Growth perpendicular to the c-axis yields the possibility of defect reduction and, therefore, the $(1\bar{1}20)$ and to some extent the $(\bar{1}\bar{1}00)$ -face of hexagonal SiC were preferentially investigated in studies of their SiO₂-SiC interface state characteristics and/or oxidation rates.¹⁸⁶⁻¹⁸⁹ Like the (110) face of 3C-SiC, these faces are non-polar. As far as β -SiC is concerned, the polar (100) face - showing some similarities with the (100) face of silicon - was the topic of some publications (cf. Ref. ^{190,191}).

These native (1x1) surfaces are obtained by thermal oxidation or HF etching on both Si- and C-faces of 3C-¹⁹², 4H-¹⁹³ and 6H-SiC ^{180,192-195} (for more references see review article Ref. ¹⁸¹). In the case of HF etched SiC surfaces, oxygen was found to be present indicating a (submono)layer on the surface that should be taken into account when examining oxidation mechanisms.^{181,192,194}

However, unrelaxed, unsaturated, clean surfaces will undergo changes in lattice spacings within the first Si-C bilayers. For 6H-SiC, *ab initio* calculations clearly indicate a decrease in bonding-length of the first bilayer from 189 pm to 184 pm on the Si-face and to 182 pm on the C-face. This equals a contraction of 40 % (C-face) or 24 % (Si-face) comparing the change in the c-axis distance.¹⁹⁶

For $(000\bar{1})$ -faces, smaller deviations were found experimentally via LEED: on average a decrease of 2 % in bonding length (= 19 % decrease in c-axis distance) on all three, equally distributed S1, S2, and S3 sites was determined.¹⁸⁰ Also, the increase of the distance between the topmost Si-C-bilayer and the underlying bilayer was experimentally found to be less pronounced than calculations indicated (5% instead of 4 % on the C-face).^{180,196}

On the Si-face, adatoms like oxygen will be found on top of the surface silicon atoms (possessing the so-called T1 site; cf. section 2.3.1.2). In particular, Si-O bond lengths of 166 pm were found for T1-oxygen.¹⁸¹ Bonding with an adatom leads to a change in interatomic distances in the first two monolayers of silicon and carbon. Depending on the site (S1, S2 or S3) increased or decreased distances between the topmost silicon and the adatoms were observed. Hydrogen was found not to change this distance as significantly as oxygen does and no expansion of Si-C-bonding lengths was found. The second monolayer shows minor (< 5 %) changes, mainly in the form of compression.¹⁸¹

Theoretic calculations showed a very significant contraction of the Si-C bonding lengths of the first bilayer for hexagonal SiC along the c-axis ¹⁹⁷ by ≈ 34 % without saturating the adatoms.^{190,198} Especially when considering that not all the sites are saturated, it is clearly indicated that adatoms, like hydrogen, prevent the surface structure from undergoing severe lattice contraction.

On the C-face, adatoms in $T1$ positions above carbon atoms were found to be most likely, excluding adatoms above silicon atoms and conserving the C-face-polarity. Also, the $T1$ adatoms above C-atoms exclude the possibility of the formation of a Si-O-bilayer consisting of three top oxygen atoms as coordinating adatoms. As for the Si-face, on the carbon terminated face also hydrogen or oxygen as adatoms will more or less preserve the (1×1) surface from undergoing significant contraction.^{181,198,199} It shall be pointed out that the energy gain due to lattice relaxation on the Si-face is more than three times smaller (0.09 eV) than on the C-terminated face of 6H-SiC.¹⁹⁷

Before surface processes can be observed, the SiC surface must be cleansed of scratches.¹⁷⁹ This cannot be done using sputtering and annealing in an Ultra-High Vacuum (UHV) due to the different vapor pressures of silicon and carbon.¹⁷⁹ However, introducing thermal oxidation, forming a silica layer, and succeeding HF removal of SiO_2 (e.g., RCA cleaning)²⁰⁰ leads to (1×1) -LEED (Low-Energy Electron Diffraction) patterns (or native surface). These surfaces are characterized by ill-definement and inhomogeneity that will lead to a diffuse background in LEED-measurements.^{180,181,192,194,201} In particular, a sub-monolayer was found to cover unreconstructed Si-C bilayers. The sub-monolayer's adatoms (H and O) were partially saturating the dangling bonds of the topmost Si or C-atoms.

Higher quality surfaces were obtained after *ex-situ* hydrogen etching.²⁰² Subsequent treatment procedures allow the formation of other surfaces structures with, for example, $(\sqrt{3} \times \sqrt{3})R30^\circ$ or (3×3) LEED patterns.

The next section will deal with reconstructed surfaces in more detail. However, as oxidized SiC surfaces show a (1×1) LEED pattern, surface reconstruction seems only to play a role in silica growth on silicon carbide during very initial oxidation (cf. section 4.).

2.3.1.2 RECONSTRUCTED SURFACES

2.3.1.2.1 Introduction

With one "free" dangling bond per one unit cell, surface reconstruction is expected to make the surface energetically more favorable. One possibility to saturate the dangling bonds would be to introduce a layer of adatoms (adlayer). The most likely atomic positions for such adatoms are three specific sites of high symmetry: $T4$, $H3$, and $T1$ (Fig. 18). The letter (T or H) denotes the position (T : on top of an underlying bilayer, H : hollow site) and the number states the coordination number of the bond (4-, 3-, or 1-fold). Either compact adlayers or adatom clusters are possible.

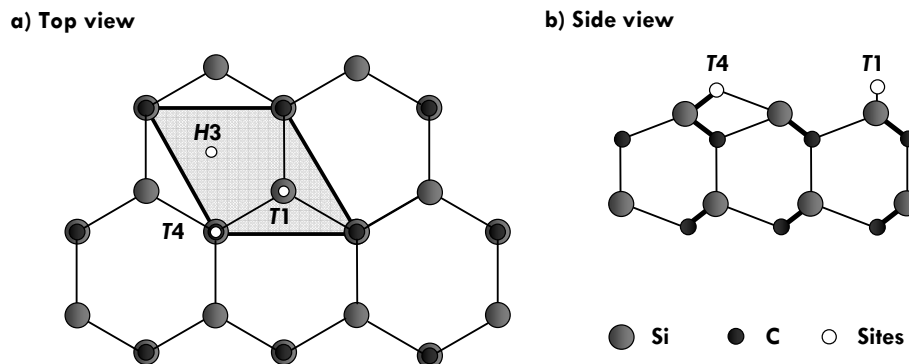


Fig. 18. Model showing different positions on the 6H-SiC Si-face for adatoms and/or surface reconstruction. In this schematic illustration, only 2 subsequent bilayers are shown for the sake of clarity. The dark lines signify the unit cell of a (1x1)-structure. a) View from top (along c-axis), b) side-view (along b-axis).

Another way to decrease surface energy is to create a reconstructed surface. Surface reconstructions also act to relax stress: compared to the lattice spacings of 3C-SiC(100), Si(100) and C(100) deviate by -20 % or +20 % respectively.²⁰³ It should be noted, that the atomic structure of the various reconstructed SiC surfaces is still a matter of scientific dispute.

Different surface types will show different oxidation behaviors during the initial oxidation step and for this reason, we describe the most basic aspects. For more profound information on SiC surfaces and surface reconstruction see Ref. ^{179,181,191,194,203,204} and for oxygen adsorption on different reconstructed 3C-SiC-surfaces see Ref. ²⁰⁵.

2.3.1.2.2 (3x3)-SiC(0001) / (3x3)-SiC(111)

As shown in 1989 by Kaplan ²⁰⁶ *in-situ* annealing in a Si flux at 800° - 850°C yields reconstructed (3x3) surfaces.^{179,206} With a Si:C ratio of 5.2 this silicon rich structure shows a silicon adlayer with strong evidence for topmost Si-Si bonds.^{179,201,206} Only one adatom-like structure was found per unit cell instead of two ^{206,207} in Dimer-Atom-Stacking-faults (DAS) known from (7x7)-Si(111) surfaces, which is taken as evidence that the (3x3)-structure is not a variant of the latter. It has, therefore, been discussed if either (3x3)-SiC(0001) surfaces are a different kind of DAS structures with two cornerholes ²⁰⁸ or if they are the result of a Si tetramer modification.²⁰⁹ However, LEED holographic data shows that an even more complex structure is most likely, in which the topmost adatom effectively sits on a T4 site, but is surrounded by a trimer of Si atoms 130 pm below the adatom. These three trimer atoms are positioned 130 pm above an additional fourth Si atom on a T4 position, which on its behalf is 200 pm above the topmost surface silicon of the original structure (cf. Fig. 19).^{179,210,211} Due to the mismatch in lattice spacings between the topmost SiC bilayer and the Si adlayer, a rotation of $9 \pm 2^\circ$ with significant displacements can be observed and the resulting Si-Si-spacings are close to ideal values of 235 pm.^{179,212} This model was found to be preferable to alternative models (after Li and Tsong ²⁰⁹ or Kulakov et al. ²⁰⁸),²¹³

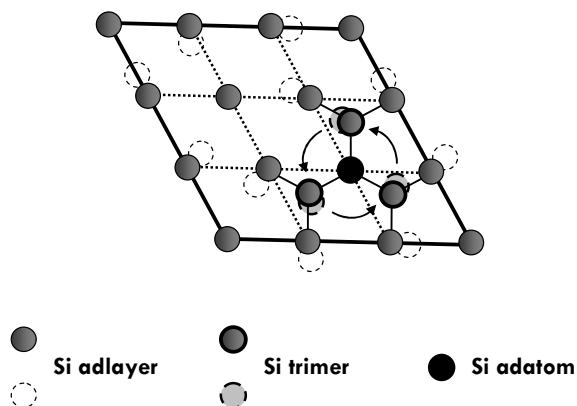


Fig. 19. Model of the 6H-SiC-(0001)-(3x3) superstructure (after Ref. ^{179,213}). As seen, a Si adatom on top of a Si trimer above a Si adlayer is rotated by $\approx 9^\circ$ leading to significant displacements. Shifted atomic positions are dashed. Thick lines indicate the (3x3) unit cell, while dotted lines show the (1x1) native unit cells.

In the end, a sp^2 -hybridized Si adlayer with fully saturated bonds is situated beyond Si adatoms, which on their behalf have one remaining dangling bond (per unit cell). The incitement for a (3x3) reconstruction on (0001) surfaces - or (111) surfaces for 3C-SiC, respectively - is the high degree of bond saturation, which is in fact for (3x3) structures even better than in the case of (7x7)-Si(111) surface structures. For crystal growth technologies, the passivation by (3x3) structures well explains the good homoepitaxial growth in Si-rich environments.

2.3.1.2.3 ($\sqrt{3}\times\sqrt{3}$)R30°-SiC(0001)

These structures are a matter of current dispute. There are several ways to obtain them. (3x3) structures can *in-situ* be transformed to a ($\sqrt{3}\times\sqrt{3}$)R30° surface phase by annealing at 1000°C for 30 minutes.^{201,206} Alternatively, *ex-situ* prepared samples will also show ($\sqrt{3}\times\sqrt{3}$)R30° structures after heating at 950° - 1000°C, but these structures are distinguishable from *in-situ* prepared samples.¹⁷⁹ Also different surface termination configurations will be obtained using *in-situ* or *ex-situ* annealing of (3x3) structures: The first was shown to yield 65 % S3 domains on 4H-SiC while latter yielded almost no S3 and 75 % S1 domains.²¹⁴ These differences could be explained by the amount of silicon content: Si-rich environments result in rather cubic stacking orders.^{214,215} As discussed by Starke, the preference of S3 stacking orders of *in-situ* prepared ($\sqrt{3}\times\sqrt{3}$)R30° structures cannot be explained in terms of “simple” stacking-order rearrangement but by an additional bilayer on top of the substrate obtained from surface reconstruction mechanisms during the (3x3)-to-($\sqrt{3}\times\sqrt{3}$)R30°-transition.¹⁷⁹ The S3 surface stacking order seems to be energetically more favorable^{181,216,217} although the chemical influence of silicon cannot yet be explained.

A third preparation method to yield ($\sqrt{3}\times\sqrt{3}$)R30° structures requires no special precursor structure and is obtained by Si-precipitation at 1000° - 1100°C.¹⁷⁹ It is worthwhile noting that clear ($\sqrt{3}\times\sqrt{3}$)R30°-patterns were obtained for both the C- and the Si-terminated surface.²¹⁸

The current debate is about potential adatoms being carbon (Ref. ^{179,219}) or silicon atoms (Ref.

^{201,206,207,218-220}). A single Si adatom at the T4 site (“T4 model”; Fig. 20a) seems likely from experimental data (XRD, LEED),^{179,218,221-223} which was predicted by *ab initio* DFT calculations^{46,190,197,223,224} but contradicts findings concerning the real electronic structure in comparison to the calculated ones for the T4-model are yet to be explained.^{223,225-227}

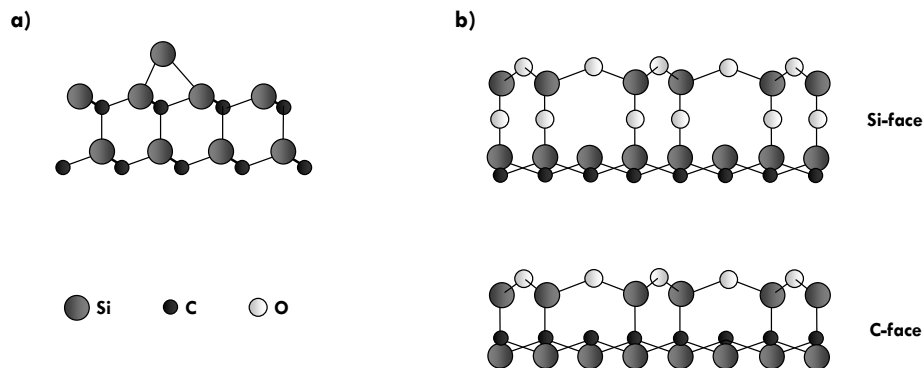


Fig. 20. Model of the 6H-SiC-(0001)- $(\sqrt{3}\times\sqrt{3})R30^\circ$ structures (after Ref. ¹⁷⁹). a) T4 model of *in-situ* prepared samples (Si-face; side view along $[1\bar{1}\bar{2}0]$), b - c) silicate overlayer model (Si₂O₃) for *ex-situ* treated samples (Si- and C-face respectively; side view along $[\bar{1}100]$). Note that latter involves a surface reconstruction mechanism that incorporates oxygen within the new structure whilst both structures yield a $(\sqrt{3}\times\sqrt{3})R30^\circ$ symmetry. On the Si-face the silicate overlayer will be connected to the SiC-lattice via a Si-O-Si bond while on the C-face this interlaying oxygen-bridge is missing.

A model based on *H3* was discussed ²²² as the contributions from residual gas adsorption.²²⁸

Ex-situ prepared $(\sqrt{3}\times\sqrt{3})R30^\circ$ surface structures for both C- and Si-face e.g. of 4H-SiC show a honeycomb-like silicate layer.¹⁷⁹ Thus this reconstructed SiC surface is terminated by ordered oxygen atoms yielding a Si₂O₃ compound. In this structure two Si adatoms per surface unit cell are covered by an overlayer consisting out of twofold coordinated oxygen (Fig. 20b).^{179,181,218,221,229,230} Remarkable is the resemblance of that surface structure with bulk SiO₂ like β -tridymite: both structures differ only in the Si-atom position.^{179,229}

$(\sqrt{3}\times\sqrt{3})R30^\circ$ surfaces show a saturation of all but one of totally three Si or C atoms within the outermost surface layer.²¹⁶ Latter atoms were shown to be saturated by hydrogen at temperatures below 600°C ²³¹ leading to a very stable surface configuration.^{179,232} Hydrogen also seems to play a key role for silicate overlayers to be created. Without it, a simple (1x1) structure, as observed on dry thermal oxidation at the SiC-SiO₂ interface, would be obtained. As speculated by Starke, the lack of an ordered structure like $(\sqrt{3}\times\sqrt{3})R30^\circ$ during initial oxidation as a seed for further silica growth could explain why native oxides grown on SiC are of poor electronic quality.^{179,181}

2.3.2 Surface structures of silica

2.3.2.1 AMORPHOUS SILICA

After the first studies conducted in the 1930s and 1940s by Hofmann et al.,²³³ Rideal,²³⁴ Kiselev²³⁵ and Carman,²³⁶ showed OH groups on top of the SiO₂-network of amorphous silica, many experiments were conducted revealing the surface chemistry of silica and reviews on this topic are available.^{237,238} The main focus of such studies were hydroxylated, amorphous silica surfaces.^{239,240} Silanol groups ($\equiv\text{Si-OH}$) that are mainly connected with superficial silicon atoms by a valence bond were termed “combined structurally-bond water”.²³⁸

As proposed by Zhuravlev,²³⁸ there are 4 types of additional O-Si-bonds on SiO₂-surfaces: (1) isolated, single silanols ($\equiv\text{Si-OH}$, i.e., one OH-group attached to one silicon atom of the SiO₂-network), (2) geminal silanols or silanediols ($=\text{Si}-(\text{OH})_2$, for example, two functional OH-groups that are attached to the same silicon atom), (3) hydrogen-bonded geminals and silanols as well as H-bonded combinations (among others vicinal or bridged), and (4) siloxane groups ($\equiv\text{Si-O-Si}\equiv$). Additionally, structurally bond OH-groups may be present within the silica network. For examinations of the surface reactivity, both bulk concentration and types of siloxane and silanol groups along with silica porosity (if present) must be considered. In detail, it has to be distinguished between adsorbed water, structurally bond water inside the SiO₂ lattice and silanols in an aqueous system. In addition, different kinds of surface groups system yield immanently the problem of energetically heterogeneous silica surfaces.

2.3.2.2 CRYSTALLINE SILICA

A triviality pointed out by Iler is, “that it would be surprising if the SiOH groups on clean surfaces of all the different crystalline and amorphous forms [of silica] would behave exactly the same”.²³⁷ Besides the structural influence, morphology and particle sizes are also important (and sometimes more important).²³⁷ Also, it is trivial to assume crystalline SiO₂ surfaces to be energetically more homogenous for each specific face than vitreous silica materials.

Analogously to silicon carbide, bulk truncated silica surfaces will show dangling bonds which likely cause point defects. This induces the tendency to saturate those dangling bonds via adsorbed adatoms (like OH-groups if available) or even will result in reconstructive processes. Prominent defect types are among others (1) oxygen deficiency-related defects like E'_v-centers (i.e., oxygen vacancies above threefold coordinated silicon like $E'_v \equiv \text{O}_3\text{-Si}\cdot$),^{239,241-246} and (2) oxygen excess-related defects like silanone groups ($=\text{Si}=\text{O}$ double bond),^{246,247} or Non-Bridging Oxygen Hole Centers (NBOHC; $\equiv\text{Si-O}\cdot$).^{239,243-245} For more literature references see, for example,²⁴⁶ and references herein. However, it is believed that silica surface influences are of secondary (or even tertiary) relevance behind interfacial properties of the SiC-SiO₂ interface (section 2.4) along with structural influences of the SiC raw material (and its surface structure and both morphological and physicochemical impacts).

2.3.2.3 IMPURITIES AND SILICA SURFACES

For both crystalline and amorphous silica surfaces, an accumulation of impurities at the gas-solid interface was observed. Especially in the case of sodium (which structurally and kinetically greatly influences silicon carbide oxidation to be discussed in section 4.1.4.5) it was shown by Fowkes et al. that this impurity will accumulate at the surface.^{237,248} This effect may well lead to a (negative) surface charge that can be removed using HF-etching showing the strong superficial character of this accumulation. As one example, 2 ppm sodium as bulk concentration in silica resulted in 2 wt% Na that could be detected at the SiO₂ surface after annealing the sample at 1000°C.²⁴⁸ Clearly, such a pronounced accumulation must be taken into account as sodium also changes the silica network structure and accelerates oxygen transport through the silica scale. Also, at elevated temperatures, this concentration of sodium is sufficient to form locally molten composite phase with silica (cf. Fig. 21).²⁴⁹

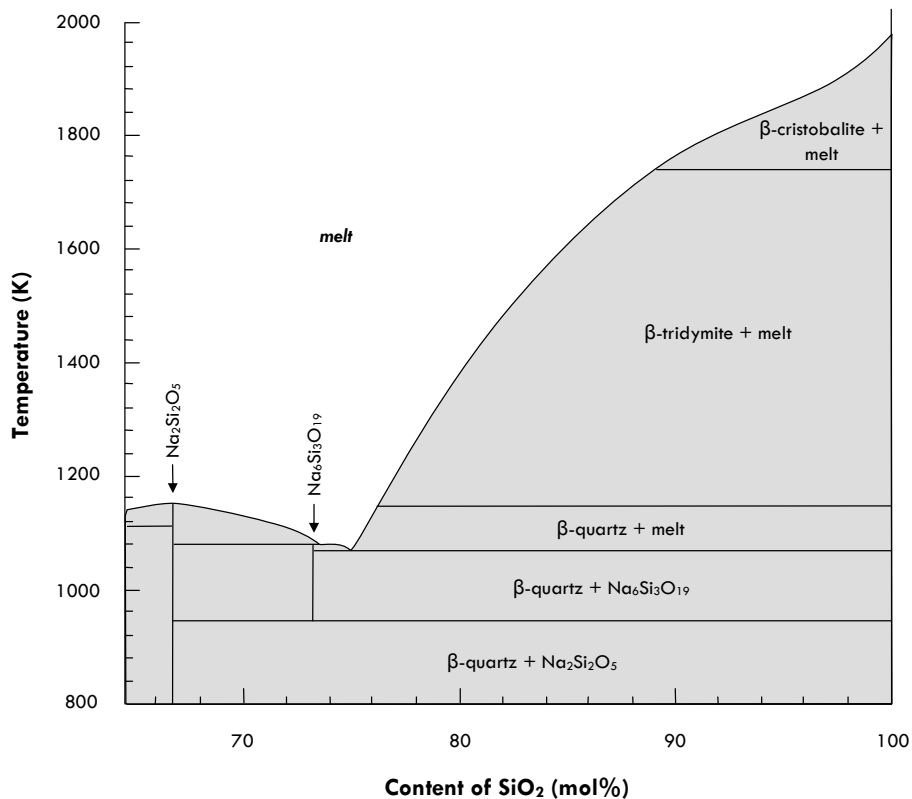


Fig. 21. SiO₂-rich side of the Na₂O-SiO₂ phase diagram with selected stability fields (after Ref. ²⁴⁹). As seen, locally increased sodium contents may readily lead to melt formation way below the melting point of pure silica.

2.4 SiC/SiO₂ interfaces

2.4.1 Introduction

2.4.1.1 BASIC STRUCTURAL ASPECTS

Silica is the stable, native oxide of silicon carbide and this provides the desired possibility of using SiC/SiO₂ devices as Metal-Oxide-Semiconductor Field Effect Transistors (MOSFETs) - quite similar to Si/SiO₂ based devices. To accomplish this, thermally grown silica provides an insulating gate above the *n*- or *p*-type semiconductor.^{58,250,251} A naturally grown oxide should, *a priori*, provide a structurally superior SiC/SiO₂ interface relative to coatings. The electronic properties of the interface often determine the overall device performance and limit fields of application.

SiC-MOSFETs (cf. Ref. ²⁵²) are particularly suited for high-voltage and high-temperature applications because of the larger band gap (2.39 - 3.33 eV depending on polytype ^{11,19,253}) and higher critical field strength E_{\max} (2.49 MV·cm⁻¹ for a doping level of 10²² m⁻³, Ref. ^{11,254}) of silicon carbide compared to silicon (band gap = 1.1 eV; $E_{\max} \approx 0.2$ MV·cm⁻¹ for the same doping level and a blocking voltage of 1 kV).^{11,255} The high thermal conductivity of silicon carbide provides electrical devices with improved heat dissipation and could, therefore, access new applications areas.²⁵⁶

2.4.1.2 P- AND N-TYPE SiC

Substrate/oxide interfaces of *p*-type SiC often show especially high densities of interface states (D_{it}).^{257,258} An in depth review about techniques to obtain interface state density values was presented by Cooper. ²⁵⁹ Incorporation of the *p*-doping material aluminium was proposed to explain this as an extrinsic mechanism ^{258,260} but seems rather unlikely in light of newer research results.^{259,261-264} An intrinsic effect is indicated by the lack of any positive effects to D_{it} exchanging Al with boron ²⁶¹ or the absence of any adverse effects of aluminium in N⁺-implanted *n*-type 6H-SiC originating from overcompensated *p*-type 6H-SiC:Al.²⁶³ As found by Zetterling and Östling ²⁶⁵, no pile-up of aluminium was detected on dry, thermally oxidized 6H-SiC but a constant yet small level of Al incorporation within the oxide scale. Contrasting to older data,^{266,267} more recent results ^{259,262,268,269} show that the interface defect densities of *p*- and *n*-type SiC are not too different. Hence, an attribution of the interface state density to intrinsic defects seems to be the most probable scenario.

2.4.1.3 DIFFERENCES BETWEEN SiC AND Si INTERFACE ABRUPTNESS

Despite the structural isomorphism between the Si-face of α -SiC-(0001) and Si-(111) the SiC/SiO₂ interface develops dramatically high densities of electrically active centers (\approx two order of magnitude higher than the Si/SiO₂ interface).²⁵⁵ In light of the structural consistency between silica created on SiC and Si this is, based on a *a priori* assumption, quite unexpected. However, the alternative to fabricate silicon carbide based MOSFETs by silica deposition ²⁷⁰ yields the same poor or even worse interface characteristics.^{229,271}

The superior interface properties of silicon are associated with a smooth and abrupt Si/SiO₂ interface without significant interlayer and are a basis for the predominance of Si-based MOSFETs in optoelectronic devices.²⁷²

Ab initio calculations indicate that in the case of silicon a suboxidic interlayer would be energetically disadvantageous.²⁷² Nonetheless existing suboxidic areas in Nominal Interface Layer (NIL) are the results of the real structure of silicon.²⁷²

In contrast to the silicon/oxide interface²⁷³ is the silicon carbide/oxide interface not nearly as smooth and abrupt,²⁷⁴⁻²⁸⁰ accompanied by poor oxygen solubility in SiC.^{272,281,282} Only after post-oxidation anneal procedures (e.g., with NO at lower temperatures than during oxidation) average SiC-surface smoothness in the range of 100 pm could be achieved.²⁷⁸

Ab initio calculations attest both hexagonal and cubic silicon carbide a lack of suitable geometries and bond lengths for the formation of an abrupt substrate/oxide interface.²⁷² These theoretical calculations indicate, that structures like unsaturated dangling bonds, oxycarbide layers (similar to oxynitride layers on Si₃N₄; cf. Ref. ^{168,283,284}) and a graded SiC-SiO₂ transition - all contributing to a high D_{it} - would be inevitable.^{229,255,272,285,286} Also apparent stress within the interface due to structural mismatch between SiC and SiO₂ could account for the poor interface quality.²⁸⁷

In this context, many authors write about suboxidic phases similar to suboxides defined for the Si-SiO₂ interface. It shall be kept in mind that pure, large-scale suboxide formation is very unlikely for SiC/SiO₂ interfaces, as the C-Si-bond would have to be broken and Si-Si-bonds would have to become dominant within oxygen presence.²⁷⁶ Hence, it should rather be spoken of oxycarbide phases like SiO_xC_y - a compound defined as an amorphous phase, in which direct bonding of silicon to both oxygen and carbon occurs.²⁷⁶

A non-reconstructed, real SiC surface yielding a non-abrupt SiC/SiO₂ interface should have a decrease of electron mobility by an order of almost 2 in the SiC substrate adjacent to the interface, which might be due to high roughness and high density of interface imperfections causing an increased electron scattering and reduced electron mobility.^{288,289} The corresponding Si/SiO₂ interface shows only a decrease of the electron mobility by a simple factor of two.²⁸⁹

High densities of interface states are in contrast to a small $\approx 5\%$ mismatch of lattice parameters between SiO₂ and SiC making epitaxial growth of silica on silicon carbide possible.¹⁷⁹ Pantelides et al.²⁸¹ explained their findings of a rather abrupt SiC/SiO₂ interface to be a result of the low solubility of oxygen and the instability of carbon monoxide within the silicon carbide substrate on the SiC side of the interface, which will become abrupt. The SiO₂ side of the interface will show carbon-related impurities and oxycarbide formation to some extent within some monolayers.

A recently conducted modeling of the 4H-SiC-(0001)/SiO₂ interface yet predicts the possibility of a completely abrupt transition between silica and silicon carbide,²⁹⁰ in a constellation, in which the mismatch induced stress between SiO₄ and SiC₄ tetrahedra would be relaxed within a few atomic layers. However, this stress is likely to induce defects like dangling bonds in a real structure oxide.

There is experimental evidence of a graded distribution of ¹⁸O at SiC/SiO₂ interfaces. The interpretation may nonetheless in favor of an abrupt silicon carbide to silica transition, if the grading is due to a disturbing effect of co-existing carbon (cf. section 2.4.2.4).²⁹¹ Isotopic tracing experiments conducted by Vickridge et al.^{292,293} and IPE measurements support this view and also indicate that the SiC/SiO₂ transition is at least electronically abrupt because the 8.9 eV large band gap of SiO₂ is established less than 1 nm away from the SiC surface.⁴¹

First-principal calculation with an abrupt interface show potential interface states to be C- or Si-related dangling bonds, Si-Si-bonds and carbon clusters.^{294,295} However, those calculations had β -quartz as initial SiO₂ structure instead of amorphous SiO₂ or β -cristobalite.

In this context, it is important to say that most published data refers to Si- or C-terminated faces of SiC (mainly 6H-, 4H- and 3C-SiC). Only few studies examined more “exotic” crystallographic orientations (like Yano et al.: 4H-SiC - $(0\bar{3}3\bar{8})$ ²⁹⁶ or 4H-SiC - $(1\bar{2}2\bar{0})$ ^{187,297}). These findings strongly show that - along with many other important properties - the interface states of various crystallographic orientations of one single SiC polytype differ greatly.

2.4.1.4 SURFACE INFLUENCE

If the evidences for almost ideal abrupt, carbon species and oxycarbide-free SiC/SiO₂ interfaces for reconstructed surfaces like highly oxygen reactive 3x3 surfaces with a Si adlayer²⁹⁸⁻³⁰⁰ prove to be true, we may even find more uniform SiO₂ layers than the ones observed on silicon.³⁰¹ The real potential of this current development is not yet known.

2.4.2 Interface states

2.4.2.1 GENERAL ASPECTS

Reducing the density of states D_{it} is vital for a widespread application of SiC-MOSFETs²⁵⁵ - especially because the low channel mobility of silicon carbide based MOS structures is a possible result of high D_{it} values.^{291,302} When talking about densities of interface states, it should be borne in mind that most interface states cannot be excited at room temperature (or at least not within several thousands of years²⁶¹) and, therefore, care should be taken for measuring their densities at low temperatures.²⁵¹

With a similar character of the Si/SiO₂ transition in comparison to the SiC/SiO₂ interface,^{255,264,303} the high density of states (trap density) of the latter seems to be a result of a high level of interface imperfections - especially when considering that thermally grown silica on both silicon and silicon carbide exhibits the same characteristics in surface and bulk regions.²⁹¹ In contrast to these similarities unoxidized silicon and/or carbon was found in the SiC/SiO₂ interface region.^{299,300,302,304} As discussed later, the electrical properties and the interface state density depend on (1) SiC polytype, (2) surface properties, (3) anisotropy, (4) contamination level, (5) doping type/level, (6) oxidation ambient, and (7) annealing procedures.

2.4.2.2 POLYTYPIC INFLUENCE AND INTERFACE STATES DISTRIBUTION

Compared to Si the much wider band gap for silicon carbide polytypes allows more energy levels for interface states (Fig. 22). These could possibly act as interface traps.^{255,262} Especially near the conduction band edge of 4H- and 6H-SiC, a high density of states is apparent.^{255,262,264,305} Hall measurements even indicate D_{it} values of almost $1 \cdot 10^{14} \text{ cm}^{-2} \cdot \text{eV}^{-1}$ for 4H-SiC near the conduction band gap edge.³⁰⁶ Hence, the choice of polytype as well as the crystallographic anisotropy of a single polytype will significantly affect D_{it} .^{255,259}

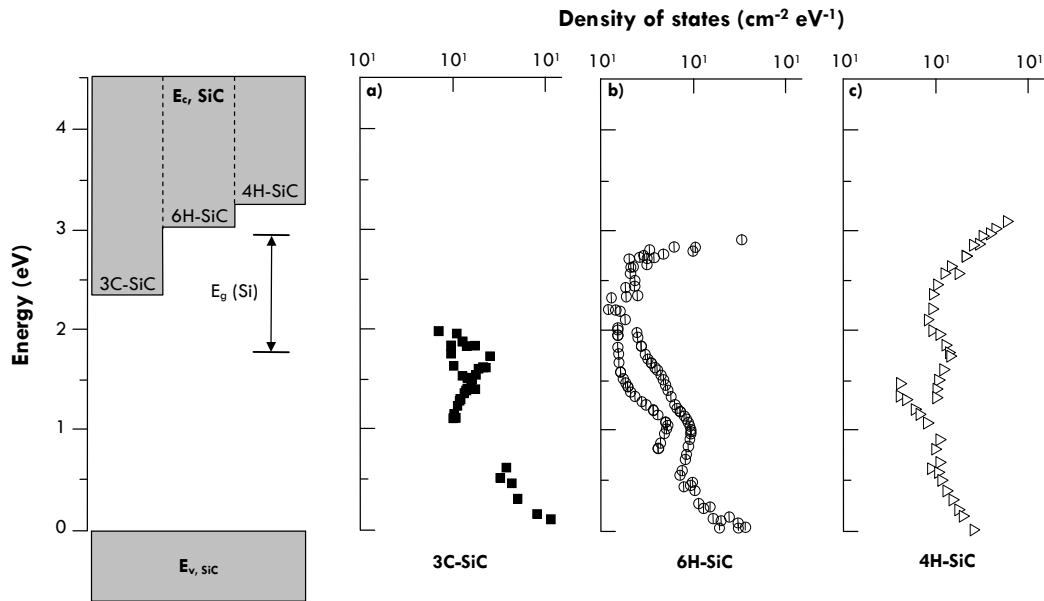


Fig. 22. D_{it} values (interface state density) for three distinct silicon carbide polytypes. On the left side, a schematic representation of the band gaps of the shown SiC polytypes and pure silicon is provided. The origin of the energy scale is set to the valence band gap edge of silicon carbide (2.9 eV above the valence band edge of SiO_2 - a value almost equal for all SiC polytypes).^{41,253} The oxide scale was thermally grown in pure oxygen and the data points are taken from admittance spectroscopy and constant-capacitance deep-level transient spectroscopy for both *n*- and *p*-type SiC (after Ref. ²⁶²).

As far as imperfections are concerned, pre-oxidation cleaning, like the H_2O_2 based standard “RCA” cleaning procedure²⁰⁰ yields significantly superior electrical properties compared to untreated samples.²⁵⁹

The existence of populated interface states between the edges of the band gap was experimentally proven by Internal PhotoEmission spectroscopy (IPE).^{255,262,264} The energies found in those studies coincide well with the interface states in the lower part of the semiconductor band gap (Fig. 22). Many of these states are surface donors, which is seen as the reason for the often observed positive charges in *p*-type SiC.²⁵⁵ In contrast, negative charges in 4H-SiC (*n*-type MOSFETs) are attributed to the high D_{it} near the conductive band edge, because these states act as acceptors.²⁵⁵

Fig. 23 provides a generalized overview over possible interface imperfections. Carbon clusters and oxide traps are believed to be the two most dominant contributions to interface states. For this reason we omit a detailed discussion of the other two minor contributions, Si-Si-bonds³⁰⁷ and stacking-fault related electrically active centers.¹³⁶

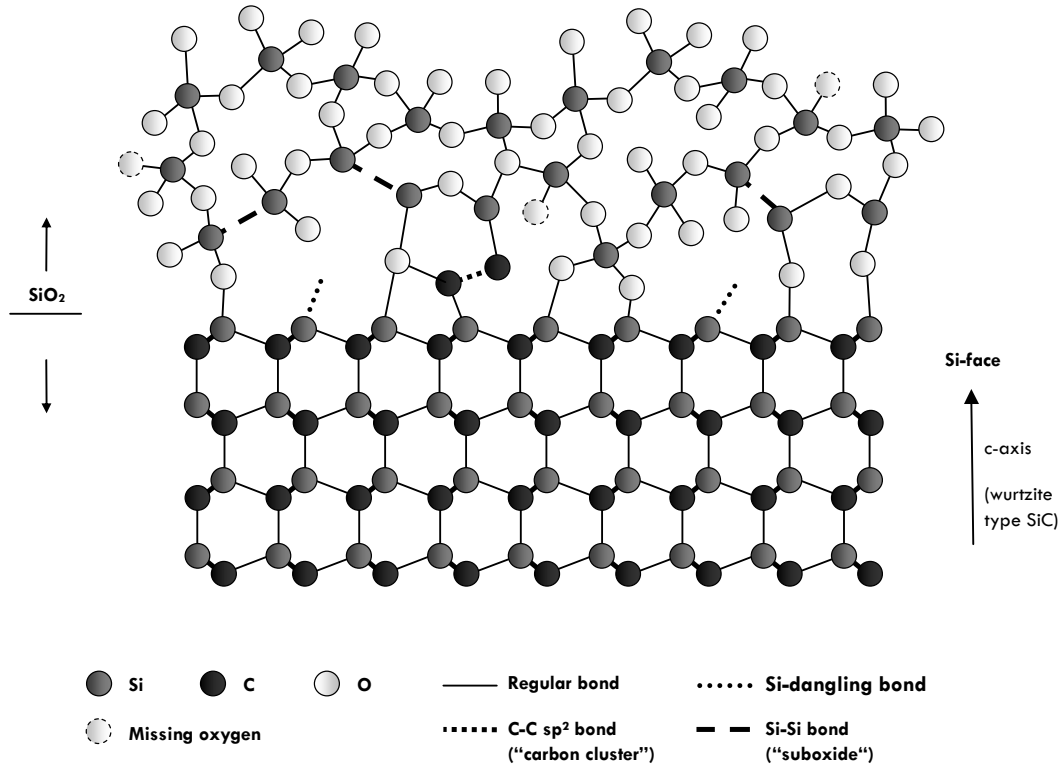


Fig. 23. Schematic representation of the SiC/SiO₂ interface and possible interface defects. The non-uniform bonding lengths of Si-C indicate the three-dimensional wurtzite type structure plotted perpendicular to the z-y-plane (the shorter and thicker bonds between Si and C indicate two Si-C-bonds directed by 60° into and out of the plane). C-dangling bonds could occur on the C-face respectively. For the sake of clarity have all atoms been chosen to have the same size.

Fig. 24 compares the density of states of different interface and near-interface defects possibly contributing to D_{it} of silicon carbide and silicon. Of those, we discuss in the next sections: dangling bonds (of silicon or carbon, respectively), carbon clusters, oxide traps and polytypic inclusions.

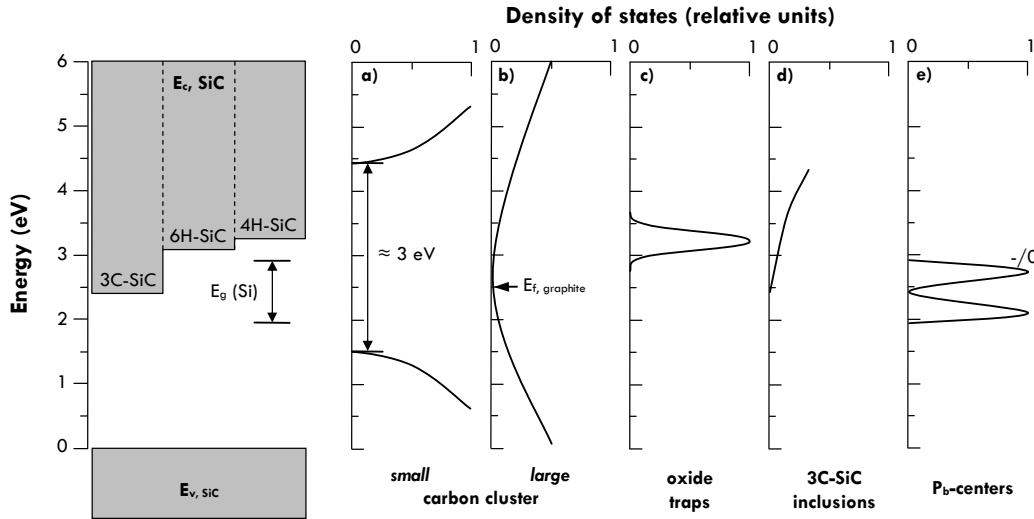


Fig. 24. Energy distribution of interface and near interface states compared to the band gap E_g of various silicon carbide polytypes and pure silicon. a) sp^2 -bonded, small carbon cluster, b) graphite like, big carbon clusters (E_f denotes the Fermi level of graphite; considered to be almost equal to the neutrality level of large carbon clusters), c) oxide traps, d) polytypic inclusions of 3C-SiC and e) P_b centers as for pure silicon-silica interfaces. The conductive band gap edges (E_c) are true to scale. At 6 eV the origin of the SiO_2 conduction band edge would be positioned (after Ref. ^{255,262}).

2.4.2.3 DANGLING BONDS

Si dangling bonds are well known from clean, unoxidized silicon surfaces as well as from the Si/ SiO_2 interface.³⁰⁸ The energetically narrow spread Si dangling bond defects (“ P_b -centers”) arise in the case of the Si/ SiO_2 interface from three-fold coordinated Si atoms, which allows hydrogen passivation by formation of electrically inactive, diamagnetic $Si_3\equiv Si-H$ entities - a procedure most commonly used for Si-MOSFETs.^{27,309,310}

Due to its pronounced tendency to form strong covalent bonds and its small atomic size, hydrogen couples to dangling bonds of both carbon and silicon ²³², making surface reconstruction obsolete. These newly formed Si-H and C-H bonds can spectroscopically be detected and lead to a significantly increased chemically inertness towards oxidation.²³² Whereas hydrogen passivation of clean and unoxidized silicon carbide surface (both p - and n -type semiconductors) for C- and Si-terminated faces is feasible,^{232,311,312} no successful attempt of this has yet been made in the case of SiC/ SiO_2 interfaces.²⁵⁵ Only when applying destructive methods like irradiation or charge injection, hydrogen passivation of the SiC/oxide interface was observed to some extent.²⁵⁵ Hydrogen passivation subsequent to Post-Metallization-Annealing (PMA)⁶⁹ or etching must also be attributed to this group of special conditions since the sample will be exposed to a high dose of energy and this may even lead to a chemical change of the interface - especially when considering, that hydrogen is a very strong catalyst for PMA.^{69,313}

Theoretical calculations indeed predict the existence of P_b -type defects near the lower part of the SiC band gap.²⁶² Dangling bonds in the SiC/SiO₂ interface might contribute to the mismatch between the substrate lattice and the oxide network (as known from Si-SiO₂)³¹⁴ as the molar volume of SiO₂ is more than twofold increased (2.15) in comparison to silicon carbide.²⁷⁵

However, one can think of alternative ways on how to reduce the mismatch-induced stress within the interface layer. For example, an atomic substitution of single Si atoms in the Si-terminated SiC surface by carbon would lead to carbon-carbon-bonding with a decreased mismatch in respect to the oxide network - a process impossible in the case of pure silicon.

Identified carbon dangling bonds within the interface of 4H-SiC/SiO₂ of porous silicon carbide³¹⁵ may be due to the unique surface of a porous sample with many different orientated surfaces contributing to the bulk surface. However, ESR data indicates C-dangling bonds^{316,317} originating from carbon in an amorphous environment and another dangling bond type for p-type SiC of unclear origin (named PERC-1).³¹⁸ As proposed by Pantelides et al.²⁸¹ C-related dangling bonds should rather be called threefold-coordinated carbon due to its preference to form graphite-like structures.

A putatively successful approach in hydrogen passivation of *n*-type 4H-SiC at temperatures above 800°C³¹⁹ was topic of some dispute.^{320,321} The energetically wide spread distribution of SiC/SiO₂ interface states would be untypical for dangling bonds with two peaks for each the (0/-) and the (+/0) transition^{308,322} observed in the Si/SiO₂ interface^{255,320} (Fig. 24). However, more research on this topic seems to be necessary.

It is valid to speculate about how processing induces possible hydrogen annealing for most of the dangling bonds and, therefore, rendering hydrogen passivation ineffective - unless depassivation by radiation or excess energy would take place.^{303,323}

It should be mentioned that hydrogen annealing at temperatures above 500°C may even lead to annealing-induced defects²⁶⁹ as the formation of a positive charge for *n*- and *p*-type SiC has been described.³²⁴ Deduced from a similar effect within the Si/SiO₂ interface³²⁴ the creation of an over-coordinated oxygen center has been proposed. It is reasonable to see a connection between trapping of holes and hydrogen related interface degradation for *p*-type SiC is more influenced than *n*-type³¹⁰ (cf. Ref. ^{269,323}).

Anyhow, the effect of conventional hydrogen annealing is meager: less than 20 % decrease for *n*-type SiC and no significant decrease for *p*-type material, in addition to featureless D_{it} spectra untypical for P_b -related interface states. This shows that traditional dangling bonds either from carbon or from silicon cannot be attributed to the bulk of interface states.^{255,262} Hence, the increased D_{it} values compared to silicon cannot (solely) be ascribed to dangling bonds, even so SiC has a higher density of atoms per unit cell and, therefore, might *a priori* exhibit a higher dangling bond density²⁶² (cf. Ref. ³⁰³).

2.4.2.4 CARBON CLUSTERS

2.4.2.4.1 General aspects

It was theoretically predicted^{262,289,325} and experimentally shown,^{150,255,256,269,281,288,302,323,324,326-328} that within the interface layer of as-grown samples carbon clusters can be formed and contribute to the high interface defect density of SiC/SiO₂.

Further evidence for the implication of carbon and interface defects is provided by comparing D_{it} values of both the Si- and the C-terminated face of a SiC single-crystal (i.e., (0001) or $(000\bar{1})$, respectively).

Significantly higher defect densities were observed for the C-face of hexagonal SiC in contrast to the Si-face^{262,326} - coinciding with more available carbon and more frequent nucleation sites on the C-face. Based on the curve characteristics of Capacitance-Voltage (CV) measurements, all crystal faces show the same origin of interface states. However, only a small portion of the theoretically available carbon will contribute to carbon cluster formation.²⁶²

The debate of carbon clusters has no analogue in Si/SiO₂ interfaces, because there is no carbon in the lattice there, and no evidence of any carbon rich regions from other sources was found.³⁰²

Removal of carbon clusters in SiC/SiO₂ leads to an improved defect density and hence to improved electronic properties. Successful examples of these methods are pre-oxidation cleaning like UV-ozone cleaning or related procedures^{261,289,317} and/or post-oxidation annealing in various atmospheres.^{259,267,289,329}

Excess carbon may also be present in form of an oxycarbide boundary layer like SiC_xO_y^{274,276,282,286,299} posing origin both to carbon and interface states. Also, a coexistence of different forms of excess carbon (carbon clusters, carbon chains, oxycarbide phases, hydroxycarbides...) is possible. As long as π -bonded carbon is present, the level of D_{it} may well be explained.

The amount of excess carbon necessary near the interface of as-grown samples to explain D_{it} values is about one monolayer with a constant carbon concentration independent of oxide thickness and this is usually within the margins of state-of-the-art analytical methods.⁶⁹ However, some core level photoemission studies^{274,298,300,301,330,331} did not detect any C-C related signal from the (0001)-SiC-SiO₂ interface with a detection limit of a $\approx 8 - 10 \text{ \AA}$ thick layer but suggest the presence of a Si-C-O phase on C-terminated and intermediated faces. For the discussion the argument of Virojanadara and Johansson³³² that photoemission studies may be improper to detect sparsely distributed carbon clusters at all should be kept in mind.

2.4.2.4.2 Cleaning procedure influence on carbon cluster

Pre-oxidation UV-ozone cleaning was originally developed for carbon removal from silicon single-crystals.³³³ Intentionally added oxygen may, therefore, be considered a device capable of removing (interstitially bonded or clustered) carbon.

Annealing in other atmospheres has also been investigated.³²⁹ The best investigated method of Post-Oxidation Annealing (POA) is the one in NO atmosphere.^{288,307,329,334-336}

There are several difficulties in the interpretation of the results. Firstly, it still remains uncertain whether nitrogen oxide gas leads to a chemical passivation of π -bonded carbon or if it induces indeed removal of excess carbon from the interface boundary.^{307,337} Secondly, a significant incorporation of nitrogen into the substrate/oxide interface has been observed^{260,338,339} and has anisotropic behavior depending on the free crystal face^{69,340} with a lower N-incorporation on the Si-face.

Thirdly, the chemistry of SiC/N/SiO₂ interfaces is quite complex with observed Si-N and Si-N-O bonds³⁴¹ and possible C-N bonds. Besides the positive effect of a significant decrease of interface states of *n*-type SiC/SiO₂ interfaces a slight increase in D_{it} was observed for *p*-type SiC (6H- and 4H-SiC).³⁰⁷

Finally, it is still unclear whether nitrogen oxide really leads to a removal of interface states or shifts their energies to a value well beyond the conductive band gap edge of the various polytypes.^{307,335,339} The latter would explain why the interface defect density of *n*-type SiC is decreased in the upper part of the band gap and increased for *p*-type SiC in the lower part.³⁰⁷

2.4.2.4.3 Carbon cluster formation and removal

The formation of carbon clusters may be a direct result of the oxidation reaction (Eq. 1): During thermal oxidation, oxygen undergoes a chemical bonding with carbon from the Si-C tetrahedral and forms both a CO molecule and a SiO₂ precipitate (cf. section 4).²⁸⁹

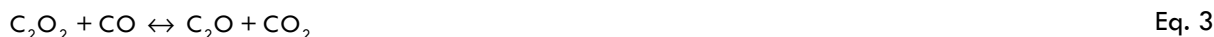


From Equation 1 it is clear that the reaction is dependent on the partial pressure of oxygen in the system. At higher oxygen partial pressures, we would have CO₂ as a reaction product, for low oxygen partial pressures, this is quite different. Already a simple thermodynamic calculation of the reaction (Eq. 2) will show that the equilibrium at 1 bar CO pressure is on the right side up to temperatures of about 1520°C.



The oxidizing character of CO for SiC has been shown also experimentally.³⁴² Therefore, the production of carbon clusters at the interface and the preservation at the interface even at severe oxidative conditions³⁴³ is expected.

The discussion can also be made dealing with CO as the sole source of carbon. Following the Boudouard equilibrium between C, CO and CO₂, carbon precipitation from CO at low temperatures is a well-known feature. The breakup of CO can thus lead to the formation of interstitial carbon clustering near the interface.²⁸⁹ The formation of these in detail is more complex. First-principle density-functional calculations³⁴⁴ show that effusing CO potentially will first undergo a weak bonding with network oxygen within the oxide scale then form a stable C₂O₂ complex with further supplied CO from the SiC/SiO₂ interface. As more CO effuses the cluster will both grow (Eq. 3) and loose bonded oxygen to passing carbon oxide²⁸¹ as the reaction takes place³⁴⁴:



As seen in Eq. 3, a reaction of the C₂O₂ cluster with a CO molecule will lead to oxygen loss.²⁸¹ Oxygen vacancies within the oxide network may also lead to carbon cluster formation.^{281,344}

Reactions between available oxygen and interstitial carbon can also lead to the formation of new CO molecules and can, therefore, possibly foster further oxidation.^{289,291,344} In an ideal case a steady-state-condition forms and consumes carbon clusters (Eq. 4 shall be considered as a simplified equation; equations for removal and formation of more complex carbon clusters are provided in detail in Ref. ³⁴⁴).



The same mechanism was proposed to explain the reduced amount of carbon clusters by POA.^{302,307,319} Ideally, the reoxidation temperature is chosen to be quite low, so that oxygen (or an oxygen containing species) is supplied but further oxide scale growth is kept low.³⁴⁴ Alternatively, the lack of supplied oxygen combined with applied elevated temperatures will induce an increased interface state density.³⁴⁵ For nitrogen oxide one may think of a reaction Eq. 5, yielding an enrichment of nitrogen within the interface layer ²⁷⁷:



Nitridation in detail seems yet to be a more complex process ³²⁴ with strong Si≡N ²⁷⁷ bonds likely to be created - with an unknown impact on the interface structure and termination of the surface of silicon carbide. Reduced oxidation rates may hinder further supply of C and lead to a decrease in the density of carbon clusters.³²⁴ Alternatively, stable CN-molecules could act as pathways for accelerated carbon diffusion.³³⁷ Afanas'ev et al. ³³⁷ also speculated about nitridated SiC/SiO₂ interfaces possibly hampering lateral carbon transport and hence preventing new carbon clusters from being created. As indicated by results from Pantelides et al.,²⁸¹ larger carbon clusters are more likely to be dissolved quite early by nitrogen, while smaller carbon clusters or single atom C will remain longest unaffected.

2.4.2.4.4 Hydrogen passivation and carbon cluster

Excess carbon is also capable of explaining the stability against hydrogen passivation and the observed quasi-continuum of interface states between the band gap edges (cf. Fig. 22, 24).²⁵⁵ It was described that the interface states of SiC/SiO₂ resemble the boundary layer between hydrogenated amorphous carbon films (α-C:H) and bulk SiO₂.^{255,264,289,303,346} Various sizes of sp²-hybridized π-bonded carbon clusters have different positions and energy widths within the band gap.²⁵⁵

2.4.2.4.5 Carbon cluster interface states

The energy range of small clusters at 1.4 eV above E_{c,SiC} ²⁶² well coincides with an increase of D_{it} (cf. Fig. 22). Small clusters also explain the positive charge in p-type SiC as they charge positively when emitting an electron.²⁵⁵ Alternatively, occupied by an electron, these states remain electrically neutral.²⁵⁵ On their behalf, empty states of small carbon cluster will not contribute to interface states for they are located well above the conductive band gap edge.²⁶²

States correlated to larger sp^2 -hybridized carbon cluster sizes (without band gap, i.e., graphite like) are located ≈ 2.5 eV above the conductive band gap edge of silicon carbide.^{255,326} Depending on whether the Fermi level of SiC coincides with the Fermi level of graphite or not, these amphoteric centers can emit or trap electrons and can consequently induce either negative or positive charges characterized by a wide spread energy distribution (cf. Fig. 24).²⁵⁵ Only when the Fermi level of SiC coincides with that of graphite will the graphite like carbon clusters remain electrically neutral.²⁶⁴ With smaller cluster sizes being statistically more probable than bigger ones, one can explain the higher density of donor interface states of SiC/SiO₂ located in the lower part of SiC band gap (Fig. 22). The atomic structure of large carbon clusters is a part of current research (cf. Ref. ^{262,325,347}).

2.4.2.5 OXIDE TRAPS

Not all interface states can be directly attributed to the presence of carbon clusters.^{255,262} Near the conductive band gap edge of 4H-SiC, the energy of the interface states are too high to be ascribed to donor states of sp^2 -C.^{255,262,305} Intrinsic SiO₂ defects (oxide traps), also known from the Si-SiO₂ boundary,^{255,348} may be responsible for this intensified D_{it} increase. Lying close to the conduction band gap edge of 4H- and 6H-SiC, an energy level of ≈ 3.2 eV (independent from the substrate type, i.e., whether it is a SiC polytype or even silicon) above the valence band gap edge was found by comparing Si/SiO₂ and SiC/SiO₂ surfaces.^{255,262,323,348} These defects are attributed to oxygen vacancies in the near-interface region (distance $\approx 1.5 - 2$ nm)²⁶² and can be correlated with excess silicon³²³ inducing acceptor centers.²⁶⁹ The existence of a “suboxidic” phase (Si¹⁺) or different phases (Si¹⁺, Si²⁺, Si³⁺; including oxycarbide phases) was experimentally shown by photoemission studies^{300,301,331,349,350} and seems to depend on the SiC anisotropy.³³² As discussed in section 4.1.2.6, these findings are not commonly accepted as other scientists were unable to find any suboxidic phase at all.

Oxygen vacancies are also responsible for fixed charges.³¹⁷ The significantly higher D_{it} values observed on the C-face of hexagonal SiC may, therefore, also be a result of a larger amount of a suboxidic phase on this face.²⁷⁴ Angle resolved studies of the Si 2p and 1s levels showed that the thickness of the oxycarbide phase does not seem to vary with increasing oxide scale thickness.³⁴⁹

There may also be donor-like oxide defects present within the SiC/SiO₂ interface originating from O/+ levels 1.7 - 1.0 eV above the valence band gap edge of silicon carbide.^{269,313,351} These states, along with acceptor-type defects (energy level at 2.9 eV above E_c of SiC), were found to be attributable to unpassivated O₃≡Si[•] centers.^{269,317} Due to the strong bonding of hydrogen these unpassivated states seem only to attribute a minor amount of interface states to bulk D_{it} .

POA in NO or N₂O was observed not only to decrease carbon cluster related interface states, but also to diminish the number of oxide related defects (so called slow interface states).³³⁷ As pointed out by Li et al.³³⁴ NO is preferable to N₂O since latter even may lead to an increase in interface state density.

Afanas'ev (Ref. ²⁶⁹) showed that it is quite difficult to strictly distinguish between contributions of carbon cluster and oxide defect states since carbon can cause degeneration of silica (Eq. 6):



Considering the superior D_{it} values of Si MOSFETs, one may ask if it is possible to make the SiC-SiO₂ interface as good as the Si-SiO₂ interface.³⁵² Calculated DOS values, however, indicate, that due to elevated D_{it} -values near the valence band gap edge (for SiC polytypes in comparison to Si) silicon carbide MOSFETs will still exhibit inferior electrical properties - even when all carbon cluster related defects could be eliminated. Future work on reconstructed surfaces will show the range of achievable improvements.

2.4.2.6 POLYTYPIC INCLUSIONS

Highly doped 4H-SiC was observed to undergo a partial polytypic transformation into 3C-SiC during thermal oxidation.¹⁴³ The attribution of highly increased D_{it} values near the 4H-SiC conduction band gap edge to polytypic transitions (4H \rightarrow 3C),²⁵⁵ does not seem to be likely for normal oxidation procedures with the exception of highly doped SiC-material¹⁴³ or H₂ etching at extreme high temperatures (1575°C).¹⁴⁴

For some cases or extreme oxidation conditions polytypic inclusions may well be present and hence contributing to elevated interface state densities.³⁵³

In the case of 3C-SiC inclusions in 4H-SiC, polytypic inclusions would lead to a continuum of states originating from the conductive band gap edge of 3C-SiC (2.39 eV) up to E_c of 4H-SiC (3.33 eV).²⁶⁴ These states are characterized by short time constants, therefore, not being likely to attribute to the main part of interface states, which on their behalf exhibit short time constants.²⁶⁴

2.4.3 Dry and wet oxidation

A later section will deal with dry and wet thermal oxidation more in detail (cf. section 4). In this section, only a few aspects of different oxidation methods will be reviewed as far as interface states are concerned.

Wet oxidation, that is, oxidation (or at least low-temperature annealing) using an atmosphere containing water vapor, is believed to produce SiC/SiO₂ interfaces with improved MOSFET properties^{307,339,354,355} but leads to a decreased dielectric strength in comparison to dry oxide scales.³⁵⁶ Hydrogen passivation of interface states might play a role to some extent.²⁷¹

Although decreasing D_{it} of *p*-type SiC, wet oxidation with slow cooling rates was shown to increase the defect state density of *n*-type SiC.³⁵⁴ These newly created defects and associated negative charges³⁵⁴ are believed to generate acceptor like oxide traps near E_c of e.g. 4H-SiC²⁶⁴ accompanied by enhanced electrical conductivity in "wet" oxides (compared to "dry" oxide scales).^{267,351,357} It was speculated whether OH-ions may cause the observed fixed negative charge.³⁵⁴ The different effect of wet oxidation on *p*- and *n*-type SiC is explained by Afanas'ev²⁶⁹ by generation of acceptor like defects which are capable of compensating positive charges from donor states. This effect would be accompanied by a shift of the energy levels of donor states into the SiC band gap due to Coulomb attraction.

For example, Tang et al.³⁵⁸ reported of D_{it} values (3C-SiC) of “wet” oxidized SiC samples (1150°C) lying more than one order of magnitude under those of samples provided by “dry” oxidation at 150°C lower oxidation temperatures. Best properties were found after wet oxidation at 1000°C.³⁵⁹ The interface state density was found to be rather independent of the oxide scale thickness (wet oxidation always leads to a larger oxide thickness than dry oxidation as discussed in section 4.2)³⁶⁰ but it strongly depends on the oxidation ambient. Moreover, those generated defects will compensate positive charges from donor states and will raise donor state levels well above the valence band gap edge due to Coulomb attraction.²⁶⁹ There is also a positive charge build-up in “wet” oxide scales on SiC.³⁵¹

Zaima et al.³⁵⁹ speculated as early as in 1990 about potential effects explaining the superior electric properties of wet oxidized SiC MOSFETs: (1) hydrogen passivation of dangling bonds, (2) removal of carbon or carbonaceous species from the interface and (3) preferential removal of C atoms from the silicon carbide surface leaving a Si-rich layer behind. First, as pointed out earlier, it seems to have a minor effect. However, the removal of carbon³⁵⁴ by forming hydrocarbon species and their fast transport away from the interface layer could explain the superior electrical properties of wet oxidized SiC-SiO₂ interfaces. As pointed out later in section 4.2, H₂O will lead to higher oxidation rates because of the higher permeation rate of water molecules in silica.³⁶¹

Results from Chaudry³⁶² indicate a $7 - 2^{1/3}$ fold increased carbon uptake of the wet oxidized oxide scale on 3C-SiC in comparison to oxidation in dry oxygen. This is believed to be due the formation (Eq. 7) of CO₂ as a product of reaction³⁶²:



CO₂ would be slower to diffuse through the oxide scale (cf. section 4.1.3) - accompanied by the formation of hydrocarbonaceous species, hence increasing the bulk amount of carbon present within the SiO₂ layer.³⁶² Due to a possible formation of SiO deteriorating the SiO₂ scale Chaudry³⁶² found a more stoichiometric oxide scale on wet oxidizes silicon carbide compared to a low-carbon showing, dry oxidized SiO₂ layer (Eq. 8 - 9).



The SiC/SiO₂ interface of dry oxide scales would exhibit more interface defects correlated with silica defects and, therefore, lead to increased D_{it} values. Newer results (Ref. ³⁶³) affirm the possibility of a substoichiometric SiO_x layer (however, x is set to be 1.5 and not 1.0 as in Ref. ³⁶² and this layer is strictly limited to the interface) as well as a carbon enriched interlayer boundary (also explaining increased interface state densities of dry oxide scales). It shall be noted that on the surface of the oxide scale heading toward the atmosphere, the nature of the oxide (i.e., SiO₂) is similar for all three cases: for C- and Si-terminated SiC as well as for pure silicon.³⁶³

In comparison to that a generally higher carbon content in the bulk oxide layer as found by Chaudry et al.³⁶² seems not necessarily to lead to an increased carbon cluster density at the interface or related carbonaceous species interfering with the electronic mobility of SiC. Latter seems to be affirmed by newer results³⁶⁴ identifying the excess carbon in oxide scales on oxidized SiC (under atmospheric conditions at elevated temperatures) possibly as hydrocarbon³⁶⁵ or displaced carbon atoms. In contrast to this, Chatty et al.³⁰⁶ identified a slightly increased number of interface states at the wet oxide - substrate interface of 4H-SiC. Once more, - like Lu et al.³²⁹ pointed out; more work needs to be done in order to decide what processes may lead to increased interface state densities in the case of wet oxidation and improved D_{it} valued in the case of POA.

3. EXPERIMENTAL AND ANALYTICAL ASPECTS

3.1 Introduction and historic aspects

3.1.1 Oxidation types

The main focus of this article is on the formation of SiO_2 out of SiC substrate due to thermal oxidation of the latter. Silica formation requires some oxidant species available in the outer atmosphere during a treatment at high temperature. This process is described as thermal oxidation, i.e., carbon extraction by oxygen and is not limited to pure O_2 -environments: CO_2 , standard air or artificial gas mixtures can be suitable. Often the distinctions between (1) dry thermal and (2) wet thermal oxidation are made.

The first requires *sensu stricto* nominally completely dry atmospheres (may it be air, CO_2 or pure oxygen) which can be achieved by using high-purity gases and predrying the gas with P_2O_5 and CaCl_2 . Unfortunately, “dry thermal oxidation” is still used in a more general way denoting almost every oxidizing atmosphere that was not additionally enriched by water vapor. It will be discussed in section 4.2 that already small amounts of water greatly affect the oxidation rates and kinetics of silica formation, hence careful evaluation of the experimental set-up is vital. The latter (wet thermal oxidation) denotes an oxidizing atmosphere that was deliberately enriched by a usually controlled amount of water vapor. A way to do so is to lead the gas flow directly through a reservoir of hot water.

It is important to distinguish strictly between wet thermal oxidation (using oxidizing gases) and hydrothermal corrosion. The term hydrothermal has no general accepted definition but in most cases the sample is surrounded by hot fluid water at $T \geq 100^\circ\text{C}$ under high pressures (either the natural pressure of boiling or controlled externally). Hydrothermal treatment of silicon carbide will be discussed briefly in section 4.3.

Two other types of silicon carbide oxidation have to be distinguished: active and passive oxidation. “Passive” denotes in this context the formation of a superficial compound hindering further access of an oxidant species (like CO_2 , H_2O , or oxygen) to the substrate (SiC). Therefore, it is not restricted so silica formation as theoretically oxycarbides or graphite could also act as a corrosion-hampering layer. The larger the solid barrier the slower will silicon carbide be oxidized. In comparison to this active oxidation is always characterized by a bulk mass loss and often following a linear time-law under steady-state conditions. Depending on environmental conditions (used gas composition, oxygen partial pressure, temperature...) active or passive oxidation will occur.

3.1.2 Furnaces and impurities

To achieve the high-temperature regimes in which SiC oxidation takes place control of atmospheric composition and temperature of the environment is necessary. However, the choice of experimental set-up and the materials for the furnace does influence the oxidation of silicon carbide itself.

Impurities like sodium, for example, derived from the tubing of alumina furnaces, accelerates the oxidation rate by modifying the network or lattice structure of silica (cf. section 4.1.4.5). These influencing parameters can be diminished by a long-time pre-heat treatment of the furnace or even be avoided by the use of fused silica furnaces. The latter are endangered in high-temperature regimes as crystallization processes within the SiO_2 -matrix can occur. Crystallized silica will undergo a β -to- α -phase transition below $\approx 270^\circ\text{C}$ and cracks formation can disintegrate the furnace tube.

Special *in-situ* measurement methods (like XRD or thermogravimetry) might require modification to the experimental set-up and it might be necessary to introduce other materials to the furnace (like windows allowing X-rays or a laser beam to enter the reaction chamber). It should be carefully noted that every further introduced phase might be a potential source of impurities.

Not only the furnace, but also the sample's mounting is a critical factor. Ideal would be to mount the sample in a way in which it lies 90° towards the incoming gas stream. Also has the spacing between individual samples (if conducting experiments on several samples at one time) to be sufficiently large so that every single specimen is introduced to a similar gas flow. In case of unevenly distributed gas current, the oxidation progress will be accelerated at the side headed towards the incoming gas ("oxidation pennant"). This effect might also be related to the increased impurity input at the front side.

Besides the need of a homogeneously distributed gas current (if not conducting the oxidation in a sufficiently large furnace under regular air), the choice of the mounting's material is important. Using non-heat-treated alumina will once more introduce, for example, sodium to the oxidation atmosphere and due to the areal proximity of sample and mounting will the input be significant. For low-temperature oxidation experiments, a horizontally sliced silica tube, in which vertically inserts (large enough to fit the sample but small enough to avoid a loose mounting) were cut, was shown to be suitable. Alternatively a mounting made out of the very same material the sample consists of (e.g. single-crystalline $\delta\text{H-SiC:N}$) can be used. The latter is also appropriate for high-temperature experiments and avoids the introduction of silica onto the sample. Thermogravimetric experiments though might require a special set-up setting.

3.2 Analytical aspects and methods

3.2.1 Gravimetry

The most historic method to observe silica formation on silicon carbide and to study the kinetics of SiO_2 growth is the use of gravimetry.³⁶⁶⁻³⁷⁰ As discussed in section 4, the bulk oxidation mechanism of silicon carbide yields a bulk weight gain per net reaction as two oxygen atoms replace one carbon atom within the SiC-lattice. Knowing the total surface area and estimating the oxide scale's mean density, one easily can calculate the SiO_2 -layer's thickness out of gravimetric data. This will be done in detail in section 4.1.2.3 and, therefore, this section shall only briefly look on some experimental aspects of gravimetrics.

The simplest way for gaining gravimetric data upon SiC oxidation is weighting a certain sample before and subsequent to exposing it to an oxidizing atmosphere at elevated temperatures. Such *ex-situ* measurements require a high-resolution ultra-micro-balance and carefully performed calibration of the system. Trivial aspects, as preheating the balance and both temperature- and air-pressure-related influences have to be considered as well as air humidity. As neither silica nor silicon carbide are pronounced hygroscopic materials, weight gain due to water adsorption can be neglected in comparison to other influencing parameters. Depending on these impact factors, accuracies in the range of 1 - 3 μg are possible to achieve when contaminations can be excluded accentuating the need of a clean and dust-free environment as long as the measurements are statistically significant (i.e., each measurement should be repeated at least 3 - 5 times).³⁷¹

Alternatively, an *in-situ* way to gain kinetic information is by thermogravimetry. As long as the correction for buoyancy is carried out adequately, real-time data can be accessed up to $\approx 1700^\circ\text{C}$ in controlled oxidizing atmospheres using an alumina furnace (with all the inflicting impurity-related complications). This is why this method was applied by many scientists from the 1950s up to present-day experiments. Also, mass loss due to bubble formation is shown in TG measurements by a characteristic zigzag-pattern corresponding with the collapse of individual bubbles.³⁷²

However, it is a bulk analysis method as only the net weight change of the whole sample can be observed. It will be shown in section 4.1.4.3 that SiC oxidation is an anisotropic process and different oxidation rates on certain crystal faces are hard to resolve. Likewise polarity-dependent oxidation rates and local inhomogeneities like defects structures (micro- or macropipes/voids etc.) result in gravimetrically unresolvable deviations from the ideal oxidation behavior. In addition, accelerated oxidation at the sample's edges will, on small-scale samples, result in a further error.

Other typical experimental errors are the uneven access of the oxidizing gas to the sample. This occurs, for example, by obstructing faces by mounting parts.

Gravimetric data has to be related to the surface area exposed. Surface area determination and development can be a problem in porous samples and is of major concern in powder studies. Here shrinking core models for surface reduction with time are necessary and this is not trivial as powders are usually neither perfectly shaped nor monosized and even then the development of surface area must include sintering effects.

In our studies on single-crystal samples of 6H-SiC:N of a size of 15 x 5 x 0.25 mm a 3 - 10 % range of error was shown to be realistic. Latter may well for small samples yield an additional source for an error of 20 % for thickness values.

A further possible source for errors is the structural development of silica scales grown on silicon carbide (cf. section 4.1.4.4). At temperatures above $\approx 1200^\circ\text{C}$, significant devitrification processes will take place and crystalline areas grow less rapid than amorphous regions. A semi-crystalline state of the bulk oxide layer influences the conversion of gravimetric data into a scale thickness (cf. section 4.1.2.3) because exact knowledge of the bulk density is required.

3.2.2 Microscopy

Microscopy, in general, is a highly valuable method for kinetic characterization of silica films on silicon carbide. The significant gain of additional pieces of information like phase morphology, structural aspects and the possibility to determine area resolved thickness values greatly show the importance of this analytical method. Also, the sample does not require any special treatment before light microscopy could be applied.

For first examinations, light microscopy is recommended. Thin silica layers (below about $1.5 \mu\text{m}$) have interference colors which correlate with the scale's thickness.

Cut or broken samples are rarely suitable for the determination of scale's thickness by light microscopy, because the diffraction limited resolution of a 100times magnifying objective lens lies close to $1 \mu\text{m}$ and often it is difficult to distinguish scale and substrate. Hence, Scanning Electron Microscopy (SEM) is commonly used for such studies.

The use of a special sample mounting (Fig. 25) has proven to be very convenient in this context. Unlike regular SEM mountings is the table of this mount holder bisected by a step in height, that is, one elevated side and one less high part. Breaking a sample in sufficiently small parts, one part can be fixed sideways on the step's side so that the truncated SiC-SiO₂-transition heads upwards towards SE- or BSE-detector. Upon the elevated section, another part of the sample can be placed so that the surface morphology of the bulk oxide layer can be studied simultaneously to the carbide-oxide-transition.

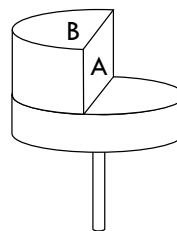


Fig. 25. SEM sample mounting to observe a cross-section of part (A) and a bulk surface area (B).

Pointed tilting-series allow to access ample view directions to directly perform measurements that are supported by chemical information like EDX oxygen mappings to distinguish between structures obtained from breaking the sample and the true oxide scale. Often SEM studies can be done without a conductive coating (Pt is recommend: it is superior to pure gold due to the formation of smaller clusters) because of the electronic properties of SiC and thin oxides scales.

Because of the tedious sample preparation, Transmission Electron Microscopy (TEM) is not often used in oxidation studies. This will change with advanced techniques like focused ion beam (FIB) becoming more widespread.

3.2.3 IR and Raman spectroscopy

Both IR and Raman spectroscopy use lattice (or network) vibrations to gain phase-dependent information. Chemical and structural modifications of the sample will influence the obtained spectra. Both methods can be applied in reflective condition and, therefore, even *in-situ* observation of silica growth on non-transparent silicon carbide (like heavily doped SiC or SSiC) can be studied.

Especially Raman spectroscopy is a wide-used method to characterize both SiC and silica and their polytypes. Vibration spectroscopy is capable to inspect also vitreous silica layers or amorphous silicon carbide.

Scale thickness determination by spectroscopic studies requires very thorough calibration with known standards. This is hardly ever done because light reflection on non-smooth surfaces affects the absolute intensities of the individual modes and, therefore, band intensity ratios. Amorphous silica layers smaller than 1 μm are usually very difficult to detect using conventional Raman spectroscopy. New enhanced spectroscopic methods like Tip-Enhanced Raman Spectroscopy TEARS may change this situation in future.

3.2.4 Ellipsometry

Ellipsometry is a very powerful optical method to characterize the thickness of thin-film layers by measuring the changes of polarized light that is reflected from a certain surface. It is suitable for layer thicknesses up to $\approx 10 \mu\text{m}$ (for UV) especially when using spectral ellipsometry. With special focusing systems, the beam diameter can be reduced from several millimeters to below 100 μm making spatially resolved spectra possible.

For silica scales on opaque SiC samples, no special pre-treatment is required. For optically transparent single-crystal silicon carbide, pre-oxidation treatments are advisable: (1) roughening the back of the sample or (2) avoiding plan parallel surfaces. First induces diffuse scattering while latter will cause a deflected back-reflection. Choosing an angle large enough (e.g. 1°), the back-reflection can be blinded out completely without inducing a surface-modifying method.

The main field of application for ellipsometry is analyzing sub-micrometer-thick layers - like silica thermally grown on silicon. Ideally, it requires smooth, homogenous surfaces and allows the introduction of several different layers, as long as they succeed in a layer-by-layer-like manner. Mathematical methods, however, also allow to introduce mixed interlayers (mixed in a sense of changing refraction index; may it be a mean refraction index or a gradually changing case) and a surface roughness. As long as the surface roughness does not exceed $\approx 1/10$ of the wavelength of the used light, a simple EMA approach (Effective-Medium-Approximation; e.g., after Bruggeman Ref. ³⁷³) can be applied.³⁷⁴ A significantly larger surface roughness causes depolarization of the light (latter can be used as a tool to characterize the magnitude of the superficial roughness itself).

As discussed in section 4.1.4, silicon carbide oxidation will not always result in smooth and homogenous silica layers. Especially sintered SiC can exhibit pronounced bubble formation even in dry thermal environments. This significantly influences the application of ellipsometry as bubble diameters in the range of 1 - 2 μm yield an undulating morphology with an according error in thickness determination. Own studies on SSiC with scale thicknesses of up to 500 nm confirmed that deviations between data derived from ellipsometry and from SEM-measurements remained well in an error margin below 6 %.

3.2.5 X-ray diffraction

The classical method for *ex-situ* phase analysis, X-ray diffraction, has recently been shown to be useful for *in-situ* silica growth determination of oxidized silicon carbide samples.³⁷⁵

The method is based on the fact that every layer above a semi-infinite crystalline medium will decrease the signal intensity of the substrate even if the adlayer is of vitreous nature. Knowing the mean density of the silica layer and the mass absorption factor, the thickness can be calculated for every Bragg angle.

Likewise, an oxide scale X-ray signal intensity increase can also be used to characterize *in-situ* (or *ex-situ*) scale thicknesses. Care must be taken for *ex-situ* studies, because SiC's mosaicity (cf. section 4.1.4.6.4) yields shifted reflections with different intensities as a source of error, because the individual reflection intensity is needed to calculate oxide layers above the silicon carbide substrate.

Another emerging technique is μ -XRD with area sensitive detectors. Here we obtain information about the crystallographic orientation of the crystalline silica phase and access information about the devitrification process. The measuring spot size of modern-day X-ray diffractometers can reach values even below 50 μm using X-ray focusing capillaries.

3.2.6 Outlook

In this review, we concentrated on some analytical method to determine the thickness of oxide scales on silicon carbide. As a matter of course there are capable methods that were not introduced yet - like X-ray reflectometry (suitable for a scale thickness of $\approx 2 - 200$ nm and a precision of ≈ 200 pm; Ref. ³⁷⁶), Rutherford backscattering spectrometry RBS (with its advantage to measure even rather curved scaled; Ref. ^{183,377}), capacitance-voltage (C-V) measurements (which, like ellipsometry, requires a suitable model; Ref. ^{77,135,358,378}), or (Angle Resolved) X-Ray Photoelectron Spectroscopy (AR)XPS (a highly surface specific method; Ref. ³⁷⁹). Depending on the actual question, the most suitable measurement method will be chosen but it is advisable to apply several, independent methods and compare the obtained results.

4. THE KINETICS OF SILICA GROWTH

4.1 Dry thermal oxidation

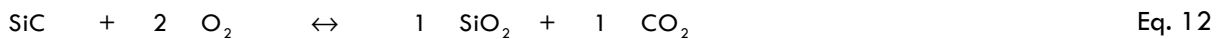
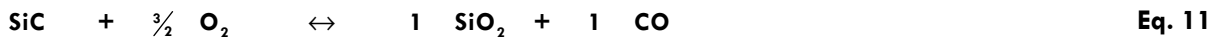
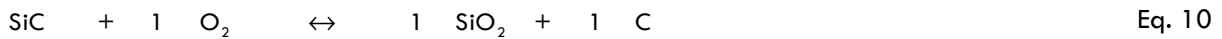
4.1.1 Introduction

Although silicon carbide is not thermodynamically stable at room temperature in oxygen-containing atmospheres, no significant oxidative reaction will take place below about 900°C.³⁰ This long known oxidation resistance of silicon carbide makes this material suitable for high-temperature applications.

Silica formation on silicon carbide is a process quite similar to the well-known silicon oxidation process. In gaseous atmospheres with low oxygen partial pressures silica will not be formed on a bare silicon carbide surface. Instead gaseous SiO and CO is formed, leading to an "active" oxidation, the mass loss of the sample. The boundary towards silica growth has been extensively discussed in the literature (examples are Refs ^{369,372,380-384}) and is usually found to be at similar $P_{(\text{O}_2)}$ -T conditions like silicon, that is, $\approx 10^{-4}$ bar $P_{(\text{O}_2)}$ at 1400°C and 10^{-3} bar $P_{(\text{O}_2)}$ at 1550°C.

However, whether passive oxidation takes place at all and how fast the oxide scale builds-up will strongly depend on (1) temperature,³⁸⁵ (2) atmospheric composition (among others oxygen partial pressure; Ref. ^{386,387}), (3) total atmosphere pressure, (4) polytype, (5) surface condition (face-polarity, smoothness), (6) intrinsic factors (pore volume ³⁸⁵ or defects ³⁸⁸) and (7) extrinsic parameters (impurities ³⁸⁹ and, when dealing with sintered ceramic bodies, sintering aids ^{390,391}). These factors will be discussed in more detail in section 4.1.4.

“Passivation” of the silicon carbide surface means that an increasing thickness of the silica layer makes it more and more difficult for oxygen to reach the silicon carbide interface where it leads to further oxidative reactions. Several silica forming reactions (Eq. 10 - 12) are theoretically possible between SiC and O₂ (Ref. ³⁹²):



Among these listed and other possible reactions, only equation 11 (introduced in Eq. 1, 6) was found to be true in gas oxidation.^{30,393-395} The formation of carbon along with silica was found in hydrothermal experiments ³⁹⁶⁻³⁹⁸ at 500° - 600°C and 100 - 200 MPa water pressure.

Auger spectroscopic examinations of the created, solid silica layer show an almost ideally stoichiometric SiO₂ composition.³⁵¹ Analogue silica forming reactions can be formulated using other oxygen containing atmospheres.^{372,399-401} For one example, pure CO₂ leads also to the formation of stoichiometric silica.^{342,392,402}

Silica is less dense than silicon carbide, hence silica formation will increase both bulk volume and bulk mass of the original SiC body (cf. Fig. 26).³⁸³ For amorphous silica with a density of 2200 kg·m⁻³ the production of a silica scale of thickness *x* will result in a penetration or reaction depth of 0.458 *x* and a corresponding gain in sample thickness of 0.542 *x*. The resemblance in density of silica in amorphous or crystalline form keeps these factors very similar for crystalline silica. A density of 2300 kg·m⁻³ for α-cristobalite shifts the factors to 0.485 and 0.515, respectively.

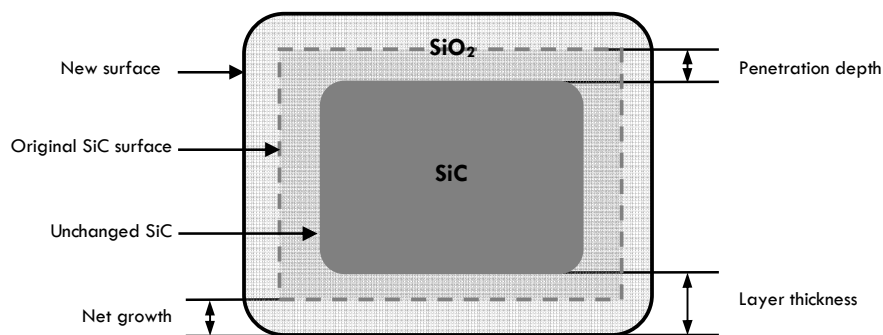


Fig. 26. Schematic illustration of the volume change during passive oxidation of silicon carbide (after Ref. ³⁸³). It is important to keep in mind that SiC oxidation is much more complex than schematically drawn above (e.g. due to anisotropy).

Analogous to silicon causes the oxidation with silica layer growth causes intrinsic compressive stress in the x-y-plane (i.e., planar to the SiC-SiO₂ interface), assuming a zero stress component in the z-direction due to mismatch of thermal expansion coefficients between oxide scale and carbide substrate.^{403,404} Viscous flow of SiO₂ grown on silicon carbide might be an important stress relief mechanism above 960°C.⁴⁰⁵

The basic factors, which could be rate limiting for silicon carbide oxidation are: (1) diffusion of oxygen within the atmosphere, (2) in-diffusion of oxygen through the forming silica layer, (3) oxidation reaction at the SiC/SiO₂ interface (4) out-diffusion of the gaseous oxidation product(s) through the silica layer and (5) out-diffusion of gas phases from the SiO₂ surface back into the atmosphere.^{406,407} The outward diffusion of gaseous products distinguishes the carbide from pure silicon oxidation, because in latter case there is no gaseous reaction product.

In steady-state conditions, linear kinetics of silica growth would indicate reaction control mechanisms, and a parabolic time-law corresponds with diffusion controlled processes.⁴⁰⁷ Supposing a surplus of oxygen, the first process (diffusion of O₂ within the outer atmosphere) will be the outmost fastest one and cannot be attributed to be rate-controlling at all. The reaction at the SiC/SiO₂ interface will most likely be much faster than the volume/grain boundary diffusion of the reactive gas or the reaction product gas phase. However, the resulting rate-controlling factor should be one order of magnitude faster than other possibly influencing processes. Otherwise, a mixed-type (e.g. linear-parabolic) will result for the kinetic model of oxide scale built-up.⁴⁰⁷

4.1.2 Growth laws

4.1.2.1 DEAL-AND-GROVE MODEL

A model proposed by Deal and Grove in 1965 for the oxidation kinetics of pure silicon is often adapted for SiC oxidation.^{408,409} This model can be applied for the description of the formation of amorphous or crystalline silica exceeding 20 - 25 nm the substrate/oxide interface.^{262,363,410-412} In case of pure silicon we have the oxidation reaction (Eq. 13):



As long as diffusion of oxygen through the growing silica layer dominates the kinetics, those will be parabolic for long-time periods under steady-state conditions. During the initial stages, at which only a very small oxide layer thickness is given, the short pathways for oxygen prevent the domination of diffusion. Reaction control has to dominate the process and an initial linear kinetics period follows. This model can successfully be transferred to SiC oxidation (although some special parameters must additionally be considered).^{262,292,338,411,412}

The general law (Fig. 27) is (Eq. 14):

$$x^2 + A \cdot x = B \cdot (t + T) \quad \text{Eq. 14}$$

In this equation, x denotes the oxide scale thickness (or the weight-gain per area unit), t denotes the oxidation time and T shifts the initial time to a certain value, taking an initially given oxide scale thickness into account.

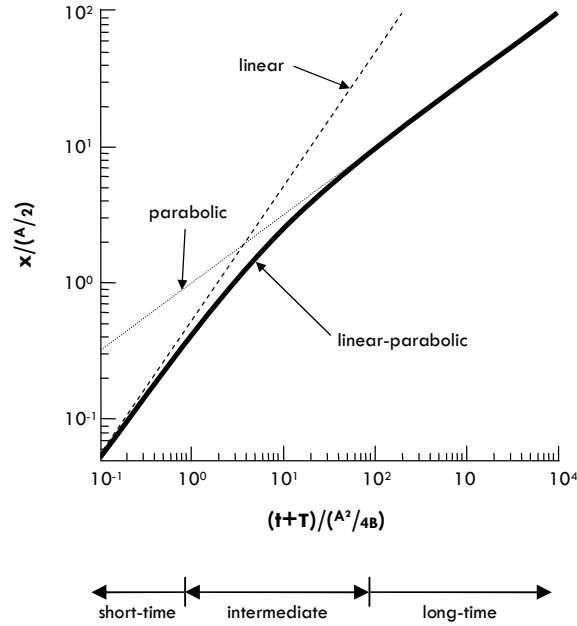


Fig. 27. For a kinetic process truly following the linear-parabolic time-law as defined by Deal and Grove ⁴⁰⁸, a linear time-law for short-times and a parabolic time-law for long-times are good approximations. However, intermediate times (that cannot be estimated *a priori*) do require a time-law incorporating both k_p and k_l (i.e., parabolic and linear rate-constants; cf. Ref. ⁴⁰⁸).

The quotient of B/A is called “linear rate-constant” and is usually abbreviated as k_l . This factor is proportional to the reaction rate of the slowest reaction, while the parabolic rate-constant (B , k_p) is proportional to the effective diffusion coefficient D^{eff} (Eq. 15). This makes two process factors be accessible by Eq. 14.⁴¹³

$$B = k_p = \frac{2 \cdot D^{eff} \cdot c}{N} \tag{Eq. 15}$$

D^{eff} denotes the effective diffusion coefficient within the oxide scale, c denotes the concentration of the gas species being transported and N labels the number of gas molecules / ions per one volume unit.^{350,408} In the case of the Henry law being applicable, c (concentration) is direct proportional to the partial pressure of the gas species in the oxidation atmosphere.⁴¹⁴ Both rate-constants, k_p and k_l , are thermally activated parameters following an Arrhenius law with characteristic activation energies E_a (cf. section 4.1.5).^{408,415}

Depending on the frame of reference, the unit of k_p is $[m^2 \cdot s^{-1}]$ or $[kg^2 \cdot m^{-4} \cdot s^{-1}]$ and the units of k_l are $[m \cdot s^{-1}]$ or $[kg \cdot m^{-2} \cdot s^{-1}]$.

Using the introduced nomenclature, Eq. 14 can be rewritten (Eq. 16):

$$\frac{x^2}{k_p} + \frac{x}{k_l} - T = t \tag{Eq. 16}$$

Solving Eq. 16 for x (scale thickness or weight-gain-per-area unit) yields (Eq. 17):

$$x = \frac{\sqrt{k_p} \cdot \left(-\sqrt{k_p} + \sqrt{4 \cdot t \cdot k_i^2 + 4 \cdot T \cdot k_i^2 + k_p} \right)}{2 \cdot k_i} \quad \text{Eq. 17}$$

When using a system without an initial oxide scale (e.g. by HF etching prior to the actual oxidation experiment) simplifies to (Eq. 18):

$$x = \frac{\sqrt{k_p} \cdot \left(-\sqrt{k_p} + \sqrt{4 \cdot t \cdot k_i^2 + k_p} \right)}{2 \cdot k_i} \quad \text{Eq. 18}$$

For further simplifications, the original equation (Eq. 14) shall be considered. Solving for x gives (Eq. 19):

$$\frac{x}{A/2} = -1 + \sqrt{1 + \frac{t+T}{A^2/4 \cdot B}} \quad \text{Eq. 19}$$

This can be simplified further for (1) very short or (2) very long times. In the first case, Eq. 20 is obtained from the assumption “ $t \ll A^2/4 \cdot B$ ” (Eq. 20):

$$x \cong k_i \cdot (t+T) \quad \text{Eq. 20}$$

In the other case (long oxidation periods) the basic assumption can be formulated to be “ $t \gg A^2/4 \cdot B$ ” and Eq. 21 results:

$$x^2 \cong k_p \cdot t \quad \text{Eq. 21}$$

As pointed out by Deal and Grove in 1965, kinetic data even in an ideal parabolic system cannot always be completely described with the simple parabolic time-law of Eq. 21. The large scatter in oxidation rates of the literature is partially due to forcing a simple parabolic law into the data.

4.1.2.2 APPLICATION OF THE DEAL-AND-GROVE MODEL TO SiC OXIDATION

It seems to be true for all crystallographic faces of the various SiC polytypes that Eq. 14 - 21 do describe the oxidation process well, including short initial phases⁴¹⁵ and gaseous diffusion as the long-term dominating rate-limiting process for temperatures below the melting temperature of silica (i.e., 1710°C).¹⁶⁸ As discussed later in more detail, the literature overflows with different values for parabolic and linear rate-constants. When taking the plenitude of influencing parameters, non-standardized testing methods and different material variations (both in polytype and fabrication method [e.g., hot pressing / sintering / liquid-phase sintering]) into account, this does not really surprise. Even deviations of more than one order of magnitude are not unusual.

Until now, it is not entirely clear whether it is oxygen or carbon monoxide diffusion or the combination of it through the forming silica layer determining the oxidation kinetics.⁴¹⁵ Oxygen diffusion was most often declared to be the most likely process.⁴¹⁴⁻⁴¹⁶ Other possible reaction products (like SiO) do not seem to be of significant influence on the kinetics.⁴¹⁶ Experimental results obtained from oxidations in both pure oxygen and compressed air above 1500°C^{30,342,406} shows only minor differences in the oxidation rates. A possible domination of CO diffusion at these high temperatures has been discussed.^{30,417}

Song et al. proposed modified Deal-and-Grove-like kinetics for basic SiC oxidation considering out-diffusion of CO.¹⁸⁶ Similar to the method applied by Deal and Grove⁴⁰⁸ they find for a steady-state with the preconditions (1) $C_{CO}^* \ll C_{O_2}^*$ (i.e., the concentration of CO in the outer oxidation atmosphere is much smaller than the concentration of oxygen = equilibrium concentration) and (2) for diffusion as the rate-limiting step the following equation for the parabolic rate-constant k_p (Eq. 22):

$$k_p = \frac{K_f \cdot c_{O_2}^* - K_r \cdot c_{CO}^*}{\frac{3/2 \cdot K_f}{D_{O_2}^{eff}} + \frac{K_r}{D_{CO}^{eff}}} \cdot N \quad \text{Eq. 22}$$

K denotes the reaction rate-constant (f... forward / r... reverse reaction as given in Eq. 1, 6), c^* the equilibrium concentration, N stands for the number of oxidant molecules incorporated into one unit volume of the oxide layer and D^{eff} for the effective diffusion coefficients of O_2 and CO through solid silica. The basic reaction equation for Eq. 22 is Eq. 23:



This reaction is believed to be extremely exothermic with $\Delta H_{298}^0 = -950 \text{ kJ} \times \text{mol}^{-1}$.⁴¹⁸ For the first case, in-diffusion of oxygen to be rate-limiting (i.e., $\frac{K_f}{D_{O_2}^{eff}} \gg \frac{K_r}{D_{CO}^{eff}}$), the following equation (Eq. 24) can be found, which is similar to the Deal-and-Grove-findings presented in Eq. 15):

$$k_p \approx \frac{c_{O_2}^*}{3/2 \cdot N} \cdot D_{O_2}^{eff} \quad \text{Eq. 24}$$

Correspondingly, for CO-out-diffusion as the rate-limiting step, Eq. 25 would be true:

$$k_p \approx \frac{c_{O_2}^* \cdot K_f}{N \cdot K_r} \cdot D_{CO}^{eff} \quad \text{Eq. 25}$$

Under steady-state-condition, all fluxes (F_1 = gas transport towards the outer surface, F_2 = diffusion through solid silica, and F_3 = reaction at the SiC-SiO₂ interface) are equal during passive oxidation. This steady-state-condition is not to be mistaken with an equilibrium condition, for an unlimited supply of oxygen will always lead the basic reaction equation to SiC consumption and SiO₂ + CO formation. As formulated by Song et al.¹⁸⁶ the steady-state can be expressed by Eq. 26:

$$F_{\text{reaction}} : F_{O_2\text{-in-diffusion}} : F_{CO\text{-out-diffusion}} = 1 : \frac{3}{2} : 1 \quad \text{Eq. 26}$$

Hence, for a first-order-reaction, the following was approximated (Eq. 27):

$$F_{\text{reaction}} = K_f \cdot c_{O_2} - K_r \cdot c_{CO} \quad \text{Eq. 27}$$

Actually, as conceded by Song et al. (Ref. ¹⁸⁶) this equation should contain 1.5 in the exponent of the concentration of O₂. Moreover, the assumption of a first-order reaction at all was discussed in this article. First-order reactions only depend on the concentration of one reactant (in this case: oxygen) and, therefore, would on all SiC faces let the very same oxidation rate to be expected (what is not true as discussed in section 4.1.4.3). Hence, a non-first-order reaction seems more likely (e.g. 2nd order). However, it is still a matter of dispute to assume an equilibrium relation to be true in a steady-state-condition in which CO-out-diffusion is supposed to be faster than oxygen-in-diffusion (otherwise, among others extensive bubble-formation would result). Therefore, c_{CO} could be approximated to be zero leading to a pure Deal-and-Grove-equation.

The discussion seems to explain basic features by differing time/temperature frames in which reaction rates influence the parabolic law. Especially on the Si-terminated face (0001) of hexagonal SiC linear oxide scale growth can be observed for longer periods than on the opposing C-terminated face.^{30,419} Differences in temperature dependence of all three processes (reaction rates and diffusion of both oxygen and CO) are a likely source for many discrepancies of measurements.

Nonetheless, it shall be noted that there is no suitable model for SiC oxidation resolving all influences on oxidation rates including impurities, crystallographic aspects, composition and crystallinity of the silica layer.^{19,168}

4.1.2.3 CONVERSION OF GRAVIMETRIC DATA

For a constant stoichiometry of the oxidation reaction as defined in Eq. 23, in which silica is the only solid oxidation product and CO leaving the system as a vapor phase, mass gain per unit area can easily be converted into scale thickness. Neither a porosity of the silica scale nor the loss of mass due to spallation are implemented into the calculation. For sintered SiC bodies, additional reactions (e.g., when carbon and/or boron are present) must be considered. One further restriction is the fact, that when SiC oxidizes, the interface will move into the solid and, therefore, the reference area will decrease. This shrinking core effect can in most cases be neglected for bulk sample surfaces larger than 10 mm² and a scale thickness in the lower μm-range.

Thermal wet or dry oxidation of silicon carbide following Eq. 23 yields an increase in weight as 1 mol carbon is substituted by 2 mol oxygen. Thus for each net reaction of a formula unit of SiC a mass gain of 19.9881 g is observed.

The next critical factor for the conversion is the density of the silica layer. As discussed in section 4.1.4.4, the silica layer may transform completely or partially into crystalline silica. For a first approach only vitreous SiO₂ shall be considered ($\rho = 2200 \text{ kg}\cdot\text{m}^{-3}$)¹⁵³.

A correlation between scale thickness (x) and mass gain (Δm) is then found using a stoichiometric correction term ξ (Eq. 28):

$$x = \frac{\left(\frac{m_2 - m_1}{A} \right) \cdot \left(\frac{n_{\text{SiO}_2} \cdot M_{\text{SiO}_2}}{n_{\text{SiO}_2} \cdot M_{\text{SiO}_2} - n_{\text{SiC}} \cdot M_{\text{SiC}}} \right)}{\rho_{\text{SiO}_2}} = \frac{\Delta m \cdot \xi}{A \cdot \rho_{\text{SiO}_2}} \quad \text{Eq. 28}$$

With ξ (Eq. 29):

$$\xi = \frac{n_{\text{SiO}_2} \cdot M_{\text{SiO}_2}}{n_{\text{SiO}_2} \cdot M_{\text{SiO}_2} - n_{\text{SiC}} \cdot M_{\text{SiC}}} = 3.006 \quad \text{Eq. 29}$$

Depending on the frame of reference, mass-gain or scale-thickness related rate-constants can be found in the literature. Assuming a known density of the silica layer, the parabolic rate-constant can be converted by the use of Eq. 30 (Ref. ³⁸³):

$$k_p^{\text{scale thickness}} \cdot \frac{\rho_{\text{SiO}_2}^2}{\zeta^2} = k_p^{\text{mass gain}} \quad \text{Eq. 30}$$

As an example for the incorporation of sintering additives we shall discuss a case of a high level of carbon to be present. Carbon will leave the SiC-SiO₂ system as CO (the amount retained in bubbles, section 4.1.4.6.3, is neglected).

First, we need to convert the mass amount of carbon (wt%_C) into a mol percentage (mol%_C; Eq. 31; no unit):

$$\text{mol}\%_{\text{C}} = \frac{M_{\text{SiC}} \cdot \text{wt}\%_{\text{C}}}{M_{\text{C}} + \text{wt}\%_{\text{C}} \cdot (M_{\text{SiC}} - M_{\text{C}})} = \frac{\text{wt}\%_{\text{C}}}{0.70045 + 0.29954 \cdot \text{wt}\%_{\text{C}}} \quad \text{Eq. 31}$$

Now, mol%_C can be used to correct the stoichiometric parameter ξ yielding a new value named ξ_{C} (Eq. 32):

$$\zeta_{\text{C}} = \frac{M_{\text{SiO}_2}}{M_{\text{SiO}_2} - M_{\text{SiC}} - M_{\text{C}} \cdot \left(\frac{\text{mol}\%_{\text{C}}}{1 - \text{mol}\%_{\text{C}}} \right)} = \frac{\text{mol}\%_{\text{C}} - 1}{0.53257 \cdot \text{mol}\%_{\text{C}} - 0.33267} \quad \text{Eq. 32}$$

This leads to a corrected scale thickness x_{C} (Eq. 33)

$$x_{\text{C}} = \frac{\Delta m \cdot \zeta_{\text{C}}}{A \cdot \rho_{\text{SiO}_2}} = \frac{\Delta m \cdot \left(\frac{\text{mol}\%_{\text{C}} - 1}{0.53257 \cdot \text{mol}\%_{\text{C}} - 0.33267} \right)}{A \cdot \rho_{\text{SiO}_2}} \quad \text{Eq. 33}$$

A pure carbon content of 5 wt% will, therefore, lead to an error of 3.27 % when converting mass-gain data into scale-thickness values. Commercial SiC contains much less carbon and accordingly the error is smaller.

The error for semi-crystalline systems can be assessed in a similar way. Although β -cristobalite is the usual crystalline form of silica on silicon carbide, at room temperature determined weight-gains or thickness-related data must consider α -cristobalite ($\rho = 2320 \text{ kg}\cdot\text{m}^{-3}$)¹⁵³ coexisting with amorphous silica ($\rho = 2000 - 2200 \text{ kg}\cdot\text{m}^{-3}$)¹⁵³. Crystallinity K (i.e., the volume fraction which is crystalline), therefore, can be defined as (Eq. 34):

$$K = \frac{V_{\alpha\text{-cristobalite}}}{V_{\text{amorphous silica}} + V_{\alpha\text{-cristobalite}}} = \text{vol}\%_{\alpha\text{-cristobalite}} \quad \text{Eq. 34}$$

With a known degree of crystallinity, a corrected density (ρ_{\emptyset}) can be obtained (Eq. 35):

$$\rho_{\emptyset} = \left(\frac{K}{\rho_{\alpha\text{-cristobalite}}} + \frac{1-K}{\rho_{\text{amorphous silica}}} \right)^{-1} \quad \text{Eq. 35}$$

Thus, a crystallinity-corrected scale thickness (x_K) can be found (Eq. 36):

$$x_K = \frac{\Delta m \cdot \zeta}{A \times \rho_{\emptyset}} = \frac{\Delta m \cdot \zeta}{A} \cdot \left(\frac{K}{\rho_{\alpha\text{-cristobalite}}} + \frac{1-K}{\rho_{\text{amorphous silica}}} \right) \quad \text{Eq. 36}$$

The error of the thickness of an amorphous silica layer mistakenly calculated to be crystalline lies almost within the same range as the error for 5 wt% carbon content, that is, 5.17 %.

4.1.2.4 DIFFERENCES BETWEEN SILICON AND SILICON CARBIDE OXIDATION

Transport mechanisms of vapor phases through solids are complex and in case of SiC oxidation still matter of dispute. Analogous to silicon oxidation it is speculated that oxygen is transported in molecular form through the up-building SiO_2 layer.^{390,409,415,420,421} In amorphous silica a change to network transport at $T > 1350^\circ\text{C}$ is likely.⁴²² The preservation of amorphous silica at very high temperatures is probably impurity induced.

Most scientists believe that oxygen diffusion through silica is the true rate-limiting process in SiC oxidation.⁴¹⁴⁻⁴¹⁶ In this case there should be no difference between the oxidation rates of silicon and silicon carbide. However, the experimentally determined rate-constants for SiC oxidation are significantly slower than those of silicon (by more than one order of magnitude).³⁰

Comparing the oxidation rates of silicon and silicon carbide, it is important to be aware of the influence of the choice of rate-constants themselves. Due to different stoichiometric coefficients, the relation between k_p -values based on the increase in scale thickness deviates from the ratio of weight-gain- k_p -values. Because of this difference the oxidation of silicon with weight-gain-per-area as point of reference will appear much faster than the comparison of scale-thickness-related oxidation rates (Fig. 28).

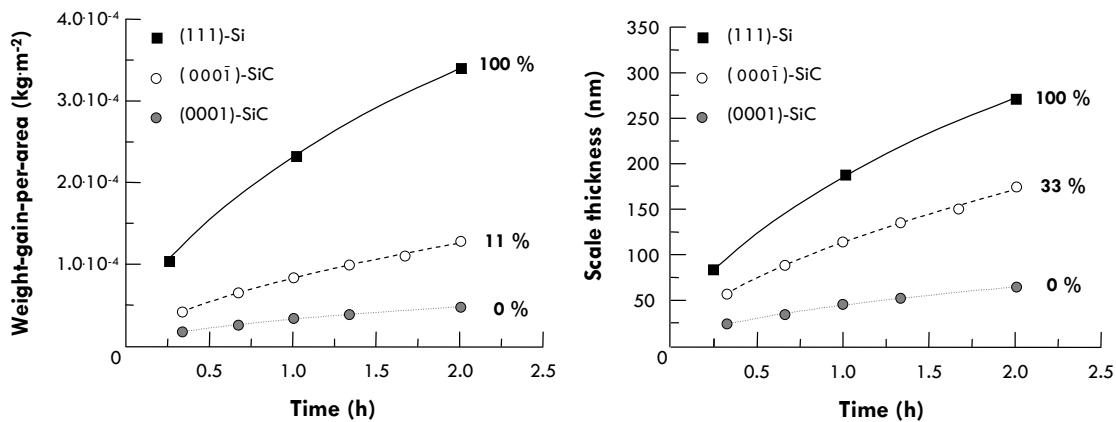


Fig. 28. Weight-gain-per-area related and scale-thickness related kinetic data for dry, thermal oxidation at 1200°C for (a) single-crystal Si (Ref. 408) and (b) SiC (Ref. 423). Scale growth on silicon seems to be more rapid and pronounced when comparing thickness derived data (k_p -values were normalized to the largest value = 100 %).

Looking at the reaction equation (Eq. 23), the necessary re-diffusion of carbon oxide might explain the differences between Si and SiC oxidation.¹⁶⁸ However, the differences in oxidation rates of different faces of SiC single-crystals require another sort of explanation. This is the case for the interlayer model proposed by Hornetz et al.²⁷⁴ (cf. section 4.1.4.3), what was experimentally evidenced by various authors.^{280,299,301,424-426} A face-dependent interlayer with oxycarbide composition was shown to be one of the most striking differences between Si-SiO₂ and SiC-SiO₂ interfaces.^{168,420,427} However, other authors did not find any of these Si-C-O-compounds at the interface, therefore, the question of surface reconstructive (section 2.3.1.2) influence may arise. For example, $\sqrt{3} \times \sqrt{3}$ -R30°-reconstructed 4H-SiC(0001) surfaces did not show significant carbon-related signals at the interface at all.³³²

Defect related differences between silica on silicon and silicon carbide were introduced in section 2.4 and showed that silicon carbide based interfaces are characterized by a much higher level of defect states limiting the application of SiC MOSFETs. This has been related to the presence of carbon at the SiC-SiO₂ interface in form of oxycarbides and/or carbon-clusters. Interpreting this as a continuous or discontinuous interlayer is capable of explaining observed differences in isotopic tracer studies between Si- and SiC-SiO₂ interfaces after reoxidation experiments: In studies oxidizing SiC with ¹⁶O at 1100°C and reoxidizing it at 950°C with ¹⁸O, the removal of carbon clusters was shown to lead to ¹⁸O incorporation into the bulk silica layer.^{328,420} Si-SiO₂ interfaces show only an ¹⁸O-increase at the interface itself (and to some minor part at the SiO₂-atmosphere-interface due to surface reactions).

In the 1980s a so called reactive layer model for Si oxidation^{428,429} was proposed to explain the suboxidic⁴³⁰⁻⁴³² and partially crystalline⁴³³ interface. With oxygen diffusing towards this boundary and silicon diffusing outwards, a reaction layer would lie on top of the 1 - 4 nm thick interlayer and not directly at the substrate-oxide-interface. This reactive layer was supposed to be impermeable to molecular oxygen diffusion after the first suboxide formation (cf. Fig. 29).

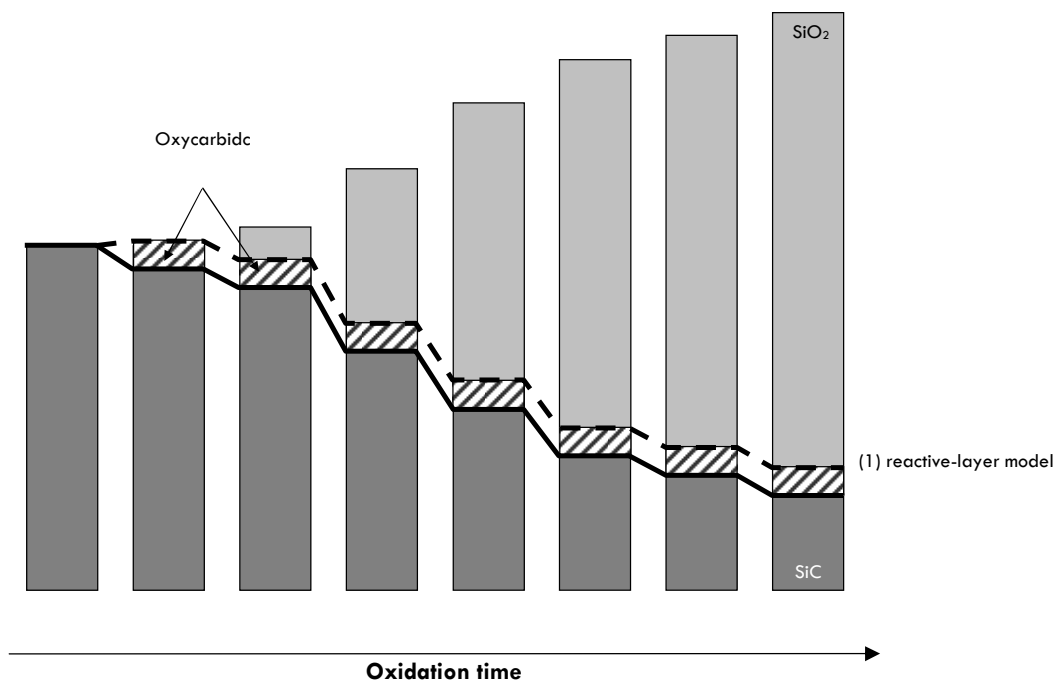


Fig. 29. Schematic illustration of the classic interface-reaction model vs. the reactive layer model for SiC oxidation (after Ref. ⁴²⁹).

However, later oxygen-isotopic-tracer studies indicated that the main reactions take place directly at the Si-SiO₂ interface, corroborating the original Deal-and-Grove-like oxidation behavior.⁴¹⁰ This led to a modified Deal-and-Grove model (called “interfacial+near-interfacial+surface reaction model” by Gusev et al.⁴¹⁰) describing oxidizing of the partially oxidized suboxides at the Si-SiO₂ interlayer-interface. With the poor oxygen solubility in SiC, the reactive layer cannot be located beneath the SiC-SiO₂ interface and Si(O)-out diffusion seems energetically not favorable.

4.1.2.5 ALTERNATIVE MODELS

Two alternative oxidation models proposed by Reisman et al.^{434,435} and Wolters et al.⁴³⁶⁻⁴³⁸ were developed to explain deviations between ideal Deal-and-Grove-like oxidation behavior and the observed oxidation kinetics of silicon. A critical assessment of the application of these two models to SiC oxidation is provided.

Oxide growth on silicon follows, according to a model proposed by Reisman et al. and Nicollian and Reisman^{434,435} an allometric correlation (Eq. 37):

$$x = a \cdot (t + T)^b \quad \text{Eq. 37}$$

In this equation, x denotes the scale's thickness, t the oxidation time, T compensates for an initial oxide layer and the two parameters a and b are variable. However, the temperature and pressure dependency of a and b was never discussed individually but their product (“ $a \cdot b$ ” = “activation energy”) can be expressed by an Arrhenius plot.⁴³⁹

The factor T is a function of the initial scale thickness x_i (Eq. 38):

$$T = \sqrt[b]{\frac{x_i}{a}} \quad \text{Eq. 38}$$

Deviations from an ideal Deal-and-Grove time-law motivated Reisman et al. to modify a (linear)-parabolic functional correlation to an allometric expression with $b \neq 1/2$. Physicochemical background for Eq. 37 is the assumption that the reaction at the Si-SiO₂ interface is rate-controlling over the whole oxidation period covered by the model. New silica grows epitaxial to the substrate and is, therefore, structurally instable. The atomic reconfiguration of the oxide locally increases the scale's viscosity correlated to scale growth. By this effect the actual rate-limiting process (= linear correlation) is hampered and the allometric equation shown in Eq. 37 can be obtained. The two parameters a and b , therefore, express the time-dependency of the oxide's viscosity.

Applying this model to the data obtained by Deal and Grove (cf. Ref. ⁴⁰⁸) shows that all data points including the very initial steps lie adequately good on the regression function (Fig. 30). For a scale thickness of above $\approx 20 - 25$ nm the Reisman and the T -corrected Deal-and-Grove model converge.

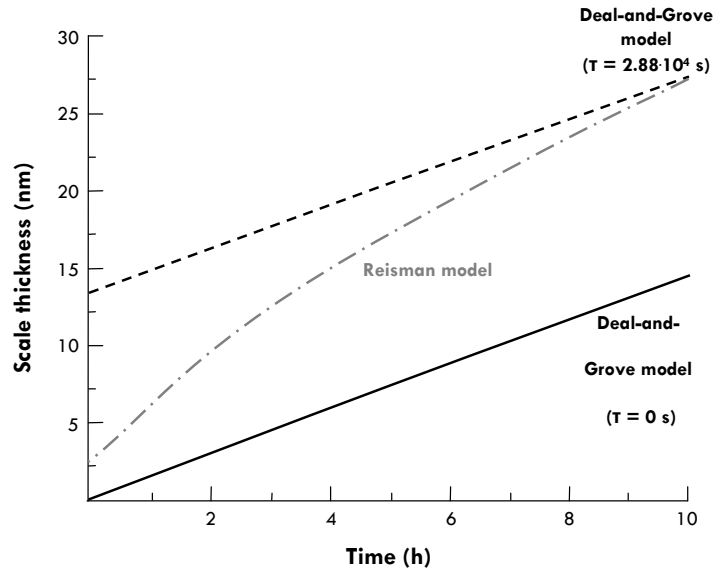


Fig. 30. Application of the Reisman model for silica growth on silicon to the basic kinetic data for dry thermal oxidation (800°C for single-crystal silicon) given by Deal and Grove (cf. Ref. 408).

Applying the Reisman model to silicon carbide oxidation, the exponential factor b lies usually very close to 0.5 and, therefore, a strict separation from the Deal-and-Grove-model becomes a mere question of statistic significance. As for thick (> 25 nm) silica layers, both models converge and hence the physicochemical better explainable Deal-and-Grove kinetic should be preferred. Also suboxidic, oxycarbide layers (at least) during initial oxidation and crystallization processes (along with crack formation) would have to be integrated in an oxidation model truly representing non-ideal oxide formation.

A second model for SiO_2 growth on Si was proposed by Wolters et al.⁴³⁶⁻⁴³⁸ Their work was motivated by the dependency between k_p and k_l that was critically discussed by Blanc in 1978 and 1987 (Ref. 440,441). As stated by Deal and Grove, linear and the parabolic rate-constant should be considered to be independent parameters with k_l proportional to the rate of the slowest reaction and k_p proportional to the diffusion coefficient.⁴¹³ Different activation energies were found for both rate-constants.^{375,419,442} Interdependencies of rate-constants are a true problem in critical evaluation of kinetic data.

Only in case of $m = 1$ ($m \dots$ slope) in a $\log(k_l)$ - $\log(k_p)$ -plot a linear-parabolic law equals an allometric correlation. For any slope unequal to 1, a linear-parabolic time-law as such is to be used instead. Wolters et al. showed cases within the vast number of different published rate-constants, in which $m \approx 1$ was found to be true^{433,443} and concluded that the parameters of the ideal Deal-and-Grove kinetics are no real physicochemical factors and should be replaced by a law similar to the Reisman model discussed earlier.

Physicochemical basis for the Wolters model is the rate-limiting process of ionic transport of oxygen through the growing silica layer - following the classic ion transport model of Wagner (cf. Ref. 444) to which non-linear conductivity was amended.⁴³⁹ This results in Eq. 39:

$$x^2 + A \cdot x^{2-\beta} = B \cdot (t + \tau) \quad \text{Eq. 39}$$

In this equation, A and B are parameters, x denotes the scale thickness as a function of the time t and T is once more a factor to correct for an initial oxide scale. For a fixed charge of the oxide, a value for β can be chosen and for " $\beta = 1$ " Eq. 39 becomes a linear-parabolic time-law. In case of " $A \gg x^\beta$ ", a simple power law is obtained. However, there is no defined correlation between these parameters and pressure or temperature.

Applying this model to the basic kinetic data from Deal and Grove⁴⁰⁸ for silicon oxidation of silicon carbide oxidation (Sibieude et al.^{375,442}) values of $m > 1$ are obtained in a log-log-plot for both rate-constants (Fig. 31). Consequently, the Reisman-model cannot successfully be applied to regular SiC oxidation.

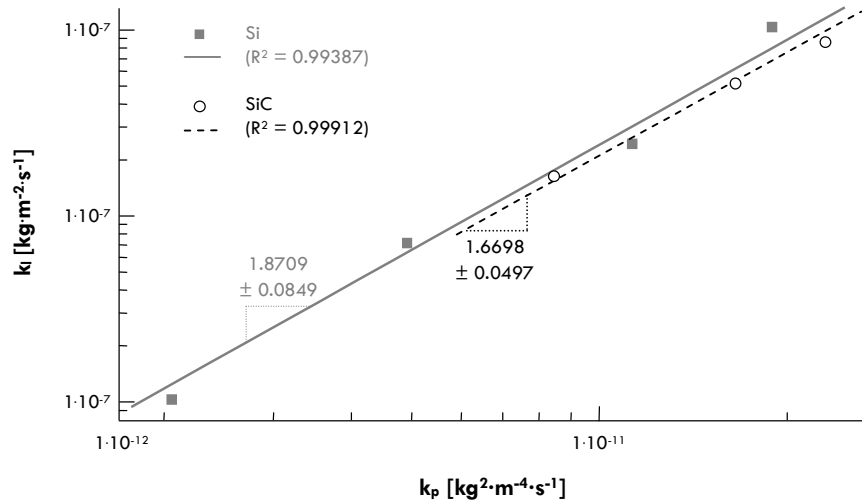


Fig. 31: Application of the Wolters model to kinetic data of silica growth on silicon (800°C for single-crystal silicon; Deal and Grove Ref. 408) and silicon carbide (1200° - 1550°C for 3C-CVD SiC; Sibieude et al. Ref. 375,442). For discussion, see text.

4.1.2.6 INITIAL OXIDATION

In the initial step of oxidation, oxygen ions will approach bulk, truncated SiC surfaces.^{30,445} Adsorption of O_2 and dissociation into single ions will lead to the formation of Si-O-bonds and Si-C-bonds respectively. Additionally surface reconstructions (cf. section 2.3.1.2) can take place depending on the used polytype and environmental conditions. As these initial bonds break up, oxycarbide formation, as observed by Öneby and Pantano²⁷⁶ or Radtke et al.³⁰⁴, takes place. These metastable amorphous Si-C-O-compounds (e.g. $SiOC_3$, SiO_2C and SiO_3C) are still a matter of current research. Da Silva et al. recently published a first-principles investigation of a crystalline SiC_xO_y phase.⁴⁴⁶

Interlayer phases like $Si_4C_{4-x}O_2$ ($x \leq 2$) with a typical thickness of ≤ 1 nm were only observed below $\approx 1000^\circ - 1100^\circ C$.^{274,447} Above $1000^\circ C$, $Si_4C_{4-x}O_2$ disappears in favor of $Si_4C_4O_4$.⁴⁴⁷ At higher temperatures, for example, above $1152^\circ C$ for 3C-SiC, all oxycarbides (like $Si_4C_4O_4$) seem to decompose to solid SiO_2 and gaseous CO .^{445,448,449}

Deal-and-Grove-like kinetics cannot be applied for oxide scale thicknesses under a certain thickness (≈ 25 nm). Ultrathin oxide scales build-up much faster than a linear relationship would expect. This behavior has extensively been examined for Si oxidation.⁴¹⁰ Close examination of these ultrathin silica films becomes more and more important as the application of silicon or silicon carbide based metal-oxide gate oxides nowadays requires such small SiO₂ layers.

Some aspects of oxygen on real surfaces of SiC were provided in section 2.3.1, discussing surface reconstructions. Influenced by the site selection of single oxygen adatoms the topmost part of the SiC lattice will undergo superficial structural changes. The chemisorption of oxygen (at room temperature) is once more an anisotropic process dependent on the crystallographic orientation and the surface type. For example, the chemisorption on the δ H-SiC(000 $\bar{1}$)-(1x1) face is much slower than on the corresponding (3x3)-Si-face.²¹⁹ As pointed out by Bermudez²¹⁹ the differences in O uptake rates will diminish when the system transients to passive oxidation, that is, with increasing oxygen coverage. Also, ($\sqrt{3}\times\sqrt{3}$)R30° surfaces were reported to oxidize less fast than other surface structures found on δ H-SiC, while their oxygen chemisorption rate is faster.²¹⁹

Calculations by Deák et al.^{450,451} and Knaup et al.⁴⁵² showed that when oxygen arrives at the SiC surface/SiC-SiO₂ interface the simplest reaction to occur would be the formation of neighboring oxygen interstitials O_i^{interface} with ≈ 193 kJ·mol⁻¹ (Eq. 40). The formation of these interstitials is characterized by Si-C-O bondings elevated above the surface level.⁴⁵⁰



This process, due to the poor oxygen solubility of SiC, would soon result in complete saturation of the SiC surface and, therefore, further oxidation would be averted. Interstitially induced stress can be seen as a reason for hindered further incorporation of oxygen.⁴⁵²

The formation of oxygen interstitials is energetically more favorable than the mere substitution of carbon (V_CO₂^{SiC}: a carbon vacancy within the SiC lattice that is occupied by oxygen) and the formation of CO. However, it is believed that a significant fraction of this reaction is in equilibrium at the later SiC-SiO₂ interface.⁴⁵⁰

More favorable than O_i^{interface} or V_CO₂^{SiC} formation is that arriving O₂ at the SiC surface will eject carbon into an interstitial position according to Eq. 41:



In a second step, for further arriving oxygen, regardless whether interstitial oxygen (Eq. 42, yielding ≈ 511 kJ·mol⁻¹) or interstitial carbon (Eq. 43 yielding ≈ 531 kJ·mol⁻¹) was created, a V_CO₂^{SiC} + O_i^{interface} - complex will be obtained.⁴⁵⁰⁻⁴⁵²



With a third oxygen molecule arriving at the interface, CO will be released, thus a second carbon atom will be removed according to Eq. 44 (yielding ≈ 473 kJ·mol⁻¹):



Consequently, a net exothermic reaction of Eq. 1 and 6 will be obtained in accordance with experimental results.^{331,453,454} With two $V_C O_2^{SiC}$ -defects created in each oxidation cycle, four new Si-O-Si units will be formed. Also, continuously oxygen interstitials and " $V_C O_2^{SiC} + C_i^{SiC}$ "-complexes will be created at the interface that could explain the observed amounts of excess carbon and oxycarbides proposed in section 2.4.2.4.

As discussed by Knaup et al.,⁴⁵² the permanent incorporation of carbon is possible in form of, for example, $(C_i)_2$ -dimers. The corresponding net reaction is (Eq. 45):



Carbon is supposed to diffuse quite easily through the silica layer and no high concentration of C is expected at elevated temperatures ($> 1200^\circ C$).⁴⁵⁰

As indicated by core level photoemission spectroscopy, the very initially formed SiO_2 (≤ 1 nm) shows Si-O-bonds very close to that of "bulk-like" (> 5 nm) with Si^{4+} as the dominant oxidation state⁴²⁵ but nonetheless (cf. section 2.4.2.5) the interface layer between "bulk" SiO_2 and "bulk" SiC is characterized by a thin interlayer of oxycarbide composition.²⁷⁴ The findings of oxidation states other than Si^{4+} (i.e., Si^{3+} , Si^{1+} and mainly Si^{2+}) at the interface region was attributed to Si-C-O bonds. Amy et al.^{299,301,425} reported first oxidation products on reconstructed Si-rich (3×3) surfaces of 6H-SiC already at $500^\circ C$, although pronounced oxidation will only be observed at temperatures above $800^\circ - 900^\circ C$. Modifying the SiC real surface, for example, by precipitating a Si-overlayer on a 6H-SiC(0001)- (3×3) surface, yields a much more abrupt and carbon-free interface (which leads to accelerated oxidation rates). Hence, it becomes very important for kinetic considerations to look closely at the surface structure present in initial oxidation studies.

The same variety of oxidation states of silicon were found on β -SiC(100) $c(2 \times 2)$ and C-rich β -SiC(100)- (1×1) ,²⁸⁰ on 4H-SiC(0001)- (3×3) ^{203,455} and on 6H-SiC(0001)- $(\sqrt{3} \times \sqrt{3})$ ²⁸² surfaces. However, the experimental findings of three suboxides (Si^{1+} , Si^{2+} and Si^{3+}) as reported from photoemission spectra still are a matter of dispute.⁴⁵⁶ Johansson and Virojanadara found only one suboxidic phase (Si_2O : Si^{1+}) besides bulk SiC and stoichiometric SiO_2 in *in-situ* oxidation studies on the Si-face of 4H-SiC.^{300,349,456} The Si^{2+} component was proposed to be wrongfully attributed to a suboxidic phase as it derives from the bulk SiC. Other, potential oxycarbide phases were suggested to derive from the Si-overlayer used by Amy et al. (cf. Ref. ^{299,301,425}) as no carbon could be found at the interlayer.^{300,331,332} In the case of the C-face of 4H-SiC, Virojanadara and Johansson did not find Si^{1+} but Si^{2+} besides bulk Si^{0+} and silica related Si^{4+} .^{300,331,457} This Si^{2+} component was attributed to originate from Si-C-O-bonds within the SiC body, which clearly contradicts findings, in which the oxycarbide layer on the Si-face is significantly thick and can be neglected only on the C-face.²⁷⁴

Clearly, more work needs to be done on this topic revealing the influence of different preparation methods and surface reconstructions on possible oxycarbide interlayers. Especially in the case of ultrathin silica layers out-diffusion of carbon may explain the lack of experimental findings of oxycarbides.²⁹⁸

Another critical factor of oxidation and especially of initial oxidation is the question how the reactive front progresses into the solid SiC body. Ideal Deal-and-Grove-like behavior would require an oxidation mechanisms advancing in a layer-by-layer fashion. Observations of rather "abrupt" SiC- SiO_2 interfaces seem to corroborate a layer-by-layer-like oxidation²⁹⁸.²⁷⁴⁻²⁸⁰ However, Hoshino et al.²⁸² reported an inhomogeneous, isle-like formation mechanism of SiO_2 domains for 6H-SiC(0001)- $(\sqrt{3} \times \sqrt{3})R30^\circ$ surfaces oxidized at $500^\circ C$ during initial oxidation. When considering the latter findings one must take into account that the surface reconstruction of (3×3) to $(\sqrt{3} \times \sqrt{3})R30^\circ$ -surfaces leads to an increased roughness and large flat terraces that might cause the isle-like character.²¹⁸

4.1.3 Gas diffusion

In the next few paragraphs, the transport mechanisms of gaseous species within the silica layer will be discussed. Compared to other oxides the oxygen diffusivity through SiO₂ is rather low, even at higher temperatures. Reliable data for CO- or CO₂-transport are missing⁴⁰⁷ but oxidation experiments conducted at various oxygen partial pressures see oxygen diffusion as the main rate-limiting step.^{386,387,458}

4.1.3.1 PRELIMINARY ASPECTS

For diffusive transportation processes through solids, Fick's first and second laws can be applied. Fick's first law makes a quantitative description of how many particles of a certain substance pass through a distinct area perpendicular towards the diffusion direction in a certain period of time (Eq. 46; Ref. ⁴⁵⁹):

$$J = \frac{1}{A} \cdot \frac{\partial N}{\partial t} = -D \frac{\partial c}{\partial x_{dd}} \quad \text{Eq. 46}$$

In Eq. 46 denotes J the net flow, N the particle number, t the time, A the area, D the diffusion coefficient, c the concentration of the substance and x_{dd} the diffusion direction. Keeping D constant, a direct correlation between temporal (t) and areal (x_{dd}) differences in the concentration can be found through the continuity equation (Fick's second law; Eq. 47). Therefore, Fick's second law is capable of describing non-steady state diffusion.

$$\frac{\partial c}{\partial t} = D \frac{\partial^2 c}{\partial x_{dd}^2} \quad \text{Eq. 47}$$

Various solutions exist for this differential equation including those for anisotropic media and differing starting and boundary conditions.^{459,460}

Volume diffusion is the main mechanism for gas transport in amorphous systems.⁴⁰⁶ Bulk volume diffusion is accomplished by ion movement and permeation, for example, of gas molecules. Local vacancies and defects enable vapor phase permeation also through crystalline phases. In (semi)crystalline systems, grain boundary diffusion becomes important but is usually slower than pure surface diffusion. In comparison, the diffusion coefficient of surface diffusion is greater than D of grain boundary diffusion and the diffusion coefficient for pure volume diffusion is even smaller. The corresponding activation energies are reciprocal related to the individual D-values.

Direct permeation of vapor phase molecules throughout a vitreous or crystalline medium requires vacancies in the order of magnitude of the gaskinetic diameter, decreasing with increasing temperature.⁴⁶¹ Both amorphous silica and β -cristobalite have almost equal densities what lead to the assumption of potentially similar transportation processes through both materials.¹⁵² In the first case, amorphous SiO₂, gas transport is accomplished by diffusion through 7-, 8- or n-fold Si-O-rings. For these structural units, a free volume of ≈ 250 pm was found - a value very close to that of 6-membered rings in β -cristobalite (220 pm).¹⁶⁴ Tab. 4 lists a comparison between the gaskinetic diameters of O₂, CO₂ and CO, showing that diffusion processes can take place and that CO and O₂ may almost be similarly well transported.^{462,463} Higher temperatures rather decrease than increase the size of mean free vacancies within the Si-O-network or -lattice as stretching Si-O-bonds will be (over)compensated by a twist of the Si-O-Si-axis.^{164,406,464}

	Gaskinetic diameter (pm)			
	0°C	20°C	1000°C	1500°C
O ₂	181	298	258	253
CO	189	319	273	268
CO ₂	233	334	300	295

Tab. 4. Gaskinetic diameters of selected gas phases (after Ref. ¹⁶⁴ and from coefficients of viscosity [for 0°C] after Ref. ⁴⁶³). The free vacancies in amorphous and crystalline SiO₂ are 250 pm and 220 pm respectively.

As shown by Doremus,⁴⁶¹ gas kinetic radii truly correlate with the square root of activation energies for diffusion of diverse gaseous species through amorphous silica in a linear fashion.

At elevated temperatures the gas diffusion is accelerated (Eq. 48) while the expansion coefficient of silica is not very strongly temperature-dependent.⁴⁶⁴

$$D = D_0 \cdot e^{-\frac{E_a}{R \cdot T}} \quad \text{Eq. 48}$$

In this equation, D denotes the diffusion coefficient, E_a the activation energy, R the ideal gas constant, and T the temperature. For kinetic studies, the diffusion coefficients must be corrected for the gas phase solubility within silica.⁴⁶⁵

Analogue to the Deal-and-Grove equation (Eq. 14) for diffusion controlled silica scale growth the correlation is (Eq. 49):

$$x = \sqrt{\left(2 \cdot D_i \cdot \left[\frac{c_i}{c_n} \right] \cdot t \right)} = k_p \cdot \sqrt{t} \quad \text{Eq. 49}$$

In this context, x denotes the scale thickness, D_i the diffusion coefficient, c_i the concentration of the gas species being present in interstitial positions, c_n the concentration of the gas species being present in the network and t the oxidation time. The parabolic rate-constant k_p comprises, therefore, three factors.⁴⁶⁵

When comparing literature data it is important to consider the different experimental methods that were used (e.g., mass spectroscopy vs. isotope exchange measurements). A questionable comparability of data from different materials like hot-pressed SiC and fibrous SiC arises from small impurities or amounts of sintering aids, which greatly influence the D -values for silica.³⁶¹ Also, water shifts the oxidation rate towards higher values even when present in concentrations as low as a few 10 ppm. Besides these factors, the crystallographic diversity and complexity of SiC itself makes comparisons of polycrystalline material (even without the presence of sintering aids) difficult.

4.1.3.2 ACTIVATION ENERGIES

Neglecting further influences like next-nearest-neighbors, it is possible to get a first impression of the differences between diffusion rates within amorphous and crystalline solids when calculating “activation energies“ for gas permeation by using the force constants needed to atomically widen the free volume. As shown by Ebi et al. ^{164,406}, E_a -values obtained using this approach clearly indicate low activation energies and, therefore, pronounced gas diffusion through silica only for a vitreous modification (cf. Tab. 5).

	E_a (kJ·mol ⁻¹)	
	amorphous SiO ₂	β-cristobalite
O ₂	49.4	795.0
CO	195.0	1230.1
CO ₂	974.9	2719.6

Tab. 5: Calculated “activation energies” obtained from using the force constants needed for expanding the free volume diameter in amorphous and crystalline silica (after Ref. 164).

These values for O₂-diffusion through vitreous silica lie closer to the literature values from Bongiorno et al. (first-principles calculation: 108 kJ·mol⁻¹)⁴⁰⁹, Norton (experimental: 113 kJ·mol⁻¹)⁴⁶⁶ and Williams (experimental: 121 kJ·mol⁻¹)⁴⁶⁷ than to those of Cawley (experimental: 280 kJ·mol⁻¹)⁴⁶⁸ or Sucov (experimental: 331 kJ·mol⁻¹)⁴⁶⁴. But even these low activation energies do not indicate a break-up of Si-O-bonds, because this would require energies from 367 - 500 kJ·mol⁻¹).^{361,464,469}

The data of Rodriguez-Viejo et al. ⁴⁷⁰ show values for the diffusion of oxygen in β-cristobalite about a factor 3 smaller (2.83 at 1400°C) than in amorphous silica.^{422,470} Corresponding activation energies differ by almost 100 kJ·mol⁻¹ (β-cristobalite: 429 kJ·mol⁻¹; amorphous silica: 328 kJ·mol⁻¹; cf. Eq. 50 - 51).⁴⁷⁰

$$D_{\beta\text{-cristobalite}} = 5.6 \cdot 10^{-4} \frac{\text{m}^2}{\text{s}} \cdot e^{-\frac{429 \text{ kJ/mol}}{R \cdot T}} \quad \text{Eq. 50}$$

$$D_{\text{amorphous}} = 1.1 \cdot 10^{-6} \frac{\text{m}^2}{\text{s}} \cdot e^{-\frac{328 \text{ kJ/mol}}{R \cdot T}} \quad \text{Eq. 51}$$

These E_a -values are much higher than the aforementioned activation energies reported from, for example, Norton (113 kJ·mol⁻¹)⁴⁶⁶ or Cawley (280 kJ·mol⁻¹)⁴⁶⁸. Such deviations show the need for more detailed studies and evidence the problems when comparing activation energies obtained from different experimental methods. Isotope tracing experiments, for example, are very susceptible for systematic errors in calculated diffusion coefficients and related activation energies as in some experiments water is used as a source for oxygen isotopes. Latter leads to accelerated diffusion and decreased activation energies.

The study of Rodriguez-Viejo et al. can serve as a basis for evaluating different diffusion rates in crystalline and amorphous silica. The difference in E_a -values between amorphous silica and β-cristobalite seems to be much smaller than the previous gasekinetic approximations would have expected - a clue, which would also support CVD oxidation results ⁴²²

4.1.3.3 DIFFUSION OF OXYGEN

A set of measurements conducted by Norton in the 1950s and 1960s (Ref. ⁴⁶⁶) still serves as reference for diffusion coefficients for molecular oxygen through vitreous silica. As pointed out by Doremus, “it is remarkable that no one has thought it necessary to repeat these experiments”.⁴⁶¹ Even minor amounts of impurities will greatly affect diffusion coefficients and gas transport activation energies ⁴¹² - hence deviations even within orders of magnitude for diffusion coefficients would not be surprising. Norton found the following equation (Eq. 52), which differs greatly from the findings of Rodriguez-Viejo et al.:

$$D_{\text{amorphous}} = 2.7 \cdot 10^{-8} \frac{\text{m}^2}{\text{s}} \cdot e^{-\frac{113 \text{ kJ/mol}}{R \cdot T}} \quad \text{Eq. 52}$$

Today it is widely accepted that at least for temperatures above 1350°C and a scale thickness above 20 - 25 nm reaction-free interstitial gas permeation (= molecular transport) is the dominant transportation mechanism,^{361,409,416} although there are also contradicting references like Ref. ⁴¹⁶ proposing a pure interstitial transport mechanism of oxygen. The low bonding energies of O₂ compared to two single oxygen ions on interstitial positions or vacancies assist this assumption ⁴⁰⁹ as well as experiments conducted at low oxygen partial pressures. For further information about oxygen mobility in silica cf. Ref. ^{152,361,461,471}).

For silicon, the diffusion of molecular oxygen truly can be seen as the rate-limiting and dominant transport mechanism as isotope labeling experiments using ¹⁸O profiling showed an accumulation of “heavy oxygen” (¹⁸O) at the Si-SiO₂ interface.^{412,433,461,468,472-476} Latter indicates that oxygen permeates without interacting with the SiO₂-network and accumulates at the solid-solid-interface. Another rise of ¹⁸O at the outer interface (SiO₂ vs. atmosphere) was proposed to result from residual water leading to H₂O diffusion and exchange reactions.⁴⁶¹ Also small amounts of Si-O-H groups were reported from these SiO₂-surfaces.

In general, isotopic tracer studies are rather difficult to interpret and as such derived D^{eff}-values are lower than the effective diffusion coefficient found by Norton. This observation could be explained by surface exchange reaction with residual amounts of water present in the oxidation atmosphere (between ¹⁸O dissolved water and ¹⁶O in the SiO₂ network).

However due to the structural and chemical deviations between Si and SiC, it cannot *a priori* be postulated that oxygen will be transported in a molecular fashion in silica thermally grown on silicon carbide. Latter is important to keep in mind especially when considering that SiC oxidation is (usually) studied at temperatures far above those of Si oxidation (i.e., below the melting temperature of silicon at 1414°C).⁴⁷⁷ At these higher temperatures (> 1350°C) or very thin scales (< 20 nm) possibly another transportation mechanism (“network oxygen” = transport of ionic oxygen) predominates.^{361,386,387,422} This process requires breaking of Si-O-bonds and hence higher activation energies found in these regimes could be explained this way. Mikkelsen indeed found extreme high activation energies of 453 kJ·mol⁻¹ (corrected 510 kJ·mol⁻¹)³⁶¹ for temperatures between 1200°C and 1400°C when suppressing molecular diffusion via application of very low oxygen pressures.⁴⁶⁹

Considering crystallization, the diffusion rate of network oxygen in β-cristobalite is probably lower than in amorphous silica ⁴²² but there are contradicting studies on this as well, showing similar diffusion rates for network oxygen in crystalline and amorphous silica due to the lack of change of the oxidation rate of CVD SiC at these temperatures.⁴⁷⁰

Summing up, possibly two major and partially coexisting transport mechanisms exist for oxygen diffusing through silica: (1) reaction-free molecular gas permeation through vacancies (“interstitial oxygen”) and (2) network-exchange related transport of ions (“network oxygen”).⁴⁷⁸ In some literature references, network diffusion is also called lattice diffusion, which is not correct for the gas transport in amorphous media (as these lack a real crystal lattice).⁴⁶⁵ Both mechanisms show a different predominance in different P_{O_2} - and T-ranges and obey different temperature dependencies. A transport via both mechanisms in low- and high-temperature regimes may exist for the various modifications of silica.

4.1.3.4 DIFFUSION OF CO

Carbon oxide cannot be transported in ionic form and should have higher activation energies than oxygen according to simplifying calculations.⁴⁶² Only very few studies reported high activation energies which could be explained by CO-out-diffusion controlled kinetics ($E_a > 400 \text{ kJ}\cdot\text{mol}^{-1}$).^{366,479} However, the data basis for this explanation is very questionable as no reliably diffusion coefficients and activation energies of CO-diffusion are available at the moment.

Currently it, therefore, seems more probable that oxygen diffusion is rate-limiting for both Si and SiC oxidation and activation energies for CO and O_2 -diffusion may be in the same range of magnitude due to similar gaskinetic radii (also, cf. Tab. 5 for a first approximation).^{164,406,461} Another argument against CO as the slowest diffusion process is that it would leave a distinct isotopic signature in $^{13}\text{C}/^{12}\text{C}$ reoxidation experiments^{283,284} or at least a significant, detectable CO content within the silica layer. Thus in those studies CO-out-diffusion seems to be faster than O_2 -in-diffusion. The lack of a significant carbon content also excludes the possibility of the transport of carbon in an elementary form as proposed by Li et al.⁴¹⁶

A special case of out-diffusion is bubble formation due to the production of high gas pressures at the SiC-SiO₂ interface. In a purely oxygen diffusion limited system, CO out-diffusion should be much faster than O_2 -in-diffusion and no bubbles would occur. However, once again the problem lies within the material diversity of silicon carbide: no bubble formation was ever found for high-purity dry thermal oxidations below the melting point of silica and bubble formation was only observed in the presence of water and sodium (modifying the network structure and gas solubility) or/and the presence of sintering aids like boron carbide (being both the source for boron and carbon and leading to a locally increased CO-production). Hence, a mere attribution of bubbles to a very slow CO transportation mechanism is not valid. As implied by Narushima et al., the formation of bubbles under CO-CO₂ atmospheres may indicate a faster diffusion mechanism of CO₂ compared to CO.⁴⁸⁰ A later section (section 4.1.4.6.3) will discuss bubble formation in more detail.

4.1.3.5 DIFFUSION OF SiO

As pointed out by Doremus, the diffusion of SiO in amorphous silica is possible at temperatures above 1200° - 1300°C.³⁶¹ Although its size is similar to that of a water molecule travelling through vacancies in vitreous silica structures, the activation energy would have to be quite high as SiO formation requires network rearrangement and the breaking up of existing SiO bonds. Isotopic tracer studies seem to exclude SiO diffusion from being a rate-limiting process.⁴¹⁶

4.1.3.6 SPECIAL CASE OF ULTRATHIN OXIDE LAYERS

Especially for ultrathin amorphous silica layers (< 20 nm), but also for thicker scales, the existence of structural defects was shown.^{162,165} Any significant change in the Si-O-network must have an influence on the transport of gas species. In particular vacancy-induced exchange reactions of oxygen in the gas phase and the Si-O-network were observed.⁴¹² Also, for such small oxides scales, the time for oxygen to travel to the reaction interface may well be smaller than the reaction's speed hence resulting in rather linear oxidation rates.

Amorphous layers are furthermore known to show regions of locally decreased/increased density with strong effects on diffusion rates and mechanisms.^{152,162,403} A variety of possible arrangements of Si-O-rings formed by SiO₄-tetrahedra exists, resulting in locally increased (= micro-channel in proper sense) or decreased density (= micro-pore).¹⁶² TEM-measurements revealed pore-like structures on silica grown via dry thermal oxidation on silicon with a diameter of ≈ 1 nm.^{162,481,482} These micro-pores potentially contribute to the linear time-law of initial silicon oxidation at least at low temperatures because for oxide scales grown at temperatures above 1000°C and/or oxide scales thicker than 50 nm no such structures were found. Nonetheless it is evident that defect formation (e.g., induced by impurities) affects the diffusion.^{403,412}

4.1.4 Influencing parameters

4.1.4.1 INTRODUCTION

Ideal Deal-and-Grove-like kinetics only apply for the formation of a single-phase oxide layer, that is, there are no grain boundaries, no cracks, no devitrification, no defects and no impurities. In case of intrinsic impurities, for example, those within the SiC lattice or present as sintering aids, the reaction front will constantly be exposed to these impurities resulting in a homogenous distribution of the impurity. Sintering aids like boron carbide affect the oxidation in two ways: (1) they lower the oxide scale's viscosity and (2) they increase the production of reaction gas (like CO).^{383,483} Also locally decreased oxygen partial pressures and extrinsic impurities have to be taken into account. Fig. 32 shows a generalized overview about such influencing parameters.

High oxygen mobility will occur along cracks, grain boundaries and in amorphous regions as well as in structural modified areas. Local oxygen consumption could decrease oxidation rates and accumulated reaction gas, assuming a silica scale of sufficiently low viscosity, could lead to either bubble formation and/or spallation.

Considering all these influencing parameters, which will be discussed in the next paragraphs in more detail, it becomes clear that high-purity single-crystal material will oxidize slower than sintered material. For sintered ceramic bodies increased oxidation will be observed on grain boundaries that readily are affected at temperatures significantly below the first macroscopic SiC oxidation.

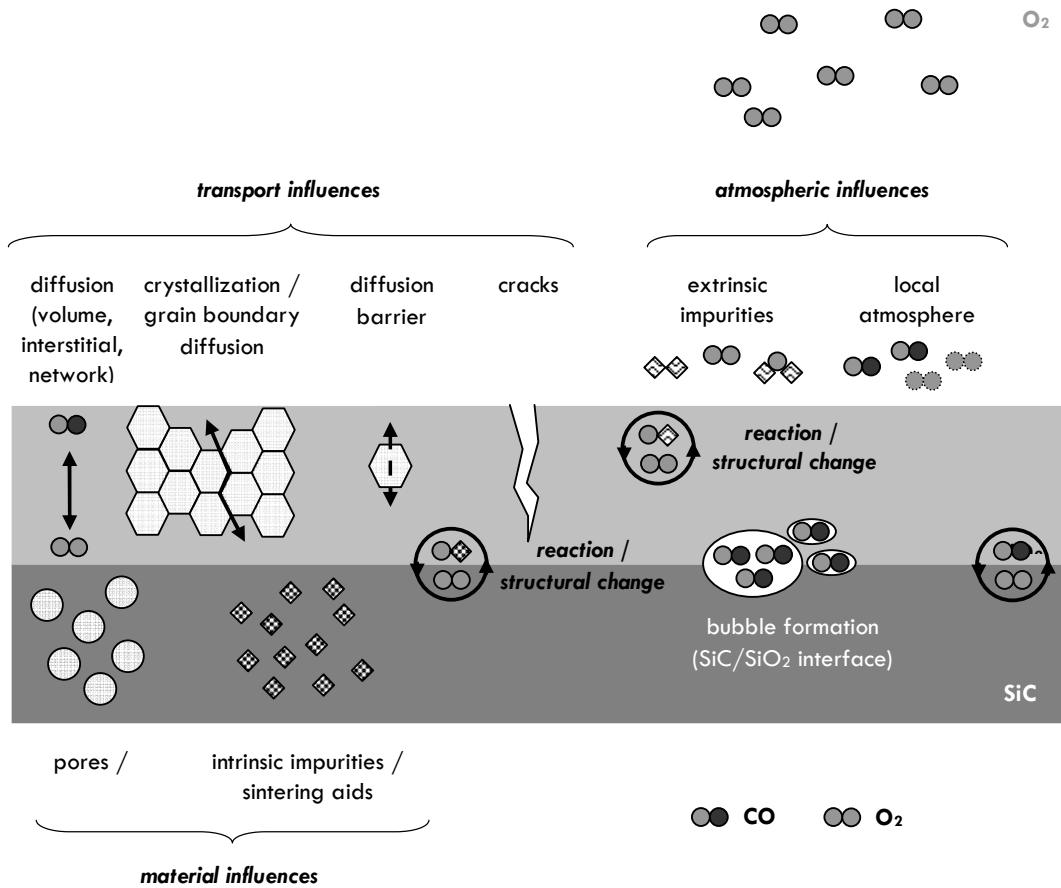


Fig. 32. Schematic illustration of real-structure deviations from an ideal Deal-and-Grove model for silicon carbide (after Ref. 383). Further complications, like surface polarity or surface reconstruction etc. may also be influencing.

4.1.4.2 HEXAGONALITY

A linear correlation between hexagonality and the oxidation rate of silicon carbide has been claimed.^{30,388,415,484,485} Within the system 3C-, 6H- and 4H-SiC, the oxidation rate was shown to decrease on the Si-face with increasing hexagonality, while on the C-face a polytype-independent kinetic was observed.⁴⁸⁶ This is qualitatively in accordance with findings by von Münch and Pfaffener⁴⁸⁵, who reported hexagonality-related dependency for wet oxidation of 6H- and 15-R SiC. However, the results of the latter study, however, are statistically poorly verified, because the scatter within single measurements is larger than the difference between the oxide scales' thickness on the different polytype samples.

Petit et al. (Ref. ⁴⁸⁴) found for wet and dry oxidized silicon carbide samples dependencies of the degree of hexagonality. While for the Si-face the differences in oxidation rates were reported to be greatest for dry oxidation, the exact opposite was found to be true for the C-face. In detail, the Si-face of 3C-SiC in wet ambient oxidizes faster than the corresponding Si-face of 6H-SiC while the C-face of 6H-SiC oxidizes faster than C-face of 3C-SiC in dry thermal environments. For wet oxidized Si-faces or dry oxidized C-faces no significant differences were found. While these differences in bulk oxide thickness are significantly discernible for low-temperature regimes (below 1050°C) they tend to vanish for higher temperatures. Also, the corresponding parabolic rate-constants do not show a conclusive trend when comparing 3C- and 6H-SiC kinetic data from the article from Petit et al. (Fig. 33). These findings are in accordance with the converging oxidation rates of, for example, 6H- and 4H-SiC using wet oxidation as observed by Shenoy et al.³⁴⁵

a) Wet oxidation

b) Dry oxidation

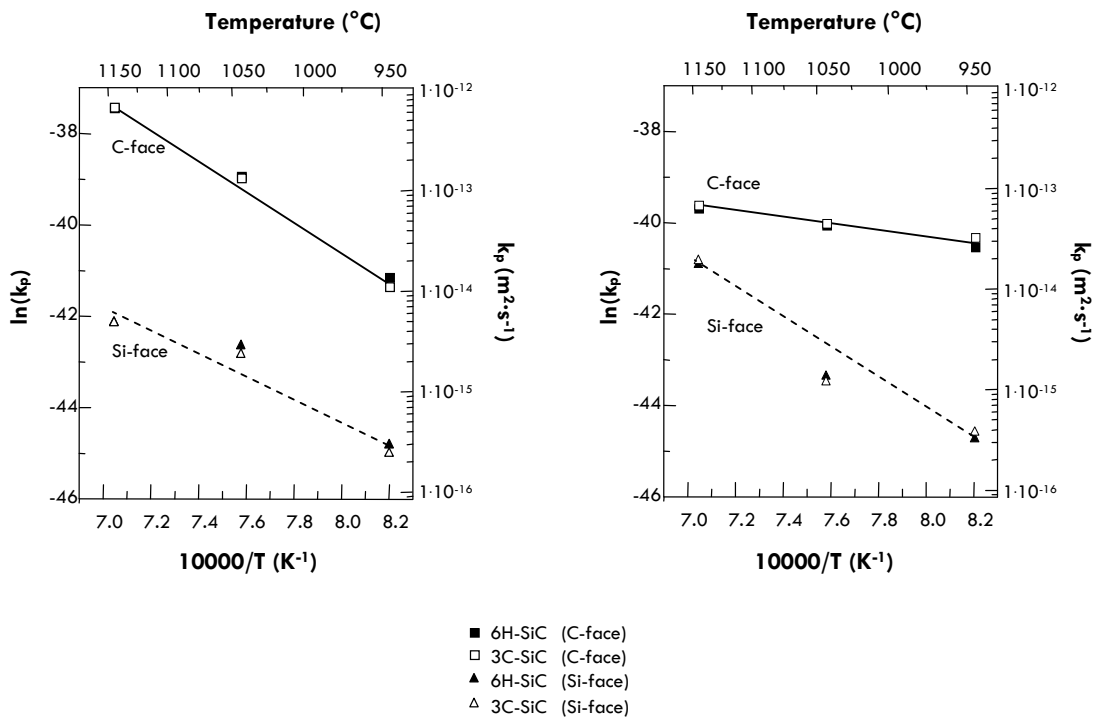


Fig. 33. Comparison between oxidation rates and their dependency on face-polarity (after Ref. ⁴⁸⁴) for a) wet oxidation and b) dry oxidation. As seen, only for dry thermal oxidation a true distinction between the oxidation progress of 3C- and 6H-SiC can be made for the C-face.

The structural distinction was even used, for example, by Powell et al. to discriminate between different polytype regions of 3C- and 6H-SiC.³⁸⁸ However, using hexagonality as such an analytical tool requires exact knowledge about the particular crystallographic orientation and potential doping/impurities levels along with the necessity of a homogenous surface morphology.

Summarizing, there seems to be an influence of hexagonality on the oxidation rate, the magnitude of it is still difficult to specify.

4.1.4.3 CRYSTAL ORIENTATION AND INTERLAYER MODEL

Face-polarity influences a lot of physicochemical parameters like surface energy (3C-SiC: Si-face = 2.2 J·m⁻² / C-face = 0.3 J·m⁻²).^{31,198,331,487,488} These differences in surface free-energy cause the instability of polytype growth on the C-face. Hence it is not surprising to find a crystallographic dependence between silicon carbide oxidation and crystal face orientation (Fig. 34, 35).^{183,489}

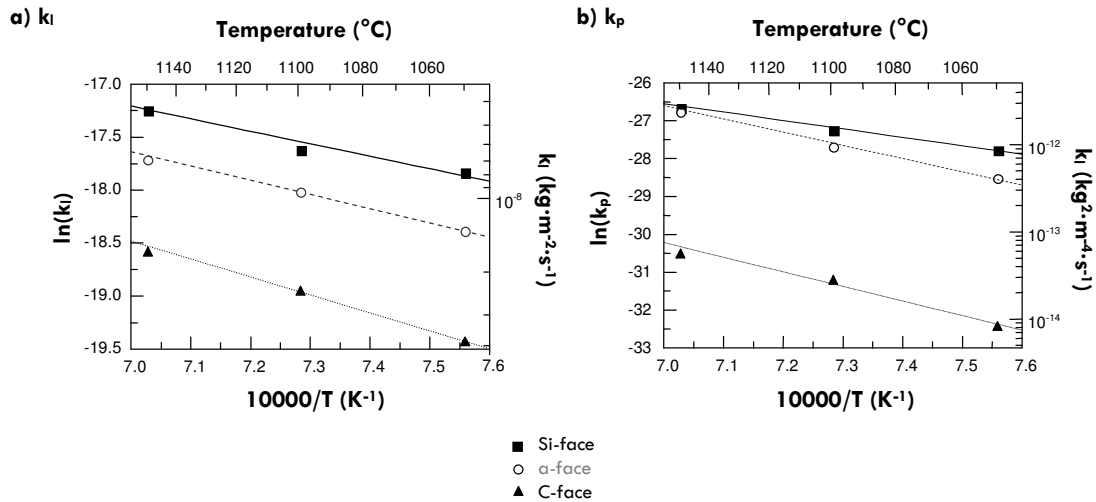


Fig. 34: Change in (a) linear rate-constant k_l and (b) parabolic rate-constant for a, Si- and C-face with increasing temperature for dry thermal oxidation of 4H-SiC.¹⁸⁶ The linear oxidation rate-constant is proportional to the interface reaction and is intermediate for the a-face (= parallel to the c-axis) in comparison to the Si- or C-face (= perpendicular to the c-axis). Unlike k_l , the k_p -values of a- and C-face become equal at 1150°C.

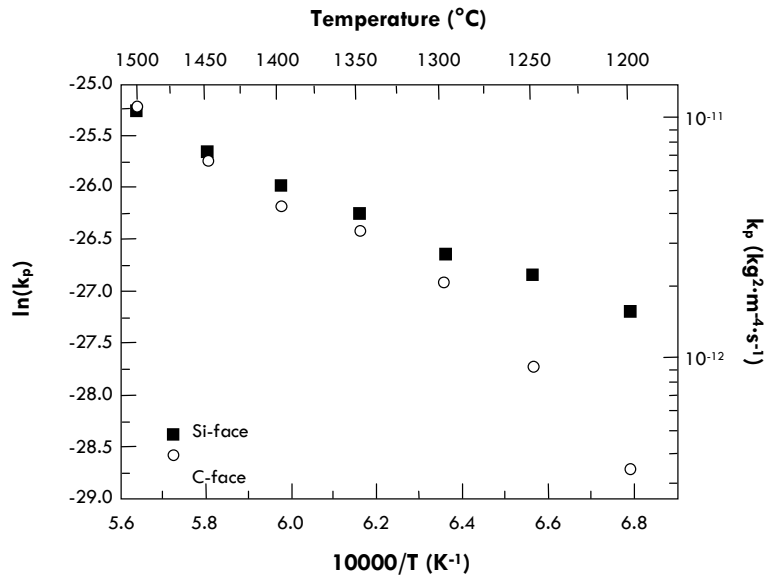


Fig. 35: Change in the parabolic rate-constant k_p for both Si- and C-face with increasing temperature for dry thermal oxidation of 4H-SiC.³⁸⁶ As seen in this figure the differences between those two faces diminish drastically at temperatures above 1200°C. The values of an a-face would lie in between those of the C- and the Si-face. Note that at low temperatures the Si-face follows a linear-parabolic time-law (i.e., k_l and k_p are needed) and the C-face a purely parabolic time law (where only k_p is required).

Experimental data proves that the oxidation rates on the C-face for α -SiC are 3- to 10-times higher than on the Si-face.^{30,31,292,415,418,445,490,491} Similar data can be obtained for corresponding activation energies. This effect can be used for determination of the face-polarity of SiC wafers cut perpendicular to the c-axis.^{31,415} However, above $\approx 1350^\circ\text{C}$ the differences in oxidation speed between Si- and C-termination seem to vanish.³⁸⁶

Until now, no generally accepted explanation for this behavior was found. However, close examination of the surface free-energies yields a first thermodynamic explanation for this phenomenon. The higher the surface free-energy, the more energy is needed to create a certain surface area of this material (e.g., C-faces grow "easier" than Si-faces). What is true for crystal growth does also apply for etching processes - hence making C-faces oxidize faster than Si-faces.

In the next few passages different models for anisotropic SiC oxidation will be introduced, because the surface free-energies of both polar faces does not explain difference in oxidation rates: the energetically rather disadvantageous Si-face would be expected to decompose more rapidly than the C-face - however, the contrary is the case.

As found by Song and Smith⁴⁹² the etch rate of SiC by low-pressure oxygen yields the very same face-dependency as found for SiC oxidation with a deviation of a factor of 6 between C- and Si-face. Etching is a process definitely not governed by diffusion, therefore, the differences in etch rates must result from different chemical surface reaction rates. If the reaction rate competes with the in-diffusion of oxygen as the rate limiting process, a face-dependent interface-reaction rate can truly explain the polarity related change in oxidation rates.¹⁸⁶ These findings are in accordance with the etching behavior of silicon carbide by other agents (e.g., molten salts).⁴⁹³

When carefully comparing the oxidation rates of different SiC faces one can find a direct dependency of areal densities of carbon atoms and k_i . The ratio of 1.64 for the carbon areal density between the C- and a-face is very close to the quotient of 1.60 for the corresponding k_i -values.¹⁸⁶ The C-face (highest carbon areal density) hence oxidizes fastest. In-diffused oxygen would, therefore, meet on the C-face carbon atoms striving to form C-O molecules and breaking Si-C bonds. After this first carbon layer was removed, the remaining half-bilayer of silicon atoms are only withheld by one underlying Si-C bonding. Breaking Si-C bonds is energetically more elaborate as three remaining Si-C bonds from the SiC-tetrahedra are present.

These findings would be in accordance with the orientation dependency of the linear rate-constant of pure silicon derived from geometrical considerations.¹⁶² However, the basic assumption of a driving force to form C-O-molecules to be higher than that of forming Si-O-bonds is not clear. A simple comparison of Gibbs free energies cannot be applied. In both cases, the very same Si-C bond would have to be broken and from that point of view, the observed differences in oxidation rate remain unclear. Moreover, a strict layer-by-layer oxidation cannot be true to an atomistic scale.

The very same geometric or mechanistic approach was used by Wright et al. in 1999.^{490,491} Starting on the Si-face, oxygen is adsorbed to silicon atoms, which are threefold coordinated to carbon atoms within the SiC lattice. Caused by the high electro negativity of oxygen, the Si-C-bonding becomes less ionic and, therefore, less forceful. With the initial Si-C-bond (“ α -bond”) being broken, incoming oxygen will occupy the former Si-site and undergo a Si-O-C-Si bond. With increased ionic character of the underlying C-Si-bond (“ β -bond”), this bonding will be strengthened. The latter bonding will be energetically much more costly to break than an alpha-bond. In a final stage, when one whole layer is fully oxidized, CO emission and structural reconstruction will take place. With one weakened and three strengthened bonds the Si-face will oxidize slower than the C-face (three weakened and one strengthened bond). However, this mechanistic model makes one fatal mistake as it assumes an inverted 4H-SiC structure. Actually, the real 4H-SiC structure shows on the Si-face onefold coordinated carbon and threefold coordinated silicon - and not a threefold coordinated carbon and one onefold coordinated silicon atom as assumed by Wright et al. Therefore, is their model improper to explain the anisotropy of SiC oxidation. It would predict the exact opposite from the observed behavior.

Tilting series examinations (cf. Fig. 34) of single-crystal 6H silicon carbide wet oxidation as performed by Ueno and Seki^{188,189} show the very same behavior as discussed: a decrease in rate-constant depending on the inclination from the C-face, which has the highest oxidation rate. These authors do not deduce this behavior from geometric consideration; they state that the activation energy of the a-face should be smallest due to the Si-C bond lying parallel to the surface. This should make it most easy for oxygen to react with silicon and carbon. As the activation energy for the oxidation on a-faces is intermediate when compared to those of Si- or C-face oxidation (with $E_a(1\bar{1}\bar{2}0)$ closer to E_a of the C-face),¹⁸⁶ a simple geometry derived model has to fail.

This problem becomes even more evident, when looking at the growth kinetics of the $(1\bar{1}\bar{2}0)$ and $(\bar{1}100)$ faces. First, with two Si-C bonds lying parallel to the surface, oxidizes slower than the latter (with one Si-C bond parallel to the surface). On both surfaces, there is an areal density of 50 % carbon and 50 % silicon atoms. However, on $(\bar{1}100)$ -faces, the C and Si atoms are dispersed less frequently than on $(1\bar{1}\bar{2}0)$ -faces. This makes a direct connection between electronegativity (which is higher for carbon compared to silicon) and oxidation rate inaccurate.

Christiansen et al. conducted studies on SiC oxidational anisotropy using a 6H-SiC Acheson sphere.^{183,377} Wet oxidation experiments showed six minima and six maxima on the equatorial region that correspond with $(1\bar{1}\bar{2}0)$ (minima) and $(\bar{1}100)$ (maxima), respectively. These findings are in accordance with studies earlier conducted by von Münch and Pfaffeneder on 6H- and 15R-SiC in 1975 (Ref. ⁴⁸⁵).

For high oxygen pressures and/or temperatures above 1200° - 1500°C oxygen diffusion becomes the dominant rate limiting process and differences between the oxidation rates of different crystallographic orientated faces will disappear (Fig. 35). This can be explained by the differences in reaction rate on the various surfaces.

Oxidation rate-constants greatly depend on the face-polarity.^{17,388,415,484,494,495} Latter was tried to be explained in terms of the interlayer model proposed by Hornetz et al.^{274,447} This idea was adapted by Afanas'ev^{289,325} in the "carbon-cluster-model" in order to explain the poor electronic quality of SiC-SiO₂ interfaces (cf. section 2.4.2.4). The observation of carbon at the interface forming a nanometer thick interlayer of oxycarbide nature by Angle Resolved X-ray Photoelectron Spectroscopy (ARXPS) was interpreted to hinder the oxidation progress and is in accordance with crystallographic anisotropy of SiC as the oxidation rates correlate with the interlayer thickness in an indirect fashion. Thus, slow oxidation rates as found on the various Si-faces could be assigned to a thicker Si-C-O interlayer (cf. Fig. 36). Although direct evidence of this oxycarbide interlayer seems to exist (cf. Ref. 150,255,256,269,281,288,299,301,302,323,324,326-328,424-426), other scientists did not find any Si-C-O-related signals at the SiC-SiO₂ interface at all (cf. Ref. 274,298,300,301,330,331). This difference between virtually no transient region up to 400 nm thick and rough interlayers³⁷⁷ reflects once more the great need for standardized oxidation tests and the application of comparable analytical methods in order to evaluate experimental findings.

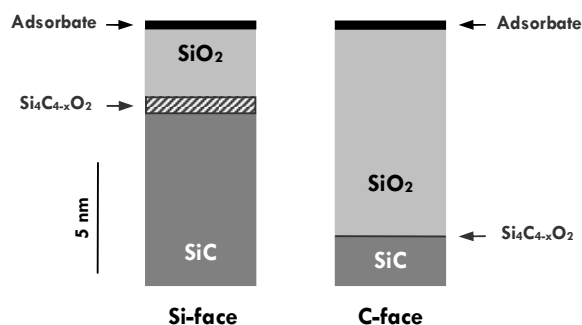


Fig. 36: Composition of the oxide scale on Si- and C-face after 15 minutes of dry thermal oxidation at 1100°C (after Ref. 447). The topmost layer consists of various species like graphite and C_xH_yO_z. Possibly, the interlayer of oxycarbide nature could explain deviations in oxidation speeds when comparing oxide scale growth on surfaces with different polarity.

Considering the face-dependent anisotropy, bulk kinetic studies on silica growth are rather complex. On the c-face, oxide formation follows from 970° up to 1245°C (1.67 - 166.67 h) after a linear-parabolic transition time with increasing temperature or longer oxidation times a parabolic law, while on the Si-face a rather linear law can be applied up to 1200°C even for longer periods.^{30,419} Comprising different rate-constants, bulk kinetic rate-constants show an increased error margin. Linear-parabolic kinetics indicate diffusion-limited growth.⁴⁹⁶ Above 1200°C, all faces follow a parabolic law after a linear transition time.^{386,387,423}

When considering that on all faces the same oxide is formed, the law should only differ in k_l because k_p is diffusion limited - a property uniform for the same silica phase. However, latter was not found to be true in SiC oxidation experiments. The proposed existence of an oxycarbide interlayer phase, however, could explain these differences.^{274,304,494}

Compared to oxidation reactions without gas production, the free-volume for gas transport now must be shared for in-diffusion of oxygen and out-diffusion of carbon oxide hence retarding the reaction itself.⁴⁰⁶ Considering gaskinetic volumes of O₂ and CO as mere estimations, oxygen will only have 57 vol% of the total passing volume available for gas permeation. However, also this very simplifying approach cannot satisfyingly explain the different oxidation rates on the various crystal faces on silicon carbide even though it gives a first hint for why silicon oxidation is much faster.

Unfortunately, too little is known about gas permeation of CO through silica (cf. section 4.1.3.4). Comparing O₂ and CO, similar molecular sizes (258 and 273 pm respectively)³⁴² can be found leading to the assumption of comparable transportation mechanisms and rates for amorphous silica.⁴⁰⁷ The observation of bubble formation on sintered SiC ceramic bodies and on single-crystals in the presence of sodium and/or water does not conclusively imply that oxygen diffusion cannot be the only rate-limiting process for all SiC materials.

In summary, a mixed term considering the diffusion of both gaseous species independent of crystal faces and the interface reaction with its anisotropic character should be applied to explain SiC oxidation. Beside all these influences, the bulk oxidation kinetic indeed does not show a very complex time-dependency but rather a simple (linear)-parabolic time-law. It would be essential for a systematic research to point out how different kinetic influences may produce indistinguishable time-dependencies.

4.1.4.4 CRYSTALLIZATION OF AMORPHOUS SILICA

4.1.4.4.1 General aspects

During passive oxidation of silicon carbide, silica starts to be formed and grows as an amorphous phase, but a phase transition into a crystalline SiO₂ modification is possible. In this context, it is incorrect to refer to crystallization of a glass, as usually crystallization is observed at temperatures above 1200°C. With the glass transition temperature, T_g, lying at that temperature (experimental value: 1202°C; Ref. ^{497,498}), amorphous silica should rather be referred to as vitreous SiO₂ as silica glass only exists below T_g.^{499,500}

Under dry thermal conditions, the linear crystallization of β-cristobalite out of amorphous, stoichiometric SiO₂ was observed by various researchers.^{30,342,368,406,415,501} Other silica phases do not occur in major amounts. Only β-tridymite was found to be a significant phase but its occurrence on high-purity single-crystals signifies impurities like water and sodium.³⁸⁹

In the only study to find a further SiO₂ polymorph, Guinel and Norton ¹⁵⁰ reported the presence of quartz. In this specific study, the influence of major impurities was excluded by a careful preheat treatment of the furnace and the subsequent analysis via XPS measurements. However, impurities at a level below 100 ppm cannot be ruled out. Also, quartz could only be determined by TEM diffraction patterns and not by other spectroscopic methods, indicating a low fraction of this phase. A mere temperature-dependency between silica polymorphs found in the silica scale on oxidized SiC samples (i.e., > 1400°C: cristobalite / 1300° - 800°C: tridymite / < 700°C: quartz) would correspond to the schematic transitions shown in Fig. 12, but was never observed in that fashion before. More comparing studies need to be performed on that specific topic as it might well hold the key in understanding the impurity-free scale-development of SiO₂ on SiC. For hydrothermal studies, quartz formation with quartz as stable equilibrium phase may be connected to solution and precipitation.¹⁵¹

Accompanying crystallization a volume reduction (298K : $\rho_{\text{amorphous silica}} = 2000 - 2200 \text{ kg}\cdot\text{m}^{-3}$, $\rho_{\beta\text{-cristobalite}} = 2200 \text{ kg}\cdot\text{m}^{-3}$)¹⁵³ causes minor cracks around crystallization centers. Crystallization is observed for oxidation periods longer than 100 h at temperatures below 1000°C .³⁶⁸ Depending on environmental conditions (e.g. water increases the crystallization rate significantly), β -cristobalite formation takes place after ca. 20 h in between 1100° and 1200°C . For temperatures higher than 1400°C , crystallization will take place after very short transition times in the range of minutes. The influence of crystallinity of the silica scale up to 1500°C was examined by various scientists.^{342,368,502}

Besides temperature and oxidation time, also the presence of additives, impurities, and the surface morphology influences the crystallization speed. It is trivial to assume the crystallization to take place at any structural imperfection (cracks, pits, elevations, pores, micro- and macropipes) and at the sample's edge starting at the silica-atmosphere interface.

With increasing crystallization the oxidation rate was reported to shift towards lower rate-constants, even with differences of factor 30 between $k_p^{\text{crystalline SiO}_2}$ and $k_p^{\text{amorphous SiO}_2}$.⁵⁰³ Lower oxidation rates for a higher degree of crystallinity of the oxide scale indicate lower gas transport velocity compared to amorphous silica with higher transportation rates. This is in contradiction to data on gas that had no or little difference. The most probable solution to these seemingly conflicting data was given by Ramberg and Worell,⁵⁰⁴ who concluded from a comparison of literature and their own data on CVD SiC that the gas transport through amorphous silica and cristobalite is roughly equal up to about 1350°C , but at higher temperatures the transport in amorphous silica becomes much faster than through cristobalite. Thus, the effect of crystallization becomes important at high temperatures, that is, under conditions, which are favorable for crystallization.

At 1677°C , the crystallization rate of amorphous silica towards β -cristobalite reaches a maximum value.¹⁶⁸ At even higher temperatures, the silica layer becomes increasingly fluid and in a semi-crystalline case the β -cristobalite grain boundaries will be closed.⁴⁰⁶ Gravity and reaction gas induced flow of the amorphous silica was also observed way below the melting point of SiO_2 . At a higher fluidity of the silica layer gas transport through the amorphous SiO_2 becomes faster and the oxidation rate increases.⁴⁰⁶ Finally, above $\approx 1728^\circ\text{C}$ (at ambient pressure; Ref. ⁵⁰⁵) the last of the β -cristobalite phase will be molten.

When considering crystallization processes at elevated temperatures, low-temperature phase transitions during cooling must be considered. In the case of β -cristobalite, a metastable phase transition exists below 300°C from the β - towards the α -phase, that is, from cubic ($F\bar{d}3m$, $\rho = 2200 \text{ kg}\cdot\text{m}^{-3}$) to tetragonal/pseudocubic ($P 4_32_12 / P 4_12_12$; $\rho = 2320 \text{ kg}\cdot\text{m}^{-3}$).^{153,159,167} The phase transition (at 268°C) is a spontaneously and reversibly proceeding process accompanied by a decrease in volume by 6.2 vol%.^{153,168}

4.1.4.4.2 Cyclic oxidation

Oxidation under static = isothermal conditions was shown to provide (dense) silica layers capable of providing adequate oxidation protection even for long-time exposure of silicon carbide to oxidant species.⁵⁰⁶ However, static conditions may not be encountered in every environment SiC-based ceramics are used in - like in combustion engines, where cyclic oxidation occurs.

As discussed before undergoes crystalline silica with its dominant phase cristobalite a phase transition below 300°C that is accompanied by a significant decrease in volume (> 5 vol%). Hence, cyclic oxidation will require careful consideration of crack formation and subsequent crack healing.^{164,168,169,507} Also the mismatch between thermal expansion coefficients C_{th} attributes for crack formation with the general relationship $C_{th}^{amorph. silica} \ll C_{th}^{silicon carbide} \ll C_{th}^{cryst. silica}$ (cf. Fig. 37).⁵⁰⁸⁻⁵¹² Silicon carbide “performs relatively well under thermal cycling” as concluded by Jacobson and the oxide layer continues to follow linear-parabolic kinetics after each cycle without significant deviations from static conditions.⁵⁰⁸ However, amorphous layers are less susceptible to crack formation than purely crystalline ones (which on their behalf show a worse adhesion to the SiC substrate).⁵⁰⁹ When examining cyclic oxidation and comparing this data with a control sample, that is subjected to isothermal oxidation, heating and cooling times at the beginning and at the end of each cycle must be kept sufficiently short in order to avoid significant oxidation reactions during these transitions periods.

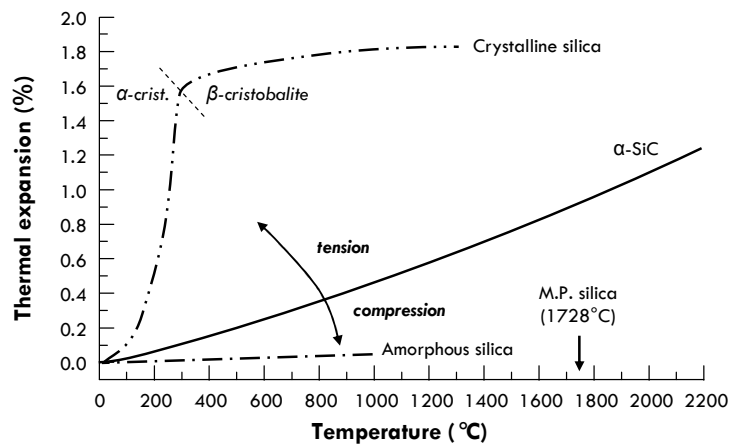


Fig. 37: Thermal expansion of amorphous/crystalline silica and silicon carbide. Depending on the state of the silica scale, tension or compression can be expected during cooling leading to crack formation (after Ref. ^{508,509}; data taken from: Ref. ^{505,510,511}). M.P. denotes the melting point of silica.

As proposed by Opila et al.⁵¹³ the lack of spallation could be understood in terms of tensile rather than compressive stress being induced in the oxide scale. The phase composition of the silica layer and the flexural strength at room temperature are comparable after static and cyclic oxidation (at 1200°C for sintered SiC).¹⁶⁹ Temperature was found to have a more profound influence on the oxidation kinetics than thermal cycling itself.⁵¹³

4.1.4.4.3 Time-law

Above 1150°C, crystallization will affect the diffusion of both oxygen and reaction gas as more and more of the silica layer undergoes a phase transition towards β -cristobalite. Deal-and-Grove kinetics can be applied for both 100 % amorphous and 100 % crystalline silica scales respectively. Only during the transition time will a time-law considering two diffusion coefficients occur. Assuming the diffusion rate of crystalline silica to be at least an order of magnitude lower than $D_{\text{amorphous silica}}$, a logarithmic time-law could be applied.³⁸³ This model assumes the effective diffusion-related diameter \varnothing_d as a function of the continuously progressing crystallization during the oxidation (= change in mass m or scale thickness dx ; Eq. 53 - 54).

$$\frac{d\varnothing_d}{dx} = k_a \cdot \varnothing_d \quad \text{Eq. 53}$$

$$\varnothing_d = k_b \cdot e^{-k_a \cdot x} \quad \text{Eq. 54}$$

A correlation between \varnothing_d and the rate-constants k_a and k_b can be found. As stated, in case of $D_{\beta\text{-cristobalite}} \ll D_{\text{amorphous silica}}$ scale growth will approximately only depend only on k_p derived from the (still) amorphous areas. Hence, the following equations can be formulated (Eq. 55 - 56):

$$x = \sqrt{k_p \cdot t} \quad \text{Eq. 55}$$

$$\frac{dx}{dt} = k_c \cdot \frac{1}{\sqrt{t}} \cdot e^{-k_a \cdot x} \quad \text{Eq. 56}$$

Solving Eq. 56 for the change of oxide scale thickness (or the increase in bulk mass analogously) will yield Eq. 57, introducing a logarithmic rate-constant k_{\ln} and a constant c :

$$x = c + k_{\ln} \cdot \ln(t) \quad \text{Eq. 57}$$

For the case of mixed kinetics an empirical complex equation (Eq. 58) was used to describe the oxidation kinetics (with T denoting an initial oxide layer; Ref. ⁵¹⁴):

$$x = k_1 \cdot t + k_p \cdot \sqrt{t} + k_{\ln} \cdot \ln(t) + T \quad \text{Eq. 58}$$

The goodness of fit strongly depends on the number of raw data points and the basic time-law that is assumed for fitting. Depending on the deviation of the individual data points, mixed-term kinetics as presented in Eq. 58 can be (equally) well applied for fitting than a basic linear-parabolic or a purely parabolic time-law. In this light, the critical assessment of the applied equation and the physicochemical relevance of the latter becomes essential.

4.1.4.4.4 Structural aspects

Amorphous networks of silica consist out of a statistic arrangement of small structural units (SiO_4 tetrahedra as discussed in section 2.2).¹⁶⁵ This model coincides with the crystallite theory (i.e., that amorphous silica consists out of microcrystalline forms of various crystal modifications or at least of parts of their unit cells) in case of small crystallites.⁵¹⁵

There exist quite a large number of explanations for the renowned tendency of vitreous SiO_2 to undergo a phase transition towards crystalline β -tridymite. Maybe the most striking one is the interpretation of amorphous silica as a very distorted form of fractured structural units of β -cristobalite explaining the small difference between the density of amorphous silica (298 K: $\rho \approx 2000 - 2200 \text{ kg}\cdot\text{m}^{-3}$)¹⁵³ and β -cristobalite (298 K: $\rho = 2200 \text{ kg}\cdot\text{m}^{-3}$)¹⁵³.

The kinetic of crystallization is to be divided into three steps: (1) incubation, (2) devitrification, and (3) equilibrium phase. During the first phase, nucleation and subsequent growth of future crystallization centers will be observed. This process is a critical function especially of the temperature and is accelerated in the presence of impurities like water or sodium. The latter, however, can prevent a complete crystallization of the silica layer by stabilizing a small amount of amorphous phase that on its behalf can contrive accelerated oxygen diffusion (compared to purely crystalline regions).^{422,516,517}

An Arrhenius-equation can be applied to characterize the correlation between the nucleation rate and the temperature. Surface inhomogeneities (like scratches) greatly increase the nucleation but influence only to a minor extent the crystal growth progress itself.⁵¹⁸ Having reached a critical size, enhanced crystal growth will take place throughout the silica layer starting at these crystallization centers. Hereby, nucleation will require higher activation energies than crystal growth. As a last step an equilibrium phase will be established.⁵¹⁸

Thermodynamic considerations show that a grain will have a significantly higher energy lying on a surface than inside a solid body.^{164,519} This explains why devitrification will start from a phase boundary and - in case of SiO_2 on SiC - most likely at the oxide-atmosphere interface. Adsorbed gas molecules will cause instable or metastable crystallization centers due to their contribution to the total energy (adsorption energy). As a result of that, shorter nucleation times are expected under vacuum.⁵¹⁸ Comparing devitrification under various atmospheres, almost the same activation energies for the nucleation process ($\approx 427 \text{ kJ}\cdot\text{mol}^{-1}$) can be estimated. This E_a -value lies within the order of magnitude of the activation energy for viscous flow according to the theory of Frenkel.⁵²⁰ Significantly lower activation energies (like $223 \text{ kJ}\cdot\text{mol}^{-1}$ as found by Ramachandran et al. ⁵²¹) may be attributed to the presence of water or related impurities.

Influencing parameters on the oxidation rate besides the temperature are (1) impurities (sodium, alumina and water promote nucleation and devitrification; cf. Ref. ^{164,518,522,523}) and (2) the morphology (discontinuities: may they be the sample's edges, scratches or pores). The latter case is shown in Fig. 38 in which chained devitrification centers are located along a scratch on the surface of 6H-SiC:N . Only a homogenous, flat and defect-free surface forms an uniform silica layer and a randomly distributed crystallization can take place.^{502,524,525}

Careful and reproducible preparation of the silicon carbide surface is essential for meaningful kinetic studies. Uniform, inhomogeneity-free surfaces obtained, for example, by polishing and subsequent etching are, therefore, adequate. Subsequent to rough (mechanical) polishing and Chemical Mechanical Polishing (CMP, improving the surface morphology, for example, by hydrogen etching) a carefully conducted cleaning step (like RCA cleaning; cf. section 2.3.1.1 and Ref. ²⁰⁰) must be implemented before oxidation experiments should be performed. For more information about surface preparation methods and scratch removal techniques cf. Ref. ^{202,526}.

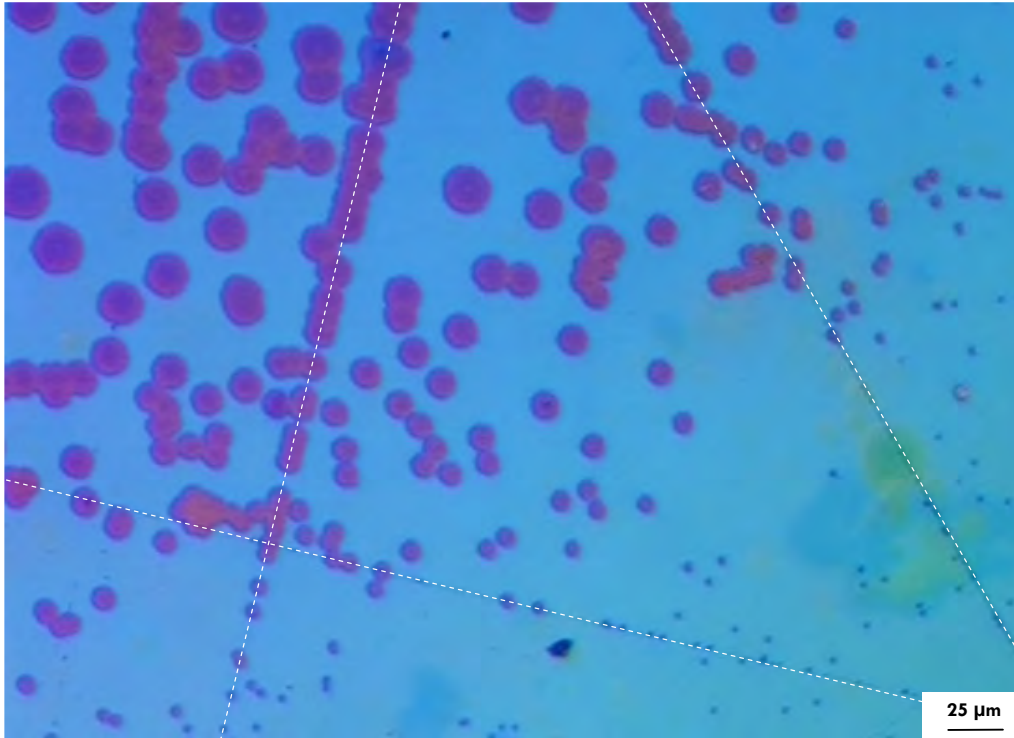


Fig. 38. Photograph of a 6H-SiC:N sample, oxidized for 5 h at 1400°C under dry thermal conditions. As seen, crystallization centers are located along significant scratches (dotted lines) on the sample's surface. The different brightness of the crystallization centers is due to different interference colors of thicker amorphous regions and thinner crystalline ones.

Besides accelerated crystal growth, both bubble formation and pitting must be considered in the presence of sintering aids. These factors will promote the tendency to create an uneven silica layer even without any structural or morphological defects on the SiC surface.

As seen in Fig. 38 and 39, the typical form of early devitrification centers are disclike structures: so called spherulites (or "rosettes" as referred to by Ainger; Ref. ⁵²³). These structures are very typical for β -cristobalite formation in amorphous silica.^{522,527-530} Would the crystallization process occur in a sufficiently thick layer, a three-dimensional sphere would be created (hence the name: spherulite ⁵⁰⁰) but due to the pronounced thinness of devitrificating SiO₂ layers on silicon carbide only rather two-dimensional structures are evident. As shown by Pantsurkin and Kalinin nucleation follows an exponential function while crystallite growth obeys to a constant term.⁵²² The latter, crystallite growth, is connected to nuclei of critical size, which, in a first approximation, may be estimated to be statistically distributed throughout the SiO₂-layer. The first, nucleation, is a very temperature-sensitive process strongly accelerated by applying at higher temperatures (i.e., above 1200°C).³⁷⁵

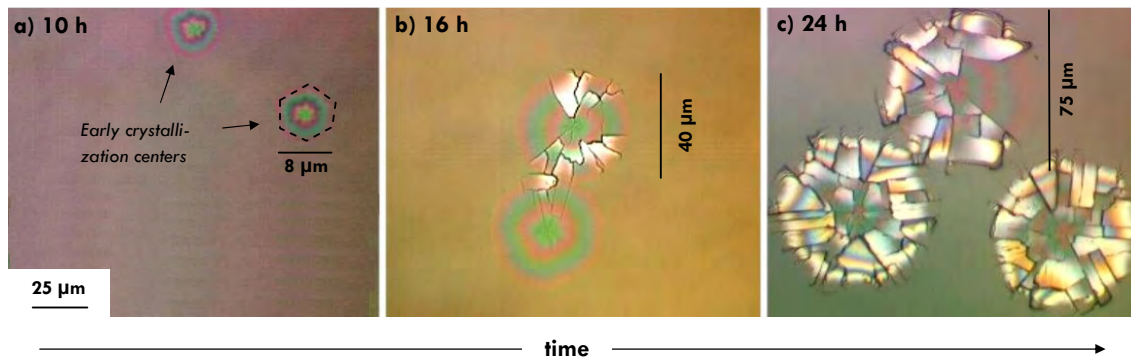


Fig. 39: Series of photographs showing the development of crystallization centers in the silica layer on silicon carbide over time (dry thermal oxidation of 6H-SiC:N at 1400°C). Early stages of crystallization can only be seen by slightly different interference colors and are characterized by a hexagonal contour (a). The amorphous silica layer has in all three pictures a different indicating increased thickness at higher oxidation times.

Every single-crystallization center will undergo a characteristic structural development. As the devitrification steadily progresses, single-crystallite plates will evolve and develop into small sub-grains as shown in Fig. 39.⁵²⁵ During the initial steps of this development, the crystallization centers are hexagonally outlined, but this preferential contour will be lost later. It must be kept in mind that cracks *ex post* may well be due to the β -to- α -phase transition of cristobalite and do not indicate extensive crack formation under oxidation conditions. However, grain boundaries, even at high temperatures, work as channels for accelerated gas transport and hence locally influence the oxidation kinetics. Further growth and steric deformation can lead to the uplift of single-crystal plates.⁵²⁴

Large spherulites reach a thickness-to-diameter-ratio of above 1 : 100, because crystallization within the amorphous layer is preferred compared to bulk thickness growth. In order to distinguish these plate-like crystallization products from much smaller (ca. 1 - 2 μm in diameter) and rather round β -cristobalite aggregates (which from here on shall be called “globulites”), we propose to use the noun “radialite” to stress the two dimensional character of these structures.

It is evident that idiomorphic radialite growth cannot take place for an unlimited period of time. Depending on the overall frequency of forming nuclei and the growth speed, the individual radialites will come into contact with each other and the formation of a more or less uniform crystallite lawn will be observed. Fig. 40 shows two idealized radialites (one single one and two grown together ones). It is important to mention that the earlier a certain region devitrificates the thinner it will be compared to later crystallized areas and especially compared to the bulk amorphous layer as non-crystalline scales grow faster at high temperatures. Radialites, therefore, are small deepenings within the vitreous silica scale.

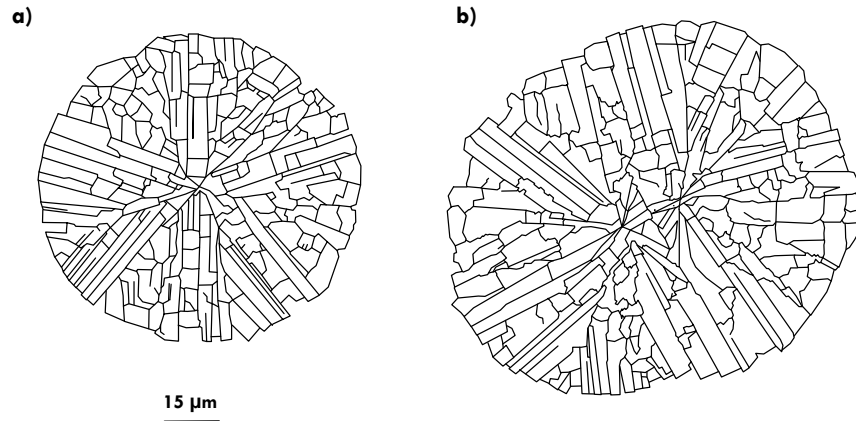


Fig. 40. a) single and b) two intergrown radialites with their typical sub-grain structure (schematic for structures obtained after dry thermal oxidation of 6H-SiC:N at 1400°C for 32 h).

All crystal plates within an idiomorphic radialite are almost radially arranged creating a typical cart-wheel-like structure. Thermal grooving may explain pronounced cracks between single-crystallites.⁵²⁵ TEM studies showed that the cubic β -cristobalite phase grows with the $\langle 111 \rangle$ axis (almost) normal to radial directions creating a fine lineation coinciding with $\{111\}$ faces.⁵²⁵

This preferential orientation can be explained by kinetic and energetic considerations. Natural β -cristobalite shows the very same formation mechanism and growth of octahedral faces ($= \{111\}$).¹⁵³ Radialite growth follows the two-dimensional restrictions of a sphere-symmetrical system. The single-crystal plates do differ from radial directions only by a very small deviation angle. In order to minimize the energy of a large number of grain boundaries of every single-crystallite an orientation parallel to the direction of closest packing (in this case $\{111\}$) will be favorable while the whole arrangement will maintain a radial superstructure.

As shown by Ogbuji an amorphous silica network exists below the grain boundaries and a very thin (few nanometers) layer is present beneath the individual crystallite plates as well (Fig. 41).^{503,525} This phase was found to be of oxycarbide composition by XPS analysis.¹⁵⁰ The network allows fast diffusion along these “channels” and thus locally increased oxidation rates.

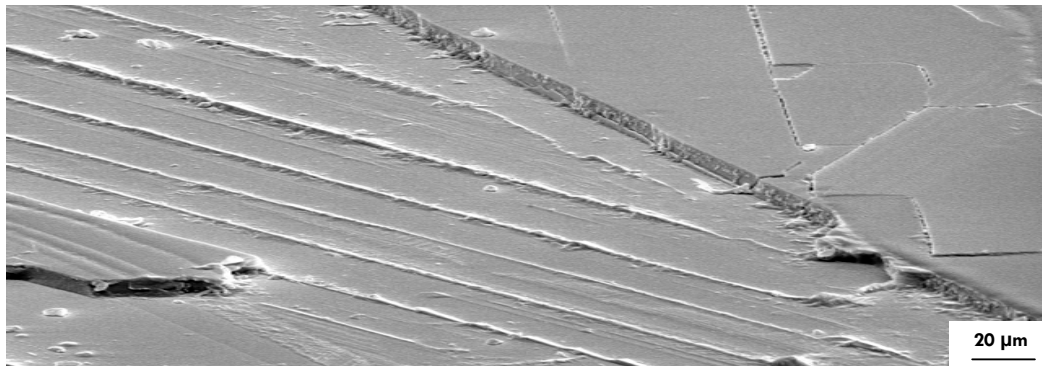


Fig. 41. The SE-mode SEM-picture shown here shows the remains of partially removed silica plates. Below the grain boundaries of the single-crystal plates of individual radialites, a network of amorphous silica (and/or oxycarbides) will be found. Directly beneath flat plates, an uneven, sub-micrometer thick interlayer can be seen. The sample material was 6H-SiC:N and the oxidation was carried out at 1400°C for 24 h.

Radialite growth and progressing crystallization are a direct function of the oxidation temperature (cf. Fig. 42) and the interpretation of any rate-constant must take external factors (impurities etc.) into account. Growth rates of $\approx 0.2 \mu\text{m}\cdot\text{h}^{-1}$ in diameter were reported for 1300°C for dry and wet oxidation experiments that well agree with extrapolated values for devitrification of stoichiometric, rehydrated amorphous SiO_2 .^{496,501}

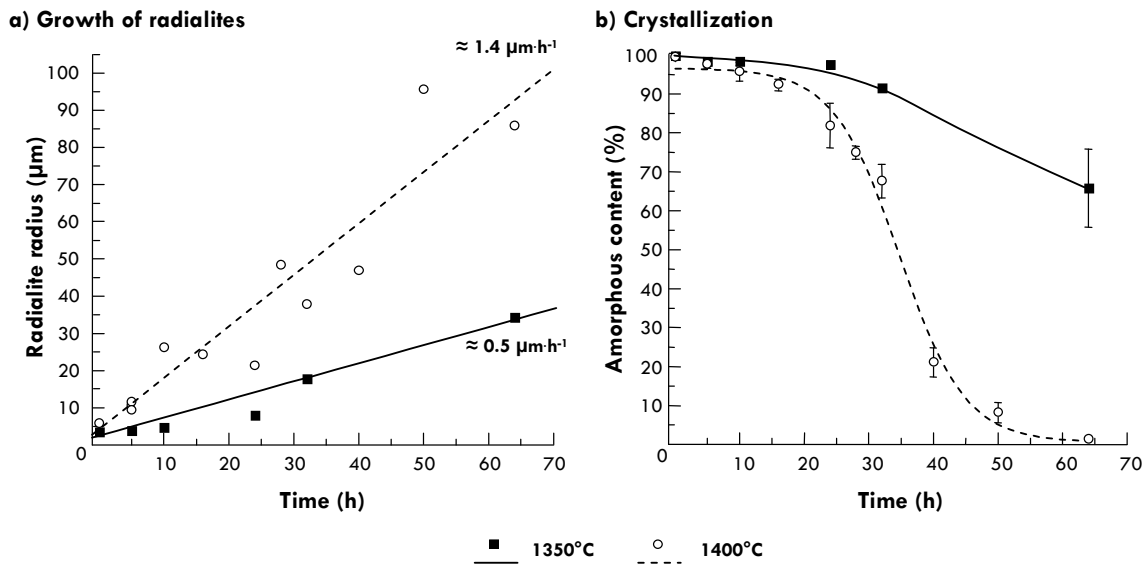


Fig. 42. Growth of radialites (a) and overall crystallization progress (b) of 6H-SiC:N single-crystal samples oxidized (dry thermal) at 1350° and 1400°C . The increase in radialite radius follows a linear time-law ($R^2 > 0.97$) and the crystallization can be described by a sigmoidal equation ($R^2 > 0.98$). As seen an increase in temperature of just 50°C will almost triple the growth-speed of radialites (from ≈ 0.5 to $\approx 1.4 \mu\text{m}\cdot\text{h}^{-1}$).

Under certain circumstances, it is important to consider delamination of radialites when analyzing SiC oxidation mechanism. Due to thermal grooving, especially under annealing or reoxidizing atmospheres⁵⁰³ or when using a steep thermal gradient, single radialites can fall out of the silica layer (“button-like” as Ogbuji described it)⁵⁰³. Such “break-away” events strongly affect the oxidation kinetics as new unoxidized areas (or, more likely: areas that are only covered by a small layer of potentially oxycarbide composition) are now exposed to the oxidation agents. Any gravimetric study will be corrupted by crystalline layer delamination. Fig. 43 shows an example of button-like radialite delamination in the silica layer upon 6H-SiC:N single-crystals.

Crystallographic studies clearly indicate that radialite formation is restricted to β -cristobalite formation. Tridymite or quartz (if observed)¹⁵⁰ grow as an oriented crystalline film.

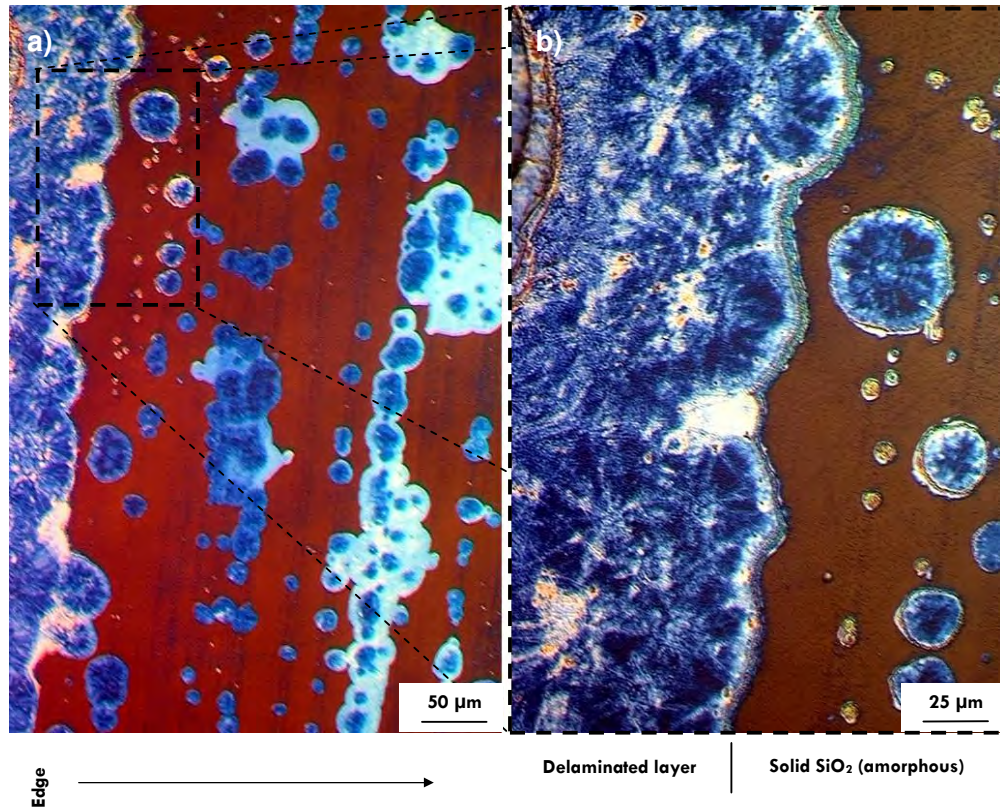


Fig. 43. Button-like delamination of β -cristobalite radialites within an amorphous silica layer (on 6H-SiC:N after 5 minutes of dry thermal oxidation in an O_2 -atmosphere using a very steep temperature gradient).

Depending on oxidation time and temperature, the crystalline silica layer can undergo a second phase transition and globulite formation will take place.^{502,524} The mechanisms of this structural process are still not clear but similar structures are known from “secondary crystallization”, for example, of $Ba_3Si_5O_{13}$.⁵²⁸ Starting at nucleation centers, grain boundaries (the ones lying close to nucleation centers start first) and discontinuities, small 1 - 2 μm large spheres (globulites) show up and start to cover the entire surface (Fig. 44 - 45). Obviously, β -cristobalite growth is connected to this kind of structural change. Influences of impurities like sodium cannot be ruled out so far and systematic studies of this subject are still missing. The formation of a damascening structure as shown in the figures in Ref. ⁵³¹ in the context of microstructures of silica bubbles at the early radialite-globulite transition is intriguing and might possibly give insight to understand the basic structural development (cf. Fig. 46).

Heuer et al. ⁵²⁴ attributed globulite formation to out-diffusion of a Si-containing species (like SiO) which would lead to sphere-like growth on top of the silica layer. However, this model is not plausible as the radialite-globulite-transition is a structural transformation and SiO-out-diffusion has never been shown to be a dominant process in SiC oxidation. The model of Costello and Tressler,⁵⁰² suggests that an amorphous overlayer on top of crystalline areas starts to create nuclei of critical size leading to secondary crystallization and the formation of globulites. This may be possible in cases where extrinsic or intrinsic impurities stabilize amorphous overlayers.

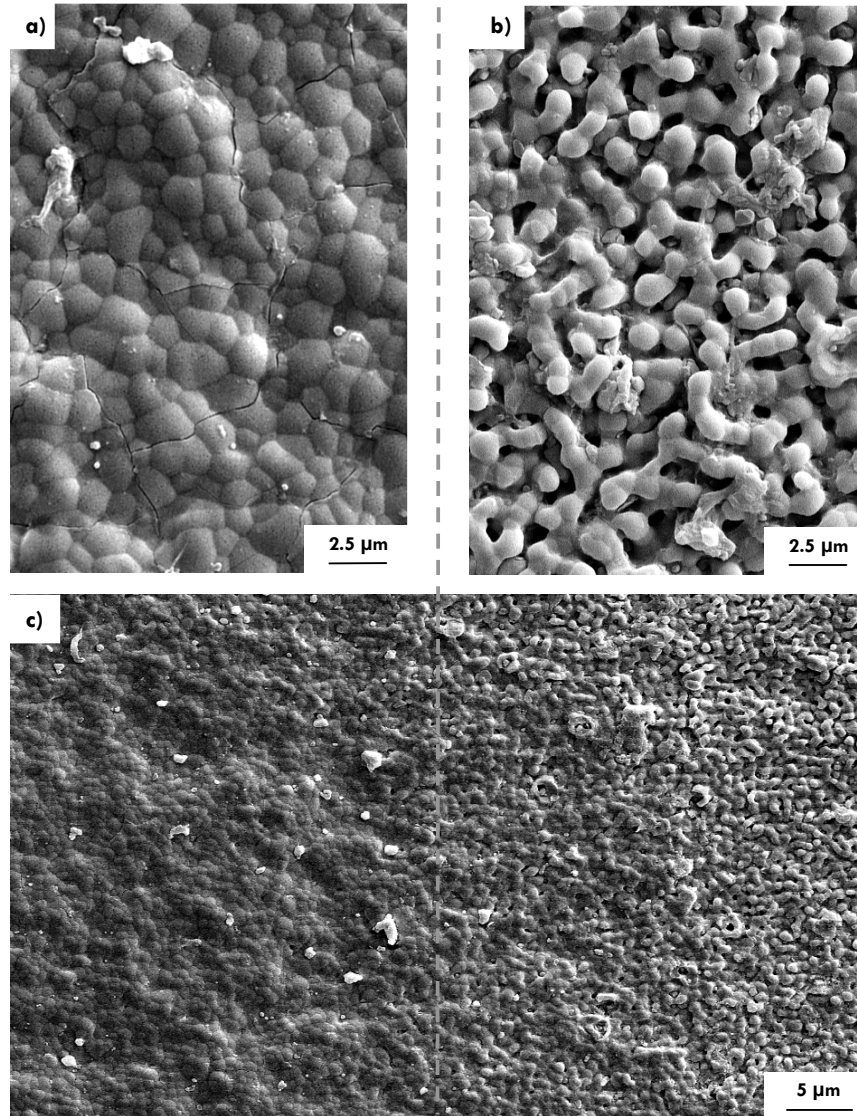


Fig. 44. SEM pictures of crystalline SiO_2 scales on 6H-SiC:N (dry thermal oxidation, 32 h, 1400°C). a) Early stage b) late stage of second-generation crystallization. As seen in (c), both stages depended on surface inhomogeneities and the proximity resulted in early crystallized areas (first-generation crystallization).

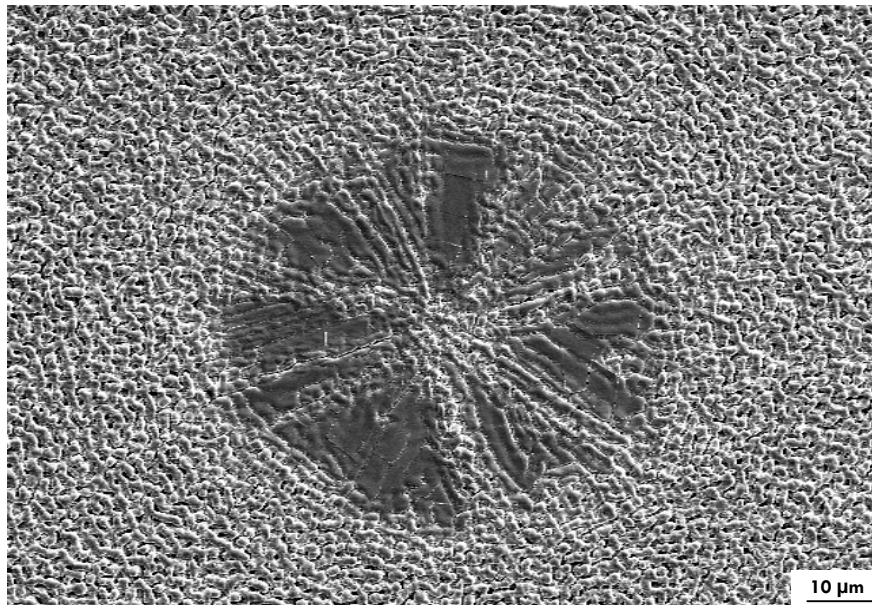


Fig. 45: SE-mode SEM picture of a dry-thermally oxidized 6H-SiC:N-sample (32 h at 1400°C) showing the remains of a radialite within a matrix of second-generation crystallites. As a final stage of SiC oxidation, the whole surface will be covered by crystalline β -cristobalite spheres (= globulites).

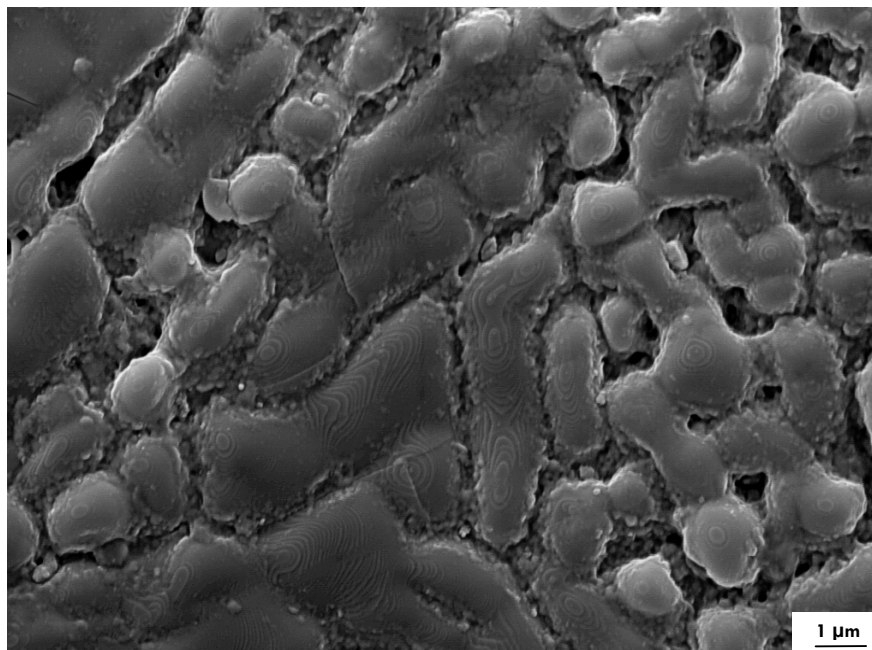


Fig. 46. Damascening microstructure in a SE-mode SEM picture of dry-thermally oxidized 6H-SiC:N (12 h at 1350°C). While further developed globulites show almost no damascening structure, the former crystalline plates show this typical “contour map” like step pattern with step heights < 100 nm.

Regardless of the unrevealed cause for globulite formation: the kinetic impact of this process cannot be underestimated. As seen in Fig. 47, in between the single globulites a significant pore volume is found. These channels reach deep into the silica layer (sometimes close to the SiC-SiO₂ interface) and will increase the oxidation speed. It is clear that the diffusion within crystalline silica cannot be longer seen as the only rate-limiting process and the gas transport rate must be corrected for accelerated diffusion within the pore volume. Still, compared to amorphous silica, even these porous crystalline layers do grow significantly slower at high temperatures.

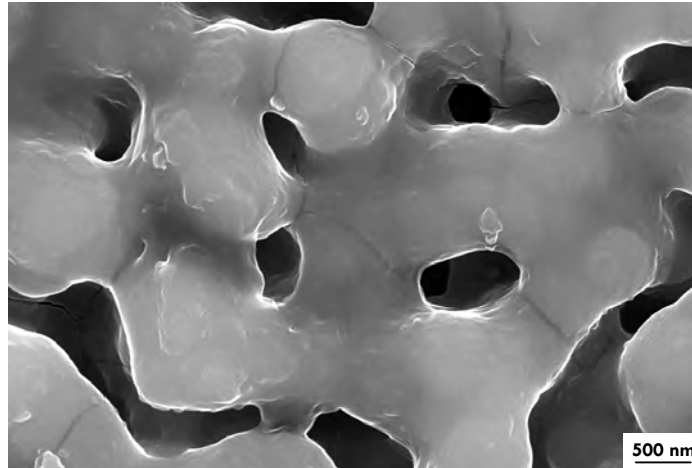


Fig. 47. SE-mode SEM micrograph of the very late stage of globulite formation (6H-SiC:N, dry thermal oxidation, 64 h, 1400°C). As seen in this sample (which was prepared without any sputter coating), the small spheres comprise a significant pore volume throughout which enhanced oxidation can take place.

XRD-measurements have been used to study this structural phase transition. While radialites show a pronounced preferential orientation, globulites do not follow any distinct orientation. 2D detectors (XRD²) like GADDS (General Area Detector Diffraction Solution) clearly show this preferential orientation in form of interrupted Debye-Scherrer rings (Fig. 48). Studies like these make XRD² not only a useful tool for *in-situ* oxide scale thickness determination (Ref. ^{375,442}) but also pieces of information about textural aspects can be obtained.

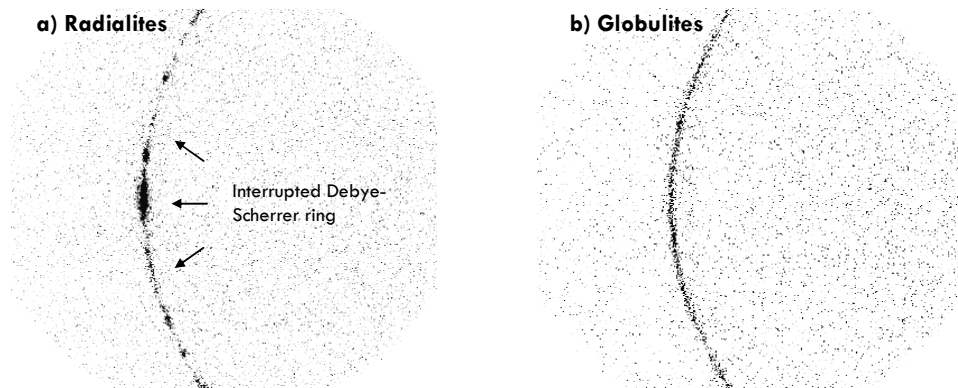


Fig. 48. GADDS diffraction pictures (D8 Advance; incident angle = 10°, angle range = 10° - 50° θ) showing texture-related differences between the (101) Debye-Scherrer ring of silica layers consisting out of a) radialites and b) globulites. The loss of a preferential orientation is due to secondary crystallization. As the measurements were carried out at room temperature, the *ex post* present phase was α -cristobalite instead of the high-temperature phase β -cristobalite.

4.1.4.5 EXTRINSIC IMPURITIES

Extrinsic impurities are present during most oxidation conditions - only under very special conditions and controlled environments their influence can be minimized or excluded.

Bubble formation, a common phenomenon when oxidizing sintered SiC ceramic bodies at high temperatures, seems to be such an impurity-related process. Observed bubble formation on CVD SiC during dry thermal oxidation in both pure O₂ or mixed CO-CO₂ atmospheres above 1675°C or 1625°C respectively, took place in experiments conducted in alumina furnaces.⁵³² Hence, the influence especially of sodium cannot be ruled out. Sodium is renowned to modify the network structure of amorphous silica and, therefore, influences the gas diffusion rate throughout the scale and promotes devitrification.^{406,518} Also, less viscous silica layers are regions in which bubbles can potentially be formed (cf. section 4.1.4.6.3).

Sodium, next to aluminium, is one prominent contamination for it is almost omnipresent in alumina furnaces, which are one of the very few suitable materials for high-temperature oxidation experiments. Various studies on the molten salt corrosion of SiC exist and in most cases the corrosion of sodium salts like Na₂SO₄, Na₂CO₃ or NaCl was investigated on sintered or hot-pressed ceramic bodies.⁵³³⁻⁵³⁸ All these studies clearly showed that the presence of sodium leads directly to increased oxidation or corrosion rates, that is, accelerated passive oxidation or even active oxidation. Sodium within the silica layer could accelerate diffusion of oxygen by the formation of non-bridging oxygens in the SiO₂ network (cf. Ref. ^{539,540} and figures within). With an O-Na bonding energy of just 84 kJ·mol⁻¹, the creation of such non-bridging oxygens (or "vacancies") is very likely, considering O-Si-bond energies of ≈ 435 kJ·mol⁻¹.

Opila showed in a very detailed study the kinetic influences of sodium (as the most probable interfering phase) in alumina furnaces. Even high-purity alumina will strongly affect the oxidation rate compared to pure fused silica as furnace material. Silica furnaces can only be applied for temperatures up to 1500°C and requires special care taking. Above 1200°C fused silica devitrifies, which was shown not to affect the applicability at high-temperatures but to cause fractures below the β-to-α-transition temperature of cristobalite (≈ 270°C).

Fig. 49 shows the kinetic influence of impurities using an alumina furnace.³⁸⁹ Heat-treatment for more than 2000 h at high temperatures was capable of decreasing the impurity-related acceleration of the oxidation process to a value statistically not indiscernible from rate-constants obtained from a pure fused silica furnace. Thus, an error of one order of magnitude in the oxidation rates must be considered when conducting experiments in alumina furnaces compared to impurity-free environments (Fig. 49b).

Zheng et al. conducted a series of experiments with sodium doped 4H-SiC single-crystals at temperatures between 1100° - 1300°C using a mullite furnace (Al₆Si₂O₁₃).⁵⁴¹ The application of latter does not exclude the possibility of the input of further extrinsic impurities within the oxidation atmosphere but this effect would be equal for all studied materials and can for comparison-related purpose be neglected. Central finding of this study was analogously to the aforementioned results of Opila that sodium, even in concentrations as low as 50 ppm, greatly accelerates silicon carbide oxidation. For 50 ppm and 1300°C, the parabolic rate-constant k_p (= 4.91·10⁻¹² kg²·m⁻⁴·s⁻¹) was about 1.8 times larger than the rate corresponding k_p -value for undoped SiC crystals (= 2.72·10⁻¹² kg²·m⁻⁴·s⁻¹). The difference was even greater (≈ 2.0 times) for 4H-SiC:Na with 0.1 wt% sodium (= 5.41·10⁻¹² kg²·m⁻⁴·s⁻¹; cf. Fig. 50). As stated by Zheng et al. no significant change in the activation energy was found (128 - 144 kJ·mol⁻¹ for doped and 118 kJ·mol⁻¹ for undoped SiC). Hence, the main oxidation mechanism seems not to be affected while the diffusivity was almost doubled. Na was shown to be incorporated into the silica layer where it caused structural changes explaining higher oxidation rates.⁵⁴¹

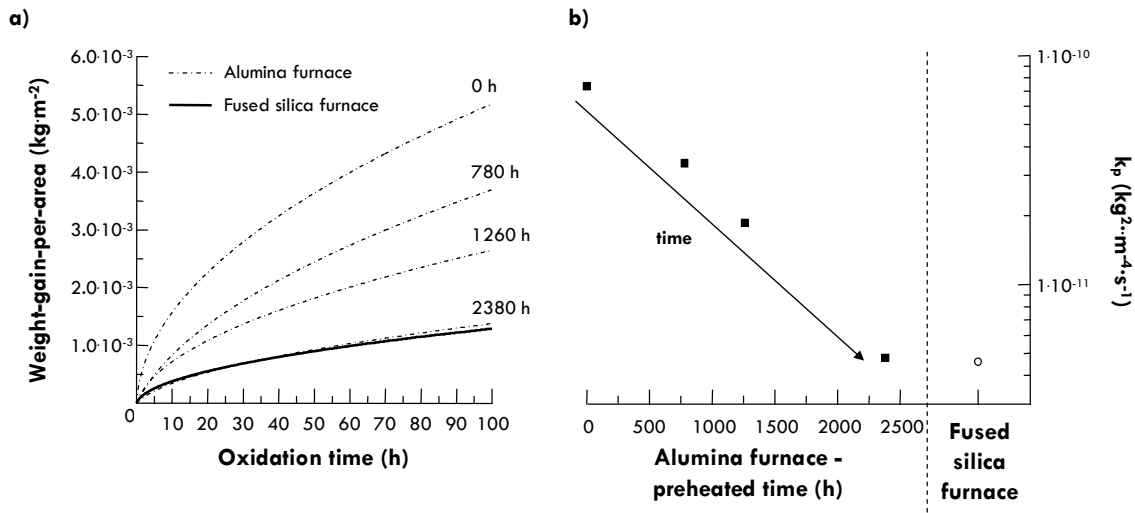


Fig. 49. Kinetics of CVD SiC oxidation under dry-thermal conditions in a fused silica furnace and a conventional alumina furnace (Ref. ³⁸⁹). Due to the influence of impurities (most likely sodium), the oxidation rates in an alumina furnaces are much higher than in pure environments. After > 2000 h of preheat-treatment will the kinetics of both furnaces converge (a) and the oxidations rates will be decreases by almost one order of magnitude (b). The rate-constants were obtained using a parabolic time-law in order to ensure comparability of the values although a linear-parabolic time-law yielded slightly better R²-values.

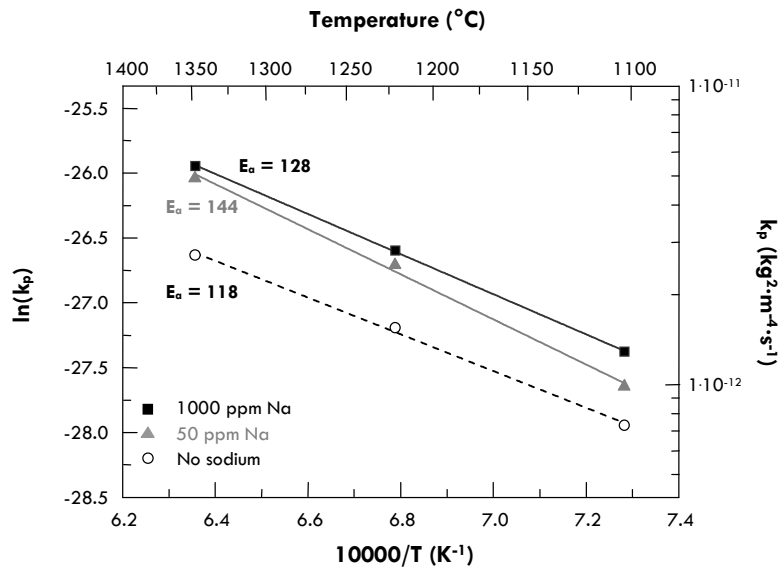


Fig. 50. Influence of sodium on the parabolic oxidation rates of single-crystal 4H-SiC (Ref. ⁵⁴¹). All E_a -values are given in kJ·mol⁻¹ and were recalculated from the data given in the cited reference.

Isotope tracer studies indicate that ionic gas transport of oxygen through the silica layer is almost unaffected by sodium while gas permeation (“molecular oxygen”) is sufficiently increased in order to explain higher oxidation rates.

One very sensitive proxy for sodium presence is tridymite, which can be found, e.g., using micro-Raman spectroscopy even at concentrations below 5 wt%.

Sodium as an intrinsic impurity can be neglected especially in case of PVT grown single-crystals. For sintered ceramic bodies, sodium is usually no major sintering additive and, therefore, other intrinsic substances like boron or carbon are important in SiC oxidation processes.

4.1.4.6 INTRINSIC FACTORS

4.1.4.6.1 General aspects

The choice of the SiC material greatly affects both oxidation kinetics and observed structural aspects (cf. Ref. ^{168,392-395,542}). SiC as a historic ceramic material is widely applied as solid sintered bodies derived from liquid-phase (LP) or solid-sintering (S) processes or hot-pressing (HP). Unlike semiconductor-grade single-crystals, these ceramic bodies are characterized by (1) a general polycrystalline, polymorphic texture, (2) the presence of intrinsic impurities, and (3) pores. All these factors are here summarized as “intrinsic factors”, because they are no unwanted parameters and have their legitimacy from the process of manufacture or structural aspects.

4.1.4.6.2 Pores

Most sintered or hot-pressed polycrystalline ceramic bodies usually show a pore volume from below 1 up to 5 vol% and thus closed porosity, which does not significantly alter the surface area.

Pores (Fig. 51) do influence the oxidation from a textural point of view. They act as inhomogeneities and hence sites for preferred crystallization much like samples edges, corners or scratches. Inhomogeneous silica formation on the rough surface of pores may induce crack formation and locally enhanced oxidation will take place parallel to devitrification (as seen in Fig. 52).

In single-crystals grown by PVT, porosity can be present in the form of micro- and macropipes and polygonized voids. On both, macro-/micropipes and cavities, an increased tendency to devitrificate will be found. Large-diameter pipes can penetrate a whole single-crystal and deliver oxygen far into the SiC body with according inner surface oxidation. Lying along the c-axis, this inner surface will oxidize faster than the Si- but slower than the C-terminated face of the corresponding α -SiC polytype. The roughness of the inner surface prevents a homogenous layer to be established and accelerated oxide layer formation (with an uneven, rolling morphology) can be observed (Fig. 53). Small micropipes can be overgrown by the silica layer.

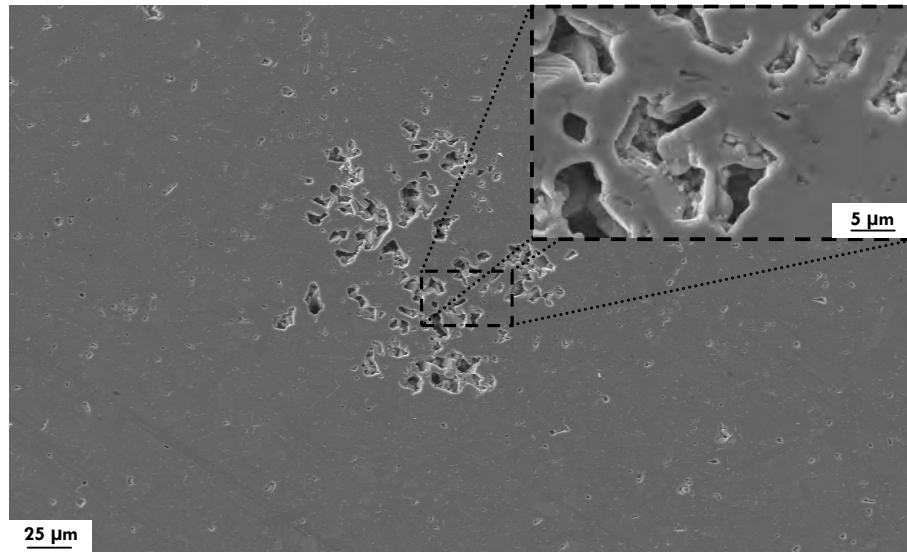


Fig. 51. SEM picture (SE mode) of a pore-cluster in typical LPSiC with a total porosity of below 1 %. The middle part is 5-fold magnified shown in the upper right part of this figure and illustrates that the pores are poorly or even not at all interconnected with each other (the corresponding scales are shown).

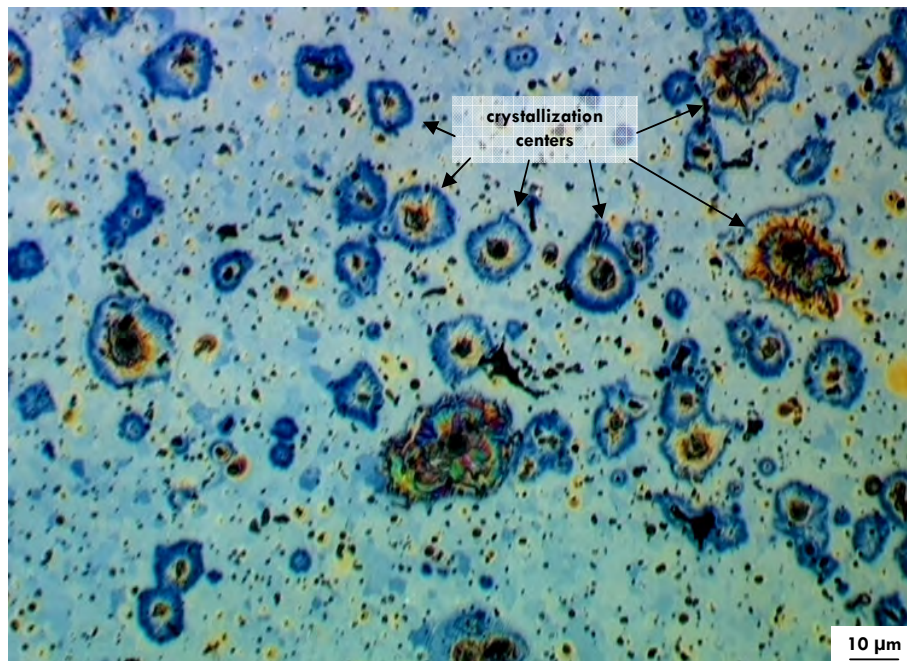
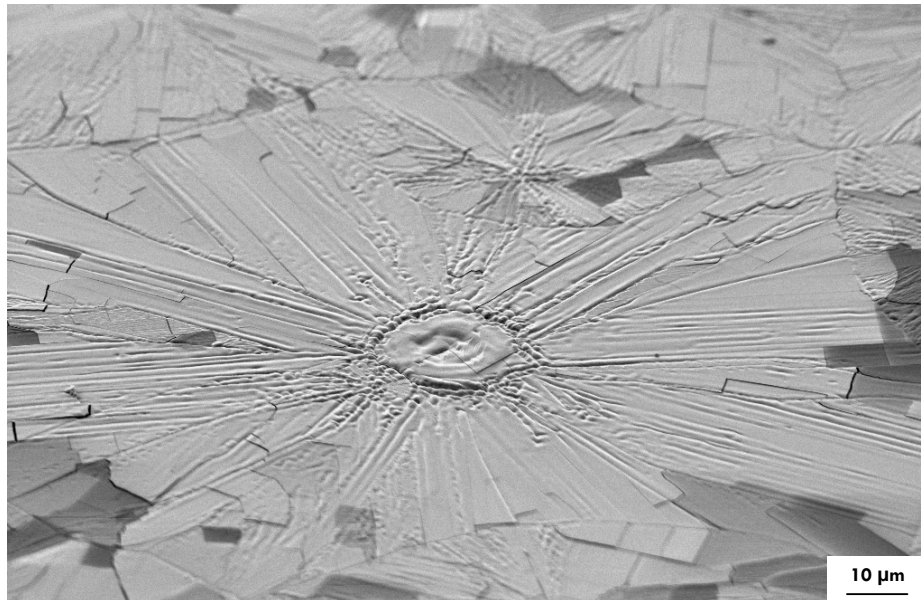


Fig. 52. Photograph of the oxidized surface of SSiC with a total pore volume of $\approx 3\%$. The sample was oxidized at 1400°C for 5 minutes in an alumina furnace under dry thermal conditions. Around former pore structures, already after this short-term oxidation crystallization can be observed ("crystallization centers"). Different colors correlate with different thicknesses (i.e., different interference colors). The bulk scale thickness in the shown sample was measured to be below 100 nm.

a) Over-grown macropipe



b) Open macropipe

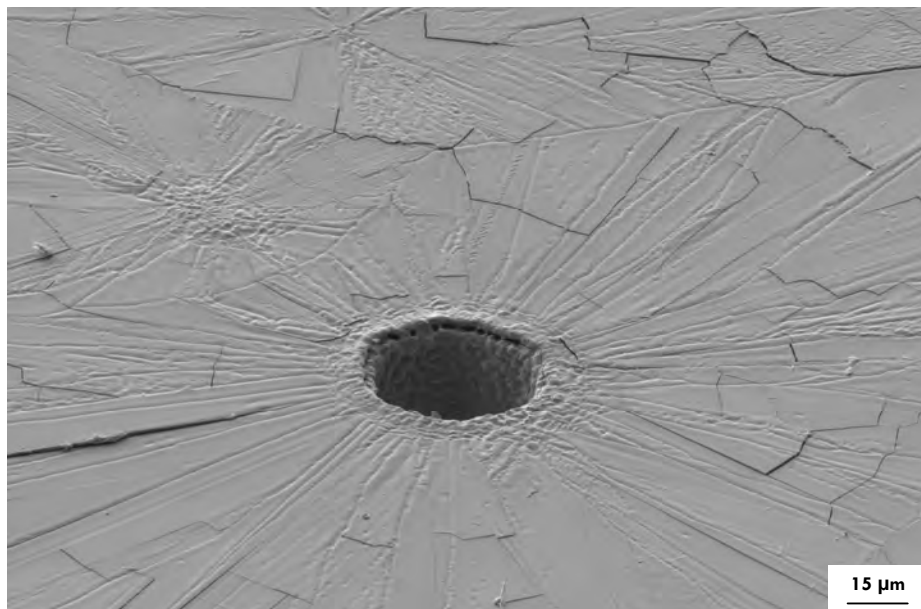


Fig. 53. SEM pictures (SE-mode) of oxide scales on 6H-SiC:N samples (10 h at 1400°C, dry thermal oxidation) with high macropipe densities. a) Overgrown macropipe (different grey scales due to capacitor effects between the crystal plates and the SiC substrate), b) open macropipe. In both cases, the defects lie in the very middle of crystallization centers. Obviously, pipes of a certain diameter ($\approx 7 \mu\text{m}$ in the upper and $35 \mu\text{m}$ in the lower picture) are too big to be overgrown by the silica layer. The interior of the open macropipe is coated by an uneven silica layer and indicates accelerated oxidation.

4.1.4.6.3 Intrinsic impurities and bubble formation

For this discussion, we have to separate the liquid-phase sintered qualities of SiC (LPSiC) from the rest, because the amount and character of additives is quite different. In LPSiC additives like YAG (yttrium-aluminium-garnet, $Y_3Al_5O_{12}$) are used. These strongly affect the oxidation behavior of silicon carbide ceramic bodies and lead the formation of phases besides silica (e.g., mullite $Al_6Si_2O_{13}$ for alumina containing samples or yttrium silicate $Y_2Si_2O_7$ for yttrium containing samples).^{543,544} Especially near the melting point of these additives or above their eutectic points respectively in a multi-phase system, this influence is of particular magnitude.¹⁶⁸ The oxidation and scale growth in LPSiC is similar to silicon nitride ceramics and the reader is referred to the literature on such materials for an assessment (cf. Ref. ^{383,545}).

For SSiC often minor amounts of boron carbide B_4C and/or carbon are used. Typically the smaller the amount of free carbon, the higher the oxidative resistance of silicon carbide.³⁹² Below the temperature, at which pronounced SiC oxidation will take place, significant oxidation reaction will occur when sintering aids like boron carbide are present. In case of larger sintering aid particles, the formation of diffusion fringes around these impurities indicate accelerated oxidation (Fig. 54).

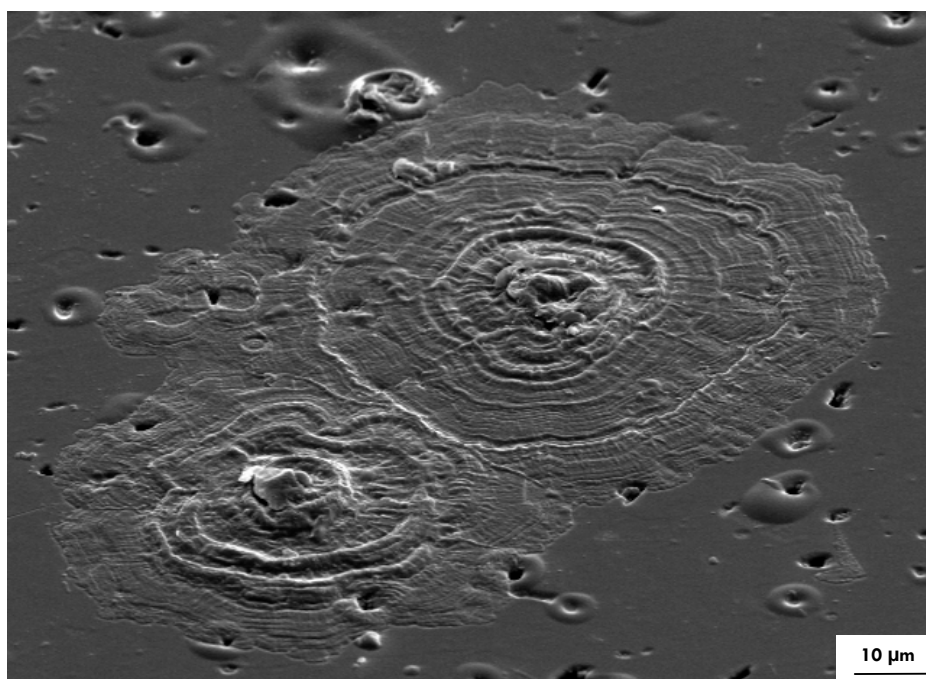


Fig. 54: SE-mode SEM picture of diffusion fringes around sintering aid particles ($\approx 2 \mu\text{m}$ large boron carbide grains) on the oxide scale above SSiC (5 minutes of dry thermal oxidation at 1400°C). The small elevations with depressions in their middles represent early (and collapsed) bubbles.

Below the melting point of silica, bubble formation without the presence of impurities has not yet been proven and still remains matter of dispute.^{343,546,547} Bubble formation, however, is a very common observation in the presence of sintering aids.^{416,496,547} Both bubble and pit-formation is attributed to CO trapped at the SiC-SiO₂ interface.^{168,502,546} CO accumulated at the interface itself increases the carbon activity c_a (finally to unity) and leads to reaction of the carbon-saturated SiC with stoichiometric silica during which gaseous carbon monoxide and silicon monoxide are created.^{372,508}

Boron (as present at the grain boundaries of sintered SiC samples) seems to be of particular importance for bubble formation as it forms B_2O_3 , which has low melting points in binary silica-boria systems down to the eutectic at 372°C .⁴¹⁶ Consequently, boron both lowers the viscosity of silica and increases the gas pressure at the substrate-oxide interface.⁵⁴⁷

Solid H_3BO_3 formed at room temperature before introducing a sintered SiC sample into the oxidizing environment also could attribute to bubble formation by decomposing at temperatures above 200°C into liquid boron oxide and, therefore, conservating boron hydroxides located deeper below the surface.⁵⁴⁷ For nominally dry atmospheres, this effect is supposed to be of minor importance but might become important during wet oxidation (cf. section 4.2).

Other impurities on their behalf are of rather minor relevance. Early experiments on SiC powder showed that 1 mol% CaO initially accelerated the oxidation (oxidation at 1300°C in air) but then yielded slower oxidation rates than observed in standard air or oxygen.³⁹³ These experiments, however, cannot compete with the purity of present-day samples and testing methods and, therefore, have to be evaluated with caution. Carbon inclusions in CVD SiC alone were shown not to be a likely source for bubble formation below $\approx 1515^\circ\text{C}$.⁵⁴⁷ The same thermodynamic calculations were applied for silicon saturated SiC yielding that below 1817°C no gas pressure of > 1 atm can be established at the SiC-SiO₂ interface.⁵⁴⁷

Conditions for bubble formation are (1) a sufficiently high gas pressure at the SiC-SiO₂ interface and (2) a viscosity low enough to allow a hollow structure to be blown (i.e., in the range of 10^6 Pa·s).^{343,500} Mieskowski et al. estimated a gas pressure of 1.3 MPa to be sufficient for 1 μm large bubbles (diameter) under a standard atmosphere to overcome both the pressure from the environment and the overlying silica layer.⁵⁴⁶ For even larger bubbles the corresponding pressures are lower (20 $\mu\text{m} = 0.1$ MPa). Typical bubble diameters, as observed by Mieskowski et al., lie well in the range of 1 - 20 μm for oxidation times up to 100 h at $1200^\circ - 1400^\circ\text{C}$.⁵⁴⁶ Fig. 55 outlines the geometry of a (collapsed) bubble formed on SSiC after 10 h of oxidation at 1400°C while on Fig. 56 typical bubbles are shown from the same oxidation conditions.

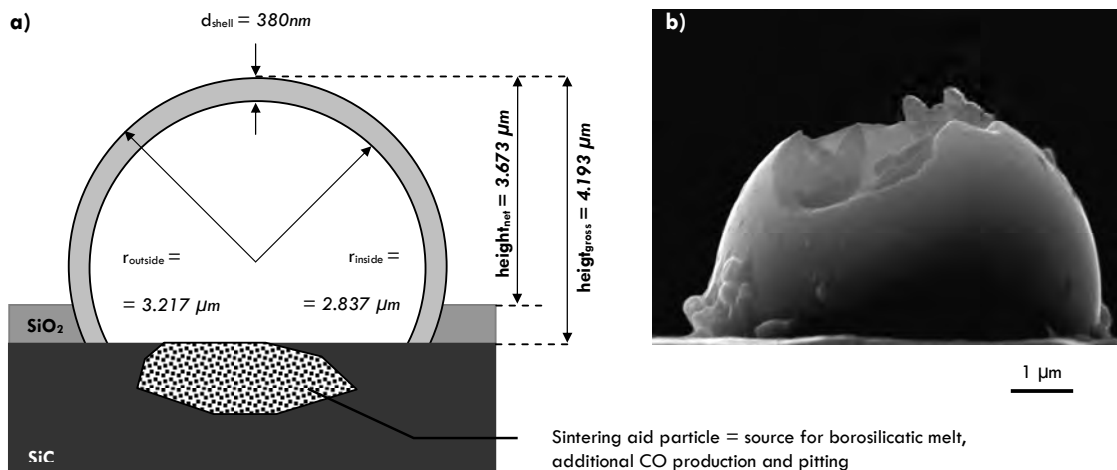


Fig. 55: Schematic illustration (a) and SEM picture (b) of a collapsed bubble grown on SSiC after 10 h at 1400°C under dry thermal conditions. As discussed in the text, bubble formation is strongly connected to the presence of impurities, e.g., in the form of sintering aids like boron carbide (B_4C).

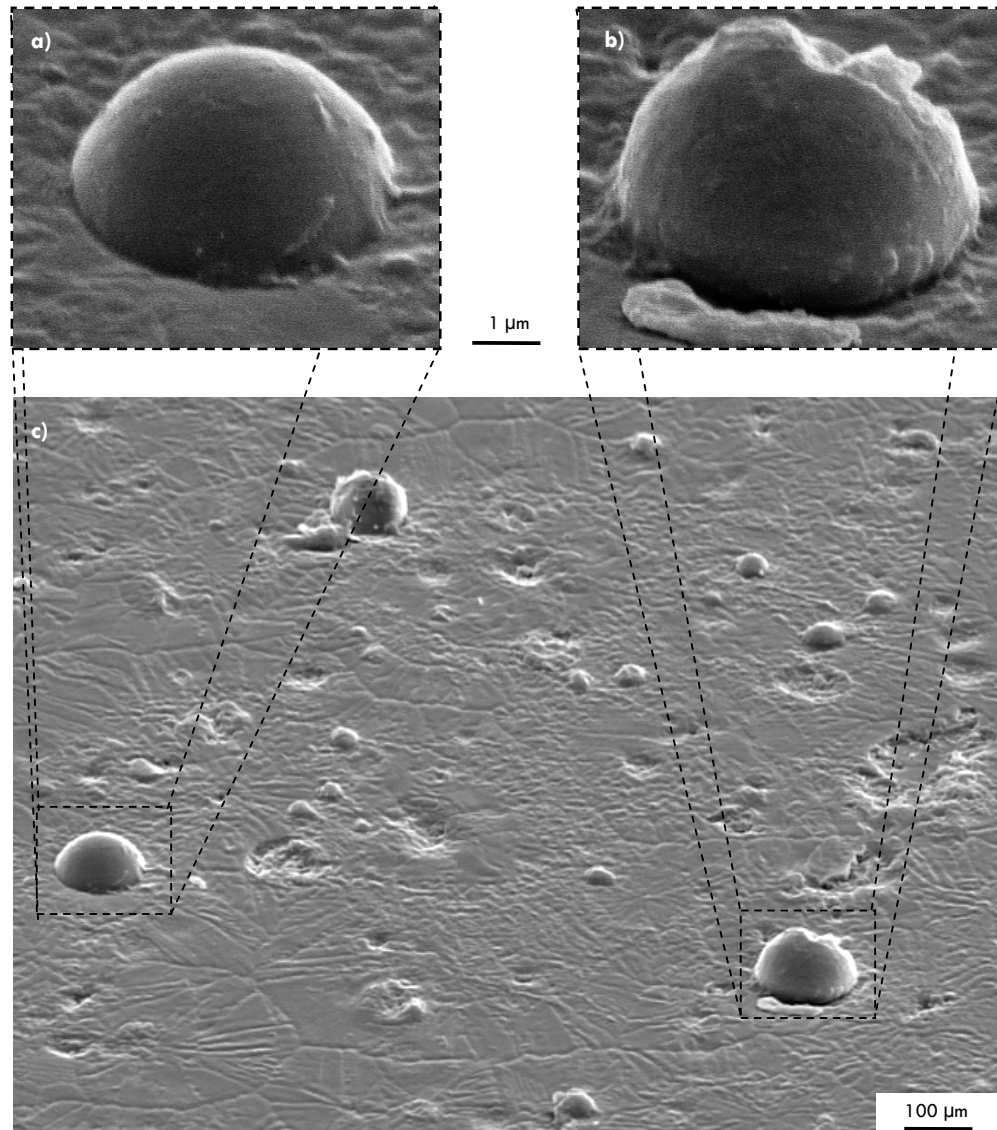


Fig. 56. SEM pictures of a still intact (a) and a partially collapsed gas bubble (b) found on SSiC after 10 h of dry thermal oxidation of SSiC. As seen on the overview (c), all bubbles are surrounded by a crystalline silica layer (indicated by small trenches between the crystal plates). Also smaller bubbles and remaining pits (possible remains of collapsed bubbles and/or overgrown pores) are present. The corresponding scale bars are provided as well.

In order to comply to the criterion of low viscosity, the silica layer cannot be fully crystalline, but bubble formation can also be observed on samples with significant devitrification within amorphous regions.³⁴³ Bubble formation increases the oxidation rate because the oxidation hampering function of a dense silica layer would significantly be stronger.^{168,546} Burst bubbles allow oxygen to get near or even below to the oxide-substrate interface and closed bubbles with their thin shell cannot protect the SiC body from further oxidation equally well as a solid silica layer. Oxidations rates obtained from experiments with bubble formation tend to yield a high error and the thickness of bubble containing scales is naturally very different from those calculated from mass gain.⁴⁹⁶

Especially above the melting point of silica (1710°C), bubble formation was observed by various scientists on CVD SiC.^{372,508,532,548} These findings indicate a genuine effect at such high temperatures above 1650°C while maintaining the basic oxidation reaction as given in Eq. 11. However, the influence of impurities cannot completely be ruled out.

As found by Goto and Homma³⁷² there is a dependency of the transition between (1) the temperature and (2) the oxygen partial pressure and solid silica growth and bubble formation. The use of CO_2 instead of O_2 , however, did not significantly influence the transition.

4.1.4.6.4 Polycrystalline, polymorphic texture

Oxidation kinetics of single-crystals are of anisotropic nature with faster oxidizing C- and slower oxidizing Si-faces. Polycrystalline bodies like conventional sintered SiC materials show bulk isotropic and initially locally anisotropic oxidation: each grain has a distinct orientation or belongs to a specific polytype and, therefore, its oxidation follows a specific rate-constant. Fig. 57 shows an example of such a mosaic oxide scale on polycrystalline SSiC after dry thermal oxidation for 5 min at 1400°C . For longer oxidation times there is a bulk, intermediate oxidation rate obeying to an overall (linear)-parabolic law.

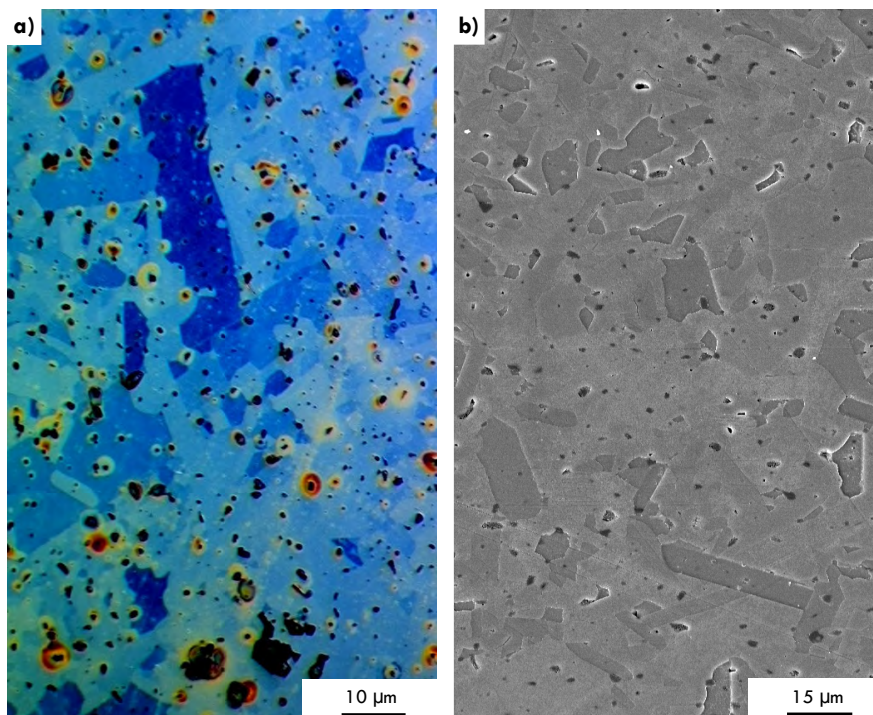


Fig. 57: Photograph (a) and SE-mode SEM picture (b) of a SSiC ceramic sample. As seen on the photograph, different heights of silica layers correspond with different grey scales fully in accordance with the overall texture of the bimodal grain size distribution of the starting material (which was made visible by etching). The oxidation conditions were dry thermal oxidation for 5 minutes at 1400°C in an alumina furnace.

4.1.4.7 ATMOSPHERE COMPOSITION

Until now, the focus of this review article was placed on basic oxidation mechanisms themselves under pure oxygen atmospheres. Other gases, like H₂O or CO₂, however, also yield the possibility of silica formation. Depending on the oxidant species used, the oxide scale growth may be accelerated or decelerated as shown in Fig. 58.⁴⁰¹

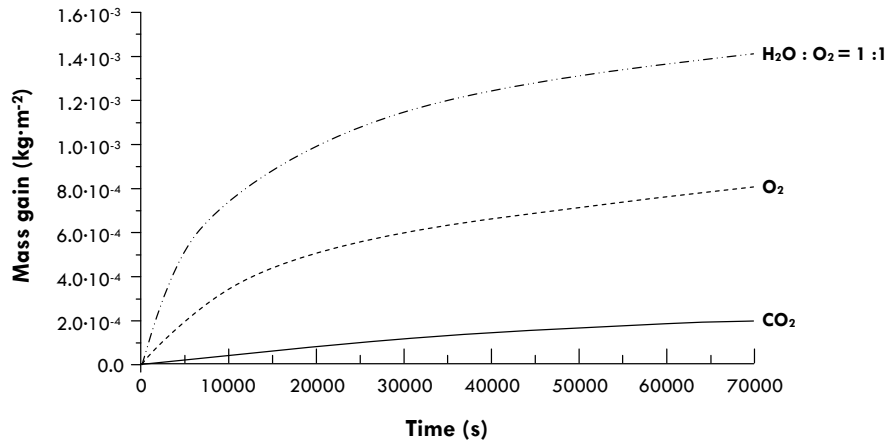


Fig. 58. Oxide scale growth observed during thermal oxidation of CVD SiC at 1200°C using various atmospheres at 0.1 MPa (after Ref. ⁴⁰¹). As seen, the choice of oxidizing species greatly determines oxidation kinetics.

First, wet oxidation was shown to provide electrically superior SiC-SiO₂ interfaces (section 2.4) while the overall oxidation rate is higher than under oxygen. A later section (section 4.2) will discuss wet oxidation in more detail, but the smaller molecular diameter of a water molecule (276 pm at 700°C) compared to O₂ (320 pm at 700°C) possibly explain this.⁴⁶¹ Unequivocal linear-parabolic time-laws found for wet oxidation clearly indicate a diffusion-controlled mechanism (that is probably in-diffusion of water).^{30,168,549}

In contrast to this, pure CO₂-atmospheres will cause very slow silica formation.^{342,401,402} In fact, at temperatures between 1200° - 1400°C the silica growth was too small to clearly decide on the rate-limiting process behind SiO₂-formation as found by Opila and Nguyen.⁴⁰¹ Possibly, dissociation of CO₂ into CO and oxygen (latter reacts with the solid SiC body) might control the oxidation process and limits its kinetic although no strict linear time-law was found to be true for SiC oxidation under CO₂ atmospheres.

Long-time oxidation in CO-CO₂ mixtures will even lead to a slight weight loss or at lower temperatures (< 1200°C) to a mere constant scale thickness.^{342,401,550} Opila and Nguyen (Ref. ⁴⁰¹) concluded from the shape of the kinetic growth of the silica layer, that a simple, diffusion-controlled mechanism can be excluded. The same conclusion can be found for a simple reaction-controlled mechanism. Otherwise decreased scale-thicknesses (e.g., at 1200°C after 80 h [CVD SiC, Ref. ⁴⁰¹] and at > 1500°C after less than ≈ 5 h [α-SiC, Ref. ³⁴²]) would be inexplicable. Eq. 59 was proposed to explain decreased an overall weight-loss during thermal oxidation in CO₂-argon or CO-CO₂ mixtures.^{342,401,551} This reaction may be in competition to a silica-forming reaction explaining weight-loss and parallel silica formation.



Goto and Homma found a stronger dependence on P_{O_2} for CO_2 -argon atmospheres than for O_2 -argon mixtures at $1600^\circ - 1712^\circ\text{C}$ (when considering dissociated CO_2 , i.e., O_2 , as oxidant species).³⁷² The concluded reason for this was proposed to be (1) out-diffusion-controlled kinetics for O_2 -argon and (2) in-diffusion controlled kinetics (most likely O^{2-}) for CO_2 -argon atmospheres. However, this argumentation contradicts the findings of in-diffusion of molecular oxygen to be rate-controlling (at least at lower temperatures) and the initial presumption of dissociated CO_2 is not evidenced.

In standard air, the surplus of oxygen (20.95 vol%) compared to the trace amounts of carbon dioxide (0.04 vol%) makes it possible neglect the contribution of CO_2 and to treat this environment as a purely oxygen-containing system ($P_{\text{O}_2} < P_{\text{air}}$).⁵⁵² More important is the influence of small amounts of water on the oxidation kinetics.⁴¹⁴

Comparing oxidation kinetics and microstructural development using Ar- O_2 and N_2 - O_2 atmospheres, it was observed that the latter (N_2 - O_2) lead to slower crystallization rates of the bulk silica layer.⁵⁵³ It is possible that solid solution nitrogen stabilizes the amorphous silica and prevents enhanced crystallization from happening.

4.1.5 Activation energy and temperature influence

Often the temperature dependency for the time constants k_x (i.e., k_l , k_p and k_{in}) is evaluated by an Arrhenius equation (Eq. 60) using f as a pre-exponential factor, E_a as the activation energy, R as the gas constant and T as the temperature.

$$k_x = f \cdot e^{-\frac{E_a}{R \cdot T}} \quad \text{Eq. 60}$$

Strictly linear trends in $1/T$ versus $\ln(k_x)$ plots occur if one elementary step in a process is dominant over the temperature range investigated and this results in a single activation energy. However, this is not true even for silicon oxidation. Here both plots involving k_l and k_p do show a curvature and the initial period has other parameters than the later stages.¹⁶²

Differing activation energies might thus also be expected for differing regimes of thickness, temperature and crystallinity in the oxidation of silicon carbide. Therefore, statements about higher activation energies for higher devitrification rates,⁵⁰² smaller activation energies for amorphous silicon carbide than for crystalline forms³⁰ and intermediate values for disordered silicon carbide surfaces^{418,554} have to be treated with caution and should be used only in the experimentally investigated temperature range.

This and additional complications like polytype distribution, sintering aid amount, and so on, are one reason for the huge scatter in published E_a -values, ranging from $80 \text{ kJ}\cdot\text{mol}^{-1}$ (Ref. ³⁶⁸) up to $612 \text{ kJ}\cdot\text{mol}^{-1}$ (Ref. ⁵⁵⁵⁻⁵⁵⁷). Different applied analytical procedures and the lack of standardized oxidation tests are further reasons for this diversity. One of the few similarities between all the published activation energies is the fact, that E_a on the Si-face is much higher than on the C-face - correlating with the different oxidation rates.³⁷⁷

In this respect it is surprising that early ⁴²¹ and some newer studies ^{389,558} argue for a single activation energy within the temperature range of 900° - 1600°C and claim that all observed changes of E_a -values are solely due to extrinsic impurity or defect concentration effects.^{164,389,541,558-560}

The comparison study by Ramberg and Worell (Ref. ⁴²²) argues in the same direction: without impurities there is a low activation energy in the order of 100 kJ·mol⁻¹ that is valid for amorphous or crystalline silica. Amorphous phases at high temperatures exist because of impurities, have a different transport mechanism and accordingly a higher activation energy (in the order of 300 kJ·mol⁻¹), which makes them increasingly more effective in the oxidation of SiC with increasing temperature.

In detail, Ramberg and Worrell (Ref. ⁴²²) compared 9 sets of experimental data from CVD and single-crystal SiC (only C-terminated faces) to their own results (performed on siliconized SiC and CVD SiC via dry, thermal oxidation). At 1350°C, a general transition in oxidation rate constants was observed using an Arrhenius plot: below this kinetic break, activation energies of ≈ 100 kJ·mol⁻¹ were found and at higher temperatures, E_a -values of 310 kJ·mol⁻¹ could be determined. It was concluded that pure systems show a crystallinity-independent development of the parabolic rate-constant (i.e., $k_p^{\beta\text{-cristobalite}} = k_p^{\text{amorphous silica}}$) as the k_p -values for samples with fully crystallized silica layers could well be extrapolated from silicon carbide samples with amorphous SiO₂ scales. The increase in activation energy was attributed to the transition of the main diffusion mechanisms from molecular to interstitial diffusion rather than to a change of crystallinity.

When amending data from the Si-face and general k_p -values from other publications (Ref. ^{375,386,387,419,422,448,530,543,553,558,561,562}) Fig. 59 can be obtained. The activation energies and linear regression functions shown in Fig. 59 were calculated using selected references (provided in the figure). Not shown is the Si-face data found by Harris and Call ⁴¹⁹ as a rather ideal linear behavior.

As shown in Fig. 35 the k_p -values for both the Si- and the C-face converge at around 1350°C but it should be kept in mind, that below 1350°C usually a linear rate-constant additionally to a parabolic one is needed - hence the data presented compares k_p -values of a purely parabolic (C-face) and derived from a linear-parabolic system (Si-face). Forcing a parabolic time-law into the Si-face's kinetic yields (1) significantly worse R^2 -values and (2) drastic smaller k_p -values. As the parabolic rate-constant is believed to be proportional to the slowest diffusion mechanism (cf. section 4.1.2.1), Fig. 59 gives both an overview of typical k_p -values (ranging from $\approx 10^{-15}$ kg²·m⁴·s⁻¹ at 725°C up to $\approx 10^{-10}$ kg²·m⁴·s⁻¹ at 1725°C) and illustrates the aforementioned transition of activation energies especially when comparing the fast-oxidizing C-face with high-temperature data.

Although using more data points than Ramberg and Worrell ⁴²² induces more and larger scatter, two more or less distinct branches can be found for high- and low-temperature regimes respectively. Unlike the low-temperature range, there is no polarity-caused differentiation between branch 1 and branch 2 at temperatures above 1350°C. In detail, comprising data from several publications (as listed in Fig. 59), the following activation energies were found: (A) $T < 1350^\circ\text{C}$: (1) Si-face: 270 kJ·mol⁻¹, (2) C-face: 104 kJ·mol⁻¹; (B) $T > 1350^\circ\text{C}$: (1) branch 1: 285 kJ·mol⁻¹, (2) branch 2: 154 kJ·mol⁻¹.

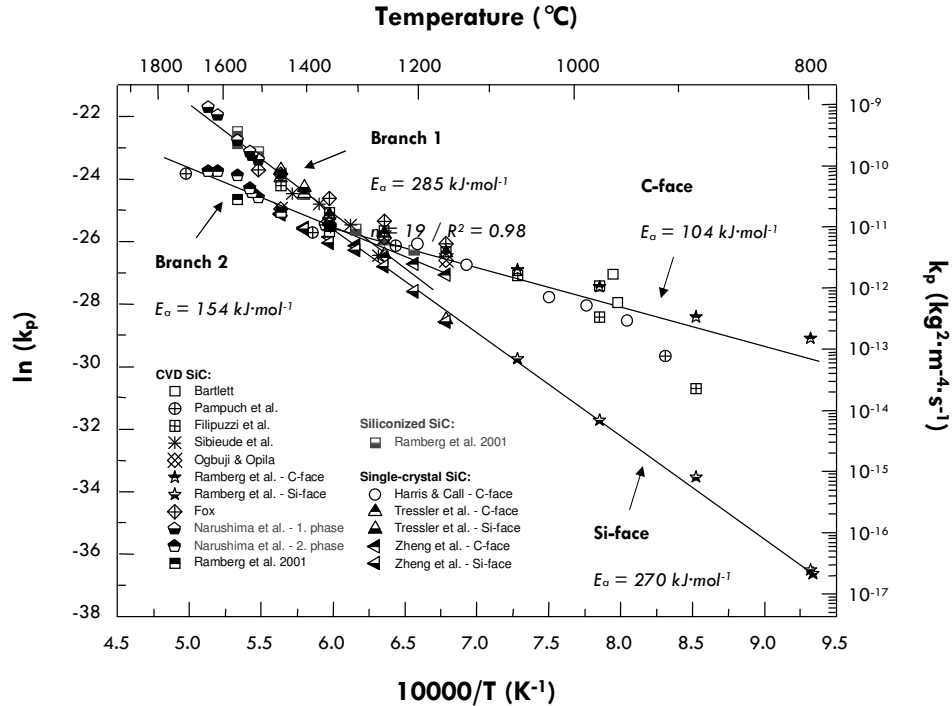


Fig. 59. Arrhenius-plot of various parabolic rate-constants (Bartlett: Ref. ⁵⁶¹; Pampuch et al.: Ref. ⁴⁴⁸; Filipuzzi et al.: Ref. ⁵³⁰; Sibieude et al.: Ref. ³⁷⁵; Ogbuji & Opila: Ref. ⁵⁵⁸; Ramberg et al.: Ref. ⁴²²; Fox: Ref. ⁵⁶⁰; Narushima: Ref. ⁵⁴⁸; Ramberg et al. 2001: Ref. ⁴²²; Harris & Call: Ref. ⁴¹⁹; Tressler et al.: Ref. ⁵⁴³; Zheng et al.: Ref. ^{386,387}). Data basis for linear regression on n data points for (1) the Si-face: Ref. ^{386,387,543}; (2) the C-face: Ref. ^{386,387,419,543}; (3) Branch 1: Ref. ^{375,422,548} (only k_p -values from 1. phase found by Narushima et al.); (4) Branch 2: Ref. ^{422,448,548,553,558} (while the k_p -value at 930°C found by Pampuch et al. was omitted for this high-temperature branch and only phase 2 data from Narushima et al. were used). For discussion, see text.

Besides a possible change in dominant rate-controlling mechanism (from molecular to ionic diffusion of oxygen), Goto proposed a general transition from oxygen-diffusion to CO-diffusion as the rate-limiting process.⁵⁵³ Thermodynamic considerations based on the work by Luthra⁴⁰⁷ show, that the potentially genuine bubble formation at high temperatures cannot be explained if CO-out-diffusion is (much) faster than O₂-in-diffusion. Otherwise the sufficient accumulation of carbon monoxide needed for bubble formation would never occur. However, the question of bubble formation to be a true genuine effect is still not resolved and interferes gravely when looking for rate-limiting processes.

Goto also found that for both, semi-crystalline and fully-crystalline silica scales (first obtained from Ar-O₂ atmospheres and latter from using N₂-O₂-mixtures) almost the same activation energies and the very same parabolic rate constants was obtained (1600° - 1700°C).⁵⁵³ Consequently, the diffusion through solid and crystalline silica would have to be the same - which is not expected from the considerations presented in section 4.1.2.4. Comparing the silica scale's thickness of crystalline and amorphous regions of the same experiment (Fig. 60), the crystalline silica is less thick than neighboring amorphous regions, strongly evidencing that SiC covered by amorphous silica oxidizes faster, presumable because the diffusion oxygen is faster. Similar results would be expected for CO-out-diffusion.

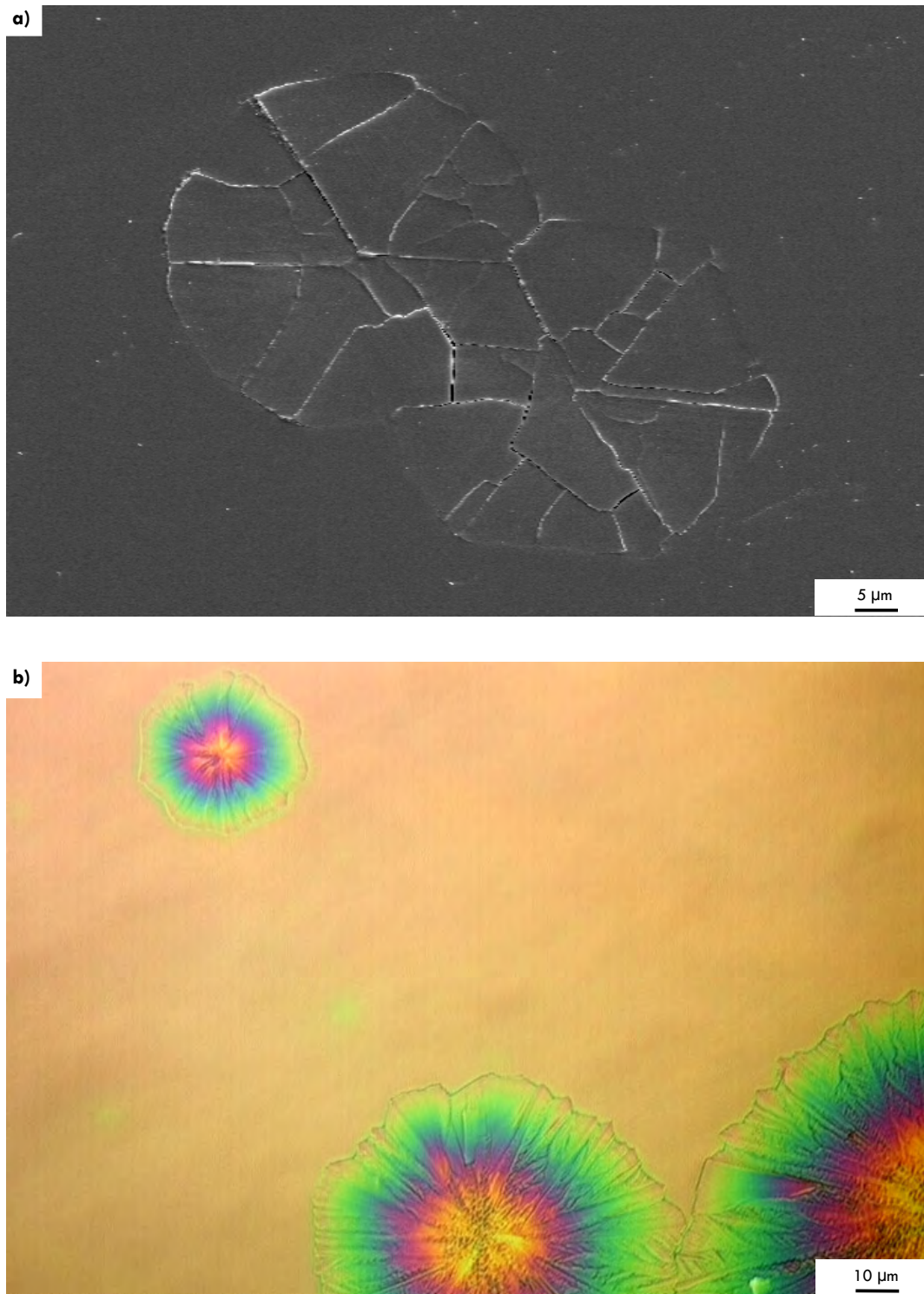


Fig. 60. SE-mode SEM picture (a) and microphotograph (b) of an oxidized 6H-SiC:N sample (5 minutes, 1400°C) showing amorphous and crystalline areas. As clearly indicated by different grey scale values (b) and the morphology (b), the crystalline areas are thinner (ca. 250 nm) than the corresponding vitreous silica layer (ca. 380 - 400 nm).

Some activation energies derived from single-crystalline SiC (various polytypes) are shown in Fig. 61, in which they are compared with activation energies for oxygen (Ref. ^{375,386,387,419,543,548,558,560,561}) diffusion through solid silica (Ref. ^{466,468,470}). As seen, the oxidation rates for silicon carbide lie in the range of E_a -values for O₂-diffusion, although there is a huge range of scatter.

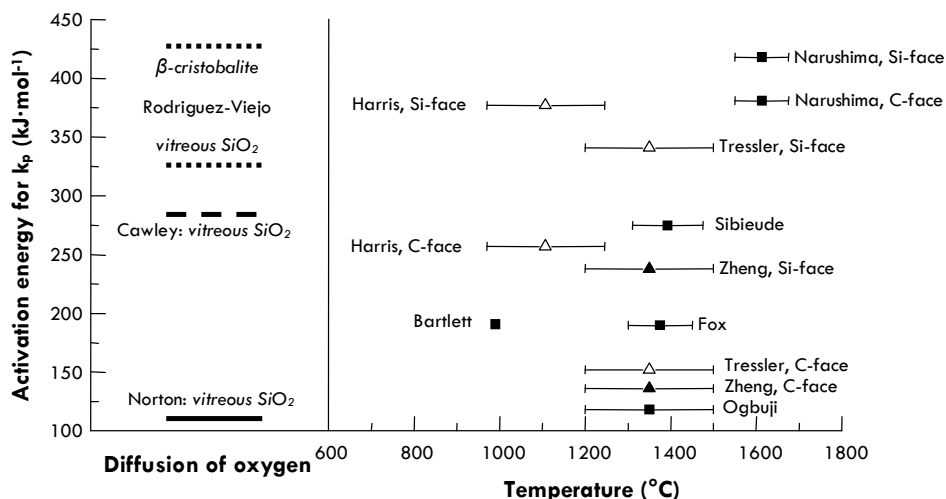


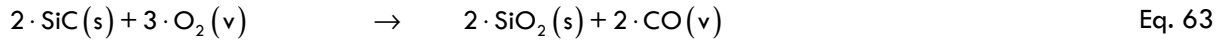
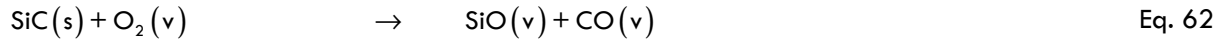
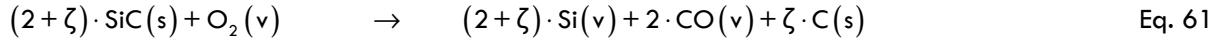
Fig. 61. Comparison between activation energies of SiC oxidation and O₂-diffusion through solid silica (either crystalline or vitreous). As seen, the large scatter of E_a -values describing silicon carbide oxidation lies well in the range of the scatter of O₂-diffusion-related activation energies (Narushima: Ref. ⁵⁴⁸; Harris: Ref. ⁴¹⁹; Tressler: Ref. ⁵⁴³; Sibieude: Ref. ³⁷⁵; Zheng: Ref. ^{386,387}; Fox: Ref. ⁵⁶⁰; Bartlett: Ref. ⁵⁶¹; Ogbuji: Ref. ⁵⁵⁸; Rodriguez-Viejo: Ref. ⁴⁷⁰; Cawley: Ref. ⁴⁶⁸; Norton: Ref. ⁴⁶⁶).

In analogy with silicon, we might expect to see a more differentiated picture by consequently using a linear-parabolic model, distinguishing between k_i and k_p -development with temperature and then looking at initial stages and crystalline and amorphous phases with and without impurities.

One thing, which has no analogue in the silicon oxidation, should appear at very high temperatures, because CO-diffusion probably has a very high activation energy 397 - 543 kJ·mol⁻¹ ⁴⁷⁹ and might become responsible for the rates in the high temperature regime. Clearly, more systematic work needs to be done on this topic, but this is a fact that applies to many fields of SiC research.

4.1.6 Passive oxidation at very low oxygen partial pressures

Varying the oxygen partial pressure changes the oxidation rates of silicon carbide during thermal oxidation. ^{386,387,458} Lowering P_{O_2} however beyond a critical value will result in active oxidation or even in the formation of a solid carbon scale (similar to carbon scales on SiC known from hydrothermal experiments; cf. Ref. ^{397,398,563-566}). ^{492,567} Latter would require temperatures above 1600°C at an oxygen partial pressure of 0.133 Pa. Fig. 62 shows calculated stability fields at low oxygen partial pressures as discussed by Song et al. (Ref. ⁵⁶⁷; field 1: oxycarbide formation, field 2: silica formation, field 3: active oxidation, field 4: carbon formation and transition to vacuum annealing). Eq. 61 - 64 show the detailed reaction equations as presented in Fig. 62 ("s"... solid phase, "v"... vapor phase) in descending order considering oxidation temperatures.



In Eq. 61, a stoichiometric term (ζ) was introduced. In case of $\zeta = 0$, pure, active oxidation will occur while for $\zeta \geq 0$ graphitization can be observed. The latter is analogous to silica formation and is greatly affected by face polarity, and the C-layer on the C-face will grow much faster than on the corresponding Si-face.

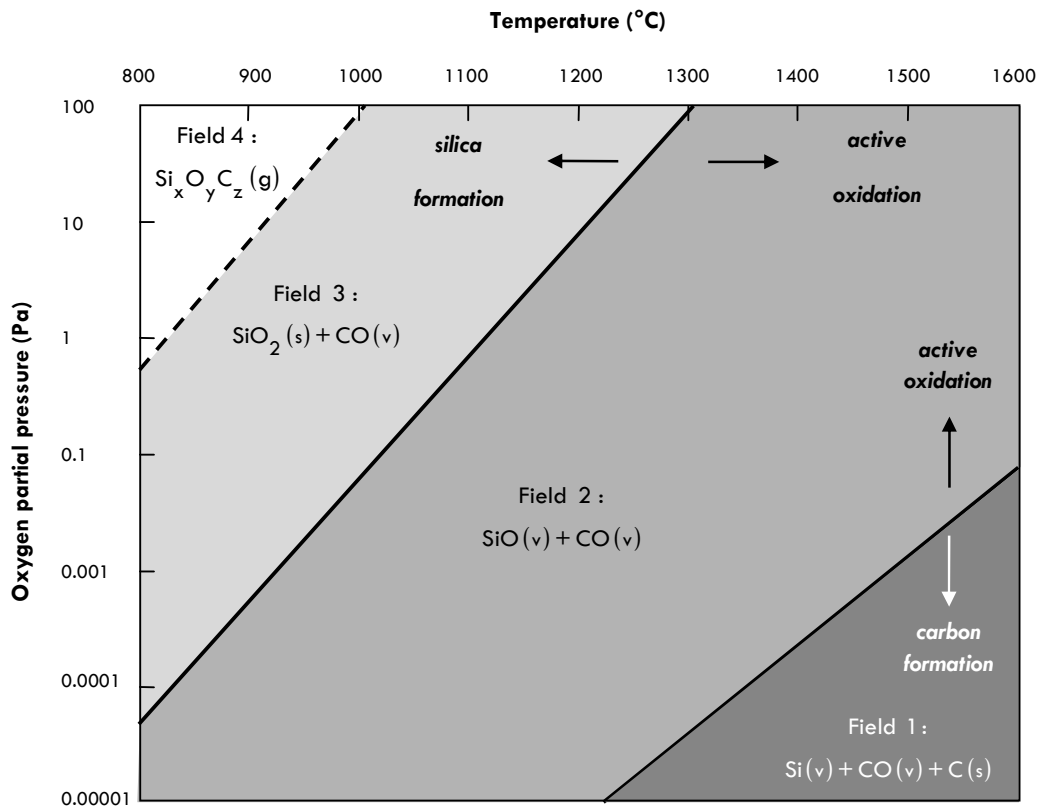


Fig. 62: Calculated plot showing oxygen partial pressure vs. temperature (after Ref. 567). Four distinct stability fields are shown: field 1 (oxycarbide formation), field 2 (silica formation), field 3 (active oxidation), and field 4 (carbon formation). In this context denotes “s” a solid phase and “v” a vapor phase. For detailed oxidation equations and discussion see text.

Graphitization itself is not the topic of this review article, but it is important to point out that the graphite layers grown on the Si- and C-faces also show structural differences: while on the Si-face a layer-like graphitization takes place, while on the C-face, island-like graphite growth (so called “carbon nanocaps”, which later align and form solid films of self-organized carbon nanotubes; cf. Ref. ⁵⁶⁸) can be observed. For more detailed information about the formation mechanism of graphite on SiC and its structure see Ref. ^{17,493,568-573}.

These differences in structural aspects may also well explain the accelerated C-growth on the carbon-terminated face: the more compact and more homogenous carbon layer on the Si-face shields the bulk SiC better from incoming oxygen than the carbon nanotube layer (which can be seen as a fast gateway for diffusion).⁵⁶⁸

4.2 Wet oxidation

4.2.1 Introduction

As discussed in section 3.1.1, wet oxidation describes thermal oxidation of silicon carbide in a water-containing atmosphere. Hydrothermal oxidation, i.e., corrosion/oxidation in hydrothermal fluids, shall briefly be discussed in section 4.3, for it does not necessarily lead to silica formation. Moreover, many other aspects of wet oxidation were already shown: for instance, the superior electronic properties of wet oxidized SiC-SiO₂ interfaces (maybe due to carbon-cluster-removal; cf. section 2.4.2.4), or structural influences on the silica scale (like pronounced devitrification and/or decreased viscosity; cf. section 4.1.4.4).

4.2.2 Diffusion of water

Experiments conducted at various water contents within an oxidizing atmosphere clearly indicate that there exists a direct correlation between $c_{\text{H}_2\text{O}}$ and the oxidation speed.¹⁶⁸ This can be explained by the smaller molecular diameter of the water molecule (276 pm at 700°C for H₂O instead of the gas-kinetically derived value of 330 pm) compared to oxygen (320 pm at 700°C; values deviate from those presented in Tab. 4).⁴⁶¹ Doremus (Ref. ⁴⁶¹) favored this small molecular diameter instead of 330 pm (what would leave H₂O *larger* than O₂)⁴⁶³ as this value equals the atomic diameter of an oxygen atom in solid oxides as the water molecule is believed to behave as if the hydrogen atoms would be “buried” within the electron cloud of the central oxygen. Correspondingly, lower activation energies can be found for diffusion of water (71 - 77 kJ·mol⁻¹; Ref. ^{499,574}) compared to pure molecular oxygen (113 kJ·mol⁻¹; Ref. ⁴⁶⁶) which is reasonable for smaller molecular diameters.³⁶⁰ For the diffusion coefficients of molecular species, at 1000°C values of $D_{\text{H}_2\text{O}}^{\text{silica}} = 1.7 \cdot 10^{-7} \text{ cm}^2 \cdot \text{s}^{-1}$ (Ref. ^{461,575}) and $D_{\text{O}_2}^{\text{silica}} = 6.6 \cdot 10^{-9} \text{ cm}^2 \cdot \text{s}^{-1}$ ($\approx 1/26 D_{\text{H}_2\text{O}}^{\text{silica}}$; Ref. ⁴⁶⁶) were reported. A network diffusion coefficient at 1000°C for oxygen equals $6.7 \cdot 10^{-19} \text{ cm}^2 \cdot \text{s}^{-1}$.^{461,469}

Effective diffusion coefficients D^{eff} can be obtained by multiplying the diffusion coefficient D with the total concentration of dissolved molecules C and divided by the total concentration of oxygen atoms in the oxide S (Eq. 65 after Ref. ^{461,471,575,576}).

$$D^{\text{eff}} = \frac{D \cdot C}{S} \quad \text{Eq. 65}$$

As shown by Doremus, even trace amounts of water will significantly increase the effective diffusion coefficient for oxygen: while 10 ppm H₂O correspond to $D_{\text{eff}, \text{O}_2}^{\text{silica}} = 6 \cdot 10^{-19} \text{ cm}^2 \cdot \text{s}^{-1}$, 3400 ppm H₂O yield a more than 3000times larger value (to $D_{\text{eff}, \text{O}_2}^{\text{silica}} = 2 \cdot 10^{-15} \text{ cm}^2 \cdot \text{s}^{-1}$).^{475,577}

The bulk molecular solubility of water is supposed to be directly proportional to the water vapor of the ambient gaseous atmosphere.⁵⁷⁵ In comparison, oxygen solubility is much smaller than the solubility of water in silica yielding higher permeation rates for H₂O.^{361,414,461,496,575}

In detail, the diffusion of water through silica is quite complicated. Oxygen is believed to permeate without significant interaction with the silica network through the oxide scale, at least at lower temperatures. Water vapor will diffuse as a molecule and reacts readily with silicon-oxygen bonds according to Eq. 66 (Ref. ^{575,578}) as proposed by the so called diffusion-reaction model.^{476,579}



Rupturing $\equiv\text{Si}-\text{O}-\text{Si}\equiv$ bridges weakens the structure and attributes for the lower viscosity of water-bearing silica compared to water-free SiO₂.^{574,576,580} Additionally, a decreased index of refraction, reduced acoustic velocity and a lower density can be found while the thermal expansion coefficient is increased.^{165,581-583} Introducing water and forming hydroxyl groups also will affect the diffusion e.g. of sodium (which is reduced in the near-surface region).⁵⁸⁴

The reaction shown in Eq. 66 is also the reason why the apparent solubility S_a of water is much higher than for other gases (i.e., $S_a^{\text{H}_2\text{O}} \approx 1000 \cdot S_a^{\text{O}_2}$ for amorphous silica as already pointed out by Deal and Grove in Ref. ⁴⁰⁸).⁵⁸⁵ Consequently, a concentration-dependent diffusion coefficient was proposed for water.^{574,578}

As concluded by Doremus, at temperatures lower than 500°C Eq. 66 is not believed to reach equilibrium in experimental studies and a time-dependent surface concentration of OH groups is found.⁵⁷⁵ This model (as outlined in the next paragraph) no longer assumes a concentration-dependent reaction constant of Eq. 66.

In detail, the diffusion-reaction model for water diffusing through vitreous silica (as proposed by Doremus; Ref. ⁵⁷⁵) is as follows: (1) At higher temperatures (900° - 1200°C), molecular diffusion of water takes place and the equilibrium is approximated by a reaction of H₂O and the Si-O-network. In this range, the OH-groups are believed to be almost immobile but still capable to interact with other, neighboring SiOH groups (= second order = bimolecular, reversible reaction) to form water. (2) Lowering the temperature (700° - 900°C) will stop this process in the presence of defects or strains (from quenching). Suitable annealing procedures will result in a first-order reaction as the aforementioned sampling between SiOH-pairs is prevented by too slow OH-diffusion. (3) This first-order reaction is dominant but not at equilibrium for short periods. Only after long times a constant = saturated surface concentration of SiOH groups can be found explaining the time-dependency of the effective diffusion coefficient of water.

This model explains well among other effects the observed time-dependency of OH-groups on the surface (several days at 200°C are not sufficient to reach equilibrium⁵⁸⁶) or why diffusion coefficients at lower temperatures were higher than expected when extrapolating these values from data obtained at higher temperatures.^{575,586-588} A small percentage of non-equilibrium water (i.e., not in equilibrium with the hydroxyl groups) may also be present at temperatures above 750°C and show fast diffusion causing structural relaxation and annihilation of (potential) oxygen vacancies.⁵⁸⁸

However, due to the oxidation inertness of silicon carbide towards oxidizing agents, the low-temperature regime (> 500°C) with the shown non-equilibrium diffusion-reaction model is of minor importance.

In the special case of H₂O-O₂ mixtures, the incorporation of OH⁻ into the silica network must be considered to lower the scale's viscosity and, therefore, enables faster molecular O₂ diffusion parallel to water transport.⁵⁴³ Argon-water mixtures are, therefore, more suitable to study the effect of water partial pressure itself.⁴⁹⁶

4.2.3 Crystalline silica

As far as crystalline silica is concerned, a lower viscosity due to OH-incorporation remains speculative. With a 13.75 % smaller molecular diameter, the diffusion of water in crystalline silica is believed to be much faster than in amorphous scales although no direct measurements for β-cristobalite and vitreous SiO₂ respectively were conducted.⁴⁶¹

4.2.4 Oxidation kinetics

Fast transport of an oxidizing agent corresponds to increased oxidation rates for silicon carbide. In particular, the oxidation rates for water-containing atmospheres are one order of magnitude higher than for the same material at the same temperature under dry, thermal conditions.^{414,559,589} Correspondingly, the activation energies for silicon carbide oxidation with water vapor as oxidizing agent is much lower than for dry thermal oxidation (167 kJ·mol⁻¹ for dry oxygen and 118 kJ·mol⁻¹ for water vapor oxidation for C-face single-crystal α-SiC).⁵⁴³ For silicon oxidation, Deal and Grove found qualitatively the same relationship (with 119 kJ·mol⁻¹ for dry oxygen and 68 kJ·mol⁻¹ for wet oxidation, i.e., $P_{\text{H}_2\text{O}} = 0.84 \text{ atm}$).⁴⁰⁸

Crystal anisotropy is also influencing wet oxidation with a slower oxidizing Si- and a faster oxidizing C-face. Thus, higher activation energies for the Si-face can be found.^{30,486,590} Wet atmospheres moreover show the same trend of damaged or (partially) amorphized silicon carbide to oxidize faster than unaltered, undamaged SiC.⁵⁵⁴

Analogous data (increased k_p -values by a factor of 3 - 21 at 1000°C and 3 - 8 at 1350°C depending on the water content in pure oxygen) were found for cubic SiC under wet atmospheres compared to dry thermal oxidation.⁴⁹⁶ This increase is qualitatively in agreement with the 26times higher diffusion coefficient of molecular water compared to O₂.

In the presence of water vapor, the linear kinetic region was found to last longer times of oxidation and the parabolic rate-constant was increased.^{168,591} However, silica volatilization might superimpose oxidation-related weight gain, because gaseous Si-O-H species were identified at temperatures between 1200° and 1400°C at atmospheric pressure during wet, thermal treatment of silica.⁵⁹²

Consequently, overlaying linear mass-loss and linear-parabolic mass gain (latter is dominant) would result.^{343,414,496,592}

Unlike oxidation of silicon, the linear reaction rates for water-containing and water-free environments are almost identical for SiC (with k_l^{water} sometimes even smaller than $k_l^{\text{dry oxygen}}$).^{408,411,496} As discussed in section 4.1.4.5, also contaminations like sodium or aluminium must critically be considered in such comparisons. Oxidation rates dependent also on the H₂O partial pressure.⁴⁹⁶

Plotting the logarithm of the parabolic rate constant k_p ($= \log(k_p)$) versus the logarithm of the partial pressure of water ($= \log(P_{\text{H}_2\text{O}})$), information about the oxidant species can be obtained.⁴⁹⁶ For oxygen, as discussed in section 4.1.3.3, results indicate at least for temperatures below $\approx 1400^\circ\text{C}$ molecular diffusion of oxygen (with a slope of $n \approx 0.5$).^{386,387,496} Water-containing atmospheres yield a slope n significantly larger than 0.5 ($T > 1100^\circ\text{C}$) although the state of the silica layer being partially crystalline with inflicting bubble formation induces a high error for the k_p -values.⁴⁹⁶ A parallel diffusion of a molecular and an ionic hydrogen-containing phase (H₂O and OH⁻, respectively) - analogous to the mixed transport of molecular and ionic oxygen - is a likely situation to explain this. Probably this is more important at temperatures above 1400°C .

Even a small amount of water (< 1 wt%) drastically changes the effective diffusion coefficient in “dry” oxygen. Correspondingly, it is expected that the oxidation kinetics in oxygen-containing atmospheres are strongly influenced by the water partial pressure. Opila (Ref. ⁴⁹⁶) concluded from extrapolating $\log(k_p)$ - $\log(P_{\text{H}_2\text{O}})$ data, that for 1200°C a threshold of 2.5 vol% H₂O and for 1400°C even 4.8 vol% water vapor exists, below which the oxidation kinetics are controlled by oxygen diffusion and not by H₂O permeation. Due to the large error, this rough estimation should not be seen as a strict boundary value, but a qualitative indication for the strength of the dependency of k_p on $P_{\text{H}_2\text{O}}$. Solution of water within the silica layer causes structural changes.^{168,593-595} Direct results are decreased viscosity and density, increased coefficients of expansion and accelerated devitrification.^{168,523,525,594}

Carbon monoxide as a reaction product reacts with water vapor and CO₂ formation can be expected (Eq. 67; Ref. ^{30,585}):

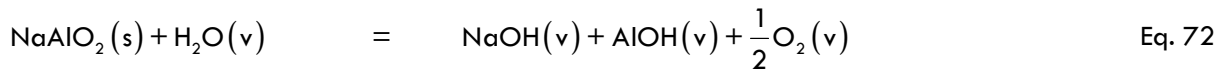
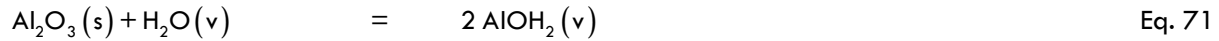
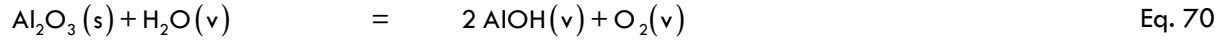
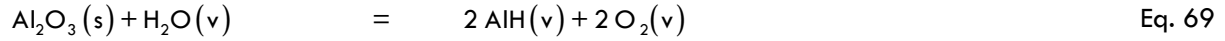
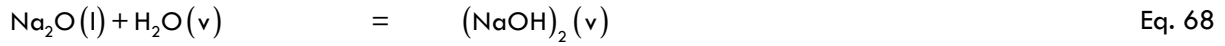


4.2.5 Structural aspects

In general, no significant difference between the microstructure of the silica scale grown on SiC via dry or wet thermal oxidation can be found.⁵⁴⁹ Long known from oxidation experiments conducted on silicon, vitreous silica is believed to crystallize much faster in the presence of water (section 4.1.4.4).^{496,523,525,543,549,559,589} As shown by Ainger ⁵²³, already a small concentration of 2500 ppm water vapor was sufficient to yield significantly crystallized silica scales during thermal oxidation of silicon at 1300°C using a silica furnace (which itself crystallized more rapidly already at 300 ppm water content within the oxidizing atmosphere at the very same temperature).

Opila (Ref. ⁴⁹⁶) conducted experiments during which the influence of sodium or related impurities could be excluded. During those experiments, the high effect on crystallization speed of water could not be corroborated leading to the assumption that previously observed accelerated devitrification would be due to contaminations, which on their behalf strongly enhance crystallization. Quantitatively, an enhancement by a factor of 1.5 - 2 in the crystallization rate (comparing dry oxidation with a water-containing atmosphere [60 vol% H₂O]; Ref. ⁵⁹⁵) seems reasonable in the light of these findings.

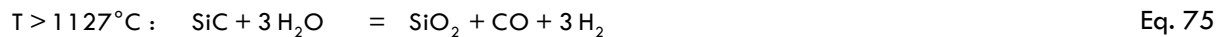
Water vapor greatly enhances the transport of other impurities like sodium, the typical contamination present in alumina furnaces.⁴¹⁴ Eq. 68 - 73 list several possible reactions involving the water-enhanced transport of sodium and aluminium ("l" = liquid; "s" = solid; "v" = vapor).⁴¹⁴



Tridymite (a sensitive proxy for sodium impurities) found within the oxide scales of wet oxidized SiC (Ref. ⁴⁰²) might, therefore, wrongfully attributed to the presence of H₂O. In reality, its occurrence might be caused by the improved transport of impurities towards the sample's surface.

Oxidation kinetics were shown to be accelerated for different SiC materials like sintered, hot-pressed, CVD or single-crystal silicon carbide.^{393,402,413,414,416,496,543,559,591,596,597} The influence of water on sintering additives must be considered. Tressler et al. observed that oxidizing (1) sintered alpha-SiC and (2) single-crystal silicon carbide in water vapor yielded a (1) 12-fold and (2) a 20-fold increased parabolic rate constant k_p .⁵⁴³ Hot-pressed SiC showed the same increase than single-crystal samples leading to the assumption, that the boron content of SSiC material could be decreased by reactions with water.

Experiments conducted within a temperature range of 1100° - 1400°C clearly showed that as long as amorphous silica is present, water vapor enables bubble formation even when virtually no impurities are present (i.e., when a silica tubing is used as reactive furnace).⁴⁹⁶ At 1200°C, $P_{\text{H}_2\text{O}} \approx 0.25$ / $P_{\text{O}_2} \approx 0.75$ was found to be sufficient to cause significant bubble formation on CVD SiC.⁴⁹⁶ The following reactions were derived from thermodynamic calculations for temperatures below (Eq. 74) and above 1127°C (Eq. 75).⁴⁹⁶



4.3 Hydrothermal oxidation

4.3.1 Introduction

As discussed before, hydrothermal oxidation deviates from gas corrosion / oxidation by the use of a fluid water substance (and/or additive substances to alter the pH-value) under high temperature and/or high pressure conditions. Under these conditions, besides incurring oxidative reactions with water, solution of the oxidation product in the fluid phase must be considered.

First experiments on hydrothermal oxidation of SiC were conducted by Sharma et al. (Ref. ⁵⁹⁸) as early as in 1974. Extensive experiments on tyranno-fibers (i.e., Si-O-C fibers) were conducted during the early 1990s (Ref. ^{564,599,600}) and pure silicon carbide samples were studied under hydrothermal conditions (Ref. ^{151,396-398,563,599,601-616}).

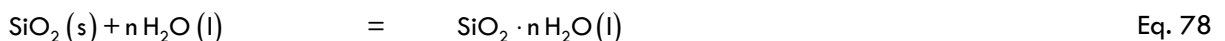
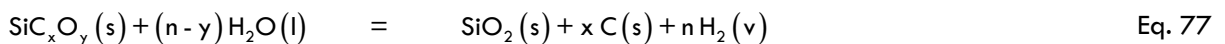
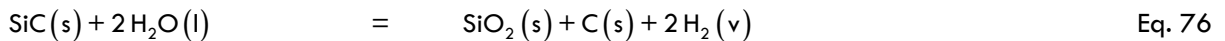
4.3.2 Chemical reactions

In pure oxygen, air or atmospheres containing CO₂ or H₂O as oxidation agents, it was shown that under atmospheric pressure silica (and potentially some minor oxycarbide phase) is the only solid phase to be expected. Only when critically decreasing the oxygen partial pressure, graphitization of the silicon carbide surface will result (cf. section 4.1.6). Under hydrothermal conditions, both the formation of a solid silica scale or a carbon layer have been described, but depending on P-T-conditions and chemical composition, active, hydrothermal corrosion can be observed (Fig. 63).

	Diagram	Possible reaction products		
		Solid	Liquid	Gaseous
a) Initial state		-	-	-
b) Active oxidation		-	SiO ₂ ·nH ₂ O H ₄ SiO ₄	CH ₄ , CO, CO ₂
c) Silica formation		SiO ₂	SiO ₂ ·nH ₂ O H ₄ SiO ₄	CH ₄ , CO, CO ₂
d) Carbon formation		C	SiO ₂ ·nH ₂ O H ₄ SiO ₄	CH ₄ , CO, CO ₂

Fig. 63. Possible reactions for hydrothermal oxidation of silicon carbide (after Ref. ^{613,617}). Besides active oxidation, the formation of solid carbon and/or silica is possible but dissolution of silica may be too fast to allow the formation of a SiO₂ scale.

Carbon formation by selective, oxidative extraction of silicon and formation of a solid C-scale, was frequently observed on SiC under hydrothermal condition. The formation of carbon layers on SiC substrates (fibers, sintered ceramic bodies, single-crystal plates...) and the possibility of synthesizing sp³-hybridized carbon (diamond) shall not be topic of this review but the interested reader may find more pieces of information in the listed references (cf. Ref. ^{563-565,601-603,609,611,618}). Eq. 76 - 78 list possible reactions leading to silica and carbon as reaction products while silica is constantly and rapidly dissolved by water preventing the built-up of a solid SiO₂-scale.⁶¹¹



Nickel and Gogotsi⁶⁰⁹ compared the activity of solid phases (SiC, SiO₂, and C) as a function of the water-to-SiC-ratio (H₂O : SiC = ζ). Depending on ζ , different reactions besides Eq. 76 – 78 are thought to be possible (Eq. 79 - 81).^{398,563,564,604,609,617}



As a result, it was found that silica would be stable in a range of $0 \leq \zeta \leq 5$ (i.e., the whole examined range) but carbon is to become unstable above $\zeta = 2$. Adjusting ζ , either active oxidation or carbon / silica formation will occur.^{604,609} The following cases can be separated (Ref.^{604,609}):

- low ζ : silica and carbon deposition
- intermediate ζ : carbon and carbon and silica forms but SiO₂ dissolves quickly enough into water to ensure the formation of a carbon layer
- high ζ : neither silica nor carbon deposition are likely as C reacts with water and forms CO / CO₂ while silica is rapidly dissolved

As for sintered, polycrystalline materials, preferential corrosion of the grain-boundaries must be expected prior to either passive or active oxidation of the actual SiC substrate.^{605,606,614,617,619} Hence, bulk weight loss should not automatically be attributed to originating from active SiC corrosion in a multi-phase system.

4.3.3 Solubility of silica in water

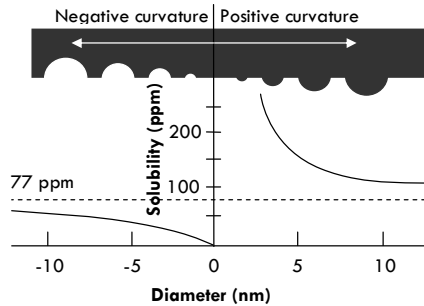
A critical factor of possible silica formation is the solubility of SiO₂ in water. This reaction has not to be considered in gas corrosion of silicon carbide, but in hydrothermal oxidation. Depending on the rate of dissolution, a protective silica layer may still be present on the silicon carbide body or become completely dissolved. In general, the solubility of silica in H₂O depends on the (1) particle size / geometry, (2) pH-value, (3) temperature, and (4) pressure.^{237,620-624} When comparing solubility values, influences from present impurities (in silica and/or water) and states of internal hydration must also be considered. It is, therefore, trivial to assume that hydroxylated silica will exhibit a different, initial solubility when introduced into water compared to a previously thoroughly dried sample, although the resulting equilibrium solubility should be unaffected.²³⁷

The first factor (Fig. 64a), particle size, increases solubility for small particles (due to the higher surface area) but also the curvature of silica particles (higher solubility for convex surfaces and smaller solubility for concave ones).²³⁷

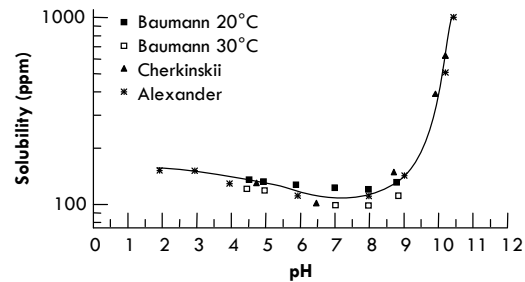
Fig. 64b depicts in detail the influence of the pH-value with a potential solubility minimum at pH 7 (lying in the range of experimental error). Below a critical value of pH 2, the solubility of silica in pure water substance is very small and as concluded by Brinker and Scherer ⁶²⁰, at low acidities no highly ionized silicate species is expected. Depending on the temperature, below pH 7 - 8 there is a more or less constant solubility. For higher pH-values, a significantly increased SiO₂-solubility can be found independently of the temperature due to the formation of silicate ion and monomer.^{237,620} Latter is in equilibrium with the solid phase and first, silicate ion, is instantaneously converted into the monomer. Finally, at pH > 10.7, none of the amorphous silica can stay in equilibrium with soluble silicate and, therefore, will completely dissolve.²³⁷

Fig. 64c shows the increased silica solubility at higher temperatures (for quartz samples). Increased temperature leads to increased solubility of silica in water up to ≈ 340°C with maximum values of ≈ 1660 ppm at 340°C.⁶²⁵ Towards the critical point of water (374°C), decreased solubility can be found (890 ppm at the critical point ⁶²⁵) along the three-phase curve (gaseous & liquid water + solid SiO₂).⁶²⁶ Higher pressure will generally increase the solubility of amorphous silica and crystalline modifications.^{237,620,625,627,628}

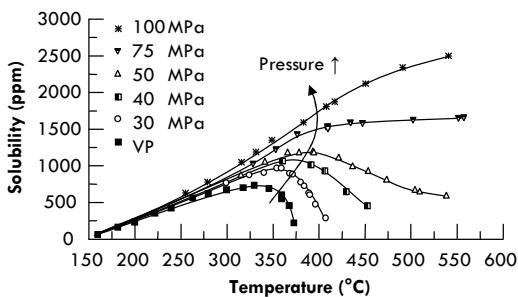
a) Curvature and particle size



b) pH



c) Temperature and pressure



d) Crystalline state

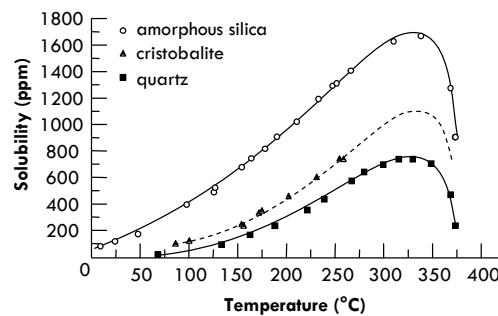


Fig. 64. Schematic illustrations showing the influence of (a) curvature and particle size; (b) pH (Ref. ²³⁷), (c) temperature and pressure (VP = vapor pressure; Ref. ⁶²⁸), and (d) crystalline state (Ref. ^{625,629}) on the solubility of silica in pure water substance. Data in Fig. 64b taken from: (a) Baumann: Ref. ⁶²²; Cherkinskii: Ref. ⁶²³; Alexander: Ref. ⁶²¹. The plot of cristobalite solubility (dashed) in the range > 250°C was extrapolated. The solubilities of Fig. 64 c and b deviate regarding the solubility values due to the usage of different crystalline states (quartz in Fig. 64c and amorphous SiO₂ in Fig. 64b respectively).

Crystalline silica is expected to show the same dissolution reactions like amorphous SiO_2 .⁶³⁰ In general, the solubility of crystalline modifications of SiO_2 is much smaller at a given temperature than the corresponding value for amorphous silica. Also, different crystalline modifications show a different solubility in water (Fig. 64d) - for example, at 100°C (along the three-phase-curve) the solubility of amorphous silica was found to be more than four times higher than $S_{\text{Cristobalite}}$ and more than 13-times higher than $S_{\text{Q-quartz}}$.^{237,624,625,628,629}

For kinetic considerations, the dissolution rate of silica has to be taken into account. As reported by Ito and Tomozawa (Ref. ⁶³¹), at 285°C and 100 MPa, dissolution rates of $0.8 \mu\text{m}\cdot\text{h}^{-1}$ and $1.5 \mu\text{m}\cdot\text{h}^{-1}$ at 200 MPa of amorphous silica can be expected. Correspondingly, to the introduced connection between total silica solubility in water, higher dissolution rates are found at higher pH-values, higher temperatures and higher pressure.

4.3.4 Silica formation

Hydrothermal experiments conducted on various silicon carbide materials (single-crystal, CVD, SiC...) resulted in the formation of a silica scale for low ζ -values.^{151,608,609} However, it should be noted, that many p-T- ζ conditions directly lead to either active oxidation (with rather linear kinetics) or carbon formation.^{605,606,614,632}

Brittle, poorly adhesive SiO_2 scales were interpreted as a result of a dissolution/precipitation process, evidenced by the presence of similar scales on the walls of gold capsules used for the experiment.¹⁵¹ Such a process could easily explain the occurrence of solid SiO_2 in a small, enclosed gold capsule, in which silica is constantly enriched in the fluid phase. Also, only a minor oxidation protection is to be expected from such inhomogeneous, brittle oxide scales as pointed out by Kraft et al. ¹⁵¹.

While hydrothermally derived silica layers ($400^\circ - 700^\circ\text{C}$ at 200 MPa) were reported to be mostly amorphous (or opal-like; potentially carbon- and water-rich), crystalline modifications (quartz, cristobalite and possibly keatite along with minor amounts of tridymite) were found as well.^{151,603,608} At temperatures above 700°C and 10 - 100 MPa, silicon carbide powder fully transformed to amorphous silica showed significant devitrification.^{608,633}

As far as the kinetics of silica formation are concerned, two parallel processes will affect bulk scale growth and weight change: (1) "regular" SiC oxidation with silica (and possibly carbon) as a reaction product and (2) dissolution of silica and formation of hydrosilicate.

Silica formation on its behalf in the presence of high-pressure and high-temperature H_2O was also supposed to explain the low friction coefficient between sliding SiC parts in tribological system.^{607,634}

4.4 Active oxidation

As seen in section 4.1.6 and as presented in Eq. 61, lowering the oxygen partial pressure will result in active oxidation of silicon carbide at sufficiently high temperatures. Already formed silica layers can be removed due to the fact, that SiO₂ is readily volatilized under reducing atmospheres. At ambient pressure (0.1 MPa) active oxidation will occur at about 1825°C and leads to mass loss that obeys to a linear time-law.^{19,30,168,382,480} Increasing temperatures will the critical oxygen partial pressure $P_{O_2}^{crit.}$ (i.e., the partial pressure at which the active-passive-transition can be observed) shift towards higher values.^{372,381,635}

Thermodynamic calculations indicate that above the SiC surface a small gaseous boundary layer must be present (similar to the active oxidation of pure silicon; Ref. ⁶³⁶).³⁸¹ It was speculated about the influence of a condensed SiO phase within that boundary layer by Nickel ³⁸² although this phase has not been detected yet.⁶³⁷

As pointed out by Narushima et al. ¹⁶⁸ it must be critically differentiated between (1) low total P_{O_2} - values (i.e., transition towards vacuum = molecular flow regime; Ref. ^{369,567,638-641}), (2) inert gas / O₂ - mixtures near or at ambient pressure (= viscous flow regime; Ref. ^{380,381,635,642}) and as a special case (3) CO₂-CO or H₂O-H₂ mixtures (Ref. ^{372,399,480,643-646}). Heuer et al. assumed oxygen diffusion through this gaseous boundary layer to be rate controlling for active oxidation for cases (1) and (2).^{168,400} This may also be true for (3), although in case of CO₂-CO atmospheres diffusion through a formed carbon layer may be rate-controlling at temperatures above 1550°C - 1650°C at very low CO₂ partial pressures.^{168,646}

Additionally, some studies were conducted inert gas - CO₂ mixtures.^{372,643} One possible reaction for CO₂ with silicon carbide is shown in Eq. 82 (Ref. ⁶⁴³):



As proposed by Balat et al. could CO due to Eq. 82 reduced initially formed silica by locally increasing the CO partial pressure and, therefore, a protective and solid SiO₂ layer cannot be established.⁶⁴³ This is in contrast to thermal oxidation in air or oxygen, as O₂ would readily oxidize carbon monoxide and prevent silica deterioration from happening.

For inert gas / oxygen mixtures, an overall increase of k_a is to be expected in case of an increased total gas flow or increased oxygen partial pressures (Fig. 65a), as long as latter stay below $P_{O_2}^{crit.}$: when reaching this critical value, an abrupt transition toward passive oxidation takes place.³⁸¹ In this context, passive oxidation can be defined either as bulk weight gain or as initial silica formation. Comparing conditions for the active-passive transition, this definition must always be checked.

Only in case of CO₂-CO and H₂O-H₂ mixtures the active oxidation rate k_a does not decrease continuously with decreasing oxygen potential but shows a distinct maximum at $P_{CO_2 \text{ or } H_2O}^{apex}$ (Fig. 65b).³⁷²

For $P_{CO_2 \text{ or } H_2O} > P_{CO_2 \text{ or } H_2O}^{apex}$, silica formation can be attributed to reaction between bulk SiC and the oxidizing species in the gas mixture (CO₂ and H₂O, respectively), while parallel mass loss will be induced by reaction of the oxide with the reducing gas species (CO and H₂, respectively).¹⁶⁸ Latter, bulk mass loss, will become dominant at $P_{CO_2 \text{ or } H_2O} < P_{CO_2 \text{ or } H_2O}^{apex}$. In the special case of CO₂-CO, carbon formation was reported to take place in such region.³⁷²

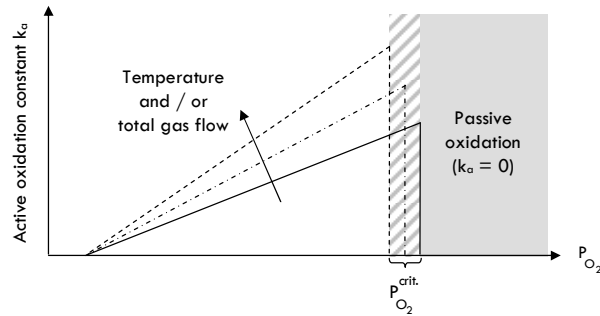
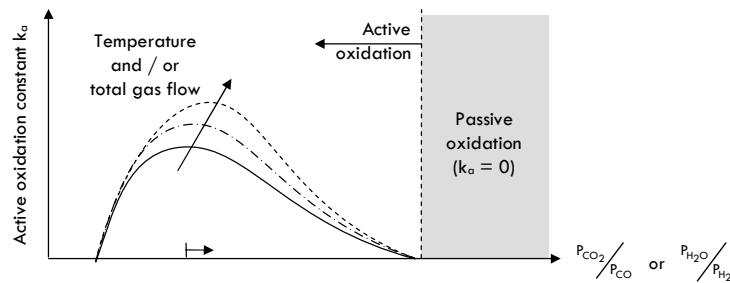
a) O₂-argonb) CO₂-CO / H₂O-H₂

Fig. 65. Schematic illustration (after Ref. ^{168,372}) of active oxidation constant k_a of (a) O₂-argon mixtures and (b) CO₂-CO or H₂O-H₂ mixtures. Shown is the influence of temperature and/or total gas flow as well as the dependency on the oxidant partial pressure. At the active-passive transition, k_a becomes abruptly (a) or continuously (b) zero. Due to the variation of the total gas flow in (a), the critical oxygen partial pressure at which the active-transition takes place decreases.

As the total gas flow increases, $P_{O_2}^{crit.}$ was shown to decrease (Fig. 65a). This was explained in terms of non-equilibrium state at the SiC surface or decreased CO/SiO boundary layers thickness.³⁸¹ For sintered ceramic bodies, the presence of impurities must be taken into account as they significantly enhance critical oxygen partial pressures.^{168,369,380,381} Similar to these findings increases $P_{O_2}^{crit.}$ for Si₃N₄ with increased impurity content.⁶⁴⁷

For comparing literature values of active oxidation rate constants (k_a) one has carefully to evaluate the experimental parameters (like total gas pressure, total gas flow, partial pressure of the oxidant gas species, used material, geometry and so on) - quite similar to the problems encountered when discussing passive oxidation and the lack of standardized oxidation tests.

The overall reaction mechanism was shown in Eq. 82. Already formed silica (e.g., during heating the sample) can react with oxygen according to Eq. 83 (Ref. ^{366,639}):



Changing the oxidizing atmosphere's overall composition from standard air or pure oxygen towards CO/CO₂ will shift the active-passive-boundary towards higher temperatures.^{372,641,643}

Fig. 66 compares the active-to-passive-transition boundary found by different workgroups. All experimentally found or thermodynamically calculated boundaries lie within the values derived from the Wagner-model⁶³⁶ and volatility diagrams^{400; 168}. The Wagner model assumes continuous CO and SiO desorption from the SiC surface³⁸⁰. Goto and Homma³⁷² criticized such models to be too simplifying at high temperatures.

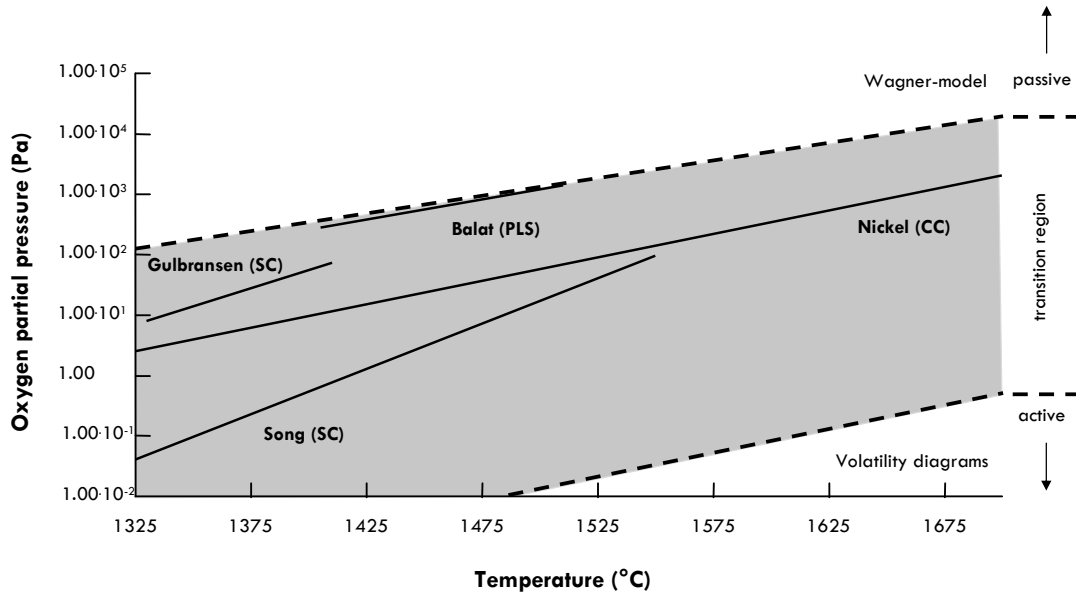


Fig. 66. Active-to-passive-transition of SiC thermal oxidation (after Ref. ^{168,382}). All shown references plot within the margins (gray) between the Wagner-model and volatility diagrams. SC denotes experiments conducted on Single-Crystals and PLS means PressureLess Sintered SiC while CC indicates CalCulated values (Nickel: Ref. ³⁸²; Balat: Ref. ⁶⁴¹; Gulbransen: Ref. ³⁶⁹; Song: Ref. ⁵⁶⁷).

A “secondary” active/passive boundary³⁸² would occur when the product gas pressure exceeds the ambient pressure at the surface. In this case, both, oxide formation and subsequent layer removal by spallation and bubble formation are to be expected. The term “secondary” in this context describes a pseudo-active regime, in which a continuously process of oxide formation and removal leads to bulk weight loss of the silicon carbide body.

5. CONCLUSIONS

This review summarizes many key features of present-day knowledge deduced over several decades of silica on silicon carbide research. As shown, structural aspects must be studied closely before evaluating oxidation-related and / or kinetic data. The structural diversity of SiC itself makes this material a complex substance to understand.

SiC-SiO₂ interfaces still are electronically inferior to their Si-SiO₂ counterpart, possibly because carbon clusters at the interface may be contributing to the high density of states at the interface. Hydrogen passivation is not suitable to achieve much better interface properties as dangling bonds (in contrast to Si-SiO₂ interfaces) are not the dominant defect type.

Silicon carbide oxidation shows a linear-parabolic behavior that can sufficiently be described using the Deal-and-Grove model originally created for silicon oxidation. However, different oxidation rates for the various faces of SiC can be found with a faster oxidizing C- and a slower oxidizing Si-face. The very same behavior can be observed for (1) etching or (2) graphitization and is probably due to the different surface energies.

Oxygen diffusion seems to determine the (long-time) oxidation kinetics, although this process alone cannot explain several phenomena. If the diffusion coefficient of oxygen alone would be rate-controlling, (1) silicon and silicon carbide would oxidize equally fast, (2) no difference between the various crystal faces would occur, and (3) CO diffusion would have to be much faster than O₂ diffusion (which is not expected based upon comparing the molecular diameters).

The general trend of increased oxidation rates at higher temperatures seems to include a kinetic transition with much higher activation energies at temperatures above $\approx 1350^{\circ}\text{C}$ and lower E_a -values below. Different models to explain this were presented, among which genuine effects (such as transition of the diffusion mechanism and crystallization) and impurity-related (such as sodium incorporation) are the most likely causes.

Silica formation on silicon carbide is a process susceptible to a myriad of influencing parameters such as (1) temperature, (2) oxygen partial pressure, (3) impurities in the oxidizing atmosphere (water, sodium, aluminium...), (4) surface morphology (porosity, asperity...), and (5) choice of SiC material (polytypism, sintering aids...). Impurities are of utmost importance when studying SiC oxidation: even trace amounts (ppm) of both water and aluminium / sodium greatly influence rate constants and structural properties of silica. Likewise, sintering aids at the percent level are a major cause for differences. A possible source for sodium contamination may well be the use of a furnace tube made of alumina. Heating such a furnace tube for long times ($>> 1000$ h) could almost eliminate that effect.

Also the (micro)structure of the formed silica layer determines the further oxidation behavior: (1) bubbles potentially lead to spallation and (2) crystalline silica layers tend to form cracks due to the phase transition during cyclic oxidation. Bubble formation as a common phenomenon of SiC oxidation is restricted to impure systems (like sintered SiC) below the melting point of cristobalite ($\approx 1710^{\circ}\text{C}$). For high-temperature oxidation of SiC, bubble formation was proposed to be a genuine effect although the influence of impurities cannot be excluded completely.

Wet oxidation yields higher passive oxidation constants due to faster transport of the H_2O molecule compared to O_2 . Unlike molecular oxygen permeation, water reacts readily with the Si-O network modifying its structure and properties. Nevertheless, an overall linear-parabolic growth law of the silica layer can be observed in wet atmospheres with corresponding lower activation energies compared to dry, isothermal oxidation.

Hydrothermal oxidation of silicon carbide poses a special case, because in addition to silica formation, water as a fluid can dissolve it. Depending on pressure, temperature and the pH-value, silica dissolution can be sufficiently high in order to prevent the built-up of a solid and homogenous silica scale, although silica formation occurs. For low $\text{H}_2\text{O}:\text{SiC}$ ratios, dissolution and parallel precipitation of silica is thought to be a reasonable explanation for poorly protective, brittle silica scales. A special case poses the formation of solid carbon films as a process of fast silica dissolution and lower C solubility in hydrothermal water.

Lowering the oxygen partial pressure beyond a critical value causes the SiC to decompose and correspondingly, linear rate constants (k_a) of active oxidation are found. Already formed silica can react with silicon carbide to yield gaseous SiO and CO. In the case of CO_2/CO and $\text{H}_2\text{O}/\text{H}_2$ mixtures, the active oxidation constant will not constantly decrease with decreasing CO_2 or H_2O partial pressure but show a local maximum of k_a .

Clearly, more work needs to be done to achieve a true understanding of SiC oxidation. The use of comparable and standardized oxidizing conditions and testing environments is one vital condition for studies on such a complex system with so many influencing parameters. Better understanding of the mechanisms beyond the oxidation of silicon carbide and the structural / electrical properties at the SiC-SiO₂ interface will hopefully enhance the use of SiC especially as a semiconductor. Once SiC was thought to be suitable for abrasives only, but we find that despite its use for many decades as a wonderful source for new discoveries and new fields of application, it has by far not worn out.

ACKNOWLEDGMENTS

This work was partially supported by the Deutsche Forschungsgemeinschaft (DFG) through Ni299/12-1. The authors would like to thank (in alphabetic order) Valerie Afanas'ev (University of Leuven), Matthias Bickermann (University of Erlangen-Nürnberg), Kai-Chieh Chang (Seagate Technology, Pittsburgh), Fabien Devynck (Ecole Polytechnique Fédérale de Lausanne), Andrei Maltsev (Caracal Inc., Ford City), and Thomas Wagner (University of Tübingen) for much appreciated and most valuable discussion.

REFERENCES

1. Nassau, K. *Gems Made by Man*, 364 (Gemological Institute of America, Carlsbad, 1980).
2. Berzelius, J.J. Untersuchungen über die Flußspatsäure und deren merkwürdigen Verbindungen. *Annalen der Physik* **1**, 169 - 230 (1824).
3. Acheson, E.G. On Carborundum. *Chemical News* **68**, 179 (1893).
4. Cowles, E.H. & Cowles, A.H. Electric Smelting-Furnace. 1 - 6 (United States of America, 1885).
5. Schubert, U. & Hüsing, N. *Synthesis of Inorganic Materials* 413 (Wiley-VCH Verlag GmbH & Co. KGaA, Weinheim, 2004).
6. Zimmermann, M. *Experimentelle Untersuchung und numerische Modellierung des Gleitkontaktverhaltens von gesintertem Siliciumcarbid (SSiC)*, 102 (Universität Karlsruhe, Karlsruhe, 1998).
7. Willander, M., Friesel, M., Wahab, Q. & Straumal, B. Silicon carbide and diamond for high-temperature device applications. *Journal of Materials Research: Materials in Electronics* **17**, 1 - 25 (2006).
8. Kiefert, L., Schmetzer, K. & Hänni, H.A. Synthetic Moissanite from Russia. *The Journal of Gemmology* **27**, 471 - 481 (2001).
9. Round, H.J. A note on carborundum. *Electrical World* **19**, 309 (1907).
10. Kleber, W., Bautsch, H.-J. & Bohm, J. *Einführung in die Kristallographie*, (Verlag Technik GmbH, Berlin, 1998).
11. Sadow, S.E. & Agarwal, A. *Advances in silicon carbide processing and applications*, 212 (Artech House inc., Norwood, 2004).
12. Baumhauer, H. Über die Krystalle des Carborundums. *Zeitschrift für Kristallographie* **50**, 33 - 39 (1912).
13. Marchi, J., Bressiani, J.C. & Bressiani, A.H.A. Densification studies of silicon carbide-based ceramics with yttria, silica and alumina as sintering additives. *Materials Research* **4**, 231 - 236 (2001).
14. Izhevskiy, V.A., Genova, L.A., Bressiani, J.C. & Bressiani, A.H.A. Review Article: Silicon Carbide. Structure, Properties and Processing. *Cerâmica* **46**, 4 - 13 (2000).
15. Kleykamp, H. & Schumacher, G. The Constitution of the Silicon-Carbon System. *Berichte der Bunsen-Gesellschaft* **97**, 799 - 805 (1993).
16. Verma, A.R. & Krishna, P. *Polymorphism and Polytypism in Crystals*, 362 (John Wiley & Sons Inc, Chichester, 1966).
17. Muehlhoff, L., Choyke, J.W., Bozack, M.J. & Yates, J.T., Jr. Comparative electron spectroscopic studies of surface segregation on SiC(0001) and SiC(000-1). *Journal of Applied Physics* **60**, 2842 - 2853 (1986).
18. Choyke, W.J. & Pensl, G. Physical Properties of SiC. *MRS Bulletin* **22**, 25 - 29 (1997).
19. Harris, G.L. *Properties of Silicon Carbide*, 282 (INSPEC, the Institution of Electrical Engineers, London, 1995).
20. Ramsdell, L.S. Studies on Silicon Carbide. *American Mineralogist* **32**, 64 - 82 (1947).
21. Jagodzinski, H. Eindimensionale Fehlordnung in Kristallen und ihr Einfluss auf die Röntgeninterferenzen. I. Berechnung des Fehlordnungsgrades aus den Röntgenintensitäten. *Acta Crystallographica* **2**, 201 - 207 (1949).
22. Jagodzinski, H. Eindimensionale Fehlordnung in Kristallen und ihr Einfluss auf die Röntgeninterferenzen. II. Berechnung der fehlgeordneten dichtesten Kugelpackungen mit Wechselwirkungen der Reichweite 3. *Acta Crystallographica* **2**, 208 - 214 (1949).
23. Zhdanov, G.S. The Numeral Symbol of Close Packing of Spheres and its Application in the Theory of Close Packings. *Comptes Rendus (Doklady) de l'Académie des Sciences de l'URSS* **48**, 39 - 42 (1945).
24. Lambrechts, W.R.L., Limpijumong, S., Rashkeev, S.N. & Segall, B. Electronic Band Structure of SiC Polytypes: A Discussion of Theory and Experiment. *Physica Status Solidi (B)* **202**, 5 - 33 (1997).
25. van Haeringen, W., Bobbert, P.A. & Backes, W.H. On the Band Gap Variation in SiC Polytypes. *Physica Status Solidi (B)* **202**, 63 - 79 (1997).
26. Jagodzinski, H. Fehlordnungserscheinungen und ihr Zusammenhang mit der Polytypie des SiC. *Neues Jahrbuch für Mineralogie* **3**, 49 - 64 (1954).
27. Pensl, G. et al. SiC Material Properties. *International Journal of High Speed Electronics and Systems* **15**, 705 - 745 (2005).
28. Pandey, D. & Krishna, P. X-ray diffraction study of stacking faults in a single crystal of 2H SiC. *Journal of Physics D* **10**, 2057 - 2068 (1977).
29. Tairov, Y.M. & Tsvetkov, V.F. Progress in Controlling the Growth of Polytypic Crystals. *Progress in Crystal Growth and Characterization* **7**, 111 - 162 (1983).
30. Haase, V. et al. *Si. Silicon. Supplemental Volume B3*, 545 (Springer-Verlag, Berlin, 1986).
31. Bickermann, M. Friedrich-Alexander-Universität Erlangen-Nürnberg (1998).
32. Bickermann, M. Universität Erlangen-Nürnberg (2002).
33. Chien, F.R., Nutt, S.R. & Yoo, W.S. Stacking Fault Energy Calculations in 6H- and 15R-SiC. *Materials Research Society Symposium Proceedings* **339**, 399 - 404 (1994).
34. Jikimoto, T. et al. Photoemission study of 6H-SiC(0001)Si face *Applied Surface Science* **117 - 118**, 794 - 797 (1997).
35. Fal'kovskii, L.A. & Camassel, J. Strong and weak modes in polytypes of SiC. *JETP Letters* **69**, 268 - 272 (1999).

36. Kelly, J.F., Barnes, P. & Fisher, G.R. Long Period Polytype Boundaries in Silicon Carbide. *Ferroelectrics* **250**, 187 - 190 (2001).
37. Dombrowski, K.F. et al. Deep donor state of vanadium in cubic silicon carbide (3C-SiC). *Applied Physics Letters* **65**, 1811 - 1813 (1994).
38. Baur, J., Kunzer, M. & Schneider, J. Transition Metals in SiC Polytypes, as Studied by Magnetic Resonance Techniques. *Physica Status Solidi (A)* **162**, 153 - 172 (1997).
39. Iwata, H., Lindefelt, U., Öberg, S. & Briddon, P.R. Cubic polytype inclusions in 4H-SiC. *Journal of Applied Physics* **93**, 1577 - 1585 (2003).
40. Afanas'ev, V.V., Bassler, M., Pensl, G. & Schulz, M. Band offsets and electronic structure of SiC/SiO₂ interfaces. *Journal of Applied Physics* **79**, 3108 - 3114 (1996).
41. Afanas'ev, V.V. & Stesmans, A. Valence band offset and hole injection in the 4H, 6H-SiC/SiO₂ interfaces. *Applied Physics Letters* **77**, 2024 - 2026 (2000).
42. Biedermann, E. The Optical Absorption Bands and their Anisotropy in the Various Modifications of SiC. *Solid State Communications* **3**, 343 - 346 (1965).
43. Lebedev, A. Heterojunctions and superlattices based on silicon carbide. *Semiconductor Science and Technology* **21**, R17 - R34 (2006).
44. Lambrechts, W.R.L., Limpijumngong, S., Rashkeev, S.N. & Segall, B. Theory of Below Gap Absorption Bands in n-Type SiC Polytypes; Or, How SiC Got Its Colors. *Materials Science Forum* **338 - 342**, 545 - 550 (2000).
45. Tairov, Y.M. Growth of bulk SiC. *Materials Science and Engineering B* **B29**, 83 - 89 (1995).
46. Bechstedt, F. et al. Polytypism and Properties of Silicon Carbide. *Physica Status Solidi (B)* **202**, 35 - 62 (1997).
47. Choyke, J.W., Hamilton, D.R. & Patrick, L. Optical Properties of cubic SiC - Luminescence of Nitrogen-Exciton complexes, and interband absorption. *Physical Review* **133**, A1163 - A1166 (1964).
48. Choyke, W.J. & Devaty, R.P. Progress in the study of optical and related properties of SiC since 1992. *Diamond and Related Materials* **6**, 1243 - 1248 (1997).
49. Cobet, C. Technische Universität Berlin (1999).
50. Powell, A.R. & Rowland, L.B. SiC Materials - Progress, Status and Potential Roadblocks. *Proceedings of the IEEE* **90**, 942 - 955 (2002).
51. Lundqvist, D. On the Crystal Structure of Silicon Carbide and its Content of Impurities. *Acta Chemica Scandinavica* **2**, 177 - 191 (1948).
52. Tyagi, U.P. & Trigunayat, G.C. Melt Growth and Characterization of Lead-Doped Crystals of Cadmium Iodide. *Acta Crystallographica* **C44**, 1157 - 1162 (1988).
53. Frank, F.C. The Growth of Carborundum: Dislocations and Polytypism. *Philosophical Magazine* **42**, 1014 - 1021 (1951).
54. Schlichting, J., Czack, G. & Kuhn, P. *Si. Silicon. Supplemental Volume B2.*, 314 (Springer-Verlag, Berlin, 1984).
55. Pandey, D. & Krishna, P. Polytypism in close-packed structures. *Current Topics in Materials Science* **9**, 415 - 491 (1982).
56. Kuhlmann-Wilsdorf, D., Pandey, D. & Krishna, P. A mechanism for the origin of screw dislocation sequences, giant screw dislocations, and polytypism in platelet crystals. *Philosophical Magazine A* **42**, 527 - 550 (1980).
57. Heine, V., Cheng, C. & Needs, R.J. The Preference of Silicon Carbide for Growth in the Metastable Cubic Form. *Journal of the American Ceramic Society* **74**, 2630 - 2633 (1991).
58. Dhanaraj, G., Huang, X.R., Dudley, M., Prasad, V. & Ma, R.-H. Silicon Carbide - Part I: Growth and Characterization. (eds. Byrappa, K. & Ohachi, T.) 181 - 232 (Springer-Verlag, Berlin, 2003).
59. Tairov, Y.M. & Tsvetkov, V.F. General principles of growing large-size single crystals of various silicon carbide polytypes. *Journal of Crystal Growth* **52**, 146 - 150 (1981).
60. Kanaya, M., Takahashi, J., Fujiwara, Y. & Moritani, A. Controlled sublimation growth of single crystalline 4H-SiC and 6H-SiC and identification of polytypes by x-ray diffraction. *Applied Physics Letters* **51**, 56 - 58 (1991).
61. Augustine, G., Hobgood, H.M., Balakrishna, V., Dunne, G. & Hopkins, R.H. Physical Vapor Transport Growth and Properties of SiC Monocrystals of 4H Polytype. *Physica Status Solidi (B)* **202**, 137 - 148 (1997).
62. Vodakov, Y.A., Mokhov, E.N., Roenkov, A.D. & Anikin, M.M. Effect of impurities on the polytypism of silicon carbide. *Pis'ma v Zhurnal Tekhnicheskoi Fiziki* **5**, 367 - 370 (1979).
63. Stein, R.A. Formation of macrodefects in SiC. *Physica B* **185**, 211 - 216 (1993).
64. Yakimova, R., Syväjärvi, M., Jacobson, H. & Janzen, E. Some Aspects of Extended Defects Formation and their Reduction in Silicon Carbide Crystals. in *Recent Research Development in Materials and Engineering* (eds. Moore, J.J., Richards, G.G. & Sohn, H.Y.) 619 - 646 (Transworld Research, Kerala, 2002).
65. Trigunayat, G.C. & Chadha, G.K. Progress in the Study of Polytypism in Crystals (I). *Physica Status Solidi (A)* **4**, 9 - 42 (1971).
66. Trigunayat, G.C. & Chadha, G.K. Progress in the Study of Polytypism in Crystals (II). *Physica Status Solidi (A)* **4**, 281 - 303 (1971).
67. Verneuil, M.A. Production artificielle du rubis par fusion. *Comptes Rendus Hebdomadaires des Seances de l'Academie des Sciences* **135**, 791 - 794 (1902).
68. Czochralski, J. Ein neues Verfahren zur Messung der Kristallisationsgeschwindigkeit der Metalle. *Zeitschrift für physikalische Chemie* **92**, 219 - 221 (1918).
69. Dhar, S. Vanderbilt University (2005).

70. Glass, R.C., Henshall, D., Tsvetkov, V.F. & Carter, C.H., Jr. SiC Seeded Crystal Growth. *Physica Status Solidi (B)* **202**, 149 - 162 (1997).
71. Tuominen, M. et al. Growth-related structural defects in seeded sublimation-grown SiC. *Diamond and Related Materials* **6**, 1272 - 1275 (1997).
72. Huang, X.R. et al. Superscrew dislocation contrast on synchrotron white-beam topographs: an accurate description of the direct dislocation image. *Journal of Applied Crystallography* **32**, 516 - 524 (1999).
73. Huang, X.R., Vetter, W.M., Huang, W., Wang, S. & Carter, C.H., Jr. Direct evidence of micropipe-related pure superscrew dislocations in SiC. *Applied Physics Letters* **74**, 353 - 355 (1999).
74. Dudley, M., Huang, X.R. & Vetter, W.M. Contribution of x-ray topography and high-resolution diffraction to the study of defects in SiC. *Journal of Physics D* **36**, A30 - A36 (2003).
75. Dudley, M. et al. White-Beam Synchrotron Topographic Studies of defects in 6H-SiC Single Crystals. *Journal of Physics D* **28**, A63 - A68 (1995).
76. Dudley, M. et al. White-Beam Synchrotron Topographic Analysis of Multi-Polytype SiC device configuration. *Journal of Physics D* **28**, A56 - A62 (1995).
77. Bergman, J.P., Lendenmann, H., Nilsson, P.A., Lindefelt, U. & Skytt, S. Crystal Defects as Source of Anomalous Forward Voltage Increase of 4H-SiC. *Materials Science Forum* **353 - 356**, 299 - 302 (2001).
78. Nakashima, S. & Harima, H. Raman Investigation of SiC Polytypes. *Physica Status Solidi (A)* **162**, 39 - 64 (1997).
79. Li, X.-B., Shi, E.-W., Chen, Z.-Z. & Xiao, B. Polytype formation in silicon carbide single crystals. *Diamond and Related Materials* **16**, 654 - 657 (2007).
80. Nakashima, S., Nakatake, Y., Harima, H., Katsuno, M. & Ohtani, N. Detection of stacking faults in 6H-SiC by Raman scattering. *Applied Physics Letters* **77**, 3612 - 3614 (2000).
81. Nakashima, S. & Harima, H. Characterization of Defects in SiC Crystals by Raman Scattering. in *Silicon Carbide. Major Recent Advances*. (eds. Choyke, J.W., Matsunami, H. & Pensl, G.) 585 - 605 (Springer-Verlag, Berlin, 2004).
82. Harima, H., Hosoda, T. & Nakashima, S. Raman imaging characterization of electric properties of SiC near a micropipe. *Materials Science Forum* **338 - 342**, 603 - 606 (2000).
83. Harima, H., Hosoda, T. & Nakashima, S. Carrier Density Evaluation in p-type SiC by Raman Scattering. *Materials Science Forum* **338 - 342**, 607 - 610 (2000).
84. Verma, A.R. *Crystal Growth and Dislocations*, 182 (Butterworths Scientific Publications, London, 1953).
85. Gabor, T. Growth mechanism of silicon carbide. *Nature* **207**, 286 - 287 (1965).
86. Forty, A.J. The growth of cadmium iodide crystals: I - Dislocations and spiral growth. *Philosophical Magazine* **43**, 72 - 81 (1952).
87. Mardix, S., Lang, A.R. & Blech, I. On giant screw dislocations in ZnS Polytype Crystals. *Philosophical Magazine* **24**, 683 - 693 (1971).
88. Müller, S.G. et al. Physical Vapor Growth and Characterization of High Conductivity 1.4 inch 4H-SiC Bulk Crystals. *Materials Science Forum* **264 - 268**, 33 - 36 (1998).
89. Hobgood, H.M. et al. Silicon Carbide Crystals and Substrate Technology: A Survey of Recent Advances. *Materials Science Forum* **457 - 460**, 3 - 8 (2004).
90. Takahashi, J. & Ohtani, N. Modified-Lely SiC Crystals Grown in [1-100] and [11-20] Directions. *Physica Status Solidi (B)* **202**, 163 - 175 (1997).
91. Ohtani, N., Katsuno, M., Fujimoto, M. & Yashiro, H. Defect Formation and Reduction During Bulk SiC Growth. in *Silicon Carbide. Major Recent Advances*. (eds. Choyke, J.W., Matsunami, H. & Pensl, G.) 137 - 162 (Springer-Verlag, Berlin, 2004).
92. Rost, H.-J., Schmidbauer, M., Siche, D. & Fornari, R. Polarity- and orientation-related defect distribution in 4H-SiC single crystals. *Journal of Crystal Growth* **290**, 137 - 143 (2006).
93. Herro, Z.G. et al. Growth of 6H-SiC crystals along the [01-15] direction. *Journal of Crystal Growth* **275**, 496 - 503 (2005).
94. Glass, R.C., Kjellberg, L.O., Tsvetkov, V.F., Sundgren, J.E. & Janzen, E. Structural macro-defects in 6H-SiC wafers. *Journal of Crystal Growth* **132**, 504 - 512 (1993).
95. Ohsato, H., Kato, T., Okuda, T. & Razeghi, M. Internal stress around micropipes in 6H-SiC substrates. *Proceedings of SPIE-The International Society for Optical Engineering* **3629**, 393 - 399 (1999).
96. Pirouz, P. On micropipes and nanopipes in SiC and GaN. *Philosophical Magazine A* **78**, 727 - 736 (1998).
97. Ziegler, G., Lanig, P., Theis, D. & Weyrich, C. Single Crystal Growth of SiC Substrate Material for Blue Light Emitting Diodes. *IEEE Transactions on electron devices* **ED-30**, 277 - 281 (1983).
98. Cabrera, N. & Levine, M.M. On the dislocation theory of evaporation of crystals. *Philosophical Magazine* **1**, 450 - 458 (1955).
99. Heindl, J. et al. The kinetic growth model applied to micropipes in 6H-SiC. *Diamond and Related Materials* **6**, 1269 - 1271 (1997).
100. Heindl, J., Strunk, H.P., Heydemann, V.D. & Pensl, G. Micropipes: Hollow Tubes in Silicon Carbide. *Physica Status Solidi (A)* **162**, 251 - 262 (1997).
101. Dudley, M. et al. The mechanism of micropipe nucleation at inclusions in silicon carbide. *Applied Physics Letters* **75**, 784 - 786 (1999).

102. Schulze, N., Barrett, D.L. & Pensl, G. Near-equilibrium growth of micropipe-free 6H-SiC single crystals by physical vapor transport. *Applied Physics Letters* **72**, 1632 - 1634 (1998).
103. Hofmann, D. et al. Analysis on defect generation during the SiC bulk growth process. *Materials Science Forum* **B61 - B62**, 48 - 53 (1999).
104. Powell, J.A. & Larkin, D.J. Process-Induced Morphological Defects in Epitaxial CVD Silicon Carbide. *Physica Status Solidi (B)* **202**, 529 - 548 (1997).
105. Si, W., Dudley, M., Glass, R., Tsvetkov, V. & Carter, C.H., Jr. Experimental Studies of Hollow-core screw dislocations in 6H-SiC and 4H-SiC Single Crystals. *Materials Science Forum* **264 - 268**, 429 - 432 (1998).
106. Vetter, W.M. & Dudley, M. Micropipes in silicon carbide crystals: Do all screw dislocations have open cores? *Journal of Materials Research* **15**, 1649 - 1652 (2000).
107. Ohsato, H., Kato, T. & Okuda, T. Screw and edge dislocations-induced internal strain around micropipes of 6H-SiC single crystals. *Materials Science in Semiconductor Processing* **4**, 483 - 487 (2001).
108. Kuhr, T.A., Sanchez, E.K., Skowronski, M., Vetter, W.M. & Dudley, M. Hexagonal voids and the formation of micropipes during SiC sublimation growth. *Journal of Applied Physics* **89**, 4625 - 4630 (2001).
109. Hofmann, D., Bickermann, M., Hartung, W. & Winnacker, A. Analysis on the formation and elimination of filamentary and planar voids in Silicon Carbide Bulk Crystals. *Materials Science Forum* **338 - 342**, 445 - 448 (2000).
110. Neudeck, P.G. & Powell, J.A. Performance limiting micropipe defects in silicon carbide wafers. *IEEE Electron Device Letters* **15**, 63 - 65 (1994).
111. Davis, R.F., Kelner, G., Shur, M., Palmour, J.W. & Edmond, J.A. Thin film deposition and microelectronic and optoelectronic device fabrication and characterization in monocrystalline alpha and beta silicon carbide. *Proceedings of the IEEE* **79**, 677 - 701 (1991).
112. Hobgood, D. et al. Status of Large Diameter SiC Crystal Growth for Electronic and Optical Applications. *Materials Science Forum* **338 - 342**, 3 - 8 (2000).
113. Yakimova, R. et al. Micropipe Healing in Liquid Phase Epitaxial Growth of SiC. *Materials Science Forum* **338 - 342**, 237 - 240 (2000).
114. Kamata, I., Tsuchida, H., Jikimoto, T. & Izumi, K. Improvement in Electrical Properties of 4H-SiC Epilayers by Micropipe Dissociation. *Japanese Journal of Applied Physics* **40**, L1012 - L1014 (2001).
115. Kamata, I., Tsuchida, H., Jikimoto, T. & Izumi, K. Influence of 4H-SiC Growth Conditions on Micropipe Dissociation. *Japanese Journal of Applied Physics* **41**, L1137 - L1139 (2002).
116. Kamata, I., Tsuchida, H., Jikimoto, T. & Izumi, K. Structural Transformation of Screw Dislocations via Thick 4H-SiC Epitaxial Growth. *Japanese Journal of Applied Physics* **39**, 6496 - 6500 (2000).
117. Müller, S.G. et al. The status of SiC bulk growth from an industrial point of view. *Journal of Crystal Growth* **211**, 325 - 332 (2000).
118. Nakamura, D. et al. Ultrahigh-quality silicon carbide single crystals. *Nature* **430**, 1009-1012 (2004).
119. Madar, R. Materials science: Silicon carbide in contention. *Nature*, 974 - 975 (2004).
120. Yakimova, R., Hysten, A.-L., Tuominen, M., Syväjärvi, M. & Janzen, E. Preferential etching of SiC crystals. *Diamond and Related Materials* **6**, 1456 - 1458 (1997).
121. Yakimova, R., Yakimov, T., Hitova, L. & Janzen, E. Defect mapping in 4H-SiC wafers. *Materials Science and Engineering B* **B46**, 287 - 290 (1997).
122. Kato, T., Ohsato, H., Okamoto, A., Sugiyama, N. & Okuda, T. The photoelastic constant and internal stress around micropipe defects of 6H-SiC single crystal. *Materials Science and Engineering B* **B57**, 147 - 149 (1999).
123. Pichler, H. & Schmitt-Riegraf, C. *Rock-forming Minerals in Thin Section*, 220 (Chapmann & Hall, London, 1997).
124. Katsuno, M., Ohtani, N., Fujimoto, T., Aigo, T. & Yashiro, H. Evolution of Crystal Mosaicity during Physical Vapor Transport Growth of SiC. *Materials Science Forum* **389 - 393**, 55 - 58 (2002).
125. Tuominen, M., Yakimova, R., Glass, R.C., Tuomi, T. & Janzen, E. Investigation of structural defects in 4H SiC wafers. *Materials Research Society Symposium Proceedings* **339**, 729 - 734 (1994).
126. Kuhr, T.A., Vetter, W.M., Dudley, M. & Skowronski, M. X-ray Characterization of 3 inch Diameter 4H and 6H-SiC Experimental Wafers. *Materials Science Forum* **338 - 342**, 473 - 476 (2000).
127. Feng, Z.C. *SiC Power Materials. Devices and Applications.*, 450 (Springer Verlag, Berlin, 2004).
128. Ha, S., Nuhfer, N.T., De Graef, M., Rohrer, G.S. & Skowronski, M. Origin of Threading Dislocations Arrays in SiC Boules Grown by PVT. *Materials Science Forum* **338 - 342**, 477 - 480 (2000).
129. Ha, S., Nuhfer, N.T., Rohrer, G.S., de Graef, M. & Skowronski, M. Origin of domain structure in hexagonal silicon carbide boules grown by the physical vapor transport method. *Journal of Crystal Growth* **220**, 308 - 315 (2000).
130. Ha, S., Rohrer, G.S., Skowronski, M., Heydemann, V.D. & Snyder, D.W. Plastic Deformation and Residual Stresses in SiC Boules Grown by PVT. *Materials Science Forum* **338 - 342**, 67 - 70 (2000).
131. Tairov, Y.M. & Tsvetkov, V.F. Investigation of growth processes of ingots of silicon carbide single crystals. *Journal of Crystal Growth* **43**, 209 - 212 (1978).
132. Lely, J.A. Darstellung von Einkristallen von Siliciumcarbid und Beherrschung von Art und Menge der eingebauten Verunreinigungen. *Berichte der Deutschen Keramischen Gesellschaft* **32**, 229 - 250 (1955).
133. Ha, S., Nuhfer, N.T., Rohrer, G.S., De Graef, M. & Skowronski, M. Identification of Prismatic Slip Bands in 4H SiC Boules Grown by Physical Vapor Transport. *Journal of Electronic Materials* **29**, L5 - L8 (2000).

134. Iwata, H., Lindefelt, U., Öberg, S. & Briddon, P.R. Theoretical Calculation of Stacking Fault Energies in Silicon Carbide. *Materials Science Forum* **389 - 393**, 439 - 442 (2002).
135. Liu, J.Q., Skowronski, M., Hallin, C., Söderholm, R. & Lendenmann, H. Structure of recombination-induced stacking faults in high-voltage SiC p-n junctions. *Applied Physics Letters* **80**, 749 - 751 (2002).
136. Iwata, H., Lindefelt, U., Öberg, S. & Briddon, P.R. Localized electronic states around stacking faults in silicon carbide. *Physical Review B* **65**, 033203-1 - 033203-4 (2001).
137. Eckstein, R. Universität Erlangen-Nürnberg (1998).
138. Nishino, S., Higashino, T., Tanaka, T. & Saraie, J. Growth mechanism and defects in SiC prepared by sublimation method. *Journal of Crystal Growth* **147**, 339 - 342 (1995).
139. Heydemann, V.D., Rohrer, G.S., Sanchez, E.K. & Skowronski, M. The structural evolution of Seed Surfaces during the initial stages of Physical Vapor Transport SiC Growth. *Materials Science Forum* **264 - 268**, 37 - 40 (1998).
140. Anthony, T.R. & Cline, H.E. Thermal Migration of Liquid Droplets through Solids. *Journal of Applied Physics* **42**, 3380 - 3387 (1971).
141. Sanchez, E.K. et al. Formation of thermal decomposition cavities in physical vapor transport of silicon carbide. *Journal of Electronic Materials* **29**, 347 - 352 (2000).
142. Knippenberg, W.F. Growth phenomena in silicon carbide. *Philips journal of research* **18**, 161 - 274 (1963).
143. Okojie, R.S. et al. Observation of 4H-SiC to 3C-SiC polytypic transformation during oxidation. *Applied Physics Letters* **79**, 3056 - 3058 (2001).
144. Powell, J.A., Larkin, D.J. & Trunek, A.J. Gaseous Etching for Characterization of Structural Defects in Silicon Carbide single crystals. *Materials Science Forum* **264 - 268**, 421 - 424 (1998).
145. Vlaskina, S.I. & Shin, D.H. 6H to 3C Polytype Transformation in Silicon Carbide. *Japanese Journal of Applied Physics* **38**, L27 - L29 (1999).
146. Pirouz, P. Polytypic Transformation in SiC. *Solid State Phenomena* **56**, 107 - 132 (1997).
147. Pirouz, P. Polytypic transformations in SiC: The role of TEM. *Ultramicroscopy* **51**, 189 - 214 (1997).
148. Kordina, O. et al. Growth of SiC by "Hot-Wall" CVD and HTCVD. *Physica Status Solidi (B)* **202**, 321 - 334 (1997).
149. Inomata, Y. Synthesis of inclusion-free SiC single crystals. *Journal of Crystal Growth* **12**, 57 - 60 (1972).
150. Guinel, M.J.-F. & Norton, M.G. Oxidation of silicon carbide and the formation of silica polymorphs. *Journal of Materials Research* **21**, 2550 - 2563 (2006).
151. Kraft, T., Nickel, K.G. & Gogotsi, Y.G. Hydrothermal degradation of chemical vapour deposited SiC fibres. *Journal of Materials Science* **33**, 4357 - 4364 (1998).
152. Lamkin, M.A., Riley, F.L. & Fordham, R.J. Oxygen Mobility in Silicon Dioxide and Silicate Glasses: A Review. *Journal of the European Ceramic Society* **10**, 347 - 367 (1992).
153. Wenk, H.-R. & Bulakh, A. *Minerals: Their constitution and origin*, 646 (Cambridge University Press, 2004).
154. Graetsch, H. & Flörke, O.W. X-ray powder diffraction patterns and phase relationship of tridymite modifications. *Zeitschrift für Kristallographie* **195**, 31 - 48 (1991).
155. Flörke, O.W. & Nukui, A. Strukturelle Pathologie von Tridymiten. *Neues Jahrbuch für Mineralogie* **158**, 175 - 182 (1988).
156. Keskar, N.R. & Chelikowsky, J.R. Structural properties of nine silica polymorphs. *Physical Review B* **46**, 1 - 13 (1992).
157. Kihara, K. Thermal change in unit-cell dimensions, and a hexagonal structure of tridymite. *Zeitschrift für Kristallographie* **148**, 237 - 253 (1978).
158. Kihara, K., Matsumoto, T. & Imamura, M. High-order thermal-motion tensor analyses of tridymite. *Zeitschrift für Kristallographie* **177**, 39 - 52 (1986).
159. Strunz, H. & Nickel, E.H. *Strunz Mineralogical Tables*, 870 (Schweizerbart'sche Verlagsbuchhandlung, Stuttgart, 2001).
160. Flörke, O.W. Die Modifikationen von SiO₂. *Fortschritte der Mineralogie* **44**, 181 - 230 (1967).
161. Heaney, P.J., Prewitt, C.T. & Gibbs, G.V. *Silica. Physical Behavior, Geochemistry and Materials Applications.*, 606 (Mineralogical Society of America, Washington, DC, 1994).
162. Irene, E.A. Models for the oxidation of silicon. *Critical Reviews in Solid State and Materials Science* **14**, 175 - 223 (1988).
163. Zachariasen, W.H. The atomic arrangement in glass. *Journal of the American Chemical Society* **54**, 3841 - 3851 (1932).
164. Ebi, R. Universität Karlsruhe (1973).
165. Bakos, T. Vanderbilt University (2003).
166. Garofalini, S.H. & Miller, A.D. Kinetics of Tridymite Formation. *Journal of Crystal Growth* **78**, 85 - 96 (1986).
167. Hatch, D.M. & Ghose, S. The alpha - beta Phase Transition in Cristobalite, SiO₂. *Physics and Chemistry of Minerals* **17**, 554 - 562 (1991).
168. Narushima, T., Goto, A., Hirai, T. & Iguchi, Y. High-Temperature Oxidation of Silicon Carbide and Silicon Nitride. *Materials Transactions* **38**, 821 - 835 (1997).
169. Maeda, M., Nakamura, K., Ohkubo, T. & Ishizuka, T. Oxidation Behavior of Silicon Carbide Under Cyclic and Static Conditions. *Ceramics International* **15**, 1 - 6 (1989).

170. Kihara, K. An orthorhombic superstructure of tridymite existing between about 105 and 180°C. *Zeitschrift für Kristallographie* **146**, 185 - 203 (1977).
171. Smith, D.K. Opal, cristobalite, and tridymite: Noncrystallinity versus crystallinity, nomenclature of the silica minerals and bibliography. *Powder Diffraction* **13**, 2 - 19 (1998).
172. Graetsch, H. Characterization of the high-temperature modifications of incommensurate tridymite L3-TO (MX-1) from 25 to 250°C. *American Mineralogist* **83**, 872 - 880 (1998).
173. Nukui, A. & Nakazawa, H. Polymorphism in Tridymite. *Journal of the Mineralogical Society of Japan* **14**, 364 - 386 (1980).
174. Dollase, W.A. & Baur, W. The superstructure of meteoritic low tridymite solved by computer simulation. *American Mineralogist* **61**, 971 - 978 (1976).
175. Kato, K. & Nukui, A. Die Kristallstruktur des monoklinen Tief-Tridymits. *Acta Crystallographica* **B32**, 2486 - 2491 (1976).
176. Hoffmann, W., Kockmeyer, M., Löns, J. & Vach, C. The Transformation of Monoclinic Low-Tridymite MC to a Phase with an Incommensurate Superstructure. *Fortschritte der Mineralogie* **31**, 96 - 98 (1983).
177. Hill, V.G. & Roy, R. Silica Structure Studies. VI. On Tridymites. *Transactions of the British Ceramic Society* **57**, 496 - 510 (1958).
178. Löns, J. & Hoffmann, W. Zur Kristallstruktur der inkommensurablen Raumtemperaturphase des Tridymits. *Zeitschrift für Kristallographie* **178**, 141 - 143 (1987).
179. Starke, U. Atomic Structure of SiC Surfaces. in *Silicon Carbide. Major Recent Advances*. (eds. Choyke, J.W., Matsunami, H. & Pensl, G.) 281 - 316 (Springer-Verlag, Berlin, 2004).
180. Hollering, M. et al. Electronic and atomic structures of the 6H-SiC (000-1) surface studied by ARPES, LEED, and XPS. *Physical Review B* **58**, 4992 - 5000 (1998).
181. Starke, U. Atomic Structure of Hexagonal SiC Surfaces. *Physica Status Solidi (B)* **202**, 475 - 499 (1997).
182. Nakajima, A., Yokoya, H., Furukawa, Y. & Yonezu, H. Step control of vicinal 6H-SiC(0001) surface by H₂ etching. *Journal of Applied Physics* **97**, 104919-1 - 104919-5 (2005).
183. Christiansen, S., Albrecht, M., Strunk, H.P. & Heibig, R. Anisotropic oxidation of silicon carbide. *Diamond and Related Materials* **6**, 1467 - 1471 (1997).
184. Kimoto, T., Itoh, H. & Matsunami, H. Step bunching in chemical vapor deposition of 6H- and 4H-SiC on vicinal SiC(0001) faces. *Applied Physics Letters* **66**, 3645 - 3647 (1995).
185. Kimoto, T., Itoh, H. & Matsunami, H. Step-Controlled Epitaxial Growth of High-Quality SiC Layers. *Physica Status Solidi (B)* **202**, 247 - 262 (1997).
186. Song, Y., Dhar, S., Feldman, L.C., Chung, G. & Williams, J.R. Modified Deal Grove model for the thermal oxidation of silicon carbide. *Journal of Applied Physics* **95**, 4953 - 4957 (2004).
187. Yano, H. et al. High channel mobility in inversion layers of 4H-SiC MOSFETs by utilizing (11-20) face. *IEEE Electron Device Letters* **20**, 611 - 613 (1999).
188. Ueno, K. & Seki, Y. Orientation dependence of thermal oxidation rates in 6H-SiC. *Institute of Physics Conference Series* **142**, 629 - 632 (1996).
189. Ueno, K. Orientation dependence of the oxidation of SiC surfaces. *Physica Status Solidi (A)* **162**, 299 - 304 (1997).
190. Pollmann, J., Krüger, P. & Sabisch, M. Atomic and Electronic Structure of SiC surfaces from ab-initio Calculations. *Physica Status Solidi (B)* **202**, 421 - 445 (1997).
191. Bermudez, V.M. Structure and Properties of Cubic Silicon Carbide (100) Surfaces: A Review. *Physica Status Solidi (B)* **202**, 447 - 473 (1997).
192. Starke, U., Bernhardt, J., Franke, M., Schardt, J. & Heinz, K. Structure and morphology of SiC surfaces studied by LEED, AES, HREELS and STM. *Diamond and Related Materials* **6**, 1349 - 1352 (1997).
193. Starke, U. et al. The (0001)-surface of 6H-SiC: morphology, composition and structure. *Applied Surface Science* **89**, 175 - 185 (1995).
194. Schardt, J. et al. LEED structure determination of hexagonal α -SiC surfaces. *Surface Science* **337**, 232 - 242 (1995).
195. Tsuchida, H., Kamata, I. & Izumi, K. Chemical states of crystalline silicon carbide surfaces. *Japanese Journal of Applied Physics* **34**, 6003 - 6007 (1995).
196. Sabisch, M., Krüger, P., Mazur, A. & Pollmann, J. Structure of 6H-SiC(0001) surfaces from ab-initio calculations. *Surface Review and Letters* **5**, 199 - 205 (1998).
197. Sabisch, M., Krüger, P. & Pollmann, J. Ab initio calculations of structural and electronic properties of 6H-SiC(0001) surfaces. *Physical Review B* **55**, 10561 - 10570 (1997).
198. Pearson, E., Takai, T., Halicioglu, T. & Tiller, W.A. Computer modeling of Si and SiC surfaces and surface processes relevant to crystal growth from the vapor. *Journal of Crystal Growth* **70**, 33 - 40 (1984).
199. Sabisch, M., Krüger, P., Mazur, A., Rohlfing, M. & Pollmann, J. First-principles calculations of β -SiC(001) surfaces. *Physical Review B* **53**, 13121 - 13132 (1996).
200. Kern, W. & Puotinen, D.A. Cleaning Solutions Based on Hydrogen Peroxide for use in Silicon Semiconductor Technology. *RCA Review* **31**, 187 - 206 (1970).
201. Starke, U., Schardt, J. & Franke, M. Morphology, bond saturation and reconstruction of hexagonal SiC surfaces. *Applied Physics A* **65**, 587 - 596 (1997).

202. Owman, F., Hallin, C., Martensson, P. & Janzen, E. Removal of polishing-induced damage from 6H-SiC(0001) substrates by hydrogen etching. *Journal of Crystal Growth* **167**, 391 - 395 (1996).
203. Soukiassian, P. & Enriquez, H. Atomic scale control and understanding of cubic silicon carbide surface reconstructions, nanostructures and nanochemistry. *Journal of Physics: Condensed Matter* **16**, S1611 - S1658 (2004).
204. Bernhardt, J., Nerdling, M., Starke, U. & Heinz, K. Stable surface reconstructions on 6H-SiC(000-1). *Materials Science and Engineering B* **B61-62**, 207-211 (1999).
205. Bermudez, V.M. Photoemission study of oxygen adsorption on (001) silicon carbide surfaces. *Journal of Applied Physics* **66**, 6084 - 6092 (1989).
206. Kaplan, R. Surface Structure and Composition of β - and 6H-SiC. *Surface Science* **215**, 111 - 134 (1989).
207. Tsukamoto, K. et al. Annealing effect on surfaces of 4H(6H)-SiC(0001)Si face. *Applied Surface Science* **113 / 114**, 467 - 471 (1997).
208. Kulakov, M.A., Henn, G. & Bullemer, B. SiC(0001)3x3-Si surface reconstruction - a new insight with a STM. *Surface Science* **346**, 49 - 54 (1996).
209. Li, L. & Tsong, I.S.T. Atomic structures of 6H-SiC(0001) and (000-1) surfaces. *Surface Science* **351**, 141 - 148 (1996).
210. Reuter, K. et al. Holographic Image Reconstruction from Electron Diffraction Intensities of Ordered Superstructures. *Physical Review B* **79**, 4818 - 4821 (1997).
211. Reuter, K., Schardt, J., Bernhardt, J., Wedler, H. & Heinz, K. LEED holography applied to a complex superstructure: A direct view of the adatom cluster on SiC(111)-(3x3). *Physical Review B* **58**, 10806 - 10814 (1998).
212. Badziag, P. Energetics of the α -SiC(0001)-(3x3) surface reconstruction. *Surface Science* **402 - 402**, 822 - 826 (1998).
213. Voegeli, W. et al. Structure of the SiC (0001) 3x3 reconstruction studied by surface X-ray diffraction. *Applied Surface Science* **252**, 5259 - 5262 (2006).
214. Starke, U., Schardt, J., Bernhardt, J., Franke, M. & Heinz, K. Stacking Transformation from Hexagonal to Cubic SiC Induced by Surface Reconstruction: A Seed for Heterostructure Growth. *Physical Review Letters* **82**, 2107 - 2110 (1999).
215. Starke, U., Bernhardt, J., Schardt, J., Seubert, A. & Heinz, K. Stacking Rearrangement on SiC Surfaces: A Possible Seed for Polytipe Heterostructure Growth. *Materials Science Forum* **338 - 342**, 341 - 344 (2000).
216. Righi, M.C. et al. Surface-induced stacking transition at SiC(0001) *Physical Review B* **66**, 045320-1 - 045320-7 (2002).
217. Grossner, U., Fissel, A., Furthmüller, J., Richter, W. & Bechstedt, F. Interplay of Surface Structures, Bond Stacking and Heteropolytypic Growth of SiC. *Materials Science Forum* **353 - 356**, 211 - 214 (2001).
218. Starke, U. Surface Reconstruction on SiC(0001) and SiC(000-1): Atomic Structure and Potential Application for Oxidation, Stacking and Growth. *Materials Science Forum* **353 - 356**, 205 - 210 (2001).
219. Bermudez, V.M. Adsorption and co-adsorption of boron and oxygen on ordered alpha-SiC surfaces. *Applied Surface Science* **84**, 45 - 63 (1995).
220. Johansson, L.I., Owman, F. & Martensson, P. High-resolution core-level study of 6H-SiC(0001). *Physical Review B* **53**, 13793 - 13802 (1996).
221. Starke, U., Bernhardt, J., Schardt, J. & Heinz, K. SiC Surface Reconstruction: Relevancy of Atomic Structure for Growth Technology. *Surface Review and Letters* **6**, 1129 - 1141 (1999).
222. Coati, A. et al. ($\sqrt{3}\times\sqrt{3}$) R30° reconstruction of the 6H-SiC (0001) surface: A simple T₄ Si adatom structure solved by grazing-incidence x-ray diffraction. *Physical Review B* **59**, 12224 - 12227 (1998).
223. Furthmüller, J., Bechstedt, F., Husken, H., Schröter, B. & Richter, W. Si-rich SiC(111)/(0001)3x3 and $\sqrt{3}\times\sqrt{3}$ surfaces: A Mott-Hubbard picture *Physical Review B* **58**, 13712 - 13716 (1998).
224. Northrup, J.E. & Neugebauer, J. Theory of the adatom-induced reconstruction of the SiC(0001) $\sqrt{3}\times\sqrt{3}$ surface. *Physical Review B* **52**, R17001 - T17004 (1995).
225. Johansson, L.I., Owman, F. & Martensson, P. Surface state on the SiC(0001)-($\sqrt{3}\times\sqrt{3}$) surface. *Surface Science* **360**, L478 - L482 (1996).
226. Themlin, J.-M., Forbeaux, I., Vanglais, V., Belkhir, H. & Debever, J.-M. Unoccupied surface state on the ($\sqrt{3}\times\sqrt{3}$) R30° of 6H-SiC(0001). *Europhysics Letters* **36**, 61 - 66 (1997).
227. Benesch, C., Fartmann, M. & Merz, H. k-resolved inverse photoemission of four different 6H-SiC (0001) surfaces. *Physical Review B* **64**, 205314 - 205324 (2001).
228. Tautz, F.S., Sloboshanin, S., Starke, U. & Schaefer, J.A. Reassessment of core-level photoemission spectra of reconstructed SiC(0001) surfaces. *Surface Science* **470**, L25 - L31 (2001).
229. Bernhardt, J., Schardt, J., Starke, U. & Heinz, K. Epitaxially ideal oxide-semiconductor interfaces: Silicate adlayers on hexagonal (0001) and (000-1) SiC surfaces. *Applied Physics Letters* **74**, 1084 - 1086 (1999).
230. Starke, U. et al. Novel Reconstruction Mechanism for Dangling-Bond Minimization: Combined Method Surface Structure Determination of SiC(111)-(3x3). *Physical Review Letters* **80**, 758 - 761 (1998).
231. Sieber, N., Hollering, M., Ristein, J. & Ley, L. Photoemission Study of the Silicate Adlayer Reconstruction on Si-terminated 6H-SiC (0001). *Materials Science Forum* **338 - 342**, 391 - 394 (2000).

232. Sieber, N. et al. Electronic and chemical passivation of hexagonal 6H-SiC surfaces by hydrogen termination. *Applied Physics Letters* **78**, 1216 - 1218 (2001).
233. Hofmann, U., Endell, K. & Wilm, D. Röntgenographische und kolloidchemische Untersuchungen über Ton. *Analytical Chemistry* **30**, 539 - 547 (1934).
234. Rideal, E.K. Polymer and condensation reactions. *Transactions of the Faraday Society* **32**, 3 - 10 (1936).
235. Kiselev, A.V. The structure of silicic acid gels. *Kolloidnyi Zhurnal* **2**, 17 - 26 (1936).
236. Carman, P.C. Constitution of colloidal silica. *Transactions of the Faraday Society* **36**, 964 - 973 (1940).
237. Iler, R.K. *The chemistry of silica*, 896 (John Wiley & Sons, New York, 1979).
238. Zhuravlev, L.T. The surface chemistry of amorphous silica. Zhuravlev model. *Colloids and Surfaces A: Physicochemical and Engineering Aspects* **173**, 1 - 38 (2000).
239. Giordano, L., Sushko, P.V., Pacchioni, G. & Shluger, A.L. Optical and EPR properties of point defects at a crystalline silica surface: Ab initio embedded-cluster calculations. *Physical Review B* **75**, 024109-1 - 024109-9 (2007).
240. Bobyshev, A.A. & Radtsig, V.A. Silanone groups -Si(O)- on the surface of mechanically activated silicon dioxide. *Kinetika i Kataliz* **29**, 638 - 647 (1988).
241. Magruder, R.H., III, Stesmans, A., Clémer, K., Weeks, R.A. & Weller, R.A. Origins of optical absorption between 4.8 and 4.9 eV in silica implanted with Si and with O ions. *Journal of Non-Crystalline Solids* **352**, 3027 - 3034 (2006).
242. Magruder, R.H., III, Stesmans, A., Clémer, K., Weeks, R.A. & Weller, R.A. Sources of optical absorption between 5.7 and 5.9 eV in silica implanted with Si and O. *Journal of Applied Physics* **100**, 033517-1 - 033517-8 (2006).
243. Skuja, L. The origin of the intrinsic 1.9 eV luminescence band in glassy SiO₂. *Journal of Non-Crystalline Solids* **179**, 51 - 69 (1994).
244. Skuja, L., Suzuki, T. & Tanimura, K. Site-selective laser-spectroscopy studies of the intrinsic 1.9-eV luminescence center in glassy SiO₂. *Physical Review B* **52**, 15208 - 15216 (1995).
245. Skuja, L., Tanimura, K. & Itoh, N. Correlation between the radiation-induced intrinsic 4.8 eV optical absorption and 1.9 eV photoluminescence bands in glassy SiO₂. *Journal of Applied Physics* **80**, 3518 - 3525 (1996).
246. Skuja, L. Optically active oxygen-deficiency-related centers in amorphous silicon dioxide. *Journal of Non-Crystalline Solids* **239**, 16 - 48 (1998).
247. Radtsig, V.A. & Senchenya, I.N. Hydrogenation of the silanone groups (≡Si-O)Si=O. Experimental and quantum-chemical studies. *Russian Chemical Bulletin* **45**, 1849 - 1856 (1996).
248. Fowkes, F.M. & Burgess, T.E. Impurity Concentration at "Clean" Oxide Surfaces. in *Clean Surfaces: Their Preparation and Characterization for Interfacial Studies* (ed. Goldfinger, G.) 351 - 360 (Marcel Dekker, Inc., New York, 1970).
249. Halter, W.E. & Mysen, B.O. Melt speciation in the system Na₂O-SiO₂. *Chemical Geology* **213**, 115 - 123 (2004).
250. Larkin, D.J., Neudeck, P.G., Powell, J.A. & Matus, L.G. Site-competition epitaxy for superior siliconcarbide electronics. *Applied Physics Letters* **65**, 1659 - 1661 (1994).
251. Tan, J., Das, M.K., Cooper, J.A., Jr. & Melloch, M.R. Metal-oxide-semiconductor capacitors formed by oxidation of polycrystalline silicon on SiC. *Applied Physics Letters* **70**, 2280 - 2281 (1997).
252. Onda, S., Kumar, R. & Hara, K. SiC integrated MOSFETs. *Physica Status Solidi (A)* **162**, 369 - 388 (1997).
253. Iwata, H.P., Lindefelt, U., Öberg, S. & Briddon, P.R. Stacking faults in silicon carbide. *Physica B* **340 - 342**, 165 - 170 (2003).
254. Konstantinov, A.O., Wahab, Q., Nordell, N. & Lindefelt, U. Ionization rates and critical fields in 4H silicon carbide. *Applied Physics Letters* **71**, 90 - 92 (1997).
255. Afanas'ev, V.V., Ciobanu, F., Dimitrijević, S., Pensl, G. & Stesmans, A. SiC/SiO₂ Interface States: Properties and Models. *Materials Science Forum* **483 - 485**, 563 - 568 (2005).
256. Vathulya, V.R., Wang, D.N. & White, M.H. On the correlation between the carbon content and the electrical quality of thermally grown oxides on p-type 6H-Silicon carbide. *Applied Physics Letters* **73**, 2161 - 2163 (1998).
257. Alok, D., McLarty, P.K. & Baliga, B.J. Electrical properties of thermal oxide grown using dry oxidation on p-type 6H-silicon carbide. *Applied Physics Letters* **65**, 2177 - 2178 (1994).
258. Shinohara, M., Yamanaka, M., Misawa, S., Okumura, H. & Yoshida, S. C-V Characteristics of MOS Structures Fabricated of Al-Doped p-Type 3C-SiC Epilayers Grown on Si by Chemical Vapor Deposition *Japanese Journal of Applied Physics* **30**, 240 - 243 (1991).
259. Cooper, J.A., Jr. Advances in SiC MOS Technology. *Physica Status Solidi (A)* **162**, 305 (1997).
260. Palmour, J.W., Davis, R.F., Kong, H.S., Corcoran, S.F. & Griffis, D.P. Dopant Redistribution during Thermal Oxidation of Monocrystalline Beta-SiC Thin Films. *Journal of the Electrochemical Society* **136**, 502 - 507 (1989).
261. Shenoy, J.N. et al. Characterization and Optimization of the SiO₂ / SiC Metal-Oxide Semiconductor Interface. *Journal of Electronic Materials* **24**, 303 - 309 (1995).
262. Afanas'ev, V.V., Bassler, M., Pensl, G. & Schulz, M. Intrinsic SiC/SiO₂ Interface States. *Physica Status Solidi (A)* **162**, 321 - 337 (1997).

263. Bassler, M., Afanas'ev, V.V. & Pensl, G. Interface state density at implanted 6H SiC/SiO₂ MOS Structures. *Materials Science Forum* **264 - 268**, 861 - 864 (1998).
264. Afanas'ev, V.V., Ciobanu, F., Dimitrijević, S., Pensl, G. & Stesmans, A. Band alignment and defect states at SiC/oxide interfaces. *Journal of Physics: Condensed Matter* **16**, S1839 - S1856 (2004).
265. Zetterling, C.-M. & Östling, M. Redistribution of aluminum during thermal oxidation of 6H silicon carbide. in *5th SiC and Related Materials Conference* (Washington, D.C., 1993).
266. Brown, D.M. et al. SiC MOS Interface Characteristics. *IEEE Transactions on electron devices* **41**, 618 - 620 (1994).
267. Lipkin, L.A. & Palmour, J.W. Improved Oxidation Procedures for Reduced SiO₂/SiC Defects. *Journal of Electronic Materials* **25**, 909 - 915 (1996).
268. Ouisse, T., Bécourt, N., Jaussaud, C. & Templier, F. Low-frequency, high-temperature conductance and capacitance measurements on metal-oxide-silicon carbide capacitors. *Journal of Applied Physics* **75**, 604 - 607 (1994).
269. Afanas'ev, V.V. SiC/SiO₂ interface defects. in *Defects in SiO₂ and Related Dielectrics: Science and Technology* (eds. Pacchioni, G., Skuja, L. & Griscom, D.L.) 581 - 597 (Kluwer Academic Publishers, Dordrecht, 2000).
270. Palmour, J.W. Method of obtaining high quality silicon dioxide passivation on silicon carbide and resulting passivated structures (Cree Research, Inc., United States of America, 1995).
271. Zetterling, C.-M. KTH, Royal Institute of Technology (1997).
272. Buczko, R., Pennycook, S.J. & Pantelides, S.T. Bonding Arrangements at the Si-SiO₂ and SiC-SiO₂ interfaces and a possible origin of their contrasting properties. *Physical Review Letters* **84**, 943 - 946 (2000).
273. Heald, S.M., Jayanetti, J.K.D., Bright, A.A. & Rubloff, G.W. X-ray reflectivity study of SiO₂ on Si. *Vacuum Science & Technology A* **8**, 2046 - 2048 (1990).
274. Hornetz, B., Michel, H.-J. & Halbritter, J. ARXPS studies of SiO₂-SiC interfaces and oxidation of 6H SiC single crystal Si-(001) and C-(00-1) surfaces. *Journal of Materials Research* **6**, 3088 - 3094 (1994).
275. Tsuchida, H., Kamata, I. & Izumi, K. Structure of Thermally Grown SiO₂ on Crystalline 6H-SiC. *Materials Research Society Symposium Proceedings* **446**, 273 - 278 (1996).
276. Önnéby, C. & Pantano, C.G. Silicon oxycarbide on SiC surfaces and at the SiC/SiO₂ interface. *Vacuum Science & Technology A* **15**, 1597 - 1602 (1997).
277. Li, H.-F. et al. Investigation of nitric oxide and Ar annealed SiO₂/SiC interfaces by x-ray photoelectron spectroscopy. *Journal of Applied Physics* **86**, 4316 - 4321 (1999).
278. Tanner, P. et al. SIMS Analysis of Nitrided Oxides Grown on 4H-SiC. *Journal of Electronic Materials* **28**, 109 - 111 (1999).
279. Imai, S., Fujimoto, M., Asuha, Takahashi, M. & Kobayashi, H. Formation of atomically smooth SiO₂/SiC interfaces at ~ 120°C by use of nitric acid oxidation method. *Surface Science* **600**, 547 - 550 (2006).
280. Silly, M.G. et al. Initial oxide/SiC interface formation on C-terminated beta-SiC (100) c(2x2) and graphitic C-rich beta-SiC (100) 1x1 surfaces. *J. Vac. Sci. Technol. B* **22**, 2226 - 2232 (2004).
281. Pantelides, S.T. et al. Bonding, Defects, and Defect Dynamics in the SiC-SiO₂ System. *Materials Research Society Symposium Proceedings* **640**, H3.3.1 - H3.3.9 (2001).
282. Hoshino, Y. et al. Initial oxidation of 6H-SiC(0001)-√3 x √3 surface studied by ion scattering combined with photoemission induced by synchrotron-radiation-light. *Surface Science* **505**, 234 - 242 (2002).
283. Spear, K.E., Tressler, R.E., Zheng, Z. & Du, H. Oxidation of Silicon Carbide Single Crystals and CVD Silicon Nitride. in *Corrosion and corrosive degradation of ceramics*, Vol. 10 (eds. Tressler, R.E. & McNallan, M.J.) 1 - 19 (The American Ceramic Society, Ohio, 1990).
284. Spear, K.E., Tressler, R.E., Zheng, Z. & Du, H. Oxidation of silicon carbide single crystals and CVD silicon nitride. *Ceramic Transactions* **10**, 1 - 18 (1990).
285. Maekawa, M. et al. Structural defects in SiO₂/SiC interface probed by a slow positron beam. *Applied Surface Science* **244**, 322 - 325 (2005).
286. Maekawa, M. et al. Structure of SiO₂/4H-SiC interface probed by positron annihilation spectroscopy. *Physical Review B* **73**, 014111-1 - 014111-9 (2006).
287. Jernigan, G.G., Stahlbush, R.E., Das, M.K., Cooper, J.A., Jr. & Lipkin, L.A. Interfacial differences between SiO₂ grown on 6H-SiC and on Si(100). *Applied Physics Letters* **74**, 1448 - 1450 (1999).
288. Chang, K.-C., Porter, L.M., Bentley, J., Lu, C.-Y. & Cooper, J., Jr. Electrical, structural, and chemical analysis of silicon carbide-based metal-oxide-semiconductor field-effect-transistors. *Journal of Applied Physics* **95**, 8252 - 8257 (2004).
289. di Ventura, M. & Pantelides, S.T. Atomic-Scale Mechanisms of Oxygen Precipitation and Thin-Film Oxidation of SiC. *Physical Review Letters* **83**, 1624 - 1627 (1999).
290. Devynck, F., Giustino, F. & Pasquarello, A. Abrupt model interface for the 4H(1000)SiC-SiO₂ interface. *Microelectronic Engineering* **80**, 38 - 41 (2005).
291. Radtke, C., Baumvol, I.J.R., Ferrera, B.C. & Stedile, F.C. The Role of Formation and Dissolution of C Clusters on the Oxygen Incorporation during Dry Thermal Oxidation of 6H-SiC. *Materials Science Forum* **483 - 485**, 657 - 600 (2005).
292. Vickridge, I.C. et al. Oxygen isotopic exchange occurring during dry thermal oxidation of 6H SiC. *Nuclear Instruments and Methods in Physics Research B* **190**, 574 - 578 (2002).

293. Vickridge, I.C., Ganem, J.J., Trimaille, I. & Cantin, J.-L. The contribution of stable isotopic tracing, narrow nuclear resonance depth profiling, and a simple stochastic theory of charged particle energy loss to studies of the dry thermal oxidation of SiC. *Nuclear Instruments and Methods in Physics Research B* **232**, 272 - 279 (2005).
294. Ohnuma, T., Tsuchida, H. & Jikimoto, T. Interface states in abrupt SiO₂/4H- and 6H-SiC(0001) from first-principles: Effects of Si dangling bonds, C dangling bonds and C clusters. *Materials Science Forum* **457 - 460**, 1297 - 1300 (2004).
295. Ohnuma, T., Tsuchida, H., Jikimoto, T., Miyashita, A. & Yoshikawa, M. Interface states at the SiO₂/4H-SiC(0001) interface from first-principles: Effects of Si-Si Bonds and of Nitrogen Atom Termination. *Materials Science Forum* **483 - 485**, 573 - 576 (2005).
296. Yano, H., Hirao, T., Kimoto, T., Matsunami, H. & Shiomi, H. Interface properties in metal-oxide-semiconductor structure on n-type 4H-SiC (03-38). *Applied Physics Letters* **81**, 4772 - 4774 (2002).
297. Yano, H., Kimoto, T. & Matsunami, H. Interface States of SiO₂/SiC on (11-20) and (0001) Si Faces. *Materials Science Forum* **353 - 356**, 627 - 630 (2001).
298. Simon, L., Kubler, L., Ermolieff, A. & Billon, T. X-ray spectroscopy of the oxidation of 6H-SiC(0001). *Physical Review B* **60**, 5673 - 5678 (1999).
299. Amy, F., Soukiasian, P., Hwu, Y.-K. & Brylinski, C. Si-rich 6H- and 4H-SiC(0001) 3x3 surface oxidation and initial SiO₂/SiC interface formation from 25 - 650°C. *Physical Review B* **65**, 165323-1 - 165323-11 (2002).
300. Virojanadara, C. & Johansson, L.I. Interfacial investigation of in situ oxidation of 4H-SiC. *Surface Science* **472**, L145 - L149 (2001).
301. Amy, F. et al. Atomic Scale Oxidation of a Complex System: O₂/α-SiC(0001)-(3x3). *Physical Review B* **86**, 4342 - 4345 (2001).
302. Chang, K.C., Nuhfer, N.T., Porter, L.M. & Wahab, Q. High-carbon concentrations at the silicon dioxide-silicon carbide interface identified by electron energy loss spectroscopy. *Applied Physics Letters* **77**, 2186 - 2188 (2000).
303. Afanas'ev, V.V., Ciobanu, F., Pensl, G. & Stesmans, A. Contributions to the Density of Interface states in SiC MOS Structures. in *Silicon Carbide. Major Recent Advances*. (eds. Choyke, J.W., Matsunami, H. & Pensl, G.) 343 - 371 (Springer-Verlag, Berlin, 2004).
304. Radtke, C., Baumvol, I.J.R., Morais, J. & Stedile, F.C. Initial stages of SiC oxidation investigated by ion scattering and angle-resolved x-ray photoelectron spectroscopies. *Applied Physics Letters* **78**, 3601 - 3603 (2000).
305. Saks, N.S., Mani, S.S. & Agarwal, A.K. Interface trap profile near the band edges at the 4H-SiC/SiO₂ interface. *Applied Physics Letters* **76**, 2250 - 2252 (2000).
306. Chatty, K., Chow, T.P., Gutmann, R.J., Arnold, E. & Alok, D. Comparative Hall Measurements on Wet- and Dry-Oxidized 4H-SiC MOSFETs. *Journal of Electronic Materials* **31**, 356 - 360 (2002).
307. Chung, G.Y. et al. Effect of nitric oxide annealing on the interface trap densities near the band edges in the 4H polytype of silicon carbide. *Applied Physics Letters* **76**, 1713 - 1715 (2000).
308. Poindexter, E.H. MOS interface states: overview and physicochemical perspective. *Semiconductor Science and Technology* **4**, 961 - 969 (1989).
309. Buchanan, D.A., Marwick, A.D., diMaria, D.J. & Dori, L. Hot-electron-induced hydrogen redistribution and defect generation in metal-oxide-semiconductor capacitors. *Journal of Applied Physics* **76**, 3595 - 3608 (1994).
310. Afanas'ev, V.V. & Stesmans, A. Ionisation and trapping of hydrogen at SiO₂ interfaces. *Materials Science and Engineering B* **58**, 56 - 59 (1999).
311. Tsuchida, H., Kamata, I. & Izumi, K. Infrared spectroscopy of hydrides on the 6H-SiC surface. *Applied Physics Letters* **70**, 3072 - 3074 (1997).
312. Tsuchida, H., Kamata, I. & Izumi, K. Si-H Bonds on the 6H-SiC(0001) Surface after H₂ Annealing *Japanese Journal of Applied Physics* **36**, 699 - 702 (1997).
313. Campi, J. & Yan, F. Study of the interface state density and effective oxide charge in post-metallization annealed SiO₂/SiC structures. *IEEE Transactions on Electron Devices* **46**, 511 - 519 (1999).
314. Stesmans, A. Structural relaxation of Pb defects at the (111)Si-SiO₂ interface as a function of oxidation temperature: The Pb-generation-stress relationship. *Physical Review B* **48**, 2418 - 2435 (1993).
315. Cantin, J.L. et al. Identification of the Carbon Dangling Bond Center at the 4H-SiC/SiO₂ Interface by an EPR Study in Oxidized Porous SiC. *Physical Review Letters* **92**, 015502-1 - 015502-4 (2004).
316. Macfarlane, P.J. & Zvanut, M.E. Characterization of paramagnetic defect centers in three polytypes of dry heat treated, oxidized SiC. *Journal of Applied Physics* **88**, 4122 - 4127 (2000).
317. Afanas'ev, V.V. & Stesmans, A. Hole traps in oxide layers thermally grown on SiC. *Applied Physics Letters* **69**, 2252 - 2254 (1996).
318. Isoya, J., Kosugi, R., Fukuda, K. & Yamasaki, S. ESR Characterization of SiC Bulk Crystals and SiO₂/SiC Interface. *Materials Science Forum* **389 - 393**, 1025 - 1028 (2002).
319. Fukuda, K., Suzuki, S., Tanaka, T. & Arai, K. Reduction of interface-state density in 4H-SiC n-type metal-oxide-semiconductor structures using high-temperature hydrogen annealing. *Applied Physics Letters* **76**, 1585 - 1587 (2000).
320. Afanas'ev, V.V., Stesmans, A., Bassler, M., Pensl, G. & Schulz, M. Comment on 'Reduction of interface-state density in 4H-SiC n-type metal-oxide-semiconductor structures using high-temperature hydrogen anneal' [Appl. Phys. Lett. **78**, 4043 (2001)]. *Applied Physics Letters* **78**, 4043 - 4044 (2001).

321. Fukuda, K., Arai, K., Suzuki, A. & Tanaka, T. Response to "comment on 'reduction of interface-state density in 4H-SiC n-type metal-oxide-semiconductor structures using high-temperature hydrogen anneal'" [Appl. Phys. Lett. **78**, 4043 (2001)]. *Applied Physics Letters* **78**, 4045 (2001).
322. Uren, M.J., Stathis, J.H. & Cartier, E. Conductance measurements on Pb centers at the (111) Si:SiO₂ interface. *Journal of Applied Physics* **80**, 3915 - 3922 (1996).
323. Afanas'ev, V.V. & Stesmans, A. Analysis of near-interfacial SiO₂ traps using photon stimulated electron tunneling. *Microelectronic Engineering* **36**, 149 - 152 (1997).
324. Afanas'ev, V.V., Stesmans, A. & Harris, C.I. Observation of Carbon Clusters at the 4H-SiC/SiO₂ interface. *Materials Science Forum* **264 - 268**, 857 - 860 (1998).
325. Bassler, M., Pensl, G. & Afanas'ev, V.V. "Carbon cluster model" for electronic states at SiC/SiO₂ interfaces. *Diamond and Related Materials* **6**, 1472 - 1475 (1997).
326. Afanas'ev, V.V. et al. Elimination of SiC/SiO₂ interface states by preoxidation ultraviolet-ozone cleaning. *Applied Physics Letters* **68**, 2141 - 2143 (1996).
327. Murray, R.T. & Taylor, S. Oxide layers on the carbon face of 6H silicon carbide substrates. *Semiconductor Science and Technology* **15**, 992 - 995 (2000).
328. Soares, G.V. et al. Ion beam analysis of the SiO₂/SiC interface. *Nuclear Instruments and Methods in Physics Research B* **249**, 444 - 446 (2006).
329. Lu, C.-Y. et al. Effect of Process Variation and Ambient Temperature on Electron Mobility at the SiO₂/4H-SiC Interface. *IEEE Transactions on electron devices* **50**, 1582 - 1588 (2003).
330. Virojanadara, C., Glans, P.-A., Johansson, L.I., Eickhoff, T. & Drube, W. High energy photoemission investigations of SiO₂/SiC samples. *Applied Surface Science* **172**, 253 - 259 (2001).
331. Virojanadara, C. & Johansson, L.I. Oxidation studies of 4H-SiC(0001) and (000-1). *Surface Science* **505**, 358 - 366 (2002).
332. Virojanadara, C. & Johansson, L.I. Studies of oxidized hexagonal SiC surfaces and the SiC/SiO₂ interface using photoemission and synchrotron radiation. *Journal of Physics: Condensed Matter* **16**, S1783 - S1814 (2004).
333. Takahagi, T., Nagai, I., Ishitani, A., Kuroda, H. & Nagasawa, Y. The formation of hydrogen passivated silicon single-crystal surfaces using ultraviolet cleaning and HF etching. *Journal of Applied Physics* **64**, 3516 - 3521 (1988).
334. Li, H.-F., Dimitrijević, S., Harrison, H.B. & Sweatman, D. Interfacial characteristics of N₂O and NO nitrided SiO₂ grown on SiC by rapid thermal processing. *Applied Physics Letters* **70**, 2028 - 2030 (1997).
335. McDonald, K. et al. Characterization and modeling of the nitrogen passivation of interface traps in SiO₂/4H-SiC. *Journal of Applied Physics* **93**, 2719 - 2722 (2003).
336. McDonald, K. et al. Kinetics of NO nitridation in SiO₂/4H-SiC. *Journal of Applied Physics* **93**, 2257 - 2261 (2003).
337. Afanas'ev, V.V. et al. Mechanisms responsible for improvement of 4H-SiC/SiO₂ interface properties by nitridation. *Applied Physics Letters* **82**, 568 - 570 (2003).
338. McDonald, K. et al. Comparison of nitrogen incorporation in SiO₂/SiC and SiO₂/Si structures. *Applied Physics Letters* **76**, 568 - 570 (2000).
339. Dhar, S. et al. Effect of nitric oxide annealing on the interface trap density near the conduction band edge of 4H-SiC at the oxide/(11-20) 4H-SiC interface. *Applied Physics Letters* **84**, 1498 - 1500 (2004).
340. Dhar, S., Feldman, L.C., Wang, S., Isaacs-Smith, T. & Williams, J.R. Interface trap passivation for SiO₂/(000-1) C-terminated 4H-SiC. *Journal of Applied Physics* **98**, 014902-1 - 014902-5 (2005).
341. Jamet, P., Dimitrijević, S. & Tanner, P. Effects of nitridation in gate oxides grown on 4H-SiC. *Journal of Applied Physics* **90**, 5058 - 5063 (2001).
342. Fitzer, E. & Ebi, R. Kinetic Studies on the Oxidation of Silicon Carbide. in *Silicon Carbide* (eds. Marshall, K.L., Faust, T.W. & Ryan, C.E.) 320 - 328 (South Carolina University Press, Columbia, S.C., 1973).
343. Schumacher, C. *Oxidationsverhalten von Bor und Kohlenstoff beinhaltenden gesinterten Siliciumcarbid-Werkstoffen bei 1500°C*, 153 (Shaker Verlag, Aachen, 2001).
344. Wang, S., di Ventra, M., Kim, S.G. & Pantelides, S.T. Atomic-Scale Dynamics of the formation and dissolution of carbon clusters in SiO₂. *Physical Review Letters* **86**, 5946 (2001).
345. Shenoy, J.N., Cooper, J.A., Jr. & Melloch, M.R. Comparison of thermally oxidized metal-oxide-semiconductor interfaces on 4H and 6H polytypes of silicon carbide. *Applied Physics Letters* **68**, 803 - 806 (1996).
346. Afanas'ev, V.V., Stesmans, A. & Andersson, M.O. Electron states and microstructure of thin α-C:H layers. *Physical Review B* **54**, 10820 - 10826 (1996).
347. Robertson, J. Amorphous Carbon. *Advances in physics* **35**, 317 - 374 (1987).
348. Afanas'ev, V.V. & Stesmans, A. Interfacial Defects in SiO₂ Revealed by Photon Stimulated Tunneling of Electrons. *Physical Review Letters* **78**, 2437 - 2440 (1997).
349. Johansson, L.I., Virojanadara, C., Eickhoff, T. & Drube, W. Properties of the SiO₂/SiC interface investigated by angle resolved studies of the Si 2p and Si 1s levels and the Si KLL Auger transition. *Surface Science* **529**, 515 - 526 (2003).
350. Schmeißer, D., Batchelor, D.R., Mikalo, R.P., Hoffmann, P. & Lloyd-Spez, A. Oxide growth on SiC(0001) surfaces. *Applied Surface Science* **184**, 340 - 345 (2001).

351. Stein von Kamienski, E.G., Portheine, F., Stein, J., Gözl, A. & Kurz, H. Charge trapping in dry and wet oxides on N-type 6H-SiC studied by Fowler-Nordheim charge injection. *Journal of Applied Physics* **79**, 2529 - 2534 (1996).
352. di Ventura, M. Can we make the SiC-SiO₂ interface as good as the Si - SiO₂ interface? *Applied Physics Letters* **79**, 2402 - 2404 (2001).
353. Konstantinov, A.O., Wahab, Q., Hallin, C., Harris, C.I. & Pécz, B. Fast Generation-Recombination Channels due to epitaxial defects in SiC Metal-Oxide-Semiconductor Devices. *Materials Science Forum* **264 - 268**, 1025 - 1028 (1998).
354. Yano, H., Katafuchi, F., Kimoto, T. & Matsunami, H. Effects of Wet Oxidation / Anneal on Interface Properties of Thermally Oxidized SiO₂ / SiC MOS system and MOSFET's. *IEEE Transactions on electron devices* **46**, 504 - 510 (1999).
355. Aung, M.T.H. & Szmidi, J. The study of thermal oxidation on SiC surface. *Journal of Wide Bandgap Materials* **9**, 313 - 318 (2002).
356. Lipkin, L.A. & Palmour, J.W. Insulator Investigation on SiC for Improved Reliability. *IEEE Transactions on electron devices* **46**, 525 - 532 (1999).
357. Friedrichs, P., Burte, E.P. & Schörner, R. Dielectric strength of thermal oxides on 6H-SiC and 4H-SiC. *Applied Physics Letters* **65**, 1665 - 1667 (1994).
358. Tang, S.M., Berry, W.B., Kwor, R., Zeller, M.V. & Matus, L.G. High Frequency Capacitance-Voltage Characteristics of Thermally Grown SiO₂ Films on β -SiC. *Journal of the Electrochemical Society* **137**, 221 - 225 (1990).
359. Zaima, S., Onoda, K., Koide, Y. & Yasuda, Y. Effects of oxidation conditions on electrical properties of SiC-SiO₂ interfaces. *Journal of Applied Physics* **68**, 6304 - 6308 (1990).
360. Wittberg, T.N., Wang, P.S. & Hsu, S.M. Surface oxidation kinetics of SiC powders in wet and dry air studied by x-ray photoelectron spectroscopy and bremsstrahlung-excited Auger electron spectroscopy. *Surface and Interface Analysis* **35**, 773 - 778 (2003).
361. Doremus, R.H. Transport of oxygen in silicate glasses. *Journal of Non-Crystalline Solids* **349**, 242 - 247 (2004).
362. Chaudry, M.I. A Study of Native Oxides of α -SiC Using Auger Electron Spectroscopy. *Journal of Materials Research* **4**, 404 - 407 (1989).
363. Vickridge, I.C., Ganem, J.-J., Battistig, G. & Szilagy, E. Oxygen isotopic tracing study of the dry thermal oxidation of 6H SiC. *Nuclear Instruments and Methods in Physics Research B* **161 - 163**, 462 - 466 (2000).
364. Sreemany, M., Ghosh, T.B., Pai, B.C. & Chakraborty, M. XPS Studies on the Oxidation Behavior of SiC Particles. *Materials Research Bulletin* **33**, 189 - 199 (1998).
365. Swift, P. Adventitious Carbon - The Panacea for Energy Referencing? *Surface and Interface Analysis* **4**, 47 - 51 (1982).
366. Pultz, W.W. Oxidation of submicroscopic fibrous silicon carbide. *Journal of the American Ceramic Society* **50** / (8)(1967).
367. Ervin, G., Jr. Oxidation Behavior of Silicon Carbide. *Journal of the American Ceramic Society* **41**, 347 - 352 (1958).
368. Gugel, E., Hennicke, H.W. & Schuster, P. Zur Bildung der SiO₂-Schicht auf SiC. *Berichte der Deutschen Keramischen Gesellschaft* **46**, 481 - 485 (1969).
369. Gulbransen, E.A., Andrew, K.F. & Brassart, F.A. The oxidation of silicon carbide at 1150° to 1400°C and at 9x10⁻³ to 5x10⁻¹ torr oxygen pressure. *Journal of the Electrochemical Society* **113**, 1311 - 1314 (1966).
370. Suzuki, H. A Study of the Oxidation of Pure Silicon-carbide Powders. *Yogyo Kyokaishi* **65**, 88 - 93 (1957).
371. Weyhe, S. *Wägetechnik im Labor. Technologie und Anwendung*, 70 (verlag moderne industrie, Landsberg / Lech, 2001).
372. Goto, T. & Homma, H. High-temperature active/passive oxidation and bubble formation of CVD SiC in O₂ and CO₂ atmospheres. *Journal of the European Ceramic Society* **22**, 2749 - 2756 (2002).
373. Bruggeman, D.A.G. Berechnung verschiedener physikalischer Konstanten von heterogenen Substanzen. I. Dielektrizitätskonstanten und Leitfähigkeiten der Mischkörper aus isotropen Substanzen. *Annalen der Physik* **24**, 636 - 664 (1935).
374. Aspnes, D.E. Optical Properties of Thin Films. *Thin Solid Films* **89**, 249 - 262 (1982).
375. Sibieude, F., Rodriguez, J. & Clavaguera-Mora, M.T. Kinetics and crystallization studies by in situ x-ray diffraction of the oxidation of chemically vapour deposited SiC. *Thin Solid Films* **204**, 217 - 227 (1991).
376. Hodroj, A. et al. Density, thickness and composition measurements of TiO₂-SiO₂ thin films by coupling X-ray reflectometry, ellipsometry and electron probe microanalysis-X. *Applied Surface Science* **253**, 363 - 366 (2006).
377. Christiansen, K. & Helbig, R. Anisotropic oxidation of 6H-SiC. *Journal of Applied Physics* **79**, 3276 - 3281 (1996).
378. Ehrstein, J. et al. A comparison of Thickness values for very thin SiO₂ films by using ellipsometric, capacitance-voltage and HRTEM Measurements. *Journal of the Electrochemical Society* **153**, F12 - F19 (2006).
379. Seah, M.P. et al. Critical review of the current status of thickness measurements for ultrathin SiO₂ on Si part V: Results of a CCQM pilot study. *Surface and Interface Analysis* **36**, 1269 - 1303 (2004).
380. Hinze, J.W. & Graham, H.C. The Active Oxidation of Si and SiC in the Viscous Gas-Flow Regime. *Journal of the Electrochemical Society* **123**, 1066 - 1073 (1976).

381. Narushima, T., Goto, A., Iguchi, Y. & Hirai, T. High-Temperature Active Oxidation of Chemically Vapor-Deposited Silicon Carbide in an Ar-O₂ Atmosphere. *Journal of the American Ceramic Society* **74**, 2583 - 2586 (1991).
382. Nickel, K.G. The role of condensed silicon monoxide in the active-to-passive oxidation transition of silicon carbide. *Journal of the European Ceramic Society* **9**, 3 - 8 (1992).
383. Nickel, K.G. & Gogotsi, Y.G. Corrosion of Hard Materials. in *Handbook of Ceramic Hard Materials*, Vol. 1 (ed. Riedel, R.) 140 - 154 (Wiley-VCH Verlag, Weinheim, 2000).
384. Schneider, B., Guette, A., Naslain, R., Cataldi, M. & Costecalde, A. A theoretical and experimental approach to the active-to-passive transition in the oxidation of silicon carbide. *Journal of Materials Science* **33**, 535-547 (1998).
385. Pelissier, K., Chartier, T. & Laurent, J.M. Silicon Carbide Heating Elements. *Ceramics International* **24**, 371 - 377 (1998).
386. Zheng, Z., Tressler, R.E. & Spear, K.E. Oxidation of Single-Crystal Silicon Carbide. Part I. Experimental Studies. *Journal of the Electrochemical Society* **137**, 854 - 858 (1990).
387. Zheng, Z., Tressler, R.E. & Spear, K.E. Oxidation of Single-Crystal Silicon Carbide. Part II. Kinetic Model. *Journal of the Electrochemical Society* **137**, 2812 - 2816 (1990).
388. Powell, J.A. et al. Application of oxidation to the structural characterization of SiC epitaxial films. *Applied Physics Letters* **59**, 183 - 185 (1991).
389. Opila, E. Influence of Alumina Reaction Tube Impurities on the Oxidation of Chemically-Vapor-Deposited Silicon Carbide. *Journal of the American Ceramic Society* **78**, 1107 - 1110 (1995).
390. Schlichting, J. & Kriegesmann, J. Oxidationsverhalten von heißgepreßtem Siliciumcarbid. *Berichte der Deutschen Keramischen Gesellschaft* **56**, 72 - 75 (1979).
391. Schlichting, J. & Schwetz, K.A. Oxidationsverhalten von gesintertem α -Siliciumcarbid. *High Temperatures, High Pressures* **14**, 219 - 223 (1982).
392. Nickel, K.G. & Quirnbach, P. Gaskorrosion nichtoxidischer keramischer Werkstoffe. in *Technische Keramische Werkstoffe* (ed. Kriegesmann, J.) Kapitel 5.4.1.1, p. 1 - 76 (Deutscher Wirtschaftsdienst, Köln, 1991).
393. Wiebke, G. Die Oxydation von Siliziumcarbid. *Berichte der Deutschen Keramischen Gesellschaft* **37**, 219 - 226 (1960).
394. Schlichting, J. Siliciumcarbid als Oxidationsbeständiger Hochtemperaturwerkstoff. Oxidations-und Heißkorrosionsverhalten. I. *Berichte der Deutschen Keramischen Gesellschaft* **56**, 196 - 200 (1979).
395. Schlichting, J. Siliciumcarbid als Oxidationsbeständiger Hochtemperaturwerkstoff. Oxidations-und Heißkorrosionsverhalten. II. *Berichte der Deutschen Keramischen Gesellschaft* **56**, 156 - 261 (1979).
396. Nickel, K.G. & Gogotsi, Y.G. Hydrothermal degradation of chemical vapor deposited SiC fibres. *Journal of Materials Science*, 4357 - 4364 (1998).
397. Kraft, T. & Nickel, K.G. Hydrothermal Carbon Coatings of alpha-SiC Crystals. in *Surface Engineering - EUROMAT 99*, Vol. 11 (ed. Dimigen, H.) 306 - 311 (Wiley-VCH, 1999).
398. Kraft, T. & Nickel, K.G. Carbon formed by hydrothermal treatment of α -SiC crystals. *Journal of Materials Chemistry* **10**, 671 - 680 (2000).
399. Jacobson, N.S., Eckel, A.J., Misra, A.K. & Humphrey, D.L. Reactions of SiC with H₂/H₂O/Ar Mixtures at 1300°C. *Journal of the American Ceramic Society* **73**, 2330 - 2332 (1990).
400. Heuer, A.H. & Lou, V.L.K. Volatility Diagrams for Silica Silicon Nitride and Silicon Carbide and Their Application to High-Temperature Decomposition and Oxidation. *Journal of the American Ceramic Society* **73**, 2785 - 3128 (1990).
401. Opila, E.J. & Nguyen, Q.N. Oxidation of Chemically-Vapor-Deposited Silicon Carbide in Carbon Dioxide. *Journal of the American Ceramic Society* **81**, 1949 - 1952 (1998).
402. Antill, J.E. & Warburton, J.B. Oxidation of Silicon and Silicon Carbide in Gaseous Atmospheres at 1000°C - 1300°C. in *AGARD Conference Proceedings No. 52* 10 (1970).
403. Irene, E.A. Silicon Oxidation studies: a revised model for thermal oxidation. *Journal of Applied Physics* **54**, 5416 - 5420 (1983).
404. Jaccodine, R.J. & Schlegel, W.A. Measurement of Strains at Si-SiO₂ Interface. *Journal of Applied Physics* **37**, 2429 - 2434 (1966).
405. EerNisse, E.P. Viscous flow of thermal SiO₂. *Applied Physics Letters* **30**, 290 - 293 (1977).
406. Ebi, R., Fitzner, E. & Hüttinger, K.J. Oxidationskinetik von SiC-Pulvern bei Temperaturen zwischen 1200°C und 1600°C. *High Temperatures, High Pressures* **4**, 21-25 (1972).
407. Luthra, K.L. Some new perspectives on oxidation of silicon carbide and silicon nitride. *Journal of the American Ceramic Society* **74**, 1095 - 1103 (1991).
408. Deal, B.E. & Grove, A.S. General Relationship for the Thermal Oxidation of Silicon. *Journal of Applied Physics* **36**, 3770 - 3778 (1965).
409. Bongiorno, A. & Pasquarello, A. Oxygen Diffusion through the disordered oxide network during silicon oxidation. *Physical Review Letters* **88**, 125901-1 - 125901-4 (2002).
410. Gusev, E.P., Lu, H.C., Gustafsson, T. & Garfunkel, E. Growth mechanism of thin silicon oxide films on Si(100) studied by medium-energy ion scattering. *Physical Review B* **52**, 1759 - 1775 (1995).

411. Fung, C.D. & Kopanski, J.J. Thermal oxidation of 3C silicon carbide single-crystal layers on silicon. *Applied Physics Letters* **45**, 757 - 759 (1984).
412. Ganem, J.-J., Trimaille, I., Andre, P. & Rigo, S. Diffusion of near surface defects during the thermal oxidation of silicon. *Journal of Applied Physics* **81**, 8109 - 8111 (1997).
413. Suzuki, A., Ashida, H., Furui, N., Mameno, K. & Matsunami, H. Thermal Oxidation of SiC and Electrical Properties of Al-SiO₂-SiC MOS Structure. *Japanese Journal of Applied Physics* **21**, 579 - 585 (1982).
414. Opila, E.J. Oxidation Kinetics of chemically Vapor-Deposited silicon carbide in wet oxygen. *Journal of the American Ceramic Society* **77**, 730 - 736 (1994).
415. Raynaud, C. Silica films on silicon carbide: a review of electrical properties and device applications. *Journal of Non-Crystalline Solids* **280**, 1 - 31 (2001).
416. Li, J., Eveno, P. & Huntz, A.M. Oxidation of SiC. *Werkstoffe und Korrosion* **41**, 716 - 725 (1990).
417. Singhal, S.C. & Lange, F.F. Effect of Alumina Content on the Oxidation of Hot-Pressed Silicon Carbide. *Journal of the American Ceramic Society* **58**, 433 - 435 (1975).
418. Powers, J.M. & Somorjai, G.A. The surface oxidation of alpha-silicon carbide by O₂ from 300 to 1373 K. *Surface Science* **244**, 39 - 50 (1991).
419. Harris, R.C.A. & Call, R.L. Oxidation of 6H alpha-silicon carbide. *Proceedings of the International conference on silicon carbide 3rd International Conference*, 329 - 336 (1974).
420. Radtke, C., Baumvol, I.J.R., Ferrera, B.C. & Stedile, F.C. Oxygen transport and incorporation mechanisms in the dry thermal oxidation of 6H-SiC. *Applied Physics Letters* **85**, 3402 - 3404 (2004).
421. Motzfeld, K. On the Rates of Oxidation of Silicon and of Silicon Carbide in Oxygen and Correlation with Permeability of Silica Glass. *Acta Chemica Scandinavica* **18**, 1595 - 1606 (1964).
422. Ramberg, C.E. & Worrell, W.L. Oxygen Transport at High Temperatures: Implications of Oxidation Kinetics. *Journal of the American Ceramic Society* **84**, 2607 - 2616 (2001).
423. Costello, J.A. & Tressler, R.E. Oxidation Kinetics of Silicon Carbide Crystals and Ceramics: I, In Dry Oxygen. *Journal of the American Ceramic Society* **69**, 674 - 681 (1986).
424. Soares, G.V., Radtke, C., Baumvol, I.J.R. & Stedile, F.C. Morphological and compositional changes in the SiO₂/SiC interface region induced by oxide thermal growth. *Applied Physics Letters* **88**, 041901-1 - 041901-3 (2006).
425. Amy, F., Soukiasian, P., Hwu, Y.-K. & Brylinski, C. SiO₂/6H-SiC(0001) 3x3 initial interface formation by Si overlay oxidation. *Applied Physics Letters* **75**, 3360 - 3362 (1999).
426. Amy, F. et al. Si/6H-SiC(0001): An unexpected cubic 4x3 Si phase overlayer. *Applied Physics Letters* **79**, 767 - 769 (2001).
427. Radtke, C. et al. Characterization of SiC thermal oxidation. *Nuclear Instruments and Methods in Physics Research B*, 579 - 582 (2002).
428. Mott, N.F. On the oxidation of silicon. *Philosophical Magazine* **55**, 117 - 129 (1987).
429. Stoneham, A.M., Grovenor, C.R.M. & Cerezo, A. Oxidation and the structure of the silicon/oxide interface. *Philosophical Magazine* **55**, 201 - 210 (1987).
430. Hollinger, G. & Himpfel, F. Multiple-bonding configurations for oxygen on silicon surfaces. *Physical Review B* **28**, 3651 - 3653 (1983).
431. Grunthaner, F.J. et al. High-Resolution X-Ray Photoelectron Spectroscopy as a Probe of Local Atomic Structure: Application to Amorphous SiO₂ and the Si-SiO₂ Interface. *Physical Review Letters* **43**, 1683 - 1686 (1979).
432. Hollinger, G. et al. Anomalous bonding in SiO₂ at the SiO₂-Si interface. *Philosophical Magazine* **55**, 735 - 764 (1987).
433. Rochet, F. et al. The thermal oxidation of silicon. The special case of very thin films. *Advances in physics* **35**, 237 - 274 (1986).
434. Reisman, A., Nicollian, E.H., Williams, C.K. & Merz, C.J. The modelling of silicon oxidation from 1x10⁻⁵ to 20 atmospheres. *Journal of Electronic Materials* **16**, 45 - 55 (1987).
435. Nicollian, E.H. & Reisman, A. A new model for the thermal oxidation kinetics of silicon. *Journal of Electronic Materials* **17**, 263 - 272 (1988).
436. Wolters, D.R. & Zegers-van Duynhoven, A.T.A. Kinetics of dry oxidation of silicon. I. Space-charge-limited growth. *Journal of Applied Physics* **65**, 5126 - 5133 (1989).
437. Wolters, D.R. & Zegers-van Duynhoven, A.T.A. Kinetics of dry oxidation of silicon. II. Conditions affecting the growth. *Journal of Applied Physics* **65**, 5134 - 5141 (1989).
438. Wolters, D.R. & Zegers-van Duynhoven, A.T.A. Kinetics of dry oxidation of silicon. *Applied Surface Science* **39**, 81 - 88 (1989).
439. Hof, A.J., Kovalgin, A.Y., Woerlee, P.H. & Schmitz, J. On the oxidation kinetics of Silicon in Ultradiluted H₂O and D₂O Ambient. *Journal of the Electrochemical Society* **152**, F133 - F137 (2005).
440. Blanc, J. A revised model for the oxidation of Si by oxygen. *Applied Physics Letters* **33**, 424 - 426 (1978).
441. Blanc, J. The oxidation of silicon by dry oxygen. Can we distinguish between models? *Philosophical Magazine B* **55**, 685 - 710 (1987).
442. Sibieude, F. & Benezech, G. X-ray diffraction study of vapour deposition of molybdenum silicides on molybdenum. *Journal of Materials Science Letters* **8**, 1323 - 1325 (1989).

443. Barbottin, G. & Vapaille, A. *Instabilities in Silicon Devices. Silicon Passivation and Related Instabilities.*, 517 (North-Holland, Amsterdam, 1986).
444. Wagner, C. Beitrag zur Theorie des Anlaufvorgangs. *Zeitschrift für physikalische Chemie* **B21**, 25 - 41 (1933).
445. Yarim, R. Technische Universität Berlin (2004).
446. da Silva, C.R.S., Justo, J.F., Pereyra, I. & Assali, L.V.C. A first principles investigation on hypothetical crystalline phases of silicon oxycarbide. *Diamond and Related Materials* **14**, 1142 - 1145 (2005).
447. Hornetz, B., Michel, H.-J. & Halbritter, J. Oxidation and 6H SiC-SiO₂ Interfaces. *Journal of Vacuum Science & Technology, A: Vacuum, Surfaces, and Films* **13**, 767 - 771 (1995).
448. Pampuch, R., Ptak, W., Jonas, S. & Stoch, J. Formation of Ternary Si-O-C Phase(s) During Oxidation of SiC. *Materials Science Monographs* **6**, 435 - 448 (1980).
449. Lavrenko, V.A., Jonas, S. & Pampuch, R. Petrographic and X-Ray Identification of Phases Formed by Oxidation of Silicon Carbide. *Ceramics International* **7**, 75 - 76 (1981).
450. Deák, P. et al. Defects in the SiC/SiO₂ interface: energetics of the elementary steps of the oxidation reaction. *Physica B* **340 - 342**, 1069 - 1073 (2003).
451. Deák, P. et al. A Cause for SiC/SiO₂ Interface States: the Site Selection of Oxygen in SiC. *Materials Science Forum* **433 - 436**, 535 - 538 (2003).
452. Knaup, J. et al. Theoretical study of the mechanism of dry oxidation of 4H-SiC. *Physical Review B* **71**, 235321-1 - 235321-9 (2005).
453. Jernigan, G.G., Stahlbush, R.E. & Saks, N.S. Effect of oxidation and reoxidation on the oxide-substrate interface of 4H- and 6H-SiC. *Applied Physics Letters* **77**, 1437 - 1439 (2000).
454. Dekker, J., Saarinen, K., Olafsson, H. & Sveinbjörnsson, E.Ö. Observation of interface defects in thermally oxidized SiC using positron annihilation. *Applied Physics Letters* **82**, 2020 - 2022 (2003).
455. Soukiasian, P. & Amy, F. Silicon carbide surface oxidation and SiO₂/SiC interface formation investigated by soft X-ray synchrotron radiation. *Journal of Electron Spectroscopy and Related Phenomena* **144 - 147**, 783 - 788 (2005).
456. Johansson, L.I. & Virojanadara, C. Synchrotron radiation studies of the SiO₂/SiC(0001) interface. *Journal of Physics: Condensed Matter* **16**, S3423 - S3434 (2004).
457. Virojanadara, C. & Johansson, L.I. Photoemission study of Si-rich 4H-SiC surfaces and initial SiO₂/SiC interface formation. *Physical Review B* **71**, 195335-1 - 195335-10 (2005).
458. Goto, A., Homma, H. & Hirai, T. Effect of oxygen partial pressure on the high-temperature oxidation of CVD SiC. *Corrosion Science* **44**, 359 - 370 (2002).
459. Crank, J. *The mathematics of diffusion*, 414 (Clarendon Press, Oxford, 1975).
460. Jost, W. & Hauffe, K. *Diffusion. Methoden der Messung und Auswertung.*, 327 (Dr. Dietrich Steinkopf Verlag, Darmstadt, 1972).
461. Doremus, R.H. *Diffusion of Reactive Molecules in Solids and Melts*, 293 (John Wiley & Sons, Inc., New York, 2002).
462. Luthra, K.L. Theoretical aspects of the oxidation of silica-forming ceramics. in *Corrosion of Advanced Ceramics - Measurement and Modelling*, Vol. 267 (ed. Nickel, K.G.) 23 - 34 (Kluwer Academic Publishers, Dordrecht, 1994).
463. Jeans, J. *An Introduction to the Kinetic Theory of Gases*, 311 (Cambridge University Press, Cambridge, 1967).
464. Sucof, E.W. Diffusion of Oxygen in Vitreous Silica. *Journal of the American Ceramic Society* **46**, 14 - 20 (1963).
465. Schaeffer, H.A. & Muehlenbachs, K. Correlations between Oxygen Transport Phenomena in non-crystalline Silica. *Journal of Materials Science* **13**, 1146 - 1148 (1978).
466. Norton, F.J. Permeation of Gaseous Oxygen through vitreous Silica. *Nature* **191**, 701 (1961).
467. Williams, E.L. Diffusion of Oxygen in Fused Silica. *Journal of the American Ceramic Society* **48**, 190 - 194 (1965).
468. Cawley, J.D., Halloran, J.W. & Cooper, A.R. Oxygen-18 Tracer Study of the Passive Thermal Oxidation of Silicon. *Oxidation of Metals* **28**, 1 - 16 (1987).
469. Mikkelsen, J.C., Jr. Self-diffusivity of network oxygen in vitreous SiO₂. *Applied Physics Letters* **45**, 1187 - 1189 (1984).
470. Rodriguez-Viejo, J., Sibieude, F., Clavaguera-Mora, M.T. & Monty, C. ¹⁸O diffusion through amorphous SiO₂ and cristobalite. *Applied Physics Letters* **63**, 1906 - 1908 (1993).
471. Doremus, R.H. Diffusion of oxygen in silica glass. *Journal of the Electrochemical Society* **143**, 1992 - 1995 (1996).
472. Han, C.J. & Helms, C.R. Isotopic tracer studies of oxygen transport through SiO₂ films at 1000°C using secondary ion mass spectrometry. *Journal of Applied Physics* **59**, 1767 - 1769 (1986).
473. Rosencher, E., Straboni, A., Rigo, S. & Amsel, G. An ¹⁸O study of the thermal oxidation of silicon in oxygen. *Applied Physics Letters* **34**, 254 - 256 (1979).
474. Rochet, F., Agius, B. & Rigo, S. An ¹⁸O Study of the Oxidation Mechanism of Silicon in Dry Oxygen. *Journal of the Electrochemical Society* **131**, 914 - 923 (1984).
475. Costello, J.A. & Tressler, R.E. Isotope Labeling Studies of the Oxidation of Silicon at 1000°C and 1300°C. *Journal of the Electrochemical Society* **131**, 1944 - 1947 (1984).

476. Rigo, S., Rochet, F., Agius, B. & Straboni, A. An ^{18}O Study of Cooperative Diffusion and Chemical Reaction during Thermal Treatments of Silica Films in Water Vapor. *Journal of the Electrochemical Society* **129**, 867 - 876 (1982).
477. Trueb, L.F. *Die chemischen Elemente. Ein Streifzug durch das Periodensystem.*, 408 (S. Hirzel Verlag, Stuttgart, 2005).
478. Cawley, J.D. Oxygen diffusion in silica and corrosion of ceramics. in *Corrosion of Advanced Ceramics - Measurement and Modelling*, Vol. 267 (ed. Nickel, K.G.) 35 - 36 (Kluwer Academic Publishers, Dordrecht, 1994).
479. Singhal, S.C. Oxidation kinetics of hot-pressed silicon carbide. *Journal of Materials Science* **11**, 1246 - 1253 (1976).
480. Narushima, T. et al. Active-to-Passive Transition and Bubble Formation for High-Temperature Oxidation of Chemically Vapor-Deposited Silicon Carbide in CO-CO_2 Atmospheres. *Journal of the American Ceramic Society* **77**, 1079 - 1082 (1994).
481. Gibson, J.M. & Dong, D.W. Direct Evidence for 1 nm Pores in "Dry" Thermal SiO_2 from High Resolution Transmission Electron Microscopy. *Journal of the Electrochemical Society* **127**, 2722 - 2728 (1980).
482. Srivastava, J.K., Prasad, M. & Wagner, J.B., Jr. Electrical Conductivity of Silicon Dioxide Thermally Grown on Silicon. *Journal of the Electrochemical Society* **132**, 955 - 963 (1985).
483. Schumacher, C. & Nickel, K.G. Influence of Boron and Carbon on the Oxidation of Sintered Silicon Carbide at 1500°C . *Ceramic Engineering & Science Proceedings* **21**, 615 - 622 (2000).
484. Petit, J.B., Neudeck, P.G., Matus, L.G. & Powell, J.A. Thermal Oxidation of Single-Crystal Silicon Carbide: Kinetic, Electrical, and Chemical Studies. *Springer Proceedings in Physics* **71**, 190 - 196 (1992).
485. von Münch, W. & Pfaffener, I. Thermal oxidation and electrolytic etching of silicon carbide. *Journal of the Electrochemical Society* **122**, 642 - 643 (1975).
486. Lauche, J., Tairov, Y.M., Tsvetkov, V.F. & Szczepanski, F. Study of the kinetics of oxidation of silicon carbide single crystals. *Neorganicheskie Materialy* **17**, 254 - 257 (1981).
487. Schulz, D. et al. Investigation of silicon carbide physical vapor transport growth on the C-terminated face of 6H seeds. *Materials Research Society Symposium Proceedings* **640**, H1.8.1 - H1.8.6 (2001).
488. Stein, R.A., Lanig, P. & Leibenzeder, S. Influence of surface energy on the growth of 6H- and 4H-SiC Polytypes by sublimation. *Materials Science and Engineering B* **B11**, 69 - 71 (1992).
489. Lucovsky, G., Niimi, H., Gözl, A. & Kurz, H. Differences between silicon oxycarbide regions at SiC-SiO₂ prepared by plasma-assisted oxidation and thermal oxidations. *Applied Surface Science* **123 / 124**, 435 - 439 (1998).
490. Wright, N.G., Johnson, C.M. & O'Neill, A.G. Mechanistic model for oxidation of SiC. *Materials Science and Engineering B* **B61-62**, 468 - 471 (1999).
491. Wright, N.G., Johnson, C.M. & O'Neill, A.G. Oxidation modelling for SiC. *Materials Research Society Symposium Proceedings* **572**, 135 - 140 (1999).
492. Song, Y. & Smith, F.W. Phase diagram for the interaction of oxygen with SiC. *Applied Physics Letters* **81**, 3061 - 3063 (2002).
493. van Bommel, A.J., Crombeen, J.E. & van Tooren, A. LEED and Auger Electron Observations of the SiC(0001) surface. *Surface Science* **48**, 463 - 472 (1975).
494. Shenoy, J.N., Das, M.K., Cooper, J.A., Jr., Melloch, M.R. & Palmour, J.W. Effect of substrate orientation and crystal anisotropy on the thermally oxidized SiO₂/SiC interface. *Journal of Applied Physics* **79**, 3042 - 3045 (1996).
495. Muehlenbachs, K. & Schaeffer, H.A. Oxygen Diffusion in vitreous silica - utilization of natural isotopic abundances. *Canadian Mineralogist* **15**, 179 - 184 (1977).
496. Opila, E.J. Variation of the Oxidation Rate of Silicon Carbide with Water-Vapour Pressure. *Journal of the American Ceramic Society* **82**, 625 - 636 (1999).
497. Brüning, R. & Crowell, T. A method to determine the kinetics of a supercooled liquid by temperature scanning measurements applied to (Li,Na)acetate and GeO₂. *Journal of Non-Crystalline Solids* **248**, 183 - 193 (1999).
498. Brüning, R. On the glass transition in vitreous silica by differential thermal analysis measurements. *Journal of Non-Crystalline Solids* **330**, 13 - 22 (2003).
499. Shelby, J.E. *Handbook of Gas Diffusion in Solids and Melts*, (ASM International, Materials Park, 1996).
500. Doremus, R.H. *Glass Science*, 339 (John Wiley & Sons, N.Y., 1994).
501. Li, H., Tomozawa, M. & Lou, V.K. Effects of nitrogen and carbon ion implantation on devitrification of silica glasses. *Journal of Non-Crystalline Solids* **168**, 56 - 63 (1993).
502. Costello, J.A. & Tressler, R.E. Oxidation Kinetics of Hot-Pressed and Sintered alpha-SiC. *Journal of the American Ceramic Society* **64**, 327 - 331 (1981).
503. Ogbuji, L.U.J.T. Effect of Oxide Devitrification Kinetics of SiC. *Journal of the American Ceramic Society* **80**, 1544 - 1550 (1997).
504. Ramberg, C.E. & Worrell, W.L. Oxygen Transport in Silica at High Temperatures: Implications of Oxidation Kinetics. *Journal of the American Ceramic Society* **84**, 2607-2716 (2001).
505. Ostrovsky, I.A. On some sources of errors in phase-equilibria investigations at ultra-high pressure; phase diagram of silica. *Geological Journal* **5**, 321 - 328 (1967).

506. Fox, D.S. Oxidation kinetics of CVD silicon carbide and silicon nitride. *Ceramic Engineering & Science Proceedings* **13**, 836 - 843 (1992).
507. Maeda, M., Nakamura, K. & Yamada, M. Oxidation Resistance Evaluation of Silicon Carbide Ceramics with Various Additives. *Journal of the American Ceramic Society* **72**, 512 - 514 (1989).
508. Jacobson, N.S. Corrosion of Silicon-Based Ceramics in Combustion Environments. *Journal of the American Ceramic Society* **76**, 3 - 28 (1993).
509. Stockmann, Y.J., Ullmann-Papst, S., Kleist, G., Steinbrech, R.W. & Nickel, H. Mechanische Eigenschaften von SiO₂-Schichten auf SiSiC. in *Korrosion und Verschleiß von keramischen Werkstoffen* (eds. Telle, R. & Quirnbach, P.) 77 - 84 (Deutsche Keramische Gesellschaft e.V. (DKG), Aachen, 1994).
510. Swainson, I.P. & Dove, M.T. On the Thermal Expansion of β -Cristobalite. *Physics and Chemistry of Minerals* **22**, 61 - 65 (1995).
511. Touloukian, Y.S., Kirby, R.K., Taylor, R.E. & Lee, T.Y.R. Thermal expansion of nonmetallic solids. 350-358, 358-371, 873-878 (New York, 1977).
512. Fei, Y. Thermal Expansion. in *Mineral Physics & Crystallography: A Handbook of Physical Constants (Agu Reference Shelf, No 2)* (ed. Ahrens, T.J.) 29 - 44 (Amer Geophysical Union, Washington, 1995).
513. Opila, E.J., Fox, D.S. & Barrett, C.A. Cyclic oxidation of monolithic silicon carbide and silicon nitride materials. *Ceramic Forum International* **14**, 367 - 374 (1993).
514. Nickel, K.G. Ceramic matrix composite corrosion models. *Journal of the European Ceramic Society* **25**, 1699 - 1704 (2005).
515. Randall, J.T., Rooksby, H.P. & Cooper, B.S. Structure of glasses: The evidence of x-ray diffraction. *Journal of the Society of Glass Technology* **14**, 219 - 229 (1930).
516. Rodriguez-Viejo, J., Sibieude, F. & Clavaguera-Mora, M.T. High-Temperature Oxidation of CVD beta-SiC. Part II. Relation between Oxygen Diffusion Coefficients and Parabolic Rate Constants. *Journal of the European Ceramic Society* **13**, 177 - 184 (1994).
517. Rodriguez-Viejo, J., Sibieude, F. & Clavaguera-Mora, M.T. High-Temperature Oxidation of CVD beta-SiC. Part I. Experimental Study. *Journal of the European Ceramic Society* **13**, 167 - 175 (1994).
518. Lipinski, D. & Schwiete, H.E. Die Bildung des Cristobalits aus amorphem Siliziumdioxid unter verschiedenen Gasatmosphären. *Tonindustrie-Zeitung und Keramische Rundschau* **88**, 145 - 153; 217 - 225; 258 - 262 (1964).
519. Göpel, W. & Ziegler, C. *Einführung in die Materialwissenschaften: Physikalisch-chemische Grundlagen und Anwendungen*, 490 (Teubner, Stuttgart, 1996).
520. Frenkel, J. *Kinetic Theory of Liquids*, (Dover Publications Mineola, 1955).
521. Ramachandran, B.E., Bala Singh, C., Pai, B.C. & Balasubramanian, N. Studies on the crystallization behaviour of high silica materials. *Materials Science and Engineering* **67**, L5 - L7 (1984).
522. Pantsukrin, S.D. & Kalinin, D.V. Kinetics and mechanism of formation of alpha-cristobalite spherulites. *Seriya Khimicheskikh Nauk* **1**, 27 - 31 (1988).
523. Ainger, F.W. The Formation and Devitrification of Oxides on Silicon. *Journal of Materials Science* **1**, 1 - 13 (1966).
524. Heuer, A.H., Ogbuji, L.U.J.T. & Mitchell, T.E. The Microstructure of Oxide Scales on Oxidized Si and SiC Single Crystals. *Journal of the American Ceramic Society* **63**, 354 - 355 (1980).
525. Ogbuji, L.U.J.T. Development of oxide scale microstructure on single-crystal SiC. *Journal of Materials Science* **16**, 2753 - 2759 (1981).
526. Monnoye, S., Turover, D. & Vicente, P. Surface Preparation Techniques for SiC Wafers. in *Silicon Carbide. Major Recent Advances*. (eds. Choyke, J.W., Matsunami, H. & Pensl, G.) 699 - 710 (Springer-Verlag, Berlin, 2004).
527. Keith, H.D. & Padden, F.J., Jr. A Phenomenological Theory of Spherulitic Crystallization. *Journal of Applied Physics* **34**, 2409 - 2421 (1963).
528. Freiman, S.W., Onoda, G.Y., Jr. & Pincus, A.G. Spherulitic crystallization in glasses. in *Symposium of the Glass Division of the American Ceramic Society Vol. 5* 141 - 150 (American Ceramic Society, Ohio, 1971).
529. Lewis, M.H., Metcalf-Johansen, J. & Bell, P.S. Crystallization Mechanisms in Glass-Ceramics. *Journal of the American Ceramic Society* **62**, 278 - 288 (1979).
530. Filipuzzi, L., Naslain, R. & Jaussaud, C. Oxidation kinetics of SiC deposited from CH₃SiCl₃/H₂ under CVI conditions. *Journal of Materials Science* **27**, 3330 - 3334 (1992).
531. Guinel, M.J.-F. & Norton, M.G. Blowing of silica microforms on silicon carbide. *Journal of Non-Crystalline Solids* **351**, 251 - 257 (2005).
532. Schiroky, G.H. Oxidation Behaviour of Chemically Vapor-Deposited Silicon Carbide. *Advanced Ceramic Materials* **2**, 137 - 141 (1987).
533. Jacobson, N.S. Kinetics and Mechanism of Corrosion of SiC by Molten Salts. *Journal of the American Ceramic Society* **69**, 74 - 82 (1986).
534. Jacobson, N.S. & Smialek, J.L. Hot Corrosion of Sintered α -SiC at 1000°C. *Journal of the American Ceramic Society* **68**, 432 - 439 (1985).
535. McKee, D.W. & Chatterji, D. Corrosion of Silicon Carbide in Gases and Alkaline Melts. *Journal of the American Ceramic Society* **59**, 441 - 444 (1976).
536. Tressler, R.E., Meiser, M.D. & Yonushonis, T. Molten salt corrosion of SiC and Si₃N₄ ceramics. *Journal of the American Ceramic Society* **59**, 278 - 280 (1976).

537. Federer, J.I. Corrosion of SiC Ceramics by Na₂SO₄. *Advanced Ceramic Materials* **3**, 56 - 61 (1988).
538. Jacobson, N.S., Stearns, C.A. & Smialek, J.L. Burner Rig Corrosion of SiC at 1000°C. *Advanced Ceramic Materials* **1**, 154 - 161 (1986).
539. Warren, B.E. X-ray diffraction study of the structure of glass. *Chemical Review* **26**, 237 - 255 (1940).
540. Warren, B.E. & Averbach, B.L. The Effect of Cold-Work Distortion on X-Ray Patterns. *Journal of Applied Physics* **21**, 595 - 599 (1950).
541. Zheng, Z., Tressler, R.E. & Spear, K.E. The effect of sodium contamination on the oxidation of single crystal silicon carbide. *Corrosion Science* **33**, 545 - 556 (1992).
542. Schwetz, K.A. Silicon Carbide Based Hard Materials. in *Handbook of Ceramic Hard Materials*, Vol. 2 (ed. Riedel, R.) 683 - 748 (Wiley-VCH Verlag GmbH, Weinheim, 2000).
543. Tressler, R.E., Costello, J.A. & Zheng, Z. Oxidation of Silicon Carbide. in *Industrial Heat Exchangers*, Vol. 1 (eds. Hayes, A.J., Liang, W.W., Richlen, S.L. & Tabb, E.S.) 307 - 314 (American Society for Metals, Pittsburgh, 1985).
544. Liu, D.-M. Oxidation of Polycrystalline α -Silicon Carbide Ceramic. *Ceramics International* **23**, 425 - 436 (1997).
545. Sangster, R.C., Kämpf, P. & Nohl, U. *Silicon Suppl. B 5d2*, 304 (Springer, Berlin, 1995).
546. Mieskowski, D.M., Mitchell, T.E. & Heuer, A.H. Bubble Formation in Oxide Scales on SiC. *Communications of the American Ceramic Society* **67**, 17 - 18 (1984).
547. Fergus, J.W. & Worrell, W.L. Effect of Carbon and Boron on the High-Temperature Oxidation of Silicon Carbide. *Journal of the American Ceramic Society* **78**, 1961 - 1964 (1995).
548. Narushima, T., Goto, T. & Hirai, T. High-Temperature Passive Oxidation of chemically vapor deposited silicon carbide. *Journal of the American Ceramic Society* **72**, 1386 - 1390 (1989).
549. Maeda, M., Nakamura, K. & Ohkubo, T. Oxidation of silicon carbide in a wet atmosphere. *Journal of Materials Science* **23**, 3933 - 3938 (1988).
550. Narushima, T., Goto, T., Yokoyama, Y., Iguchi, Y. & Hirai, T. High-Temperature Active Oxidation of Chemically Vapor-Deposited Silicon Carbide in CO-CO₂ Atmospheres. *Journal of the American Ceramic Society* **76**, 2521 - 2524 (1993).
551. Jacobson, N.S., Lee, K.N. & Fox, D.S. Reactions of Silicon Carbide and Silicon(IV) Oxide at Elevated Temperatures. *Journal of the American Ceramic Society* **75**, 1603 - 1611 (1992).
552. Mortimer, C.E. *Chemie. Das Basiswissen der Chemie.*, 744 (Georg Thieme Verlag, Stuttgart, 2001).
553. Goto, T. High temperature passive oxidation mechanism of CVD SiC. *Materials Science Forum* **522 - 523**, 27 - 36 (2006).
554. Nipoti, R., Madrigali, M. & Sambo, A. A study about the wet oxidation of crystalline and ion damaged 6H-SiC. *Materials Science and Engineering B* **B61 - 62**, 475 - 479 (1999).
555. Nakatogawa, T. Silicon carbide nonohmic resistors. II. Oxidation rates of silicon carbide. *Kogyo Kagaku Zasshi* **57**, 348 - 350 (1954).
556. Nakatogawa, T. Silicon carbide nonohmic resistors. III. Oxidation and electric capacitance of silicon carbide powder. *Kogyo Kagaku Zasshi* **57**, 484 - 486 (1954).
557. Nakatogawa, T. Silicon carbide nonohmic resistors. I. Surface structure of single crystals. *Kogyo Kagaku Zasshi* **57**, 441 - 443 (1954).
558. Ogbuji, L.U.J.T. & Opila, E.J. A Comparison of the Oxidation Kinetics of SiC and Si₃N₄. *Journal of the Electrochemical Society* **142**, 925 - 930 (1995).
559. Jorgensen, P.J., Wadsworth, M.E. & Cutler, I.B. Effects of Water Vapor on Oxidation of Silicon Carbide. *Journal of the American Ceramic Society* **44**, 258 - 261 (1961).
560. Fox, D.S. Oxidation Behavior of Chemically-Vapor-Deposited Silicon Carbide and Silicon Nitride from 1200° to 1600°C. *Journal of the American Ceramic Society* **81**, 945 - 950 (1998).
561. Bartlett, R.W. Oxide Films on Beta-Silicon Carbide. *Journal of the Electrochemical Society* **118**, 397 - 399 (1971).
562. Ramberg, C.E., Cruiciani, G., Spear, K.E., Tressler, R.E. & Ramberg, C.F., Jr. Passive-Oxidation Kinetics of High-Purity Silicon Carbide from 800° to 1100°C. *Journal of the American Ceramic Society* **79**, 2897 - 2911 (1996).
563. Gogotsi, Y.G. & Yoshimura, M. Formation of carbon films on carbides under hydrothermal conditions. *Letters to nature* **367**, 628 - 630 (1994).
564. Gogotsi, Y.G. & Yoshimura, M. Degradation of SiC-based fibres in high-temperature, high-pressure water. *Journal of Materials Science Letters* **13**, 395 - 399 (1994).
565. Gogotsi, Y.G., Welz, S., Ersoy, D.A. & McNallan, M.J. Conversion of silicon carbide to crystalline diamond-structured carbon at ambient pressure. *Nature* **411**, 283 - 287 (2001).
566. Kraft, T. & Nickel, K.G. Solvothermal Formation of sp²- and sp³-Carbon From Carbides. in *Eurocarbon '98* Vol. 2 881 - 882 (Strasbourg, 1998).
567. Song, Y. & Smith, F.W. Effects of Low-Pressure Oxidation on the Surface Composition of Single Crystal Silicon Carbide. *Journal of the American Ceramic Society* **88**, 1864 - 1869 (2005).
568. Kusunoki, M., Suzuki, T., Hirayama, T., Shibata, N. & Kaneko, K. A formation mechanism of carbon nanotube films on SiC(0001). *Applied Physics Letters* **77**, 531 - 533 (2000).
569. Kusunoki, M., Suzuki, T., Kaneko, K. & Ito, M. Formation of self-aligned carbon nanotube films by surface decomposition of silicon carbide. *Philosophical Magazine Letters* **79**, 153 - 161 (1999).

570. Kusunoki, M., Shibata, J., Rokkaku, M. & Hirayama, T. Aligned Carbon Nanotube Film Self-Organized on a SiC Wafer. *Japanese Journal of Applied Physics* **37**, L605 - L606 (1998).
571. Kusunoki, M., Rokkaku, M. & Suzuki, T. Epitaxial carbon nanotube film self-organized by sublimation decomposition of silicon carbide. *Applied Physics Letters* **71**, 2620 - 2622 (1997).
572. Adachi, S., Mohri, M. & Yamashina, T. Surface Graphitization process of SiC(0001) single-crystal at elevated temperatures. *Surface Science* **161**, 479 - 490 (1985).
573. Badami, D.V. X-Ray Studies of Graphite Formed by Decomposing Silicon Carbide. *Carbon* **3**, 53 - 57 (1965).
574. Moulson, A.J. & Roberts, J.P. Water in silica glass. *Transactions of the Faraday Society* **57**, 1208 - 1216 (1961).
575. Doremus, R.H. Diffusion of water in silica glass. *Journal of Materials Research* **10**, 2379 - 2389 (1995).
576. Doremus, R.H. Viscosity of silica. *Journal of Applied Physics* **92**, 7619 - 7629 (2002).
577. Kalen, J.D., Boyce, R.S. & Cawley, J.D. Oxygen Tracer Diffusion in Vitreous Silica. *Journal of the American Ceramic Society* **74**, 203 - 209 (1991).
578. Doremus, R.H. Oxidation of Silicon by Water and Oxygen and Diffusion in Fused Silica. *Journal of Chemical Physics* **80**, 1773 - 1775 (1976).
579. Rochet, F. & Rigo, S. Effect of pressure on thermally induced diffusivity and reactivity of water in thin amorphous silica films. *Philosophical Magazine B* **55**, 747 - 755 (1987).
580. Morey, G.W. New Crystalline Silicates of Potassium and Sodium, their Preparation and General Properties. *Journal of the American Chemical Society* **36**, 215 - 230 (1914).
581. Bakos, T., Rashkeev, S.N. & Pantelides, S.T. Reactions and Diffusion of Water and Oxygen Molecules in Amorphous SiO₂. *Physical Review Letters* **88**, 055508-1 - 055508-4 (2002).
582. Brückner, R. Charakteristische physikalische Eigenschaften der oxydischen Hauptglasbildner und ihre Beziehung zur Struktur der Gläser. Teil II: Mechanische und optische Eigenschaften als Funktion der thermischen Vorgeschichte. *Glastechnische Berichte* **37**, 459 - 476 (1964).
583. Hetherington, G. & Jack, K.H. Water in vitreous silica. Part I. Influence of "water" content on the properties of vitreous silica. *Physics and Chemistry of Glasses* **3**, 129 - 133 (1962).
584. Tian, L., Dieckmann, R., Lin, Y.-Y. & Hui, C.-Y. Influence of "water" on the diffusion of sodium in fused quartz and in alkaline-earth aluminoborosilicate glass. in *Advances in Science and Technology*, Vol. 29. Mass and Charge Transport in Inorganic Materials: Fundamentals to Devices (eds. Vincenzini, P. & Buscaglia, V.) (Techna Srl, Faenza, 2000).
585. Cappelen, H., Johansen, K.H. & Motzfeldt, K. Oxidation of Silicon Carbide in Oxygen and in Water Vapour at 1500°C. *Acta Chemica Scandinavia* **A35**, 247 - 254 (1981).
586. Helmich, M. & Rauch, F. On the mechanism of diffusion of water in silica glass. *Glastechnische Berichte* **66**, 195 - 200 (1993).
587. Wakabayashi, H. & Tomozawa, M. Diffusion of Water into Silica Glass at Low Temperatures. *Journal of the American Ceramic Society* **72**, 1850 - 1855 (1989).
588. Tomozawa, M., Li, H. & Davis, K.M. Water diffusion, oxygen vacancy annihilation and structure relaxation in silica glasses. *Journal of Non-Crystalline Solids* **179**, 162 - 169 (1994).
589. Jorgensen, P.J., Wadsworth, M.E. & Cutler, I.B. Oxidation of Silicon Carbide. *Journal of the American Ceramic Society* **42**, 613 - 616 (1959).
590. Brander, R.W. & Boughey, A.L. The etching of α -silicon carbide. *British Journal of Applied Physics* **18**, 905 - 912 (1967).
591. Narushima, T., Goto, A., Iguchi, Y. & Hirai, T. High-Temperature Oxidation of Chemically Vapor-Deposited Silicon Carbide in Wet Oxygen at 1823 to 1923 K. *Journal of the American Ceramic Society* **73**, 3580 - 3584 (1990).
592. Opila, E.J., Fox, D.S. & Jacobson, N.S. Mass Spectrometric Identification of Si-O-H(g) Species from the Reaction of Silica with Water Vapor at Atmospheric Pressure. *Journal of the American Ceramic Society* **80**, 1009 - 1012 (1997).
593. Irene, E.A. & Ghez, R. Silicon Oxidation Studies: The Role of H₂O. *Journal of the Electrochemical Society* **124**, 1757 - 1761 (1977).
594. Wagstaff, F.E. & Richards, K.J. Kinetics of Crystallization of Stoichiometric SiO₂ Glass in H₂O Atmospheres. *Journal of the American Ceramic Society* **49**, 118 - 121 (1966).
595. Wagstaff, F.E., Brown, S.D. & Cutler, I.B. The influence of H₂O and O₂ atmospheres on the crystallization of vitreous silica. *Physics and Chemistry of Glasses* **5**, 76 - 81 (1964).
596. Lu, W.-J., Steckl, A.J., Chow, T.P. & Katz, W. Thermal Oxidation of Sputtered Silicon Carbide Thin Films. *Journal of the Electrochemical Society* **131**, 1907 - 1914 (1984).
597. Weaver, G.Q. & Olson, B.A. High Strength Silicon Carbide for Use in Severe Environments. *Proceedings of the International conference on silicon carbide* **3**, 367 - 374 (1973).
598. Sharma, K.K., Flörke, O.W., Gugel, E. & Sahl, K. Behavior of silicon carbide under thermooxidative and hydrothermal conditions. *Sprechsaal - International Ceramics and Glass Magazine* **107**, 418-420, 422, 424 (1974).
599. Gogotsi, Y.G. & Yoshimura, M. Low-Temperature Oxidation, Hydrothermal Corrosion, and Their Effects on Properties of SiC (Tyranno) Fibres. *Journal of the American Ceramic Society* **78**, 1439 - 1450 (1995).

600. Kanno, Y., Yasuda, E. & Yoshimura, M. Hydrothermal Corrosion of Si-Ti-C-O Systems (Tyranno) Fibres. *Journal of the Surface Science Society of Japan* **14**, 229 - 235 (1993).
601. Gogotsi, Y.G., Kofstad, P., Yoshimura, M. & Nickel, K.G. Formation of sp^3 -bonded carbon upon hydrothermal treatment of SiC. *Diamond and Related Materials* **5**, 151 - 162 (1996).
602. Gogotsi, Y.G., Nickel, K.G. & Kofstad, P. Hydrothermal Synthesis of Diamond from Diamond-seeded β -SiC Powder. *Journal of Materials Chemistry* **5**, 2313 - 2314 (1995).
603. Gogotsi, Y.G. et al. Structure of carbon produced by hydrothermal treatment of β -SiC powder. *Journal of Materials Chemistry* **6**, 595 - 604 (1996).
604. Jacobson, N.S., Gogotsi, Y.G. & Yoshimura, M. Thermodynamic and Experimental Study of Carbon Formation on Carbides under Hydrothermal Conditions. *Journal of Materials Chemistry* **5**, 595 - 601 (1995).
605. Kim, W.-J., Hwang, H.S., Park, J.Y. & Ryu, W.S. Corrosion behaviors of sintered and chemically vapor deposited silicon carbide ceramics in water at 360°C. *Journal of Materials Science Letters*, 581 - 584 (2003).
606. Kim, W.-J., Hwang, H.S. & Park, J.Y. Corrosion behavior of reaction-bonded silicon carbide ceramics in high-temperature water. *Journal of Materials Science Letters* **21**, 733 - 735 (2002).
607. Kitaoka, S., Tsuji, T., Katoh, T., Yamaguchi, Y. & Kashiwagi, K. Tribological Characteristics of SiC Ceramics in High-Temperature and High-Pressure Water. *Journal of the American Ceramic Society* **77**, 1851 - 1856 (1994).
608. Yoshimura, M., Kase, J.-I. & Somiya, S. Oxidation of SiC powder by high-temperature, high-pressure H₂O. *Journal of Materials Research* **1**, 100 - 103 (1986).
609. Nickel, K.G. & Gogotsi, Y.G. Hydrothermal Synthesis of Diamond. in *Handbook of Ceramic Hard Materials*, Vol. 1 (ed. Riedel, R.) 374 - 389 (Wiley-VCH Verlag, Weinheim, 2000).
610. Herrmann, M., Schilm, J., Michael, G., Meinhardt, J. & Flegler, R. Corrosion of silicon nitride materials in acidic and basic solutions and under hydrothermal conditions. *Journal of the European Ceramic Society* **23**, 585 - 594 (2003).
611. Watanabe, T., Kohri, H., Yagasaki, T., Kimura, Y. & Shiota, I. Surface modification of SiC by hydro-thermal treatment. *Advances in Science and Technology* **32** (10th International Ceramics Congress and 3rd Forum on New Materials), 175 - 180 (2003).
612. Shen, A.H., Bassett, W.A. & Chou, I.-M. Hydrothermal Studies in a Diamond Anvil Cell: Pressure Determination Using the Equation of State of H₂O. in *High-Pressure Research: Application to Earth and Planetary Sciences* (eds. Syono, Y. & Manghnani, M.H.) 61 - 68 (American Geophysical Union, Washington D.C., 1992).
613. Nickel, K.G. & Gogotsi, Y.G. Approaches to Standardisation: High Temperature Oxidation and Hydrothermal Corrosion of Silica Forming Ceramics. *Key Engineering Materials* **113**, 15 - 29 (1996).
614. Barringer, E. et al. Corrosion of CVD Silicon Carbide in 500°C Supercritical Water. *Journal of the American Ceramic Society* **90**, 315 - 318 (2007).
615. Zhuravlev, L.T. & Potapov, V.V. Density of Silanol Groups on the Surface of Silica Precipitated from a Hydrothermal Solution. *Physical Chemistry of Surface Phenomena* **80**, 1119 - 1128 (2006).
616. Potapov, V.V. & Zhuravlev, L.T. Temperature Dependence of the Concentration of Silanol Groups in Silica Precipitated from a Hydrothermal Solution. *Glass Physics and Chemistry* **31**, 661 - 670 (2005).
617. Gogotsi, Y.G. & Yoshimura, M. Water Effects on Corrosion Behaviour of Structural Ceramics. *MRS Bulletin*, 39 - 45 (1994).
618. Gogotsi, Y.G. Hydrothermale Korrosion von SiC - Betrachtung der schädlichen und nützlichen Aspekte. in *Korrosion und Verschleiß von keramischen Werkstoffen* (eds. Telle, R. & Quirnbach, P.) 114 - 122 (Deutsche Keramische Gesellschaft e.V. (DKG), Aachen, 1994).
619. Schwetz, K.A. & Hassler, J. Zur Beständigkeit von Hochleistungskeramiken gegen Flüssigkeitskorrosion. *Ceramic Forum International* **79**, D9 - D19 (2002).
620. Brinker, C.J. & Scherer, G.W. *Sol-Gel Science: The Physics and Chemistry of Sol-Gel Processing*, 912 (Academic Press, San Diego, 1990).
621. Alexander, G.B., Heston, W.M. & Iler, R.K. The Solubility of Amorphous Silica in Water. *Journal of Physical Chemistry* **58**, 453 - 455 (1954).
622. Baumann, H. Über die Auflösung von SiO₂ in Wasser. *Beiträge zur Silikose-Forschung* **37**, 45 - 71 (1955).
623. Cherkinskii, Y.S. & Knyaz'kova, I.S. Silica concentration dependence on pH in the presence of solid silica. *Doklady Akademii Nauk SSSR* **198**, 358 - 360 (1971).
624. Goto, K. States of silica in aqueous solution. II. *Nippon Kagaku Zasshi* **76**, 1364 - 1366 (1955).
625. Fournier, R.O. & Rowe, J.J. The Solubility of Amorphous Silica in Water at high Temperatures and High Pressures. *American Mineralogist* **62**, 1052 - 1056 (1977).
626. Wagner, W. & Pruss, A. The IAPWS Formulation 1995 for the Thermodynamic Properties of Ordinary Water Substance for General and Scientific Use. *Journal of Physical and Chemical Reference Data* **31**, 387 - 535 (2002).
627. Willey, J.D. The effect of pressure on the solubility of amorphous silica in seawater at 0°C. *Marine Chemistry* **2**, 239 - 250 (1974).
628. Kennedy, G.C. A portion of the system silica-water. *Economic geology* **45**, 629 - 653 (1950).
629. Fournier, R.O. & Rowe, J.J. The Solubility of Cristobalite along the Three-Phase Curve, Gas plus Liquid plus Cristobalite. *American Mineralogist* **47**, 897 - 902 (1962).

630. Gerya, T.V. et al. Thermodynamic modeling of solubility and speciation of silica in H₂O-SiO₂ fluid up to 1300°C and 20 kbar based on the chain reaction formalism. *European Journal of Mineralogy* **17**, 269 - 283 (2005).
631. Ito, S. & Tomozawa, M. Stress Corrosion of Silica Glass. *Journal of the American Ceramic Society* **64**, C160 (1981).
632. Hirayama, H., Kawakubo, T. & Goto, A. Corrosion Behavior of Silicon Carbide in 290°C Water. *Journal of the American Ceramic Society* **72**, 2049 - 2053 (1989).
633. Somiya, S. Hydrothermal corrosion of nitride and carbide of silicon. *Materials Chemistry and Physics* **67**, 157 - 164 (2001).
634. Kitaoka, S., Tsuji, T., Yamaguchi, Y. & Kashiwagi, K. Tribochemical wear theory of non-oxide ceramics in high-temperature and high-pressure water. *Wear* **205**, 40 - 46 (1997).
635. Zhiqiang, F., Chunhe, T., Tongxiang, L. & Jean-Charles, R. Oxidation of SiC and decomposition of SiO₂ at low partial pressure of oxygen in He-O₂ system. *Nuclear Engineering and Design* **234**, 45 - 49 (2004).
636. Wagner, C. Passivity during the oxidation of Silicon at Elevated Temperatures. *Journal of Applied Physics* **29**, 1295 - 1297 (1958).
637. Rosenqvist, T. & Tuset, J.K. Discussion of "thermodynamics of the silicon-carbon-oxygen system for the production of silicon carbide and metallic silicon". *Metallurgical Transactions B* **18B**, 471 - 472 (1987).
638. Rosner, D.E. & Allendorf, H.D. Kinetics of the Attack of Refractory Materials by Dissociated Gases. in *Heterogeneous Kinetics and Elevated Temperatures* (ed. Belton, G.R.) 231 - 251 (Plenum Press, New York, 1970).
639. Antill, J.E. & Warburton, J.B. Active to passive transition in the oxidation of SiC. *Corrosion Science* **11**, 337 - 342 (1971).
640. Vaughn, W.L. & Maahs, H.G. Active-to-Passive Transition in the Oxidation of Silicon Carbide and Silicon Nitride in Air. *Journal of the American Ceramic Society* **73**, 1540 - 1543 (1990).
641. Balat, M., Flamant, G., Male, G. & Pichelin, G. Active to passive transition in the oxidation of silicon carbide at high temperature and low pressure in molecular and atomic oxygen. *Journal of Materials Science* **27**, 697 - 703 (1992).
642. Bennett, M.J. & Chaffey, G.H. The Effect of Fission Fragment Irradiation Upon The Active to Passive Transition in the Oxidation of Self-Bonded Refel Silicon Carbide at 850 - 950°C. *Journal of Nuclear Materials* **52**, 184 - 190 (1974).
643. Balat, M., Berjoan, R., Pichelin, G. & Rochman, D. High-temperature oxidation of sintered silicon carbide under pure CO₂ at low pressure: active-passive transition. *Applied Surface Science* **133**, 115 - 123 (1998).
644. Kim, H.E. & Readey, D.W. Active Oxidation of SiC in Low Dew-Point Hydrogen above 1400°C. in *Silicon Carbide Transactions*, Vol. 2 301 - 312 (Ohio State University, Westerville, OH, 1989).
645. Kim, H.E. & Moorhead, A.J. Effects of Active Oxidation on the Flexural Strength of α -Silicon Carbide. *Journal of the American Ceramic Society* **73**, 1868 - 1872 (1990).
646. Narushima, T., Lin, R.Y., Iguchi, Y. & Hirai, T. Oxidation of chemical vapor-deposited silicon nitride in dry oxygen at 1923 to 2003 K. *Journal of the American Ceramic Society* **76**, 1047 - 1051 (1993).
647. Sheehan, J.E. Passive and active oxidation of hot-pressed silicon nitride materials with two magnesia contents. *Journal of the American Ceramic Society* **65**, C111 - C113 (1982).

Chapter 01

Chapter 02

Chapter 03

Chapter 04

Chapter 05

Chapter 06

Chapter 07

Chapter 08

Chapter 09

Chapter 10

Chapter 11

Chapter 12

SCANNING ELECTRON AND POLARIZATION MICROSCOPY STUDY OF THE VARIABILITY AND CHARACTER OF HOLLOW MACRO-DEFECTS IN SILICON CARBIDE WAFERS

V. Presser⁽¹⁾, A. Loges⁽¹⁾, K. G. Nickel⁽¹⁾

⁽¹⁾ Institut für Geowissenschaften, Universität Tübingen

ABSTRACT:

Polarization microscopy is a suitable tool for studying strain in appropriately cut SiC single-crystals. Both the outline shape examined by electron microscopy and the induced interference pattern observed by polarization microscopy were used to study the variation and character of macro-defects present in SiC wafers. While voids are usually in a relaxed state, hollow-core dislocations are characterized by large interference halos up to $\approx 100 \mu\text{m}$ in diameter. Conoscopy, i.e. evaluation of the interference pattern created by inserting an Amici Bertrand lens, is suitable to examine these optical phenomena in more detail and to gain additional knowledge on the inclination of cut wafers towards the c-axis. The discrepancy between simulated interference patterns for (0001)-SiC and the observed ones strongly indicates that pipes are no pure screw dislocations as commonly thought, but must have an edge component.

1. INTRODUCTION

Silicon carbide (SiC), long used as a ceramic for abrasive or high-temperature applications (Ref. ^{1,2}), is an attractive semiconductor material, because its large band gap width (2.4 - 3.3 eV) and high critical field strength (3.108 V/m) along with high thermal conductivity and temperature stability, permit utilization as a high-power and high-temperature device.³ The unique property of this large band-gap semiconductors unique property to form a solid silica scale during thermal oxidation enables the fabrication of SiC/SiO₂ devices as metal-oxide-semiconductor field effect transistors (MOSFETs), similar to Si/SiO₂.⁴ SiC is the single most important non-oxide ceramic material and the most promising semi-conductor material as a replacement for silicon-based devices.

The greatest obstacle to the large-scale application of SiC-based devices is the avoidance of structural defects during single-crystal growth. The structural diversity of SiC, with more than 200 different modifications (polytypes; Ref. ⁵), combined with defects formed during the growth process, limit both possible crystal size and single-crystal quality. Silicon carbide single-crystals grown by Physical Vapor Transport (PVT) using the modified Lely method ⁶, the most widely used method of obtaining large-scale SiC wafers, are highly susceptible to contain defects, such as tube-like defects (micropipe) or polygonized, tabular / platelet-shaped voids.

2. MACRO-DEFECTS IN SILICON CARBIDE

2.1 Pipes

“Pipes” are hollow, tube-like structures with diameters from < 0.1 to $> 5 \mu\text{m}$. These defects are believed to be hollow-core screw dislocations with, in case of small-period polytypes, a Burger’s vector larger than one unit cell.⁷ Sub-micrometer micropipes may be referred to as nano- or micropipes *sensu stricto* and those with larger diameters as “macropipes”.⁸ Normally, micro- and macropipes are orientated fairly well along the c-axis in hexagonal silicon carbide crystals.⁹ However, some macropipes show a serpentine-like structure with significant deviation from the direction of the c-axis.¹⁰

Defect densities have been lowered significantly via critically controlling process stability and growth in off-c-axis orientations.¹¹ Nonetheless, the nature and origin of pipes remain a matter of dispute, and models of mosaicity, overgrowth and void-movement have been proposed as possible explanations.

2.2 Voids

Polygonized voids are also prominent defects present in PVT-grown SiC. In hexagonal SiC, these hollow structures have a hexagonal parallelepiped outline and their edge faces lying perpendicular to the (0001) face.^{12,13} In contrast to pipes, these defects can reach diameters $> 500 \mu\text{m}$ and are, therefore, macroscopically visible as “negative crystals” or “hollow crystals” with reflecting, inner faces. Typical aspect ratios between height (h, parallel [0001]) and width (w, perpendicular [0001]) are $h/w \geq 5$.¹⁰ These voids seem to be able to move along the growth direction.^{10,12,14} and, hence, may result from imperfections at the seed interface. Movement of voids requires a certain diameter (Ref. ¹⁵) and can lead to (off-axis) pipe formation.¹² The movement of such defects was explained according to Hofmann et al. (Ref. ¹⁰) by local differences in the heat transfer distribution and different kinetics at the sublimation (bottom) and growth face (ceiling). The fact that critical control of the seed interface is capable of reducing the defect density of voids significantly ¹⁶ points in this direction.

2.3 Voids terminating pipes

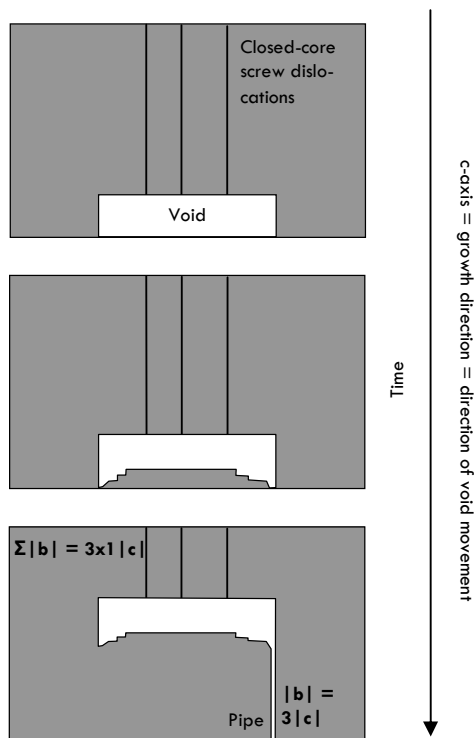


Fig. 1. Schematic illustration of a void formation mechanism (after Ref. ¹²) which also induces a micropipe to form. Note the trench at the void's outer region.

Voids often terminate pipes. The model by Kuhr et al. ¹² argues that pipes, which are not induced during initial growth of the seeding crystal, must be caused by condensation of smaller screw-dislocations. Kuhr et al. ¹² noticed dislocations in direction of the growing surface, which were not connected to the initial seed. Instead, pipes originated from the voids' rims and propagated towards the seed. Moreover, evaporation steps on the void tops and growth steps on the bottom were detected, which was taken as evidence for a movement of voids by a local vapour transport process along the thermal gradient, perpendicular to the growth face.

Dislocations, however, can neither end within a compact crystal nor within a cavity inside a wafer and the absolute value of all Burgers vectors on top of a void must be the same as on the bottom side. Condensation of individual screw-dislocations at the void edge forming open-core dislocations is due to the convex form of void's bottom part (Fig. 1). Recrystallization within a small cavity, with opposing faces that are only a few micrometers apart, should proceed towards the edges, until a critical value in dislocation density is reached.

The low temperature gradient and the lower oversaturation in the cavities explains the low level of dislocations because of the low nucleation rate according to Glass et al. (Ref. ^{17,18}) and Ma (Ref. ¹⁹). Also, a growing face with a parallel line vector will push the dislocation along the growth front; including the dislocation would induce an energetically disadvantageous stress field.

Once the growing area on the bottom part of the void reaches the voids edges, the dislocations are condensed into clusters whose stress field makes any further approach of the growth isle impossible and an open-core dislocation remains.^{20,21}

2.4 Defect characterization

To detect and analyze structural defects in silicon carbide, defect-selective etching (e.g., using molten KOH) are used and, then, other characterization methods can be applied, such as visual inspection using optical microscopy (for example, Nomarski Differential Interference Contrast NDIC). The basic principle behind the concept of preferential etching is that areas with high internal strains tend to be etched more rapidly, thus, creating characteristic etch pits on the surface.^{17,18} For higher resolution, Scanning or Transmission Electron Microscopy (SEM, TEM) or Atomic Force Microscopy (AFM) can be applied. More information, including crystallographic misalignment, can be obtained by using Synchrotron White Beam X-ray Topography (SWBXT) and High-Resolution X-Ray Diffraction (HRXRD).²²⁻²⁵

Using transmitted light microscopy, small macropipes and especially micropipes lying along the c-axis cannot be seen on single-crystals cut perpendicular to c; only tilted pipes will appear as one focuses through the sample. To determine defect densities, a quick and reliable method is needed. As shown in this study, simple polarization microscopy is capable of this task and subsequent conoscopic imaging reveals the wafer's inclination towards the c-axis. Polarization microscopy to describe stress-related interference pattern due to inclusions or dislocations has successfully been used for more than 50 years.²⁶⁻²⁸

3. EXPERIMENTAL METHOD

For electron microscopy a LEO VP 1450 instrument (Carl Zeiss AG, Oberkochen, Germany), operating at 15 kV acceleration current, and an Olympus BH2-UMA Normarsky phase contrast polarization microscope (Olympus Europa Holding GmbH, Hamburg, Germany) were used. Simulation of stress field was carried out using Matlab 7 (The MathWorks, Inc, Boston, U.S.A.).

4. RESULTS AND DISCUSSION

4.1 Morphology of macro-defects

Macro-defects in single-crystal silicon carbide exhibit a large structural variation. One cannot assume that macropipes behave like micropipes and postulate an even, well-shaped habitus. Fig. 2 depicts some examples of various pipe outlines. High-quality wafers tend to show less morphological variety and exhibit rather uniformly shaped, often polygonized (hexagonal) hollow-core screw-dislocations (Fig. 2h).

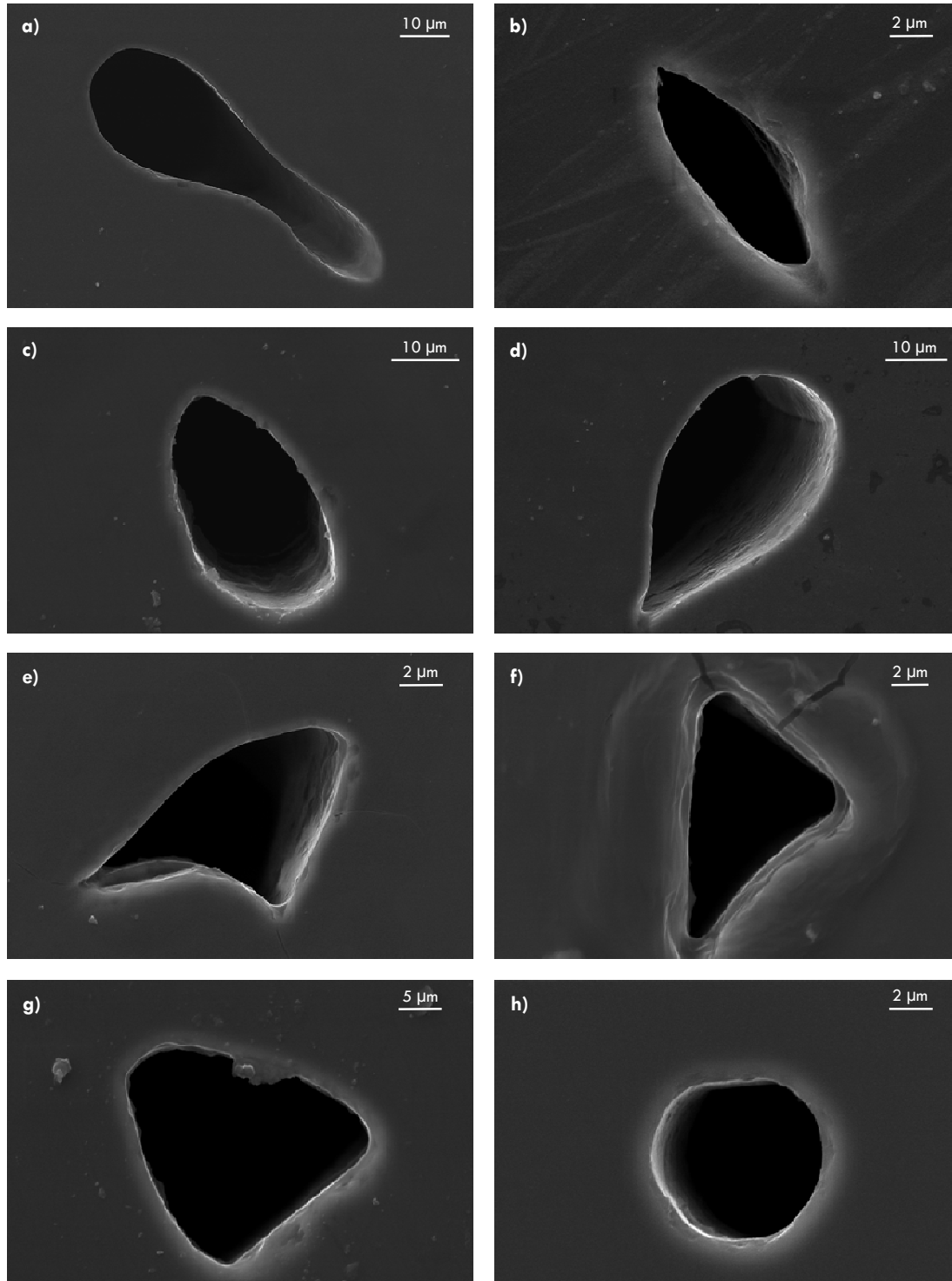


Fig. 2. Various forms of macropipes found on (0001)-SiC surfaces (SE-mode SEM microphotographs).
The pipe shown in Fig. 2h is characteristic for high-quality wafers.

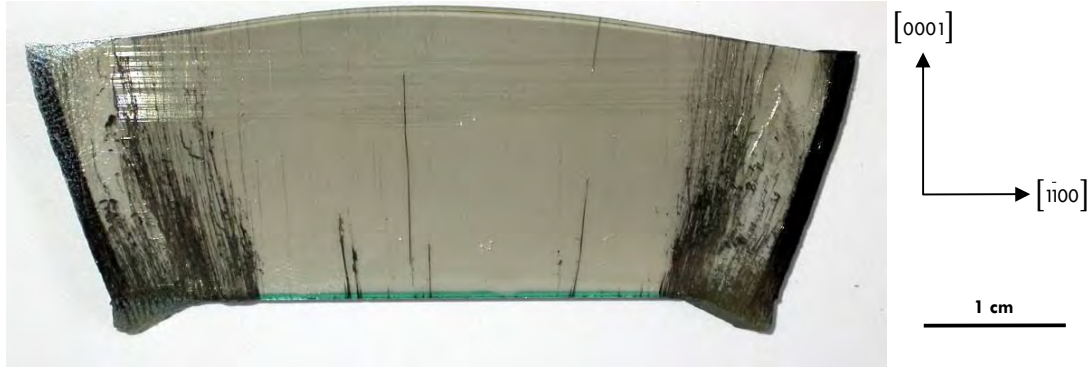


Fig. 3. Vertically sliced ingot showing pipes that deviate in their propagation direction significantly from the c-axis.

The direction of the c-axis is often the growth direction, and most pipes are oriented along it with little aberration.²⁹ The deviation seems to be related to faceted growth: pipes on areas where faceted growth occurs are almost ideal orientated along the c-axis; pipes grown on non-faceted areas can occur with a certain angle with respect to the c-axis.⁹

However, randomly orientated, short range pipes have also been observed.³⁰ SiC single-crystals grown perpendicular to the c-axis indeed did not show any pipe, but were characterized by a high level of stacking faults.^{11,31} In our samples, we found pipes following the outer curvature of the sliced ingot rather than the c-axis (Fig. 3). Their lateral expansion is limited ($\ll 100 \mu\text{m}$), but their vertical length often comprises the whole height of the single-crystals, which were up to several centimeters thick.

Large, often polygonized voids (“hollow crystals”) can be observed as a typical macro-defect lying in the basal plane. Depending on the SiC polytype, voids of different shapes can be seen. For hexagonal SiC, these voids tend to form rather hexagonal outlines and are, therefore, often referred to as “hexagonal voids”. However, it is important to note that even in one specific polytype the overall outline of these voids may vary greatly, as seen in Fig. 4.

In contrast to pipes voids are vertically limited. As shown in Fig. 5a, a void with a maximum of $\approx 300 \mu\text{m}$ lateral expansion has a width of $< 50 \mu\text{m}$ and only a deeper trench on the right. Voids, as discussed earlier, often terminate pipes; a typical case is depicted in Fig. 5b and 5c.

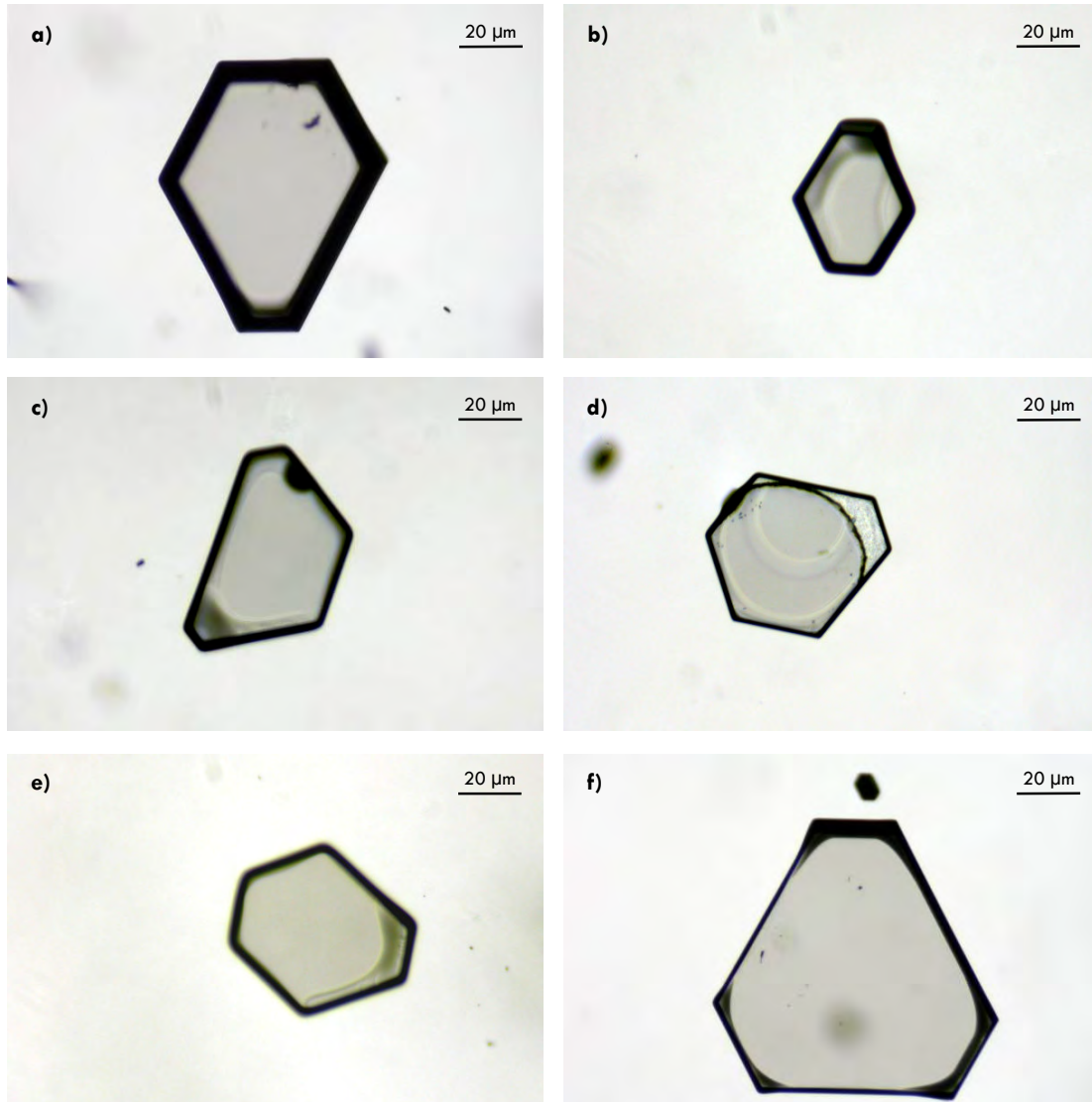


Fig. 4. Various forms of polygonized voids as observed in 6H-SiC (light microscopically images).

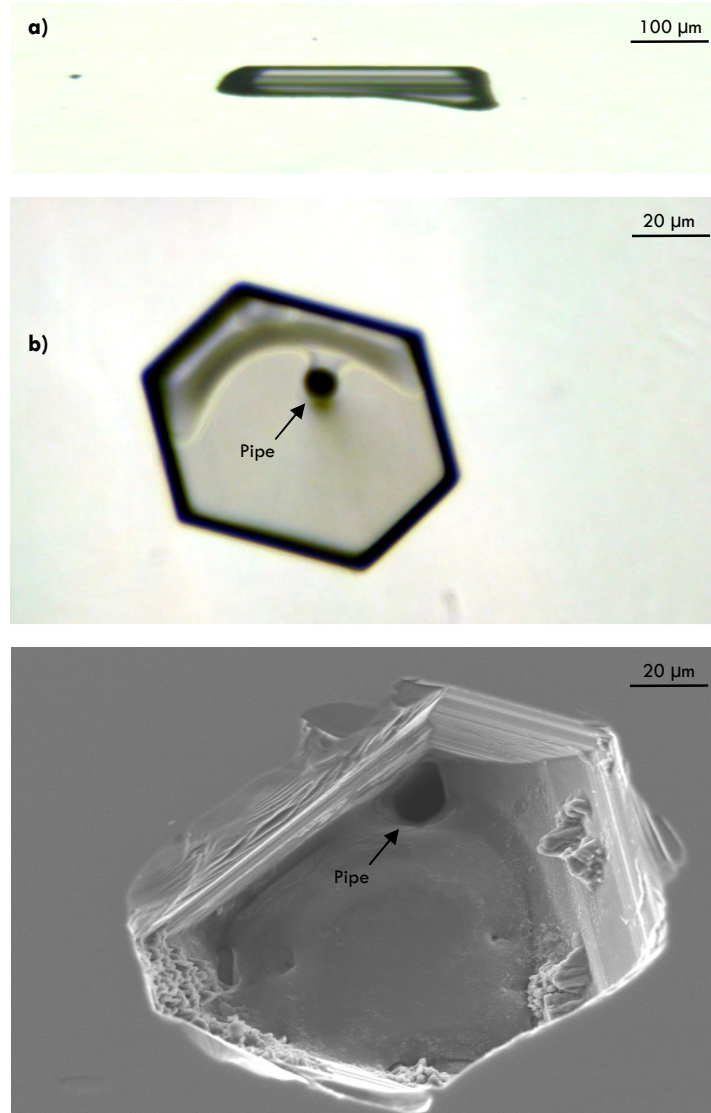


Fig. 5. Polarization microphotographs (a, b) and SE-mode SEM picture of voids. a) Vertically sliced void showing its preferential extension in the basal plane. b, c) Polygonized void terminating large open-core dislocation.

4.2 Polarization microscopy

4.2.1 Pipes

As discussed in detail by Kato et al.³², pipes are clearly visible under the light microscope in the crossed poles condition. A unique interference pattern is created by the distribution of internal stresses (Fig. 6). These “bright star patterns” are changed by rotating the sample and are much larger than the pipes they are connected to. Therefore, they indicate very precisely the position even of smaller pipes. As shown in Fig. 7, the visible strain field of $\approx 1 \mu\text{m}$ large pipe can easily reach $50 \mu\text{m}$ or more.

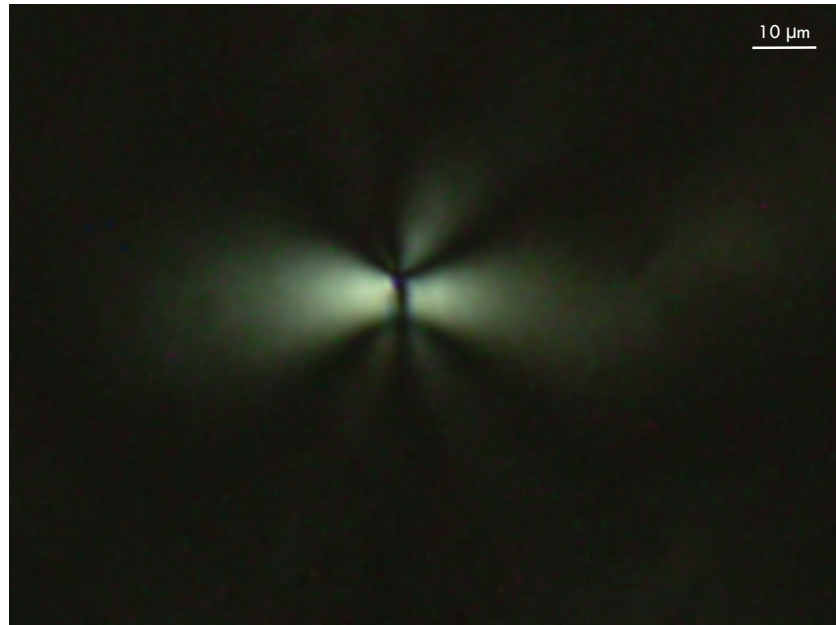


Fig. 6. Bright interference pattern around a large, elongated pipe similar to the one shown in Fig. 2b with a maximum diameter of approximately 5 μm.

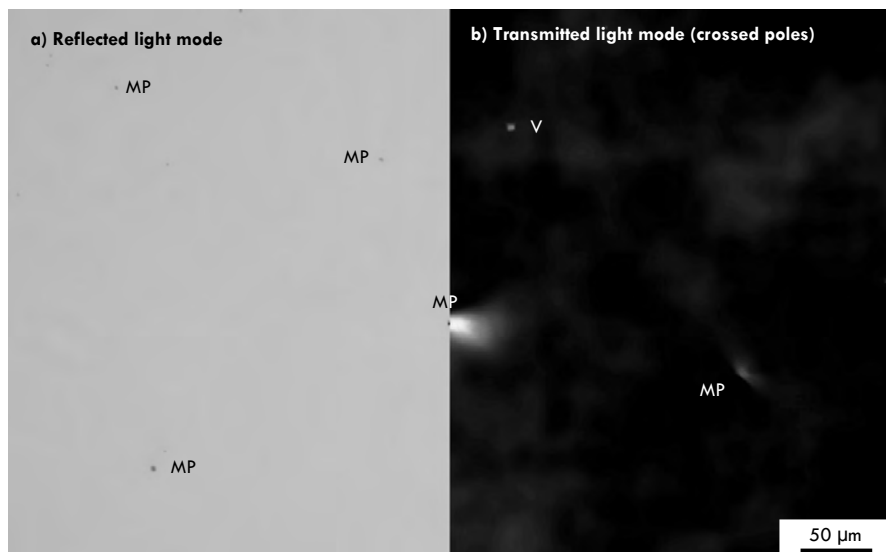


Fig. 7. Section of SiC wafer containing macropipes (MP). (a) Without crossed poles and (b) crossed poles. The macropipe (MP) in the middle is easily seen by the interference pattern, while in reflected light mode those small open-core dislocations are very difficult to see. A small void (V) is only visible, because a micropipe originates from it.

The origin of these halo-like patterns is strain, acting perpendicular to the c -axis, because without it no birefringence would be seen on the (0001)-face of silicon carbide, where the c -axis and the optical axis converge.³²

This behavior is well known from natural, deformed quartz grains and is referred to as undulatory extinction due to a locally anomalous biaxial optical character.³³ Using conoscopic microscopy, the anomalous biaxial optical character is easily visible. In case of (0001)-SiC, normally the bisecting isogyres will not change when rotating the sample around the c -axis. Strain around pipes causes the isogyres of a strained section to show an anomalous biaxial figure (i.e., a small opening of the central cross = melatope; Fig. 8). Also, as seen in Fig. 8c, inclination to a cut perpendicular to the c -axis is easily detected by non-centric rotation of the isogyres.

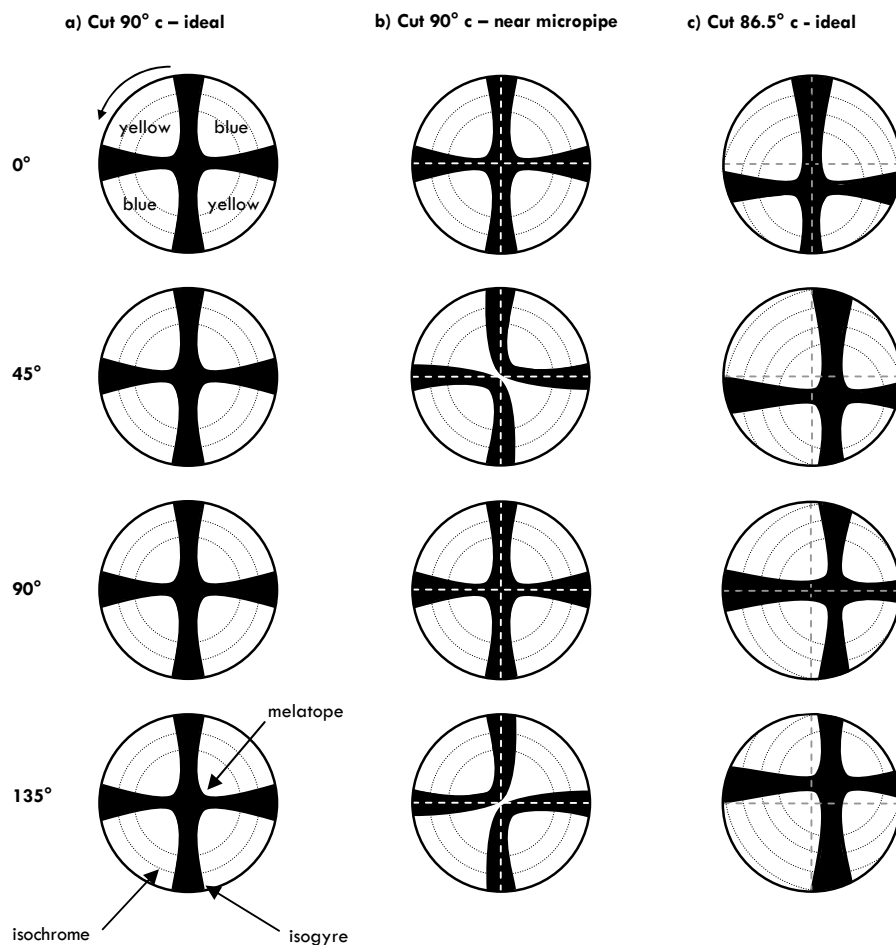


Fig. 8. Schematic conoscopic images of a 6H-SiC:N-Wafer cut perpendicular c (columns a, b) and with a 3.5° inclination towards the c -axis (column c). The rotation is anticlockwise. The colors denoted in the first figure are the birefringence colors with a red λ compensator (λ -plate: 551 nm) inserted. Column a): Ideal positive optical uniaxial character of 6H-SiC: centered, closed isogyres. Column b): In strained areas around e.g. micropipes, the optical uniaxial crystal becomes locally anomalous biaxial and the isogyres opens slightly.

Column c): A wafer cut with an offset towards the c -axis with closed, but not centered isogyres.

A more detailed study of the outline of the interference pattern around pipes is shown in Fig. 9. The outline of the interference pattern changes when rotating the sample along the c-axis (Fig. 9a). A very simple equation for edge dislocations²⁶ was found suitable. K in Eq. 1 can be seen as a scaling factor.

$$r^2 = K^2 \cdot \cos^2(2\phi) \cdot \cos^2(\phi - \beta) \quad \text{Eq. 1}$$

where r and ϕ to describe any point in polar coordinates and β describes the angle between the polarizer and the slip direction. K is defined as (Eq. 2):

$$K = \frac{\left(\frac{2aA\pi tC}{\lambda}\right)^2}{T} \quad \text{Eq. 2}$$

where a is the amplitude of the incident plane-polarized light, t denotes the plate's thickness, C is the mean strain-optic coefficient, λ describes the wavelength and T denotes the intensity of transmitted light.

The factor A is calculated using Eq. 3, where b is the absolute value of the Burger's vector and ν the Poisson's ratio.

$$A = \frac{b}{4\pi \cdot (1 - \nu)} \quad \text{Eq. 3}$$

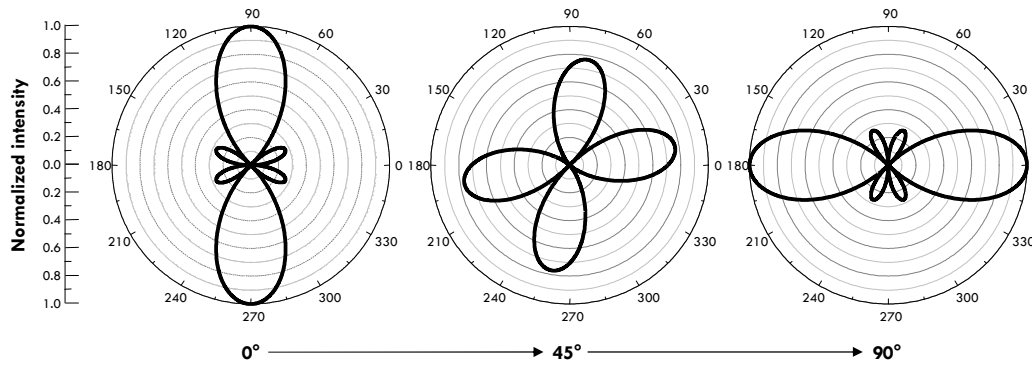
Simple polarization microscopy is, therefore, capable of characterizing strained regions in SiC in general and especially around pipes as long as the stress field is large enough for optical resolution.

Introducing a red-I-plate yields additional information about the direction of strain (cf. Fig. 9b). The presence of a homogenous, superimposing stress field would be indicated by bright and dark branches in the interference pattern (Fig. 9c).

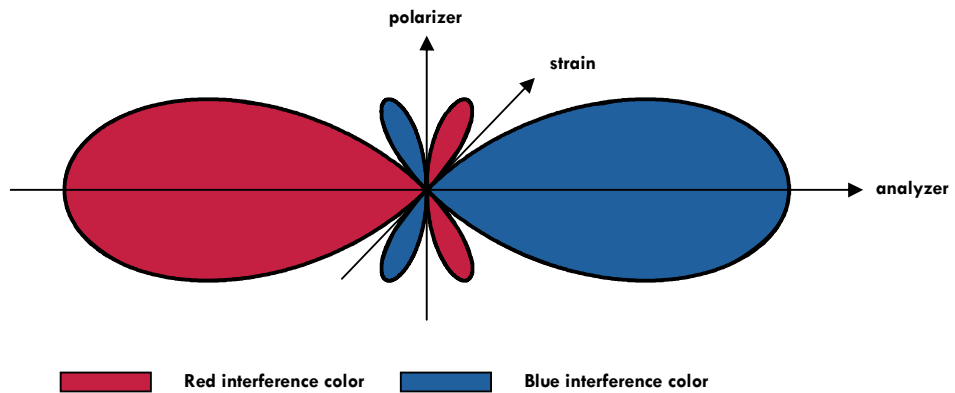
The equations above fit the phenomenological observations perfectly. However, this raises questions about the true nature of open-core dislocations, which we will discuss this topic in more detail below. Firstly, we will compare the stress field around (1) pure screw dislocations and around (2) screw dislocations having an edge component. A simulation of the stress field around both dislocation types, using the model of Hirth et al. (Ref. ³⁴) and the elastic constants of δ H-SiC from Kamitani et al. (Ref. ³⁵), is shown in Fig. 10. It illustrates the lines of constant intensity for (a) a pure screw-dislocation (Burgers vector

$$\vec{b} = \begin{pmatrix} 0 \\ 0 \\ 1 \end{pmatrix}, \text{ line vector } \vec{l} = \begin{pmatrix} 0 \\ 0 \\ 1 \end{pmatrix} \text{ and (b) a mixed-character dislocation } (\vec{b} = \begin{pmatrix} 0 \\ 0 \\ 1 \end{pmatrix}, \vec{l} = \begin{pmatrix} 1 \\ 1 \\ 0 \end{pmatrix}).$$

a) Interference pattern change while rotating the sample (crossed poles)



b) Interference pattern with inserted red-I-plate



c) Interference pattern with superimposing stress field

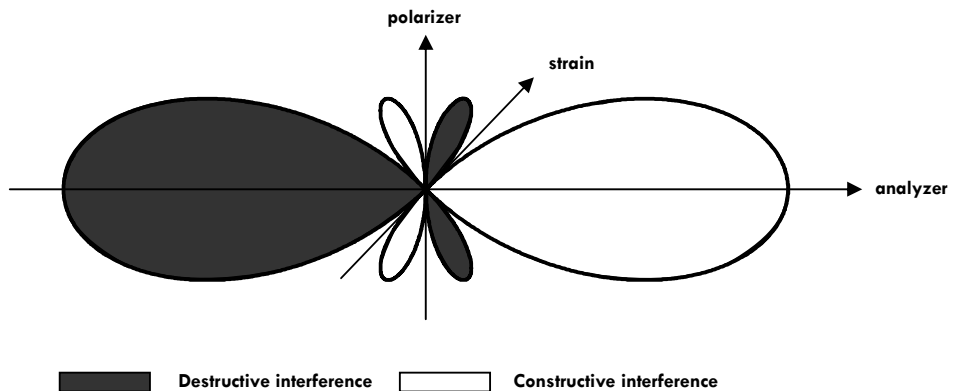
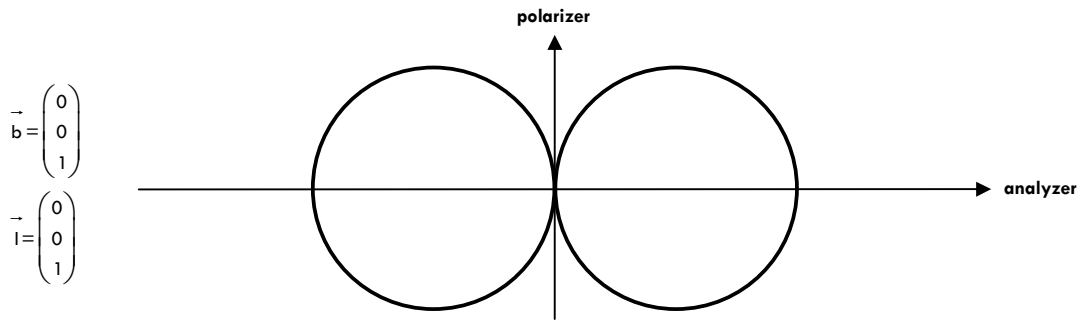


Fig. 9. a) Shape of the interference pattern around open-core dislocations in crossed poles condition. b) Interference pattern with red and blue areas after introduction of a red-I-plate. c) Destructive and constructive interfering areas of the strain field around pipes in the presence of a superimposing strain field.

a) Interference pattern of a pure screw-dislocation



b) Interference pattern of a mixed-type dislocation

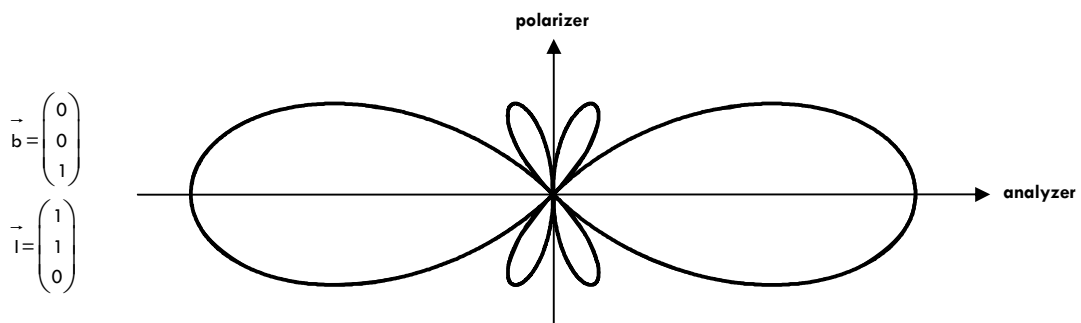


Fig. 10. Simulated contour shape (= lines of constant intensity) for a) a pure screw-dislocation and b) for a mixed-type dislocation (i.e., having both edge and screw components).

From Fig. 10 (screw versus mixed type dislocation) and Fig. 11 (observation versus simulation) and other interference patterns in the literature ^{26-28,36-38}, it is evident that the interference pattern around hollow-core dislocations (pipes) cannot be explained solely by the presence of a pure screw-dislocation (even with $|\vec{b}| > |\vec{c}|$), but critically requires the presence of an edge-component.

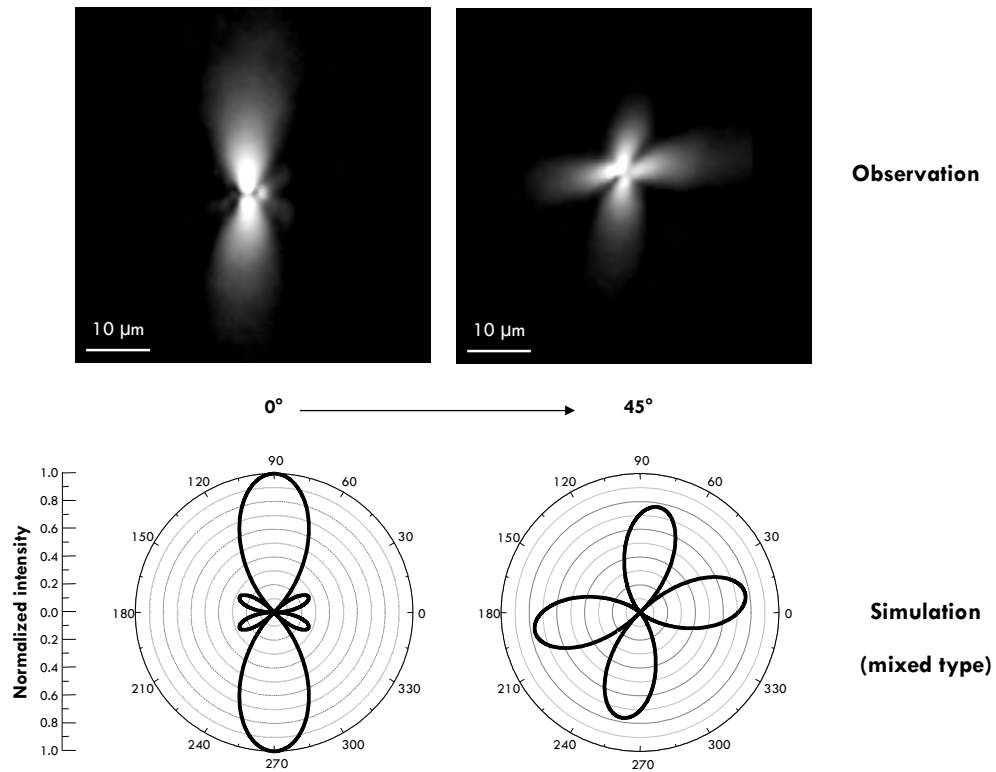


Fig. 11. Comparison between observed and simulated interference pattern. The pipe studied showed only a small deviation from the c-axis as confirmed by focussing different levels within the transparent crystal.

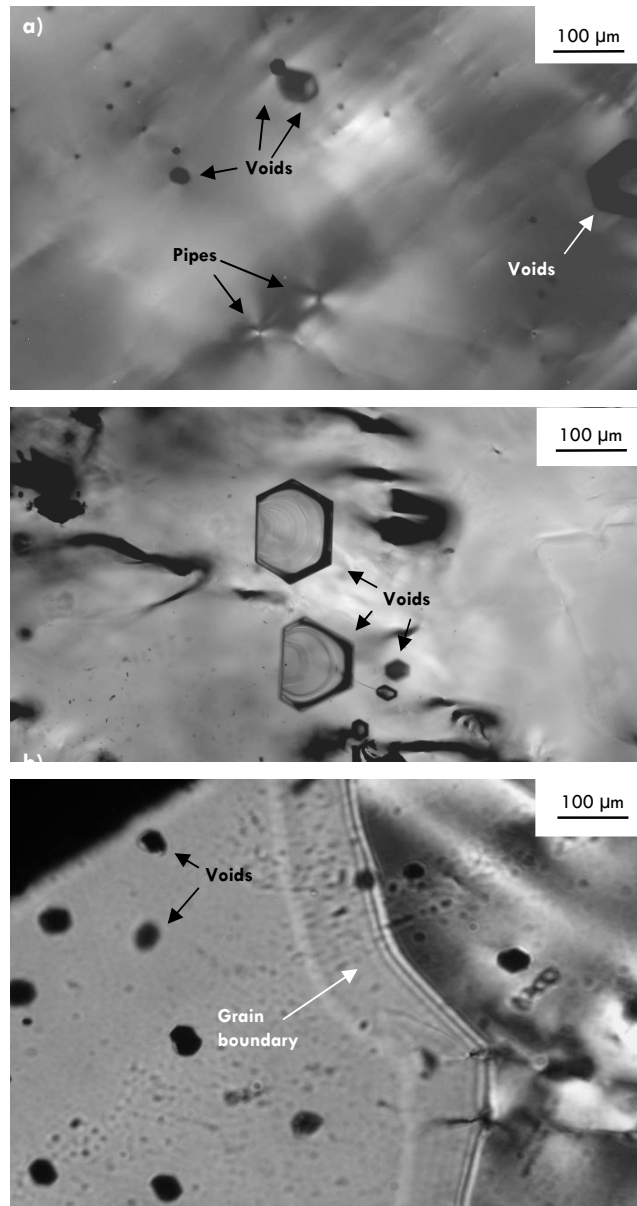


Fig. 12. Voids as seen using crossed poles. Pipes are surrounded by significant interference patterns (a); such halos are not present around voids (b). Any brightening around voids is related to clustered screw-dislocations (c).

4.2.2 Voids

As seen in Fig. 12, there is no significant strain field originating from voids. A pipe-related interference pattern appears only where a micropipe originates from the void. Even in highly strained areas at the edge of SiC single-crystals the voids were free of any stress field induced anomalous birefringence, which brightly illuminated other parts of the bulk material. This is shown in Fig. 12c, where strained areas of SiC are separated by a grain boundary.

This behavior is expected if the local vapor transport process leaves the voids moving during single-crystal growth at the bottom with a very low level of dislocations. However, the trench, located at the voids outer border (Fig. 1), often comprises several screw-dislocations (both closed-core and open-core). These dislocations are the source for the interference pattern around voids.

5. CHARACTER OF PIPES IN SILICON CARBIDE SINGLE-CRYSTALS

As discussed by Frank (Eq. 4; Ref. ^{20,21}), a high level of mechanically induced strain makes it energetically more advantageous to form hollow-core instead of closed-core dislocations during single-crystal growth, as more elastic stress-related energy can be saved than surface energy must be spent. This explains why these concave surfaces, which usually are readily closed during PVT growth, are still present and form those open-core screw-dislocations. It is important to note that a completely undistorted single-crystal would still be energetically highly favorable.

$$r = \frac{G \cdot b^2}{8 \cdot \pi^2 \cdot \gamma} \quad \text{Eq. 4}$$

Eq. 4 correlates an equilibrium radius of the open-core dislocation r with the shear modulus G , the absolute value of the Burgers vector \bar{b} and the surface energy γ .

The literature contains many contradicting findings on the character of pipes. Heindl et al. suggested a significant edge component in small micropipes, while true macropipes were described as almost ideal screw-dislocation using Frank's equation.³⁹ From Synchrotron White-Beam X-ray Topography (SWBXT) and simulations, Huang et al. claimed that the micropipes observed in their study were pure screw-dislocations.^{23,40} Ohsato et al. critically evaluated the strain-field around micropipes by polarization microscopy and found that it was not compatible with a pure screw-dislocation and needed the introduction of an edge component.^{37,38} Although the work of Ohsato et al. contained some inconsistencies in describing the interference patterns, our own investigations strongly confirm the presence of an edge component.

AFM and SWBXT work presented by Ma et al. (Ref. ⁴¹⁻⁴³) supported the interpretation of pipes as pure screw dislocations. They combined their analysis with polarization microscopy but did not further attempt to simulate the observed interference patterns in respect to the dislocation type. However, they confirmed interference pattern around both, pure (closed-core) screw dislocations and pipes.⁴³

The contradictions of the literature could be due to the existence of pipes with different dislocation characteristics. This needs critical consideration in view of the considerable morphological variety of macro- and micropipes. Furthermore, Frank's equation is only an approximation for pipes, as it assumes an isotropic material as far as the elastic properties are concerned. This precondition would be met for a screw-dislocation whose line direction is perfectly parallel to c , as the only stress component in this case is shear strain along [0001]. For deviations from this ideal orientation, the magnitude of elastic anisotropy becomes important. Anisotropy was found to be larger at higher temperatures for 3C-SiC (Ref. ⁴⁴) and 6H-SiC (Ref. ^{45,46}); thus, significant anisotropy must be considered during PVT growth. From the data of Kamitani et al. ³⁵ and Eq. 5 a value of $A_{\max} \approx 16\%$ can be approximated at room temperature for the stress field of a dislocation with line and Burgers vector both lying perpendicular to the c -axis.

$$A_{\max} = 1 - \frac{C_{44}^*}{\frac{1}{2} \cdot (C_{11}^* - C_{12}^*)} \tag{Eq. 5}$$

where C_{nm}^* is used in contrast to the general notation C_{ijkl} .

For any angle α between line direction and c-axis, Eq. 6 can be used to calculate the value for the effective anisotropy:

$$A_{\text{eff}} = \sin(\alpha) \cdot A_{\max} = \sin(\alpha) \cdot \left[1 - \frac{C_{44}^*}{\frac{1}{2} \cdot (C_{11}^* - C_{12}^*)} \right] \tag{Eq. 6}$$

Edge dislocations can be evaluated using the very same procedure described earlier, although the resulting equations are more elaborate, as both shear and principal stress and strain must be considered.

It is questionable whether screw-dislocations or screw components are present in dislocations that are not parallel c. The lack of pipes perpendicular to c may well be phenomenological evidence against this. Also, it is remarkable that micro- and macropipes only occur in materials with sheet-like structure, for example, highly structurally anisotropic materials (SiC, ZnS, CdI₂).⁴⁷⁻⁴⁹ As dislocations are no equilibrium phenomenon, the system favors their removal and, therefore, they will move out of the crystal along glide planes as soon as critical activation energy for this movement can be overcome. For edge dislocations, gliding is possible perpendicular to the line direction and parallel to the Burgers vector. Gliding of screw dislocations happens perpendicular \bar{b} . Fig. 13 depicts a schematic illustration of possible gliding planes for 6H-SiC.

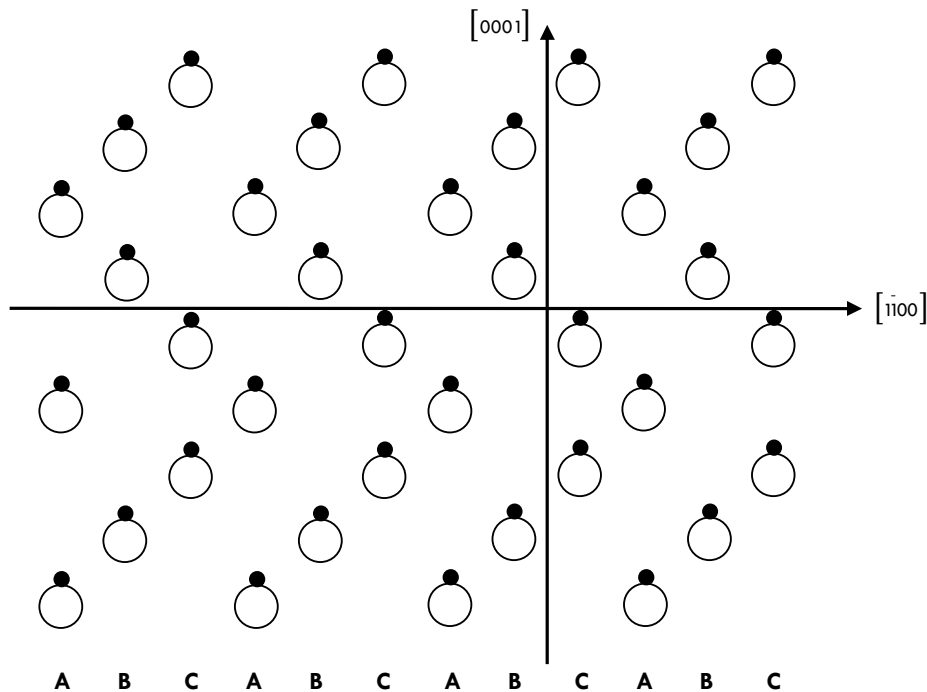


Fig. 13. Schematic illustration of the crystal structure of 6H-SiC with two possible glide planes.

Movement of a dislocation with an integer Burgers vector requires gliding of the parts of the crystal structure by one unit cell parameter. A 6H-SiC gliding along [0001], therefore, requires movement of 1.5079 nm in c- and 0.3073 nm in a-direction, i.e., moving within the a-b plane requires a “step” that is only one fifth of the step width along c. It is trivial to assume the activation energies to follow the same correlation. Moreover, in the a-b plane there exists one more path for gliding, because in $\langle \bar{1}\bar{1}00 \rangle$ it is possible for the dislocation to move in two steps along $\langle \frac{1}{2}\bar{1}\frac{1}{2}0 \rangle$ and $\langle \frac{1}{2}\bar{1}\frac{1}{2}0 \rangle$ (= 0.2661 nm each). Thus, stacking faults will temporarily be created. This mechanism may be energetically favorable because stacking faults contain only low energies. Along c no such “shortcut” can occur as no partial shift will result in a close-packed structure.

Therefore, dislocations with a Burgers vector in the basal plane are relatively mobile within the crystal structure, while in case of \bar{b} parallel c dislocations are not kinetically favored for gliding. This means that screw-dislocations will be found parallel c and only edge dislocations can be found within the basal plane. Assuming a sufficiently high annealing temperature, pipes, which are not perfectly arranged along the c-axis must show some edge component as any pure screw dislocation component with \bar{b} lying in the basal plane would have vanished.

Gliding of dislocations with a non-integer absolute value of \bar{b} will result in a high level of stacking faults. The observation of Takahashi et al.¹¹ of pipe-free SiC crystals grown along $[\bar{1}100]$ but with stacking-faults favors the assumption that dislocations parallel to the growth direction will be created during the crystal growth on the seed crystal and anneal later, depending on the actual orientation.

Unfortunately, most published studies do not describe the exact orientation of the observed pipes relative to the c-axis. Standard wafers are cut to a thickness of 250 μm making a large-scale examination of the exact defect orientation impossible. Fig. 3 showed a typical case of a medium-grade SiC single-crystal ingot cut perpendicular to (0001). Here, the pipes propagate along the curved outer face of the crystal rather than purely along c. The scatter for literature values for the true character of pipes may be explained this way.

Another complication of Frank's equation is that no additional strain is considered. Clusters of dislocations within the basal plane were reported to be radially distributed around pipes⁵⁰ and to dissociate into Shockley partial dislocations. Their formation is due to the system's impetus to reduce the stress around pipes, which will influence the equation radius of the formed open-core dislocation. These considerations are even more complicated by the observation of unevenly shaped pipes, which raises even more questions on the applicability of Frank's equation.

Considering the above statements, the observation of a strain field of a dislocation with both screw and edge components can be explained in two ways. First, edge dislocations around pipes may superimpose the stress field created by the screw dislocation to yield an interference pattern similar to the one of a mixed-type dislocation stress field. This, however, would require a non-uniformly distributed stress field, because a homogenous stress field would cause both constructive and destructive superimposition of the stress fields (cf. Fig. 9c). Second, the studied pipes probably have both edge and screw components, as they do not lie perfectly parallel to c. This would well explain all observations as long as the simulated data of closed-core dislocations with and without an edge component are truly extendable to open-core defects.

6. CONCLUSION

We reported on the variability of the general outline and interference pattern of hollow macro-defects commonly known from SiC single-crystals. Both defect types, voids and pipes, exhibit a wide range of structural variability, which accounts for the discrepancies in the literature concerning the nature of hollow-core dislocations. These were described earlier as pure screw-dislocations⁴¹, but the work Ohsato et al.^{37,38} raised serious doubts upon this interpretation, because the interference pattern were unexplainable unless a edge-component was introduced to pipes.

We confirm these findings and attribute the observed interference phenomenon to the character of pipes with an inclination towards the c-axis, which always have an edge component. Furthermore, voids were shown to be in a relaxed state due to their origin from a local vapour transport growth process, even within a superimposing strain-field.

Conoscopy allows gaining more information about a general inclination of the single-crystal and especially about anomalous biaxial behavior with undulatory extinction. Considering how quick and easy-to-apply polarization and conoscopical microscopy is compared to other defect-characterization methods, we think that routine application of these methods e.g. for quality management will become important. Kubota et al. recently described a method to automate this way of rapid defect mapping.⁵¹ Also, conosopic imaging allows accessing information about the angle, in which a certain wafer has been cut.

Acknowledgments

This work was supported by the Deutsche Forschungsgemeinschaft (DFG) through Ni299/12-1. The authors would like to thank Dr. Th. Wenzel and Dr. N. Peranio (University Tübingen) for valuable discussion and help during the simulation phase.

REFERENCES

1. Acheson, E.G. On Carborundum. *Chemical News* **68**, 179 (1893).
2. Schwetz, K.A. Silicon Carbide Based Hard Materials. in *Handbook of Ceramic Hard Materials*, Vol. 2 (ed. Riedel, R.) 683 - 748 (Wiley-VCH Verlag GmbH, Weinheim, 2000).
3. Feng, Z.C. *SiC Power Materials. Devices and Applications.*, 450 (Springer Verlag, Berlin, 2004).
4. Dhanaraj, G., Huang, X.R., Dudley, M., Prasad, V. & Ma, R.-H. Silicon Carbide - Part I: Growth and Characterization. (eds. Byrappa, K. & Ohachi, T.) 181 - 232 (Springer-Verlag, Berlin, 2003).
5. Harris, G.L. *Properties of Silicon Carbide*, 282 (INSPEC, the Institution of Electrical Engineers, London, 1995).
6. Tairov, Y.M. & Tsvetkov, V.F. Investigation of growth processes of ingots of silicon carbide single crystals. *Journal of Crystal Growth* **43**, 209 - 212 (1978).
7. Verma, A.R. & Krishna, P. *Polymorphism and Polytypism in Crystals*, 362 (John Wiley & Sons Inc, Chichester, 1966).
8. Herro, Z.G. et al. Growth of 6H-SiC crystals along the [01-15] direction. *Journal of Crystal Growth* **275**, 496 - 503 (2005).
9. Müller, S.G. et al. Physical Vapor Growth and Characterization of High Conductivity 1.4 inch 4H-SiC Bulk Crystals. *Materials Science Forum* **264 - 268**, 33 - 36 (1998).
10. Hofmann, D., Bickermann, M., Hartung, W. & Winnacker, A. Analysis on the formation and elimination of filamentary and planar voids in Silicon Carbide Bulk Crystals. *Materials Science Forum* **338 - 342**, 445 - 448 (2000).
11. Takahashi, J. & Ohtani, N. Modified-Lely SiC Crystals Grown in [1-100] and [11-20] Directions. *Physica Status Solidi (B)* **202**, 163 - 175 (1997).
12. Kuhr, T.A., Sanchez, E.K., Skowronski, M., Vetter, W.M. & Dudley, M. Hexagonal voids and the formation of micropipes during SiC sublimation growth. *Journal of Applied Physics* **89**, 4625 - 4630 (2001).
13. Eckstein, R. Universität Erlangen-Nürnberg (1998).
14. Hofmann, D. et al. Analysis on defect generation during the SiC bulk growth process. *Materials Science Forum* **B61 - B62**, 48 - 53 (1999).
15. Anthony, T.R. & Cline, H.E. Thermal Migration of Liquid Droplets through Solids. *Journal of Applied Physics* **42**, 3380 - 3387 (1971).
16. Sanchez, E.K. et al. Formation of thermal decomposition cavities in physical vapor transport of silicon carbide. *Journal of Electronic Materials* **29**, 347 - 352 (2000).
17. Glass, R.C., Kjellberg, L.O., Tsvetkov, V.F., Sundgren, J.E. & Janzen, E. Structural macro-defects in 6H-SiC wafers. *Journal of Crystal Growth* **132**, 504 - 512 (1993).
18. Glass, R.C., Henshall, D., Tsvetkov, V.F. & Carter, C.H., Jr. SiC Seeded Crystal Growth. *Physica Status Solidi (B)* **202**, 149 - 162 (1997).
19. Ma, X. Superscrew dislocations in silicon carbide: Dissociation, aggregation, and formation. *Journal of Applied Physics* **99**, 1 - 6 (2006).
20. Frank, F.C. The Growth of Carborundum: Dislocations and Polytypism. *Philosophical Magazine* **42**, 1014 - 1021 (1951).
21. Frank, F.C. Capillary Equilibria of Dislocated Crystals. *Acta Crystallographica* **4**, 497 - 501 (1951).
22. Huang, X.R., Vetter, W.M., Huang, W., Wang, S. & Carter, C.H., Jr. Direct evidence of micropipe-related pure superscrew dislocations in SiC. *Applied Physics Letters* **74**, 353 - 355 (1999).
23. Huang, X.R. et al. Superscrew dislocation contrast on synchrotron white-beam topographs: an accurate description of the direct dislocation image. *Journal of Applied Crystallography* **32**, 516 - 524 (1999).
24. Dudley, M. et al. White-Beam Synchrotron Topographic Studies of defects in 6H-SiC Single Crystals. *Journal of Physics D* **28**, A63 - A68 (1995).
25. Dudley, M. et al. White-Beam Synchrotron Topographic Analysis of Multi-Polytype SiC device configuration. *Journal of Physics D* **28**, A56 - A62 (1995).
26. Bullough, R. Birefringence Caused by Edge Dislocations in Silicon. *Physical Review* **110**, 620 - 623 (1958).
27. Ming, N. & Ge, C. Direct observation of defects in transparent crystals by optical microscopy. *Journal of Crystal Growth* **99**, 1309 - 1314 (1990).
28. Tanner, B.K. & Fathers, D.J. Contrast of crystal defects under polarized light. *Philosophical Magazine* **29**, 1081 - 1094 (1974).
29. Powell, A.R. & Rowland, L.B. SiC Materials - Progress, Status and Potential Roadblocks. *Proceedings of the IEEE* **90**, 942 - 955 (2002).
30. Augustine, G., Hobgood, H.M., Balakrishna, V., Dunne, G. & Hopkins, R.H. Physical Vapor Transport Growth and Properties of SiC Monocrystals of 4H Polytype. *Physica Status Solidi (B)* **202**, 137 - 148 (1997).
31. Takahashi, J., Kanaya, M. & Fujiwara, Y. Sublimation growth of SiC single crystalline ingots on faces perpendicular to the (0001) basal plane. *Journal of Crystal Growth* **135**, 61 - 70 (1994).
32. Kato, T., Ohsato, H., Okamoto, A., Sugiyama, N. & Okuda, T. The photoelastic constant and internal stress around micropipe defects of 6H-SiC single crystal. *Materials Science and Engineering B* **B57**, 147 - 149 (1999).

33. Pichler, H. & Schmitt-Riegraf, C. *Rock-forming Minerals in Thin Section*, 220 (Chapmann & Hall, London, 1997).
34. Hirth, J.P., Barnett, D.M. & Lothe, J. Stress fields of dislocation arrays at interfaces in bicrystals. *Philosophical Magazine A* **40**, 39 - 47 (1979).
35. Kamitani, K. et al. The elastic constants of silicon carbide: A Brillouin-scattering study of 4H and 6H SiC single crystals. *Journal of Applied Physics* **82**, 3152 - 3154 (1997).
36. Bond, W.L. & Andrus, J. Photographs of the stress field around edge dislocations. *Physical Review* **101**, 1211 (1956).
37. Ohsato, H., Kato, T., Okuda, T. & Razeghi, M. Internal stress around micropipes in 6H-SiC substrates. *Proceedings of SPIE-The International Society for Optical Engineering* **3629**, 393 - 399 (1999).
38. Ohsato, H., Kato, T. & Okuda, T. Screw and edge dislocations-induced internal strain around micropipes of 6H-SiC single crystals. *Materials Science in Semiconductor Processing* **4**, 483 - 487 (2001).
39. Heindl, J. et al. Dislocation Content of Micropipes in SiC. *Physical Review Letters* **80**, 470- 471 (1998).
40. Huang, X.R. et al. Direct evidence of micropipe-related pure superscrew dislocations in SiC. *Applied Physics Letters* **74**, 353 - 355 (1999).
41. Ma, X., Dudley, M., Vetter, M. & Sudarshan, T. Extended SiC Defects: Polarized Light Microscopy Delineation and Synchrotron White-Beam X-Ray Topography Ratification *Japanese Journal of Applied Physics* **42**, L1077 - L1079 (2003).
42. Ma, X. & Sudarshan, T. Nondestructive Defect Characterization of SiC Substrates and Epilayers. *Journal of Electronic Materials* **33**, 450 - 455 (2004).
43. Ma, X. A method to determine superscrew dislocation structure in silicon carbide. *Materials Science and Engineering B* **129**, 216 - 221 (2006).
44. Li, Z. & Bradt, R.C. The single-crystal elastic constants of cubic (3C) SiC to 1000°C. *Journal of Materials Science* **22**, 2557 - 2559 (1987).
45. Veldkamp, J.D.B. & Knippenberg, W.F. Anomalous Young's modulus behaviour of SiC at elevated temperatures. *Journal of Physics D* **7**, 407 - 411 (1974).
46. Hasselman, D.P.H. & Batha, H.D. Strength of Single Crystal Silicon Carbide. *Applied Physics Letters* **2**, 111 - 113 (1963).
47. Forty, A.J. The growth of cadmium iodide crystals: I - Dislocations and spiral growth. *Philosophical Magazine* **43**, 72 - 81 (1952).
48. Verma, A.R. *Crystal Growth and Dislocations*, 182 (Butterworths Scientific Publications, London, 1953).
49. Mardix, S., Lang, A.R. & Blech, I. On giant screw dislocations in ZnS Polytype Crystals. *Philosophical Magazine* **24**, 683 - 693 (1971).
50. Vetter, W.M. & Dudley, M. Transmission electron microscopy studies of dislocations in physical-vapour-transport-grown silicon carbide *Philosophical Magazine A* **81**, 2885 - 2902 (2001).
51. Kubota, T., Talekar, P., Ma, X. & Sudarshan, T.S. A nondestructive automated defect detection system for silicon carbide wafers. *Machine Vision and Applications* **16**, 170-176 (2005).

Chapter 01

Chapter 02

Chapter 03

Chapter 04

Chapter 05

Chapter 06

Chapter 07

Chapter 08

Chapter 09

Chapter 10

Chapter 11

Chapter 12

MICROSTRUCTURAL EVOLUTION OF SILICA ON SINGLE CRYSTAL SILICON CARBIDE. PART 1: DEVITRIFICATION AND OXIDATION RATES

V. Presser⁽¹⁾, A. Loges⁽¹⁾, Y. Hemberger⁽¹⁾, K. G. Nickel⁽¹⁾

⁽¹⁾ Institut für Geowissenschaften, Universität Tübingen

ABSTRACT:

Dry thermal oxidation of single-crystal silicon carbide ($6H\text{-SiC}$) at 1400°C in low-water oxygen using an alumina tube furnace initially yields a predominantly vitreous oxide scale. After 28 h approximately one quarter of the oxide scale's surface has become crystalline with disc-like cristobalite aggregates (radialites) statistically distributed within the vitreous matrix. Crystalline areas were found to be thinner than vitreous regions using optical microscopy and AFM/HF-etching analysis, providing evidence for different oxidation rates of silicon carbide covered by vitreous silica and cristobalite. As the bulk oxide scale continues to grow during devitrification, the radialites assume their characteristic morphology with a deepened center. Line-profiles of the oxide scale's thickness across radialites obtained from AFM/HF-etching were used to determine the oxidation rate of SiC covered by crystalline silica and the crystallization rate applying a two-stage parabolic equation. As a result, it was found that the parabolic rate-constant B_{vitreous} is ≈ 4.2 -times larger than the corresponding rate-constant in crystalline areas ($B_{\text{cristobalite}}$) suggesting similar differences in effective oxygen diffusion coefficients. For the crystallization rate v we determined a value of $1.5 \pm 0.1 \mu\text{m/h}$.

1. INTRODUCTION

For over a century silicon carbide (SiC) was used almost exclusively for abrasive and high-temperature applications. In the last decade SiC has also turned into a promising semiconductor material as high-quality SiC wafers have become available.¹⁻³ Its beneficial high-temperature behavior is due to the formation of a protective oxide scale consisting of silica (SiO₂). The latter is the only stable native oxide of silicon carbide (SiC) and is formed at temperatures above 900°C.^{4,5} Analogous to Si oxidation, oxide scale growth on SiC generally follows a linear-parabolic time-law leading to passivation of the carbide's surface.^{6,7} As indicated by this time-law, the oxidation mechanism is believed to become mainly diffusion-controlled after an initial period.

At temperatures above 1200°C the initially vitreous silica crystallizes beginning at the oxide-atmosphere interface and disc-like crystal plates of β-cristobalite appear (radialites; often referred to as spherulites).⁴ If the diffusion-coefficient of crystalline silica is smaller compared to vitreous SiO₂, the oxide scale will grow faster in vitreous regions which act as pathways of accelerated diffusion.⁸

A second microstructural transition takes place when the large radialite crystal plates (often larger than 200 μm in diameter while only 1 – 2 μm thick) transform into small solid crystal spheres (globulites; approx. 2 μm in diameter).^{4,9,10} This process is most likely related to impurities like alkaline or alkaline earth elements which are present in many raw materials and furnace atmospheres.¹¹ During cooling below 500°C, β-cristobalite finally undergoes a phase transformation into α-cristobalite, accompanied by a decrease in volume by 4.9 vol%, causing crack formation.¹²⁻¹⁵

In the first part of this study we show how Atomic Force Microscopy (AFM) in combination with HF-etching ("AFM/HF-etching method") yields information about the local morphology of the scale and its interfaces. We chose 28 h exposure at 1400°C for dry thermal oxidation as we knew from previous studies that this period is long enough to have a substantial scale growth yet only sparsely intergrown radialites. The overall oxidation process was described earlier.⁴ The second part of this study will focus on the influence of impurities and defects on the microstructural evolution, especially as far as globulite formation is concerned.

2. EXPERIMENTAL

High-quality 6H-SiC:N (SiCrystal AG, Erlangen, Germany) was used to cut 10.0 x 5.0 x 0.25 mm³ samples which were then polished. 28 h of thermal oxidation in an alumina tube furnace at 1400°C in high-purity non-dehumidified oxygen yielded a 1.24 μm thick oxide scale as determined by spectral ellipsometry. During the oxidation, the sample rested on two 250 μm thick vertically aligned 6H-SiC:N plates to reduce the contact area with the support plate, to avoid contamination and allow free access for the gas to all sample sides.

AFM measurements were performed using a TopoMetrix Explorer® (TopoMetrix Corporation, Santa Clara, United States of America) in contact mode with a tripod scanner (500 x 500 pixel data resolution). Nomarski DIC was carried out using a BH2-UMA microscope (Olympus Europa Holding GmbH, Hamburg, Germany).

Removal of the oxide scale was accomplished using aqueous hydrofluoric acid (HF, 40%) at ambient temperature. Occasionally the HF solution was stirred to overcome local saturation. After 24 h the silica scale was completely removed. Shorter HF exposure times led to remaining isles of dense silica.

Examination of the very same sample position before and subsequent to HF-etching was ensured by mapping large areas and comparing the very unique pattern of the individual radialites. HF-etching of unoxidized SiC wafers caused no measurable corrosive attack; the RMS roughness (root mean square; R_q) remained unchanged at $\approx 42 \pm 7$ nm.

3. RESULTS AND DISCUSSION

3.1 Nomarski DIC

After oxidation, we applied Nomarski DIC microscopy to study the oxide scale. Fig. 1a shows the oxide scale after 28 h of thermal oxidation which is characterised by the presence of radialites within a vitreous silica layer. Approximately 25% of the sample's surface was found to be crystalline silica. In accordance with the literature we confirmed the crystalline parts of the oxide scale to be α -cristobalite by XRD and Raman spectroscopy.⁴ We found two types of radialites: (1) radialites like R1 (Fig. 1a) which have a mean radius of 47 ± 5 μm (based on 25 radialites) and (2) radialites like R2 which have undergone structural transition towards globulite formation. More than $\approx 90\%$ of the radialites are R1-type and less than 10 % are similar to R2 with larger diameters and significant globulization. Fig. 1e – 1g show examples of R2-type radialites with pronounced globulite formation.

Most radialites (Fig. 1b) are easily distinguished from the vitreous regions. This is due to the decrease in volume as a result of the β -to- α phase transition of the original devitrification product β -cristobalite. Consequently, crack formation occurs and must critically be considered during cyclic oxidation.¹⁶ However, as seen in Fig. 1c and 1d, not all crystalline areas show crack formation. It is trivial to assume these crack-free crystalline regions to be under tensile stress at room temperature because of the β -to- α phase transition.

During the initial stages of radialite formation and growth the crystalline discs exhibit a characteristic hexagonal shape (Fig. 1b, 1d). The reason why a cubic crystal (β -cristobalite) growing within a vitreous layer (silica) shows a hexagonal shape is illustrated in Fig. 2: the preferential growth of β -cristobalite along the octahedral faces (i.e., $\{111\}$) results in a hexagonal shape for the (111) viewing direction.^{4,17,18}

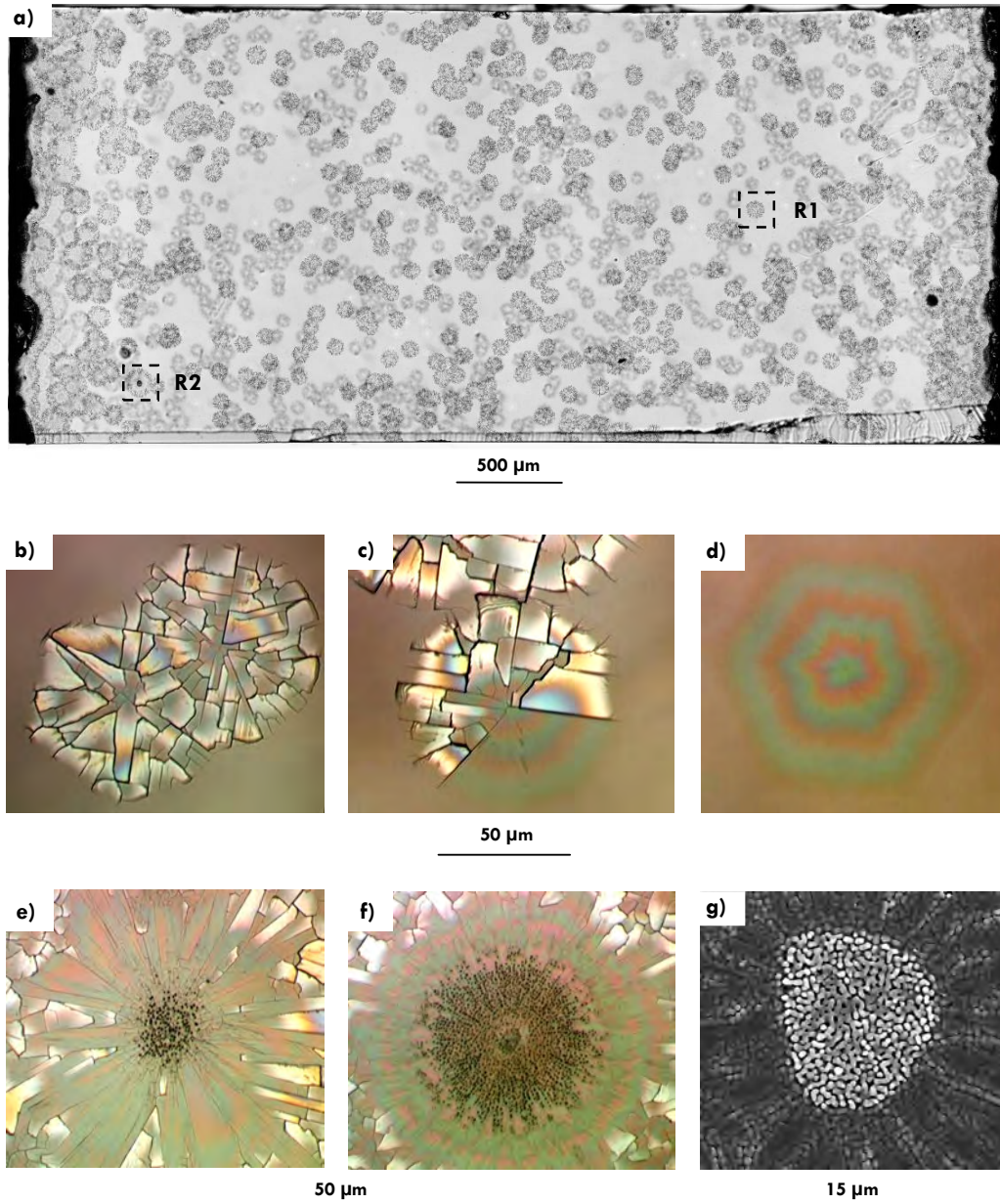


Fig. 1. (a) Nomarski DIC pictures of the sample's surface showing partially intergrown radialites within a vitreous silica scale. R1 and R2 denote two radialites that will be subject to AFM/HF-etching analysis and which are two typical radialite types [(b – d): R1-type, (e): R2-type]. After the experiment the radialites are often highly differentiated into several crystal plates (b) due to the β -to- α phase transition of cristobalite. Overall, both differentiated and uncracked radialites are visible as depressions within the vitreous matrix (c, d). Note the overall hexagonal shape of the individual radialites. R2-type radialites show globulite formation (e, f), that is, small crystalline spheres (g; SE-mode SEM image).

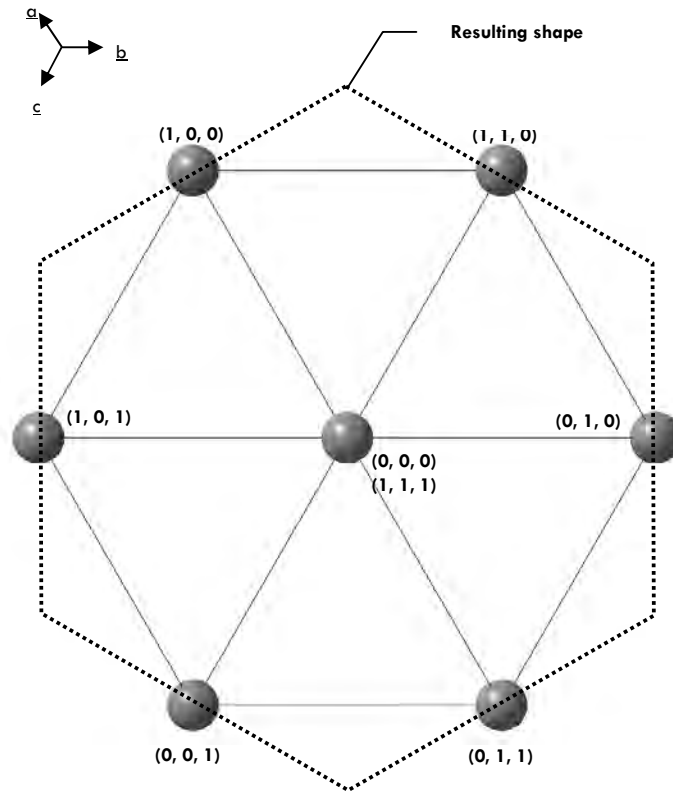


Fig. 2. The shape of cristobalite radialites shown in Fig. 1 is explained by preferential growth of {111}- β -cristobalite, because a hexagonal outline results in the (111) viewing direction.

Fig. 3 compares a magnified section from Fig. 1 with calculated interference colors for crystalline silica on silicon carbide using the optical constants of α -cristobalite. For α -cristobalite ($n = 1.48$), thickness-dependent interference colors can be calculated using Eq. 1 (Ref. ^{19,20}).

$$\lambda_{\text{constructive interference}} = \frac{2 \cdot n \cdot d \cdot \cos(\beta)}{m - \frac{1}{2}} \quad \text{Eq. 1}$$

where m denotes the interference color order and β is the angle of the refracted ray (refraction due to the phase boundary air-to-oxide). In case of perpendicular incident light, β becomes 42.51 when using Snell's law.

The interference color of the radialite encompasses three orders (m), yielding a total z-difference of approximately 500 nm. The scale thickness of most radialites, however, is not accessible via analysis of interference colors due to crack formation (cf. Fig. 1b). Therefore, and because of the higher precision of z-values, we applied the AFM/HF-etching method. It should be noted that the z-values determined via optical microscopy and AFM/HF-etching differed by less than 30 nm.

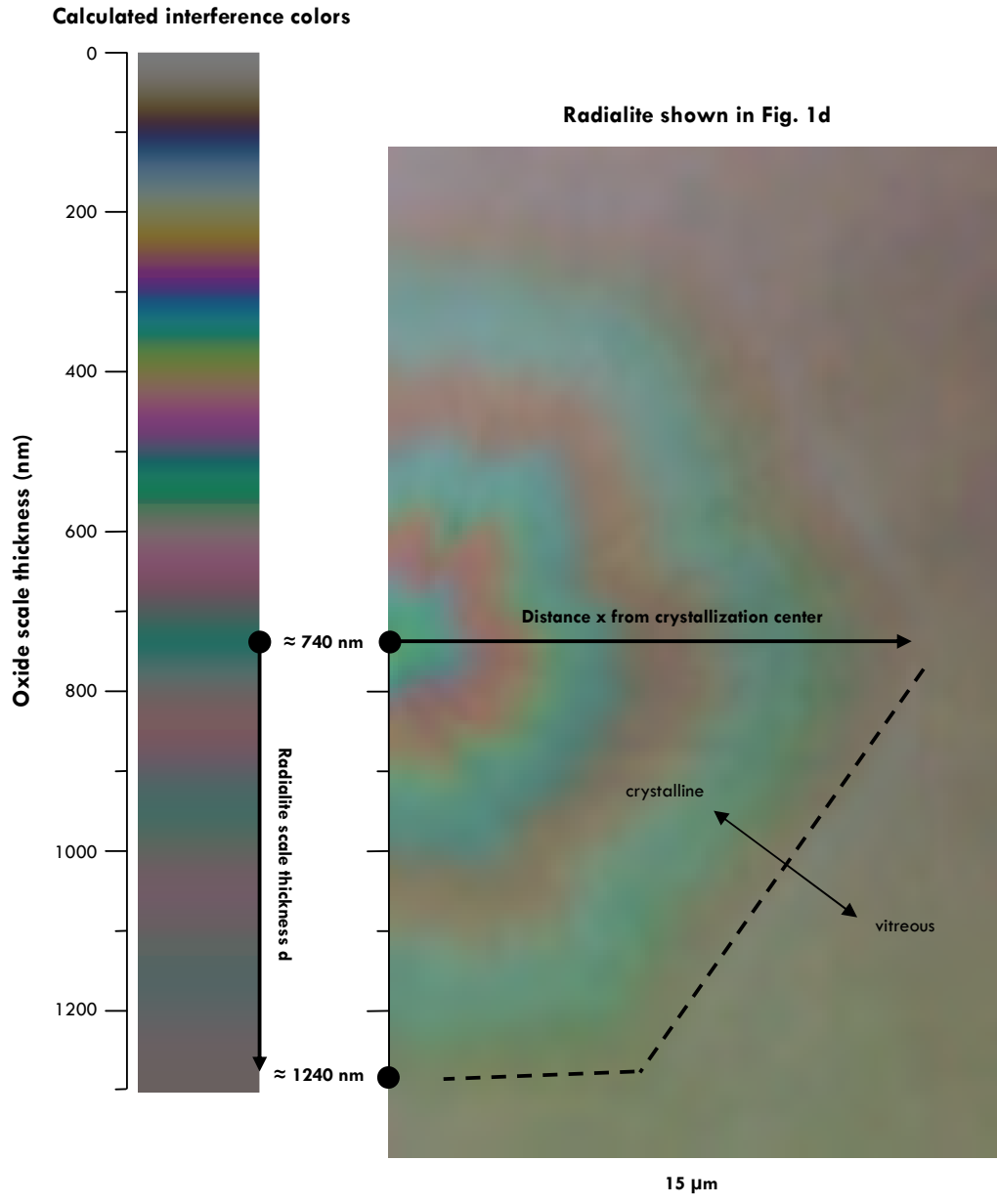


Fig. 3. Comparison between calculated and observed interference colors of the radialite shown in Fig. 1d. Note the almost equidistant spacings between interference color orders. The interference colors were calculated using the refraction index for α -cristobalite (1.48) using Eq. 1.

3.2 AFM/HF-etching

AFM analysis of the oxide scale's surface (Fig. 4a) shows the appearance of several small crystal plates, which are detached from each other. This differentiation with significant cracks between single crystal plates is presumably due to the aforementioned volume contraction associated with the β -to- α phase transition during cooling. This is evidenced by the fact that the SiC-side of the SiC-SiO₂ interface (Fig. 4b) does not show the characteristic grain boundaries present in the overlying oxide scale. Differentiation of the radialites into several crystal plates is a well-known phenomenon and is due to energy minimization while an overall radial symmetrical superstructure is maintained.^{4,21}

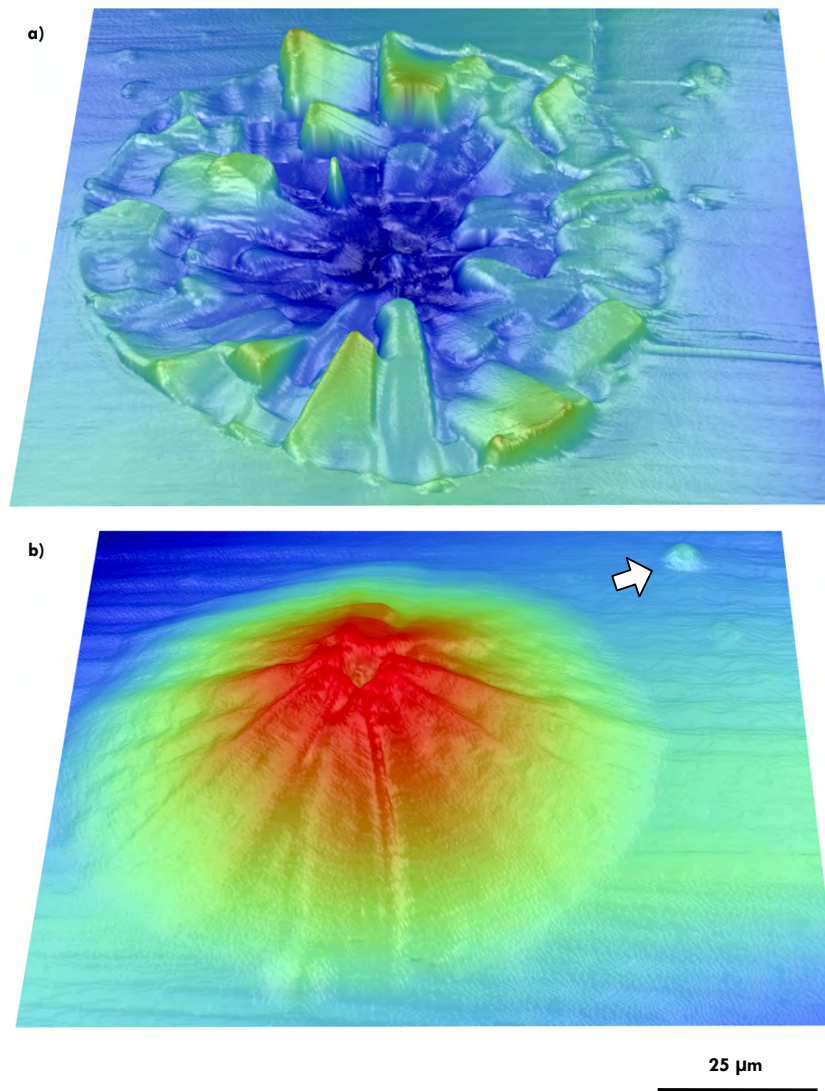


Fig. 4. Shaded AFM scans of R1: (a) the upper silica scale surface and (b) the SiC-side of the former SiC-SiO₂-interface (110 × 110 μm²). The scale bar is only valid for the horizontal front line of the individual pictures due to perspective distortion.

Also, the pictures are vertically super-elevated. An arrow marks a small crystallization center.

The SiC-SiO₂ interface exhibits the inverse morphology of the upper oxide scale's surface: a radialite forms a depression in the vitreous silica matrix with the deepest part in the center. Correspondingly, the former SiC-SiO₂ interface shows an elevation of solid silicon carbide that has its peak at the crystallization center.

The central crater-like depression may be linked to the fact that the strain of the original uncracked inclined crystal plate is largest and grain boundary formation begins here. Grain boundaries themselves accelerate oxidation due to faster gas diffusion.

From previous experiments it is known that the crystallization rate V of vitreous stoichiometric silica is linear for dry atmospheres but becomes parabolic for high water-vapor concentrations or oxygen-deficient silica.^{22,23} It is difficult to assess at which time exactly a nucleus of critical size is formed and crystallization starts, but the crystallization rate of the radialite shown in Fig. 4 (\varnothing 85 μm , 28 h oxidation) must have been at least 1.5 $\mu\text{m}/\text{h}$ ($= \frac{1}{2} \cdot 85 \mu\text{m} : 28 \text{h}$). Larger values for V are also possible as critical nucleation during the very initial oxidation period ($\ll 1 \text{h}$) is unlikely and has been observed to be impurity related, only. The radius we used is half the distance between two flat parallel sides of the radialite hexagons (cf. Fig. 2).

From experiments conducted on stoichiometric rehydrated vitreous silica (GE2214 and GE224 glasses) by Li et al., a crystallization rate of $2.6 \pm 0.1 \mu\text{m}/\text{h}$ for atmospheres containing 0.6 – 2.0 vol% water vapor was estimated for 1400°C.²³ Increasing water content correlates with larger crystallization rate (e.g., $> 15 \mu\text{m}/\text{h}$ in 0.1 MPa water vapor at 1426°C).^{24,25} Consequently, a large scatter of crystallization rates can be found in the literature. Inside a solid cube of melted quartz glass exposed to an inert gas atmosphere, crystallization rates as low as 0.2 $\mu\text{m}/\text{h}$ were reported by Wagstaff which might indicate a lower boundary for an intrinsic crystallization rate.²⁶ Also, surface effects might account for faster crystallization rates in superficial areas compared to the bulk volume.²⁷

In our experiments the water vapor content was significantly lower than in the experiments by Li et al. and, thus, $\approx 1.5 \mu\text{m}/\text{h}$ is a reasonable crystallization rate to assume. This assumption is corroborated as the largest distance for the crystalline scale to have spread into the vitreous matrix at the very edge of the sample yields the same crystallization rate. These areas are expected to undergo crystallization already during an initial oxidation phase due to scratches and discontinuities. Larger crystallite radialites can be attributed to the presence of impurities and, therefore, these do not yield reliable values for determination of the intrinsic crystallization rate of pure silica. The crystallization rate found in this study is in perfect agreement with results presented in a previous study, where we obtained $v = 1.4 \pm 0.2 \mu\text{m}/\text{h}$ from average radialite diameters for 11 samples (6H-SiC:N) and oxidation times of up to 64 h.⁴

As the oxide scale grows, the crystallization front propagates laterally further into the growing vitreous matrix. Vertically, the very thin oxide scale is penetrated very fast explaining why the diameter of the radialites is almost the same for the upper surface and the lower SiC-SiO₂ interface. Fig. 5 shows a line profile through the HF-etched former oxide-carbide interface yielding a radialite diameter at the oxide-atmosphere interface (d_{upper}) of 87 μm and a diameter at the carbide-oxide interface (d_{lower}) of 85 μm .

The observation of larger radialite diameters on the oxide-atmosphere interface compared to the oxide-carbide interface was found to be true for all studied radialites, suggesting that crystallization starts at the $\text{SiO}_2\text{-O}_2$ interface. TEM results (part II) also give evidence to this. Superficially adsorbed gas molecules may act as unstable or metastable crystallization centers due to their contribution to the total energy (adsorption energy) causing the crystallization to start at the oxide-atmosphere interface.²⁸ The small differences in diameter (i.e., $d_{\text{upper}} \approx d_{\text{lower}}$) evidence that crystallization must have started during an early oxidation stage.

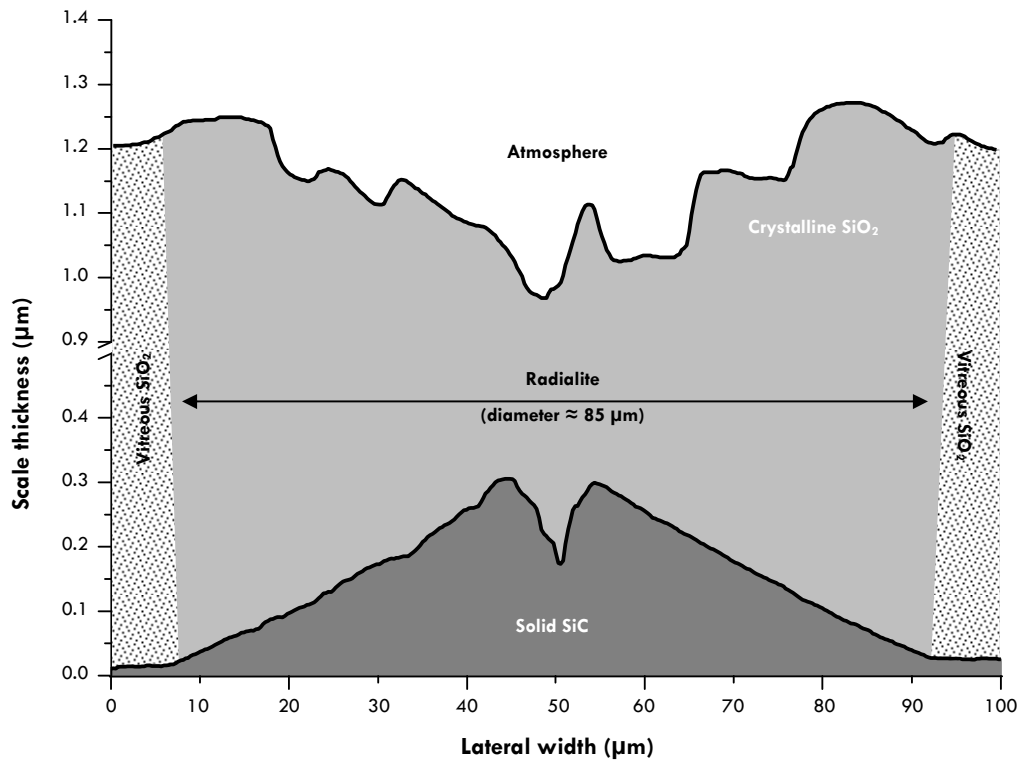


Fig. 5. Line-scan through radialite R1. Note the vertical super elevation.

Another reason for the difference between d_{upper} and d_{lower} is faster crystal growth in the upper parts of the oxide scale than in the lower. This is not unlikely, because the vitreous matrix could be stabilised by impurity enrichment along the crystallization front. Part II of this study will discuss impurity-related influences in more detail.

Bulk oxide scale growth is much slower than lateral crystallization. Diffusion through crystalline silica must be slower than through vitreous SiO_2 to make the growing radialite adopt its characteristic shape with a slim inner part and thicker outer regions (schematically shown in Fig. 6). If it were not for the β -to- α transition of cristobalite, the morphology of the line-profile through the radialite at the oxide-atmosphere interface would mirror the one at the oxide-carbide interface.

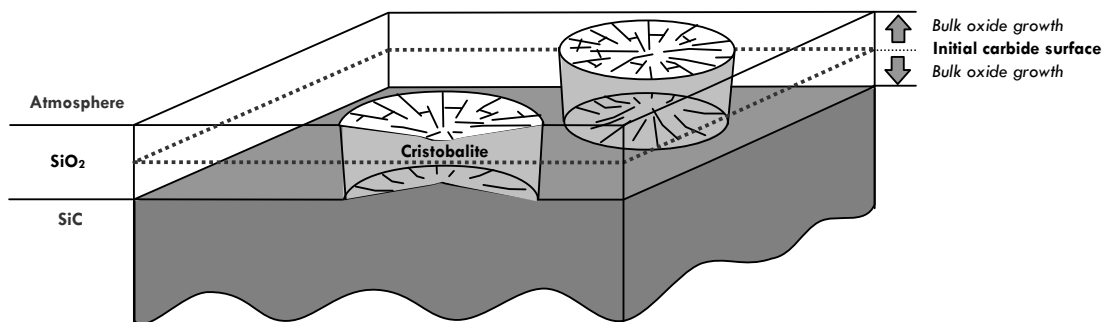


Fig. 6. Schematic illustration of radialites within the vitreous silica matrix thermally grown on silicon carbide. Note that the schematic illustration is vertically super elevated – in fact, a radialite thickness of 1 – 2 μm is contrasted by a much larger horizontal expansion of up to 100 μm in our sample (= 50 times the bulk scale thickness).

A second structural transition takes place when small crystalline spheres ($\varnothing \approx 1 - 2 \mu\text{m}$) consume the radialite plates (Fig. 1f – 1g). The exact reason for this transition is still a matter of dispute, but an impurity related cause for this microstructural effect is most likely.^{4,17} Although consisting of the very same crystalline phase as radialite plates, the oxide scale comprising globulites is significantly thicker.

Figure 7 depicts a radialite ($\varnothing 137 \mu\text{m}$) that has formed around a $\approx 1 \mu\text{m}$ small micropipe (hollow-core dislocation defect; cf. Ref. ²⁹) and which has already undergone the transition towards globulite formation starting at the center. There is no significant influence on the oxidation rate by the presence of such a small pipe; however, it has acted as a crystallization center. The outer part of the SiC-SiO₂ interface still displays the outline of the caldera-like radialite; the inner part is rough and porous. The inner part's scale thickness reaches values higher than the surrounding vitreous matrix (1.40 μm instead of 1.24 μm). This effect is more evident in Fig. 8 where a combined profile plot of the upper and lower AFM scan is presented. Porosity comprised in-between the individual globulites allows oxygen to diffuse faster towards the oxide-carbide-interface leading to locally accelerated oxidation with an accordingly thicker oxide scale. An impurity-related contribution to increased oxidation rates is likely, because micropipes are places that can retain machining or handling impurities despite cleaning. The radialites' outer diameter reaches 137 μm which is $\approx 50 \mu\text{m}$ more than the mean diameter of radialites observed on this sample (as presented, for example, in Fig. 3). As mentioned above, the radialite-globulite transition is believed to be impurity-related and, therefore, an accelerated crystallization rate (2.4 $\mu\text{m}/\text{h}$) is expected.

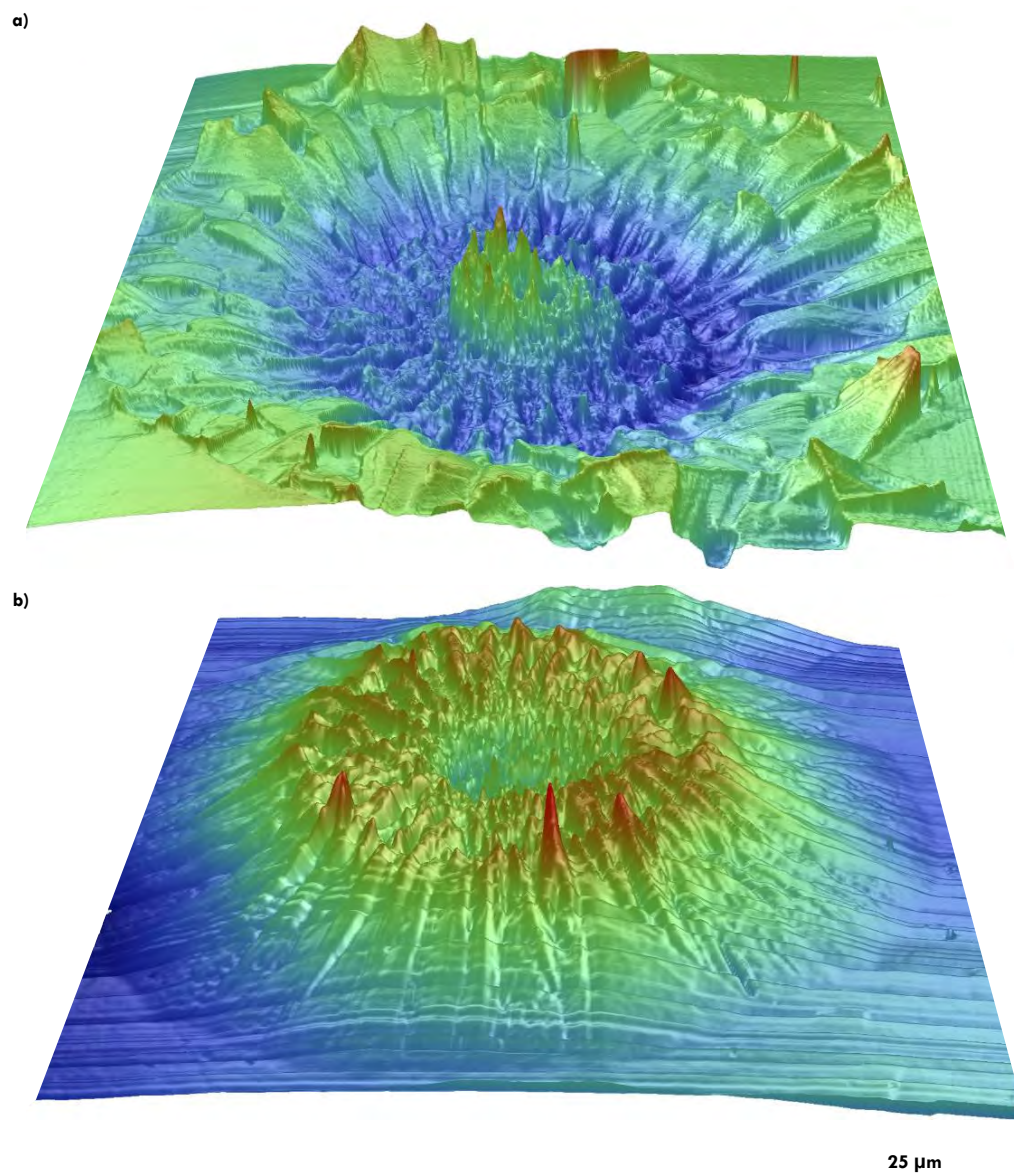


Fig. 7. AFM scans of R2: (a) the upper silica surface and (b) the SiC-side of the former SiC-SiO₂-interface (150 x 150 μm^2). Horizontal ripple-like lineation is due to vibrations during the AFM scan. The picture is perspectively distorted and has a maximum vertical height of 800 nm.

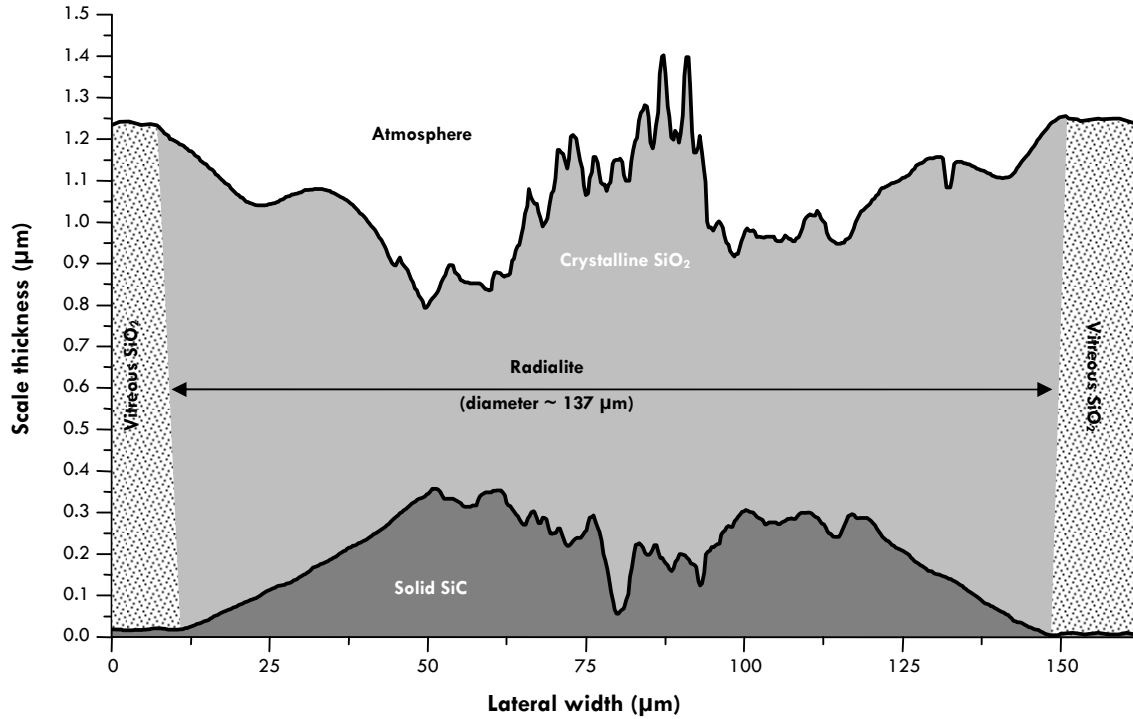


Fig. 8. Line-scan through radialite R2. Note the vertical super elevation.

3.3 Oxidation rates

When evaluating the radialite thickness, the slope of the elevation at the former SiC-SiO₂ interface is of special interest as the *in-situ* morphology at high temperatures is preserved there. The sequence of interference orders in uncracked radialites is almost equidistant (Fig. 3) and the slope of the SiC-SiO₂ interface also appears to be linear in the AFM/HF-etching results (Fig. 5, 9a). Fitting a linear function to the measured line profile data, however, yields significant residuals (Fig. 9b). Because both the vitreous and the crystalline region will grow following a (linear)-parabolic time-law, the slope at the carbide-oxide interface cannot be a simple linear one.

Over long periods the linear-parabolic time-law can be approximated by a simple parabolic one which has been applied for the following calculations. In case of a parabolic time-law, there are only two rate-constants to be considered for devitrifying silica: $B_{\text{cristobalite}}$ for the crystalline region and B_{vitreous} for the vitreous scale.⁴ From other studies $B_{\text{cristobalite}}$ is expected to be smaller than B_{vitreous} because of the higher diffusion coefficient of oxygen in non-crystalline silica.³⁰⁻³² The exact difference between $B_{\text{cristobalite}}$ and B_{vitreous} is a matter of dispute. A factor of ≈ 3 for the corresponding diffusion coefficients was reported by Rodriguez-Viejo et al. (Ref. ³²; ¹⁸O diffusion experiments) at 1400°C.

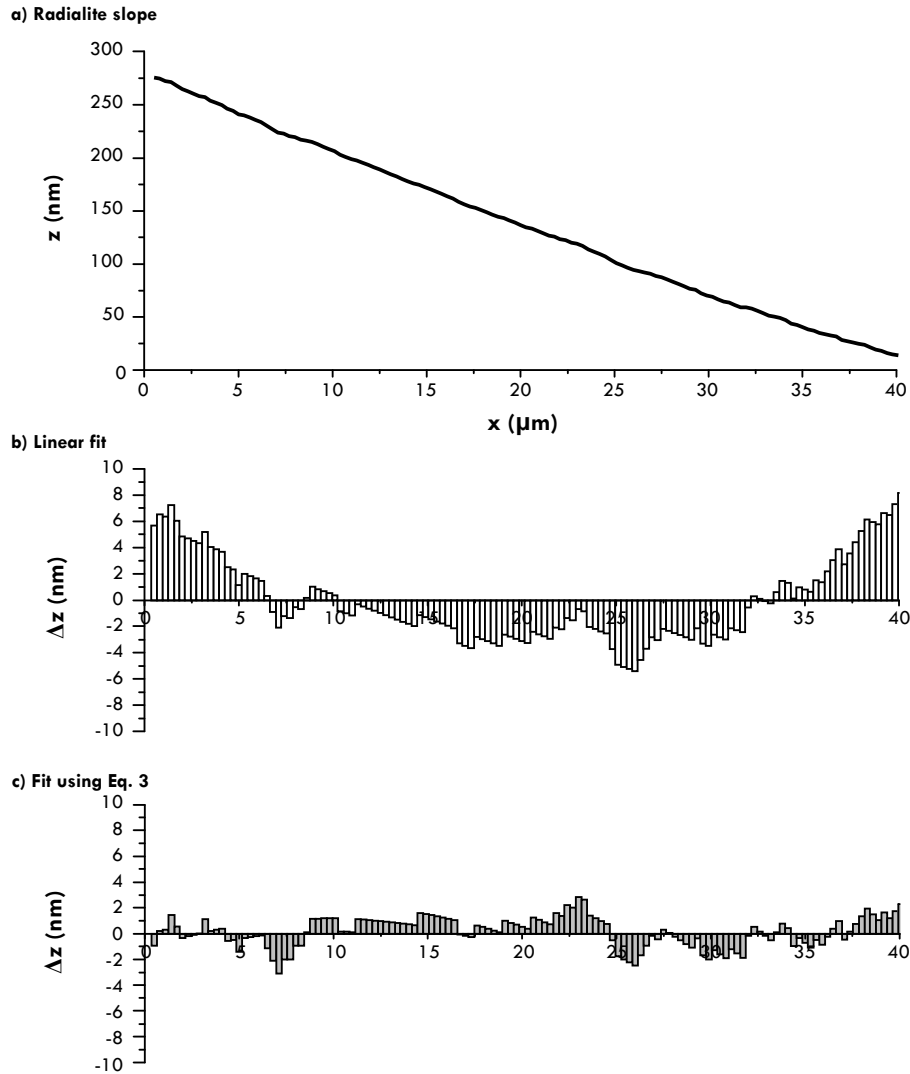


Fig. 9. Line profile of the slope of radialite R1 (a) and the fitting results using a linear fit (b) and Eq. 13 (c). Note the large residuals in case of a single linear fit. For discussion see text.

For an undisturbed vitreous part of the scale its thickness d_{vitreous} can be calculated as a function of time t using Eq. 2:

$$d_{\text{vitreous}} = \sqrt{B_{\text{vitreous}} \cdot t_{\text{vitreous growth}}} \tag{Eq. 2}$$

The time which the crystallization front needs to progress along a distance x is determined by the crystallization rate V . From other studies it is known that the crystallization rate of silica follows a linear time-law.^{4,23,26,27} Consequently, $t_{\text{vitreous growth}}$ can be expressed as Eq. 3 as a fraction of the distance x from radialite center for all points within the radialite and the crystallization rate V :

$$t_{\text{vitreous growth}} = \frac{x}{V} \tag{Eq. 3}$$

We will now present an equation that gives the total oxide scale thickness at a distance x from the crystallization center (cf. Fig. 3). For that, we assume that crystallization has started at $t = 0$ at the radialite center. Later, this assumption will be discussed in more detail. Eq. 3 gives the oxide scale's thickness for the whole time during which silica is present in its vitreous form. Once crystallization has taken place the scale will continue to grow following a parabolic time-law with a different rate-constant. For the further scale growth we cannot simply add two parabolic-growth equations like Eq. 2; instead we must correct the parabolic-growth for additional contribution of the vitreously grown, now crystallized scale at position x . Deal and Grove proposed a factor T to this correction (which, in their case, was used to correct for an initially present scale; Eq. 4).

$$d = \sqrt{B \cdot (t + T)} \quad \text{Eq. 4}$$

However, T is a correction term for the time that was required to build up this initial scale and no direct term for the thickness itself. Thus, when considering two different parabolic rate-constants ($B_{\text{vitreous}} > B_{\text{cristobalite}}$) we must correct the thickness d_{vitreous} of the now crystallized scale by introducing an expression for the time it would have taken an ideal crystalline silica scale to build up this scale thickness ($T_{\text{crystallization}}$). The difference in density between vitreous silica and β -cristobalite is negligible – at the very moment of crystallization we assume $d_{\text{vitreous}} = d_{\text{cristobalite}}$ – and this is why we can write for the time correction term (Eq. 5):

$$T_{\text{crystallization}} = \frac{(d_{\text{vitreous}})^2}{B_{\text{cristobalite}}} \quad \text{Eq. 5}$$

Inserting Eq. 2 into Eq. 5 we get (Eq. 6):

$$T_{\text{crystallization}} = \frac{B_{\text{vitreous}} \cdot t_{\text{vitreous growth}}}{B_{\text{cristobalite}}} \quad \text{Eq. 6}$$

For the total scale thickness d_{total} (comprising initial vitreous growth and continuing growth of the devitrified scale), we can write (Eq. 7 analogue to Eq. 4):

$$d_{\text{total}} = \sqrt{B_{\text{cristobalite}} \cdot (t_{\text{cristobalite growth}} + T_{\text{crystallization}})} \quad \text{Eq. 7}$$

Inserting Eq. 6, Eq. 7 transforms to (Eq. 8):

$$d_{\text{total}} = \sqrt{B_{\text{cristobalite}} \cdot \left(t_{\text{cristobalite growth}} + \frac{B_{\text{vitreous}} \cdot t_{\text{vitreous growth}}}{B_{\text{cristobalite}}} \right)} \quad \text{Eq. 8}$$

We also know (Eq. 9):

$$t_{\text{cristobalite growth}} + t_{\text{vitreous growth}} = t_{\text{total}} \quad \text{Eq. 9}$$

From Eq. 3 we can also replace $t_{\text{vitreous growth}}$ by x/v (Eq. 10):

$$d_{\text{total}} = \sqrt{B_{\text{cristobalite}} \cdot \left(t_{\text{cristobalite growth}} + \frac{B_{\text{vitreous}} \cdot \left(\frac{x}{v} \right)}{B_{\text{cristobalite}}} \right)} \quad \text{Eq. 10}$$

Now, we replace $t_{\text{cristobalite growth}}$ (Eq. 11):

$$t_{\text{cristobalite growth}} = t_{\text{total}} - t_{\text{vitreous growth}} = t_{\text{total}} - \frac{x}{v} \tag{Eq. 11}$$

Inserting Eq. 11 into Eq. 10 we get (Eq. 12):

$$d_{\text{total}} = \sqrt{B_{\text{cristobalite}} \cdot \left(t_{\text{total}} - \frac{x}{v} \right) + \frac{B_{\text{vitreous}} \cdot \left(\frac{x}{v} \right)}{B_{\text{cristobalite}}}} \tag{Eq. 12}$$

Rearranging Eq. 12 we finally obtain Eq. 13 as an expression to calculate the total scale thickness d_{total} at any point that is x units away from the crystallization center.

$$d_{\text{total}} = \sqrt{B_{\text{cristobalite}} \cdot \left(t_{\text{total}} - \frac{x}{v} \right) + B_{\text{vitreous}} \cdot \left(\frac{x}{v} \right)} \tag{Eq. 13}$$

As seen in Fig. 9c, Eq. 13 fits excellently to the experimental data when used to calculate the radialite slope instead of scale thickness. Fig. 10 illustrates the contribution from vitreous scale growth and the subsequent growth from the devitrified oxide layer (following a different, smaller parabolic rate-constant $B_{\text{cristobalite}}$).

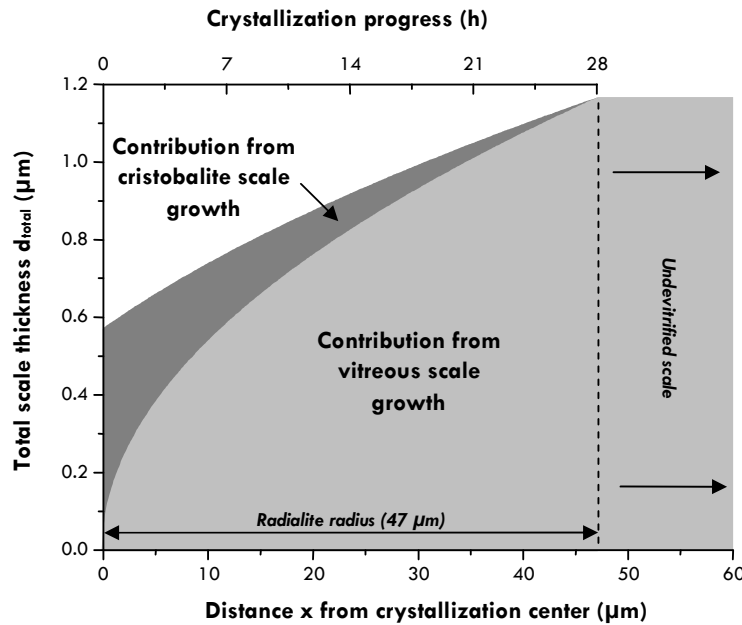


Fig. 10. Schematic illustration of Eq. 13: total scale thickness d_{total} as a function of x (i.e., distance from crystallization center). While the oxide scale grows, it undergoes devitrification and continues to grow (following a different, smaller parabolic rate-constant). At each point x , therefore, we obtain a contribution to the total thickness d_{total} from the time this area grew following the vitreous parabolic rate-constant and a contribution from the time it continued to grow following the parabolic rate-constant of cristobalite. The upper x -axis shows at which time during oxidation the devitrification front has reached a certain x position (assuming instant crystallization at the radialite's center). Parameters used: $B_{\text{vitreous}} = 1.34 \cdot 10^{-17} \text{ m}^2/\text{s}$, $B_{\text{cristobalite}} = 3.20 \cdot 10^{-18} \text{ m}^2/\text{s}$, $v = 1.5 \pm 0.1 \text{ } \mu\text{m}/\text{h}$.

It was assumed that devitrification started during the initial oxidation phase. We know from other experiments⁴ that this assumption is valid for large-scale radialites which have not undergone globulization. In fact, a significant amount of crystallization centers was readily observed after a few minutes of oxygen treatment in an alumina tube furnace at temperatures $\geq 1350^\circ\text{C}$.⁴ At the sample's edges, the oxide scale's devitrification starts almost immediately during oxidation due to a high density of discontinuities and scratches. Both, the radii of typical radialites ($47 \pm 5 \mu\text{m}$; data basis: 25 radialites) and the distance which the crystallization front has moved into the vitreous matrix ($\approx 40 - 50 \mu\text{m}$) are very similar; this is why it is likely that the selected radialites underwent devitrification at the very beginning of the oxidation process.

Also, we assume the crystallization front to progress as a vertical boundary into the vitreous matrix. As seen from Fig. 5, 6, 8 and as discussed in part II of this two-part study, the crystallization front is slightly inclined and, therefore, the upper and the lower radialite diameter differ slightly. The latter difference, however, lies in the range of a few micrometers (i.e., $\leq 5\%$ of the total radialite radius) and can consequently be neglected in first approximation. One possible explanation for this observation is that the crystallization starts at the oxide-atmosphere interface. Part II of this two-part study, however, will discuss this phenomenon in the context of impurity and gas exsolution more thoroughly.

It is evident that V and the corresponding B -values can not be calculated independently. Determination of the exact crystallization rate by measuring the radialite radius is made difficult by the unknown time needed to create a nucleus of critical size. Assuming the crystallization to have started during the very initial oxidation phase (shortly after $t = 0$), the radialite shown in Fig. 4 ($\varnothing 85 \mu\text{m}$, $t_{\text{oxidation}} = 28 \text{ h}$) yields $V = 1.5 \mu\text{m/h}$. This value can be seen as the slowest possible crystallization rate, because if the crystallization with linear kinetics starts at any later moment the crystallization rate would have to be faster.

Considering the problematic determination of V , we calculated B_{vitreous} and used this fixed value for further refinement of V and $B_{\text{cristobalite}}$. B_{vitreous} was calculated from the total vitreous scale thickness ($d = 1.24 \mu\text{m}$; as determined via SEM cross-section) to be $1.34 \cdot 10^{-17} \text{ m}^2/\text{s}$. This value is in excellent agreement with the parabolic rate constant derived from the oxidation study of 11 samples and oxidation times up to 64 h, which were between $1.28 \cdot 10^{-17}$ and $1.34 \cdot 10^{-17} \text{ m}^2/\text{s}$ at 1400°C .⁴

For the calculation of d as a function of the distance to the crystallization center x , we used the z -values from the slope of the former SiC-SiO₂ interface, multiplied by two and subtracted that value from the bulk oxide thickness ($1.24 \mu\text{m}$, Eq. 14).

$$d_{(x)} = d_{\text{bulk vitreous scale}} - 2 \cdot z \quad \text{Eq. 14}$$

This way, the d -values did not have to be corrected for the β -to- α phase transition of cristobalite.¹⁴ The factor two is the result of the fact, that SiO₂ on SiC grows both ways: $\approx 50\%$ of the scale thickness progresses into the carbide and $\approx 50\%$ of the scale surmounts the former carbide surface level because the freshly build SiO₂ takes twice as much space the SiC it consumes.⁴

Fitting Eq. 13 using the z -profiles of five radialites, we obtained the values presented in Tab. 1 ($R^2 = 0.975$). The crystallization rate $V = 1.5 \pm 0.1 \mu\text{m/h}$ is found to be in excellent agreement with the aforementioned slowest possible crystallization rate (i.e., $1.5 \mu\text{m/h}$).

Fixed:	$B_{\text{vitreous}} = 1.34 \cdot 10^{-17} \text{ m}^2/\text{s}$
Refined:	$B_{\text{cristobalite}}, \nu$
Results:	$B_{\text{cristobalite}} = 3.20 \cdot 10^{-18} \pm 4.87 \cdot 10^{-20} \text{ m}^2/\text{s}$ $\nu = 1.5 \pm 0.1 \text{ } \mu\text{m}/\text{h}$
	$B_{\text{vitreous}} : B_{\text{cristobalite}} = 4.2 : 1$
	$R^2 = 0.975$

Tab. 1. Results of fitting Eq. 3 to five radialite slopes (using a constant value for B_{vitreous}). For discussion see text.

According to Deal and Grove ⁶, the parabolic rate constant B can be expressed by assuming oxygen diffusion as the rate-controlling mechanism (Eq. 15):

$$B = \frac{2 \cdot D_{\text{eff}} \cdot c}{N} \quad \text{Eq. 15}$$

where D_{eff} is the effective diffusion coefficient, c denotes the equilibrium concentration of the oxygen in the oxide scale and N gives the number of oxidant molecules in one unit volume of the silica layer.

Thus a comparison of B_{vitreous} and $B_{\text{cristobalite}}$ to assess the effective diffusion coefficients should consider differences in the oxygen solubility in vitreous and crystalline silica. Neglecting this effect yields $B_{\text{vitreous}} : B_{\text{cristobalite}} = 4.2 : 1 \approx D_{\text{eff}}^{\text{vitreous}} : D_{\text{eff}}^{\text{crystalline}}$, which is quite close to the value of ≈ 2.8 from the study of Rodriguez-Viejo et al. ³² at 1400°C. The differences may be explained by minor differences in oxygen solubility.

In a study on the effect of oxide devitrification on the oxidation kinetics of SiC, Ogbuji reported a ≈ 30 -fold decrease in the parabolic rate-constant with increased crystallization (at 1300°C).⁸ In this study, Ogbuji oxidized CVD-SiC coupons in high-purity oxygen, then switched to an annealing process (under argon) in order to obtain highly crystalline oxide scales and finally switched back to an oxidizing atmosphere (pure oxygen). It is difficult to compare these data with our study because of the different temperature regimes. Even though there is a significant difference in temperature, a deviation by a factor of 10 between our results and those of Ogbuji is still much higher than expected. A tentative explanation would be that the large difference in B-values is a result of different transport mechanisms – molecular permeation in the lower-temperature regime (< 1350°C) and ionic oxygen diffusion at higher temperatures (> 1350°C). Therefore, it might be the case that the difference in ionic oxygen diffusion between vitreous silica and cristobalite is much smaller than between molecular diffusion in crystalline and non-crystalline SiO₂. Furthermore, the discrepancy in B-values may be explained in terms of experimental procedure and different fitting methods. Ogbuji encountered a distorting effect, so called “turbulence”, when performing the annealing sequence and monitoring the weight gain. This is also the reason for significant scatter and poor correlation factors ($R^2 \approx 0.55$) in the experimental data from the re-oxidation stage. It is not entirely clear what caused this distortion; the reason for this may be found in the experimental setup but it is also possible that the annealing procedure in argon puts the system into conditions of an active oxidation.

As mentioned in the experimental section, we used an alumina tube furnace for our experiments. It is well known that impurities from the furnace (e.g., sodium) strongly affect and accelerate oxidation by modifying the network structure of silica.^{11,33} Although our furnace had been heat-treated at 1500°C and was in use for several months, some impurity-related influence to the oxidation rate and the crystallization rate might not have been eliminated. For more details on the impurity-related influence of SiC oxidation see Ref. ¹¹ and part II of this study.

4. DISCUSSION

AFM analysis of both the outer surface of the oxide scale thermally grown on silicon carbide and the former oxide-carbide interface after silica removal by HF etching is a powerful method to study microstructural aspects of silica devitrification and growth. As silica undergoes a phase transition with significant crack formation at the surface of the crystalline areas, only analysis of the undisturbed SiC-SiO₂ interface allows studying the details of the original morphology of the oxide scale. We see great potential for application of this method for all kinds of oxide scales on HF inert materials.

The method has the principal advantage to investigate an undisturbed natural growth of a scale. Any breaks, disturbances etc. become visible as disturbances of the morphology development. In this way the method provides insight into the history of scale growth in a single sample.

From many studies it is known that silica thermally grown on silicon carbide readily crystallizes at 1400°C yielding disc-like crystalline aggregates (β -cristobalite radialites) within a vitreous silica matrix. When examined at room temperature, the oxide scale usually shows radialites differentiated into small crystalline plates due to the β -to- α phase transition of cristobalite. Some radialites, however, preserve their *in-situ* form and allow inspection of the oxide scale's thickness (d) via polarization microscopy and the interference colors evidence a total difference of d_{center} and d_{edge} in the range of 500 nm. This difference is due to different oxidation rates in vitreous and crystalline areas. The latter grow more slowly because of the smaller diffusion coefficient in crystalline silica compared to vitreous SiO₂.

These optical findings are in excellent agreement with results from AFM/HF-etching. At the former SiC-SiO₂ interface, we determined z-profiles of the slope of several radialites. Both, crystalline and vitreous regions grow in good accordance with a parabolic time law. The resulting slope below radialites at the former carbide-oxide interface is almost linear in shape and can be expressed by a modified equation based on the Deal-and-Grove model yielding an excellent fit for the experimental data.

Using a fixed value for the parabolic rate-constant, we determined the crystalline parabolic rate-constant to be ≈ 4.2 -times smaller than B_{vitreous} . This value is within the same order of magnitude as a predicted value for the ratio between the oxygen-diffusion constant of vitreous and crystalline silica at this temperature. For the crystallization rate, we determined a value of $\approx 1.5 \mu\text{m/h}$ for dry oxidation regimes. Part II of this two-part study will focus on the influence of impurities on crystallization and globulite formation.

Acknowledgments

This work was supported by the Deutsche Forschungsgemeinschaft (DFG) through Ni299/12-1. The authors like to thank M. Presser and M. Schloßer (University of Tübingen) for helpful discussion.

REFERENCES

1. Sadow, S.E. & Agarwal, A. *Advances in silicon carbide processing and applications*, 212 (Artech House inc., Norwood, 2004).
2. Harris, G.L. *Properties of Silicon Carbide*, 282 (INSPEC, the Institution of Electrical Engineers, London, 1995).
3. Schwetz, K.A. Silicon Carbide Based Hard Materials. in *Handbook of Ceramic Hard Materials*, Vol. 2 (ed. Riedel, R.) 683 - 748 (Wiley-VCH Verlag GmbH, Weilheim, 2000).
4. Presser, V. & Nickel, K.G. Silica on silicon carbide. *Critical Reviews in Solid State and Material Sciences* **33**, 1 - 99 (2008).
5. Haase, V. et al. *Si. Silicon. Supplemental Volume B3.*, 545 (Springer-Verlag, Berlin, 1986).
6. Deal, B.E. & Grove, A.S. General Relationship for the Thermal Oxidation of Silicon. *Journal of Applied Physics* **36**, 3770 - 3778 (1965).
7. Luthra, K.L. Some new perspectives on oxidation of silicon carbide and silicon nitride. *Journal of the American Ceramic Society* **74**, 1095 - 1103 (1991).
8. Ogbuji, L.U.J.T. Effect of Oxide Devitrification on oxidation Kinetics of SiC. *Journal of the American Ceramic Society* **80**, 1544 - 1550 (1997).
9. Tressler, R.E., Costello, J.A. & Zheng, Z. Oxidation of Silicon Carbide. in *Industrial Heat Exchangers*, Vol. 1 (eds. Hayes, A.J., Liang, W.W., Richlen, S.L. & Tabb, E.S.) 307 - 314 (American Society for Metals, Pittsburgh, 1985).
10. Costello, J.A. & Tressler, R.E. Oxidation Kinetics of Silicon Carbide Crystals and Ceramics: I, In Dry Oxygen. *Journal of the American Ceramic Society* **69**, 674 - 681 (1986).
11. Opila, E. Influence of Alumina Reaction Tube Impurities on the Oxidation of Chemically-Vapor-Deposited Silicon Carbide. *Journal of the American Ceramic Society* **78**, 1107 - 1110 (1995).
12. Flörke, O.W. Die Modifikationen von SiO₂. *Fortschritte der Mineralogie* **44**, 181 - 230 (1967).
13. Strunz, H. & Nickel, E.H. *Strunz Mineralogical Tables*, 870 (Schweizerbart'sche Verlagsbuchhandlung, Stuttgart, 2001).
14. Keskar, N.R. & Chelikowsky, J.R. Structural properties of nine silica polymorphs. *Physical Review B* **46**, 1 - 13 (1992).
15. Peacor, D.R. High-temperature single-crystal study of the cristobalite inversion. *Zeitschrift für Kristallographie* **138**, 274 - 298 (1973).
16. Maeda, M., Nakamura, K., Ohkubo, T. & Ishizuka, T. Oxidation Behavior of Silicon Carbide Under Cyclic and Static Conditions. *Ceramics International* **15**, 1 - 6 (1989).
17. Ogbuji, L.U.J.T. Development of oxide scale microstructure on single-crystal SiC. *Journal of Materials Science* **16**, 2753 - 2759 (1981).
18. Wenk, H.-R. & Bulakh, A. *Minerals: Their constitution and origin*, 646 (Cambridge University Press, 2004).
19. Hecht, E. *Optics*, 698 (Pearson Education Inc., San Francisco, 2002).
20. Nesse, W.D. *Introduction to Optical Mineralogy*, 362 (Oxford University Press, Oxford, 2005).
21. Pantsukrin, S.D. & Kalinin, D.V. Kinetics and mechanism of formation of alpha-cristobalite spherulites. *Seriya Khimicheskikh Nauk* **1**, 27 - 31 (1988).
22. Wagstaff, F.E., Brown, S.D. & Cutler, I.B. The influence of H₂O and O₂ atmospheres on the crystallization of vitreous silica. *Physics and Chemistry of Glasses* **5**, 76 - 81 (1964).
23. Li, H., Tomozawa, M. & Lou, V.K. Effects of nitrogen and carbon ion implantation on devitrification of silica glasses. *Journal of Non-Crystalline Solids* **168**, 56 - 63 (1993).
24. Opila, E.J. Variation of the Oxidation Rate of Silicon Carbide with Water-Vapor Pressure. *Journal of the American Ceramic Society* **82**, 625-636 (1999).
25. Wagstaff, F.E. & Richards, K.J. Kinetics of Crystallization of Stoichiometric SiO₂ Glass in H₂O Atmospheres. *Journal of the American Ceramic Society* **49**, 118 - 121 (1966).
26. Wagstaff, F.E. Crystallization and melting kinetics of cristobalite. *Journal of the American Ceramic Society* **52**, 650 - 654 (1969).
27. Doremus, R.H. *Glass Science*, 339 (John Wiley & Sons, N.Y., 1994).
28. Lipinski, D. & Schwiete, H.E. Die Bildung des Cristobalits aus amorphem Siliziumdioxid unter verschiedenen Gasatmosphären. *Tonindustrie-Zeitung und Keramische Rundschau* **88**, 145 - 153; 217 - 225; 258 - 262 (1964).
29. Presser, V., Loges, A. & Nickel, K.G. Scanning electron and polarization microscopy study of the variability and character of hollow macro-defects in silicon carbide wafers. *Philosophical Magazine* **88**, 1639 - 1657 (2008).
30. Ebi, R. Universität Karlsruhe (1973).
31. Ebi, R., Fitzer, E. & Hüttinger, K.J. Oxidationskinetik von SiC-Pulvern bei Temperaturen zwischen 1200°C und 1600°C. *High Temperatures, High Pressures* **4**, 21-25 (1972).
32. Rodríguez-Viejo, J., Sibieude, F., Clavaguera-Mora, M.T. & Monty, C. ¹⁸O diffusion through amorphous SiO₂ and cristobalite. *Applied Physics Letters* **63**, 1906 - 1908 (1993).
33. Opila, E.J. & Myers, D.L. Alumina Volatility in Water Vapor at Elevated Temperatures. *Journal of the American Ceramic Society* **87**, 1701-1705 (2004).

Chapter 01

Chapter 02

Chapter 03

Chapter 04

Chapter 05

Chapter 06

Chapter 07

Chapter 08

Chapter 09

Chapter 10

Chapter 11

Chapter 12

MICROSTRUCTURAL EVOLUTION OF SILICA ON SINGLE CRYSTAL SILICON CARBIDE. PART 2: INFLUENCE OF IMPURITIES AND DEFECTS

V. Presser⁽¹⁾, A. Loges⁽¹⁾, R. Wirth⁽²⁾, K. G. Nickel⁽¹⁾

⁽¹⁾ Institut für Geowissenschaften, Universität Tübingen

⁽²⁾ Helmholtz-Zentrum Potsdam

ABSTRACT:

Passive oxidation of single crystal silicon carbide (6H-SiC) resulted in the formation of a vitreous silica layer which crystallized gradually at temperatures near 1300° - 1400°C. During this process, statistically distributed devitrification centers appeared and disc-like aligned crystal plates (radialites) formed. The crystallization process did not necessarily start at structural defects although these often act as areas of preferred nucleation. A second structural transition from disc-like radialites to small crystalline spheres (globulites) was not connected to structural defects but a consequence of the presence of impurities. Alkaline and earth-alkaline elements are common contaminations within the atmospheres of typical furnaces fitted with alumina tubes. Globulite formation was a process of recrystallization catalyzed by an impurity-related melt formed on top of the devitrified areas. Crystallization caused exsolution of reaction gas and local impurity enrichments as the solubility for these phases is much higher in the devitrifying vitreous silica matrix. Both clean and impurity loaded oxidation produced specific morphologies of scales and interfaces.

1. INTRODUCTION

Silica is the only stable solid oxide of silicon carbide (SiC) and it forms at temperatures above 900°C leading to a passivation of the carbide's surface.¹⁻³ The formation of this dense oxide scale provides SiC with its beneficial oxidation behavior: growth of the silica layer increasingly delays the transport of oxygen towards the oxide-carbide interface and outward diffusion of carbon monoxide. Commonly, the growth of the oxide scale is assumed to be diffusion controlled which results in an overall parabolic time-law.

Nonetheless not all features of silicon carbide oxidation are well understood. Anisotropic oxide scale growth, that is, the dependency of the oxidation rate on the crystallographic orientation, is such a case.³⁻⁵ Sintering aids like boron carbide are another influencing factor as they may cause bubble formation.⁶ Similarly, impurities originating from the furnace tube are a known cause for disturbances in oxidation behavior.⁷ However, we still lack a detailed knowledge of the processes involved.

Understanding of the basic oxidation behavior of SiC ceramics and possible influencing factors has profited a lot from the availability of high-quality SiC materials. Now systematic studies on undoped SiC single crystals (wafers) with known crystallographic orientation and controllable doping level have become the basis for new models of the oxidation of sintered SiC ceramic bodies. In this context, 6H-SiC single crystals were used for a morphological study of the oxide scale to gain a basic understanding of the intrinsic and impurity-related features. We chose only one specific crystallographic orientation, in particular 6H-SiC-(0001), so that the oxide growth anisotropy had not to be considered.

Silica is subjected to a devitrification process at temperatures $\geq 1200^\circ\text{C}$ during oxidation and it was shown that surface inhomogeneities, like scratches, act as crystallization centres.³ The crystallization starts most likely at the oxide-atmosphere interface (cf. part I). After nuclei of critical size have grown, vitreous silica transforms into β -cristobalite and disc-like crystalline aggregates (radialites) appear.³ A second probably impurity-related morphological transition takes place when the flat crystal plates transform into small 1 – 2 μm sized spheres of statistically orientated β -cristobalite (globulites).^{3,8,9}

All three phases are expected to show different oxidation rates: oxygen diffusion (rate-controlling factor) is faster in vitreous silica than in cristobalite. As in-between the globulites pathways of accelerated diffusion are contained oxidation will be accelerated in these areas compared to regions covered by a dense radialite lawn. However, all three phases (vitreous silica, radialites, globulites) coexist over a long period of time and the observed overall kinetics can be approximated with a mean parabolic time-law which cannot resolve the individual processes (cf. Ref. ³). Due to the large difference between the oxidation rate of vitreous and crystalline silica (factor of ≈ 3), the oxidation reaction will mostly be governed by the oxidation rate constant of non-crystalline SiO_2 for as long as a sufficiently large area is covered by vitreous silica (allowing fast SiC oxidation, for example, as a skeletal network beneath crystal plates).¹⁰

Part I of this two-part study discussed the effect of devitrification on the oxidation rate of single crystal (0001)-6H-SiC and examined it by means of a combination of HF-etching and AFM-analysis. Part II will focus on the influence of (1) impurities and (2) defects on the microstructural evolution of SiO_2 thermally grown on SiC. Both influences are discussed in the light of globulite formation. Regarding the influence of defects, we studied hollow-core defects (pipes and voids), that are frequently found in SiC wafers.¹¹

2. EXPERIMENTAL

As sample material we used (0001)-6H-SiC:N wafers (SiCrystal AG, Erlangen, Germany; nitrogen doped with $N \approx 10^{17} \text{ cm}^{-3}$). These were subjected to dry, thermal oxidation at temperatures between 1350°C and 1400°C. To elucidate the influence of impurities, experiments were carried out in both an alumina tube and a fused quartz tube. For the latter, the oxygen was dehumidified using P_2O_5 . As an artificial impurity source we used high-purity sodium chloride (99.999% purity; Merck KGaA, Darmstadt, Germany).

For SE-mode SEM images we used a LEO VP 1450 electron microscope (Carl Zeiss AG, Oberkochen, Germany) operating at 15 kV acceleration voltage.

X-ray fluorescence (XRF) analysis was carried out using a Bruker AXS S4 Pioneer[®] instrument (Bruker AXS GmbH, Karlsruhe, Germany). Regarding the operation parameters rhodium was chosen as anode material and the instrument operated at 4 kW power output.

X-Ray microdiffraction (μ XRD) examination was done using a Bruker D8 Discover[®] XRD²-microdiffractometer (Bruker AXS GmbH, Karlsruhe, Germany) with Co- K_α radiation, an area sensitive Hi-Star detector (GADDS) and monocapillary optics ($\varnothing_{\text{beam}} \sim 300 \mu\text{m}$; Institute for Scientific Instruments GmbH, Berlin, Germany). The diffraction images recorded with the area-sensitive detector are referred to as GADDS frames in this study. For more details on μ XRD see Ref. ¹².

Sampling for TEM analysis was accomplished using focused ion beam (FIB) milling. FIB preparation (cf. Ref. ¹³) was conducted using a FIB200 instrument (FEI Company, Eindhoven, The Netherlands) at the GFZ Helmholtz-Zentrum Potsdam. TEM studies were carried out using a FEI F20 X-Twin instrument operating at 200 kV and equipped with a FEG electron source. Energy dispersive X-ray (EDX) analyses were performed in scanning transmission electron microscope (STEM) mode with a nominal spot size of 1 nm using a high angle annular dark field detector (HAADF) and an EDAX X-Ray analyzer (EDAX, Wiesbaden, Germany).

3. RESULTS AND DISCUSSION

3.1 Preliminary remarks: change of the oxide scale morphology

Previous studies (e.g., Ref. ³, part I) showed that the morphology of silica thermally grown on silicon carbide changes drastically due to (1) devitrification and (2) globulization. Fig. 1 summarizes key microstructural aspects of silica thermally grown on silicon carbide using dry oxygen and an alumina tube furnace (1400°C; 4 – 100 h). Initial crystallization starts at surface inhomogeneities like scratches or at the sample's edges (Fig. 1a). Progressing devitrification leads to the formation of large radialites which, over time, separate into several crystal plates (Fig. 1b).¹⁴ As the radialites continue to expand into the vitreous matrix, they start forming a crystalline lawn and eventually globulite formation starts. The latter begins at the deepened centers of the radialites and partially along grain boundaries (Fig. 1c). With progressing globulization, more and more of the radialites are consumed by globulites (Fig. 1d – f) and, in the end, the entire silica scale consists of a continuous globulite lawn. The latter is characterized by significant porosity (Fig. 2). We will show later in what way this microstructural evolution differs for high-purity systems, that is, where the presence of impurities down to the ppm-scale can be excluded. In the next two sections we will look more closely on (1) the vitreous-crystalline transition and (2) globulite formation.

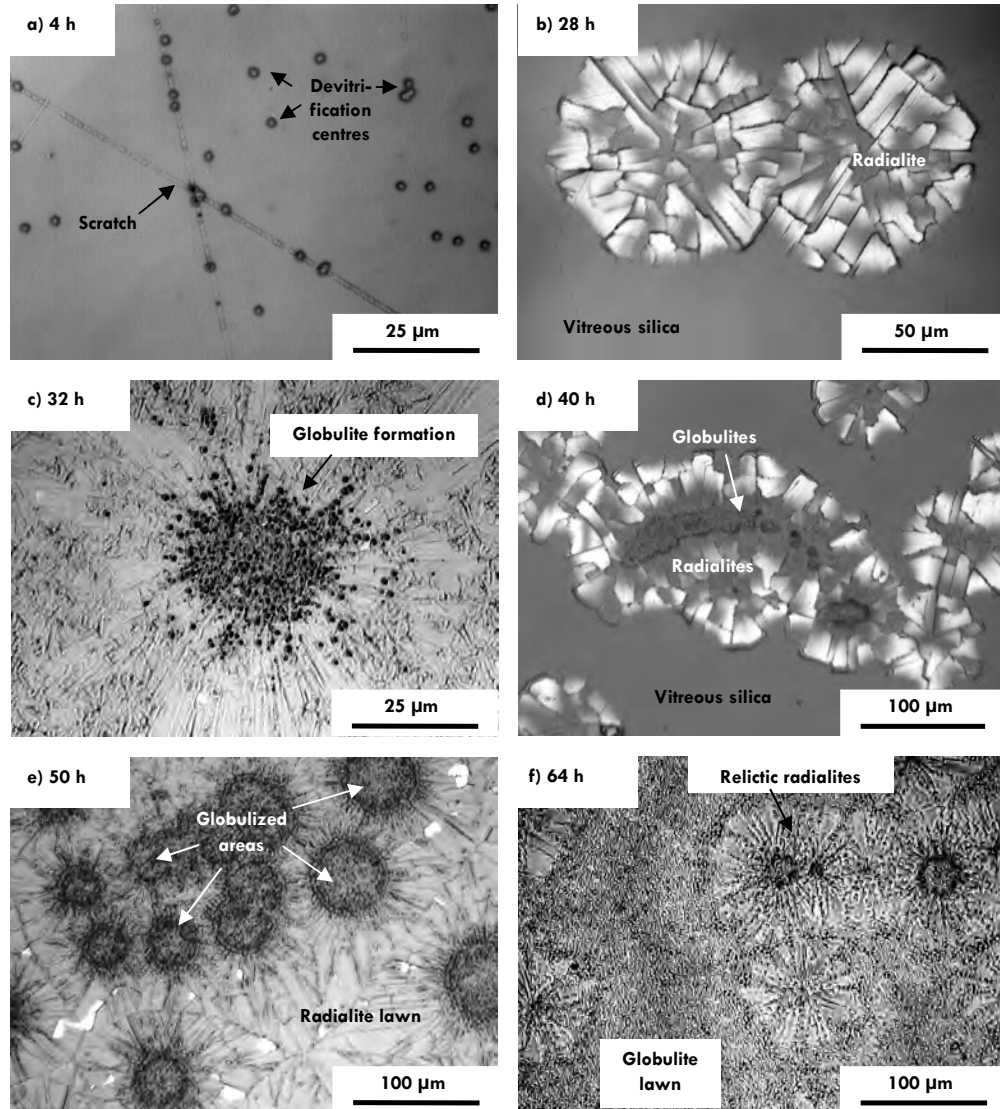


Fig. 1. Optical microphotographs of SiO_2 thermally grown on SiC (1400°C, alumina tube furnace, oxidation times given in the figure). For discussion see text.

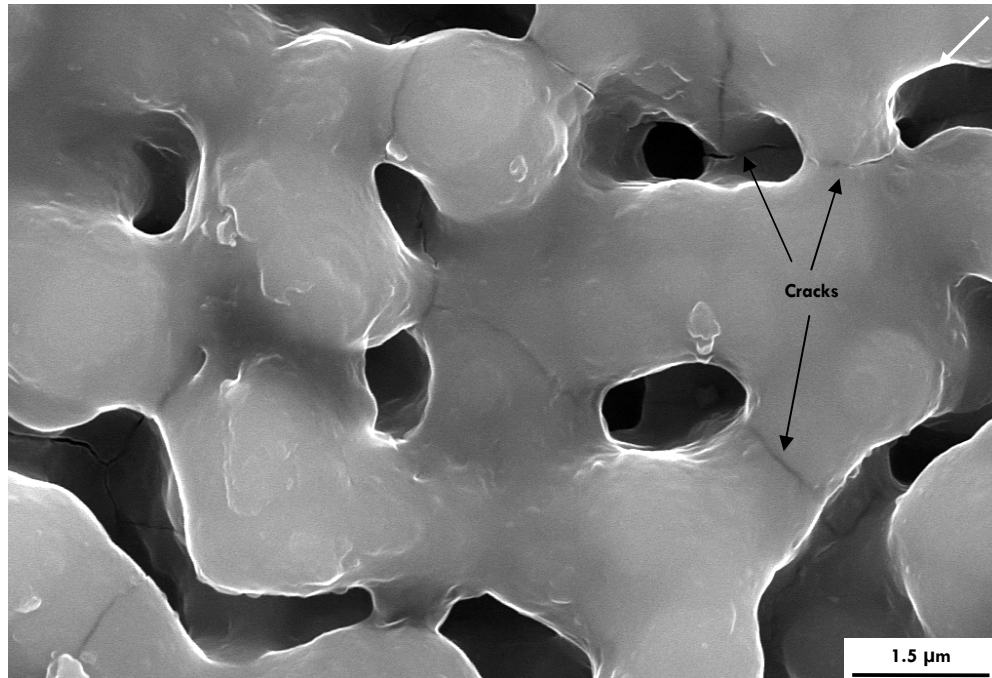


Fig. 2. SE-mode SEM image of a SiC sample oxidized at 1400°C for 64 h in an alumina tube furnace.

Cracks are due to the β -to- α phase transition below 300°C.

3.2 Silica layer: vitreous-crystalline transition

3.2.1 TEM studies of the transition zone

In the first part of this study, we reported a crystallization speed of $\approx 1.5 \mu\text{m/h}$ for silica at 1400°C. The devitrification yields cristobalite and the low-temperature form of latter was confirmed via μXRD *ex-situ*. During the bulk oxide scale growth in z-direction the lateral crystallization progresses and the radialites assume their characteristic form with a thicker outer and a thinner inner region. Because the crystallization most likely starts at the oxide-atmosphere interface, the diameter of the individual radialites is larger at the oxide-atmosphere than at the oxide-carbide interface.

Within the oxide scale, we focused our study on the vitreous-crystalline interface. Fig. 3a depicts the area where a TEM foil (Fig. 3b) has been obtained from the bulk sample. In Fig. 3c two TEM bright field images of FIB foils show a typical segment of a radialite and the direct transition between crystalline and vitreous silica. The sample shown was oxidized at 1400°C for 32 h in an alumina tube furnace. Within the crystalline area of the scale, stress contrast is a result of differences in the thermal expansion behavior of cristobalite and vitreous silica. Also, the lack of diffraction contrast (lattice fringes) clearly identifies vitreous silica and can, therefore, be used to differentiate between crystalline and non-crystalline silica.

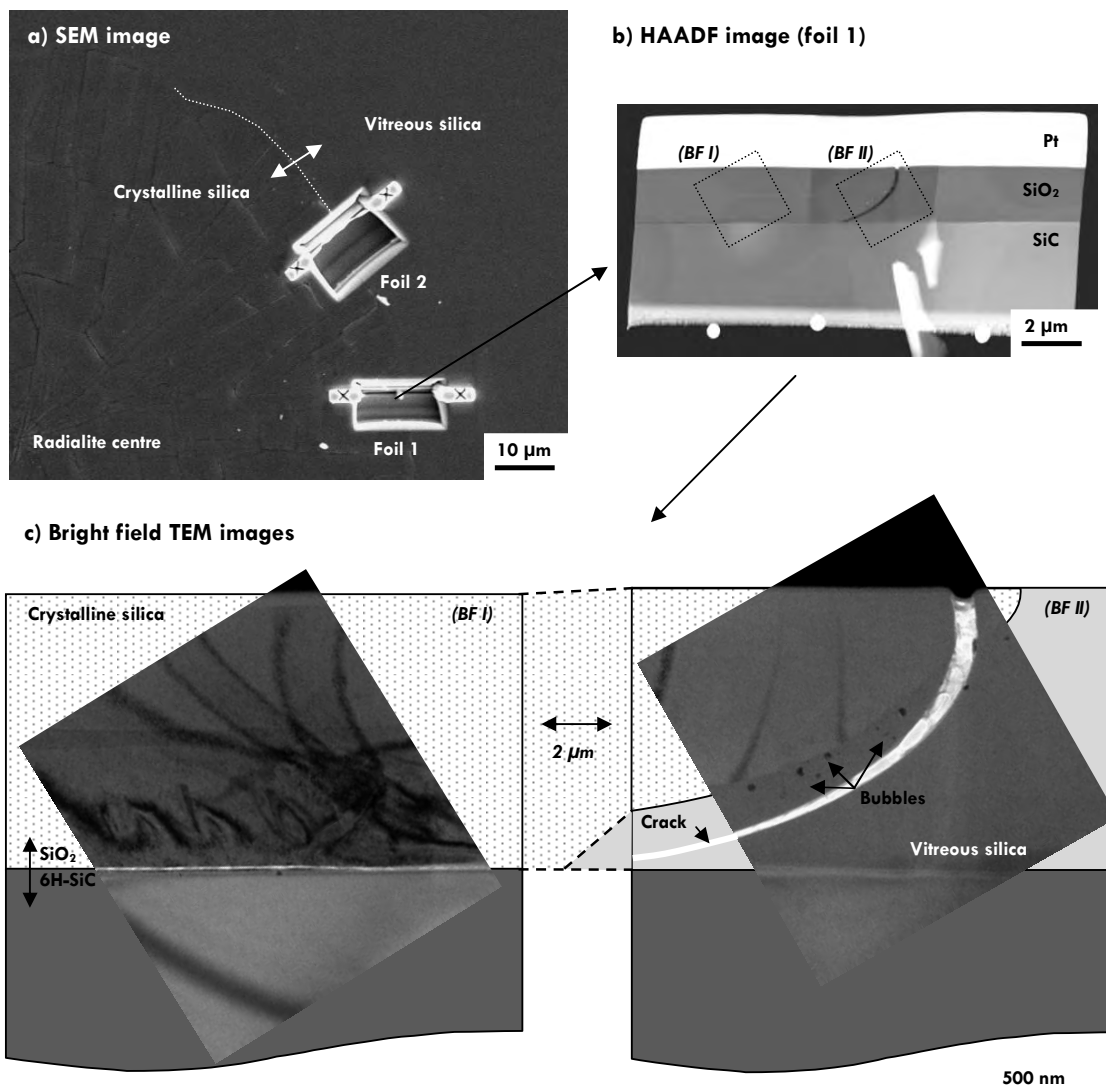


Fig. 3. Crystalline-vitreous transition zone within the oxide scale as studied using electron microscopy (1400°C, 32 h, alumina tube furnace). a) SE-mode SEM image showing where TEM foils have been cut. b) High-Angle-Annular-Dark-Field STEM image of foil 1. The dotted squares indicate where bright field images have been obtained. c) Bright field TEM images of the SiO₂-SiC and crystalline-vitreous silica transition zone. For discussion see text.

As shown in Fig. 3, the oxide scale contains cracks due to the rapid β -to- α phase transition of cristobalite at $\approx 250^\circ\text{C}$ and large differences in thermal expansion.¹⁵ This phase transition is accompanied by a volume decrease of approximately 4.9 vol%¹⁶ at the transformation which corresponds to a total change in relative volume by 7.8 vol%¹⁷ at ambient temperature. The observed crack did not form directly at the crystalline-vitreous interface but some μm inside the vitreous matrix, probably following a path of maximum tension. Differences in the volumetric thermal expansion coefficient α of crystalline and vitreous silica contribute to this phenomenon.¹⁸⁻²²

In particular, differences between $\alpha_{\text{silica, vitreous}}$ and $\alpha_{\text{cristobalite}}$ are significantly larger than between silicon carbide and α -cristobalite. Delamination of dense silica layers thermally grown on SiC is not expected as a common phenomenon and limited to chipping of single radialite plates.³ Thus, *in-situ* at temperatures higher than the β -to- α phase transition we would not expect significant crack formation in the oxide scale, especially since both phases (β -cristobalite and vitreous silica) have almost the same density. Only some grain boundaries between crystal plate sections will appear due to energy minimization (cf. part I).

Besides crack formation, Fig. 3 shows accumulated bubbles on the vitreous side of the devitrification zone. This gas was previously dissolved within the vitreous silica which has a higher gas solubility compared to crystalline modifications like cristobalite.²³⁻²⁵ With crystallization progressing into the vitreous matrix, gas is depleted in the radialite and enriched within the crystalline-vitreous transition zone. Once a critical concentration has been reached, bubble formation of the otherwise completely soluble gas species (most probably CO) is observed.

Cristobalite acts as a diffusion barrier for outgasing CO as the diffusion coefficient of crystalline silica is significantly smaller than that of vitreous silica.²⁶ Therefore, accumulation of reaction gas originating from the oxide-carbide interface can be observed at the crystalline-vitreous transition zone. Gas accumulation along the crystalline-vitreous boundary may also provide predetermined breaking points for scale delamination.

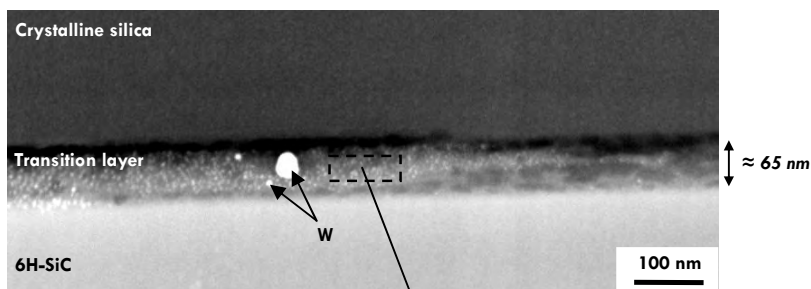
Accumulation of reaction gas at the crystalline-vitreous interface will in turn stabilize the vitreous phase as the latter has a higher gas solubility (i.e. Le Châtelier's principle). This might contribute to the pronounced wedge-shape of the crystalline-vitreous transition zone (i.e., larger upper radialite diameter) as devitrification happens faster in the superficial part (where exsolved gas can easily diffuse out of the glass into the atmosphere).

What is observed for dissolved gas also applies for impurities. The intake of alkaline and earth-alkaline elements during the oxidation of samples mounted in an alumina tube is well known.⁷ XRF measurements confirmed significant concentrations of Na (1500 ppm), Al (700 ppm), and K (100 ppm) to be present on the oxide scale's surface of samples oxidized mounted in an alumina tube. In comparison, the concentrations of these elements were negligible within the SiC-wafer before the oxidation was performed ($\ll 30$ ppm). These concentrations were measured on the sample's surface and should not be regarded as actual concentration within the first tens of nm of the surface or the oxide-carbide interface but to reflect an average value of a graded surface. Nevertheless, the notable accumulation of these elements confirms the input and incorporation of a significant amount of impurities when using an alumina tube furnace.

TEM/EDX studies performed on the SiO₂-SiC interface underneath a radialite revealed accumulated impurities within a thin, vitreous layer (Fig. 4). The white particles (i.e. white in dark field images) in that transition layer correspond to a high concentration of tungsten which has been used in earlier experiments in that specific alumina tube furnace. More important is the detected accumulation of calcium which originates from impurities of the alumina tube itself. Other impurities, like potassium or sodium, were below the detection limit. However, it should be considered that the detection of a "mobile" element such as sodium by EDX is often difficult, because Na ions are known to move within the silica for charge compensation when an electron beam is applied.⁷

In contrast to these results, the transition layer between vitreous silica and silicon carbide showed no such accumulation (neither of W nor of Ca). This strongly suggests that these impurities were once dissolved within the vitreous matrix and exsolved when crystallization took place along the transition region.

a) HAADF image



b) EDX spectrum

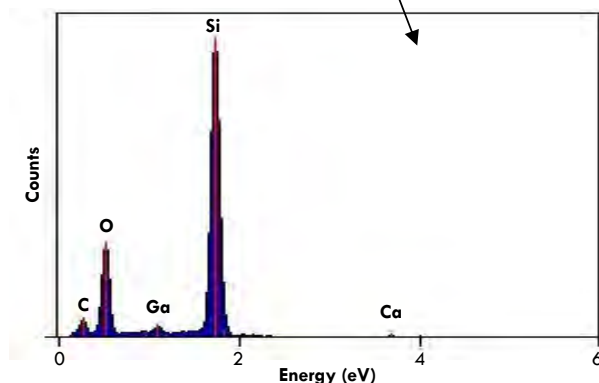


Fig. 4. HAADF image (a) and corresponding EDX spectrum of the SiC-SiO₂ transition zone (b) showing calcium enrichment (1400°C, 32 h, alumina tube furnace). The detected gallium is a residue of the FIB preparation method (using a focused Ga-ion beam).

3.2.2 Stabilization of a skeletal vitreous network

As for the SiO₂-SiC interface, the accumulation of impurities possibly contributes to the stabilization of a vitreous transition zone below the cristobalite crystal plates. This ridge-like, skeletal network can best be seen when the crystal plates have been removed, for example, by ultrasonic cleaning or at the edges of a broken sample. Previous studies, for example, by Ogbuji confirm the non-crystalline nature of this network^{10,27} and EDX measurements evidence the presence of oxygen and corroborate a silica-like composition.

Fig. 5 shows an example of the skeletal network of a broken sample. Arrows in Fig. 5 indicate a section in which the crystal plate does not delaminate at the oxide-carbide interface but near the crystalline-vitreous transition within the oxide scale. Silicon-oxycarbide is a phase unlikely to be present at such ridges, because Si_xC_yO_z it is believed to disappear at such high temperatures leaving stoichiometric silica the only stable oxide.^{1,28}

The role of the skeletal vitreous network was addressed in previous studies.^{3,7,10,27,29,30} Ogbuji¹⁰ interpreted remaining vitreous areas to contrive the main part of the oxidation, because oxygen diffuses much faster in non-crystalline silica as was evidenced in part I of this two-part study. The same observation was made by Ainger for pure silicon and devitrification of the vitreous silica oxide scale, who referred to radialites as “rosette defects”.¹⁵

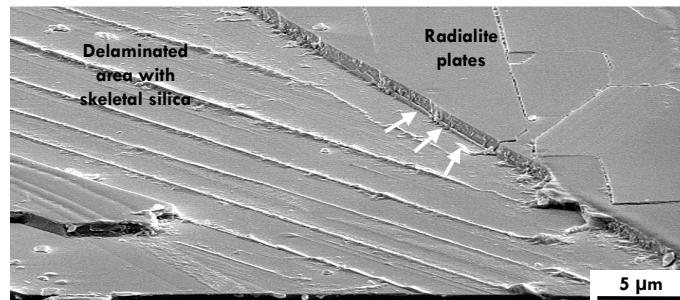


Fig. 5. Delaminated cristobalite plates from the edge region of broken samples (1400°C, 24 h, alumina tube furnace). Below the crystal plates a framework of vitreous silica is found on the SiC-substrate, which remains back even after mechanical removal of the radialite segments. Arrows indicate a section where a crack formed not at the SiO₂-SiC interface, but within the oxide scale (separating crystalline and vitreous silica).

3.3 Globulite formation

3.3.1 Preliminary remarks to globulite formation

The formation of few μm sized silica spheres consisting of statistically oriented cristobalite is termed globulite formation and is a well-known phenomenon during the oxidation of both silicon and silicon carbide, that is, materials with silica as their native oxide.^{27,29} Globulization is a recrystallization process during which the pronounced preferred orientation seen in radialites is completely lost.³ This can be seen via μXRD using area-sensitive detectors (Fig. 6) where the GADDS frames and psi-scans of the (101) reflection of α-cristobalite are shown for (a) radialites and (b) globulites.

From the χ-scans we know of a pronounced preferred orientation of the radialite crystal plates. In contrast to this, the globulite lawn shows no such preferred orientation which strongly suggests a true recrystallization mechanism. Also, the Debye-Scherrer-ring of the (101)-reflection is spotty in case of the radialite lawn and homogeneously after recrystallization. This can be explained when looking at the radialite plates (Fig. 1 and part I): after the β-to-α phase transition, several of the plates are slightly tilted and, therefore, they contribute to the local-maxima in the χ-scan (e.g., at 248°, 262°, 292° and 298° χ). This also shows that within the illuminated area (10° incident angle, 300 μm beam diameter: 0.4 mm²) there are only very few crystalline plates with different orientation due to the large lateral expansion of the radialite segments (tens of micrometers large). Otherwise, the Debye-Scherrer-ring would lack the spotty feature. The latter is the case for the globulite lawn: here, small crystalline spheres (1 – 2 μm in diameter) with no preferred orientation contribute to a homogeneously distributed Debye-Scherrer-ring of the (101) reflection. Also, the decrease in crystallite size is reflected by an increase in the reflection half-width (FWHM = full width at half maximum) which correlates with the mean coherence length. In particular, the (101) reflection of the radialite lawn shows a FWHM of 0.32°2θ and after globulization 0.40°2θ (FWHM not corrected for the contribution of the instrument function).

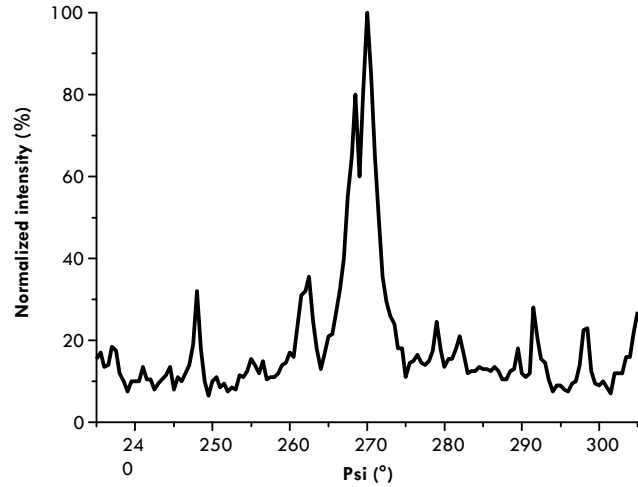
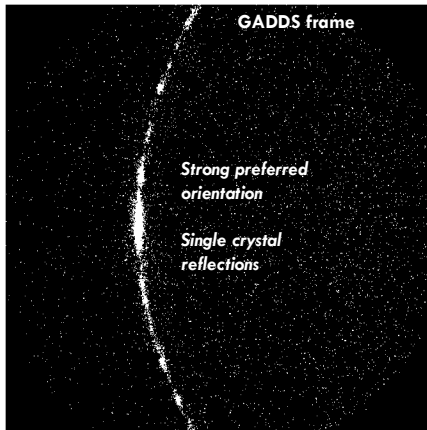
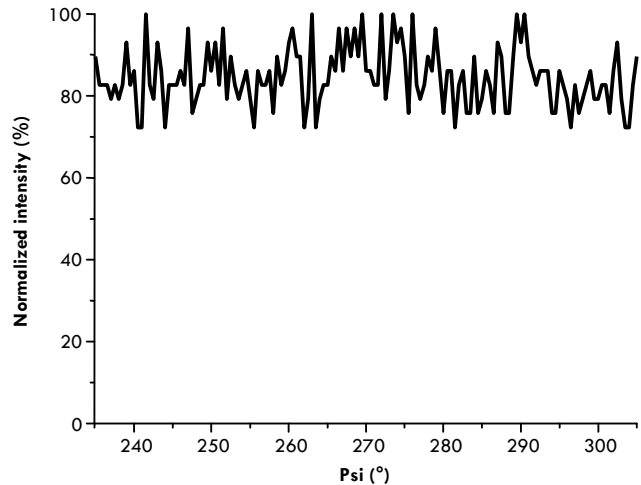
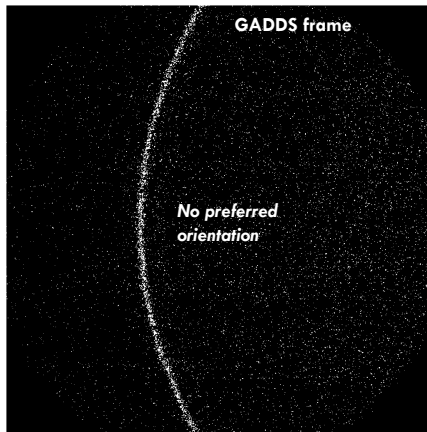
a) Radialite lawn: α -cristobalite (101) reflectionb) Globulite lawn: α -cristobalite (101) reflection

Fig. 6. GADDS frames and χ -scans of (a) radialite and (b) globulite lawn. The pronounced preferred orientation of the radialite plates is lost after globulization. The presented GADDS frames cover $235^\circ - 305^\circ \chi$ and $5^\circ - 35^\circ 2\theta$ (Co-K α).

Globulite formation has never been observed to take place without a preceding phase of “normal” devitrification, that is, radialite formation. Usually after a certain amount of time, radialites start to undergo this structural transition beginning at the centre part and along grain boundaries. These grain boundaries present under *in-situ* conditions are not to be mistaken with the phase-transition related crystal plate differentiation below 300°C . Because of energy minimization radialite plates of a critical size are known to show grain boundary formation. As seen in part I of this study, these boundaries are evidenced by lineation-like elevations on the former carbide-oxide interface.

As seen in Fig. 1, the flat radialite plates are consumed by an uneven lawn of small crystalline spheres in the final stage of globulization. In-between these, there is a significant open pore volume (Fig. 2).

3.3.2 Influence of defects

To elucidate the influence of defects we examined the oxide scale's morphology near hollow defects (voids and pipes) on polished surfaces. Both defect types have a hollow core and either a large lateral (voids) or axial (pipes) extension. Typical defect dimensions of voids are several tens or even hundreds of μm laterally and tens of μm axially, while pipes have typical diameters of tens of nm up to few μm with a depth in the mm-range. In contrast to mechanically introduced scratches the surrounding area of these defects is perfectly crystalline and in case of voids in a relaxed state.¹¹ Therefore, no accelerated oxidation due to special stress or surface states of silicon carbide must be taken into account. Pipes, however, are centers of a significant strain field that can be made visible by polarization microscopy due to photoelasticity. For further information on hollow defects in silicon carbide see Refs. ^{3,11,31}.

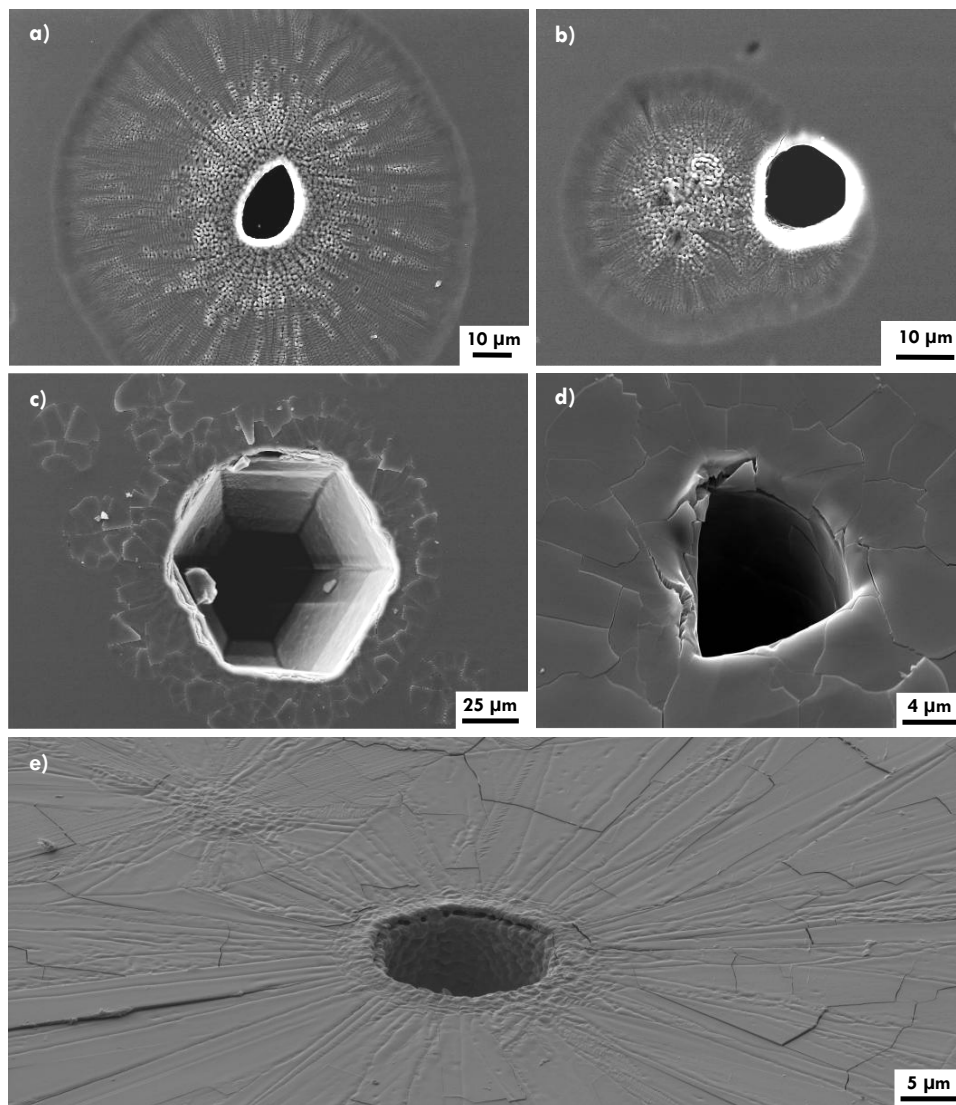


Fig. 7. SE-mode SEM images of the oxide scale's morphology around structural defects in samples oxidized at 1350°C for 10h (a-d) and 1400°C for 24h (e). a) Devitrified area with globulite formation around pipe, b) Devitrification and globulite formation off-centered from pipe c) Radialite formation around void, d) Radialite formation around and in pipe, e) Devitrified area with globulite formation around pipe mouth and on the inner surface.

The sample shown in Fig. 7 was oxidized for 10 h at 1350°C in an alumina tube furnace. Fig. 7a shows a common case where radialite and subsequent globulite formation starts around the defect. Other cases like the one shown in Fig. 7b give evidence that this is not necessarily the case: here both radialite formation and globulization have taken place $\approx 10 \mu\text{m}$ apart from the pipe's outer edge in the vitreous silica matrix. From this we conclude that (1) hollow defects in SiC single-crystals are possible crystallization centers but (2) do not *per se* cause globulization. Hollow defects, however, may retain remains of the polishing paste or related impurities.

Our conclusions are corroborated by the observation that the crystals around pipes and / or voids do not necessarily undergo the radialite-globulite transition. Two such cases are shown in Fig. 7c and 7d, where the surroundings of a void (Fig. 7c) and a pipe (Fig. 7d) have devitrified without the appearance of globulites. It is remarkable that also the inner surface of the pipe shown in Fig. 7d has homogenous crystal coverage with individual crystal plates of the same size and type as observed on the upper surface. In contrast, another pipe (oxidized at 1400°C, 24 h) shows the typical globulite morphology both on the pipe's inner surface and near the edge (Fig. 7e). As a final conclusion we see that hollow defects in SiC act rather as classical crystallization sites although crystallization does not necessarily start here. Globulization, however, must clearly be caused by a different mechanism.

3.3.3 Influence of impurities

To investigate the influence of impurities we performed oxidation experiments in a quartz tube furnace using P_2O_5 -dried oxygen at 1400°C for 28 hours. Sodium is a common impurity and, thus, we introduced small amounts of sodium chloride (some 5 μm large grains of high purity NaCl) on selected samples. The difference in the oxide scale's morphology was drastic, as shown in Fig. 8. Thoroughly cleaned surfaces of samples without additionally introduced NaCl showed no globulite formation at all, but small statistically distributed radialites (Fig. 8a). Samples with sodium chloride displayed a more or less homogenous crystalline oxide scale fully covered with globulites (Fig. 8b - d). Furthermore, clean undoped samples, which were positioned downstream the gas flow behind NaCl-containing samples showed extensive globulite formation, too. This is a good example of the high mobility of sodium and, in general, of alkaline and earth alkaline impurities.

Further evidence for the dominant relation of impurities and globulization comes from an experiment at 1350°C for 100 h in a high-purity environment (dehumidified oxygen, fused quartz tube) which showed no evidence of globulite formation but only a high degree of radialite cover. Ogbuji's experiments¹⁰, for which the influence of impurities can be excluded, as well, point in the same direction.

The quantification of the influence of the impurities remains difficult. Assuming a minimum crystallization speed of 1.5 $\mu\text{m}/\text{h}$ from the first part of this study 28 h of crystallization would yield a radialite radius r of 42 μm . However, only $r = 6.5 \mu\text{m}$ was observed in high-purity environments. This is probably due to a late nucleation, because from oxidation tests at 1400°C carried out for less than 28 h samples without any significant devitrification at all were observed in the high-purity environment.

Alternatively a lower crystallization rate for radialites in high-purity environments can be assumed as the crystallization speed of 1.5 $\mu\text{m}/\text{h}$ may already have been influenced by impurities to some extent. This is likely to be true as impurities are known to influence both nucleation and crystallization rate. Concerning the nucleation process, impurities are believed to be the most important causative factor.²³ The crystal growth rate V can be influenced by impurities via a change of the viscosity of vitreous media. In particular, oxygen or water accelerate silica crystallization considerably.³² The same applies for sodium: even trace amounts of Na in the ppm range influence silica viscosities significantly.³³

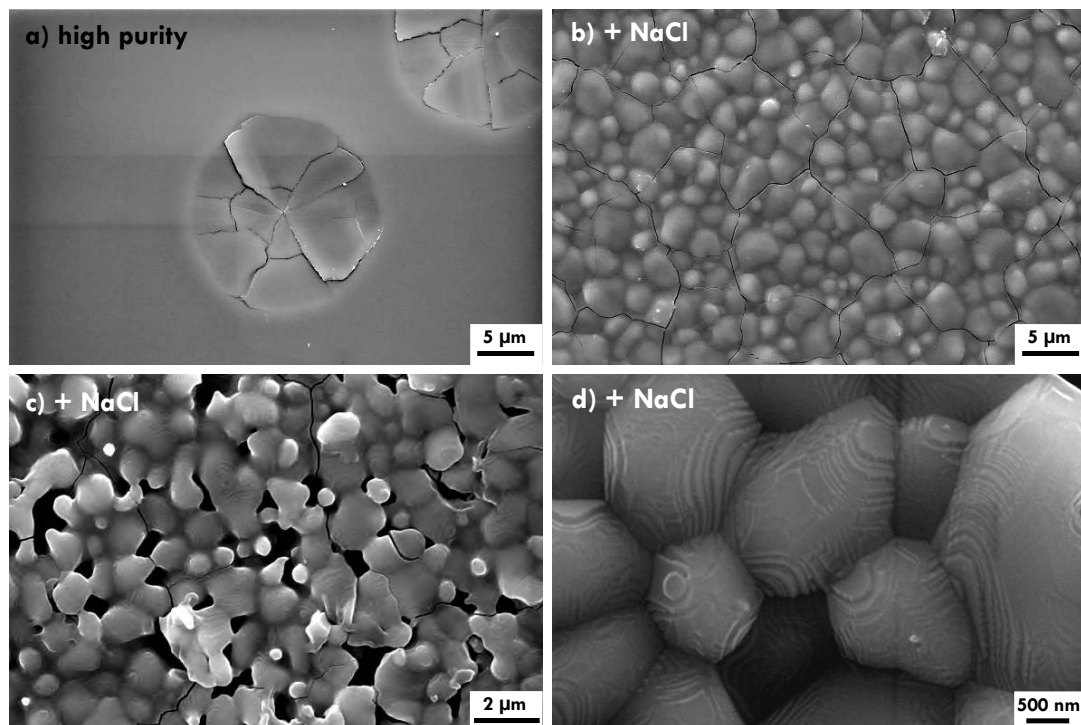


Fig. 8. SE-mode SEM images of the oxide scale obtained after 28 h of dry, thermal oxidation of (0001)6H-SiC:N at 1400°C. a) In high-purity environments ideal radialite formation can be observed. b – d) In the presence of intentionally introduced NaCl, extensive globulite formation and accelerated crystallization is observed. Note the growth-step structures on “young” globulites in 8c and 8d.

3.3.4 Influence on the oxidation rate

As pointed out in Opila’s study ⁷ on the influence of alumina reaction tube impurities, alkaline or earth-alkaline elements will cause accelerated oxidation rates as well as accelerated crystallization. However, in principal we should have two opposing effects: sodium accelerates SiC oxidation as both molecular and ionic diffusion of oxygen is faster in sodium-doped silica, while it also catalyses silica devitrification.³⁴ The latter should decelerate SiC oxidation because oxygen diffusion is much slower in cristobalite than it is in vitreous silica.²⁶

Both phases coexist over a long period of time as discussed earlier and consequently most of the oxidation reaction should happen beneath the regions covered by vitreous silica. This includes the *in-situ* grain boundaries of large differentiated radialite plates, which must have accelerated oxidation rates due to the presence of the skeletal amorphous network.

In most environments the coexistence of both phases, (1) vitreous silica and (2) growing radialites, is superimposed by the structural transition of radialites into (3) globulites. The latter is accompanied by the formation of pores (Fig. 2, 8c) and the introduction of many new grain boundaries between individual globulites which on their behalf act as pathways for accelerated oxygen transport.

Therefore, it is in some cases incorrect to assume a slower oxidation rate for SiC covered with crystalline silica without taking the actual morphological microstructure into account. The effects of radialite and globulite formation do at least partly compensate for each other and we think that this is one of the reasons, why the overall oxidation process can usually be fitted to a simple parabolic time-law despite the complicated processes in detail.

However, as electronic applications of SiC become more important and we need to know the kinetics more precisely, at least the observable difference between the net weight gain per unit area during the “vitreous silica” stage compared to the “crystalline silica” phase (comprising both radialite and subsequent globulite formation) can and should be resolved, as pointed out by Ogbuji (Ref. ¹⁰) and Presser and Nickel (Ref. ³).

A further complication in the presence of impurities is the appearance of tridymite as one of the crystallization products.⁷ It is not expected that the bulk diffusion coefficient of oxygen through cristobalite is significantly different from that of tridymite. But the presence of tridymite, in turn, can be used as an indicator for the presence of impurities as tridymite is known not to form under high-purity conditions.³

3.3.5 Globulite formation mechanism

To summarize the observations on the influence of impurities and globulite formation, we propose a mechanism for the microstructural evolution of silica on single crystal silicon carbide at high temperature (1300° - 1400°C) in the presence of common impurities. This mechanism is in agreement with a study by Costello and Tressler ³⁵ speculating about an enhanced surface crystallization process which would be promoted by Na and / or K from the furnace tube resulting in “second generation spherulites” (i.e., globulites) and is schematically illustrated in Fig. 9.

- (1) Bulk growth of vitreous silica. During the initial oxidation stage, silicon carbide oxidizes in an oxygen containing atmosphere by forming vitreous silica.
- (2) Nucleation of crystallization centers. At high temperatures nuclei of cristobalite form in the entire amorphous silica layer. Either preferred formation or preferentially bigger nucleus sizes occur at the interface between the vitreous silica layer and the atmosphere.
- (3) Radialite growth. Once nuclei of critical size are present, devitrification of vitreous silica starts at the oxide-atmosphere interface with bulk radialite growth. SiC covered by the vitreous matrix oxidizes faster than areas covered with cristobalite plates. As a result, the typical caldera-like morphology of radialites (thinner inner part / thicker outer part) develops. Gas and impurities, dissolved in the vitreous silica, exsolve from the devitrified areas and become enriched in the zone ahead of the crystallization front.
- (4) Impurity accumulation. The exsolved impurities like potassium or sodium accumulated at the devitrification front possibly stabilize the skeletal vitreous network beneath and in-between radialites plates. With a continuing input, the impurity concentration on the surface will increase until the formation of a first melt occurs as drops or surface films.

- (5) Globulite formation. The formed melt must be saturated with silica. Hence, melt spots are the sites at which dissolution and reprecipitation of silica takes place first. Reprecipitation produces relaxed crystals that are statistically orientated. During growth they form globular objects. Isolated growing globulites have a natural pore space between them. When they grow independent from each other, a swelling process is accompanying the growth. Nonetheless, the globulites will continue to be covered by melt, because it is an equilibrium melt which must wet perfectly. These globulite forming areas are then sites of preferred oxidation, because they contain a melt and they are porous. In this way they consume the hill tops which the silica-SiC interface developed during radialite growth (see part I, also). The net result is a local super-elevation of the globulite lawn with a structure resembling sintered spheres. It is highly likely that the growing globulite cover is further differentiated with perfect “young” spheres, which develop into more deformed shapes with time and probably also with depth within the scale. The structures shown in Fig. 2 and 8c are, therefore, seen as a fairly late stage of the process, while initial features like growth-steps such as shown in Fig. 8d dominate in spots with low amounts of melt.

As for this mechanism, we referred to a “melt phase” that is caused by cristobalite liquidization due to impurities. In general, melt formation is possible and caused already by minor amounts of, for example, sodium ³⁶ as seen from the binary phase diagram presented in Fig. 10. Here, we see that a melt phase can coexist with crystalline silica. As we neither know the exact viscosity nor the exact chemical composition, the phase might not be truly molten but very poorly viscous. Also, this melt formation is restricted to very thin layers, for example, on the topmost surface and must not be mistaken with a mechanism causing bulk radialite liquidization. Melt-catalyzed recrystallization would be in agreement with (1) the observed loss of preferred orientation (μ XRD), (2) the morphological changes caused by globulization and (3) the observation of growth-steps.

In theory, the latter may also be caused by a gas-vapor transport mechanism. Significant vapor-phase formation, however, is not expected at the studied oxidation temperatures ($\ll 1700^\circ\text{C}$). In fact, the input of impurities, however, showed an increase in weight-gain per unit area during oxidation of SiC at these temperatures ($\ll 1700^\circ\text{C}$) evidencing a true passive oxidation mechanism.⁷

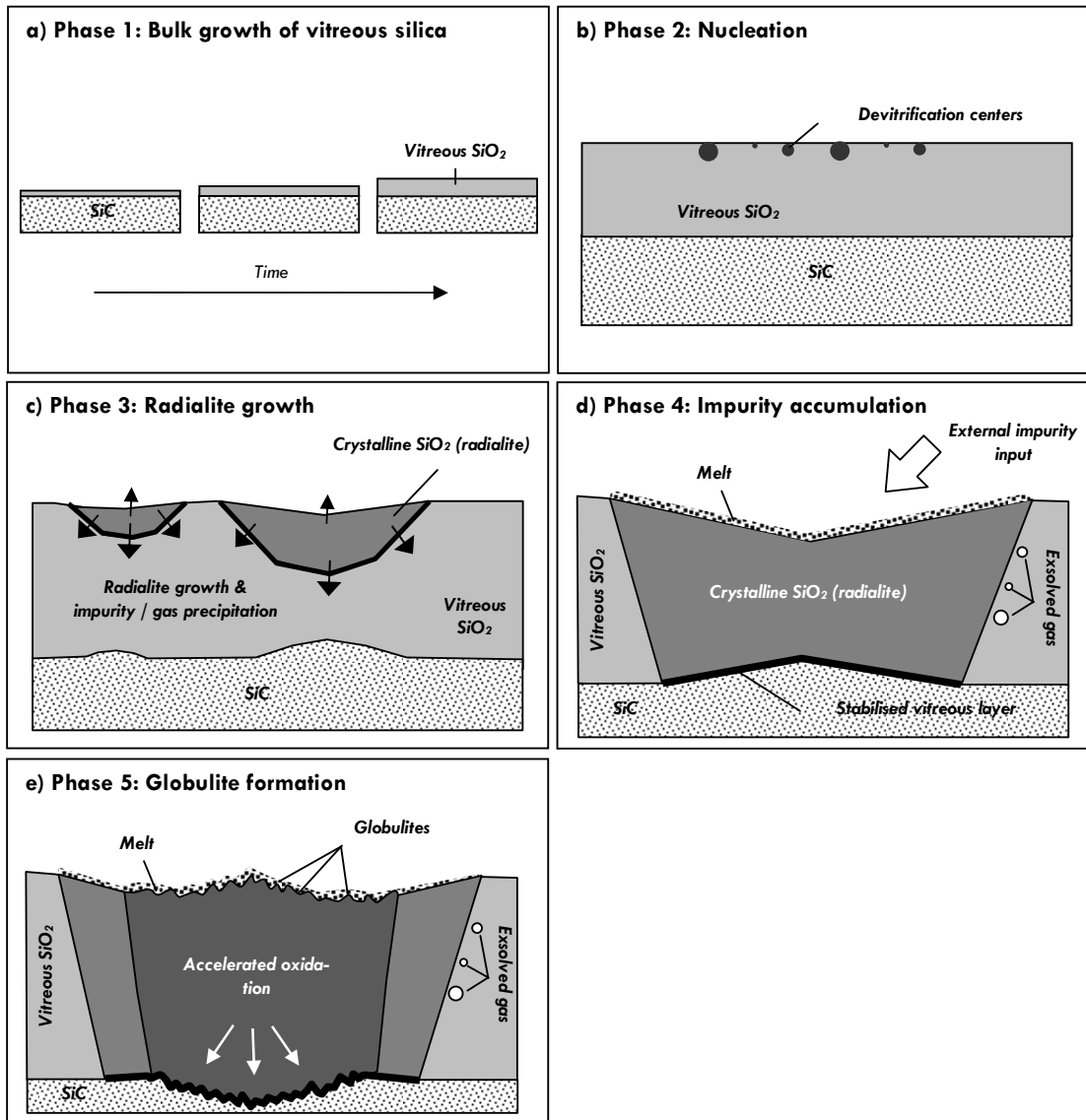


Fig. 9. Globulite formation mechanism. For discussion see text.

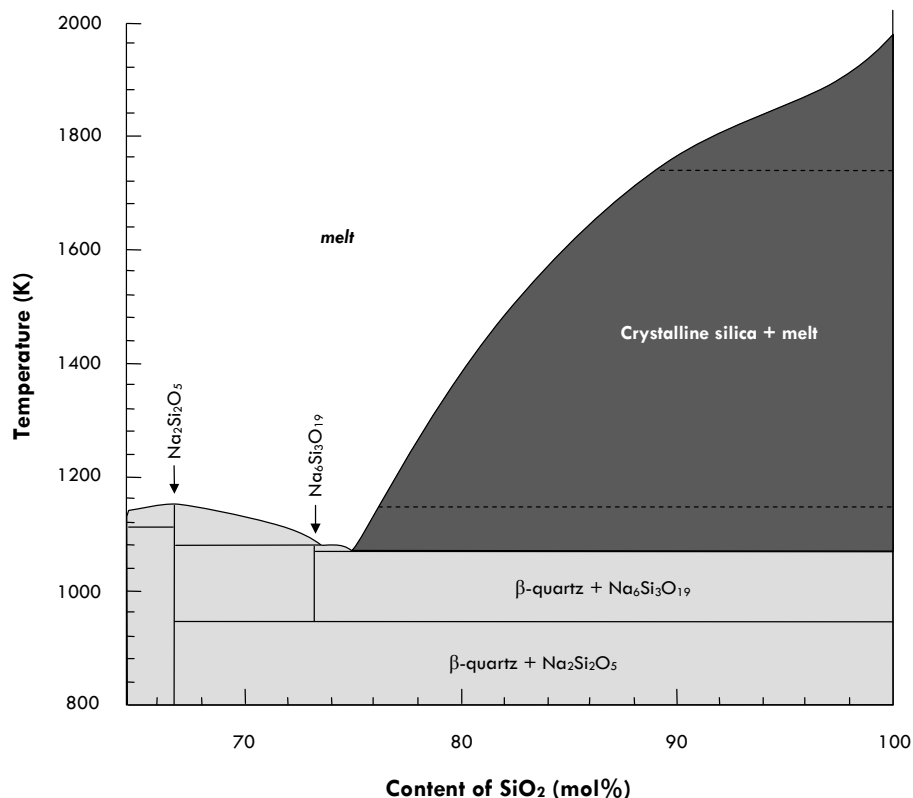


Fig. 10. Simplified binary phase diagram (Na₂O – SiO₂; after Ref. ³⁶). Even minor amounts of sodium lead to the formation of a coexisting melt. For discussion see text.

4. CONCLUSION

In this study we analyzed the vitreous-crystalline transition zone within the oxide scale formed during the dry, thermal oxidation of silicon carbide (6H-SiC:N) carried out in an alumina tube. This interface is characterized by accumulation of impurities and gas that were once both dissolved in the vitreous silica matrix. The presence of exsolved products explains why beneath the crystal plates a skeletal vitreous network remains which is also present at grain boundaries (i.e., between the individual plates out of which radialites are comprised) and acts as a pathway for accelerated diffusion – hence accelerating SiC oxidation as such.

With a continuous input of impurities coming from the furnace tube, the impurity concentration on top of the crystal plates is constantly increasing until a critical level is reached at which melt formation starts. Catalyzed by a liquid phase, the energetically unfavorable large crystal plates recrystallize and small crystalline spheres (globulites) appear. These spheres are interconnected by the melt phase wetting the crystalline spheres. Globulization in this advanced stage induces local swelling with pore formation and is limited to impurity-loaded environments / samples.

SiC oxidized in high-purity atmospheres in the absence of e.g. Na and / or K did not show globulite formation even after 100 h of dry thermal oxidation at 1350°C. This means that the influence of impurities must not only be considered for bulk oxidation rates, but accounts for a particularly rough morphological evolution of the silica layer. Nonetheless, even in the clean case some morphology will develop due to radialite growth because SiC covered by vitreous silica oxidizes faster and some in-situ grain boundaries form as a result of radialite differentiation.

Hollow defects in SiC can be seen as simple surface inhomogeneities and, as such, as possible centers for devitrification. They are, however, not causing globulite formation *per se*. Eventually, impurities or polishing paste remnant may be trapped in these defects and act as extrinsic impurity sources.

Acknowledgments

This work was supported by the Deutsche Forschungsgemeinschaft (DFG) through Ni299/12-1. The authors gratefully acknowledge XRF measurements carried out by Dr. H. Taubald and the most helpful input and μ XRD measurements provided by Dr. C. Berthold (both University of Tübingen).

REFERENCES

1. Haase, V. et al. *Si. Silicon. Supplemental Volume B3.*, 545 (Springer-Verlag, Berlin, 1986).
2. Harris, G.L. *Properties of Silicon Carbide*, 282 (INSPEC, the Institution of Electrical Engineers, London, 1995).
3. Presser, V. & Nickel, K.G. Silica on silicon carbide. *Critical Reviews in Solid State and Material Sciences* **33**, 1 - 99 (2008).
4. Christiansen, K. & Helbig, R. Anisotropic oxidation of 6H-SiC. *Journal of Applied Physics* **79**, 3276 - 3281 (1996).
5. Shenoy, J.N., Das, M.K., Cooper, J.A., Jr., Melloch, M.R. & Palmour, J.W. Effect of substrate orientation and crystal anisotropy on the thermally oxidized SiO₂/SiC interface. *Journal of Applied Physics* **79**, 3042 - 3045 (1996).
6. Schumacher, C. & Nickel, K.G. Influence of Boron and Carbon on the Oxidation of Sintered Silicon Carbide at 1500°C. *Ceramic Engineering & Science Proceedings* **21**, 615 - 622 (2000).
7. Opila, E. Influence of Alumina Reaction Tube Impurities on the Oxidation of Chemically-Vapor-Deposited Silicon Carbide. *Journal of the American Ceramic Society* **78**, 1107 - 1110 (1995).
8. Tressler, R.E., Costello, J.A. & Zheng, Z. Oxidation of Silicon Carbide. in *Industrial Heat Exchangers*, Vol. 1 (eds. Hayes, A.J., Liang, W.W., Richlen, S.L. & Tabb, E.S.) 307 - 314 (American Society for Metals, Pittsburgh, 1985).
9. Costello, J.A. & Tressler, R.E. Oxidation Kinetics of Silicon Carbide Crystals and Ceramics: I, In Dry Oxygen. *Journal of the American Ceramic Society* **69**, 674 - 681 (1986).
10. Ogbuji, L.U.J.T. Effect of Oxide Devitrification on oxidation Kinetics of SiC. *Journal of the American Ceramic Society* **80**, 1544 - 1550 (1997).
11. Presser, V., Loges, A. & Nickel, K.G. Scanning electron and polarization microscopy study of the variability and character of hollow macro-defects in silicon carbide wafers. *Philosophical Magazine* **88**, 1639 - 1657 (2008).
12. Berthold, C., Bjeoumikhov, A. & Brügemann, L. Fast XRD² Microdiffraction with Focusing X-Ray Microlenses. *Particle & Particle Systems Characterization in press*(2008).
13. Wirth, R. Focused ion beam (FIB): a novel technology for advanced application of micro- and nanoanalysis in geosciences and applied mineralogy. *European Journal of Mineralogy* **16**, 863 - 876 (2004).
14. Pantsukrin, S.D. & Kalinin, D.V. Kinetics and mechanism of formation of alpha-cristobalite spherulites. *Seriya Khimicheskikh Nauk* **1**, 27 - 31 (1988).
15. Ainger, F.W. The Formation and Devitrification of Oxides on Silicon. *Journal of Materials Science* **1**, 1 - 13 (1966).
16. Peacor, D.R. High-temperature single-crystal study of the cristobalite inversion. *Zeitschrift für Kristallographie* **138**, 274 - 298 (1973).
17. Keskar, N.R. & Chelikowsky, J.R. Structural properties of nine silica polymorphs. *Physical Review B* **46**, 1 - 13 (1992).
18. Swainson, I.P. & Dove, M.T. On the Thermal Expansion of β-Cristobalite. *Physics and Chemistry of Minerals* **22**, 61 - 65 (1995).
19. Jacobson, N.S. Corrosion of Silicon-Based Ceramics in Combustion Environments. *Journal of the American Ceramic Society* **76**, 3-28 (1993).
20. Stockmann, Y.J., Ullmann-Papst, S., Kleist, G., Steinbrech, R.W. & Nickel, H. Mechanische Eigenschaften von SiO₂-Schichten auf SiSiC. in *Korrosion und Verschleiß von keramischen Werkstoffen* (eds. Telle, R. & Quirnbach, P.) 77 - 84 (Deutsche Keramische Gesellschaft e.V. (DKG), Aachen, 1994).
21. Touloukian, Y.S., Kirby, R.K., Taylor, R.E. & Lee, T.Y.R. Thermal expansion of nonmetallic solids. 350-358, 358-371, 873-878 (New York, 1977).
22. Ostrovsky, I.A. On some sources of errors in phase-equilibria investigations at ultra-high pressure; phase diagram of silica. *Geological Journal* **5**, 321 - 328 (1967).
23. Doremus, R.H. *Glass Science*, 339 (John Wiley & Sons, N.Y., 1994).
24. Shelby, J.E. Pressure dependence of helium and neon solubility in vitreous silica. *Journal of Applied Physics* **47**, 135 - (1976).
25. Barrer, R.M. & Vaughan, D.E.W. Solution and diffusion of helium and neon in tridymite and cristobalite. *Transactions of the Faraday Society* **67**, 2275 - 2290 (1967).
26. Rodríguez-Viejo, J., Sibieude, F., Clavaguera-Mora, M.T. & Monty, C. ¹⁸O diffusion through amorphous SiO₂ and cristobalite. *Applied Physics Letters* **63**, 1906 - 1908 (1993).
27. Ogbuji, L.U. Development of oxide scale microstructure on single-crystal SiC. *Journal of Materials Science* **16**, 2753 - 2759 (1981).
28. Raynaud, C. Silica films on silicon carbide: a review of electrical properties and device applications. *Journal of Non-Crystalline Solids* **280**, 1 - 31 (2001).
29. Heuer, A.H., Ogbuji, L.U.J.T. & Mitchell, T.E. The Microstructure of Oxide Scales on Oxidized Si and SiC Single Crystals. *Journal of the American Ceramic Society* **63**, 354 - 355 (1980).
30. Sibieude, F., Rodriguez, J. & Clavaguera-Mora, M.T. Kinetics and crystallization studies by in situ x-ray diffraction of the oxidation of chemically vapour deposited SiC. *Thin Solid Films* **204**, 217 - 227 (1991).

31. Dhanaraj, G., Huang, X.R., Dudley, M., Prasad, V. & Ma, R.-H. Silicon Carbide - Part I: Growth and Characterization. (eds. Byrappa, K. & Ohachi, T.) 181 - 232 (Springer-Verlag, Berlin, 2003).
32. Lipinski, D. & Schwiete, H.E. Die Bildung des Cristobalits aus amorphem Siliziumdioxid unter verschiedenen Gasatmosphären. *Tonindustrie-Zeitung und Keramische Rundschau* **88**, 145 - 153; 217 - 225; 258 - 262 (1964).
33. Donnadieu, P. Influence of impurities on plastic flow of silica glass. *Journal of Non-Crystalline Solids* **99**, 113 - 117 (1988).
34. Zheng, Z., Tressler, R.E. & Spear, K.E. The effect of sodium contamination on the oxidation of single crystal silicon carbide. *Corrosion Science* **33**, 545 - 556 (1992).
35. Costello, J.A. & Tressler, R.E. Oxidation Kinetics of Hot-Pressed and Sintered alpha-SiC. *Journal of the American Ceramic Society* **64**, 327 - 331 (1981).
36. Halter, W.E. & Mysen, B.O. Melt speciation in the system Na₂O-SiO₂. *Chemical Geology* **213**, 115 - 123 (2004).

Chapter 01

Chapter 02

Chapter 03

Chapter 04

Chapter 05

Chapter 06

Chapter 07

Chapter 08

Chapter 09

Chapter 10

Chapter 11

Chapter 12

METAMICTIZATION IN ZIRCON: RAMAN INVESTIGATION FOLLOWING A RIETVELD APPROACH. PART 1: PROFILE LINE DECONVOLUTION TECHNIQUE.

V. Presser⁽¹⁾

⁽¹⁾ Institut für Geowissenschaften, Universität Tübingen

ABSTRACT:

The line profile form of Raman spectra can be analyzed using the very same approach and software used for diffractogram deconvolution via the Rietveld approach. In both cases the “true” profile containing information about the sample must be separated from the instrument’s profile function (and potentially from the emission profile) which can be achieved by deconvolution. In this first part of a two-part study we demonstrate how the instrument’s profile function can be described via a Gaussian function profile (yielding the very same result as several convoluted hat functions) using several examples (diamond, calcite, silicon and silicon carbide) for which true Raman bandwidth values are presented (assuming the true band profile to be Lorentzian). Also, asymmetrical bands can be described and analyzed via the presented deconvolution approach. The second part of this study will discuss and apply this method for studying the radiation-induced damage in zircon grains (metamictisation).

1. INTRODUCTION

Rietveld refinement is a well established method for whole-pattern-fitting structure refinement and as such it is a widespread standard tool for qualitative and quantitative phase determination using X-ray, neutron or synchrotron data.¹ The term Rietveld refinement, in general, stands for a profile refinement procedure based on the least squares method, where a calculated pattern is adapted to the experimental data. Profile refinement is the basis for the Rietveld method; having starting parameters reasonably close to the final values, it is possible to refine crystal structure data such as atomic positions, temperature factors etc. and, in the end, also quantitative determination in polyphase systems is possible. By minimization of S (residual), the best least squares fit is believed to yield the best Rietveld fit (Eq. 1):

$$S = \sum_i w_i \cdot [y_i^{\text{measured}} - y_i^{\text{calculated}}]^2 \rightarrow \text{minimum} \quad \text{Eq. 1}$$

where y is a measured or calculated intensity (y^{measured} or $y^{\text{calculated}}$, respectively) and w is a statistic weight of each measured data point (Eq. 2; with σ as the standard deviation).

$$w_i = \frac{1}{\sigma_i^2} = \frac{1}{y_i^{\text{measured}}} \quad \text{Eq. 2}$$

One of the most challenging tasks in this context is the correct deconvolution of the profile function of the sample and the instrument, respectively.^{2,3} The measured profile can be seen as a mixed Gaussian-Lorentzian profile function in first approximation (possibly with asymmetric features). Modern day Rietveld software packages are powerful tools for fast profile deconvolution even when several complex profile functions are involved.

Raman spectra also comprise those two convoluted pieces of information: (1) the profile function of the actual sample signal and (2) the profile function of the instrument. It is only by correct deconvolution of those two profiles that an instrument-independent profile function of the sample can be obtained. This is essential when comparing data acquired from different instruments or even from one single instrument using different sets of slit widths. Polynomial approaches or linear-combination of Gaussian-Lorentzian profiles, however, are only approximations and do not truly represent the actual physical process which leads to convoluted profiles.

As nowadays, fast computers are standard tools, true deconvolution of Raman spectra is no longer time consuming and a mere matter of minutes or even seconds. In this paper, we will illustrate how software originally designed for Rietveld refinement can easily be used for such purposes. Although the concept of convolution and the basic features of the Raman instrument function(s) are well known (or at least intensively studied), the technical approach to deconvolute the profile function of the instrument from the sample's profile using the described Rietveld-approach has not been described yet.

In the first part of this two-part study, we present the basics of a Rietveld approach to profile line deconvolution and provide examples of applications to calibration standards. The second part will present experimental data of radiation-induced line-broadening in natural zircon (ZrSiO_4) in the context of radiometric age determination.

2. ANALYTICAL METHODS

Raman spectra were obtained using a confocal Raman microprobe Labram[®] 2 (HORIBA Jobin Yvon GmbH, Bensheim, Germany) with a 1800 lines/mm grating using an external argon ion laser (488.0 nm). The laser beam was focused onto the sample by a 100-fold magnifying microscope objective (NA = 0.90) and a lateral resolution of $< 2 \mu\text{m}$ was obtained with a power of 2 mW at the sample surface. We used a backscattering $z(y, xy)\bar{z}$ geometry for all spectra and for investigation of the influence of different polarization directions, we rotated the polarization direction by using a lambda-half-plate. The exact angle of the polarization direction was adjustable with a computer controlled stepping motor ($\approx 1^\circ$ accuracy).

Peak-fitting and deconvolution were performed using TOPAS[®] 4 (BRUKER AXS GmbH, Karlsruhe, Germany). As sample material we used natural diamond (Kimberly, South Africa), natural calcite (Grünten, Allgäu, Germany) and high quality undoped synthetic (111)-Si (WACKER CHEMIE AG, Burghausen, Germany) and both undoped and heavily nitrogen doped (0001)-6H-SiC ($n \approx 10^{19} \text{ cm}^{-3}$; SiCrystal AG, Erlangen, Germany).

3. RESULTS AND DISCUSSION

3.1 General remarks

From various studies on the true profile line shape of Raman modes, we know that for Raman bands not lying in direct vicinity to the Rayleigh line a Lorentzian profile function can be assumed.⁴ This was found to be true for both the Stokes and the Anti-Stokes domain. However, it should be kept in mind that a Lorentzian profile function is not the only sample profile function. Especially if there is a statistically distributed continuum of distorting influence parameters, significant deviation from an ideal Lorentzian profile can be observed and a rather Gaussian band shape results. One prominent example is the LO phonon plasmon coupled (LOPC) mode of silicon carbide, where a plasmon-phonon-interaction distorts the profile shape by introducing an asymmetric component and by generally broadening the LOPC mode (for more detailed information on LOPC see Ref. ^{5,6}). Also, full width at half maximum (FWHM; further referred to bandwidth) and profile form may vary for different temperature regimes.⁷

Studies made, for example, by Singh et al. ⁸ and Asthana and Kiefer ⁹ showed how the profile function of the instrument can be separated from the true Raman profile in order to obtain the true Raman bandwidth Γ . In this context, we refer to Γ as the bandwidth of the true Raman profile function (which may or may not correspond with $\text{FWHM}_{\text{Lorentz}}$).

For this study, we used an argon ion laser whose emission profile is Lorentzian with negligible bandwidth. Thus it was not necessary to consider the laser's line FWHM for convolution. As solid-state lasers emit emission-lines with significant bandwidths, correct deconvolution requires taking this into account as a third contributing factor apart from sample and instrument). Tanabe and Hiraishi ¹⁰ used the negligible "true" FWHM of emission lines to determine the profile function of the instrument. As shown in that study, the FWHM of neon emission lines is not a constant value for every Raman wavenumber value but decreases with larger wavenumbers. This observation was corroborated by our study during which we analyzed the total bandwidth ($\text{FWHM}_{\text{total}}$; Gaussian profile shape) of > 40 neon emission lines (Fig. 1).

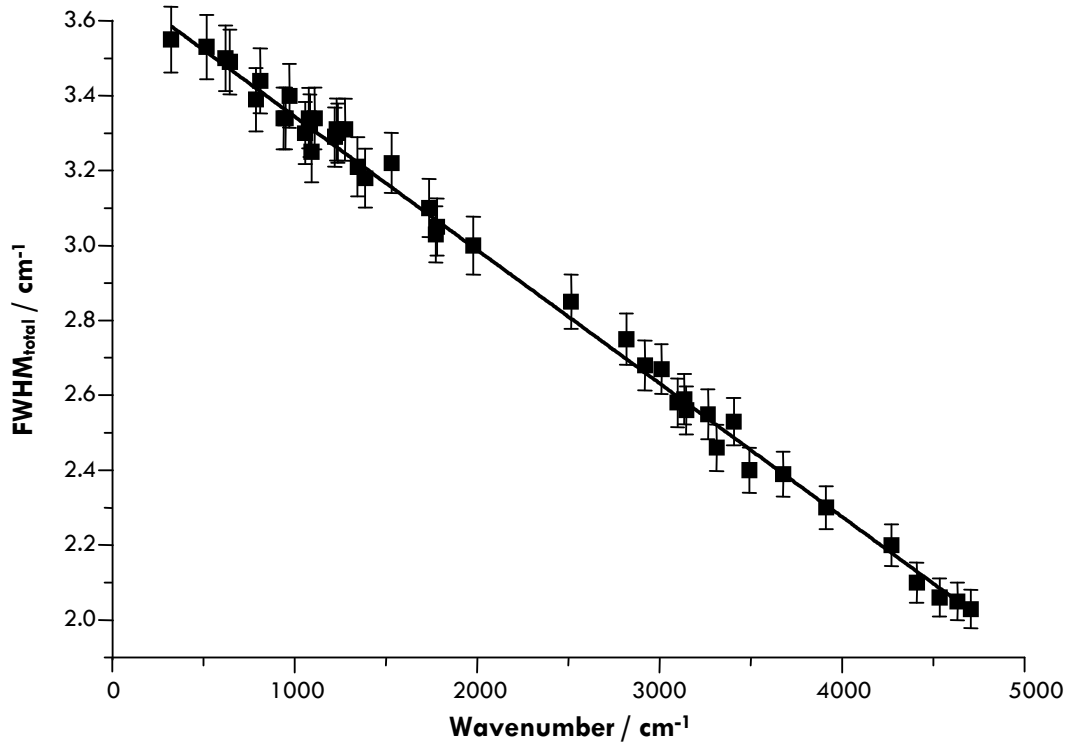


Fig. 1. Relationship between total bandwidth $FWHM_{total}$ and Raman shift ($R^2 = 0.99341$) for 42 neon emission lines (120 s acquisition time).

For our specific instrument and the set of slit widths used we found as expected (Ref. ^{7,10}) a linear relationship with a negative slope expressed in Eq. 3:

$$FWHM_{total} \text{ (cm}^{-1}\text{)} = a \text{ (cm}^{-1}\text{)} + b \cdot \text{Raman shift (cm}^{-1}\text{)} \quad \text{Eq. 3}$$

with $a = 3.682$ and $b = -3.489 \cdot 10^{-4}$. Consequently, it is not correct to determine just one overall instrumental bandwidth. Assuming the bandwidth to be constant yields a sufficiently small error only if the observed spectral range is narrow.

This can indeed be seen as the most important difference to Rietveld analysis, for example, of X-ray diffraction (XRD) data, where diffracted monochromatic radiation is analyzed which does not show this (linear) spectral deviation in FWHM values. XRD data also show a change (increase) in $FWHM_{total}$ values due to the angular dispersion of the collimator (Caglioti equation, Eq. 4).

$$FWHM_{total}^{diffraction \ data} = \sqrt{U \cdot \tan^2 \theta + V \cdot \tan \theta + W \cdot \tan^0 \theta} \quad \text{Eq. 4}$$

The profile function of the instrument is convoluted by hat functions corresponding to slits within the spectrometer (e.g., entrance slit of the spectrometer). When using a CCD, the pixel width of the detector also acts as a slit (with very small slit width). Convolution of two hat functions yield a trapezoid function – which is actually a better approximation than a triangle function (cf. Fig. 2).¹¹ When considering the focal slit width, the convolution of three hat functions yields a Gaussian-like profile function. The larger the slit width, the wider the corresponding hat function will be. It should be noted that the described Rietveld approach to profile line deconvolution could equally be adapted for any kind of instrument function (even asymmetric ones).

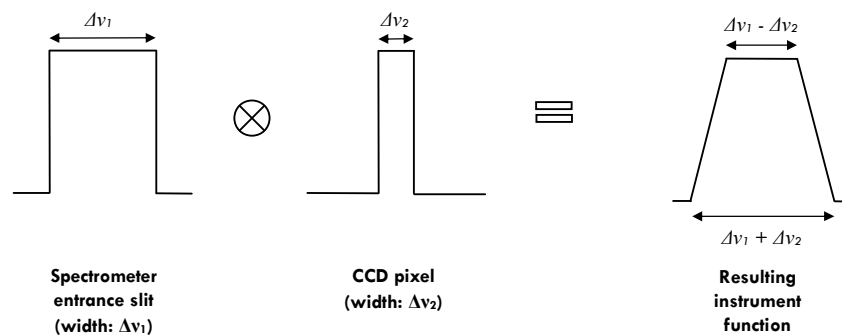


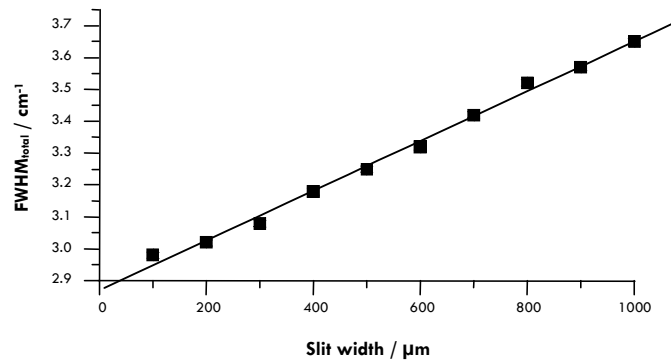
Fig. 2. Schematic illustration of the convolution result of two hat functions (corresponding to two slits with different slit widths).

3.2 Diamond

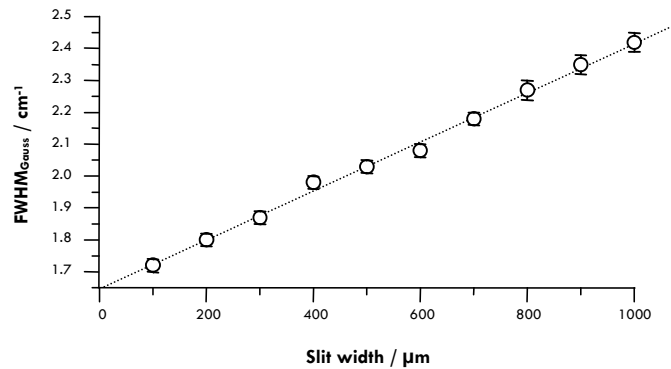
In order to study the dependency of the FWHM of the slit width, we varied the focal slit width from 100 to 1000 μm in 100 μm steps. For all these measurements we studied the same sample position. Repeating measurements with the same set of slit width values yielded a reproducibility of 0.01 – 0.05 cm^{-1} .

Figure 3 shows the results of the deconvolution of the diamond E_{2g} -mode ($\text{FWHM}_{\text{total}}$, $\text{FWHM}_{\text{Gauss}}$ and $\text{FWHM}_{\text{Lorentz}}$). Extrapolation of the total bandwidth for a slit width of 0 μm would yield a FWHM value of 2.87 cm^{-1} which still contains the instrument function's profile broadening caused by the finite pixel width and confocal slit width. In particular, the true Raman bandwidth Γ (as long as the profile shape is Lorentzian) is $\approx 1 \text{ cm}^{-1}$ smaller and lies within the range of $1.77 \pm 0.03 \text{ cm}^{-1}$. This is in good agreement with the range of Γ values reported for natural diamond (1.61 – 2.16 cm^{-1}).¹²

Total bandwidth



b) Gaussian bandwidth



c) Lorentzian bandwidth

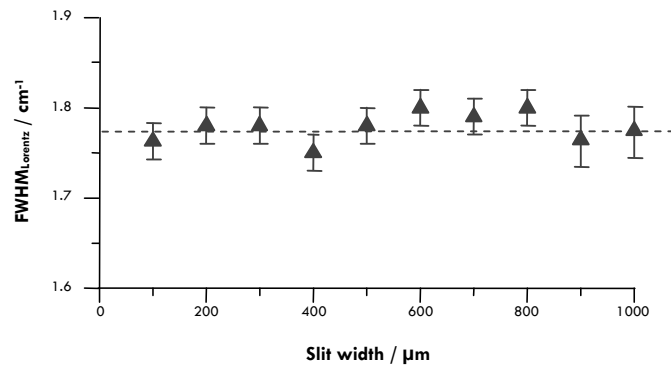


Fig. 3. Wavenumber dependency of bandwidth (a: FWHM_{total}, b: FWHM_{Gauss} ≈ instrumental bandwidth, c: FWHM_{Lorentz} ≈ true Raman bandwidth; 60 s acquisition time). For discussion see text.

3.3 Calcite

Analyzing just one single Raman mode like the diamond E_{2g} -mode does not meet the requirements posed by dealing with common Raman spectra. We expanded our study to calcite whose Raman spectrum shows more than just one single first-order mode. Again, we varied the slit width from 100 – 1000 μm in 100 μm steps. The linear relationship between the Raman shift and the individual $\text{FWHM}_{\text{Gauss}}$ -values was taken into account by using Eq. 3. Refinement of a and b (Eq. 3) for the five analyzed modes (155, 281, 711, 1435 cm^{-1} [E_g], and 1085 cm^{-1} [A_{1g}]) yielded negative values for b which is in perfect accordance with the overall behavior presented in Fig. 1. Best results were obtained by using a and b as determined via measurement of neon emission lines ($a = 3.682$ and $b = -3.489 \cdot 10^{-4}$).

In particular, we found a total bandwidth of 11.29 cm^{-1} for the E_g -mode at 281 cm^{-1} which happens to be the same value (11.3 cm^{-1}) given by Gillet et al. (who did not correct for the profile function of the instrument).¹³ When correcting our data for the instrument's contribution we end up with a true (Lorentzian) FWHM of 9.02 cm^{-1} .

It should also be pointed out that the intensity especially of the A_{1g} -band strongly depends on the polarization direction. Consequently, we investigated FWHM values for various polarization directions more thoroughly.

Unlike to other studies (like Bowie et al.¹¹) we did not rotate the sample but the polarization direction of the laser beam. As the laser beam diameter on the sample is smaller than 2 μm , mechanical stability ensuring to probe the very same position (down to the sub-micrometer level) is questionable when rotating the sample. Introducing a lambda-half-plate and rotating the latter by use of a stepping motor ensures probing exactly the same position avoiding influences from sample heterogeneity. The overlying effect of angular dependence of the grating's efficiency to reflect and disperse the light itself does not influence the true bandwidth but should be kept in mind when comparing Raman spectra using different polarization directions.

As a result, we found no angular variation of $\text{FWHM}_{\text{Lorentz}}$ (e.g., $\text{FWHM}_{\text{Lorentz}}^{A_{1g}} = 1.56 \pm 0.02 \text{ cm}^{-1}$) when using the same parameters for the instrument function's contribution. The fit did not indicate any significant residuals to be present. This agrees well with the findings of Bowie and Griffith¹¹ which indicate no significant change within the experimental error. Their values for the uncorrected $\text{FWHM}^{A_{1g}}$ varied between 7.08 and 7.70 cm^{-1} ($\Delta = 0.62 \text{ cm}^{-1}$) while our values ranged from 1.55 to 1.59 cm^{-1} .

3.4 Plasma lines and silicon

A special case is posed by plasma lines which are emitted from the gas laser, reflected by the surface of the sample (in our case: single crystal silicon) and introduced into the measured Raman spectrum. Deconvolution of these narrow lines showed a negligible $\text{FWHM}_{\text{Lorentz}}$ while the convolution with the profile function of the instrument yielded an excellent fit. Here also overlapping modes are frequently observed (e.g., overlapping plasma lines or an overlap between the A_1 -mode of silicon and a plasma line).

Fig. 4 shows a spectrum of (111)-Si with plasma lines which were introduced by simply removing the interference filter of the spectrometer. Next to two plasma lines (at 529 and 560 cm^{-1}) the A_1 -mode of silicon can be seen. Due to the high reflectivity of silicon and the poor scattering of this semiconductor, the plasma lines are more intense than the actual Si-mode.

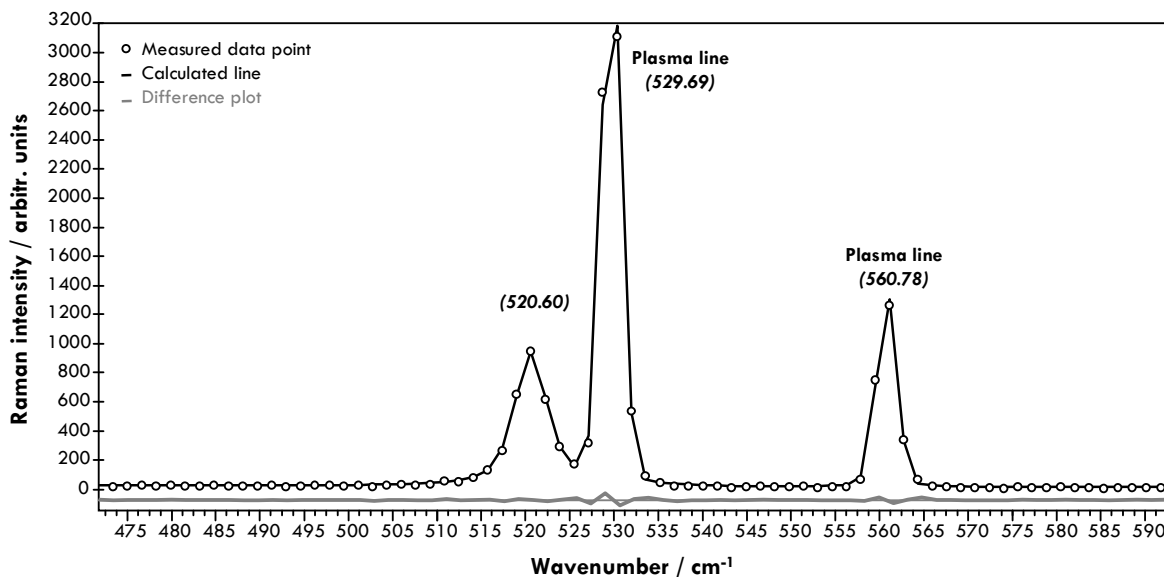


Fig. 4. A₁-mode of (111)-Si and two plasma lines (10 s acquisition time). The calculated curve's angular shaped profile is due to the fact, that not a continuum of calculated data points is plotted but the calculated data points are reduced to the number and the position of the measured data points ("simulated measurement").

For all plasma lines we calculated negligible $\text{FWHM}_{\text{Lorentz}}$ -values ($\approx 0.05 \text{ cm}^{-1}$) and for the slightly overlapping Si-band $3.05 \pm 0.08 \text{ cm}^{-1}$. Comparing with the literature, 3.05 cm^{-1} lies fully within the range of reported values for undistorted Si (at room temperature, e.g., $2.9 - 3.7 \text{ cm}^{-1}$)¹⁴⁻¹⁶.

3.5 Overlapping and asymmetric modes

Asymmetric Raman modes are well known, for example, for structurally bound water. Here the asymmetry arises from a spectrum of O-H-bonding lengths. Various studies tried to describe this asymmetry by using several curves (e.g., Gaussian / Voigt). The functions' relative intensities and positions indicated differences in the OH-mode distribution. Introducing profile functions other than Gauss and / or Lorentz, such as a circle function, asymmetries can be described by one calculated mode alone. In the case of silicon carbide, where phonon-plasmon interaction occurs for the LO mode around 965 cm^{-1} , asymmetry and line-broadening increase with higher doping levels.

Overlapping modes can only be correctly discriminated if more about the individual modes involved is known. Therefore, exact knowledge on the instrument's profile function is essential. Even strongly overlapping modes can be treated this way, although there is a critical threshold of overlapping beyond which restraints (e.g., exact number of overlapping modes etc.) must be introduced to allow for correct deconvolution.

Fig. 5 depicts a spectrum of undoped (0001)-6H-SiC:N. Here, we see overlapping modes (TO at 768, 789 and 797 cm^{-1} ; Fig. 6a) and one LOPC mode (965 cm^{-1}).^{5,6} Using the outlined approach we determined the following values for $\text{FWHM}_{\text{Lorentz}}$: 2.17 cm^{-1} (TO mode at 768 cm^{-1}), 1.62 cm^{-1} (TO mode at 789 cm^{-1}), 1.19 cm^{-1} (TO mode at 797 cm^{-1}) and 2.97 cm^{-1} (LO mode at 965 cm^{-1}).

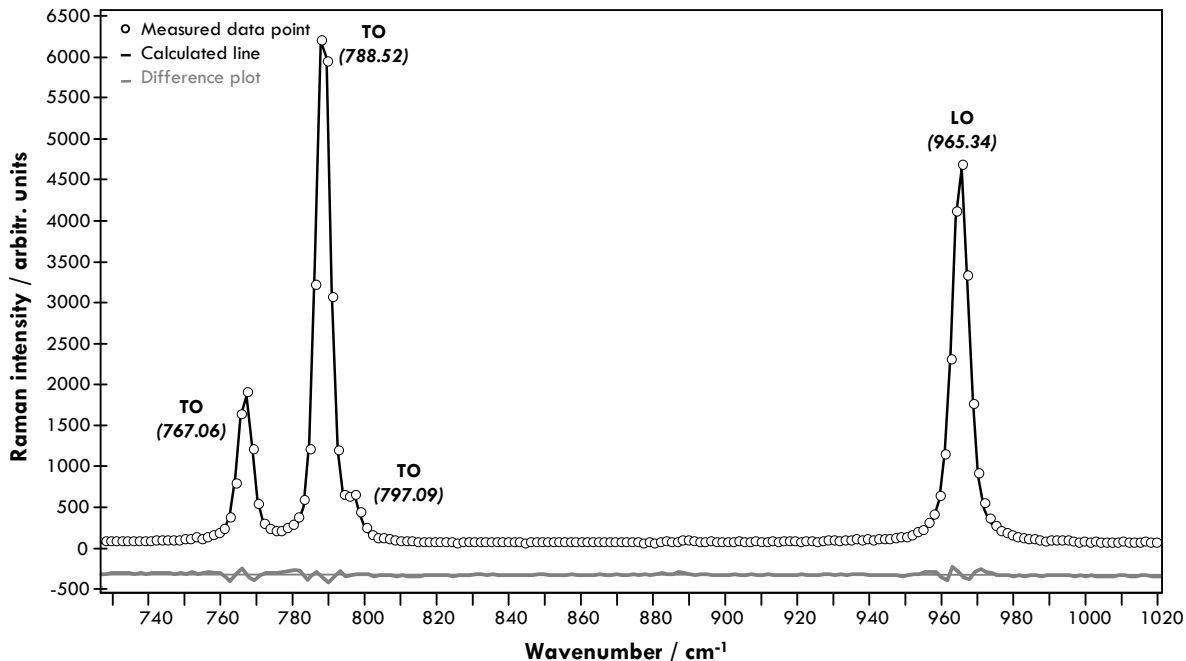


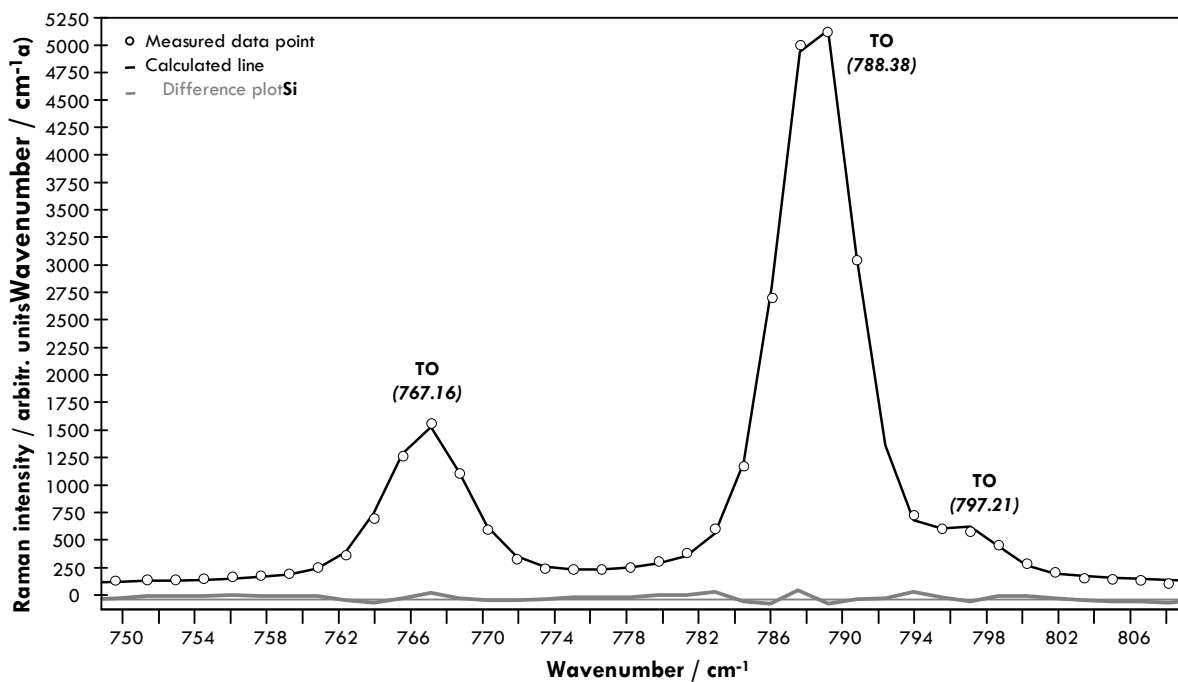
Fig. 5. Raman spectrum of undoped (0001)-6H-SiC (1 s acquisition time). For discussion see text.

The value of 1.19 cm^{-1} may seem too small or at least questionable when considering the small overall intensity and the considerable overlap. However, when examining the Lorentzian bandwidth of this TO-mode at 797 cm^{-1} for another face of 6H-SiC (Fig. 6b: a-face with polarization direction parallel c-axis - i.e. $z(y, xy)\bar{z}$ with $x = \langle 010 \rangle$, $y = \langle 100 \rangle$, $z = \langle \bar{1}\bar{1}0 \rangle$) - the TO-mode is significantly more intense due to SiC's anisotropy (along with directional dispersion of the TO mode at 789 cm^{-1}).^{6,17} For this setting deconvolution yielded $\text{FWHM}_{\text{Lorentz}} = 1.31 \text{ cm}^{-1}$. That value is identical with the first Lorentzian bandwidth within experimental error. In such difficult cases, Lorentzian bandwidth values can only be determined using the described approach of deconvolution.

When examining doped SiC, bandwidth determination of the shifted and broadened LOPC mode is more complicated. In this paper we do not attempt to describe the broadening by the equation introduced by Harima et al.⁵ but by a simple convolution of a circle function with a Lorentzian profile function. This is not the physically most meaningful description but (as demonstrated) yields an excellent fit; so this should be regarded as an empirical way for profile fitting of asymmetric modes.

Fig. 7a depicts the LOPC mode of heavily nitrogen doped (0001)-6H-SiC fitted with a Voigt profile following the outlined approach to describe the Gaussian part. Introducing one single circle function yields an excellent fit and empirically describes the mode's natural asymmetry (Fig. 7b). That way, the broadening from the profile function of the instrument can correctly be removed and "true" Raman bandwidth values can be obtained. This model is also extendible to all other kinds of asymmetric bands (e.g., water).

a) c-face of 6H-SiC



b) a-face of 6H-SiC (polarization parallel c-axis)

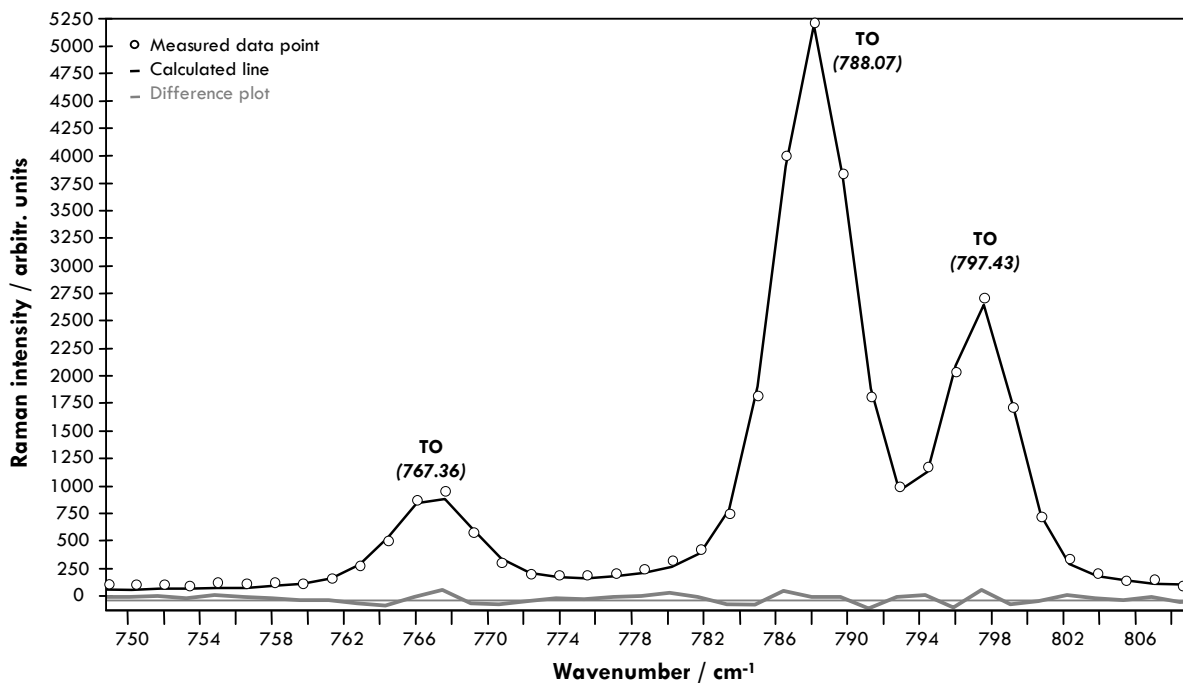


Fig. 6. Raman spectra of undoped 6H-SiC: a) c-face, b) a-face (1 s acquisition time).

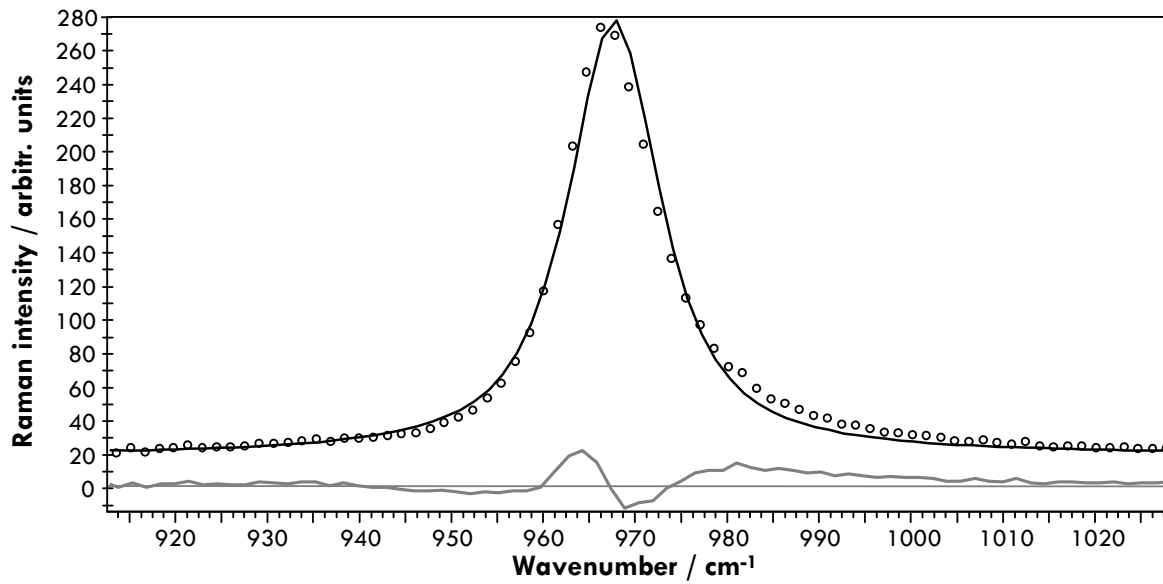
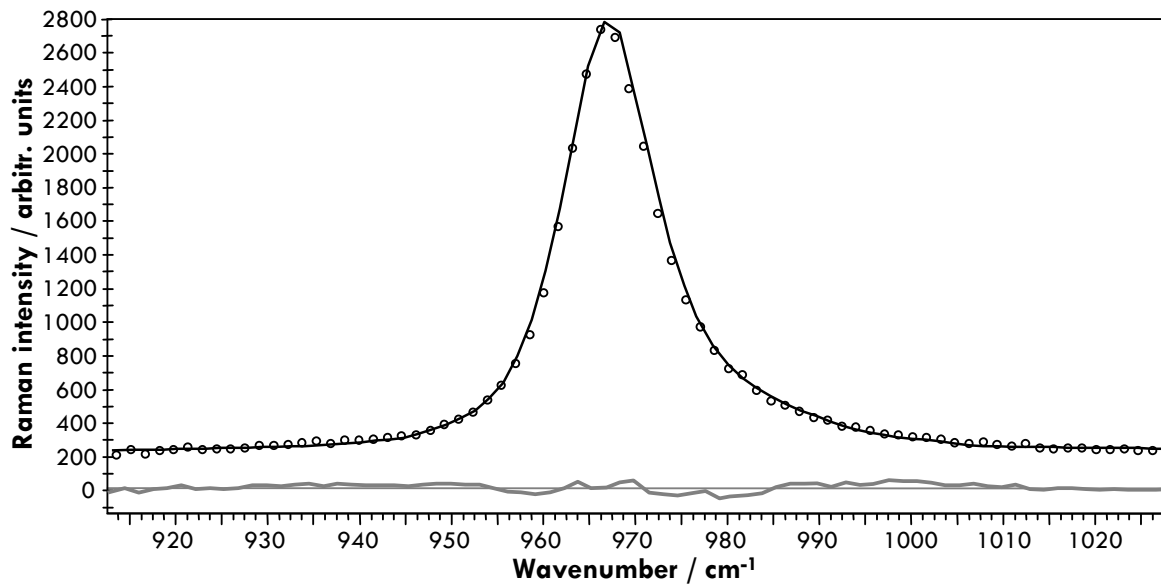
a) Gauss \times Lorentzb) Gauss \times Lorentz \times Circle

Fig. 7. LOPC-mode of heavily nitrogen doped (0001)-6H-SiC fitting (a) one Voigt profile and (b) convolution of Lorentzian, Gaussian and a circle function (1 s acquisition time). For discussion see text.

4. GUIDELINES

As most Rietveld programs are capable of reading xy-data, preparing the data is reduced to converting the file format. It should be kept in mind that some programs give out error message when large x-values are entered – this is due to the fact that angles higher than 180° are inconsistent with X-ray or neutron diffraction. Therefore, it might be necessary to divide the Raman shift by a factor of 100 (so that, e.g., 2000 cm^{-1} reduces to 20 cm^{-1}) to avoid any further complications

Once in the Rietveld software, it is necessary to define an emission profile. When using a gas laser only one emission wavelength and a small bandwidth should be selected. To each single band a peak phase must be assigned which has two convoluted parts: (1) instrument function and (2) profile function of the sample.

The profile function of the instrument can be assumed to be Gaussian. In fact, the obtained values had the same experimental errors when using two (or three) convoluted hat functions instead of one Gaussian. To calculate $\text{FWHM}_{\text{Gauss}}$ caused by the instrument we used Eq. 3 describing the wavenumber-dependency of the bandwidth and the parameters “a” and “b” were refined for all bands. Better results were obtained when refinement was performed over more than just one data set which also yields statistically verified values.

Compared to traditional deconvolution using the same Gaussian-Lorentzian functions, the resulting FWHM-values obtained using a Rietveld-approach were within the experimental error (although traditional deconvolution is much more time consuming).

The true Raman bandwidth in our samples was put on a level with the Lorentzian bandwidth. If that assumption is correct, the profile function of the sample's Raman modes is just one Lorentz function convoluted with the instrument function. These values were unconstrained for all modes in one single spectrum. However, it is possible to use $\text{FWHM}_{\text{Lorentz}}$ of each individual mode as a joint value to be refined for several spectra (e.g., when varying the spectral slit width or for larger data sets).

5. CONCLUSION

In this paper we illustrated how application of easy-to-use Rietveld software enables the line profile deconvolution of Raman spectra to obtain values corrected for the profile function of the instrument and its impact on the profile form and bandwidth.

Most Rietveld programs were developed not only for deconvolution but for batch processing of large amounts of data, for example, for large sets of individual spectra. This makes deconvolution of complete mapping data sets containing hundreds or even thousands of single spectra possible. The good results we obtained with TOPAS® can easily be reproduced by any other Rietveld software capable of deconvolution of (user-defined and predefined) profile functions (which, in fact, most Rietveld programs are not).

It is important to point out that apart from the more elaborate determination of the instrument function's contribution to the convoluted profile function Rietveld software capable of the direct convolution approach allows to save those parameters and retrieve this set of instrument broadening parameters in a graphical interface every time other spectral data are analyzed. Batch processing on its behalf can also be used to correct band positions, for example, with the help of plasma lines or even to correct the measured intensity.

The most striking advantage of using Rietveld software for Raman spectra deconvolution is that these programs can directly be used for this purpose which makes tedious creation of individual programs obsolete. In particular, programming stable least-square kernels for batch processing is not an easy task and can, thus, be avoided by resorting to well-established software solutions.

We also strongly encourage the use of deconvolution Rietveld software for further fields of spectroscopy or signal analyzing techniques in general. With regard to Raman spectroscopy we hope that the widespread use as a standard technique will improve reproducibility and comparability of data especially when more complex profile functions showing significant asymmetry are involved. As will be shown in part two of this two-part study, the fast and reliable way of determining FWHM-values following a Rietveld approach can successfully be adapted to the quantitative description of metamictisation in natural zircon¹⁸.

Acknowledgments

We gratefully acknowledge the helpful discussion and input from Dr. C. Berthold, A. Loges and M. Schloßer (Eberhard-Karls-Universität Tübingen).

REFERENCES

1. Rietveld, H.M. A Profile Refinement Method for Nuclear and Magnetic Structures. *Journal of Applied Crystallography* **2**, 65 - 71 (1969).
2. Cheary, R.W. & Coelho, A. A fundamental parameters approach to x-ray line-profile fitting. *Journal of Applied Crystallography* **25**, 109 - 121 (1992).
3. Cheary, R.W., Coelho, A.A. & Cline, J.P. Fundamental Parameters Line Profile Fitting in Laboratory Diffractometers. *Journal of Research of the National Bureau of Standards and Technology* **109**, 1 - 25 (2004).
4. Jouanne, M. et al. Structural transformations in nanosized zirconium oxide. *Physical Review B* **64**, 155404-1 - 155404-7 (2001).
5. Harima, H., Nakashima, S. & Uemura, T. Raman scattering from anisotropic LO-phonon-plasmon-coupled mode in n-type 4H- and 6H-SiC. *Journal of Applied Physics* **78**, 1996 - 2005 (1995).
6. Nakashima, S. & Harima, H. Raman Investigation of SiC Polytypes. *Physica Status Solidi (A)* **162**, 39 - 64 (1997).
7. Tobin, M.C. *Laser Raman Spectroscopy*, (Robert E. Krieger Publishing Company, Malabar, 1982).
8. Singh, R.K., Singh, S.N., Asthana, B.P. & Pathak, C.M. Deconvolution of Lorentzian Raman linewidth: techniques of polynomial fitting and extrapolation. *Journal of Raman Spectroscopy* **25**, 423 - 428 (1994).
9. Asthana, B.P. & Kiefer, W. Deconvolution of the Lorentzian Linewidth and Determination of Fraction Lorentzian Character from the Observed Profile of a Raman Line by a Comparison Technique. *Applied Spectroscopy* **36**, 250 - 257 (1982).
10. Tanabe, K. & Hiraishi, J. Experimental Determination of True Raman Linewidths from Measurements of Linewidths Observed at Different Slit Openings. *Applied Spectroscopy* **35**, 436 - 438 (1981).
11. Bowie, B.T. & Griffiths, P.R. Determination of the Resolution of a Multichannel Raman Spectrometer Using Fourier Transform Raman Spectra *Applied Spectroscopy* **57**, 190 - 196 (2003).
12. Kirillov, D. & Reynolds, G.J. Linewidths of phonon lines of natural and synthetic diamonds. *Applied Physics Letters* **65**, 1641-1643 (1994).
13. Gillet, P., Biellmann, C., Reynard, B. & McMillan, P. Raman spectroscopic studies of carbonates Part I: high-pressure and high-temperature behavior of calcite, magnesite, dolomite, and aragonite. *Physics and Chemistry of Minerals* **20**, 1 - 18 (1993).
14. Hart, T.R., Aggarwal, R.L. & Lax, B. Temperature Dependence of Raman Scattering in Silicon. *Physical Review B* **1**, 638 - 642 (1970).
15. Lang, G. et al. Anharmonic line shift and linewidth of the Raman mode in covalent semiconductors. *Physical Review B* **59**, 6182 - 6188 (1999).
16. Menendez, J. & Cardona, M. Temperature dependence of the first-order Raman scattering by phonons in silicon, germanium, and α -tin: Anharmonic effects. *Physical Review B* **29**, 2051 - 2059 (1984).
17. Feldman, D.W., Parker, J.H., Jr., Choyke, W.J. & Patrick, L. Raman Scattering in 6H-SiC. *Physical Review* **170**, 698 - 704 (1968).
18. Presser, V. & Glotzbach, C. Metamictisation in zircon: Raman investigation following a Rietveld approach. Part II: Sampling depth implication and experimental data. *Journal of Raman Spectroscopy* **40**, xxx (2009).

Chapter 01

Chapter 02

Chapter 03

Chapter 04

Chapter 05

Chapter 06

Chapter 07

Chapter 08

Chapter 09

Chapter 10

Chapter 11

Chapter 12

METAMICTIZATION IN ZIRCON: RAMAN INVESTIGATION FOLLOWING A RIETVELD APPROACH. PART 2: SAMPLING DEPTH IMPLICATION AND EXPERIMENTAL DATA.

V. Presser⁽¹⁾, C. Glotzbach⁽¹⁾

⁽¹⁾ Institut für Geowissenschaften, Universität Tübingen

ABSTRACT:

Profile line deconvolution following a Rietveld-approach is applied to Raman spectra obtained from natural zircon grains from the European Alps. The corrected bandwidths are in perfect agreement with values obtained from an established correction method (after Irmner) as far as the area of validity of the latter is concerned. For Raman active modes smaller than that, the Rietveld-approach also yields accurate values for the true Raman bandwidth. Moreover, changes to instrument parameters are compensated by the correction routine. As for the studied zircon grains, Raman spectroscopy was shown to be a suitable tool for the examination of zoning (i.e., regions with show a variable degree of radiation-induced damage because of a different amount of incorporated uranium and / or thorium). This is complicated by the fact that the measured Raman signal is not restricted to the depth expected from the axial resolution (several micrometers) but a significant contribution comes from a comparatively large excitation volume (tens of micrometer deep). This sampling volume, however, lies within the same order of magnitude as zoning which itself is blurred by the range of amorphisation-causing alpha-particles.

1. INTRODUCTION

Zircon (ZrSiO_4) is a widespread accessory mineral that can be found in igneous rocks, metamorphic rocks and detrital in some sediments. Its high melting point and both physical and chemical resistivities make this mineral most suitable for age determination.¹ The latter is facilitated as zircon incorporates among other elements, trace amounts of uranium and thorium into the lattice during crystal growth by substituting Zr^{4+} .² Typical concentrations of uranium are around hundreds to thousands ppm, and in extreme cases even up to 1 wt%. Radioactive decay of uranium and to a lesser extent thorium to lead leads to radiation-induced damage when α -particles move through the crystal lattice leaving trails of damage behind. A negligible fraction of radiation damage is produced by the spontaneous fission of heavy nuclides, referred to as “fission tracks” which can be made visible by etching and used for determination of U content (as described, for example, in Ref. ^{3,4}). In this context, the term “metamict state” or “metamictisation” as introduced by Broegger ⁵ describes the radiation-induced amorphisation of otherwise crystalline media.

Radiation-damage, however, is not a constant value that accumulates over time. In particular, radiation damages in zircon anneal at temperatures between 350° and 400°C ⁶ and, therefore, estimates of the degree of metamictisation also have to take into account information about the time-temperature-path (tT) of analyzed samples (e.g., Ref. ⁷). Complicating things further, the degree of metamictisation influences the annealing kinetics and the diffusion of elements (e.g. He can be trapped and Pb can be lost).

As described by Nasdala et al., Raman spectroscopy is an excellent tool to study radiation-induced metamictisation of zircon on a micro-scale.² With increased structural damage to the crystal lattice, the shape and position of individual Raman-active modes change in four ways: (1) the bands become broader, (2) they decrease in total Raman intensity, (3) they shift towards smaller wavenumbers and (4) they become asymmetric when amorphisation reaches a critical level.^{2,7,8} As zircons are not entirely opaque but often highly transparent the vertical sampling depth is a critical factor to consider when performing a (semi-)quantitative description of metamictisation using Raman spectroscopy.

In this study, we used natural zircons to (1) estimate the state of metamictisation of individual crystals by means of a Rietveld-based Raman profile deconvolution approach and (2) to investigate the sampling depth of Raman spectroscopy, especially in respect to zoning. For this purpose, estimates of radiation damage were derived from Raman spectroscopy corrected by a Rietveld approach as presented in part 1 of this two-part study (Ref. ⁸). Corresponding uranium concentrations were measured using the fission track method.

2. ANALYTICAL METHODS

Raman spectra were obtained using a confocal Raman microprobe Labram[®] 2 (HORIBA Jobin Yvon GmbH, Bensheim, Germany) with a 1800 lines/mm grating fitted with an external argon ion laser (488.0 nm). The laser beam was focused onto the sample by a 50fold (100fold) magnifying microscope objective with a numeric aperture $\text{NA} = 0.55$ ($\text{NA} = 0.90$) and a lateral resolution of $1.1\ \mu\text{m}$ ($0.7\ \mu\text{m}$) was obtained with a power of 2 mW at the sample surface. We used a backscattering $z(y, xy)\bar{z}$ geometry for all spectra.

To investigate the influence of polarization direction we rotated the latter by using a lambda-half-plate. The exact angle of the polarization direction was adjustable with a computer controlled stepping motor ($\approx 1^\circ$ accuracy). For all measurements we choose a polarization perpendicular to the c-axis which yielded maximum intensity for the Si-O V_3 stretching (B_{1g}). Calibration of the Raman shift was performed using the plasma lines from the Argon ion laser after removal of the interference filter. Peak-fitting and profile line deconvolution was performed using TOPAS[®] 4 (BRUKER AXS GmbH, Karlsruhe, Germany).

Analyzed Zircons came from a transect crossing the Gotthard massif (along the Gotthard tunnel) in the central Alps and from the Mont Blanc massif in the western Alps. Both massifs formed by Variscan and pre-Variscan intrusives and metasediments and were affected by Alpine greenschist facies metamorphism.⁹ Most analyzed crystals are well-formed with sharp, clearly recognisable faces (i.e., euhedral to subeuhedral in form) and are between 50 and 300 μm long. Zircons were mounted in Perfluoroalkoxy (TEFLON-PFA[®], in the following referred to as PFA), ground and polished to reveal internal surfaces.

For methodological details about the fission track method we refer to Wagner and Van den haute¹⁰, Gallagher et al.¹¹ and Reiners¹². Analytical details are given in Glotzbach et al.¹³.

3. RESULTS AND DISCUSSION

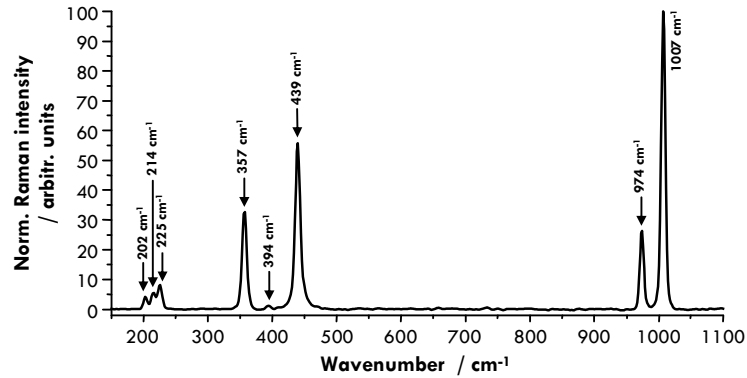
3.1 Raman spectra of zircon and PFA

Fig. 1 shows Raman spectra of a typical zircon grain (Fig. 1a) and the PFA mount (Fig. 1b). The spectrum of the latter is characterized by six Raman active modes with significant intensity in the range between 150 and 1100 cm^{-1} among which the mode at 732 cm^{-1} is the strongest.¹⁴ The Raman active modes and their assignments (after Ref. ^{15,16}) are presented in Tab. 1. In this study we focus on the two Raman active modes (Si-O stretching) at 974 and 1007 cm^{-1} where no overlying PFA mode must be considered. Also, it was easy to identify PFA modes originating from the excited volume below the zircon grains.

Band position / cm^{-1}	Mode assignment	
201	E_g	External mode (<i>trans.</i>)
214	B_{1g}	External mode (<i>rot.</i>)
225	E_g	External mode (<i>rot.</i>)
357	E_g	Si-O V_4
393	B_{1g}	Si-O V_4
974	A_{1g}	Si-O V_1
1007	B_{1g}	Si-O V_3

Tab. 1. Observed band positions and mode assignment (after Ref. ^{15,16}).

a) Zircon



b) PFA

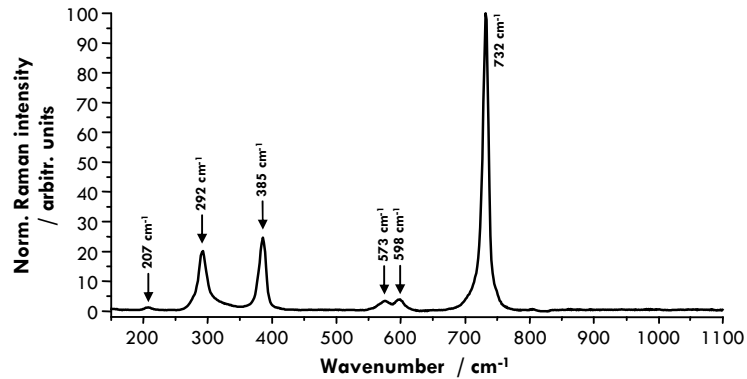


Fig. 1. Raman spectra of zircon and PFA (used to embed zircon grains) for the Raman shift between 150 and 1100 cm^{-1} (60 and 10 s acquisition times, respectively). For discussion see text.

3.2 Sampling depth

When comparing results on metamictisation of zircon obtained by Raman spectroscopy with other results procured via other methods, e.g. uranium content determined by means of the fission track method, TEM or μ -XRD (for larger grains), exact knowledge of the actual sampling depth is required. For example, the penetration depth for μ -XRD (i.e., X-ray diffraction with a beam spot size usually in the hundreds of 100 μm scale) is a function of the wavelength employed, the sample's density and atomic weight, as well as the incident angle. For dense zircon, $\text{Cu}_{K\alpha}$ -radiation and a reflection at $26^\circ 2\theta$ (Bragg-Brentano geometry) the first 3 μm contribute 50% to the signal's total intensity and 90% of the signal information is obtained from within the first 10 μm in axial direction. However, the micro-scale zoning of the zircons analyzed in this study precluded the application of μXRD^2 as the lateral resolution desired is one order of magnitude smaller (below 10 μm instead of 100 μm).

For confocal Raman spectroscopy, the axial resolution is a function of (1) the numeric aperture, (2) the confocal slit width, (3) the optical absorption coefficient α of the material at the incident wavelength, and (4) the wavelength of the exciting radiation.¹⁷ Also, the laser power must be considered to compensate for the detection limit. For natural samples such as zircon grains α is no constant value – especially when considering zoning and radiation-induced structural damage, which can often be seen in form of reduced opacity.

It is important to strictly differentiate between the terms “axial resolution” and “axial detection limit” or more generally, “(axial) sampling depth”. A value for the axial resolution is obtained from defocussing experiments. It describes two times the axial distance $z_{a.r.}$ between the sample position which yields maximum total signal intensity and the position which yields half that intensity. To obtain this value the sample is moved downwards relative to the focus point starting at $z = 0$ while the total signal intensity is monitored. However, even at a distance $|z| \gg |z_{a.r.}|$, significant signal intensity originating from the sample can still be detected with the Raman spectrometer. Accordingly, we can define a total sampling depth that corresponds to the volume from which a detectable Raman intensity is contributed to the measured spectrum (i.e., 99% signal intensity corresponds to a tens of micrometer large sampling depth).

The higher the input laser power, the higher the total Raman intensity. This way signals from a larger total axial segment exceeds the detection limit. For a $2\ \mu\text{m}$ thin polyethylene film ($NA = 0.90$, $\lambda = 488.0\ \text{nm}$, focal slit width = 100) the z -dependency of the Raman signal is shown in Fig. 2 along with the schematic illustration of the Gaussian beam geometry (going from over- to under focus). Only as a first approximation the sampling volume can be approximated as a cylinder.

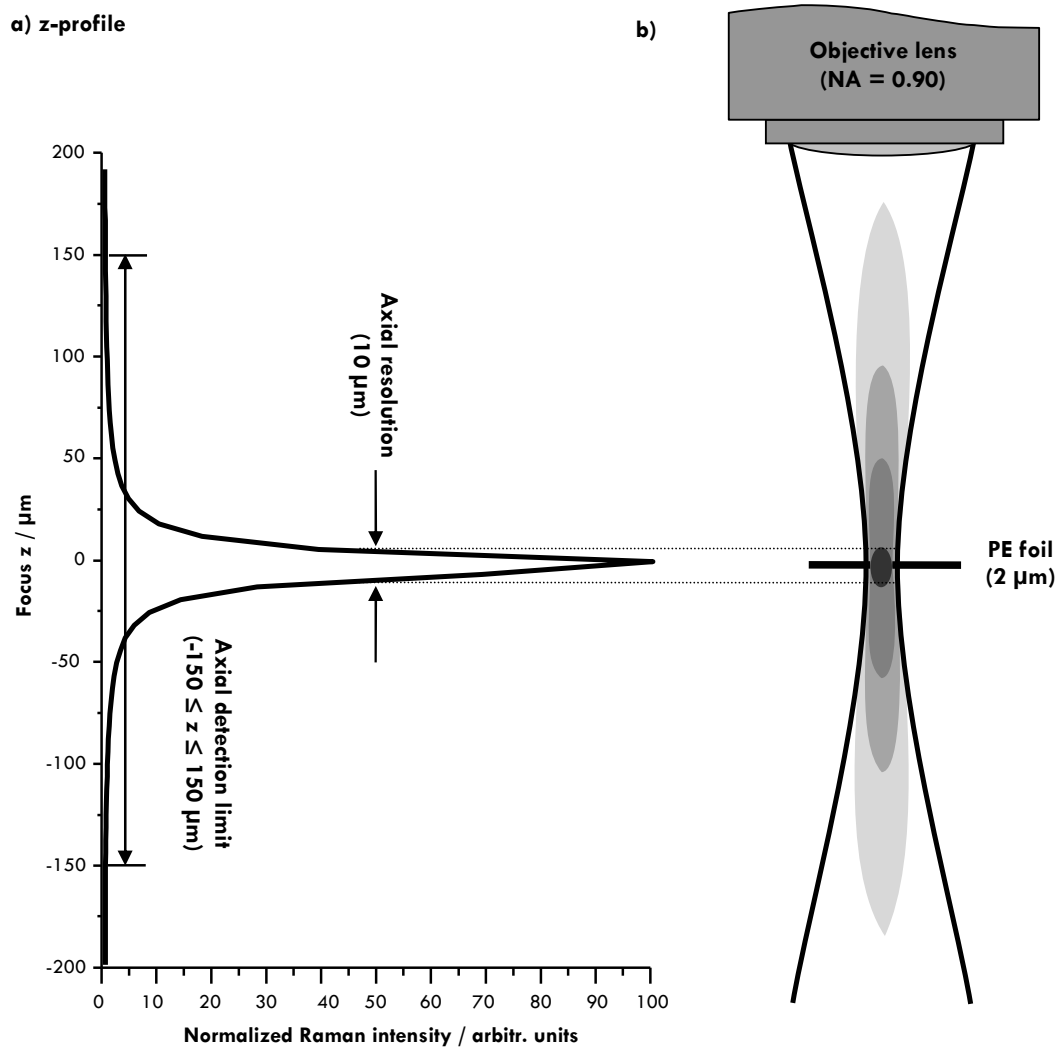


Fig. 2. Measured z -profile of the Raman signal of a $2\ \mu\text{m}$ PE foil (a) and schematic illustration of the Gaussian beam geometry (showing isophotes = iso-intensity contours; after Ref. ¹⁸). For discussion see text.

In the example presented, an axial resolution of $\approx 10 \mu\text{m}$ is contrasted by a sampling depth of $300 \mu\text{m}$ (99% signal intensity) and $80 \mu\text{m}$ (90% signal intensity). For most applications, the axial resolution yields a good first impression of the actual sampling depth, but it should be acknowledged that the total measured volume stretches far beyond the limits of the axial resolution.

For transparent materials it must be considered that the maximum Raman intensity will not be obtained when the laser is focused on the surface of the sample, but from within the material (several micrometer below the surface). As the focus point lies below the surface plane the total excited volume inside the sample is much larger.

Reliable values for the actual sampling depth can be obtained from wedge-shaped samples embedded in a matrix which itself shows strong, Raman-active modes. The zircon grains used for this study were sufficiently thin for that purpose and embedded in PFA which acts as a Raman-active matrix. Removal and measurement of the zircon grain's thickness after Raman measurements allowed direct determination of the sampling depth. Fig. 3 shows the approach schematically and Fig. 4 lists Raman spectra for two different numeric apertures (0.55 and 0.90). As a result, we found a sampling depth of $\approx 40 \mu\text{m}$ for $\text{NA} = 0.90$ and $\approx 50 \mu\text{m}$ for $\text{NA} = 0.55$ (focal slit width = $100 \mu\text{m}$ in both cases) for the used material and setup. These values fall within the range of reported sampling depths, e.g. by Deluca et al. ($\approx 30 \mu\text{m}$ for ferroelectric $\text{PbZr}_{1-x}\text{Ti}_x\text{O}_3$).¹⁹

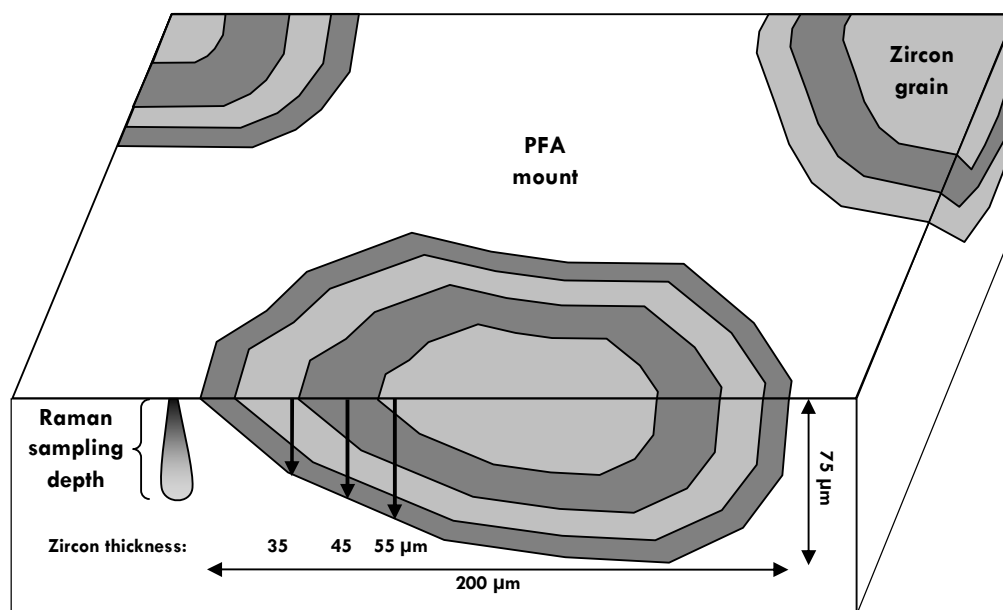


Fig. 3. Schematic illustration of a cross-section through a typical sample of PFA-embedded zircon grains used for the determination of the sampling depth.

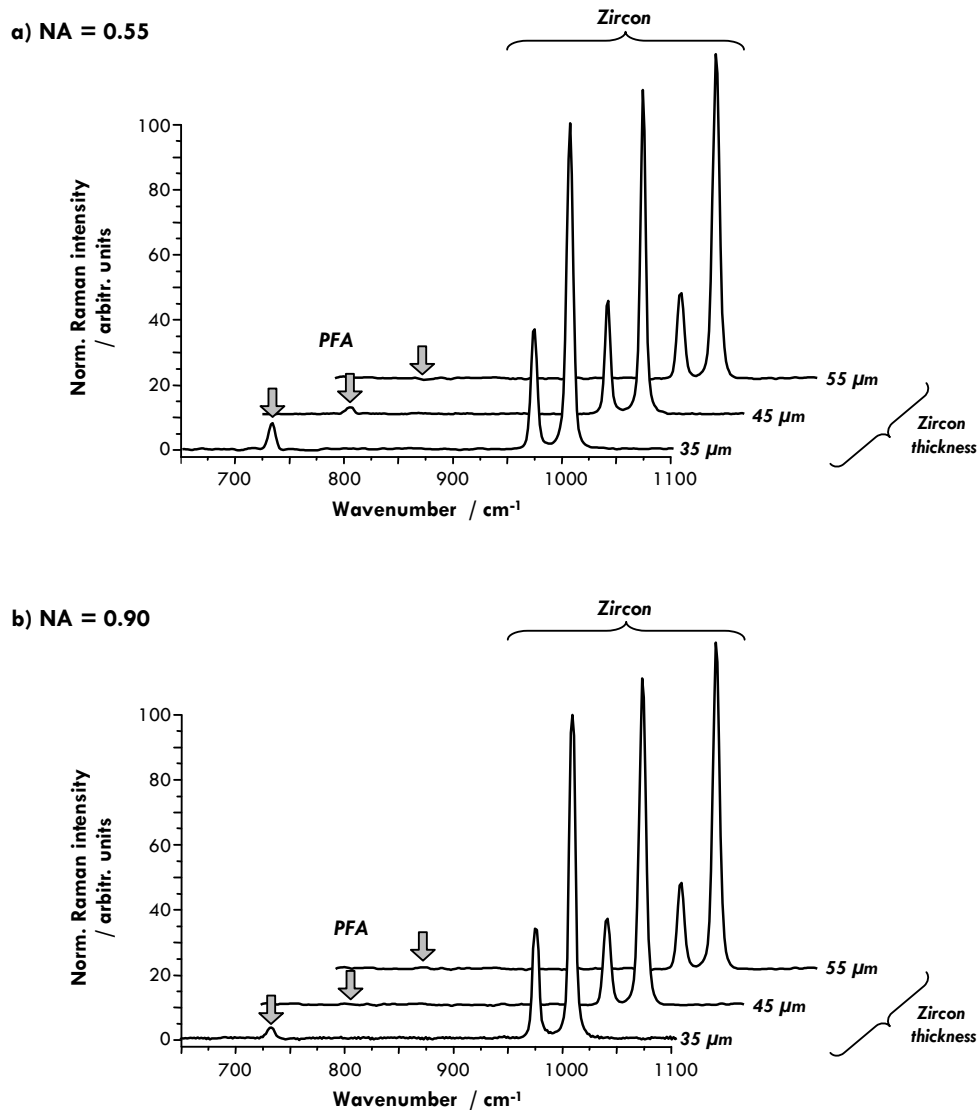


Fig. 4. Selected spectra in the range of 650 – 1100 cm^{-1} (60 s acquisition time) of a zircon grain probing regions of variable bulk thickness using (a) NA = 0.55 and (b) NA = 0.90. For NA = 0.55 we observed a penetration depth (i.e., PFA signal below 1%) of 50 μm and for NA = 0.90 of 40 μm .

Our findings are contrasted by values of approx. 2 μm for the axial resolution using an objective lens with NA = 0.95 as given by Nasdala et al.²⁰ and Markwort et al.²¹. However, these studies did not further investigate the actual sampling depth but the “axial resolution” which is (at least) one order of magnitude smaller than the axial detection limit for optically transparent material. When comparing the total area under the z-axis profile with the area covered by the axial resolution limit, only $\approx 50\%$ of the total signal derives from between these boundaries. This means, of course, that approximately 50% of the observed Raman signal comes from a region beyond the axial resolution limit.

It should also be noted that the high lateral resolution of $\leq 1.1\ \mu\text{m}$ for 488.0 nm is only achieved along the focal plane. For a numeric aperture of 0.55 (50fold magnifying lens) we observed a lateral resolution of about 100 μm with the focus point being 100 μm above the sample surface.

Recently published studies by Macdonald & Vaughan (Ref. ²²) and Everall (Ref. ²³) evidence significant contribution of out-of-focus regions to Raman depth profiles even when using a confocal setup. This contribution is not only limited to rays propagating along the paraxial axis; some rays from virtually every illuminated point within the excited double-cone volume contribute to the total out-of-focus part of the measured Raman signal. Similarly, refraction along phase boundaries causes a significant increase in lateral resolution.²³ Both studies, therefore, corroborate our findings of an axial sampling depth in the region of tens of μm .

3.3 Profile line deconvolution

Profile line deconvolution was performed following a Rietveld approach as described in Ref. ⁸. Fig. 5 shows a typical zircon Raman spectrum in the range of $180 - 1040 \text{ cm}^{-1}$ along with a comparison between the observed profile and the actual sample contribution.

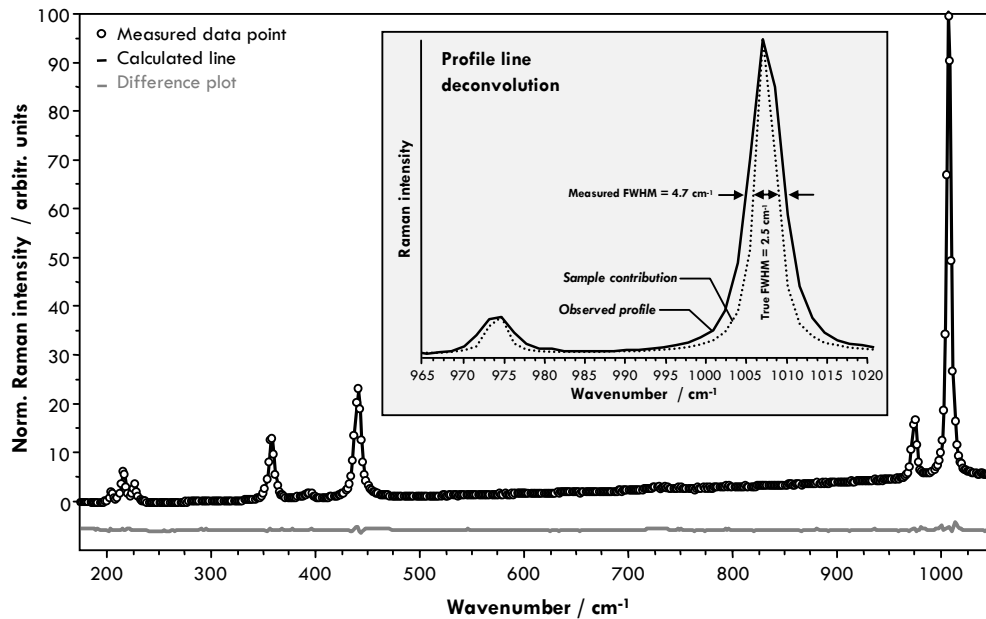


Fig. 5. Profile line deconvolution of a typical zircon spectrum (60 s acquisition time). The inset shows the contribution to the observed Raman profile and the difference between observed and true Raman bandwidth.

The determination of the true Raman bandwidth is not a new topic for Raman spectroscopy. In a study published in 1985 Irmer (Ref. ²⁴) introduced a very convenient way to correct for the instrument function's contribution to the total Raman bandwidth (Eq. 1) which has been used e.g. by Nasdala et al. for their studies on the metamictisation of zircon.^{2,7,20,25-28}

$$\frac{b}{b_s} = \sqrt{1 - 2 \cdot \left(\frac{s}{b_s}\right)^2} \quad \text{Eq. 1}$$

In Eq. 1 b denotes the true full width at half maximum (FWHM; further referred to as bandwidth), b_s is the observed total FWHM and s is the spectral resolution (instrumental correction factor).

It is important to note that Eq. 1 can only be applied for $b \geq 2s$ (Nasdala et al., Ref. ⁷) or, in general, for $b \gg s$ (Irmer, Ref. ²⁴). Regarding our spectrometer (operating at 488 nm, using a grating with 1800 lines/mm for deconvolution of the Raman mode at ≈ 1000 cm⁻¹), with $s = 2.95$ cm⁻¹, we would expect reliable values only for an observed FWHM larger than ≈ 7 cm⁻¹ (corresponding with a true Raman bandwidth of $b = 5.9$ cm⁻¹). As demonstrated in Fig. 6, many of the spectra obtained from zircon grains yielded FWHM values at 1007 cm⁻¹ below ≈ 7 cm⁻¹ for the Si-O ν_3 stretching mode. This also explains why the Irmer-equation does not fit calculated (true) Raman bandwidths following a Rietveld-approach over the whole range of data points. Only by excluding the first data points (i.e., excluding the non-valid range below 6.6 cm⁻¹ according to the definition of the Irmer-equation) from the regression we observed an excellent agreement between the data points and the Irmer-equation. As for the total data set, we found a simple linear equation to fit best.

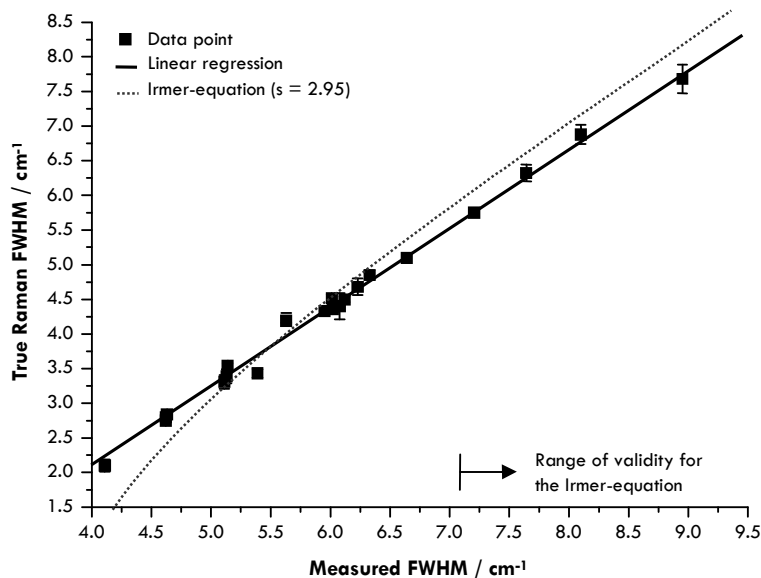


Fig. 6. Plot showing the correlation between observed (total) bandwidth and calculated true FWHM (60 s acquisition time). The data points fit to the correlation after Irmer (Ref. ²⁴) but also to a simple linear correlation.

The applicability of the Rietveld-approach for Raman active modes with a FWHM smaller than $2s$ is illustrated by profile line deconvolution of silicon. For undoped and unstrained silicon we determined the true Raman bandwidth to be 3.05 ± 0.08 cm⁻¹ in the first part of this two-part study. This value falls fully within the range of reported values for undistorted Si (at room temperature e.g. 2.9 – 3.7 cm⁻¹ ²⁹⁻³¹). Using Eq. 1 after Irmer, a value of 1.40 cm⁻¹ is obtained, which is too small for silicon by more than 1 cm⁻¹. However, this discrepancy is fully understandable as the corresponding, observed FWHM was 4.40 cm⁻¹ which clearly does not fall within the area of validity of the Irmer-equation.

The problem with the equation given by Irmer or when trying to fit a linear function (as one might be inclined to do when looking at Fig. 6) is that the correction will only be valid for one specific set of instrument parameters. Changing, for example, the objective lens or the focal slit width requires a new and adequate correction factor. Also, the measured FWHM is a function of the Raman shift and, therefore, different correction factors are required for deconvolution of Raman modes located at different spectral positions.

We, therefore, believe that a simple Rietveld-approach that itself compensates for the instrument's profile contribution independently from the spectral region is a very efficient method of profile line deconvolution of Raman spectra yielding reliable values for the true Raman bandwidth.

3.4 Zoning

Zoning in uranium content is a common phenomenon of natural zircons causing different degrees of metamictisation. The zircon grains used for this study were embedded in PFA so that they could be ground and polished (1) to be easier to handle when performing Raman spectroscopic and FTA measurements and (2) to get an impression of the grains' zoning (revealed by etching). Unfortunately, it is not possible to gain information on how the zoning continues in the bulk volume without cutting the crystal. Also, as the zones are often very narrowly spaced (i.e., a few micrometer), we must consider that the Raman signal with its larger sampling volume averages over several zones. However, as the path length of α -particles moving in solid zircon also lies in the range of tens of micrometer, the difference in radiation damage because of different amounts of radioactive elements incorporated into individual zones is blurred in the same order of magnitude as with regard to the large Raman sampling depth.

Fig. 7 shows a typical zoned zircon grain. Because of etching, zone boundaries are visible in the optical microphotograph. Two line profiles were measured. The results for a vertical (profile 1) and a horizontal profile (profile 2) of the true Raman FWHM and the uranium concentration are shown. Obviously, the different zones show a varying degree of metamictisation because of the different contents of incorporated radioactive elements. For the Raman plot, data points were measured in 1 μm intervals and the uranium content was determined in 10 μm intervals. The latter was calculated by means of the fission track method using Eq. 2 (Eq. 6 in Ref. ³²).

$$U_s = \left(\frac{d_G \cdot I_G}{d_s \cdot I_s} \right) \cdot U_G \cdot \frac{\rho_s}{\rho_G} \quad \text{Eq. 2}$$

In Eq. 2, U_s (U_G) is the uranium content of the sample (uranium doped standard glass), d_s (d_G) is the density of the sample (standard glass), I_s (I_G) is the latent track length of zircon (standard glass) and ρ_s (ρ_G) is the induced track density of the sample (standard glass) counted by an external detector. Values employed are given in Tab. 2 (reference data taken from Ref. ³²⁻³⁵). Thorium which makes a minor contribution to the total radiation damage can be neglected in first approximation.⁶

Parameter	Value	Unit	Reference
U_G	36.5 ± 0.7	ppm	³³
d_s	4.2	g/cm^3	-
d_G	2.45	g/cm^3	³⁴
I_s	26.3	μm	^{32,35}
I_G	17.2	μm	^{32,35}

Tab. 2. Parameters and values used for the calculation of the uranium concentration from fission track studies.

The resulting resolution of both methods (fission track and Raman) is in the same order of magnitude, which is confirmed by the excellent correlation between both measurements (Fig. 7).

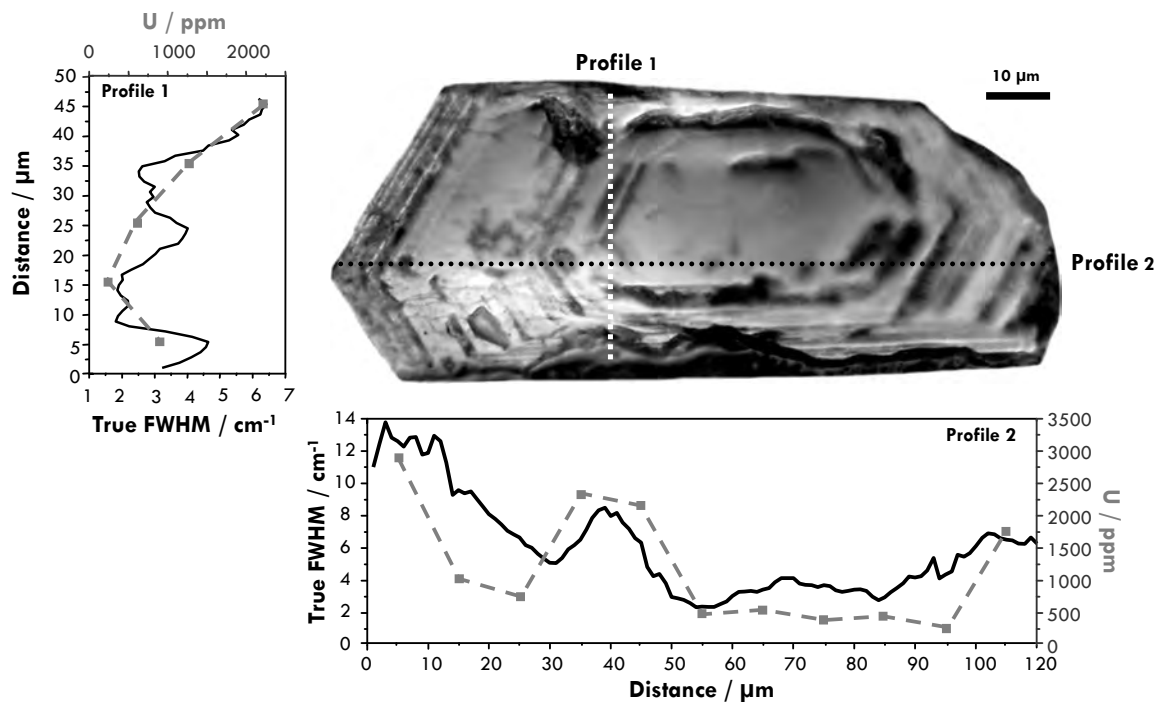


Fig. 7. Profile plots (True Raman FWHM [solid line] and uranium concentration [dashed line]) of a typical zoned zircon grain (microscopic image; 60 s acquisition time for each spectrum). The different zones show a different degree of metamictisation. For discussion see text.

3.5 True bandwidth versus Raman wavenumber

Metamictisation leads to both line broadening and a corresponding wavenumber downshift. This effect is also known from amorphisation as a result of mechanic strain.³⁶⁻⁴⁰ As a result, a linear relationship can be observed between the true Raman FWHM (Γ) and the Raman wavenumber ($\tilde{\nu}$) (Eq. 3). For the 1007 cm^{-1} V_3 Si-O stretching mode the range of true Raman bandwidth observed in the studied zircon grains was 2.1 - 13.2 cm^{-1} and the corresponding Raman wavenumbers range from 1001.5 to 1008.4 cm^{-1} (Tab. 3). As shown in Fig. 8, the data points calculated for the samples used in this study are in excellent agreement with the very detailed studies of Nasdala et al.²⁸

$$[\Gamma (\text{cm}^{-1})] = 1454.44 (\text{cm}^{-1}) - 1.44 \cdot [\tilde{\nu} (\text{cm}^{-1})] \quad \text{Eq. 3}$$

A similar relationship can be found for all other Raman-active modes in the zircon spectrum.

This correlation between Raman bandwidth and spectral position is important if profile line deconvolution yields a high analytical error, e.g. in case of very weak Raman modes. An example can be found in Ref.⁴¹ where the radiation-damage in apatite is characterized by analysis of the spectral position of weak Raman active modes instead of their bandwidth.

Sample	Grain	Position	Wavenumber / cm^{-1}	$\text{FWHM}_{\text{corr}}$ / cm^{-1}	α -fluence / 10^{-16} mg	ρ_s / 10^5 cm^{-2}	ρ_G / 10^5 cm^{-2}	U / ppm
C6P04A	1	1	1006.85 ± 0.04	3.31 ± 0.10	$1.03 \cdot 10^{-1}$	99.08	3.128	921
	2	1	1006.29 ± 0.04	3.39 ± 0.10	$4.81 \cdot 10^{-2}$	46.16	3.128	429
	3	1	1006.94 ± 0.01	2.75 ± 0.03	$3.75 \cdot 10^{-2}$	36.03	3.128	335
	5	1	1006.59 ± 0.02	4.33 ± 0.04	$6.92 \cdot 10^{-2}$	66.43	3.128	618
	6	1	1006.74 ± 0.01	3.99 ± 0.04	$7.27 \cdot 10^{-2}$	69.80	3.128	649
	7	1	1006.84 ± 0.01	2.34 ± 0.03	$1.39 \cdot 10^{-2}$	13.30	3.128	124
	8	1	1006.15 ± 0.01	3.5 ± 0.04	$2.51 \cdot 10^{-2}$	24.07	3.128	224
	9	1	1005.02 ± 0.06	7.64 ± 0.21	$1.00 \cdot 10^{-1}$	96.26	3.128	895
	10	1	1008.37 ± 0.02	3.25 ± 0.05	$2.23 \cdot 10^{-2}$	21.39	3.128	199
		2	1007.76 ± 0.01	3.32 ± 0.03	$1.88 \cdot 10^{-2}$	18.01	3.128	168
		3	1008.29 ± 0.01	2.38 ± 0.04	$1.41 \cdot 10^{-2}$	13.51	3.128	126
	11	1	1006.09 ± 0.02	4.52 ± 0.05	$5.75 \cdot 10^{-2}$	55.17	3.128	513
	12	1	1006.76 ± 0.02	5.11 ± 0.05	$1.26 \cdot 10^{-1}$	121.59	3.128	1131
		2	1006.98 ± 0.02	3.59 ± 0.04	$1.40 \cdot 10^{-1}$	135.1	3.128	1256
		3	1006.77 ± 0.02	4.18 ± 0.05	$7.85 \cdot 10^{-2}$	75.43	3.128	702
	13	1	1006.36 ± 0.02	4.36 ± 0.05	$7.39 \cdot 10^{-2}$	70.93	3.128	660
	14	1	1006.39 ± 0.06	4.4 ± 0.19	$1.11 \cdot 10^{-1}$	106.96	3.128	995
	15	1	1007.85 ± 0.03	4.68 ± 0.10	$8.43 \cdot 10^{-2}$	81.06	3.128	754
		2	1007.26 ± 0.04	4.84 ± 0.11	$8.43 \cdot 10^{-2}$	81.06	3.128	754
		3	1007.98 ± 0.03	4.32 ± 0.10	$9.48 \cdot 10^{-2}$	91.19	3.128	848
16	1	1007.00 ± 0.02	2.8 ± 0.04	$4.10 \cdot 10^{-2}$	39.41	3.128	366	
17	1	1006.71 ± 0.03	4.85 ± 0.07	$8.09 \cdot 10^{-2}$	77.68	3.128	722	
18	1	1007.62 ± 0.03	2.21 ± 0.09	$5.04 \cdot 10^{-2}$	48.41	3.128	450	
19	1	1007.21 ± 0.02	4.23 ± 0.07	$4.57 \cdot 10^{-2}$	43.91	3.128	408	
20	1	1006.72 ± 0.01	3.54 ± 0.04	$4.69 \cdot 10^{-2}$	45.03	3.128	419	
CGP09B	4	1	1001.51 ± 0.06	13.1 ± 0.22	$4.74 \cdot 10^{-1}$	455.97	3.136	4230
		2	1006.29 ± 0.01	5.99 ± 0.04	$6.32 \cdot 10^{-2}$	60.80	3.136	564
		3	1005.97 ± 0.03	7.05 ± 0.09	$2.84 \cdot 10^{-1}$	273.58	3.136	2538
		4	1005.23 ± 0.04	8.04 ± 0.15	$2.63 \cdot 10^{-1}$	253.32	3.136	2350
CGP22	9	1	1004.6 ± 0.05	7.71 ± 0.16	$1.84 \cdot 10^{-1}$	174.79	3.095	1643
		2	1003.83 ± 0.04	8.93 ± 0.15	$2.29 \cdot 10^{-1}$	217.85	3.095	2048
	12	1	1003.11 ± 0.05	10.3 ± 0.18	$3.84 \cdot 10^{-1}$	364.78	3.095	3429
		2	1003.09 ± 0.03	10.5 ± 0.11	$3.73 \cdot 10^{-1}$	354.65	3.095	3333
MRP233B	7	1	1008.17 ± 0.02	2.25 ± 0.05	$1.83 \cdot 10^{-2}$	16.89	3.012	163
		2	1007.94 ± 0.02	2.36 ± 0.05	$1.95 \cdot 10^{-2}$	18.01	3.012	174
		3	1007.70 ± 0.02	2.91 ± 0.07	$2.55 \cdot 10^{-2}$	23.64	3.012	228
	12	1	1008.26 ± 0.03	2.87 ± 0.11	$8.40 \cdot 10^{-3}$	8.22	3.012	75

Tab. 3. Results obtained from zircon grains analyzed for this study. Raman wavenumber and corrected bandwidth values are for the ν_3 Si-O stretch vibration around 1007 cm^{-1} . Uranium content is calculated using Eq. 2, and $d_G = 2.45 \text{ g/cm}^3$, $d_s = 4.2 \text{ g/cm}^3$, $l_G = 26.3 \text{ }\mu\text{m}$, $l_s = 17.2 \text{ }\mu\text{m}$, $U_G = 36.5 \text{ ppm}$; ρ_s (ρ_G) is the track density of the sample and the dosimeter glass.

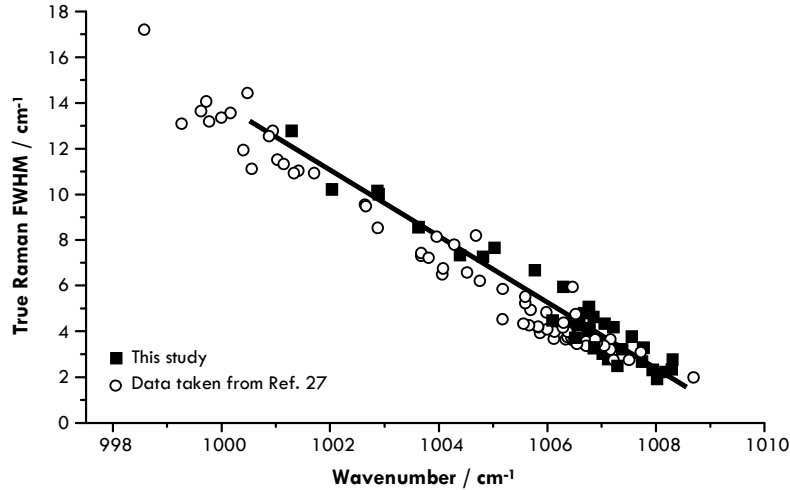


Fig. 8. Correlation between Raman shift and true Raman bandwidth showing the excellent agreement of data from Nasdala et al. (Ref. 28) and this study (60 s acquisition time).

3.6 Metamictization of zircons from the Gotthard transect

Metamictisation itself is a reversible process as thermally controlled annealing causes recrystallisation. Long-term annealing of radiation damage in zircon, however, is still not well understood, but complete annealing is believed to be accomplished at temperatures between $\approx 350^\circ - 400^\circ\text{C}$ (“Color Removal Zone”).⁶ Since the analyzed samples have been subject to greenschist-facies conditions during peak Alpine metamorphism with temperatures $\approx 400^\circ\text{C}$ in the Mont Blanc and Gotthard massif, respectively (e.g, Ref. 9,42 and references therein), all samples should have been annealed around 30 – 35 Ma ago. To test this assumption, we calculated the total α -damage (= α -fluence) of subregions in individual crystals using Eq. 4 (Ref. 7) and assuming constant accumulation of radiation damage since Variscan metamorphism (≈ 300 Ma).

$$D_\alpha = 8 \cdot \frac{c_U \cdot N_A \cdot 0.9928}{M_{238} \cdot 10^6} \cdot (e^{\lambda_{238} \cdot t} - 1) + 7 \cdot \frac{c_U \cdot N_A \cdot 0.0072}{M_{235} \cdot 10^6} \cdot (e^{\lambda_{235} \cdot t} - 1) + 6 \cdot \frac{c_{Th} \cdot N_A}{M_{232} \cdot 10^6} \cdot (e^{\lambda_{232} \cdot t} - 1) \quad \text{Eq. 4}$$

In Eq. 4, c_U and c_{Th} denote the concentration of uranium and thorium respectively (in ppm), N_A is the Avogadro constant, M_i is the molecular weight of the parent isotopes, λ_i is the respective decay constant and t is the age. This equation presupposes a present uranium isotope ratio of 99.28% ^{238}U and 0.72% ^{235}U .

Plotting the true Raman bandwidth against the corresponding α -damage, a linear correlation (“Nasdala line”) was found for completely unannealed samples (Eq. 5).⁷

$$[\Gamma \text{ (cm}^{-1}\text{)}] = 1.2 + 140 \cdot [D_\alpha \text{ (} 10^{16} \text{ / mg)}] \quad \text{Eq. 5}$$

The samples in this study lie below the Nasdala line in a region where annealing has (at least partially) reset the radiation-damage several million years ago (Fig. 9). This observation is in accordance with both the metamorphic history of the sampled rocks ($\approx 400^\circ\text{C}$) and the annealing temperature of radiation damage in zircon ($\approx 350^\circ - 400^\circ\text{C}$).

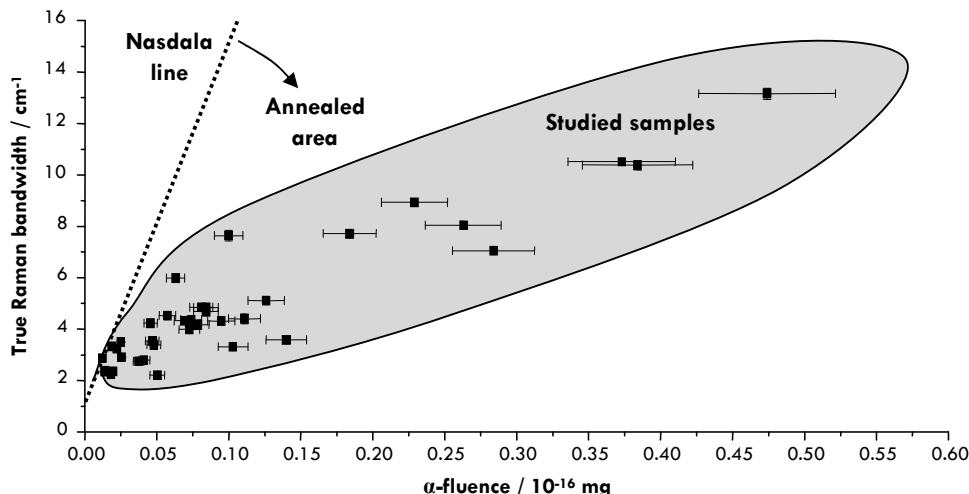


Fig. 9. True Raman bandwidth of the $\nu_3(\text{SiO}_4)$ Raman band (at $\approx 1007 \text{ cm}^{-1}$; 60 s acquisition time) in relation to calculated α -damage ($= \alpha$ -fluence) assuming that radiation damage has been accumulated since Variscan metamorphism (300 Ma). Samples do not plot on the linear correlation found for unannealed zircons (Ref. 7), implying annealing of radiation damage during Alpine metamorphism. The error margin of calculated α -fluence corresponds to estimated Th-concentrations assuming that Th/U is between 0 and 1.

4. CONCLUSION

In this study we examined the radiation-induced amorphisation of natural zircon grains from the European Alps by means of Raman spectroscopy following a Rietveld approach. In agreement with earlier studies, especially those of Nasdala et al., we found a linear relationship between the metamictisation-caused downshift and the corresponding line broadening.

Zoning of zircon grains, a common phenomenon, can also be studied by means of Raman spectroscopy as long as the different zones show a varying degree of radiation damage. The latter corresponds with a different content of uranium and / or thorium. However, when examining zircon zoning, the sampling depth for Raman spectroscopy must critically be considered. The total sampling depth is about one order of magnitude larger than the often-cited axial-resolution (tens of micrometer as opposed to only a few micrometers). Significant signal contribution indeed derives from the volume defined by the axial resolution limit (approximately 50 %), but significant information comes from the much larger total excitation volume. This is well-known, e.g. from studies on the exciting volume in electron microscopy or the penetration depth in X-ray diffraction.

For the Raman profile line deconvolution following a Rietveld-approach we found that our results are in perfect agreement with reported corrected FWHM values for zircon grains. Moreover, our approach yields values that are within the same range as true Raman bandwidths calculated using the Irmmer-equation as long as the range of validity ($b \gg s$) of the latter is taken into account. Unlike the simple Irmmer-equation, however, our approach compensates for every change of instrumental parameters (e.g. confocal slit width) as demonstrated in the first part of this two-part study.

Acknowledgements:

We gratefully acknowledge the helpful discussion and input from Dr. C. Berthold, A. Loges and M. Schloßer (Eberhard-Karls-Universität Tübingen).

REFERENCES

1. Deer, W.A., Howie, R.A. & Zussman, J. Zircon. in *Rock-Forming Minerals. Orthosilicates.*, Vol. 1A 418 - 442 (John Wiley & Sons, New York, 1982).
2. Nasdala, L., Irmer, G. & Wolf, D. The degree of metamictization in zircon: a Raman spectroscopic study. *European journal of mineralogy* **7**, 471 - 478 (1995).
3. Price, P.B. & Walker, R.M. Chemical etching of charged-particle tracks in solids. *Journal of Applied Physics* **33**, 3407 - 3412 (1962).
4. Fleischer, R.L., Price, P.B. & Walker, R.M. Fission-track ages of zircons. *Journal of Geophysical Research* **69**, 4885 - 4888 (1964).
5. Broegger, W.C. Amorf. in *Salmonsens store illustrerede Konversationsleksikon* (ed. Bangstrup, C.) 427 - 428 (Isaac Salmonsens, Kopenhagen, 1893).
6. Garver, J.I. & Kamp, P.J.J. Integration of zircon color and zircon fission-track zonation patterns in orogenic belts: application to the Southern Alps, New Zealand. *Tectonophysics* **349**, 203 - 219 (2002).
7. Nasdala, L. et al. Metamictization of natural zircon: accumulation versus thermal annealing of radioactivity-induced damage. *Contributions to Mineralogy and Petrology* **141**, 125 - 144 (2001).
8. Presser, V. Metamictisation in zircon: Raman investigation following a Rietveld approach. Part I: Profile line deconvolution technique. *Journal of Raman Spectroscopy* **40**, xxx (2009).
9. Frey, M. & Ferreiro Mählmann, R. Alpine metamorphism of the Central Alps *Schweizerische Mineralogische und Petrographische Mitteilungen* **79**, 135 - 154 (1999).
10. Wagner, G.A. & Van den haute, P. *Fission-Track Dating*, (Enke Verlag, Stuttgart, 1992).
11. Gallagher, K., Brown, R. & Johnson, C. Fission track analysis and its applications to geological problems. *Annual Review of Earth and Planetary Sciences* **26**, 519 - 572 (1998).
12. Reiners, P.W. Past, Present, and Future of Thermochronology. *Reviews in Mineralogy & Geochemistry* **58**, 1 - 18 (2005).
13. Glotzbach, C. et al. Neogene exhumation history of the Mont Blanc massif, western Alps. *Tectonics* **in press**(2008).
14. Kim, D., Chung, H. & Kim, N. Simple and reliable Raman measurement of an etchant solution directly through teflon tubing. *Applied Spectroscopy* **61**, 447 - 450 (2007).
15. Dawson, P., Hargreave, M.M. & Wilkinson, G.R. Vibrational spectrum of zircon (ZrSiO₄). *Journal of Physics C* **4**, 240 - 256 (1971).
16. Hoskin, P.W.O. & Rodgers, K.A. Raman spectral shift in the isomorphous series (Zr_{1-x}Hf_x)SiO₄. *European Journal of Solid State and Inorganic Chemistry* **33**, 1111 - 1121 (1996).
17. Zhu, W. & Pezzotti, G. Spatially resolved stress analysis in Al₂O₃/3Y-TZP multilayered composite using confocal fluorescence spectroscopy. *Applied Spectroscopy* **59**, 1042 - 1048 (2005).
18. Lipkin, D.M. & Clarke, D.R. Sample-probe interactions in spectroscopy: Sampling microscopic property gradients. *Journal of Applied Physics* **77**, 1855 - 1863 (1995).
19. Deluca, M., Sakashita, T. & Pezzotti, G. Polarized Raman scattering of domain structures in polycrystalline lead zirconate titanate. *Applied Physics Letters* **90**, 051919-1 - 051919-3 (2007).
20. Nasdala, L., Pidgeon, R.T. & Wolf, D. Heterogeneous metamictization of zircon on a microscale. *Geochimica et Cosmochimica Acta* **60**, 1091 - 1097 (1996).
21. Markwort, L., Kip, B., Da Silva, E. & Roussel, B. Raman imaging of heterogeneous polymers: a comparison of global versus point illumination. *Applied Spectroscopy* **49**, 1411 - 1430 (1995).
22. Macdonald, A.M. & Vaughan, A.S. Numerical simulations of confocal Raman spectroscopic depth profiles of materials: a photon scattering approach. *Journal of Raman Spectroscopy* **38**, 584 - 592 (2007).
23. Everall, N. The Influence of Out-of-Focus Sample Regions on the Surface Specificity of Confocal Raman Microscopy *Applied Spectroscopy* **62**, 591 - 598 (2008).
24. Irmer, G. Zum Einfluß der Apparatefunktion auf die Bestimmung von Streuquerschnitten und Lebensdauern aus optischen Phononenspektren. *Experimentelle Technik der Physik* **33**, 501 - 506 (1985).
25. Nasdala, L., Gotze, J., Pidgeon, R.T., Kempe, U. & Seifert, T. Constraining a SHRIMP U-Pb age: micro-scale characterization of zircons from Saxonian Rotliegend rhyolites. *Contributions to Mineralogy and Petrology* **132**, 300 - 306 (1998).
26. Nasdala, L., Wenzel, T., Pidgeon, R.T. & Kronz, A. Internal structures and dating of complex zircons from Meissen Massif monzonites, Saxony. *Chemical Geology* **156**, 331 - 341 (1999).
27. Nasdala, L. et al. Incomplete retention of radiation damage in zircon from Sri Lanka. *American Mineralogist* **89**, 219 - 231 (2004).
28. Nasdala, L., Hanchar, J.M., Kronz, A. & Whitehouse, M.J. Long-term stability of alpha particle damage in natural zircon. *Chemical Geology* **220**, 83 - 103 (2005).
29. Hart, T.R., Aggarwal, R.L. & Lax, B. Temperature Dependence of Raman Scattering in Silicon. *Physical Review B* **1**, 638 - 642 (1970).
30. Lang, G. et al. Anharmonic line shift and linewidth of the Raman mode in covalent semiconductors. *Physical Review B* **59**, 6182 - 6188 (1999).

31. Menendez, J. & Cardona, M. Temperature dependence of the first-order Raman scattering by phonons in silicon, germanium, and α -tin: Anharmonic effects. *Physical Review B* **29**, 2051 - 2059 (1984).
32. Enkelmann, E., Jonckheere, R. & Ratschbacher, L. Absolute measurements of the uranium concentration in thick samples using fission-track detectors. *Nuclear Instruments and Methods in Physics Research B* **229**, 489 - 498 (2005).
33. Bellemans, F., De Corte, F. & Van den haute, P. Corning CN glasses for the evaluation of the neutron spectrum in fission track dating. *Applied Radiation and Isotopes* **46**, 1351 - 1354 (1995).
34. De Corte, F., Bellemans, F., Van Den Haute, P., Ingelbrecht, C. & Nicholl, C. A new U doped glass certified by the European Commission for the Calibration of Fission-Track Dating. *Solid Earth Sciences Library* **10**, 67 - 78 (1998).
35. Jonckheere, R. On the densities of etchable fission tracks in a mineral and co-irradiated external detector with reference to fission-track dating of minerals. *Chemical Geology* **200**, 41 - 58 (2003).
36. Gogotsi, Y.G., Kailer, A. & Nickel, K.G. Pressure-induced phase transformations in diamond. *Journal of Applied Physics* **84**, 1299 - 1304 (1998).
37. Gogotsi, Y. & Rosenberg, M.S. Phase transformations in semiconductors under contact loading. *Tribology Issues and Opportunities in MEMS, Proceedings of the NSF/AFOSR/ASME Workshop on Tribology Issues and Opportunities in MEMS*, 431 - 442 (1998).
38. Kailer, A., Gogotsi, Y.G. & Nickel, K.G. Micro-Raman spectroscopy of indentation-induced phase-transformations. *Materials, Functionality & Design, Proceedings of the European Conference on Advanced Materials and Processes and Applications* **5**, 171 - 174 (1997).
39. Kailer, A., Gogotsi, Y.G. & Nickel, K.G. Use of hardness indentation coupled with micro-Raman spectroscopy in high-pressure materials research. *Materials Research Society Symposium Proceedings* **499**, 225 - 230 (1998).
40. Kailer, A., Nickel, K.G. & Gogotsi, Y.G. Raman microspectroscopy of nanocrystalline and amorphous phases in hardness indentations. *Journal of Raman Spectroscopy* **30**, 939 - 946 (1999).
41. Zattin, M., Bersani, D. & Carter, A. Raman microspectroscopy: A non-destructive tool for routine calibration of apatite crystallographic structure for fission-track analyses. *Chemical Geology* **240**, 197 - 204 (2007).
42. Poty, B.P., Stalder, H.A. & Weisbrod, A.M. Fluid inclusion studies in quartz from fissures of the western and central Alps. *Schweizerische Mineralogische und Petrographische Mitteilungen* **54**, 717 - 752 (1974).

Chapter 01

Chapter 02

Chapter 03

Chapter 04

Chapter 05

Chapter 06

Chapter 07

Chapter 08

Chapter 09

Chapter 10

Chapter 11

Chapter 12

EOS CALCULATIONS FOR HYDROTHERMAL DIAMOND ANVIL CELL (HDAC) OPERATION

V. Presser⁽¹⁾, M. Heiß⁽²⁾, K. G. Nickel⁽¹⁾

⁽¹⁾ Institut für Geowissenschaften, Universität Tübingen

⁽²⁾ Walter Schottky Institut, Technische Universität München

ABSTRACT:

The Hydrothermal Diamond Anvil Cell (HDAC) is an excellent tool for high-temperature, high-pressure (hydrothermal) experiments. For an accurate determination of pressure induced by a certain temperature in an isochoric sample chamber volume, an Equation Of State (EOS) of water can be used instead of direct measurement. This paper reviews the theoretic background and provides all needed equations for the application of EOS of water to HDAC experiments summarizing *state-of-the-art* knowledge and incorporating *up-to-date* thermodynamic data. The p-T conditions determined using the IAPWS-95 formulation for the thermodynamic properties of ordinary water are in agreement with values obtained from direct methods or other established EOS formulations. In particular, (1) the calculation of density through the (a) melting point or (b) homogenization method along with determining (2) pressure as a function of density and temperature or (3) density as a function of pressure and temperature is explained. As a new aspect in the context of HDAC operations, the critical influence of nucleation and a strategy to overcome this problem are discussed. Furthermore, we have derived new polynomial equations, which allow the direct calculation of the fluid phase's density from the melting temperature. These are implemented in a spreadsheet program, which is freely available for interested users.

1. INTRODUCTION

The diamond anvil cell (DAC) today is a standard tool for high-pressure experiments of small sample volumes ($\ll 0.1 \text{ mm}^3$) conducted over the last ≈ 50 years on a myriad of different materials.¹⁻⁶ With the introduction of the ruby fluorescence method by Forman et al.⁷, accurate pressure determination by measuring the pressure-induced shift of ruby fluorescence lines was made possible and enabled widespread application of the DAC. In the 1990's, a modified DAC was introduced, which was capable of conducting experiments under hydrothermal conditions [Hydrothermal Diamond Anvil Cell (HDAC)].

Bassett et al. developed the HDAC in 1993 and conducted extensive studies on the determination of pressure from the Equations Of State (EOS) assuming (1) an isochoric sample chamber, (2) a known density of the fluid phase and (3) a reliably measured temperature.⁴⁻⁶ In those studies, the p-T-data gained from using EOS of water was compared with measured p-T-values^{4,5,8} showing the beneficial use EOSs due to the easy applicability and high accuracy. The basis for the EOS was the observation of negligible changes of the sample chamber's volume.⁸ It was also shown that for aqueous solutions the EOS of pure water can be modified if necessary to still provide accurate p-T-determination.⁶

Until now, the application of HDAC experiments and the use of EOS were evidenced by many different authors for a myriad of different issues (e.g., Refs. ³⁻¹¹). However, in the available literature there is no practical description of using *up-to-date* thermodynamic data for the calibration of a HDAC. This article, therefore, provides all formulas needed for p-T calculations and density determination in the course of HDAC use based on EOS for the thermodynamic properties of pure water (further called IAPWS-95 = International Association for the Properties of Water and Stream).¹² Using EOS instead of a direct method (like the well established ruby static pressure scale introduced by Forman et al.⁷ for pressures up to 2.3 GPa and later extended up to 19.5 GPa by Piermarini et al.¹³) for HDAC experiments has the advantage that no additional material must be inserted into the sample chamber. This especially is important in cases, in which chemical reactions between the calibration probe (e.g., ruby) and the sample must be avoided. As not every sample material can be used to indicate the ambient pressure by shifted Raman lines, using an EOS of water has proven to be suitable for precise pressure determination.

2. ASSEMBLY OF THE HYDROTHERMAL DIAMOND ANVIL CELL (HDAC)

The general set-up of a HDAC is described in more details elsewhere (Refs. ^{4,5}). Here we only summarize the most basic features of a conventional HDAC shown in Fig. 1.

Two opposing diamond anvils (preferably with round anvil faces) are located above and below a metal gasket (usually made out of rhenium or stainless steel), through which a hole of 500 μm diameter along the whole height of the metal plate is introduced. The diamond anvils are backed by tungsten carbide (WC) mountings. These also exhibit a central bore to enable *in situ* visual inspection and spectroscopic / diffraction based probing of the sample chamber's interior while it is at elevated pressures and temperatures.

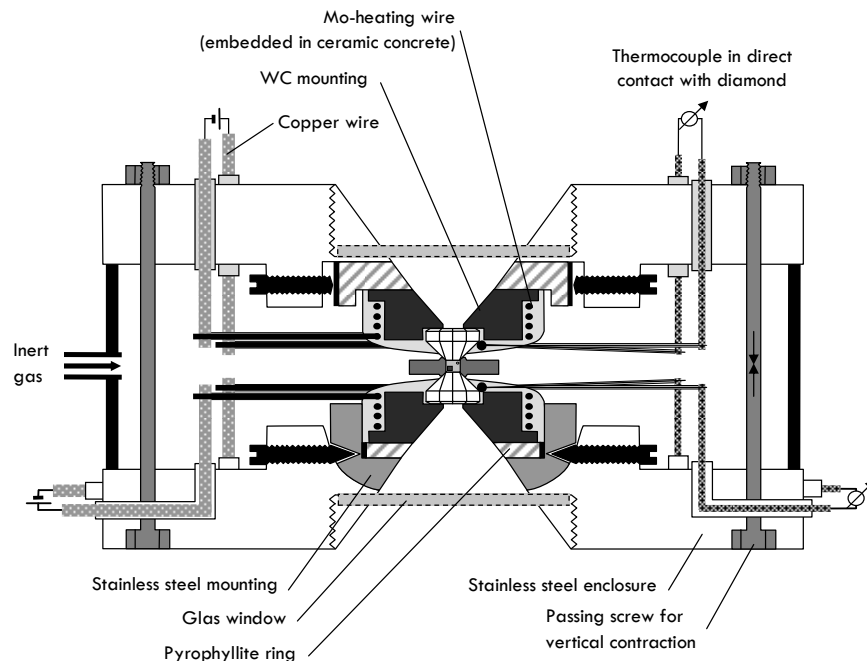


Fig. 1. Schematic assembly of a Bassett-type HDAC.

Molybdenum wires, insulated by ceramic concrete and/or an alumina hull, are wrapped around the WC-mounting and connected to a current source. This way, conductive heating of both diamond anvils via their surrounding is possible. Alternatively, a laser system could be used to heat the sample chamber directly.

Both WC mountings are located on pyrophyllite rings to ensure insulation and the lower WC holder is put onto a calotte made of stainless steel. The upper mounting can be shifted horizontally while the lower panlike mounting allows tilting. Both adjusting functions ensure that both anvil faces remain coaxial and coplanar with respect to each other. Otherwise the diamonds could get damaged when high pressures are applied or when both diamond faces are in direct contact (as needed for correct adjustment).

Unlike conventional DACs, pressure is applied to the sample material in the hydrothermal diamond anvil cell by increasing the temperature. During the process the sample chamber's volume behaves almost ideally isochoric, as discussed later. Knowing the pressure mediating fluid and measuring the sample chamber's inner temperature by thermocouples in direct contact with the anvils, the exact pressure can be calculated using an EOS for water as discussed in the following paragraphs.

Most important is that the HDAC's interior (outside the diamonds) can be filled with inert gas. Argon with some additional hydrogen to remove free oxygen is often used. This way both the decomposition of the anvils and the rapid oxidation of the molybdenum wires are prevented at temperatures above 500°C.

3. P-T DETERMINATION

3.1 General aspects

Direct methods, like the ruby fluorescence method, use physicochemical properties of the sample material or deliberately introduced probes, which yield information about the p-T conditions the sample is subjected to. Carefully conducted calibration, e.g., of the pressure induced shift of the fluorescence line or Raman-active modes, therefore, is a valuable way for direct observation and determination of the sample chamber's inner pressure. A direct method should, thus, always be applied to elucidate the validity of a set of assumed EOS.

Various equations of state exist, among which data from Saul & Wagner (1989; Helmholtz free energy & optimized structure; Ref. ¹⁴) and Hill (1990; Helmholtz free energy & optimized structure & combination with a scaled equation; Ref. ¹⁵) were shown to be applicable within a $\pm 1\%$ range of precision.

In this article, we use the IAPWS-95 formulation for the thermodynamic properties of ordinary water for general and scientific use ¹², which is valid for temperatures from 0° up to 1000°C, the normal temperature range for hydrothermal experiments at pressures up to 1 GPa. HDAC experiments at pressures up to 2 GPa are possible; for such cases the EOS can reasonably well be extrapolated according to Wagner and Pruss ¹² and even extrapolating up to 100 GPa still yields reasonably well results. Also, the EOS presented here can reasonably well be extrapolated within the stable fluid region down to ≈ 200 K. Table 1 lists formula symbols and critical values used in the paragraphs to come.

Category	Symbol	Meaning	Unit	Value
Nomenclature	<i>M</i>	Molar weight	kg·mol ⁻¹	-
	<i>m</i>	Mass	kg	-
	<i>n</i>	Mole	mol	-
	<i>p</i>	Pressure	Pa	-
	<i>T</i>	Temperature	K	-
	<i>V</i>	Volume	m ³	-
	θ	$T/T_{(c)}$; inverse reduced temperature	-	-
	ρ	Density	kg·m ⁻³	-
	T	$1 - \theta$	-	-
Subscripts	<i>c</i>	Denotes values at the critical point	-	-
IAPWS-95 constants	$\rho_{(c)}$	Density at critical point	kg·m ⁻³	322
	$p_{(c)}$	Pressure at critical point	MPa	22.064
	$T_{(c)}$	Temperature at critical point	K	647.096
	<i>R</i>	Specific gas constant	J·mol ⁻¹ ·K ⁻¹	8.314472

Tab. 1. Nomenclature and values for selected critical parameters (data taken from Ref. ¹²).

Figure 2 shows the calculated pressure of water in an isochoric system ($\rho = 958.35$ kg·m⁻³; corresponds with an homogenization temperature $T_h = 100^\circ\text{C}$ as discussed later) as a function of the temperature using the fundamental equation for water by Saul and Wagner (Ref. ¹⁴; based on IAPS-84) and IAPWS-95 (as presented in this paper). As seen from Fig. 2a and especially from Fig. 2b the differences are rather small but drastically increase when pressures > 1 GPa ($\approx 600^\circ\text{C}$) are reached and the EOS presented by Wagner and Pruss ¹² according to IAPWS-95 must be extrapolated. At 1000°C the differences between both EOS data sets are still slightly below 1%.

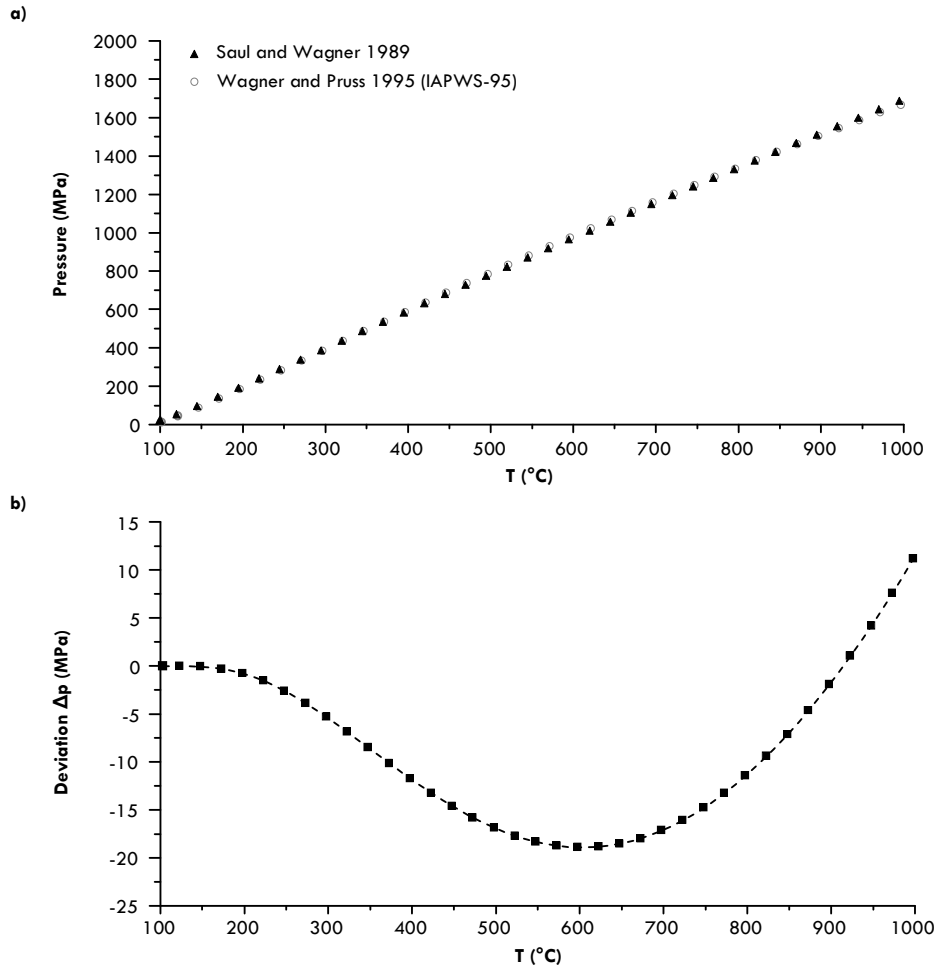


Fig. 2. a, b) Comparison between pressures calculated for water ($\rho = 958.35 \text{ kg}\cdot\text{m}^{-3}$) using EOS presented by Saul and Wagner¹⁴ and Wagner and Pruss (= IAPWS-95; Ref. ¹²). Fig. 2b depicts the difference plot between both datasets.

As pointed out by Burnley and Schmidt, the deviation between the calculated internal pressures using EOS after Haar et al. (Ref. ¹⁶; frequently used HDAC experiments)^{4-6,17,18} and after Saul and Wagner¹⁴ near 0.5 GPa are below 2 %. According to Bassett (Ref. ¹⁹, based on the work by Shen et al.(Ref. ¹¹) the EOS introduced by Haar et al. (Ref. ¹⁶) are accurate to within $\pm 1 \%$ for temperatures up to 850°C while the formulation after Saul and Wagner (Ref. ¹⁴; basis for IAPWS-95) is believed to be more precise at higher temperatures. Figure 3 depicts a comparison between various EOS (Duan et al. ²⁰, Haar et al. ¹⁶, Saul and Wagner ¹⁴, and IAPWS-95 ¹²) for the low pressure regime (corresponding with a density of 582 $\text{kg}\cdot\text{m}^{-3}$) and two calculated data points (Ref. ^{21,22}) for the α - β phase-transition of quartz. As concluded by Shen et al., the disagreement between the p-T values determined via the α - β phase-transition is greater than the difference between the values obtained from different EOSs.¹¹ For more information on the comparison of IAPWS-95 to other EOS see Ref. ¹².

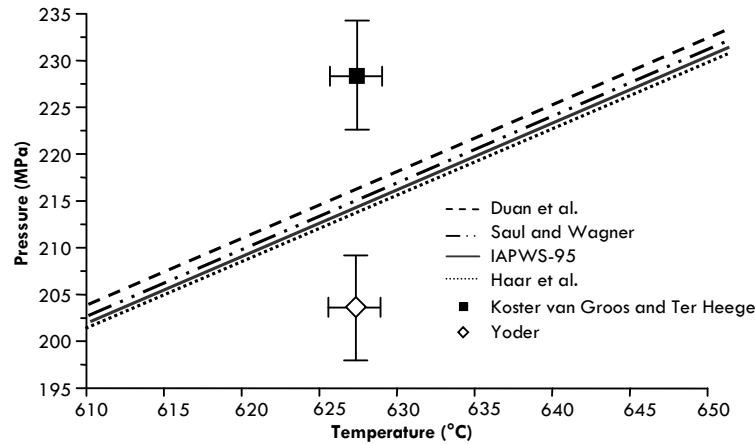


Fig. 3. Comparison between p-T values obtained from different EOS formulations ($\rho = 582 \text{ kg}\cdot\text{m}^{-3}$; Duan et al.: Ref. ²⁰; Saul and Wagner: Ref. ¹⁴; IAPWS-95: Ref. ¹²; Haar et al.: Ref. ¹⁶) and p-T ranges determined via the α - β phase-transition of quartz (Koster van Groos and Ter Heege: Ref. ²²; Yoder: Ref. ²¹). For discussion see text.

Determining p-T values in the cell involves the calculation of the isochoric pressure within the sample chamber using (1) a measured temperature and (2) a determined fluid density. For the sake of clarity, we refer to water as the only fluid phase. In hydrothermal experiments, which induce chemical changes to the fluid (e.g., by dissolution of silica), specific equations of state may be necessary, because changes in the chemical composition or the pH-value may significantly affect the accuracy of the EOS. More information on user-defined EOS can be found in Refs. ^{8,17,23}.

Temperature measurements are usually done using thermocouples in direct contact with the diamond anvils. An accuracy of 0.75% (at least 2.2°C) above 0°C and 2.0% (at least 2.2°C) below 0°C is reasonably assumed for type K thermocouples unless other undesired effects like ageing of thermocouples occur.²⁴

Density determination is done using a known homogenization temperature T_h . The easiest way to determine T_h is to enclose a small air bubble within the isochoric sample chamber volume and observe the bubble disappearance during heating up. As shown by Shen et al. ⁸ the error, which is induced, because the bubble consists of standard air instead of pure water vapor can usually be neglected. Both, T_h during heating (i.e. the bubble vanishes) or during cooling (i.e. the bubble reappears) can be used. For the latter, the later discusses nucleation problem must be considered. In practice, a simple reheating and recooling may be necessary, if more than only one bubble appears below T_h .

In some cases the cell volume decreases significantly during heating and no bubble reappears during cooling. Then the melting point of ice is used for an accurate density determination.

3.2 Determination of the density using the homogenization method

It is well known that during the first (and to some minor amount also during the second) run of a HDAC experiment, the sample chamber's behavior is not truly isochoric, because the gasket material extrudes and changes the sample chamber volume slightly. Usually, a slight decrease occurs. Hence, not the homogenization temperature during the first up-heating but the value obtained from reheating after the first cooling path is more accurate. This way, the volume of the sample chamber won't change significantly during the second run and only a minor decrease (≈ 1 vol%) will occur during the second run.⁸

Using the EOS of pure water, the density of the equilibrium fluid ρ' at the homogenization temperature (homogenization = homogenization towards liquid phase) is calculated using Eq. 1 (Ref. ¹²):

$$\rho' = \rho_{(c)} \cdot \left[1 + b_1 \cdot T^{1/3} + b_2 \cdot T^{2/3} + b_3 \cdot T^{5/3} + b_4 \cdot T^{16/3} + b_5 \cdot T^{43/3} + b_6 \cdot T^{110/3} \right] \quad \text{Eq. 1}$$

with $\rho_{(c)}$ ($= 332 \text{ kg}\cdot\text{m}^{-3}$) being the density at the critical point (CP at 22.064 MPa and 647.096 K). The values for b_i are: $b_1 = 1.99274064$, $b_2 = 1.09965342$, $b_3 = -0.510839303$, $b_4 = -1.75493479$, $b_5 = -45.5170352$, $b_6 = -6.74694450 \cdot 10^{-5}$.

3.3 Calculation of the pressure

Once the fluid's density has been determined, a direct relation between temperature and sample chamber pressure can be found. Fig. 4 shows a general scheme of p-T-paths with nearly linear isochors arising from the homogenization points on the boiling curve of H₂O.

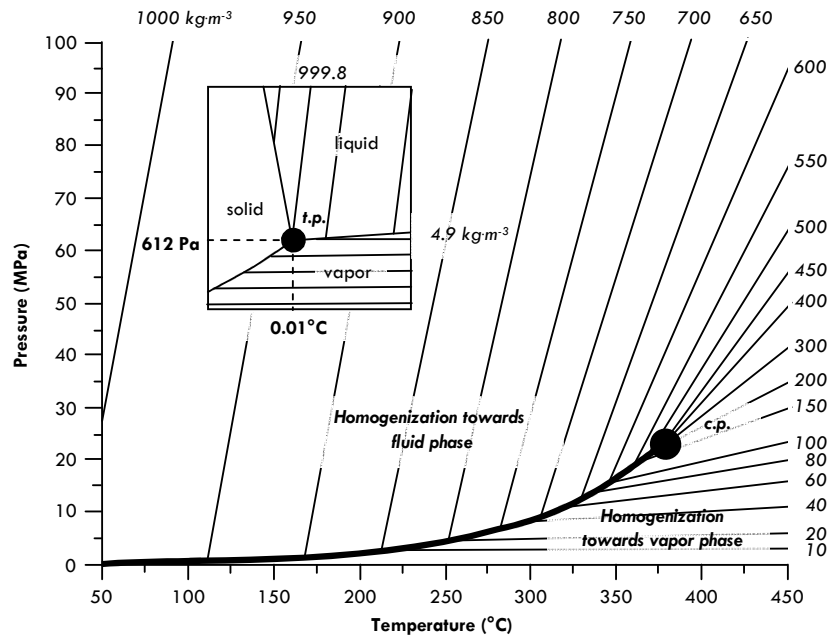


Fig. 4. Phase diagram showing the boiling curve below the critical point (c.p.) and from this phase boundary arise isochors calculated with the IAPWS-95 EOS. (after Ref. ⁶)The small inset illustrates the three phase boundary at the triple point (t.p.).

Eq. 2 gives the fundamental equation for the specific free Helmholtz energy f provided by the IAPWS-95 formulation, using the dimensionless form: $\phi = f / [RT]$.

$$\frac{f_{(\bar{\delta}, \tau)}}{R \cdot T} = \phi_{(\bar{\delta}, \tau)} = \phi_{(\bar{\delta}, \tau)}^{\text{ideal}} + \phi_{(\bar{\delta}, \tau)}^{\text{residual}} \quad \text{Eq. 2}$$

As introduced in Tab. 1, τ denotes the inverse reduced temperature ($\tau = T_{(c)}/T$) and $\bar{\delta}$ denotes the reduced density ($\bar{\delta} = \rho'/\rho_{(c)}$). For pressure calculation in the single-phase region (i.e. saturated liquid) using a known density and a certain temperature, only the residual part of the dimensionless Helmholtz free energy is needed (Eq. 3).

$$\frac{p_{(\bar{\delta}, \tau)}}{\rho' \cdot R \cdot T} = 1 + \bar{\delta} \cdot \phi_{(\bar{\delta}, \tau)}^{\text{residual}} \quad \text{Eq. 3}$$

Using the 56-coefficient equation of state, the residual part of ϕ can in general be expressed by Eq. 4:

$$\phi^{\text{residual}} = \sum_{i=1}^7 \Omega_i + \sum_{i=8}^{51} \Xi_i + \sum_{i=52}^{54} \Psi_i + \sum_{i=55}^{56} \Delta_i \quad \text{Eq. 4}$$

with (Eqs. 5 - 8):

$$\Omega_i = n_i \cdot \bar{\delta}^{d_i} \cdot \tau^{t_i} \quad \text{Eq. 5}$$

$$\Xi_i = n_i \cdot \bar{\delta}^{d_i} \cdot \tau^{t_i} \cdot e^{-\delta^c} \quad \text{Eq. 6}$$

$$\Psi_i = n_i \cdot \bar{\delta}^{d_i} \cdot \tau^{t_i} \cdot e^{-[a_i\{\bar{\delta} - \varepsilon_i\}^2 - \beta_i\{\tau - \nu_i\}^2]} \quad \text{Eq. 7}$$

$$\Delta_i = n_i \cdot \left(\left\{ (1 - \tau) + A_i \cdot [(\bar{\delta} - 1)^2]^{\left(\frac{1}{2\beta}\right)} \right\}^2 + B_i \cdot \{(\bar{\delta} - 1)^2\}^{b_i} \right) \cdot \bar{\delta} \cdot e^{-c_i \times \{\bar{\delta} - \varepsilon_i\}^2 - D_i \times \{\tau - \nu_i\}^2} \quad \text{Eq. 8}$$

For values of the individual parameters see Tab. 2.

In the case of $\phi_{(\bar{\delta})}^{\text{residual}}$, Eq. 4 must be derived from the reduced density $\bar{\delta}$ yielding Eqs. 9 – 12:

$$\frac{d\Omega_i}{d\bar{\delta}} = n_i \cdot d_i \cdot \bar{\delta}^{(d_i-1)} \cdot \tau^{t_i} \quad \text{Eq. 9}$$

$$\frac{d\Xi_i}{d\bar{\delta}} = n_i \cdot e^{-\delta^c} \cdot \tau^{t_i} \cdot \bar{\delta}^{(d_i-1)} \cdot (d_i - c_i \cdot \bar{\delta}^{c_i}) \quad \text{Eq. 10}$$

i	α_i	b_i	c_i	d_i	t_i	n_i	α_i	β_i	γ_i	ϵ_i	A_i	B_i	C_i	D_i
1				1	-0.5	$1.2533547935523 \cdot 10^{-2}$								
2				1	0.875	7.8957634722828								
3				1	1	-8.7803203303561								
4				2	0.5	$3.1802509345418 \cdot 10^{-1}$								
5				2	0.75	$-2.6145533859358 \cdot 10^{-1}$								
6				3	0.375	$-7.8199751687981 \cdot 10^{-3}$								
7				4	1	$8.8089493102134 \cdot 10^{-3}$								
8		1		1	4	$-6.6856572307965 \cdot 10^{-1}$								
9		1		1	6	$2.0433810950965 \cdot 10^{-1}$								
10		1		1	12	$-6.6212605039687 \cdot 10^{-5}$								
11		1	2		1	$-1.9232721156002 \cdot 10^{-1}$								
12		1	2		5	$-2.5709043003438 \cdot 10^{-1}$								
13		1	3		4	$1.6074868486251 \cdot 10^{-1}$								
14		1	4		2	$-4.0092828925807 \cdot 10^{-2}$								
15		1	4		13	$3.9343422603254 \cdot 10^{-7}$								
16		1	5		9	$-7.5941377088144 \cdot 10^{-6}$								
17		1	7		3	$5.6250979351888 \cdot 10^{-4}$								
18		1	9		4	$-1.5608652257135 \cdot 10^{-5}$								
19		1	10		11	$1.1537996422951 \cdot 10^{-9}$								
20		1	11		4	$3.6582165144204 \cdot 10^{-7}$								
21		1	13		13	$-1.3251180074668 \cdot 10^{-12}$								
22		1	15		1	$-6.2639586912454 \cdot 10^{-10}$								
23		2	1		7	$-1.0793600908932 \cdot 10^{-1}$								
24		2	2		1	$1.7611491008752 \cdot 10^{-2}$								
25		2	2		9	$2.2132295167546 \cdot 10^{-1}$								
26		2	2		10	$-4.0247669763528 \cdot 10^{-1}$								
27		2	3		10	$5.8083399985759 \cdot 10^{-1}$								
28		2	4		3	$4.9969146990806 \cdot 10^{-3}$								
29		2	4		7	$-3.1358700712549 \cdot 10^{-2}$								
30		2	4		10	$-7.4315929710341 \cdot 10^{-1}$								
31		2	5		10	$4.7807329915480 \cdot 10^{-1}$								
32		2	6		6	$2.0527940895948 \cdot 10^{-2}$								
33		2	6		10	$-1.3636435110343 \cdot 10^{-1}$								
34		2	7		10	$1.4180634400617 \cdot 10^{-2}$								
35		2	9		1	$8.3326504880713 \cdot 10^{-3}$								
36		2	9		2	$-2.9052336009585 \cdot 10^{-2}$								
37		2	9		3	$3.8615085574206 \cdot 10^{-2}$								
38		2	9		4	$-2.0393486513704 \cdot 10^{-2}$								
39		2	9		8	$-1.6554050063734 \cdot 10^{-3}$								
40		2	10		6	$1.9955571979541 \cdot 10^{-3}$								
41		2	10		9	$1.5870308324157 \cdot 10^{-4}$								
42		2	12		8	$-1.6388568342530 \cdot 10^{-5}$								
43		3	3		16	$4.3613615723811 \cdot 10^{-2}$								
44		3	4		22	$3.4994005463765 \cdot 10^{-2}$								
45		3	4		23	$-7.6788197844621 \cdot 10^{-2}$								
46		3	5		23	$2.2446277332006 \cdot 10^{-2}$								
47		4	14		10	$-6.2689710414685 \cdot 10^{-5}$								
48		6	3		50	$-5.5711118565645 \cdot 10^{-10}$								
49		6	6		44	$-1.9905718354408 \cdot 10^{-1}$								
50		6	6		46	$3.1777497330738 \cdot 10^{-1}$								
51		6	6		50	$-1.1841182425981 \cdot 10^{-1}$								
52			3		0	$-3.1306260323435 \cdot 10^1$	20	150	1.21	1				
53			3		1	$3.1546140237781 \cdot 10^1$	20	150	1.21	1				
54			3		4	$-2.5213154341695 \cdot 10^3$	20	250	1.25	1				
55	3.5	0.85				$-1.4874640856724 \cdot 10^{-1}$		0.3			0.32	0.2	28	700
56	3.5	0.95				$3.1806110878444 \cdot 10^{-1}$		0.3			0.32	0.2	32	800

Tab. 2. Parameters for the 56-coefficient formulation of the EOS of water (data taken from Ref. ¹²).

$$\frac{d\Psi_i}{d\bar{\delta}} = -n_i \cdot e^{(-\alpha_i \bar{\delta}^2 + 2\alpha_i \varepsilon_i \bar{\delta} - \beta_i \tau^2 + 2\beta_i \gamma_i \tau - \alpha_i \varepsilon_i^2 - \beta_i \gamma_i^2)} \cdot \bar{\delta}^{(d_i-1)} \cdot \tau^t \cdot (2 \cdot \alpha_i \cdot \bar{\delta}^2 - 2 \cdot \alpha_i \cdot \varepsilon_i \cdot \bar{\delta} - d_i) \quad \text{Eq. 11}$$

$$\frac{d\Delta_i}{d\bar{\delta}} = \frac{n \cdot e^{-C_i(\bar{\delta}^2 - 2\bar{\delta} + 1) - D_i(\tau^2 - 2\tau + 1)} \cdot \Pi^{(b_i-1)} \cdot \Gamma}{1 - \bar{\delta}} \quad \text{Eq. 12}$$

with (Eqs. 13 – 14):

$$\Pi = A_i^2 \cdot [\{\bar{\delta} - 1\}^2]^{2\alpha_i} + [B_i - 2 \cdot A_i \cdot \{\tau - 1\}] \cdot [\{\bar{\delta} - 1\}^2]^{\alpha_i} + [\tau^2 - 2 \cdot \tau + 1] \quad \text{Eq. 13}$$

$$\Gamma = \xi \cdot \eta \cdot \bar{\delta} \cdot \eta + \eta + A_i^2 \cdot [\xi - 4 \cdot \zeta - \kappa] \cdot \kappa^{4\alpha_i} + [\{\xi - 2 \cdot \zeta - \kappa\} \cdot \{B_i - 2 \cdot A_i \cdot \langle \tau - 1 \rangle\}] \cdot \kappa^{2\alpha_i} \quad \text{Eq. 14}$$

and (Eqs. 15 – 18):

$$\xi = 2 \cdot \bar{\delta} \cdot C_i \cdot \{\bar{\delta}^2 - 2 \cdot \bar{\delta} + 1\} \quad \text{Eq. 15}$$

$$\eta = \tau^2 - 2 \cdot \tau + 1 \quad \text{Eq. 16}$$

$$\zeta = 2 \cdot \alpha_i \cdot b_i \cdot \bar{\delta} \quad \text{Eq. 17}$$

$$\kappa = \bar{\delta} - 1 \quad \text{Eq. 18}$$

The corresponding equations are much simpler for the older 58-coefficient EOS proposed by Saul and Wagner in 1989.¹⁴ In this case the residual part of ϕ is as follows (Eq. 19):

$$\phi^{\text{residual}} = \sum_{i=1}^9 \Omega_i + \sum_{i=10}^{54} \Xi_i + (e^{-0.4 \cdot \bar{\delta}^6} - e^{-2 \cdot \bar{\delta}^6}) \sum_{i=55}^{58} \Theta_i \quad \text{Eq. 19}$$

While the derivations of Ω_i and Ξ_i after $\bar{\delta}$ are the same as before (Eqs. 9 – 10), $d\Theta_i/d\bar{\delta}$ yields Eq. 20:

$$\frac{d\Theta_i}{d\bar{\delta}} = (-2.4 \cdot e^{-0.4 \cdot \bar{\delta}^6} + 12 \times e^{-2 \cdot \bar{\delta}^6}) \cdot n_i \cdot \bar{\delta}^{(d_i+5)} \cdot \tau^{t_i} + (e^{-0.4 \cdot \bar{\delta}^6} - e^{-2 \cdot \bar{\delta}^6}) \cdot n_i \cdot d_i \cdot \bar{\delta}^{(d_i-1)} \cdot \tau^{t_i} \quad \text{Eq. 20}$$

Tab. 3 lists the needed parameters for the 58-coefficient equations of state formulation.

i	c _i	d _i	t _i	n _i	i	c _i	d _i	t _i	n _i
1	1	0		8.216377478·10 ⁻¹	30	2	2	8	1.220538576·10 ⁻¹
2	1	2		-2.543894379·10 ⁻¹	31	2	4	5	-2.562237041·10 ⁻¹
3	2	0		-8.830868648·10 ⁻²	32	2	5	4	2.555034636·10 ⁻¹
4	5	9		-8.903097248·10 ⁻⁷	33	2	6	2	-6.323203907·10 ⁻²
5	8	0		-1.241333357·10 ⁻⁶	34	2	6	12	3.351397575·10 ⁻⁵
6	11	0		2.895590286·10 ⁻⁹	35	2	7	3	-6.152834985·10 ⁻²
7	11	12		1.403610309·10 ⁻¹¹	36	2	7	10	-3.533048208·10 ⁻⁴
8	13	7		8.183943371·10 ⁻¹³	37	2	8	3	3.146309259·10 ⁻²
9	13	13		-2.397905287·10 ⁻¹³	38	2	10	2	-2.261795983·10 ⁻³
10	1	1	0	-7.519743341·10 ⁻¹	39	2	10	8	1.86897020·10 ⁻⁴
11	1	1	1	-4.151278588·10 ⁻¹	40	2	11	0	-1.384614556·10 ⁻³
12	1	1	3	-1.030513740	41	2	11	1	2.713160073·10 ⁻³
13	1	2	1	-1.648036888	42	2	11	3	-4.866118539·10 ⁻³
14	1	2	5	-4.686350251·10 ⁻¹	43	2	11	4	3.751789129·10 ⁻³
15	1	3	5	3.560258142·10 ⁻¹	44	2	11	6	-5.692669373·10 ⁻⁴
16	1	4	2	-6.364658294·10 ⁻¹	45	3	2	13	-5.876414555·10 ⁻¹
17	1	4	3	2.227482363·10 ⁻¹	46	3	2	14	5.687838346·10 ⁻¹
18	1	4	5	-8.954849939·10 ⁻²	47	3	2	15	-1.642158198·10 ⁻¹
19	1	5	6	1.557686788·10 ⁻³	48	3	3	14	5.878635885·10 ⁻¹
20	1	6	4	1.347719088·10 ⁻³	49	3	3	16	-2.844301931·10 ⁻¹
21	1	7	1	-1.301353385·10 ⁻³	50	3	4	13	-2.049198337·10 ⁻¹
22	1	8	8	9.987368673·10 ⁻⁷	51	3	4	26	-4.039233716·10 ⁻³
23	1	9	0	2.263629476·10 ⁻⁴	52	3	5	15	5.459049594·10 ⁻²
24	1	11	1	2.893304950·10 ⁻⁶	53	3	5	23	-8.914260146·10 ⁻³
25	2	1	0	1.995437169·10 ⁻¹	54	3	5	25	4.974411254·10 ⁻³
26	2	1	9	-2.707767662·10 ⁻²	55	1	50		-7.093183380·10 ⁻³
27	2	1	10	1.849068216·10 ⁻²	56	2	40		1.718796342·10 ⁻²
28	2	1	11	-4.402394357·10 ⁻³	57	3	32		-1.482653038·10 ⁻²
29	2	2	0	-8.546876737·10 ⁻²	58	4	26		4.517292884·10 ⁻³

Tab. 3. Parameters for the 58-coefficient formulation of the EOS of water (data taken from Ref. ¹⁴).

3.4 Determination of the density using the melting point method

Slightly more complicated is the determination of the density when no homogenization towards the liquid phase occurs. An air bubble can easily be introduced during the setup of the experiment, but the density may change in such a manner as to prevent the formation of an air bubble after the initial heating run. An increase of density due to decreasing sample chamber volume would be a typical example. Alternatively, the experiment's conditions can deliberately be chosen to observe higher density fluid states, which exclude bubble formation.

It was shown that in those cases the carefully conducted measurement of the melting point of the frozen liquid yields the needed density-related information. Technically, all that has to be done is cooling the sample chamber below the freezing point of the liquid phase. This can be accomplished by using pre-cooled compressed air or by directly injecting liquid nitrogen into the HDAC's interior via the inert gas inlet.^{4,5}

Another approach uses IAPWS-95 EOS of ordinary water to calculate the water's density from the melting temperature of an ice phase. However, this method is slightly more complex as no direct equation of $\rho'_{(p,T)}$ can be used. For the density, the following equation is relevant (Eq. 21).

$$\rho' = \frac{\sqrt{\left(\rho_{(c)} \cdot R \cdot T \cdot \left[\rho_{(c)} \cdot R \cdot T + 4 \cdot p \cdot i_{(\delta)}^{\text{residual}}\right]\right)} - \rho_{(c)} \cdot R \cdot T}{2 \cdot R \cdot T \cdot \phi_{(\delta)}^{\text{residual}}} \quad \text{Eq. 21}$$

As both sides of the equation above contain a density-related term, an approach like the Newton–Raphson method²⁵ must be used to determine $\rho'_{(p,T)}$. One solution to this problem is to apply Eq. 22 to calculate a first value for the pressure ($p_{(cc)}$; cf. Eq. 3).

$$p_{(cc)} = \rho'_{\text{initial}} \cdot R \cdot T \cdot \left(1 + \delta \cdot \phi_{(\delta)}^{\text{residual}}\right) \quad \text{Eq. 22}$$

A good starting point for that is to assume the density of $1000 \text{ kg} \cdot \text{m}^{-3}$. All equations needed for this pressure calculation are presented below.

The next step is to determine the melting temperature by heating the previously cooled sample chamber. To calculate the correspondent melting pressure knowledge of the actually present ice phase is needed. As described by Haselton et al.²⁶, the morphology of the ice crystals can be used to gain this phase-related information. Then Eqs. 23 – 27 can be used to calculate the melting pressure of the various ice phases (p given in [MPa] and temperature T in [K]).¹²

$$p_{\text{melt}}^{\text{ice I}} = 6.11657 \cdot 10^{-4} - 382.897282 \cdot \left(1 - \left[\frac{T}{273.16}\right]^{-3}\right) + 120.5790027 \cdot \left(1 - \left[\frac{T}{273.16}\right]^{-21.2}\right) \quad \text{Eq. 23}$$

$$p_{\text{melt}}^{\text{ice III}} = 209.9 - 61.9733948 \cdot \left(1 - \left[\frac{T}{251.165}\right]^{60}\right) \quad \text{Eq. 24}$$

$$p_{\text{melt}}^{\text{ice V}} = 350.1 - 415.642221 \cdot \left(1 - \left[\frac{T}{256.164}\right]^{8}\right) \quad \text{Eq. 25}$$

$$p_{\text{melt}}^{\text{ice VI}} = 632.4 - 679.678224 \cdot \left(1 - \left[\frac{T}{273.31}\right]^{4.6}\right) \quad \text{Eq. 26}$$

$$p_{\text{melt}}^{\text{ice VII}} = 2216 \cdot e^{\left(0.0173683 \cdot \left[1 - \left\{\frac{T}{355}\right\}^{-1}\right] - 0.0544606 \cdot \left[1 - \left\{\frac{T}{355}\right\}^5\right] + 8.06106 \times 10^{-8} \cdot \left[1 - \left\{\frac{T}{355}\right\}^{22}\right]\right)} \quad \text{Eq. 27}$$

Tab. 4 lists the p-T ranges, in which Eqs. 23 – 27 are valid.

Ice phase	Temperature range (K)	Pressure range (MPa)
Ice I	273.16 – 251.165	$6.11657 \cdot 10^{-4} - 209.9$
Ice III	251.165 – 256.164	209.9 – 350.1
Ice V	256.164 – 273.31	350.1 – 632.4
Ice VI	273.31 – 355	632.4 – 2216
Ice VII	355 – 715	2216 – 19910

Tab. 4. Ranges of validity for Eqs. 23 – 27 for various ice phases.

As the next step a value for the deviation of the calculated and the actual pressure ($p_{(cc)}$ and $p_{(melt)}$ respectively) according to Eq. 28 is used to calculate a deviation function Δ .

$$\Delta = \frac{p_{(cc)} - p_{(melt)}}{p_{(melt)}} \quad \text{Eq. 28}$$

Increasing the initial density to +1% in a second calculation of the pressure $p_{(cc)}^{\text{II}}$, a discrete value of Δ (i.e. $\Delta_{(\text{II})}$) can be found. Applying Eq. 29 yields a value for the slope m of the deviation function Δ .

$$m = \frac{y_2 - y_1}{x_2 - x_1} = \frac{\Delta_{(\text{II})} - \Delta}{\left(\frac{\rho'}{\rho_{(c)}}\right) \cdot (1 + 1\%) - \left(\frac{\rho'}{\rho_{(c)}}\right)} = \frac{\Delta_{(\text{II})} - \Delta}{\frac{\rho'}{\rho_{(c)}} \cdot 1\%} \quad \text{Eq. 29}$$

Using the Newton–Raphson algorithm to find approximations to the zeros of a real-valued function, a linear equation with m as the slope (Eq. 30) is considered

$$\Delta = \frac{\Delta_{(\text{II})} - \Delta}{\frac{\rho'}{\rho_{(c)}} \cdot 1\%} \cdot \left(\frac{\rho'}{\rho_{(c)}} + x_0\right) \quad \text{Eq. 30}$$

and solved after x_0 (Eq. 31):

$$x_0 = \frac{\Delta}{m} - x \quad \text{Eq. 31}$$

The obtained value of x_0 is used as the new input value for the density ρ to recalculate both $\phi_{(\delta)}^{\text{residual}}$ and $p_{(cc)}$. Iteration of this procedure yields after several runs a value $p_{(cc)} \cong p_{(melt)}$. Usually less than 4 iteration steps are needed to obtain deviations between $p_{(cc)}$ and $p_{(melt)}$ smaller than 1%.

Fig. 5 provides a general phase diagram with the liquid-solid-phase boundary calculated using the introduced Newton-Raphson-method. In order to provide an easier way for density calculation using the melting-point-method, Eq. 32 – 34 give polynomial equations for values along the phase boundary for ice I, III and V. The deviation between such calculated values and densities and those calculated via the Newton-Raphson-method lies way below 1‰.

$$\text{Ice I:} \quad \rho' = 1000.03592 - 6.59231 \cdot T_{\text{melt}} - 0.16593 \cdot T_{\text{melt}}^2 - 0.00255 \cdot T_{\text{melt}}^3 \quad \text{Eq. 32}$$

$$\text{Ice III:} \quad \rho' = 1793.80193 + 75.23283 \cdot T_{\text{melt}} - 2.71298 \cdot T_{\text{melt}}^2 - 0.03382 \cdot T_{\text{melt}}^3 \quad \text{Eq. 33}$$

$$\text{Ice V:} \quad \rho' = 1188.62937 - 3.47086 \cdot T_{\text{melt}} - 0.01414 \cdot T_{\text{melt}}^2 - 0.00018 \cdot T_{\text{melt}}^3 \quad \text{Eq. 34}$$

In Eqs. 32 – 34 the melting temperature input is in degrees Celsius [°C], the output (density ρ') is then in [kg·m⁻³].

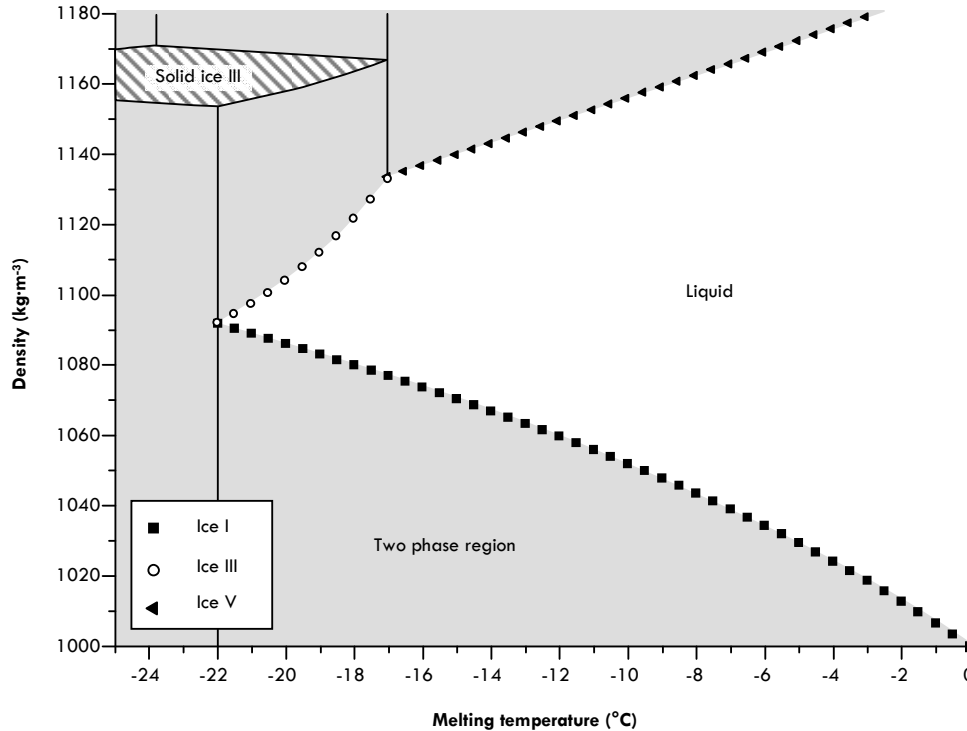


Fig. 4. Simplified phase diagram in the unary water system showing the liquidus line valid for ice I, III, and V. The melting temperature corresponds with a certain phase-dependent melting pressure, which together with a known temperature yields the density-information (after Eq. 32 – 34 and Ref. ²⁶).

3.5 Metastability-related implications

Nucleation and metastability in general are major implications to the application of EOS to HDAC experiments. During cooling at temperatures below T_h , a certain amount of energy must be spent for the creation of a new phase boundary before a new phase (gas bubble, ice) can occur. Only nuclei of a critical volume will result in a progressing nucleation process (i.e. when the energy gained by the phase transition is less than the required surface energy). This nucleation process kinetically hampers phase transitions and, therefore, causes the observation of too low transitions temperatures in HDAC experiments.

Especially in case of the formation of ice, liquid water requires significant undercooling (usually more than 30°C) before solid ice can be observed. As described by Haselton et al. metastable phase relations were almost always observed except for a liquid pressure larger than 1 GPa.²⁶ Furthermore the joint nucleation of ice I and V is due to the failure of nucleating ice II.²⁶ More detailed information on the metastable behavior of ice polymorphs can be found in Refs. ²⁶⁻²⁸.

Similar observations can be made for the dehomogenization of liquid water into a liquid phase and a gas bubble although the nucleation process of a gas phase to separate is kinetically less hampering than that of solid ice. To avoid these implications we suggest that phase transition temperatures should only be measured during heating, i.e. homogenization towards the liquid phase. Then, no additional phase must be created and, therefore, nucleation is no longer important. In order to determine the fluid's density after an experiment, the cell chamber should be cooled down below the point of vapor nucleation and then heated up again to determine a true value for T_h . As shown by Shen et al. (Ref. 8) homogenization temperatures determined this way are precise to within 0.3°C.

4. OTHER HDAC-EXPERIMENT RELATED CALCULATIONS

4.1 Calculation of the mean cell chamber volume (non-solid volume)

The sample chamber's volume cannot *a priori* be calculated using a simple geometric approach assuming a known diameter and height of the approximately cylindrical borehole. First, the sample chamber's sides are never perfectly smooth even though when they have carefully been drilled into the solid metal. Second, the volume will change during sealing the chamber by compressing the metal plate between the anvils. Also, the volume will be altered by relaxation and flowing of the metal in the course of a conducted experiment. Hence, a geometry-independent method for the determination of the sample chamber's volume must be found that can be applied when the HDAC sample chamber's interior is loaded with (1) liquid water, (2) a vapor bubble, and (3) the sample(s).

A convenient method for this is using again the homogenization method described earlier for density determination. This way, the non-solid mean cell chamber volume can be determined for one single experiment even after the sample has been inserted into the water-filled boring hole. Knowing the size of the vapor bubble (V_{vapor}), the corresponding density of the liquid phase (ρ_{liquid}) and of the vapor phase (ρ_{vapor}) and the total density (ρ_{nonsolid}) at a given temperature, the sample chamber's volume (V_{nonsolid}) can be calculated using Eqs. 35 – 36.

$$V_{\text{nonsolid}} \cdot \rho_{\text{nonsolid}} = V_{\text{vapor}} \cdot \rho_{\text{vapor}} + V_{\text{liquid}} \cdot \rho_{\text{liquid}} \quad \text{Eq. 35}$$

$$V_{\text{total}} = V_{\text{vapor}} + V_{\text{liquid}} \quad \text{Eq. 36}$$

Incorporating Eq. 35 into Eq. 36 yields Eq. 37 as proposed by Audétat and Keppler.²⁹

$$V_{\text{nonsolid}} = \frac{V_{\text{vapor}} \cdot (\rho_{\text{vapor}} - \rho_{\text{liquid}})}{\rho_{\text{nonsolid}} - \rho_{\text{liquid}}} \quad \text{Eq. 37}$$

V_{vapor} can be obtained by measuring the bubble's diameter and assuming perfect sphere geometry (Eq. 38).

$$V_{\text{vapor}} = \frac{4}{3} \cdot \left(\frac{\varnothing_{\text{vapor}}}{2} \right)^3 \cdot \pi \quad \text{Eq. 38}$$

However, for the application of Eq. 38 requires an evaluation of several aspects is necessary: (1) Is there just only one single air bubble present? and (2) Does the air bubble adhere to the diamond anvil? If there are more small air bubbles present, the total vapor volume would be underestimated and if the air bubble adheres to the window, the air bubble would appear too large and the calculated value for V_{vapor} is too big. Moreover, this calculation implies that no sample material is present inside the sample chamber. However, only the non-solid mean chamber volume is measured this way, i.e. the total volume would be $V_{\text{nonsolid}} + V_{\text{sample}}$.

Values for ρ_{vapor} and ρ_{liquid} can easily be calculated using EOS provided by Wagner and Pruss (Ref. 12; Eq. 1 for $\rho_{\text{liquid}} = \rho'$ and Eq. 39 for $\rho_{\text{vapor}} = \rho''$).

$$\rho' = \rho_{(c)} \cdot e^{\left(c_1 \cdot \tau^{1/3} + c_2 \cdot \tau^{2/3} + c_3 \cdot \tau^{4/3} + c_4 \cdot \tau^3 + c_5 \cdot \tau^{37/6} + c_6 \cdot \tau^{7/3} \right)} \quad \text{Eq. 39}$$

with $\rho_{(c)}$ ($= 332 \text{ kg}\cdot\text{m}^{-3}$) being the density at the critical point and $\tau = 1 - (T/T_{(c)})$. The values for c_i are: $c_1 = -2.03150240$, $c_2 = -2.68302940$, $c_3 = -5.38626492$, $c_4 = -17.2991605$, $c_5 = -44.7586581$, $c_6 = -63.9201063$. Again, a small error results from the vapor phase not being water vapor but standard air.

Determining the diameter of the air bubble for at least five temperatures provides a statistically adequate basis to calculate a mean sample chamber volume. Optical refraction between the vapor bubble and the water render the determination of the actual size of the vapor bubble not trivial. To our experience reproducibility better than 5 % is obtained.

4.2 Calculation of the water-sample-ratio

For many problems, knowledge of the water-to-sample ratio (χ) is critical. For example, the hydrothermal corrosion of silicon carbide shows χ -dependent stability fields in which active corrosion, carbon formation, or carbon / silica formation takes place. To determine the ratio, we recommend the use of samples with a simple geometry (e.g., rectangular prism) to minimize the error in the determination of the volume of the sample.

The determination of the sample chamber's volume by the method described above assumed $V_{\text{total}} = V_{\text{water}}$, neglecting the contribution of the sample material. Disregarding furthermore the thermal expansion of the sample material Eqs. 40 – 41 can be used to determine a simplified water-to-sample ratio χ (weight-related: Eq. 40; molar: Eq. 41).

$$\frac{V_{\text{water}} \cdot \rho_{\text{water}}}{V_{\text{sample}} \cdot \rho_{\text{sample}}} = \frac{m_{\text{water}}}{m_{\text{sample}}} = \chi_{\text{weight}} \quad \text{Eq. 40}$$

$$\frac{V_{\text{water}} \cdot \rho_{\text{water}} / M_{\text{water}}}{V_{\text{sample}} \cdot \rho_{\text{sample}} / M_{\text{sample}}} = \frac{n_{\text{water}}}{n_{\text{sample}}} = \chi_{\text{molar}} \quad \text{Eq. 41}$$

5. CONCLUSIONS AND OUTLOOK

With its unique possibility of *in situ* probing sample material during hydrothermal treatment, the HDAC is an ideal tool for small-sample-volume corrosion experiments under hydrothermal conditions. Using EOS density or pressure determination, the p-T- ρ -conditions in the course of HDAC experiments can be obtained at all times without the need of direct measuring of these properties. EOS following the IAPWS-95 formulation yielded p-T conditions that lie well in the range of direct methods or other, established EOS for pure water (Refs. ¹⁴ and ¹⁶).

All of the introduced considerations and formulas can equally be used for Gem Anvil Cells (GAC) – like the Moissanite Anvil Cell (MAC).³⁰⁻³³ Using materials other than diamond yields the possibility of reducing the expenses although care has to be taken choosing the anvil's chemical composition in order to avoid chemical changes of the fluid phase or thermal decomposition within the actual range of p-T-conditions.

See EPAPS Document No. E-RSINAK-79-030808 (Microsoft® Excel file) for “EOS Calculations for HDAC Operations” (ECHO) allowing pressure and density determination of isochorically enclosed pure water as well as calculation of the sample chamber's volume and the sample-water-ratio. This document can be reached through a direct link in the online article's HTML reference section or via the EPAPS homepage (<http://www.aip.org/pubservs/epaps.html>).

ACKNOWLEDGMENTS

This work was partially supported by the Deutsche Forschungsgemeinschaft (DFG) through Ni299/12-1. The authors would like to thank (in alphabetical order) Dr. Andreas Audétat (Bayerisches Geoinstitut Bayreuth), Dr. Thomas Wagner (ETH Zürich) and Prof. Wolfgang Wagner (Ruhr-Universität Bochum) for much appreciated and most valuable discussion.

REFERENCES

1. Weir, C.E., Lippincott, E.R., van Valkenburg, A. & Bunting, E.N. Infrared Studies in the 1- to 15Micron Region to 30,000 Atmospheres. *Journal of Research of the National Bureau of Standards* **63A**, 55 - 62 (1959).
2. Besson, J.M. Pressure generation. in *High-pressure techniques in chemistry and physics* (eds. Holzapfel, W.B. & Isaacs, N.S.) 1 - 45 (Oxford university press, Oxford, 1997).
3. Bassett, W.A. The diamond anvil cell and the nature of the earth's mantle. *Annual Review of Earth and Planetary Sciences* **7**, 357 - 384 (1979).
4. Bassett, W.A., Shen, A.H., Bucknum, M. & Chou, I.-M. A new diamond anvil cell for hydrothermal studies to 2.5 GPa and from -190 to 1200°C. *Review of Scientific Instruments* **64**, 2340 - 2345 (1993).
5. Bassett, W.A., Shen, A.H., Bucknum, M. & Chou, I.-M. Hydrothermal Studies in a New Diamond Anvil Cell up to 10 GPa and from -190°C to 1200°C. *PAGEOPH* **141**, 487 - 495 (1993).
6. Bassett, W.A., Chou, I.-M., Anderson, A.J. & Mayanovic, R. Aqueous Chemistry in the Diamond Anvil Cell up to and Beyond the Critical Point of Water. in *Chemistry at Extreme Conditions* (ed. Manaa, M.R.) 223 - 240 (Elsevier, Amsterdam, 2005).
7. Forman, R.A., Piermarini, G.J., Barnett, J.D. & Block, S. Pressure Measurement Made by the Utilization of Ruby Sharp-Line Luminescence. *Science* **176**, 284 - 285 (1972).
8. Shen, A.H., Bassett, W.A. & Chou, I.-M. Hydrothermal Studies in a Diamond Anvil Cell: Pressure Determination Using the Equation of State of H₂O. in *High-Pressure Research: Application to Earth and Planetary Sciences* (eds. Syono, Y. & Manghnani, M.H.) 61 - 68 (American Geophysical Union, Washington D.C., 1992).
9. Schmidt, C. & Ziemann, M.A. In-situ Raman spectroscopy of quartz: A pressure sensor for hydrothermal diamond-anvil cell experiments at elevated temperatures. *American Mineralogist* **85**, 1725 - 1734 (2000).
10. Schmidt, C., Rickers, K., Bilderback, D.H. & Huang, R. In situ synchrotron-radiation XRF study of REE phosphate dissolution in aqueous fluids to 800°C. *Lithos* **95**, 87 - 102 (2007).
11. Shen, A.H., Bassett, W.A. & Chou, I.-M. The α - β quartz transition at high temperatures and pressures in a diamond-anvil cell by laser interferometry. *American Mineralogist* **78**, 694 - 698 (1993).
12. Wagner, W. & Pruss, A. The IAPWS Formulation 1995 for the Thermodynamic Properties of Ordinary Water Substance for General and Scientific Use. *Journal of Physical and Chemical Reference Data* **31**, 387 - 535 (2002).
13. Piermarini, G.J., Block, S., Barnett, J.D. & Forman, R.A. Calibration of the pressure dependence of the R1 ruby fluorescence line to 195 kbar. *Journal of Applied Physics* **46**, 2774 - 2780 (1975).
14. Saul, A. & Wagner, W. A Fundamental Equation for Water Covering the Range from the Melting Line to 1273 K at pressures up to 25000 MPa. *Journal of Physical and Chemical Reference Data* **18**, 1537 - 1564 (1989).
15. Hill, P.G. A unified fundamental equation for the thermodynamic properties of water. *Journal of Physical and Chemical Reference Data* **19**, 1233 - 1274 (1990).
16. Haar, L., Kell, G.S. & Gallagher, J.S. *NBS/NRC Steam Tables: Thermodynamic and Transport Properties and Computer Programs for Vapor and Liquid States of Water in SI Units*, 320 (Taylor & Francis, Washington, 1984).
17. Mayanovic, R.A., Anderson, A.J., Bassett, W.A. & Chou, I.-M. Synchrotron X-ray spectroscopy of Eu/HNO₃ aqueous solutions at high temperatures and pressures and Nb-bearing silicate melt phases coexisting with hydrothermal fluids using a modified hydrothermal diamond anvil cell and rail assembly. *Review of Scientific Instruments* **78**, 053904/1 - 053904/9 (2007).
18. Schmidt, C., Chou, I.-M., Bodnar, R.J. & Bassett, W.A. Microthermometric analysis of synthetic fluid inclusions in the hydrothermal diamond-anvil cell. 995 - 1007 **85**(1998).
19. Bassett, W.A. High pressure-temperature aqueous systems in the hydrothermal diamond anvil cell (HDAC). *European Journal of Mineralogy* **15**, 773 - 780 (2003).
20. Duan, Z., Møller, N. & Weare, J. An equation of state for the CH₄-CO₂-H₂O system: I. Pure systems from 0 to 1000°C and 0 to 8000 bar. *Geochemica et Cosmochimica Acta* **56**, 2605 - 2617 (1992).
21. Yoder, H.S., Jr. High-low quartz inversion up to 10,000 bars. *Transactions of the American Geophysical Union* **31**, 827 - 835 (1950).
22. Koster van Groos, A.F. & Ter Heege, J.P. High-low quartz transition up to 10 kilobars pressure. *Journal of Geology* **81**, 717 - 724 (1973).
23. Gottschalk, M. Equations of State for Complex Fluids. *Reviews in Mineralogy and Geochemistry* **65**, 49 - 97 (2007).
24. von Körtvelyessy, L. *Thermoelement Praxis*, 504 (Vulkan Verlag, Essen, 1998).
25. Deuffhard, P. *Newton Methods for Nonlinear Problems. Affine Invariance and Adaptive Algorithms*, 430 (Springer Verlag GmbH, Heidelberg, 2004).
26. Haselton, H.T., Chou, I.-M., Jr., Shen, A.H. & Bassett, W.A. Techniques for determining pressure in the hydrothermal diamond-anvil cell: Behaviour and identification of ice polymorphs (I, II, V, VI). *American Mineralogist* **80**, 1302 - 1306 (1995).
27. Evans, L.F. Selective Nucleation of the High-Pressure Ices. *Journal of Applied Physics* **38**, 4930 - 4932 (1967).

28. Bridgman, P.W. Water, in the Liquid and Five Solid forms, under Pressure. *Proceedings of the American Academy of Arts and Sciences* **47**, 439 - 558 (1912).
29. Audétat, A. & Keppler, H. Solubility of rutile in subduction zone fluids, as determined by experiments in the hydrothermal diamond anvil cell. *Earth and Planetary Science Letters* **232**, 393 - 402 (2005).
30. Hu, J. et al. X-ray diffraction and laser heating: application of a moissanite anvil cell. *Journal of Physics: Condensed Matter* **14**, 10479 - 10481 (2002).
31. Ti-Yu, D. Applications of Moissanite Anvil Cell for Raman Spectroscopy under High-Temperature and High-Pressure. *Spectroscopy and Spectral Analyses* **25**, 902 - 905 (2005).
32. Xu, J., Mao, H.K., Hemley, R. & Hines, E. The moissanite anvile cell: a new tool for high-pressure research. *Journal of Physics: Condensed Matter* **14**, 11543 - 11548 (2002).
33. Xu, J., Mao, H.K. & Hemley, R. The gem anvil cell: high-pressure behaviour of diamond and related meaterials. *Journal of Physics: Condensed Matter* **14**, 11549 - 11552 (2002).

Chapter 01

Chapter 02

Chapter 03

Chapter 04

Chapter 05

Chapter 06

Chapter 07

Chapter 08

Chapter 09

Chapter 10

Chapter 11

Chapter 12

STRUCTURAL CHARACTERISATION OF TRIBOLOGICALLY INFLUENCED SILICON CARBIDE CERAMIC SURFACES

V. Presser⁽¹⁾, C. Berthold⁽¹⁾,
R. Wirth⁽²⁾, K. G. Nickel⁽¹⁾

⁽¹⁾ Institut für Geowissenschaften, Universität Tübingen

⁽²⁾ Helmholtz-Zentrum Potsdam

ABSTRACT:

Tribologically influenced ceramic surfaces are usually only looked at in terms of the wear effects: surface topography, friction coefficient, loss rates. Current efforts go towards a deeper understanding of mechanisms and kinetics. To gain this, the effects of the wear of ceramics on the phases and microstructures have to be analysed in detail. As an example for this, we studied tribologically influenced silicon carbide ceramics worn under water lubrication. Because structural changes occur within the uppermost μm and tribochemical reaction layers are often restricted to the nm-range, appropriate analytical tools have to be used and those come only now available. We will show how the currently developed techniques of X-ray microdiffraction combined with Raman spectroscopy can resolve many issues. Another recent improvement, transmission electron microscopy (TEM) on cross-sections prepared via the focused ion beam technology (FIB), helps to verify the findings of the former techniques.

1. INTRODUCTION

Tribology (Greek: τριβο = “to rub”, λόγος = “meaning”) is the science of interacting surfaces in relative motion and an important field of research in engineering. Thematically, it encompasses more than bulk physical wear and resulting changes in morphology. The alteration in chemistry, phase content and structure are important factors for materials in sliding contact, too. Typical examples are sintered silicon carbide (SiC) ceramic bodies, which are often employed as sliding seals in the presence of water because of their high corrosion and wear resistance.¹⁻³ SiC has been shown to have a low friction coefficient under water lubrication which is explained by chemical reactions between the carbide and water forming an oxide scale that acts as a lubricant.¹⁻⁵ Besides superficial alteration of the chemical composition, mechanical contact will deteriorate the ceramic matrix and finally cause bulk mass loss.

Many studies in the field of engineering science focus almost exclusively on describing the evolution of the friction coefficient over time (corresponding to wear distance) and quantify the bulk wear at best by means of profilometry. Electron microscopy and / or atomic force microscopy (AFM) are applied to visualise the wear debris and the worn surfaces' morphology. In addition, EDX (Energy Dispersive X-ray spectrometry) or EELS (Electron Energy Loss Spectroscopy) are used to look at the chemical composition.

Within the last decades some studies on the tribology of ceramics included a wider range of analytical methods like Raman spectroscopy⁶, FT-IR⁷, Secondary Ion Mass Spectroscopy (SIMS)⁸ or Auger Electron Spectroscopy (AES)^{4,5}. Comparing results from different analytical methods, it is imperative to be aware about the actual size and geometry of the analysed volume – some methods are rather surface sensitive but show a large lateral resolution while others have a larger sampling depth but only a very small lateral spot size. Only completely homogeneous bodies will yield identical analytical results when analysed at different sample positions (lateral / axial) and tribologically influenced surfaces certainly have a gradient with respect to chemical composition and structural deterioration.

This review concentrates on a few methods particularly suited for spatially resolved analysis, where new technologies, for example, in the fields of X-ray optics^{9,10} and TEM preparation^{11,12}, facilitate fast or highly resolved studies.

2. ANALYTICAL METHODS

2.1 The base: sampling volume considerations

A major requirement for the correct interpretation of differently sampled analyses from thin surface layers or, in general, heterogeneous samples, is the exact knowledge of both size and geometry of the excited volume.

The largest sampling depth of the methods discussed in this review is given for Raman spectroscopy: here, depending mainly on the optical absorption coefficient α of the material, the used laser wavelength λ_{laser} , the numeric aperture NA of the objective lens used and the instrumental setup (i.e., confocal settings), penetration depths reach up to several tens of μm or more.^{13,14} In general, it is, therefore, essential to use an objective lens with a high numeric aperture (> 0.9) in order to decrease the size of the excited volume.

The total sampling depth can be very different depending on the material and the chosen excitation wavelengths. For highly opaque silicon single crystals the effective penetration depth ($\bar{\delta} = \frac{1}{2} \alpha$) lies in the sub-micrometre scale depending on the excitation laser wavelength.^{15,16} For these materials, $\bar{\delta}$ was shown to decrease significantly when choosing smaller laser wavelengths (e.g., UV radiation: effective penetration depth for silicon encompasses only a few nanometres).^{17,18} Also for highly transparent silicon carbide (4H- and 6H-SiC), the effective penetration depth can be reduced to tens of nanometres below $\lambda_{\text{laser}} = 244 \text{ nm}$ even for a non-confocal setup.¹⁹

Confocal Raman spectroscopy uses a focussed laser beam and a large part of the scattered information originates from the focus spot. The laser beam has indeed its smallest diameter within the focus plane (usually around $1 \mu\text{m}$ depending on the numeric aperture and the laser wavelength), but already some μm inside the material, the laser beam diameter is increased significantly ($\gg 5 \mu\text{m}$). Therefore, the gained information comes from a larger volume segment. Recent studies by Everall (Ref. ²⁰), Macdonald and Vaughan (Ref. ²¹) and Presser and Glotzbach (Ref. ²²) show that even for a confocal setup a significant signal contribution originates from out-of-focus areas.

In the literature, often the term “axial resolution” is used, which does not refer to the penetration depth and usually lies around $\approx 2 \mu\text{m}$.²³ Axial resolution denotes two times the axial distance $z_{\text{a.r.}}$ between the point of the sample which yields maximum total signal intensity and the position which yields half that intensity.²³ In order to obtain this value the sample is moved downwards relative to the focus point starting at $z = 0$ while the total signal intensity is monitored. However, even at a distance $|z| \gg |z_{\text{a.r.}}|$, a significant part of the signal intensity originates from the sample surrounding and is recorded by the Raman spectrometer.

The penetration depth for XRD is easier to determine as the often unknown optical transparency has not to be taken into account. X-rays are absorbed mainly by the photo-electric effect, but also scattered by elastic diffusion (Rayleigh diffusion) and inelastic diffusion (Compton diffusion). Knowing the wavelength used and the sample's density and chemistry in terms of the mean atomic number, it is possible to calculate the depth from which a certain percentage of the measured total signal is obtained. Choosing a smaller incident angle makes XRD more surface sensitive. In case of SiC ($\rho = 3200 \text{ kg/m}^3$), the depth for 50% contribution to the diffracted beam is $6.2 \mu\text{m}$ for 10° incident angle but only $0.4 \mu\text{m}$ for 0.5° incident angle (using Cu- K_α radiation). The lateral resolution can be derived from the beam diameter and the incident angle. As for μ -XRD, beam diameters of $\ll 1 \text{ mm}$ are obtained by employing X-ray optics (capillary optics or focussing mirrors).

When performing EDX on bulk samples, the excitation volume is a function of the acceleration current, the mean atomic number and density of the analysed material. By means of a Monte-Carlo simulation, it is possible to calculate the size and form of the pear-shaped excited area.²⁴⁻²⁶ The high lateral resolution, like for Raman spectroscopy, is only observed in the focus plane for EDX analysis. In case of SiC, an excited volume of $\approx 10 \mu\text{m}^3$ and a penetration depth of $\approx 3 \mu\text{m}$ can be expected.

In all three cases the penetration depth is larger than the typical thickness of a tribolayer ($\leq 100 \text{ nm}$) and, therefore, reflects only an average over the signal from the ceramic matrix and the tribologically influenced scale. This is a good explanation for situations where, for example, oxygen concentrations measured via EDX to be as high as several % apparently do not correlate with any detectable oxygen-rich phase by means of Raman spectroscopy - the thin film showing an oxygen-containing phase is simply not detectable within the Raman detection limit.

The penetration depth can be modified and decreased by simply making the sample very thin. Focused Ion Beam (FIB) preparation, as discussed in the next chapter, can be used to cut small samples (foils) from the bulk surface. Samples of defined thickness (usually 100 - 500 nm) can be prepared limiting the penetration depth to that specific thickness.¹²

2.2 Transmission Electron Microscopy (TEM) and Focused Ion Beam (FIB) preparation

TEM is a most versatile method allowing, for example, systematic dislocation studies, evaluation of grain sizes and by selective area electron diffraction (SAED) identification of crystalline phases. One limitation is that it requires the phase to be stable enough to sustain the high-energy electron beam used in a TEM (~ 100 keV). The often more important limitation is the small volume investigated.

Conventional bulk sample preparation of heterogeneous materials by argon ion milling produces rather randomly selected sample cross-sections (e.g., Ref. ⁸) and it is, therefore, advantageous to replace this by the FIB technology. The excited volume in a FIB cut foil caused by the electron beam in an analytical electron microscopy (i.e., < 100 nm) is determined by approximately the beam diameter.

FIB preparation is a big leap forward in tribological studies, because only then area selective TEM studies ^{11,12,27-29} are possible. For this, foils can be cut using single (i.e., one ion column) or dual-beam (i.e., conventional SEM equipped with an additional ion column) instruments with a precision of $\ll 100$ nm.³⁰ To avoid surface damage in the range of the first tens of nanometres during FIB-assisted Pt deposition, the sample should be sputter coated, for example, with carbon or platinum before attempting FIB imaging and preparation. The depth of the FIB cut can be selected (usually in the range of 10 – 20 μm) allowing not only the analysis of a discrete depth profile from the sample's surface but give the decisive advantage of pre-selection of the true spot of interest and its microstructural situation (for example a certain area of a wear track).

The example of Fig. 1 displays SEM, STEM and TEM images of tribologically exposed SiC surfaces. Smooth areas (Fig. 1a - c) are covered by an approximately 100 nm thick dense tribolayer. On rough surface areas (Fig. 1d - f) redeposited (loose) wear debris has accumulated in depressions (Fig. 1e) building up a scale of 0.5 – 1.0 μm thickness. Below the tribolayer, micro-fracture and shear cracks can be observed in the uppermost 2 μm of the ceramic matrix. EDX-analysis and EELS-mapping (not shown here; see Ref. ³¹) of the tribolayer shown in Fig. 1 revealed that SiC debris is embedded within an oxygen-rich matrix that is visible in Fig. 1f where it appears as a light-grey phase. Oxygen input can also be observed along cracks some μm into the ceramic body.

Structural deterioration during tribological exposure does not mean a complete loss of structural order on a short-range scale (full-scale amorphisation). As wear debris is trapped between the sliding surfaces, the crystallite size is decreased during lapping while mechanic deformation (elastic / plastic) takes place at the same time. A typical example is shown in Fig. 1c and 1f where wear debris in form of (strained but intact) SiC particles is held together by an oxygen-rich phase. This simultaneous insight into two levels of structural changes is almost impossible without the FIB technique.

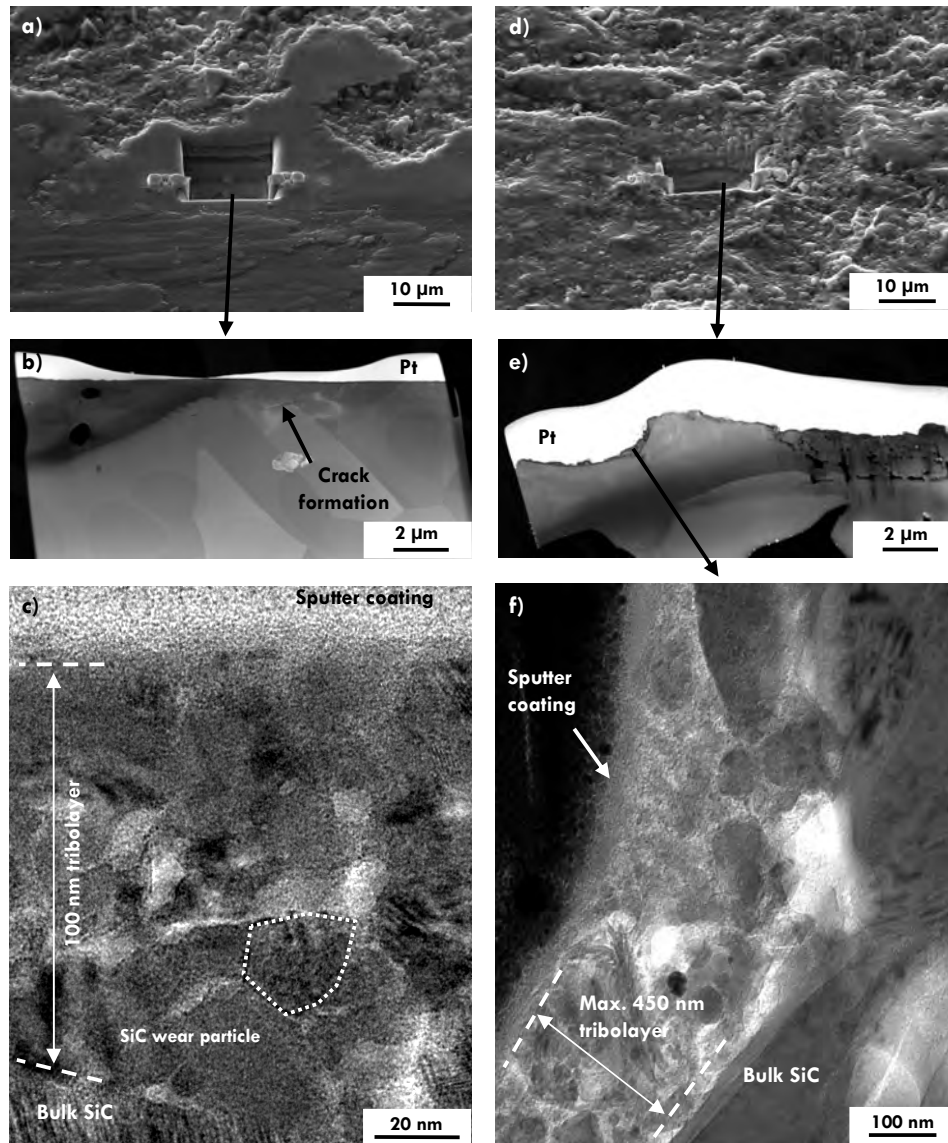


Fig. 1. Electron images (cross sections) of the surface area (a - c: smoothed part; d - f; rough part) of SiC wear tracks (a, d: SEM; b, e: STEM; c, f: dark field TEM). The net-like structure on Fig. 1b and 1e originates from the TEM sample holder foil while white spots on Fig. 1e are due to Ga contamination. The tribolayer is composed of rounded wear debris that is held together by an oxygen rich phase (Ref. ³¹) on top of the SiC ceramic matrix.

Plastic deformation of SiC under static conditions is usually observed at elevated temperatures above 500°C³²⁻³⁷ because the brittle nature of SiC precludes such deformation under most circumstances. But in sliding contact SiC does show plastic deformation (see Erickson et al.⁸). One reason may be that tribologically exposed surfaces experience high local energies when small asperity peaks come in physical contact causing both high “flash” temperatures (up to 1000°C) and high pressures (Hertzian contact; up to n·10 GPa). However, plastic deformation of SiC along the basal plane (0001) $[1\bar{1}20]$ slip plane system is known from hardness indentations (“indentation plasticity”). In Fig. 2a a Vickers hardness indentation (15.5 N) in undoped, single-crystal (0001)-6H-SiC is shown. Here, plastic deformation is already verified by the elevated zone around indentation cores. HR-TEM reveals the mechanisms, because we observe that the indentation has transformed the single-crystalline SiC into a mosaic crystal due to domain gliding along slip planes (Fig. 2c, d). This structural deterioration, thus, merely decreases the crystallite = domain size. Clearly FIB preparation is extremely helpful to investigate this case which allows us to interpret the results of x-ray diffraction and Raman spectroscopy below.

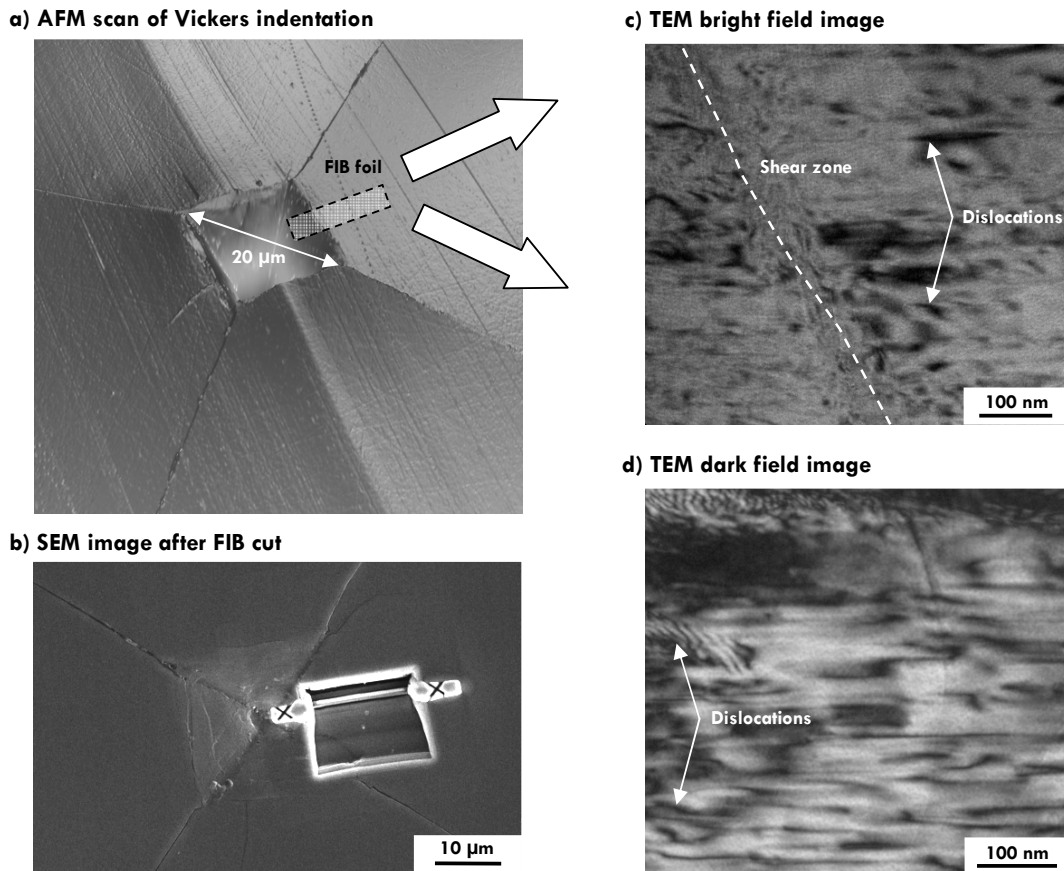


Fig. 2. Plastic deformation of SiC in a Vickers hardness indentation (15.5 N) in (0001)-6H-SiC. a) AFM scan, b) SEM image of sample after FIB foil preparation, c) bright field TEM image showing a shear zone and indentation-related dislocations, d) dark field TEM image displaying mosaic crystal formation due to dislocation formation.

2.3 Raman spectroscopy

Like XRD, Raman spectroscopy yields phase-related, structural information. However, as vibrational modes and their corresponding bonding lengths are studied, there is no need for the analysed material to be in a crystalline state (selection rule for XRD). In tribolayers, amorphous compounds are likely to be present as a result of tribochemical reactions and mechanical treatment. Hence, Raman spectroscopy ideally complements XRD for analysis of worn surfaces.

Raman spectroscopy is also sensitive to tribologically induced structural deterioration as described above: due to mechanical contact bonding lengths increase and over time the crystallite size decreases. Extensive Raman studies on this topic were carried out in the course of bulk pressure-induced amorphisation³⁸ and hardness indentation experiments on ceramics and single-crystals³⁹⁻⁴². With increased structural damage to the crystal lattice, the shape and position of individual Raman-active modes changes in four ways: (1) the bands become broader, (2) they decrease in total Raman intensity, (3) they shift in their spectral position and (4) they become asymmetric when the structural deterioration reaches a critical level.^{39,43,44} In case of structural deterioration due to mechanical contact, Raman-active modes of tribologically influenced SiC will shift towards higher wavenumbers, because mechanical exposure leads to a densification.⁴¹ Radiation-induced amorphisation (so called metamictisation), instead, is known to cause a down-shift of Raman modes.^{43,44}

Analogous to the analysis of XRD patterns, it is imperative for the quantitative description of the Raman FWHM to separate the instrument's contribution from the observed linewidth. For that, Irmer⁴⁵ proposed a simple equation using a correction parameter ("spectral resolution"⁴⁴) which is, among others, a function of wavelength, grating, focal length and slit width. Quantitative description of the degree of structural deterioration by means of linewidth analysis following this approach has successfully been applied to natural materials like zircon.^{43,44,46-48} The Irmer equation, however, cannot be applied when analysing asymmetric or very narrow Raman modes (i.e. when the FWHM is in the same order of magnitude as the spectral resolution). In such cases "conventional" profile line deconvolution must be applied and the instrument function can often be separated by approximating by a Gaussian profile.⁴⁹

Quantitative characterisation of tribolayers by means of Raman spectroscopy is difficult due to the large penetration depth of the laser beam. In particular, a bulk penetration depth in the μm -range^{13,14} is contrasted by a scale thickness in the nm-range. The resulting Raman linewidth, therefore, is an average of a small contribution of the thin tribolayer causing line-broadening and the uninfluenced bulk matrix.

Fig. 3 shows Raman spectra of tribologically influenced SiC surfaces as compared to a Vickers-indentation in a (0001)-6H-SiC wafer and unstrained ideal single-crystal (0001)-6H-SiC. Besides pronounced line-broadening caused by mechanical deterioration of the crystal lattice new modes appear around 540 cm^{-1} and 680 cm^{-1} .

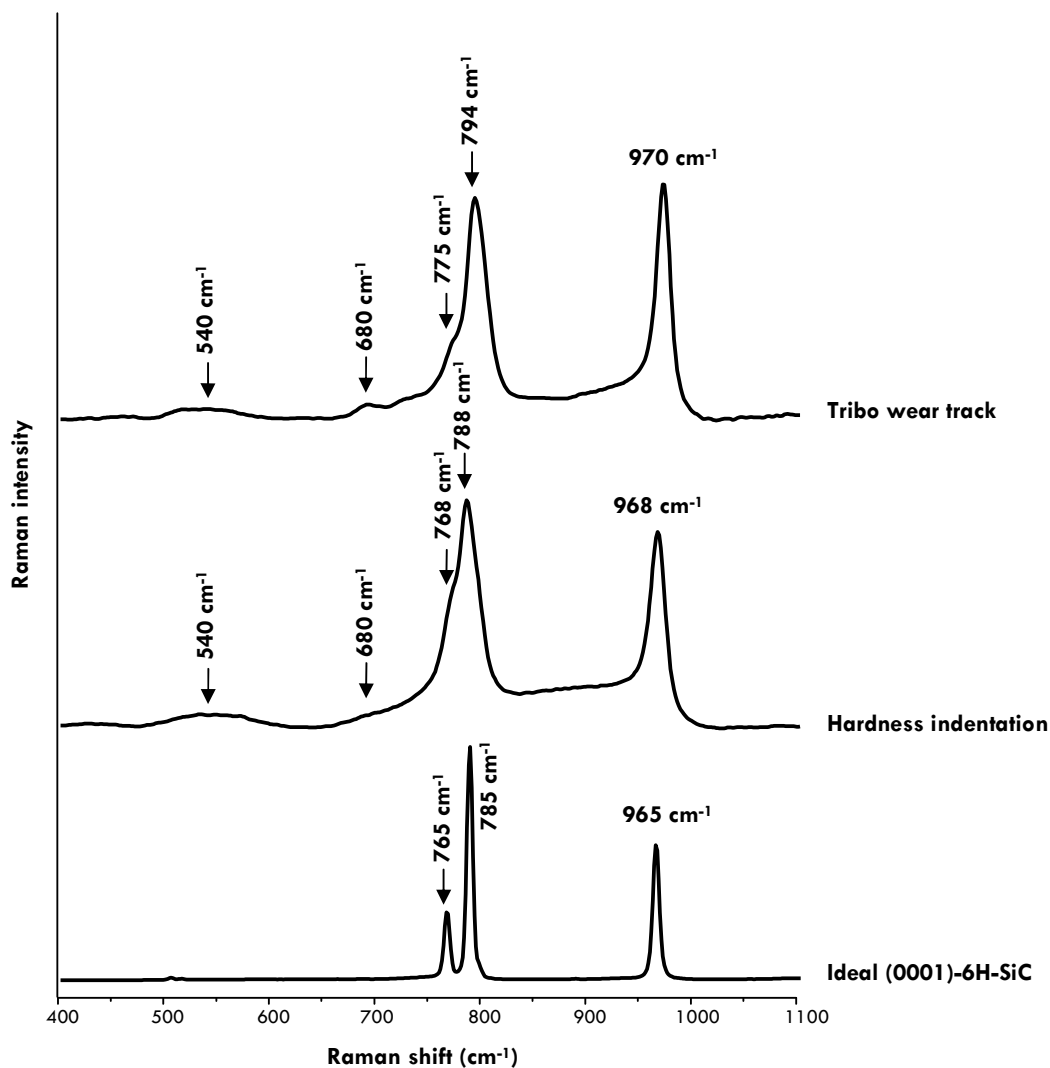


Fig. 3. Raman spectra of a wear track of tribologically influenced SiC, the central part of a Vickers hardness indentation and ideal undistorted undoped (0001)-6H-SiC. Note the spectral up shift of the Raman modes due to mechanical deterioration (densification).

The appearance of new Raman-active modes is well-known for nano-sized crystallites as scattering from confined acoustical phonons becomes relevant^{50,51} and selection rules eventually change⁵²⁻⁵⁶. In fact, new Raman-active modes for mechanically exposed surfaces were described to appear at around 400, 475, 490, 540, 680, 845 and 950 cm⁻¹.^{39,41,57-59} For the mode at 680 cm⁻¹ Lauer⁵⁸ suggested an attribution to a Si-C-O phase (silicon oxycarbide). Considering the chemical process, the presence of silicon oxycarbide may be possible, but the mode assignment by Lauer has not been corroborated by Raman studies performed in the Si-C-O system, yet.⁶⁰⁻⁶²

A qualitative description of the degree of tribological wear is possible by evaluation of the true Raman-FWHM (FWHM_{corr}). An example for that is shown in Fig. 4 where a direct correlation between tribolayer thickness and FWHM_{corr} is demonstrated.

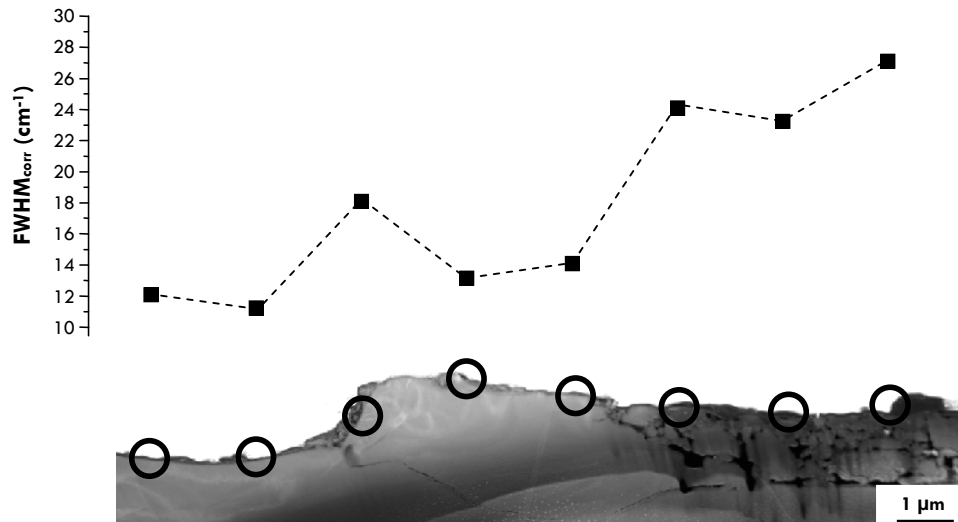


Fig. 4. True Raman linewidth ($FWHM_{corr}$) line scan across wear track (STEM image). Note the correlation between tribolayer thickness / structural deterioration and Raman linewidth.

2.4 Small Angle μ -X-Ray Diffraction (μ XRD)

Using the previously mentioned dependency of the penetration depth for X-rays on the incident angle, it is possible to enhance the surface sensitivity of XRD by choosing a small incident angle and maintaining it while the detector moves along the diffraction.

With X-ray optics like polycapillary lenses now becoming available, XRD can also be applied to study small areas. Beam diameters defined by the Gaussian beam halfwidth of $\leq 20 \mu\text{m}$ are attainable for short working distances (hence the term μ -XRD).^{11,12,63-67} It should be kept in mind that the beam spot on the surface becomes elongated and will be relatively large when using small incident angles (like 0.5° or 1.0°).

For synchrotron radiation beam diameters less than 100 nm have been reported.⁶⁸ Alternatively, focussing mirrors have been applied successfully for studies carried out on the grain scale (i.e., $\geq 1 \mu\text{m}$).⁶⁹ Ideally combined with a micro-focus tube⁷⁰ and an area-sensitive detector⁷¹⁻⁷⁴ which integrates over a large angular range and provides information on preferential orientation, measuring times are in the range of minutes.^{11,12}

This way, systematic studies by means of xy -mapping and varying incident angles are possible and the well-known effect of superficial amorphisation causing linewidth broadening of (hkl)-reflections^{75,76} after mechanic contact of sliding surfaces can now be characterised on a μm -scale via μ -XRD.

To do so, the linewidth and profile form must be corrected for the influence of the instrument function, for example, by the Fundamental Parameters Approach (FPA).⁷⁷⁻⁸⁰ Based on deconvolution, the instruments profile function is determined by measuring a standard material which shows no size or strain related line broadening. Once the instrument's contribution has been determined, quantitative description of the "true" linewidth is possible.

In reality there is no such thing as an ideal standard material and, hence, sample contributions must be considered. For instance, the linear absorption coefficient will usually not be the same for the standard and the studied sample and further corrections are, therefore, needed. Using small incident angles introduces new problems, because the standard material must not be strained within the first tens of nm beneath the surface to avoid broadened or shifted reflections. Consequently, bulk mechanical polishing to obtain a smooth surface is not a good option and optical polishing and / or chemically etched surfaces are preferable as long as a smooth surface is maintained.

Quantitative analysis of the Full Width at Half Maximum (FWHM) yields information on the so-called “crystallite size”.^{81,82} This apparent crystallite size is an average of the length of coherent scattering directions and, therefore, can only be used as an approximation of the “real” crystallite size. For a comparison between apparent grain sizes and coherent scattering lengths see, for example, Ref. ⁵¹.

The FWHM of every (*hkl*)-reflection yields its own apparent crystallite size as the coherent scattering domain is usually not spherical. For example, layered phases like graphite show coherently scattering domains with a small axial and a large lateral expansion. This information can be obtained by introducing spherical harmonics to the Rietveld refinement (better known from texture analysis).^{83,84}

“Silicon carbide” is a collective term for hundreds, if not thousands of (slightly) different SiC modifications (so called polytypes).⁸⁵⁻⁸⁷ Although only 3C-, 4H-, 6H- and 15R-SiC are usually making up the main part of the phase assemblage, it is still necessary to treat monolithic SiC bodies as polyphase materials when using the Rietveld method for quantitative analysis of the apparent crystallite size.⁸⁸⁻⁹² Due to the pronounced line broadening at small incident angles, this can only be done under less surface-sensitive conditions. Choosing an incident angle of, for example, 10°, the contribution of the nm-scale tribolayer is almost negligible. The SiC polytype distribution determined at higher incident angles is taken as a good approximation, because the ceramic matrix usually shows a homogenous phase distribution and the excitation volumina are comparable in net size.

The spatial resolution of XRD cannot be decreased much below $\approx 20 \mu\text{m}$. Otherwise, only a few, one or even no single crystallite would be in reflection position and it would be necessary to perform time-consuming tilting series.

Fig. 5 shows XRD diffractograms of tribologically influenced SiC recorded with varying incident angle. In the case presented, the bulk SiC polytype composition was determined at 10° incident angle to be $\approx 7 \text{ wt}\%$ 4H-SiC, $\approx 86 \text{ wt}\%$ 6H-SiC and $\approx 6 \text{ wt}\%$ 15R-SiC. Using this polytype distribution for analysis of a XRD diffractogram measured with 1° incident angle, an apparent crystallite size of $\approx 15 - 60 \text{ nm}$ was calculated. This is in the same order of magnitude than the apparent grain sizes within the tribolayer seen in Fig. 1 (TEM) that lie in the range of 5 – 30 nm. With the sampling depth for X-rays being larger than the actual tribolayer, an inflated apparent crystallite sizes will be observed, because the large SiC grains from within the ceramic matrix contribute to the total signal.

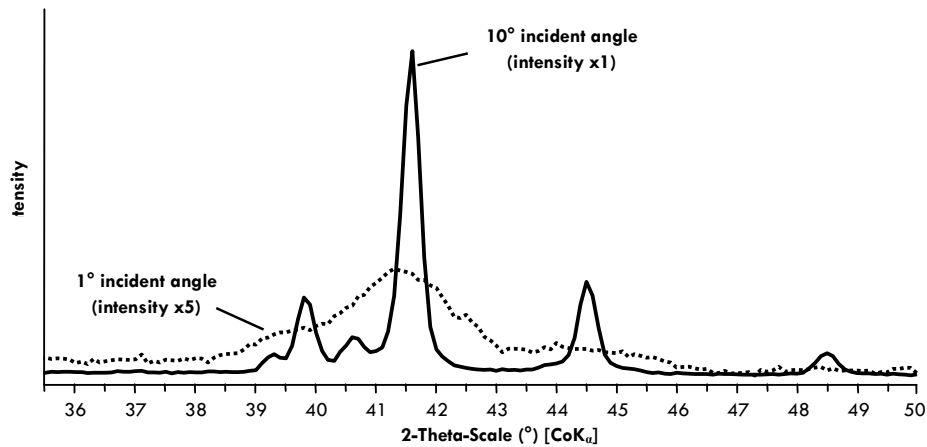


Fig. 5. XRD diffractograms of tribologically exposed SiC. The line-broadening of the individual (hkl) -reflections is apparent for small incident angles (= high surface sensitivity).

3. CONCLUSION

It is current opinion that tribologically stressed samples can give us many more information about mechanisms and kinetics than formerly obtained by gravimetry, profilometry and friction coefficient measurements. The direct observation of oxygen input (EDX, EELS), apparent grain sizes (HR-TEM) and phase assemblage (SAED) by FIB-assisted TEM has become a powerful method in the characterisation of the chemical and structural deterioration of tribologically influenced ceramic surfaces.

However, despite the strongly increased speed of sample preparation by FIB, access to (HR)-TEM instruments is limited. The alternative, the structural characterisation of SiC tribolayers by small angle μ -XRD and especially Raman-spectroscopy as more wide-spread methods is improving our knowledge about tribological processes greatly as well. The rather poor spatial resolution ($\approx 10 \mu\text{m}$) of X-ray diffraction does not withstand it to be very suitable for quantitative description of apparent crystallite sizes (= mean length of coherent scattering). Raman-spectroscopy, on the other hand, has a smaller lateral resolution ($\approx \mu\text{m}$) and permits, therefore, a higher resolving analysis of wear tracks and structural deterioration. However, Raman-spectroscopy has a large axial penetration depth ($\approx 10 \mu\text{m}$) and is, consequently, in most cases limited to qualitative analysis. Even though μ -XRD and Raman cannot fully replace TEM-studies, both methods are ideal to screen large numbers of samples in order to find a suitable position for further in-depth analysis with more sophisticated analytical techniques.

New developments, for example, in X-ray optics / X-ray detectors and improvements for more surface-sensitive Raman methods like Tip Enhanced Raman Spectroscopy (TERS, in combination with AFM) will certainly further decrease (lateral / axial) resolution and measuring times. The future belongs to fast, spatially resolved characterisation methods that require little or no sample preparation. Ideally, complementary methods will be combined in one instrument which ensures that exactly the same sample position is analysed. A promising first example for that is PRAXIS, a prototype that combines μ -XRF (X-Ray Fluorescence = chemical information) and Raman (= structural information).⁹³⁻⁹⁷

ACKNOWLEDGMENTS

This work was supported by the Deutsche Forschungsgemeinschaft (DFG) through Ni299/12-1.

REFERENCES

1. Schwetz, K.A. Silicon Carbide Based Hard Materials. in *Handbook of Ceramic Hard Materials*, Vol. 2 (ed. Riedel, R.) 683 - 748 (Wiley-VCH Verlag GmbH, Weinheim, 2000).
2. Schwetz, K.A. & Hassler, J. Zur Beständigkeit von Hochleistungskeramiken gegen Flüssigkeitskorrosion. *Ceramic Forum International* **79**, D9 - D19 (2002).
3. Xu, J. & Kato, K. Formation of tribochemical layer of ceramics sliding in water and its role for low friction. *Wear* **245**, 61 - 75 (2000).
4. zum Gahr, K.-H., Blattner, R., Hwang, D.-H. & Pöhlmann, K. Micro- and macro-tribological properties of SiC ceramics in sliding contact. *Wear* **250**, 299 - 310 (2001).
5. Chen, C.-T.A. & Marshall, W.L. Amorphous silica solubilities IV. Behavior in pure water and aqueous sodium chloride, sodium sulfate, magnesium chloride, and magnesium sulfate solutions up to 350°C. *Geochimica et Cosmochimica Acta* **46**, 279 - 287 (1982).
6. Ersoy, D.A., McNallan, M.J. & Gogotsi, Y.G. Carbon coatings produced by high temperature chlorination of silicon carbide ceramics. *Materials Research Innovations* **5**, 55 - 62 (2001).
7. Hsu, S.M., Zhang, J. & Yin, Z. The nature and origin of tribochemistry. *Tribology Letters* **13**, 131 - 139 (2002).
8. Erickson, L.C., Blomberg, A., Hogmark, S. & Bratthall, J. Tribological characterization of alumina and silicon carbide under lubricated sliding. *Tribology International* **26**, 83 - 92 (1993).
9. Bjeoumikhov, A., Bjeoumikhova, S. & Wedell, R. Capillary Optics in X-Ray Analytics. *Particle & Particle Systems Characterization* **22**, 384 - 390 (2005).
10. Berthold, C., Bjeoumikhov, A. & Brügemann, L. Fast XRD² Microdiffraction with Focusing X-Ray Microlenses. *Particle & Particle Systems Characterization in press*(2008).
11. Mayer, J., Giannuzzi, L.A., Kamino, T. & Michael, J. TEM sample preparation and FIB-induced damage. *MRS Bulletin* **32**, 400 - 407 (2007).
12. Wirth, R. Focused ion beam (FIB): a novel technology for advanced application of micro- and nanoanalysis in geosciences and applied mineralogy. *European Journal of Mineralogy* **16**, 863 - 876 (2004).
13. Deluca, M., Sakashita, T. & Pezzotti, G. Polarized Raman scattering of domain structures in polycrystalline lead zirconate titanate. *Applied Physics Letters* **90**, 051919-1 - 051919-3 (2007).
14. Lewis, I.R., Lewis, L. & Edwards, H.G.M. *Handbook of Raman Spectroscopy: From the Research Laboratory to the Process Line*, 1080 (CRC Press, New York, 2001).
15. Agullo-Rueda, F., Moreno, J.D., Montoya, E., Guerrero-Lemus, R. & Martinez-Duart, J.M. Influence of wavelength on the Raman line shape in porous silicon. *Journal of Applied Physics* **84**, 2349 - 2351 (1998).
16. Aspnes, D.E. & Studna, A.A. Dielectric functions and optical parameters of silicon, germanium, gallium phosphide, gallium arsenide, gallium antimonide, indium phosphide, indium arsenide, and indium antimonide from 1.5 to 6.0 eV. *Physical Review B* **27**, 985 - 1009 (1983).
17. Ishitsuka, N., Sakata, H., Nishimura, A., Miura, H. & Kumazawa, T. Development of apparatus for measuring stress in semiconductor devices by applying microscopic Raman spectroscopy using an ultraviolet laser. *Nippon Kikai Gakkai Ronbunshu, A-hen* **62**, 2750 - 2756 (1996).
18. Holtz, M., Carty, J.C. & Duncan, W.M. Ultraviolet Raman stress mapping in silicon. *Applied Physics Letters* **74**, 2008 - 2010 (1999).
19. Harima, H. Raman scattering characterization on SiC. *Microelectronic Engineering* **83**, 126 - 129 (2006).
20. Overall, N. The Influence of Out-of-Focus Sample Regions on the Surface Specificity of Confocal Raman Microscopy *Applied Spectroscopy* **62**, 591 - 598 (2008).
21. MacDonald, A.M. & Vaughan, A.S. Numerical simulations of confocal Raman spectroscopic depth profiles of materials: a photon scattering approach. *Journal of Raman Spectroscopy* **38**, 584 - 592 (2007).
22. Presser, V. & Glotzbach, C. Metamictisation in zircon: Raman investigation following a Rietveld approach. Part II: Sampling depth implication and experimental data. *Journal of Raman Spectroscopy* **40**, in press (2009).
23. Markwort, L., Kip, B., Da Silva, E. & Roussel, B. Raman imaging of heterogeneous polymers: a comparison of global versus point illumination. *Applied Spectroscopy* **49**, 1411 - 1430 (1995).
24. Eggert, F. *Standardfreie Elektronenstrahl-Mikroanalyse mit dem EDX im Rasterelektronenmikroskop*, (Book on Demand GmbH, Norderstedt, 2005).
25. Goldstein, J. et al. *Scanning Electron Microscopy and X-Ray Microanalysis*, 689 (Springer Science + Business Media, Inc., New York, 2003).
26. Schmidt, P.F. *Praxis der Rasterelektronenmikroskopie und Mikrobereichsanalyse*, 810 (expert verlag, Esslingen, 1994).
27. Lozano-Perez, S. A guide on FIB preparation of samples containing stress corrosion crack tips for TEM and atom-probe analysis. *Micron* **39**, 320 - 328 (2008).
28. Presser, N. & Hilton, M.R. Applications of focused ion beam machining to the characterization of carbide, nitride and oxide films. *Thin Solid Films* **308 - 309**, 369 - 374 (1997).
29. Volkert, C.A. & Minor, A.M. Focused ion beam microscopy and micromachining. *MRS Bulletin* **32**, 389 - 399 (2007).

30. Wirth, R. Focused Ion Beam (FIB) combined with SEM and TEM: Advanced analytical tools for studies of chemical composition, microstructure and crystal structure in geomaterials on a nanometre scale. *Chemical Geology in press*(2008).
31. Presser, V., Nickel, K.G., Krummhauser, O. & Kailer, A. A Model for Wet Silicon Carbide Tribo-Corrosion. *Wear in press*(2008).
32. Mussi, A., Rabier, J., Thilly, L. & Demenet, J.L. Plasticity and deformation microstructure of 4H-SiC below the brittle-to-ductile transition. *Physica Status Solidi C* **4**, 2929 - 2933 (2007).
33. Presser, V. & Nickel, K.G. Silica on silicon carbide. *Critical Reviews in Solid State and Material Sciences* **33**, 1 - 99 (2008).
34. Samant, A.V. & Pirouz, P. Activation parameters for dislocation glide in α -SiC. *International Journal of Refractory Metals & Hard Materials* **16**, 277 - 289 (1998).
35. Samant, A.V., Wei, X.L. & Pirouz, P. An optical and transmission electron microscopy study of deformation-induced defects in 6H-SiC. *Philosophical Magazine A* **78**, 737 - 746 (1998).
36. Demenet, J.L., Zhang, M., Hobgood, H.M. & Pirouz, P. Fragile-ductile transition of single crystal 4H-SiC. *Journal de Physique IV* **106**, 53 - 62 (2003).
37. Patten, J., Gao, W. & Yasuto, K. Ductile regime nanomachining of single-crystal silicon carbide. *Journal of manufacturing science and engineering* **127**, 522 - 532 (2005).
38. Ravindran, T.R., Arora, A.K. & Gopalakrishnan, R. Pressure-induced amorphization of bismuth orthosilicate. *Journal of Physics: Condensed Matter* **14**, 6579 - 6589 (2002).
39. Kailer, A., Gogotsi, Y.G. & Nickel, K.G. Micro-Raman spectroscopy of indentation-induced phase-transformations. *Materials, Functionality & Design, Proceedings of the European Conference on Advanced Materials and Processes and Applications* **5**, 171 - 174 (1997).
40. Kailer, A., Gogotsi, Y.G. & Nickel, K.G. Use of hardness indentation coupled with micro-Raman spectroscopy in high-pressure materials research. *Materials Research Society Symposium Proceedings* **499**, 225 - 230 (1998).
41. Kailer, A., Nickel, K.G. & Gogotsi, Y.G. Raman microspectroscopy of nanocrystalline and amorphous phases in hardness indentations. *Journal of Raman Spectroscopy* **30**, 939 - 946 (1999).
42. Gogotsi, Y. & Domnich, V. Indentation-induced phase transformations in ceramics. in *High Pressure Surface Science and Engineering* (eds. Gogotsi, Y. & Domnich, V.) 443 - 466 (Institute of Physics Publishing, Bristol, 2004).
43. Nasdala, L., Irmer, G. & Wolf, D. The degree of metamictization in zircon: a Raman spectroscopic study. *European journal of mineralogy* **7**, 471 - 478 (1995).
44. Nasdala, L. et al. Metamictization of natural zircon: accumulation versus thermal annealing of radioactivity-induced damage. *Contributions to Mineralogy and Petrology* **141**, 125 - 144 (2001).
45. Irmer, G. Zum Einfluß der Apparatefunktion auf die Bestimmung von Streuquerschnitten und Lebensdauern aus optischen Phononenspektren. *Experimentelle Technik der Physik* **33**, 501 - 506 (1985).
46. Nasdala, L., Pidgeon, R.T. & Wolf, D. Heterogeneous metamictization of zircon on a microscale. *Geochimica et Cosmochimica Acta* **60**, 1091 - 1097 (1996).
47. Nasdala, L. et al. Incomplete retention of radiation damage in zircon from Sri Lanka. *American Mineralogist* **89**, 219 - 231 (2004).
48. Nasdala, L., Hanchar, J.M., Kronz, A. & Whitehouse, M.J. Long-term stability of alpha particle damage in natural zircon. *Chemical Geology* **220**, 83 - 103 (2005).
49. Presser, V. Metamictisation in zircon: Raman investigation following a Rietveld approach. Part I: Profile line deconvolution technique. *Journal of Raman Spectroscopy* **40**, in press (2009).
50. Fujii, M., Kanzawa, Y., Hayashi, S. & Yamamoto, K. Raman scattering from acoustic phonons confined in Si nanocrystals. *Physical Review B* **54**, R8373 - R8376 (1996).
51. Jouanne, M. et al. Structural transformations in nanosized zirconium oxide. *Physical Review B* **64**, 155404-1 - 155404-7 (2001).
52. Mani, K.K. & Ramani, R. Lattice dynamics of graphite. *Physica Status Solidi (B)* **61**, 659 - 668 (1974).
53. Knight, D.S. & White, W.B. Characterization of diamond films by Raman spectroscopy. *Journal of Materials Research* **4**, 385 - 393 (1989).
54. Champagnon, B., Panczer, G., Chemarin, C. & Humbert-Labeaumaz, B. Raman study of quartz amorphization by shock pressure. *Journal of Non-Crystalline Solids* **196**, 221 - 226 (1996).
55. Boukenter, A. et al. Low-frequency Raman scattering from fractal vibrational modes in a silica gel. *Physical Review Letters* **57**, 2391 - 2394 (1986).
56. Boukenter, A. et al. Raman observation of fractons in silica aerogels. *Journal of Non-Crystalline Solids* **95 - 96**, 1189 - 1195 (1987).
57. Gogotsi, Y.G., Kailer, A. & Nickel, K.G. Phase transformations in materials studied by micro-Raman spectroscopy of indentations. *Materials Research Innovations* **1**, 3 - 9 (1997).
58. Lauer, J.L. Wear-Induced Changes in the Raman, Infrared, and Fluorescence Spectra of Silicon Nitride Surfaces. *Applied Spectroscopy* **50**, 1378 - 1388 (1996).
59. Di Gregorio, J.F. & Furtak, T.E. Raman scattering by surface phonon-polaritons in large SiC microcrystals. *Solid State Communications* **89**, 163 - 166 (1994).
60. Hurwitz, F.I., Heimann, P., Farmer, S.C. & Hembree, D.M., Jr. Characterization of the pyrolytic conversion of polysilsesquioxanes to silicon oxycarbides. *Journal of Materials Science* **28**, 6622 - 6630 (1993).

61. Pantano, C.G., Singh, A.K. & Zhang, H. Silicon oxycarbide glasses. *Journal of Sol-Gel Science and Technology* **14**, 7 - 25 (1999).
62. Ryan, J.V. & Pantano, C.G. Synthesis and characterization of inorganic silicon oxycarbide glass thin films by reactive rf-magnetron sputtering. *Vacuum Science & Technology A* **25**, 153 - 159 (2007).
63. Langhoff, N., Bjeoumikhov, A., Bjeoumikhova, S., Langhoff, N. & Wolff, H. Capillary optics for real time X-ray diffractometry. *Journal of X-Ray Science and Technology* **13**, 185 - 190 (2005).
64. Bjeoumikhov, A., Wedell, R. & Bjeoumikhova, S. Mono- and polycapillary optics-state of the art and applications. *Guangxue Jingmi Gongcheng* **15**, 1932 - 1945 (2007).
65. Schell, N., Eichhorn, F., Bjeoumikhov, A., Prinz, H. & Ollinger, C. Parabolic capillary optics with less than 50 μm focus and large focal distance for synchrotron radiation scattering. *AIP Conference Proceedings* **879**, 975 - 980 (2007).
66. Wroblewski, T., Bjeoumikhov, A. & Hasse, B. Micro diffraction imaging of bulk polycrystalline materials. *Materials Science Forum* **524 - 525**, 273 - 278 (2006).
67. Bjeoumikhov, A. et al. New generation of polycapillary lenses: Manufacture and applications. *X-Ray Spectrometry* **32**, 172 - 178 (2003).
68. Hignette, O., Cloetens, P., Rostaing, G., Bernard, P. & Morawe, C. Efficient sub 100 nm focusing of hard x rays. *Review of Scientific Instruments* **76**, 063709-1 - 063709-5 (2005).
69. Chang, C.H., MacDowell, A.A., Thompson, A.C., Padmore, H.A. & Patel, J.R. Grain orientation mapping of passivated aluminum interconnect lines by X-ray micro-diffraction. *AIP Conference Proceedings* **449**, 424 - 426 (1998).
70. Arndt, U.W., Long, J.V.P. & Duncumb, P. A microfocus x-ray tube used with focusing collimators. *Journal of Applied Crystallography* **31**, 936 - 944 (1997).
71. Sibieude, F., Rodriguez, J. & Clavaguera-Mora, M.T. Kinetics and crystallization studies by in situ x-ray diffraction of the oxidation of chemically vapour deposited SiC. *Thin Solid Films* **204**, 217 - 227 (1991).
72. Taguchi, T. A new position sensitive area detector for high-speed and high-sensitivity X-ray diffraction analysis. *Powder Diffraction* **21**, 97 - 101 (2006).
73. Rodriguez-Navarro, A.B. XRD2DScan. New software for polycrystalline materials characterization using two-dimensional x-ray diffraction. *Journal of Applied Crystallography* **39**, 905 - 909 (2007).
74. Rajiv, P., Hinrichsen, B., Dinnebier, R., Jansen, M. & Joswig, M. Automatic calibration of powder diffraction experiments using two-dimensional detectors. *Powder Diffraction* **22**, 3 - 19 (2007).
75. Dinnebier, R.E. & Billinge, S.J.L. *Powder Diffraction: Theory and Practice*, (Royal Society of Chemistry, Cambridge, 2008).
76. Klug, H.P. & Alexander, L.A. *X-ray Diffraction Procedures for Polycrystalline and Amorphous Materials*, 716 (John Wiley & Sons Inc., New York, 1954).
77. Cheary, R.W. & Coelho, A.A. Axial Divergence in a Conventional X-ray Powder Diffractometer. I. Theoretical Foundations. *Journal of Applied Crystallography* **31**, 851 - 861 (1998).
78. Cheary, R.W. & Coelho, A. A fundamental parameters approach to x-ray line-profile fitting. *Journal of Applied Crystallography* **25**, 109 - 121 (1992).
79. Cheary, R.W. & Coelho, A. Axial Divergence in a Conventional X-ray Powder Diffraction. II. Realization and Evaluation in a Fundamental-Parameter Profile Fitting Procedure. *Journal of Applied Crystallography* **31**, 862 - 868 (1998).
80. Cheary, R.W., Coelho, A.A. & Cline, J.P. Fundamental Parameters Line Profile Fitting in Laboratory Diffractometers. *Journal of Research of the National Bureau of Standards and Technology* **109**, 1 - 25 (2004).
81. Scherrer, P. Bestimmung der Größe und der inneren Struktur von Kolloidteilchen mittels Röntgenstrahlen. *Nachrichten von der Gesellschaft der Wissenschaften zu Göttingen* **2**, 98 - 100 (1918).
82. Alexander, L. The Synthesis of X-Ray Spectrometer Line Profiles with Application to Crystallite Size Measurements. *Journal of Applied Physics* **25**, 155 - 161 (1954).
83. Sitepu, H. In situ structural and texture analyses of monoclinic phase for polycrystalline Ni-rich $\text{Ti}_{49.86}\text{Ni}_{50.14}$ alloy from neutron diffraction data. *Powder Diffraction* **23**, 35 - 40 (2008).
84. Honkimäki, V. Profile Function of Bragg Reflections in Powder Diffraction. *Journal of Applied Crystallography* **29**, 625 - 631 (1996).
85. Varn, D.P. & Canright, G.S. The crystal problem for polytypes. *Acta Crystallographica A* **A57**, 4 - 19 (2001).
86. Feng, Z.C. *SiC Power Materials. Devices and Applications*, 450 (Springer Verlag, Berlin, 2004).
87. Choyke, W.J., Matsunami, H. & Pensl, G. *Silicon Carbide. Recent Major Advances*, 899 (Springer Verlag, Berlin, 2004).
88. Hernandez-Jimenez, A., Ortiz, A.L., Sanchez-Bajo, F. & Cumbre, F.L. A simple, accurate and effective polymorphic method to determine phase compositions of SiC-based ceramics. *Journal of the European Ceramic Society* **24**, 2885 - 2894 (2004).
89. Hernandez-Jimenez, A., Ortiz, A.L., Sanchez-Bajo, F., Guiberteau, F. & Cumbre, F.L. Determination of Lattice Parameters of Polytypes in Liquid-Phase-Sintered SiC Using the Rietveld Method. *Journal of the American Ceramic Society* **87**, 943 - 949 (2004).
90. Ortiz, A.L. et al. Quantitative Phase-Composition Analysis of Liquid-Phase-Sintered Silicon Carbide Using the Rietveld Method. *Journal of the American Ceramic Society* **83**, 2282 - 2286 (2000).

91. Ortiz, A.L., Sanchez-Bajo, F. & Cumbreira, F.L. X-Ray Powder Diffraction Analysis of Liquid-Phase-Sintered Silicon Carbide Ceramics. *Key Engineering Materials* **206 - 213**, 723 - 726 (2002).
92. Ortiz, A.L., Sanchez-Bajo, F., Pature, N.P., Cumbreira, F.L. & Guiberteau, F. Quantitative polytype-composition analyses of SiC using X-ray diffraction: a critical comparison between the polymorphic and the Rietveld methods. *Journal of the European Ceramic Society* **21**, 1237 - 1248 (2001).
93. Andrikopoulos, K.S., Daniilia, S., Roussel, B. & Janssens, K. In vitro validation of a mobile Raman-XRF micro-analytical instrument's capabilities on the diagnosis of Byzantine icons. *Journal of Raman Spectroscopy* **37**, 1026 - 1034 (2006).
94. Ramos, P.M. Universitat Rovira i Virgili (2006).
95. Van der Snickt, G., De Nolf, W., Vekemans, B. & Janssens, K. μ -XRF/ μ -RS vs. SR μ -XRD for pigment identification in illuminated manuscripts. *Applied Physics A* **92**, 59 - 68 (2008).
96. Zieba-Palus, J. & Borusiewicz, R. Examination of multilayer paint coats by the use of infrared, Raman and XRF spectroscopy for forensic purposes. *Journal of Molecular Structure* **792 - 793**, 286 - 292 (2006).
97. Zieba-Palus, J., Borusiewicz, R. & Kunicki, M. PRAXIS - combined μ -Raman and μ -XRF spectrometers in the examination of forensic samples. *Forensic Science International* **175**, 1 - 10 (2008).

Chapter 01

Chapter 02

Chapter 03

Chapter 04

Chapter 05

Chapter 06

Chapter 07

Chapter 08

Chapter 09

Chapter 10

Chapter 11

Chapter 12

TRIBOLOGICAL AND HYDROTHERMAL BEHAVIOUR OF SILICON CARBIDE UNDER WATER LUBRICATION

V. Presser⁽¹⁾, O. Krummhauser⁽²⁾, K. G. Nickel⁽¹⁾,
A. Kailer⁽²⁾, C. Berthold⁽¹⁾, C. Raisch⁽³⁾

⁽¹⁾ Institut für Geowissenschaften, Universität Tübingen

⁽²⁾ Fraunhofer Institut für Werkstoffmechanik, Freiburg

⁽³⁾ Institut für Physikalische & Theoretische Chemie, Universität Tübingen

ABSTRACT:

In this study the tribological and hydrothermal behaviour of silicon carbide was examined. No significant reaction layer was found after tribochemical experiments conducted on sintered silicon carbide (SSiC) and after hydrothermal treatment using a hydrothermal diamond anvil cell (HDAC). Mechanical contact of sliding parts induced superficial amorphisation and chemical analysis showed a slight increase in oxygen content within the topmost part of the surface. Static experiments using single-crystal silicon carbide (SCSiC) and a hydrothermal diamond anvil cell revealed an active oxidation mechanism and silica as the result of solution and precipitation.

1. INTRODUCTION

Sintered silicon carbide (SSiC) ceramics are widely used for applications in severe chemical and high-temperature environments. The very high corrosion and wear resistance, the special mechanical properties and also the low friction coefficient (< 0.1) in sliding applications in aqueous media explain why SiC is ideally suited as a material in face seals.

On the sliding surfaces a chemical reaction of silicon carbide and water takes place.¹ Tribochemical reactions as described in literature are believed to explain the advantageous behaviour of SSiC in aqueous media lubricated sliding applications.

Wear models considering mechanical and chemical wear are primarily based on the work of T. F. J. Quinn in which he predominantly discussed tribooxidation of metals.²⁻⁵ These models basically comprise the heat development in rubbing rough surfaces and “hot spots” with temperature augmentation up to 1000°C. Oxidation occurs in these contact areas with high temperatures. In 2000, Xu and Kato expanded this model for oxidative wear of ceramic materials.¹

The formation of tribochemical layers depends on both thermodynamical and mechanical parameters. Self mated SiC face seals undergo tribochemical polishing of the surfaces in conditions of boundary lubrication in water.⁶ Due to very low wear rates in water lubricated sliding contacts of silicon carbide, a semi-continuous model-based-approach to determine the wear characteristics in initial tribological exposure is performed. Oxidation and degradation of silicon carbide may occur under very high loading and poor lubrication conditions. Elevated temperatures certainly increase the rate of oxidation, the role of high-pressure however is not clear.

Calculating temperature and pressure based on micromechanical effects between rubbing surfaces can be achieved using a micro asperity based model approach.⁷ Input data for the calculation are received with stylus profilometry, thus having the advantage of real geometric surface data with a lateral resolution of 2 μm and the possibility to create localised temperature maps.

Based on calculated results, hydrothermal and tribological experiments were conducted and compared. Our approach comprises static (hydrothermal) and dynamic (tribological) conditions of chemical degradation of silicon carbide in aqueous environments. The relations between tribological and hydrothermal corrosion of SiC are not well understood yet. A combined tribological-hydrothermal corrosion model should be beneficial for the improvement of lifetime prediction and security of ceramic face seals.

The scope of the present work is, therefore, to qualify the tribological behaviour in terms of the corrosion behaviour under different loading cases. Static corrosion experiments under high temperatures and pressures were conducted to determine the parallels in the (tribo)chemical behaviour to hydrothermal oxidation of silicon carbide. In the present paper, first results of this project are presented: (1) tribological experiments, (2) corrosion experiments using a diamond anvil cell, and (3) comparison and discussion of results.

2. EXPERIMENTAL PROCEDURE

2.1 Characteristics of used material

2.1.1 Sintered silicon carbide (SSiC)

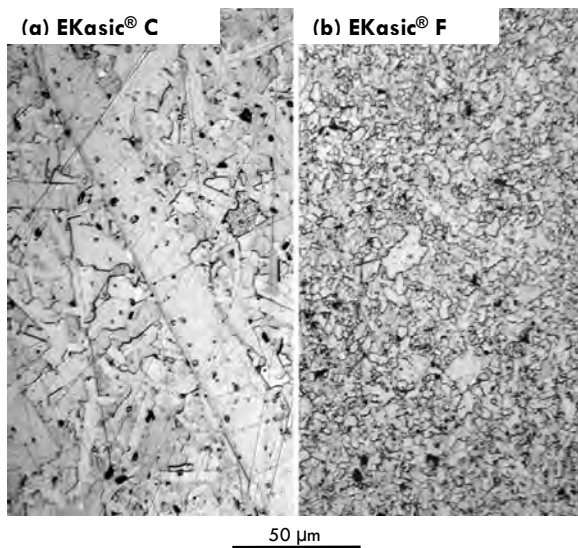


Fig. 1. Optical microphotographs of etched surfaces of (a) EKasic® C and (b) F.

SiC sliding ring samples were obtained from ESK Ceramics GmbH & Co. KG (Kempten, Germany). Two different types of sintered silicon carbide (SSiC) materials were used in tribological investigations. The first material was a fine grained EKasic® F with a tight grain size distribution around 5 μm and the second was EKasic® C which showed a bimodal grain size distribution with large needle-like crystals up to 1500 μm in a fine grained matrix with grains of about 10 μm (Fig.1). This different grain size distribution is the major difference between those two materials, while polytype distribution (≈ 80 wt% 6H-SiC, ≈ 20 wt% 4H-SiC + 15R-SiC) and chemical composition (additions of boron carbide as sintering aid) are both very similar.

The sliding surfaces of the sliding ring samples were lapped into a defined roughness and the characterisation of physical surface parameters was carried out with a Hommel T 8000 s profilometer

(Hommel GmbH, Köln, Germany). This apparatus is capable of measuring topographies down to a micro-scale level. The numerical values of the initial roughness parameters from these studies are shown in Table 1.

Material	R _z (μm)	R _a (μm)
EKasic® C	2.77	0.79
EKasic® F	1.25	0.52

Tab. 1. Initial roughness parameters of used samples.

2.1.2 Single-crystal silicon carbide (SCSiC)

Commercially available, undoped 6H-SiC single crystal plates (SiCrystal AG, Erlangen, Germany) were ground to a thickness of 100 μm, polished with 1 μm diamond paste and cut into small cuboids of approximately 240 x 240 x 100 μm³. This way, reproducible volumes of ≈ 6·10⁻³ mm³ (± 50%) with similar surface characteristics were obtained. Each sample was carefully cleaned in tridistilled water and acetone for 30 minutes using an ultrasonic bath to remove remnants of the polishing paste.

2.2 Experimental methodology

2.2.1 Tribometer

Figure 2 depicts the experimental setup for tribological tests. A static slide ring is attached to a torque meter while the applied load and the sliding velocity can be varied in wide ranges. As lubricant deionised water was used and the electrical conductivity was both monitored and kept below $0.09 \text{ S}\cdot\text{m}^{-1}$. During the experiment, the lubricant was applied with a pressure of 0.1 MPa between the friction couple. Also, the test apparatus provides the option for external cooling.

Two different tribological regimes were chosen: (1) a static mode (Fig. 2c) and (2) a dynamic mode (Fig. 2d). In order to determine the general running behaviour, static pressure conditions at 0.5 MPa , external cooling and a sliding velocity of $6 \text{ m}\cdot\text{s}^{-1}$ were chosen. In intervals of $\approx 2000 \text{ m}$ sliding distance the sample surfaces were measured with the stylus profilometer and numerically evaluated. Experiments in dynamic conditions were carried out in absence of external cooling and with a sliding velocity of $6 \text{ m}\cdot\text{s}^{-1}$. The abort criterion in case of scuffing was a measured torque of $2 \text{ N}\cdot\text{m}$.

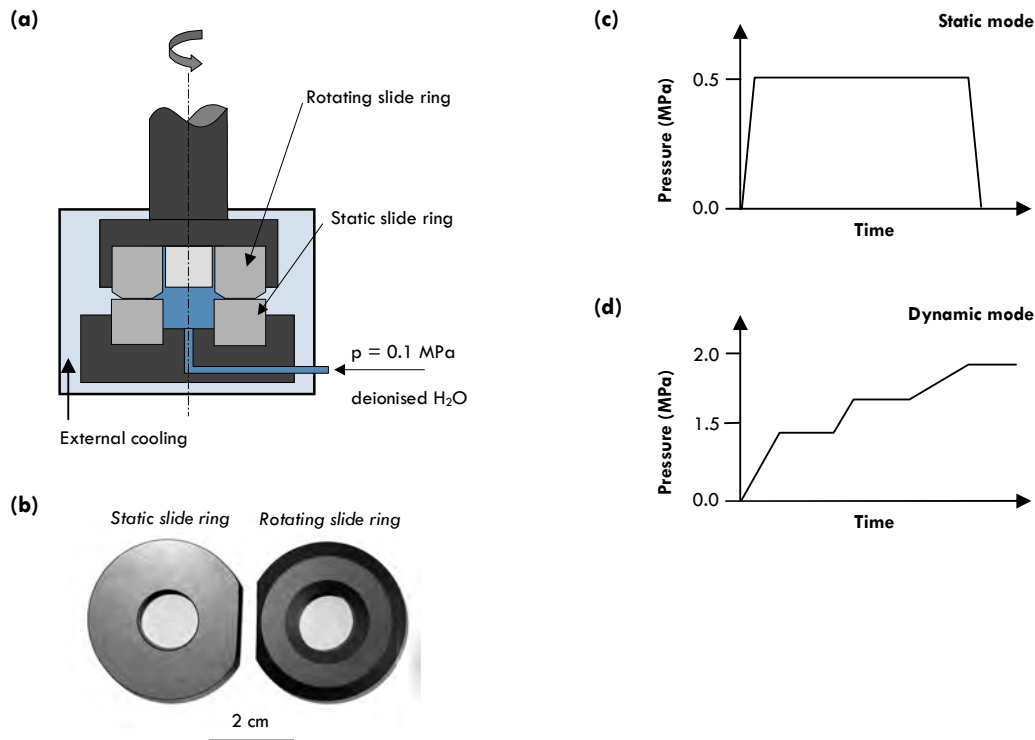


Fig. 2. Experimental setup (a), applied slide rings (b) and used run modes: static (c) and dynamic (d).

2.2.2 Hydrothermal Diamond Anvil Cell (HDAC)

Hydrothermal treatment of the single-crystal silicon carbide samples was carried out using a Bassett-type hydrothermal diamond anvil cell consisting of two opposing diamond anvils (0.25 ct) with nearly round polished faces (\varnothing 1 mm).^{8,9} The sample chamber (i.e., a boring hole within a 250 μm thick rhenium gasket with a diameter of 500 μm) was vertically sealed by diamond anvils (Fig. 3). These anvils are seated on ring like tungsten carbide mountings, allowing a visual inspection of the sample chamber's interior during the experiment. Around the WC mounting, a Mo-heating wire embedded in ceramic concrete was used as resistance furnaces.

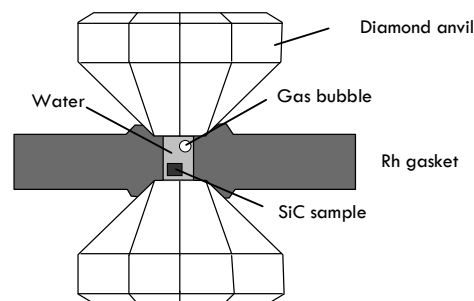


Fig. 3. Illustration of the HDAC's sample chamber.

As pressure mediating material, pure tridistilled water was used. Introducing a small gas bubble within the isochoric gasket chamber, the exact density of the homogenised fluid was calculated using equations of state (EOS) of pure water.^{10,11} Knowing the exact homogenisation temperature, it was possible to obtain the pressure information P at every temperature T along isochoric lines. For more information on HDAC operation see Ref. ¹².

The samples were heated up to 500°C with 20 K·min⁻¹. This final temperature was maintained \pm 1 K for 5 h and corresponds to a pressure of 500 – 770 MPa. Afterwards, the sample was cooled down to room temperature with the same gradient.

2.3 Analytical methods

For Scanning Electron Microscopy (SEM) a LEO VP 1450 instrument (Carl Zeiss AG, Oberkochen, Germany) was applied operating at 15 kV acceleration voltage. Equipped with an INCA Energy 300 system (Oxford Instruments, High Wycombe, Great Britain) for energy-dispersive X-ray spectroscopy (EDX), elements heavier than beryllium could reliably be detected. All samples were examined without the application of a sputter coating.

Raman spectroscopy was carried out using a Dilor Labram[®] 2 (Horiba Jobin Yvon GmbH, München, Germany; 1800 groves·mm⁻¹) and an Ar⁺-ion-laser (Innova Series 70; Coherent GmbH, Dieburg, Germany) operating at 488.0 and 514.5 nm and 12.0 \pm 0.3 mW output power on the sample's surface. Using a 50x magnifying objective lens (numeric aperture NA = 0.55), the resulting lateral resolution was < 2 μm .

X-Ray Diffraction (XRD) examination was done using a Bruker D8 Advance Microdiffractometer (Bruker AXS GmbH, Karlsruhe, Germany) with Co K α radiation, an area sensitive Hi-Star detector (GADDS) and monocrapillary optics ($\varnothing_{\text{beam}} \approx$ 300 μm ; Institute for Scientific Instruments GmbH, Berlin, Germany).

X-ray photoelectron spectra were recorded via an Omicron EA125HR electron energy analyser (Omicron NanoTechnology GmbH, Taunusstein, Germany) using Al K α radiation (1486.6 eV; XR 50 X-ray tube manufactured by SPECS GmbH, Berlin, Germany) in Constant Analyser Energy (CAE) mode with a pass energy of 50 eV. Increased surface sensitivity was achieved using a tilting angle of 60°.

Measurements of lubricants were performed with a Platform ICP-MS Micromass Ltd. (Manchester, United Kingdom) using - 2 V operating bias and a gas flow rate of 4.1 ml·min⁻¹ (H₂-He).

Glow-discharge optical emission spectrometry (GDOES) as a tool for combined sputtering and atomic emission to determine element depth profiling was carried out using the GD Profiler HR RF-GDOES system from Horiba Jobin Yvon (München, Germany).

3. RESULTS AND DISCUSSION

3.1 Wear test

Table 2 provides an overview about the conditions of wear tests.

Friction couple	Load condition	External cooling
EKasic® F / EKasic® F	dynamic	no
EKasic® C / EKasic® C	dynamic	no
EKasic® C / EKasic® C	static	yes
EKasic® C / EKasic® C	static	no

Tab. 2. Test conditions used in tribological experiments.

To determine the maximum tolerance of both materials, experiments were conducted without external cooling in dynamic load conditions. Each material was equipped with a blind hole (\varnothing 2 mm, depth 8 mm) 3 mm below the surface, in which a thermocouple was inserted in order to allow temperature recording near the rubbing surfaces during the experiment. The gap between the thermocouple and the material was bypassed by placing-in a heat conductive paste.

After a short period of time both silicon carbide varieties reached a high level of friction (Fig. 4). In particular, the coarse variety of silicon carbide showed a favourable behaviour against poor lubricated friction conditions in comparison to the fine variety. The abort criterion of 2 N·m torque was reached with the fine type of silicon carbide after 10 minutes test time, while the coarse type lasted 30 minutes until the experiment was automatically stopped. With the rise of friction coefficients a dramatic temperature gain up to 300°C occurred simultaneously.

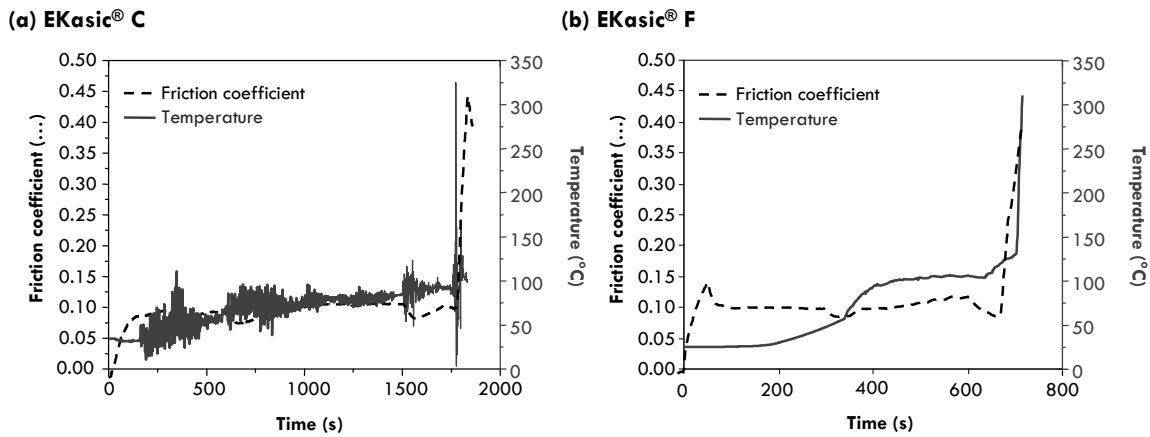


Fig. 4. Monitored friction coefficient and temperature of (a) EKasic® C and (b) F tribotests.

To determine the tribological behaviour during the initial lifetime of a slide ring seal, experiments in static conditions with applied load intervals as shown in Figure 2c were conducted. All interval experiments were performed with external cooling. Every 30 minutes the experiments were stopped (≈ 2000 m wear distance) and the resulting tribologically influenced surfaces were examined. The development of friction coefficient vs. experiment time and the resulting surface morphologies are shown in Figure 5a. Each morphology picture has a lateral scale of 2 mm.

After an initial phase with oscillating friction coefficients in the range of 0.06 (“run-in”, Fig. 5), the tribologically exposed surface undergoes a smoothing process (Fig. 5b). The sliding behaviour stabilises after 2000 meters sliding distance and the roughness values decrease from unused to the 2000 m worn case about $1.2 \mu\text{m}$ (R_z). In the further progress of the experiment, the decrement of roughness values retards. As a result of smoothing the friction coefficient decreases to values of ≈ 0.10 .

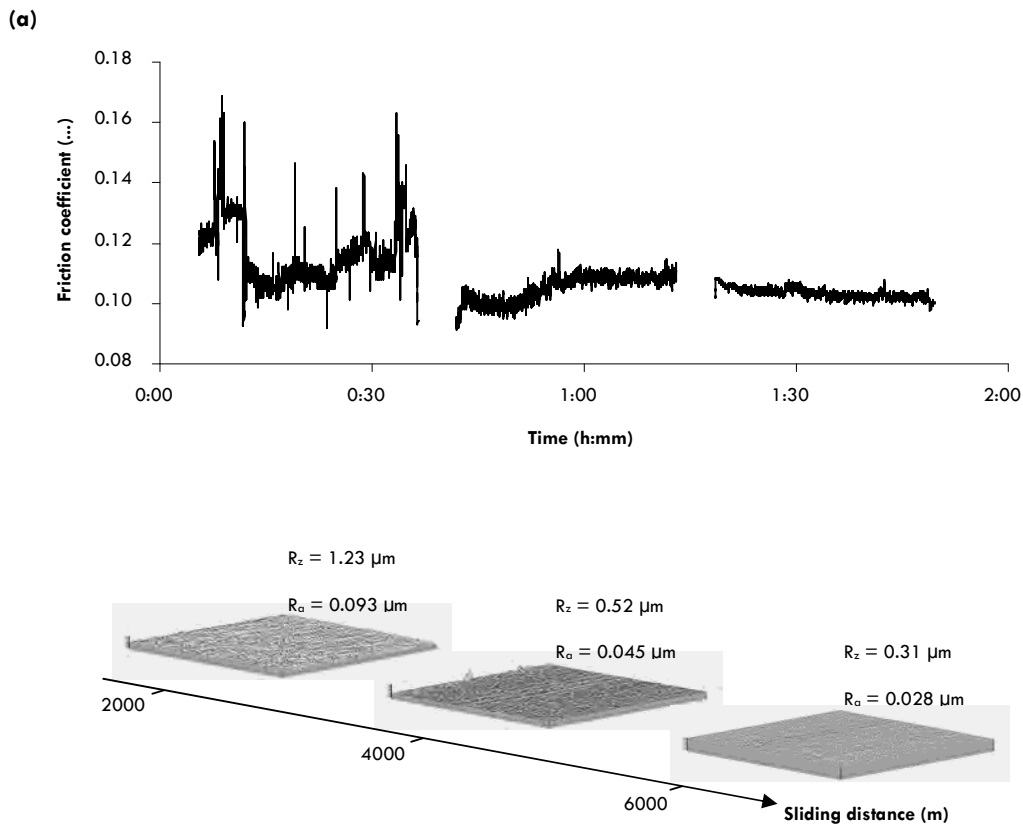


Fig. 5. Development of the tribologically influenced surface of EKasic® C.

A special set of experiments aiming for the quantification of tribochemical wear was carried out with EKasic® C slide ring seals without external cooling in static conditions. In those experiments the lubricant was sampled to determine the dissolved silicon. The pressure conditions were estimated in preliminary tests and chosen at 0.6 MPa and 1.1 MPa (Fig. 6).

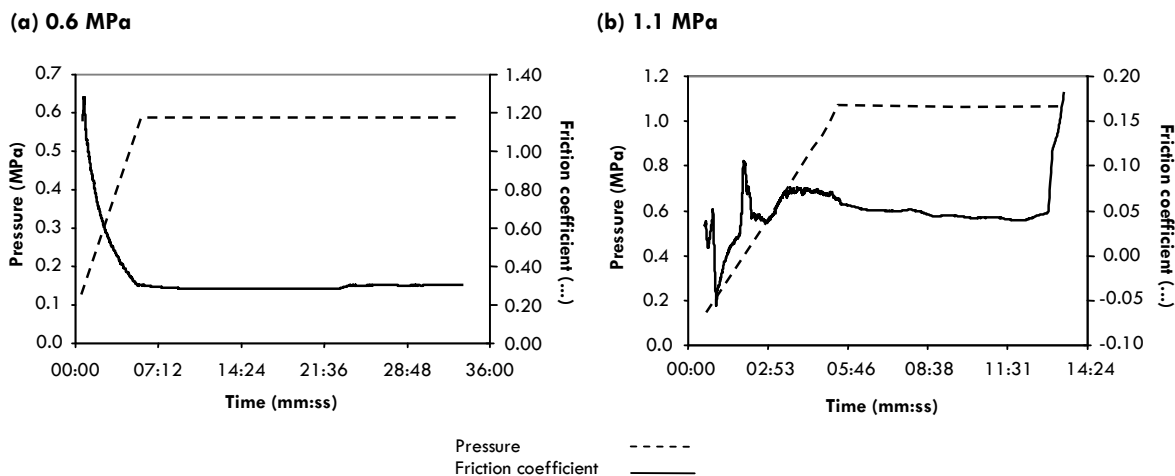


Fig. 6. Friction and pressure conditions in static experiments without external cooling at 0.6 (a) and 1.1 MPa (b) contact pressure (EKasic[®] F).

Samples of lubricating water were collected at the beginning, in the middle and at the end of the experiment. After 14 minutes the experiment conducted with 1 MPa pressure was terminated due to the reach of the abort criterion of 2 N·m measured torque. The water samples were analysed with ICP-MS (detection limit d. l. = 10.9 ppb) for their silicon content, the results are shown in Tab. 3.

Sample	0.5 MPa	1 MPa
<i>Start</i>	< d. l.	< d. l.
<i>Middle</i>	< d. l.	98.7
<i>End</i>	46.1	111.6

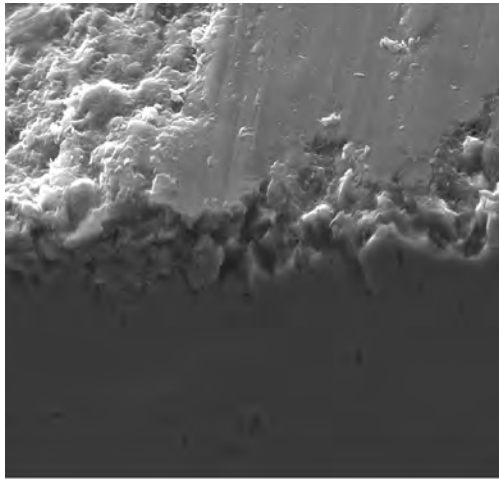
Tab. 3. ICP-MS results of Si-content in lubricating water in $\mu\text{g}\cdot\text{l}^{-1}$ (d. l. = detection limit) for EKasic[®] C in static mode condition.

3.2 Analytical examination of tribologically exposed surfaces

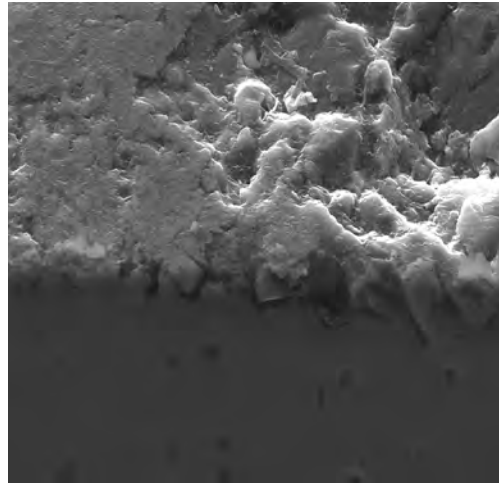
3.2.1 SEM and EDX

As seen in Fig. 7, the mixed regime tribologically influenced sample surfaces show a different characteristic than the samples worn under cooled conditions. A massive distortion of the surface was detected and the corresponding EDX sampling depth was in the range of 5 - 10 μm . On some parts of the samples' surfaces, smoothed regions could be found which were elevated in comparison to the rest of the surface. At these positions, direct mechanical contact of the two sliding parts took place inducing strain.

(a) EKasic® C



(b) EKasic® F



20 μm

Fig. 7. Tribologically exposed surfaces of both studied SSiC varieties (SE-mode SEM images).

EDX analysis of the samples' surfaces showed an oxygen content of 3 - 8 wt%. This significant oxygen concentration is limited to the very superficial region as shown in Fig. 8. The absolute values shown in Fig. 8 indicating oxygen present even in depths as large as some micrometer must be evaluated very carefully due to the large volume excited by the electron beam. In comparison, the initial oxygen content of EKasic® C and F was in the range of < 1 wt%.

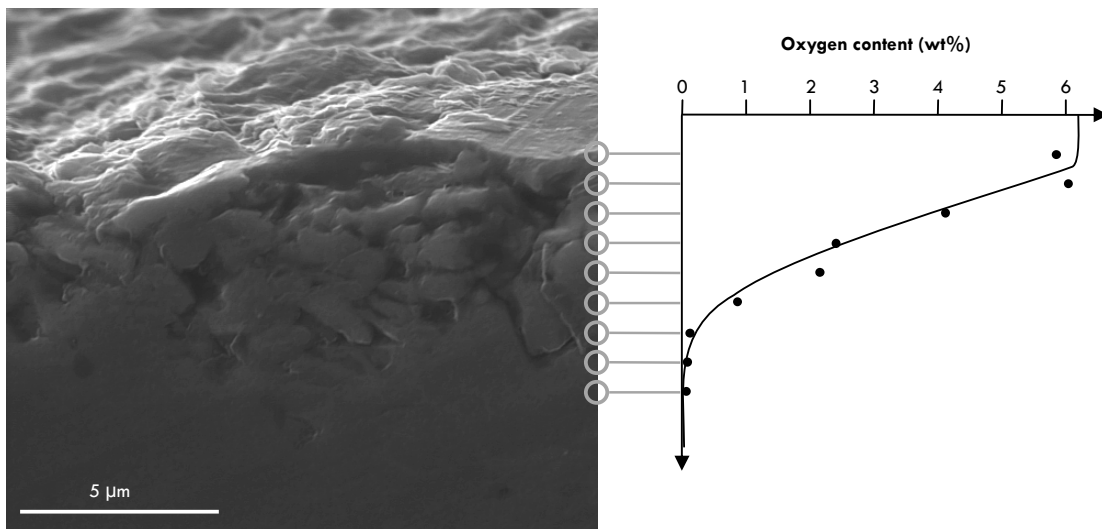


Fig. 8. SE-mode SEM image and EDX analysis of oxygen content along EKasic® C cross section.

The scale bar is only valid for the vertical cut section.

3.2.2 XRD

XRD was performed in order to determine possible reaction products. The obtained diffraction patterns evidenced the polycrystalline texture that comprises several different SiC-polytypes. Neither at 10° incident angle nor at grazing incident was any additional phase besides the various SiC-polytypes found. Although XRD is generally limited to the detection of crystalline phases, also no evidence of an amorphous phase (as potentially shown in form of an amorphous halo) could be found.

In order to obtain more surface sensitive information about the tribologically influenced samples, grazing incident measurements at 1° were performed. These clearly showed a significant broadening of the individual (hkl)-reflections due to nanoscale crystallite sizes and / or lattice strain (cf. Fig. 9).

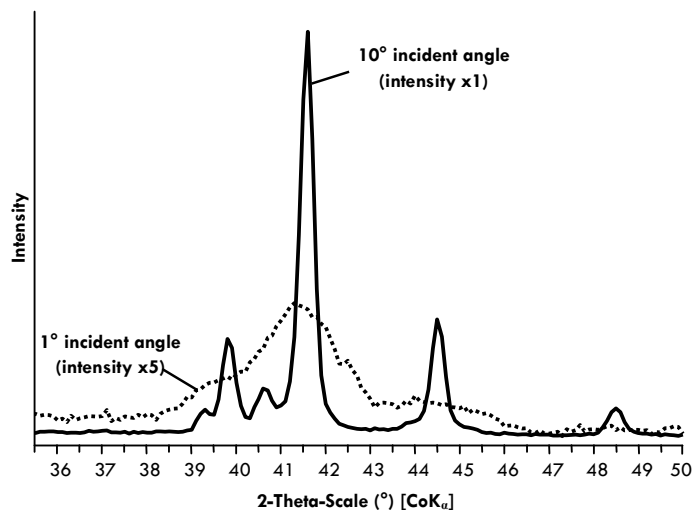


Fig. 9. X-ray diffractograms of tribologically treated SSiC (EKasic® F).

3.2.3 Raman spectroscopy

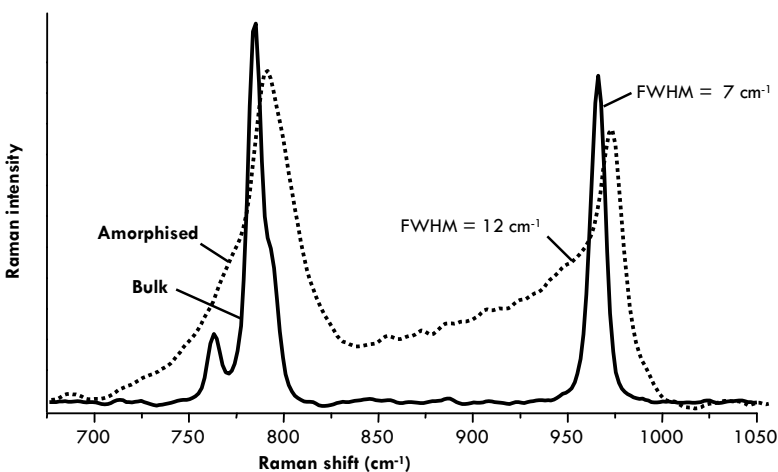


Fig. 10. Raman spectra comparing tribologically treated with untreated SSiC ($\lambda = 488.0$ nm; EKasic® F).

No additional phase was found via Raman spectroscopy on tribologically exposed surfaces compared to the bulk material. Neither any form of silica (amorphous or crystalline) nor any oxycarbide phase could be found, hence excluding the existence of such a phase within the resolution limit of this method (i.e., $\approx 0.5 - 1.0$ μm). However, the flattened areas showed strongly broadened SiC bands (Fig. 10), indicating superficial amorphisation due to mechanical stress.¹³

3.2.4 XPS

XPS measurements of bulk SSiC showed the presence of Si and C as main elements and minor amounts of oxygen and boron (latter originates from the sintering aid boron carbide). Compared to that, SSiC surfaces after tribological treatment show no longer the boron-related signal peak at ≈ 190 eV (cf. Fig. 11). This indicates a superficially limited leaching of boron within the topmost 5 - 7 nm, because B was still found via EDX, which is a less surface sensitive method.

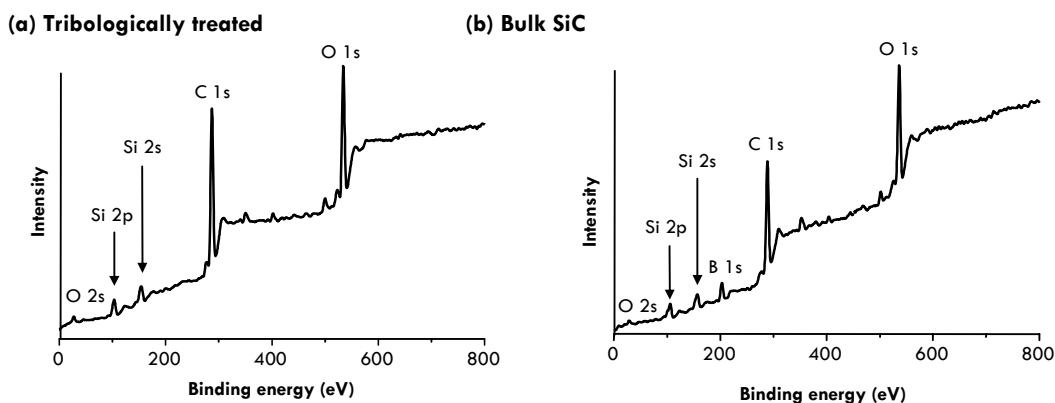


Fig. 11. Wide-scan XPS spectra of (a) tribologically treated and (b) bulk SSiC (EKasic® F).

The detection of carbon, however, cannot be seen as a proxy for SiC presence as C may well be correlated with adsorbed CO or contaminations. Discrimination between SiC and SiO₂ (both times Si is present as Si⁴⁺) can be done by evaluating the Si 2p photoelectron spectra as due to the different chemical environment the measured bonding energy of Si-C and Si-O₂ are also different. Slight differences, however, were found comparing the tribologically influenced surface with bulk SiC: the SiC-related Si 2p peak is slightly broadened compared to bulk SiC. This may well indicate amorphisation or at least some differences in the chemical environment.

Even with grazing incident measurements all tribologically exposed surfaces showed the presence of C. Due to the high superficial sensitivity these findings exclude the presence of a silica layer thicker than ≈ 7 nm covering the entire SSiC surface. Only a very thin layer of pure silica may be found before and after tribological treatment. The same would be true for single-crystal SiC which was exposed to air for several hours. Its presence is no direct evidence for any reaction layer in a tribological sense.

3.2.5 GDOES

Glow-discharge optical emission spectrometry was used to gain information about the depth profile concentration of various elements of the tribochemically exposed surfaces (Fig. 12). The measured spot on the sample's surface had a diameter of ≈ 4 mm. Especially the increased concentration of oxygen and hydrogen on the topmost part is notable. Approximately 200 nm deeper inside the material no significant amount of neither O nor H was detected. It is difficult to give the error of the absolute depth values as we dealt with uneven surfaces but combined with results from Raman and XPS a reaction layer of < 200 nm seems to be reasonable at this point.

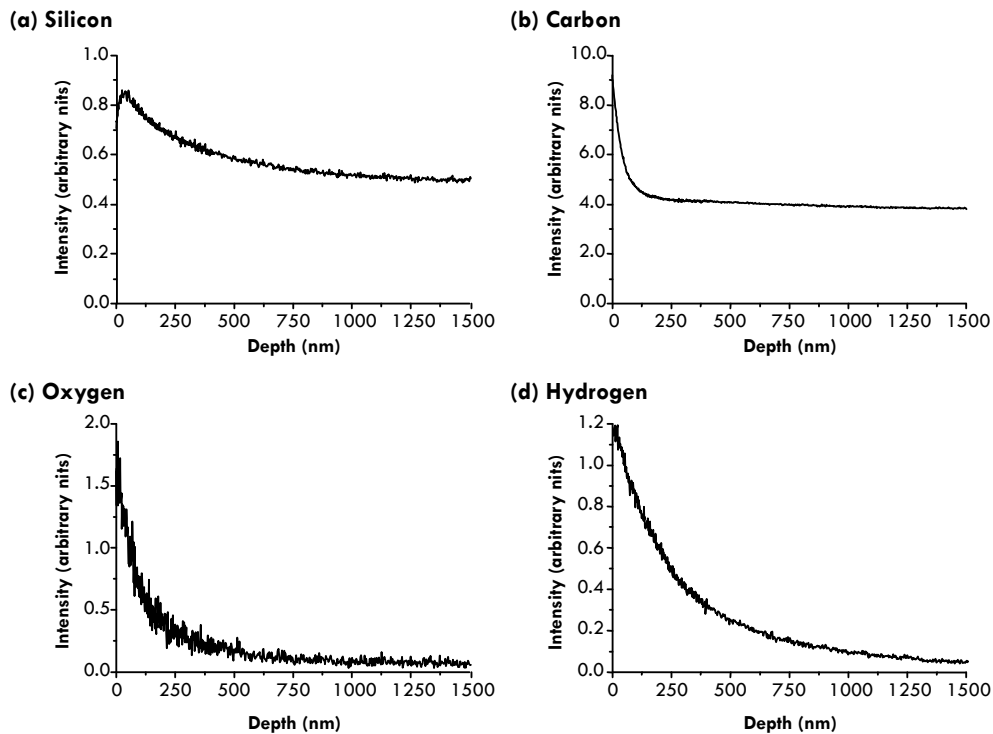


Fig. 12. GDOES element depth profiles as found in tribologically treated EKasic® F.

3.3 HDAC experiments

3.3.1 Optical microscopy

In-situ monitoring of the HDAC's sample chamber revealed that hydrothermal treatment lead to darkening of the transparent sample, indicating increased roughness. After hydrothermal exposure, gas bubbles readily appeared during cooling already at 350 - 400°C, which cannot be related to dehomogenisation of pure water and a water-saturated liquid. Latter would be expected to happen at temperatures $\ll 200^\circ\text{C}$ as indicated from the homogenisation temperature during heating. It was also found that higher SiC-to-H₂O-ratios correlate with higher dehomogenisation temperatures. The separating gas phase is probably a carbonaceous species originating from the hydrothermal decomposition of silicon carbide.

3.3.2 SEM and EDX

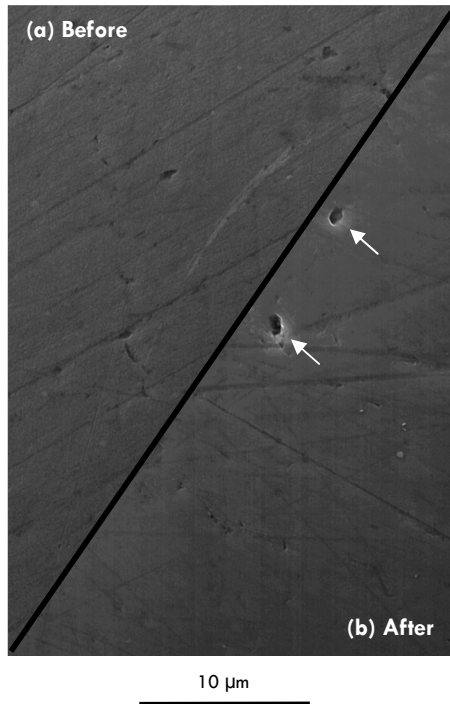


Fig. 13. SE-mode SEM image of the 6H-SiC wafer's surface (a) before and (b) after hydrothermal treatment.

After hydrothermal treatment, the SiC samples showed a significant roughening. Fig. 13 depicts a comparison between the same sample before (Fig. 13a) and after (Fig. 13b) the treatment (SE-mode SEM microphotographs). Small scratches and superficial imperfections are due to the mechanical polishing procedure. Arrows indicate hydrothermally induced pitting.

The observation of higher surface roughness after hydrothermal treatment is in agreement with the findings by Barringer et al.¹⁴ who conducted corrosive experiments on CVD SiC. In our experiments, analysing the weight change of the sample material was not possible but considering the significant change in surface morphology, a bulk weight loss is conclusive. This is corroborated by the observation of gas formation via the corrosive mechanism as seen *in-situ*.

On top of the diamond anvils and on the samples' surfaces, flakes of a white powder with typical particle sizes $\ll 1 \mu\text{m}$ were found in many places. These flakes are loosely attached to the substrate and, therefore, interpreted to be precipitates. On one sample this phase formed a non-uniform lawn beginning at the sample's edges. Thus the solution and re-precipitation of silica in the hydrothermal fluid is the most likely origin of this phase shown in the SEM-microphotographs in Figure 14.

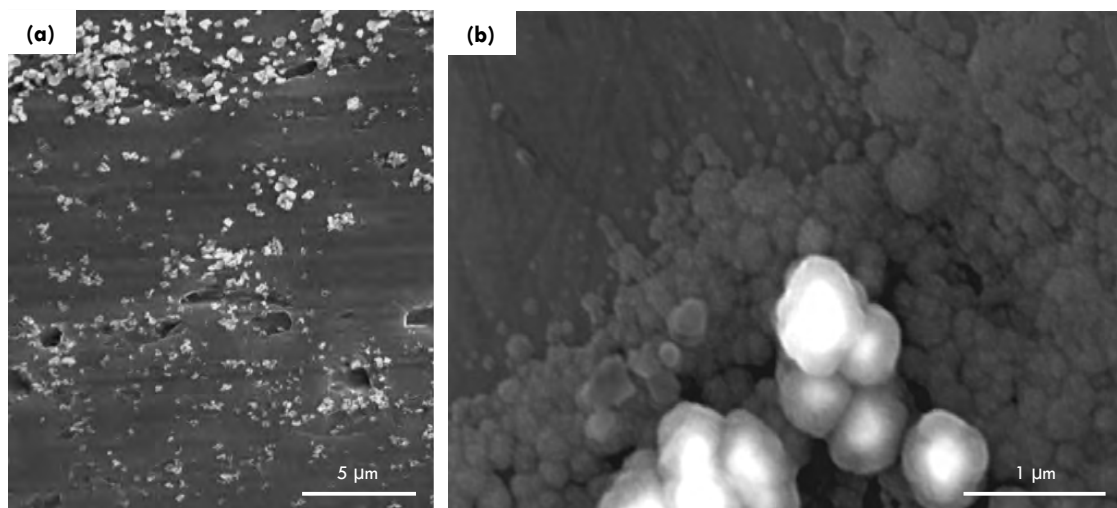


Fig. 14. Precipitated phase on hydrothermally treated SCSiC samples (6H-SiC wafer).

In EDX measurements several weight percent oxygen and a decrease in carbon concentration was detected in the flaked areas, while no oxygen content could be detected in those areas which were not covered. We take this as a strong evidencing for a silica-like composition of the flakes.

3.3.3 Raman spectroscopy

As shown in Fig. 15, Raman spectroscopy of the original and hydrothermally treated samples showed no additional Raman-active modes. Excess carbon, to which detection Raman spectroscopy is especially sensitive, would have yielded peaks at ≈ 1335 and 1590 cm^{-1} (amorphous carbon; Ref.¹⁵) and free silicon would be detectable through a single peak at $\approx 520 \text{ cm}^{-1}$ (Ref.¹⁶). All peaks could be attributed to (0001)-6H-SiC.¹⁷ The surface roughening did not influence the Raman spectrum. As also seen in Fig. 15, no Raman signal indicating SiO_2 was found. Amorphous silica shows a characteristic strong mode at 440 cm^{-1} , α -quartz (an expected equilibrium phase) at 464 cm^{-1} and α -cristobalite (the dominant crystalline phase during dry thermal oxidation of silicon carbide) at 416 cm^{-1} .¹⁸⁻²⁰

Using different wavelengths (488.0 and 514.5 nm), no additional information could be gained. Each observed line of SiC was also found in the Anti-Stokes region; hence the false attribution to fluorescence peaks could be excluded. Besides the SiC samples, also the surfaces of the diamond anvils were examined. All anvils showed the same sparse coverage with the white powder as the silicon carbide surfaces, but no silica-related Raman lines could be detected. In particular, no Raman-active mode besides the T_{2g} -line of diamond occurred.

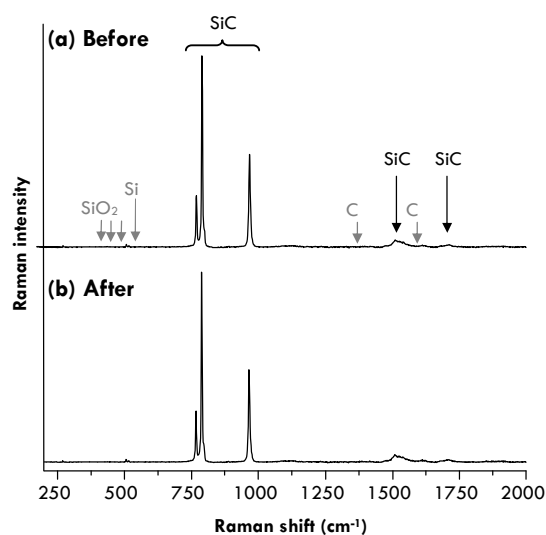


Fig. 15. Raman spectra (a) before and (b) after hydrothermal treatment ($\lambda = 514.5 \text{ nm}$; 6H-SiC wafer).

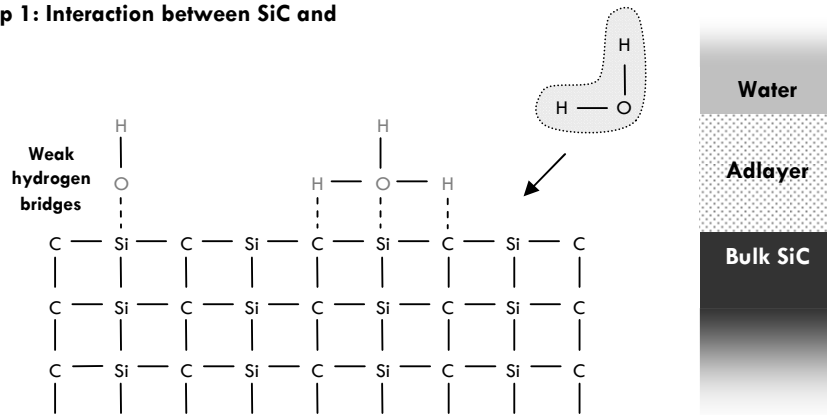
4. TRIBOCHEMICAL MODEL

Combining the findings of mechanically and chemically influenced surfaces, we propose a three-step mechanism for tribochemical wear of silicon carbide in aqueous media (cf. Fig. 16). At first, a bulk reaction between water and silicon carbide will happen. The kinetics are strongly affected by the ambient temperature. However even under room temperature the very surface of the SiC body will react with water, dangling bonds will be saturated and (OH)-groups will bond to the truncated surface. This reaction is dominated by weak hydrogen bridge bonds. It is important to keep in mind that this initial reaction will be limited to the very outer part of the surface, i.e., one / few monolayers.

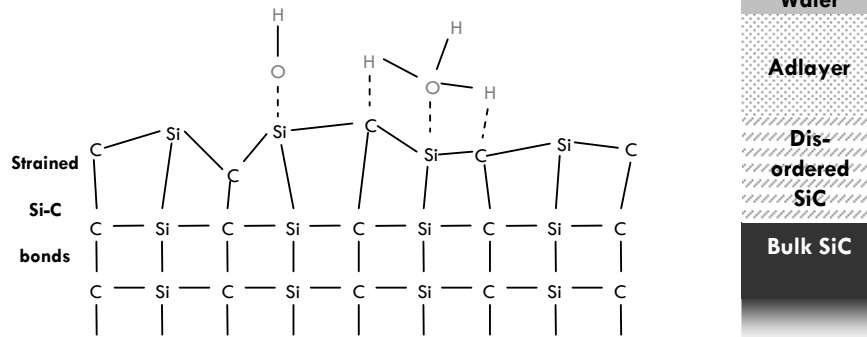
Mechanical stress causes superficial amorphisation and, therefore, disordered layers of partially hydroxylated silicon carbide can be found. It is trivial to assume that those layers with strained bonds are more susceptible to the attacking aqueous solution. Hence the formation of a reaction layer on top of unaffected crystalline silicon carbide can be expected. Also, mechanical contact of asperity peaks will drastically increase the temperature and enables tribochemical reaction to take place.

Simultaneously to this process, silica can readily be dissolved into the fluid phase. Combined with mechanical deterioration the overall thickness of the reaction layer will be limited to a sub-micrometer level. However, dissolution and re-precipitation of silica, as observed in the diamond anvil cell, is another competing mechanism which becomes especially important for low water-to-SiC ratios or (over)saturated fluids.

(a) Step 1: Interaction between SiC and H₂O



(b) Step 2: Amorphisation



(c) Step 3: Tribochemical corrosion

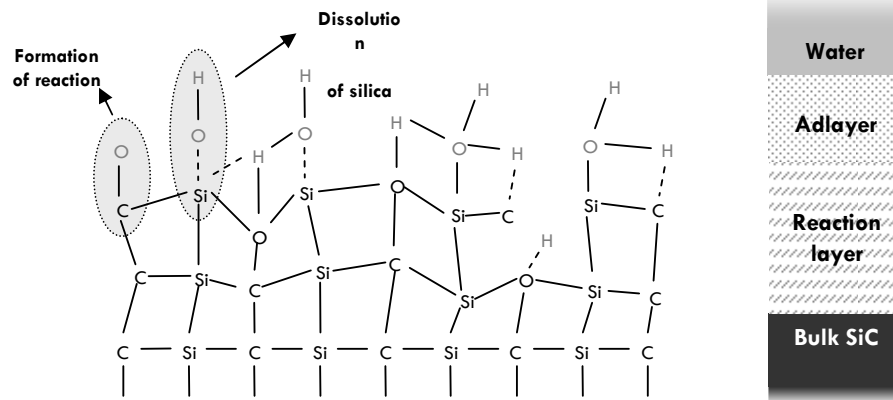


Fig. 16. Three-step tribomodel. For discussion see text.

The observed bubble formation in HDAC experiments may indicate another, cavitation-like wear mechanism. If the content of reaction gas becomes too high, the overcritical fluid will dehomogenise into two discrete phases. Boiling of the fluid phase and collapsing bubbles then may cause at least parts of the reaction layer to delaminate.

Typical silicon carbide materials for sliding applications in aqueous media are sintered ceramic bodies containing sintering additives like boron carbide and exhibiting grain boundaries. As discussed by Schwetz and Hassler (Ref. ²¹) preferential corrosion of sintering aids can be expected as well as coarsening of grain boundaries. In case of tribocorrosion whole grains may completely break out of the matrix and grain boundaries in general act as weak points for corrosive attack of hydrothermal water. We also observed these effects which will superimpose the described model of tribochemical wear.

5. CONCLUSION AND OUTLOOK

Tribochemical treatment of silicon carbide seal parts showed no significant oxide layer. Neither pure silica nor any oxycarbide phase was determined via XRD or Raman spectroscopy. However, both methods have a limited detection limit for scales thinner than ≈ 100 nm, especially when only amorphous phases are present. Increased superficial oxygen content may be due to oxygen incorporation into amorphised SiC. We have also noticed that mechanical contact leads to amorphisation of the topmost surface layer and any reaction layer's thickness should be thinner than ≈ 100 nm.

Static conditions as observed via HDAC experiments indicate bulk active corrosion. High-pressure, high-temperature water dissolves silica and carbon faster than SiO₂- or C-formation would take. The only silica-like phase found after the experiments was a product of solution and precipitation accompanied by heterogeneous nucleation while a superficial graphitisation can be excluded. For tribological application the extensive bubble formation observed in the HDAC may be important as well as silica precipitation.

Further work will focus on atomic scale investigation of bulk reaction product interfaces as tribologically and hydrothermally influenced samples will be prepared with a FIB (Focused Ion Beam) and analysed with Transmission Electron Microscopy (TEM). This way, more detailed information about the exact chemical composition and structure of SiC degradation products will be obtained.

ACKNOWLEDGEMENTS

This work was partially supported by the Deutsche Forschungsgemeinschaft (DFG) through Ho1149/92 and Ni299/12-1. The authors would like to thank ESK Ceramics GmbH & Co. KG (Kempten, Germany) for sample material and Burgmann Industries GmbH & Co. KG (Wolfratshausen, Germany) for sample machining. Also, N. Walker, B. Maier and I. Gill-Kopp from the workshop of the Institute for Geoscience (IFG) are thanked for preparing sub-millimeter samples of single-crystal SiC.

REFERENCES

1. Xu, J. & Kato, K. Formation of tribochemical layer of ceramics sliding in water and its role for low friction. *Wear* **245**, 61 - 75 (2000).
2. Quinn, T.F.J. Computational methods applied to oxidative wear. *Wear* **199**, 169 - 180 (1996).
3. Quinn, T.F.J. Oxidative wear. *Wear* **18**, 413 - 419 (1971).
4. Quinn, T.F.J. Oxidative wear modelling: I. *Wear* **153**, 179 - 200 (1992).
5. Quinn, T.F.J. Oxidative wear modelling: Part II. The general theory of oxidative wear. *Wear* **175**, 199 - 208 (1994).
6. zum Gahr, K.-H., Blattner, R., Hwang, D.-H. & Pöhlmann, K. Micro- and macro-tribological properties of SiC ceramics in sliding contact. *Wear* **250**, 299 - 310 (2001).
7. Zimmermann, M. *Experimentelle Untersuchung und numerische Modellierung des Gleitkontaktverhaltens von gesintertem Siliciumcarbid (SSiC)*, 102 (Universität Karlsruhe, Karlsruhe, 1998).
8. Bassett, W.A., Shen, A.H., Bucknum, M. & Chou, I.-M. Hydrothermal Studies in a New Diamond Anvil Cell up to 10 GPa and from -190°C to 1200°C. *PAGEOPH* **141**, 487 - 495 (1993).
9. Bassett, W.A., Shen, A.H., Bucknum, M. & Chou, I.-M. A new diamond anvil cell for hydrothermal studies to 2.5 GPa and from -190 to 1200°C. *Review of Scientific Instruments* **64**, 2340 - 2345 (1993).
10. Haselton, H.T., Chou, I.-M., Jr., Shen, A.H. & Bassett, W.A. Techniques for determining pressure in the hydrothermal diamond-anvil cell: Behaviour and identification of ice polymorphs (I, II, V, VI). *American Mineralogist* **80**, 1302 - 1306 (1995).
11. Shen, A.H., Bassett, W.A. & Chou, I.-M. Hydrothermal Studies in a Diamond Anvil Cell: Pressure Determination Using the Equation of State of H₂O. in *High-Pressure Research: Application to Earth and Planetary Sciences* (eds. Syono, Y. & Manghnani, M.H.) 61 - 68 (American Geophysical Union, Washington D.C., 1992).
12. Presser, V., Heiß, M. & Nickel, K.G. EOS calculations for hydrothermal diamond anvil cell operation. *Review of Scientific Instruments* **78**, 085104-1 - 085104-9 (2008).
13. Gogotsi, Y.G., Kailer, A. & Nickel, K.G. Phase transformations in materials studied by micro-Raman spectroscopy of indentations. *Materials Research Innovations* **1**, 3 - 9 (1997).
14. Barringer, E. et al. Corrosion of CVD Silicon Carbide in 500°C Supercritical Water. *Journal of the American Ceramic Society* **90**, 315 - 318 (2007).
15. Knight, D.S. & White, W.B. Characterization of diamond films by Raman spectroscopy. *Journal of Materials Research* **4**, 385 - 393 (1989).
16. Parker, J.H., Feldman, D.W. & Ashkin, M. Raman Scattering by Silicon and Germanium. *Physical Review* **155**, 712 - 714 (1967).
17. Nakashima, S. & Harima, H. Raman Investigation of SiC Polytypes. *Physica Status Solidi (A)* **162**, 39 - 64 (1997).
18. Hemley, R.J., Mao, H.K., Bell, P.M. & Mysen, B.O. Raman Spectroscopy of SiO₂ Glass at High Pressure. *Physical Review Letters* **57**, 747 - 750 (1986).
19. Kingma, K.J. & Hemley, R.J. Raman spectroscopic study of microcrystalline silica. *American Mineralogist*, 269 - 273 (1994).
20. Etchepare, J., Merian, M. & Kaplan, P. Vibrational normal modes of SiO₂. II. Cristobalite and tridymite. *Journal of Chemical Physics* **68**, 1531 - 1537 (1978).
21. Schwetz, K.A. & Hassler, J. Zur Beständigkeit von Hochleistungskeramiken gegen Flüssigkeitskorrosion. *Ceramic Forum International* **79**, D9 - D19 (2002).

Chapter 01

Chapter 02

Chapter 03

Chapter 04

Chapter 05

Chapter 06

Chapter 07

Chapter 08

Chapter 09

Chapter 10

Chapter 11

Chapter 12

A MODEL FOR WET SILICON CARBIDE TRIBO-CORROSION

V. Presser⁽¹⁾, K. G. Nickel⁽¹⁾,
O. Krummhauser⁽²⁾, A. Kailer⁽²⁾

⁽¹⁾ Institut für Geowissenschaften, Universität Tübingen
⁽²⁾ Fraunhofer Institut für Werkstoffmechanik, Freiburg

ABSTRACT:

Silicon carbide sustains chemical and mechanical deterioration during tribological exposure under water lubrication. In particular, tribochemical wear leads to the formation of a thin (tens to hundreds of nanometre) layer composed of nanoscale SiC wear debris embedded in a silica-like matrix (SiO_xH_y) with possibly some minor oxycarbide content. The SiC wear particles are plastically deformed and rounded as a result of mechanical tribolapping. Below that layer, subsurface damage builds up in the form of dislocations, ruptures and shear cracks. As a result of plastic deformation (similar to indentation plasticity) SiC single crystals within that transition zone are transformed into mosaic crystals with smaller domains due to slip plane gliding. Comparing results for static hydrothermal conditions (using a hydrothermal diamond anvil cell) and tribotest for the mild and severe wear regime (i.e., with and without external cooling) we derived a qualitative wear-model of wet silicon carbide tribo-corrosion. While mechanical contact yields pathways for water inflow and generally disrupts the structural integrity of SiC grains, hydrothermal reactions of trapped water and subsequent pressure relief leads to a mechanism of dissolution and reprecipitation. The latter produces the observed amount of SiO_xH_y which acts as an adhesive for the SiC wear debris.

1. INTRODUCTION

1.1 General aspects of wet SiC tribo-corrosion

Sintered silicon carbide (SiC) is a common ceramic material for extreme environments. Owing to SiC's pronounced chemical inertness and high-temperature stability no significant oxidation reaction is observed below 900°C under ambient pressure in oxygen or air. SiC is also known for its excellent wear resistance and, especially in case of sliding wear in aqueous media, a low friction coefficient. Therefore, silicon carbide ceramics are often employed as face seals.

Advanced ceramics like SiC are generally brittle, which often limits application due to potential premature device failure. Plastic deformation of SiC, observed in indentation experiments¹⁻⁴ (indentation plasticity), has frequently been reported for tribological exposure^{1,5,6}, but not for static compression experiments below $\approx 500^\circ\text{C}$ ⁷⁻¹². In general, tribochemical wear of SiC ceramics is subject to the following main deterioration mechanisms: (1) chemical reactions, (2) plastic deformation, (3) micro-crack formation, and (4) micro-abrasion^{5,6}. Each of these mechanisms is influenced by a large number of factors such as contact geometry, surface roughness, grain size, sliding speed, mode and amount of applied load, surface temperature / pressure, exposure duration, composition of the lubricant and so on¹³.

Erickson et al.⁶ differentiate between mild and severe wear regimes. The first was not reported to cause any formation of a chemically influenced tribolayer on top of the mechanically deteriorated SiC matrix. However, the role of such a tribochemical layer is most important for experiments conducted under water-lubrication¹⁴. Here, SiC shows a higher wear resistance and a lower friction coefficient than alumina, due to more pronounced surface smoothing^{5,15,16}. This was explained in terms of tribochemical wear producing a thin oxygen-rich layer comprising rounded SiC wear particles. Soft hydroxides cause SiC surfaces to show a self-lubricating behaviour¹⁷. Smoothened surfaces, in turn, are known to show the effect of hydrodynamic lubrication and this, combined with tribolayer formation, explains the low friction coefficient.

Fig. 1 shows schematically the simple model for the formation of a reaction layer for sliding ceramics under water lubrication as proposed by Xu and Kato¹⁸ based on the work of Quinn et al.¹⁹⁻²¹. In the contact zone between the two sliding SiC surfaces high local temperature and pressure conditions are prevailing on asperity peaks. Consequently, SiC reacts with water to form a silica or silica-like layer, which delaminates as a result of repeated mechanical contact. With time the sliding surfaces are, therefore, smoothed by a combined mechanism of wear debris formation and peak abrasion. Instead of a no-wear situation, as expected for perfect hydrodynamic lubrication on smooth surfaces, bulk abrasion and delamination dominate during the initial run-in phase.

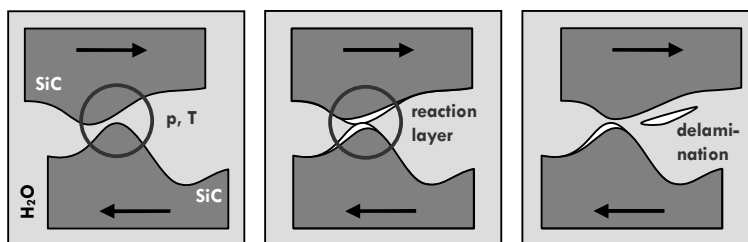
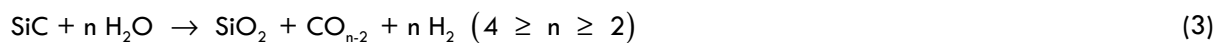


Fig. 1. Formation of a tribochemical layer schematically after Xu and Kato¹⁸.

Kitaoka et al.^{5,22} proposed the following tribochemical reactions for SiC based on the detection of H₂ and, at temperatures > 300°C, CO₂:



Or, more generally:



From static hydrothermal experiments on SiC it was reported that SiC becomes unstable shortly before the H₂O:SiC molar ratio reaches 2:1 while carbon destabilises shortly thereafter²³. Correspondingly, at intermediate temperatures (100 to 300°C and 200MPa) reaction (1) and a methane forming reaction become possible²⁴:



For wet wear of SiC we can assume a high H₂O:SiC molar ratio with an abundance of lubricating water. However, this may not be true for the entire sliding surface and trapped water, as will be discussed below, can become a key factor for understanding tribochemical wear.

In the tribochemical equations listed solid silica is always a reaction product of silicon carbide and high-temperature, high-pressure water along with gases (CO_x, CH₄, H₂). Increasing the H₂O:SiC molar ratio facilitates the formation of a pure carbon layer on hydrothermally treated silicon carbide surfaces due to high silica solubility²³⁻²⁶.



Solubility of silica strongly depends on the chosen p-T and pH conditions and is as low as several nm per year below 100°C at pH 7^{8,27,28}. At 285°C and 100 MPa, a silica solubility rate of ≈ 800 nm/h can be expected in distilled water²⁹ and there are even higher solubility rates for more extreme p-T regions³⁰. Considering that reported tribolayers on SiC range from μm to nm in thickness, bulk silica formation rivals such high silica solution rates. A corresponding loss of silica due to (partial) SiO₂ solution was discussed and reported, for example, by Andersson et al.³¹ and Presser et al.³². However, the common presence of a solid oxygen-rich, silica-like tribolayer renders the solution rate to be usually lower than that of silica formation. In fact, no single-phase carbon layer has ever been found on SiC after tribological exposure under water lubrication. Solution and reprecipitation of silica due to local effects will be addressed in more detail below.

1.2 On the p-T conditions

As mentioned above, the p-T conditions present on SiC sliding surfaces must strongly determine the tribochemical behaviour. To investigate the p-T influence on, for example, silica formation, static experiments using autoclaves^{23,33} or the hydrothermal diamond anvil cell^{32,34} can be used. However, to conciliate these experiments with tribological investigations it is essential to know the actual p-T range on the surface commonly assessed by numerical methods. Such approaches use boundary conditions (thermal diffusivity, velocity, etc.) and the input data from profilometry or the surface topology data³⁵⁻³⁸, because real contact areas are several orders of magnitude smaller than the geometric contact areas. Because of surface roughness, the pressure is applied only on asperities and, therefore, local contact stresses may exceed the yield stress of the material. Following the rough contact models of Greenwood³⁹, asperities can be approximated as ellipsoids and the Hertzian contact theorem is applied to estimate pressures. The heat formation and temperature rise in frictional microcontacts can subsequently be calculated using the contact flash temperature models of Kuhlmann-Wilsdorf^{36,37}.

Own calculations gave high flash temperatures of up to or more than 1000°C in sliding contacts of rough surfaces and corresponding pressures up to several GPa, but those are expected to prevail only for short periods of time and in small areas. Therefore, in the model after Xu and Kato¹⁸ shown in Fig. 1, tribochemical deterioration is expected to happen predominantly on asperities. The good thermal conductivity of SiC counteracts high temperatures and thus several hundred centigrade are likely to be present as flash temperatures on the sliding SiC surfaces at best.

However, longer lasting high pressure conditions are envisaged by mechanical deterioration processes, which entrap water in near surface cracks and pores. This way - similar to the operation conditions in a hydrothermal diamond anvil cell - increasing temperatures will cause a corresponding increase in pressure. Temperatures of 500°C, for example, will induce an isochoric, isostatically acting pressure of several hundred MPa. Rise (= dissolution) and fall (= reprecipitation) of p-T conditions allow transport of silica and oxygen input deep into the ceramic body along pathways such as cracks.

Static experiments performed using comparable p-T ranges studied the hydrothermal oxidation of SiC. Only some older studies^{40,41} reported silica formation around SiC grains. The overall observation, however, made for the temperature range of 220° - 800°C and up to several hundred MPa was an active oxidation mechanism for SiC fibres, single crystals and powder^{5,22,33,42,43}. Active corrosion starts at grain boundaries and secondary phases like yttrium-aluminium-garnet or boron carbide are preferentially attacked^{33,43}. Silica formation in these cases is limited to a mechanism of dissolution and reprecipitation^{32,34}. However, reported corrosion rates vary strongly, which is partially caused by non-comparable experimental conditions and different choices of material (SSiC: different polytype and sintering aid composition; single-crystal vs. polycrystalline body etc.).

We conclude from static experiments that during tribochemical wear, "hydrothermal" conditions (hundreds of MPa and hundreds of °C) can be expected, which should result in active SiC corrosion. This, of course, qualitatively contradicts the detection of SiO_x as a reaction product in tribolayers raising questions about the kinetics of silica formation and dissolution. Unfortunately, it is impossible to probe the actual reaction zone with respect to pressure, temperature and pH-value, so we can only rely on calculations and indirect methods to evaluate what really happens **during** tribological exposure.

2. EXPERIMENTAL PROCEDURE

For hydrothermal runs undoped 6H-SiC single crystal plates (SiCrystal AG, Erlangen, Germany) were ground to a thickness of 100 μm , polished with 1 μm diamond paste (of $R_z \approx 500$ nm and $R_a \approx 10$ nm) and cut into small bodies of approximately 240 x 240 x 100 μm^3 . Each sample was carefully cleaned in tridistilled water and acetone for 30 minutes using an ultrasonic bath to remove remnants of the polishing paste ⁴⁴.

Hydrothermal experiments were performed with a hydrothermal diamond anvil apparatus (HDAC) after Basset et al. (Ref. ^{45,46}). Pure tridistilled water was used as a medium and the pressure was calculated by equations of state (EOS) of pure water and the determination of the homogenisation temperature ^{47,48}. More details on HDAC operations can be found in Ref. ⁴⁹. Samples were heated with 20 $\text{K}\cdot\text{min}^{-1}$ up to 500°C. This temperature, which corresponds to an isochoric pressure of 500 – 770 MPa, was maintained ± 1 K for 5 h before cooling to 300 K with the same gradient.

For tribological tests EKasic[®] F (ESK Ceramics GmbH & Co. KG, Kempten, Germany) was used. This material has a fine grain size of about 5 μm . It consists of ≈ 80 wt% 6H-SiC, 20 wt% 4H-SiC + 15R-SiC and additions of boron carbide as sintering aid. The sliding surfaces were lapped to values of $R_z = 2.79$ μm and $R_a = 0.79$ μm as determined by a stylus profilometer (Hommel T 8000s, Hommel GmbH, Köln, Germany).

Tribological tests were conducted in a sliding ring tribometer with deionised water as lubricant. The setup is described in detail in Ref. ^{35,44}. During the experiment the lubricant was applied with a pressure of 0.1 MPa between the friction couple. Test runs were executed at 1.5 MPa with a sliding velocity of 6 $\text{m}\cdot\text{s}^{-1}$. We performed experiments with and without external cooling to investigate mild and severe wear regimes. For experiments without external cooling, the abort criterion in case of scuffing was a measured torque of 2 $\text{N}\cdot\text{m}$.

AFM measurements were performed using a TopoMetrix Explorer[®] (TopoMetrix Corporation, Santa Clara, U.S.A.) in contact mode with a tripod scanner (500 x 500 pixel data resolution).

For SE mode SEM images we used a LEO VP 1450 electron microscope (Carl Zeiss AG, Oberkochen, Germany) operating at 15 kV acceleration voltage.

Sampling of an EKasic[®] F sample for TEM analysis was accomplished by using focused ion beam (FIB) milling. FIB preparation (cf. Ref. ⁵⁰) was conducted under ultra-high vacuum conditions in an oil-free vacuum system using a FEI FIB200 instrument (FEI Company, Eindhoven, The Netherlands) at the Helmholtz-Zentrum Potsdam. As a result TEM-ready foils of approximately 20 x 10 x 0.15 μm^3 were obtained. The FIB-cut foils then were placed on a perforated carbon grid on a copper mesh. TEM was carried out in a FEI F20 X-Twin instrument operated at 200 kV and equipped with a FEG electron source. Electron energy-loss spectroscopy (EELS) data was acquired with a Gatan imaging filter (GIF Tridium; Gatan GmbH, München, Germany).

3. RESULTS AND DISCUSSION

3.1 HDAC experiments

Hydrothermal treatment of single-crystal SiC yields a bulk active oxidation mechanism causing enhanced surface roughness and pronounced pitting. The surface roughness increases from $R_z \approx 500$ nm and $R_a \approx 10$ nm to $R_z \approx 1900$ nm and $R_a \approx 22$ nm after a 5h HDAC experiment at 500°C. This observation for single-crystal SiC is in agreement with the finding of active corrosion for CVD SiC at 500°C in supercritical water by Barringer et al.³³.

Chemical reaction(s) are also evidenced by higher dehomogenisation temperatures, that is, during cooling the fluid separates into a liquid and a gaseous phase at much higher temperatures than observed during initial heating (e.g., at 310°C instead of 80°C). The rise is attributed to the formation of a gaseous reaction product (here: carbonaceous species). A graphitised surface layer was not found by Raman spectroscopy, which is sensitive to carbon layers even on the nm scale.

Silica was observed which was probably formed by precipitation. At least some of the silica present (partially containing aluminium and iron as remnants from sample machining) must be seen as a quenching product when the small amount of water in the HDAC sample chamber evaporates during sample extraction at ambient temperatures. More details on static SiC hydrothermal corrosion using a Bassett-type diamond anvil cell can be found in Ref.³².

3.2 Tribological exposure experiments

Typical images from worn samples in SEM, AFM, STEM and TEM mode are shown in Figs. 2 and 3. While tribological exposure leads in general to a morphological smoothening, samples from severe conditions without external cooling had both smoothened wear tracks (plateaus) and lower areas of increased surface roughness. The inset in Fig. 2a shows the rough part next to the smoothened wear track in a higher magnification. Note the plastically deformed remains of a former wear track (Fig. 2a). Also, in Fig. 2a the two sampling sites from which the FIB foils were taken (Fig. 3b and 3c, respectively) are marked.

Fig. 3 compares areas subjected to mild and severe wear regimes with the aid of STEM/TEM studies, which were carried out on FIB prepared cross-sections. For tribological experiments conducted at 1.5 MPa with external cooling a thin tribolayer of ≈ 35 nm above a 500 – 800 nm thick region of severely mechanically deformed silicon carbide was found (Fig. 3a). This region of mechanic deformation shows plastic deformation, dislocation formation and pronounced cracks, which are partially filled with material. Morphological and structural differences between smooth wear tracks and rough parts (Fig. 3b and 3c, respectively) were more pronounced in samples from tests without cooling water.

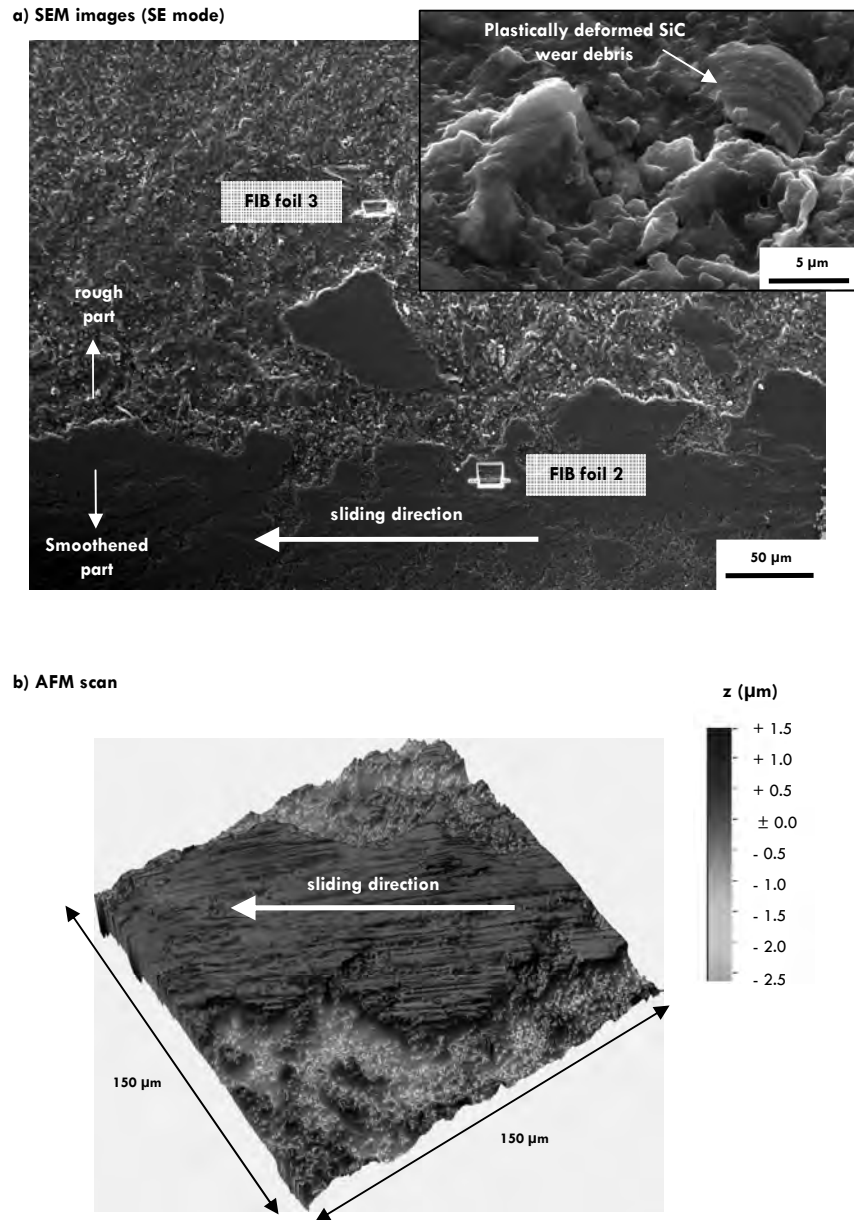
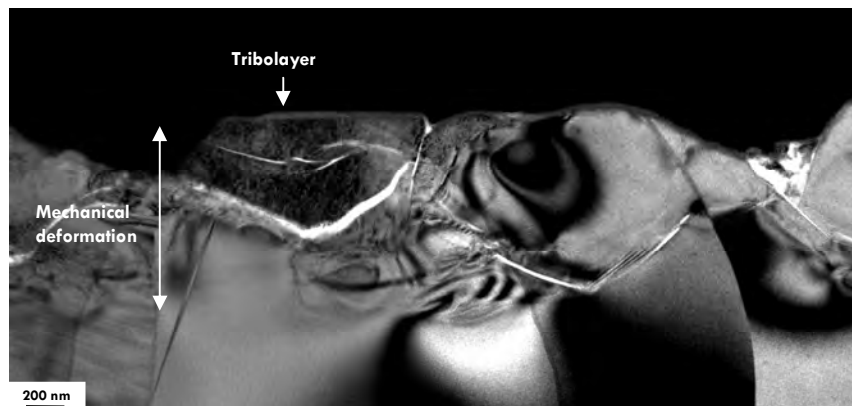
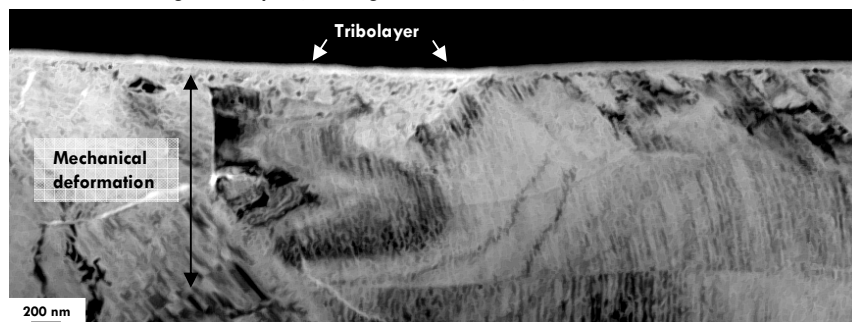


Fig. 2. a) SE mode SEM images and b) AFM scan of EKasic® F wear tracks from experiments without external cooling.

a) With external cooling (TEM dark field; FIB foil 1)



b) Without external cooling: smooth part (TEM bright field; FIB foil 2)



c) Without external cooling: rough part (STEM; FIB foil 3)

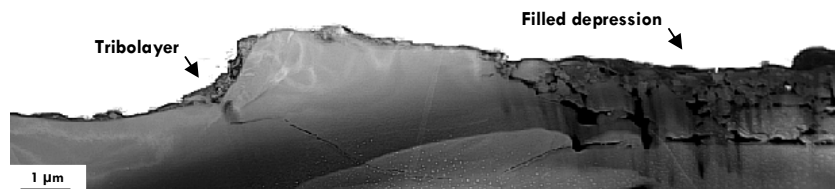


Fig. 3. Electron microphotographs of the superficial area of EKasic® F wear tracks (a) with and (b, c) without external cooling. White spots in 3c are due to Ga-contamination. For discussion see text.

Figs. 3b and c show that the tribolayer's thickness on smoothed yet elevated areas is ≈ 100 nm, while on rough areas a total thickness of ~ 500 nm is observed. Even deeper "valleys" between elevated parts, as seen on the right part of Fig. 3c, are filled with larger SiC particles forming a porous layer with up to $1.5 \mu\text{m}$ thickness. The mechanical deterioration is expressed in crack and dislocation formation (cf. Fig. 3a). Latter is also shown with a higher magnification in Fig. 4.

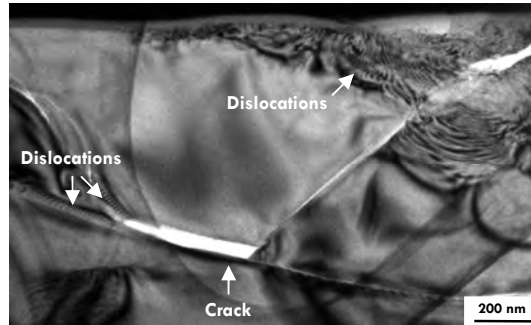
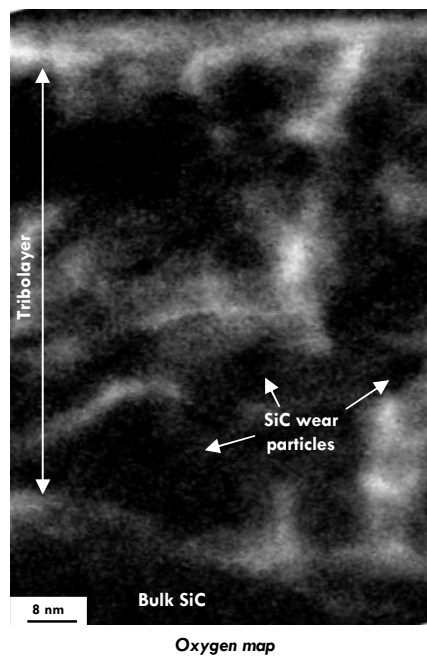
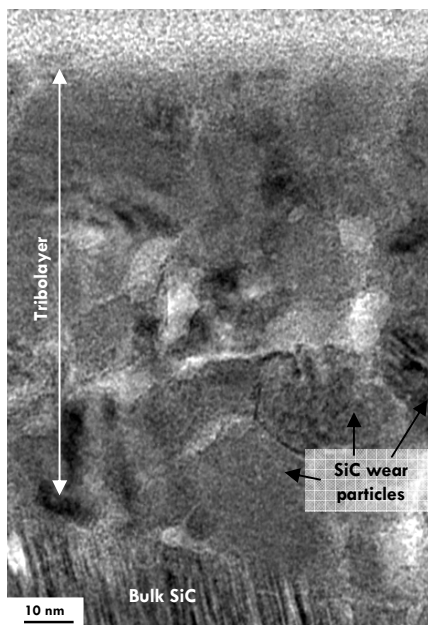


Fig. 4. TEM dark field image of the superficial area of EKasic® F wear tracks with external showing mechanical deterioration in form of crack and dislocation formation.

a) Without external cooling: smoothed part



b) With external cooling

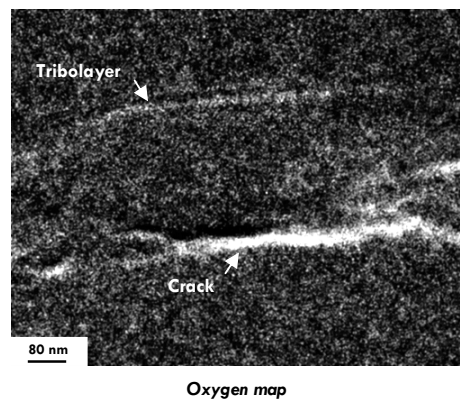
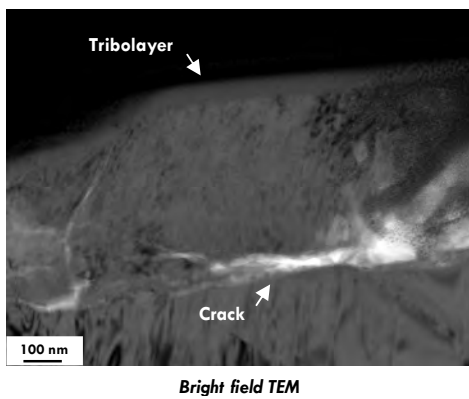


Fig. 5. Electron microphotographs of the tribolayer formed on SiC. Oxygen-rich areas correspond to the tribolayer (in which SiC wear particles are rubbed in; 5a) and (partially redeposited) cracks (5b).

Fig. 5 depicts EELS mappings and TEM images of the smooth wear track without external cooling (Fig. 5a) and the thin tribolayer observed in mild wear experiments with external cooling by water (Fig. 5b). The oxygen distribution maps shows that nanometre scale SiC wear debris is contained within an oxygen-rich matrix. The same oxidation product can be found in cracks and shear zones in the mechanically deteriorated area within the ceramic body.

Further EELS analysis of the tribolayer revealed the presence of carbon and silicon (Fig. 6). Oxygen seems to be restricted to the boundaries of nm-sized grains of SiC. Nonetheless the oxygen-rich phase seems not to be a uniform grain-boundary phase and we interpret it rather to be an adhesive, holding the angular wear debris together. The nm-scaled microstructure makes it very difficult to determine the exact chemical composition of the oxygen-rich phase, but EELS mapping clearly indicates that all oxygen-rich areas also show a strong silicon signal, which is weaker than the silicon signal from the SiC matrix.

From GDOES analysis⁴⁴ we know that the tribolayer contains significant amounts of hydrogen. Hence, an overall SiO_xH_y stoichiometry seems feasible. The weak carbon signal makes it impossible to exclude the presence of oxycarbides, which were reported to be possible reaction products in tribochemical wear⁵¹, as part of the assemblage. Some larger regions are free of carbon down to the detection limit and therefore we conclude that the overall composition of the oxygen-rich regions is close to (wet) silica.

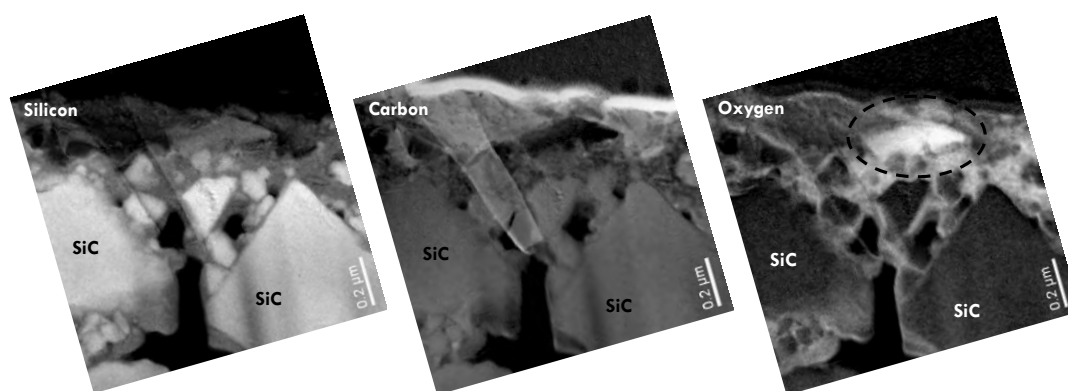


Fig. 6. EELS mappings of EKasic® F tribologically exposed without external cooling. A section from the rough part shown in Fig. 3c with some large SiC debris particles. The high carbon concentration on top of the tribolayer is due to previous carbon coating.

Differences between mild and severe deterioration can clearly be made comparing the EELS results and TEM images from experiments with and without external cooling. However, unlike the model proposed by Erickson (Ref. 6), chemical changes play an important role in the “mild wear” regime, too. Mechanical deterioration dominates the first μm below the surface, but a thin tribolayer ($< 50\text{ nm}$) is present and oxygen input evidently takes place along cracks several hundreds of nanometre deep inside the ceramic body. These cracks, therefore, provide a pathway network for water ingress into the ceramic body as long as they are connected to the surface. Without external cooling we found crystalline silica in some parts of the reaction layer (Fig. 7) by selected area diffraction (SAD). Comparing our results with Ref. 52, the reflections with $d = 3.27\text{ \AA}$ could be attributed to α -quartz-(011), those with $d = 2.06\text{ \AA}$ to α -quartz-($\bar{2}20$).

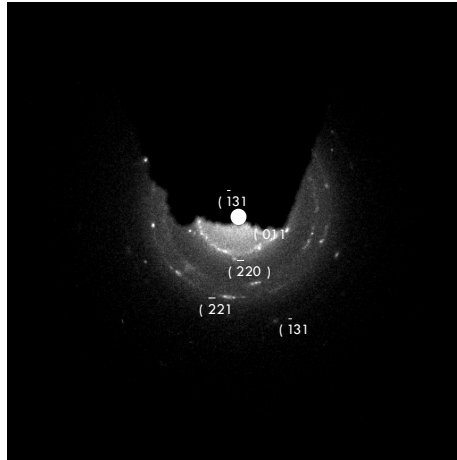


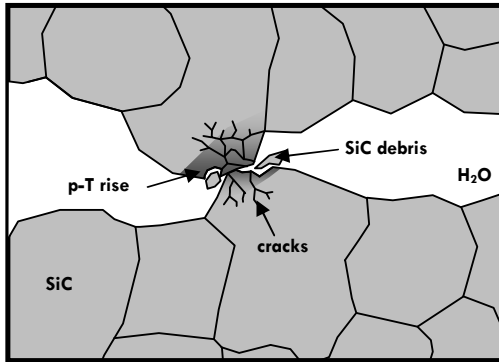
Fig. 7. Selected-area diffraction (SAD) performed in the highlighted (dashed) area in Fig. 6 (without external cooling; rough part) evidencing the presence of crystalline silica (α -quartz).

It is well known⁵³ that the presence of quartz is a good indicator for a moderate hydrothermal regime. At atmospheric pressure only cristobalite forms and it does not transform into modifications other than the low-T-form of cristobalite. In fact, amorphous silica transforms even under hydrothermal conditions first to cristobalite and then to quartz⁵⁴ and the synthesis of silica powder in hydrothermal conditions gives cristobalite and / or quartz^{55,56}. This is also known from hydrothermal oxidation of SiC, where cristobalite is formed first and quartz appears later during longer runs at several hundred centigrade²³. Under very high pressures (> 2 GPa) other modifications of silica form (coesite / stishovite) and at high temperatures ($> 750^{\circ}\text{C}$, depending on the pressure) quartz disappears. Hence, the p-T-regime must have been limited to about $250^{\circ} - 750^{\circ}\text{C}$ at pressures of several hundred MPa. Although this is a relatively large p-T range, the detection of crystalline silica proves that (1) the tribolayer consists of silica as a major phase, (2) the p-T conditions were hydrothermal, and (3) these hydrothermal conditions must have been sustained for an extended period of time near the surface.

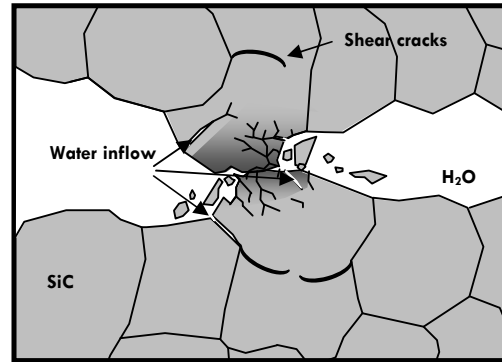
3.3 Qualitative Wear-model of wet silicon carbide tribo-corrosion

Our first ideas on how hydrothermal tribo-corrosion works based on static experiments and tribological tests³² may now become refined, because the TEM studies allow to describe the composition and structural characteristics of tribolayers formed on SiC during sliding contact under water lubrication. The findings of rounded, lapped and mechanically deformed SiC wear debris glued together by a silica-like phase and re-deposition of the latter in cracks and depressions leads us to the following qualitative model which is illustrated schematically in Fig. 8.

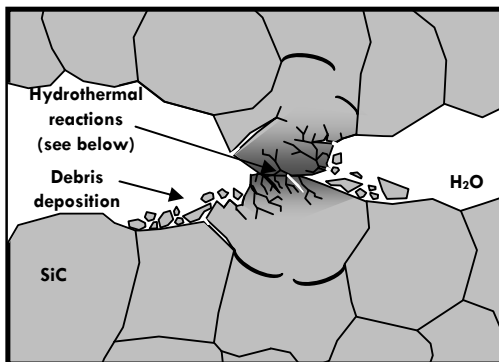
Step 1: First contact / debris formation



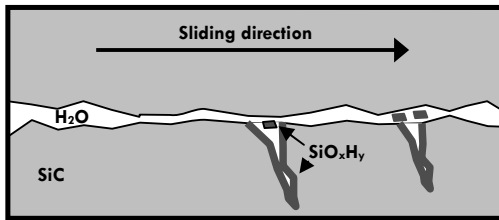
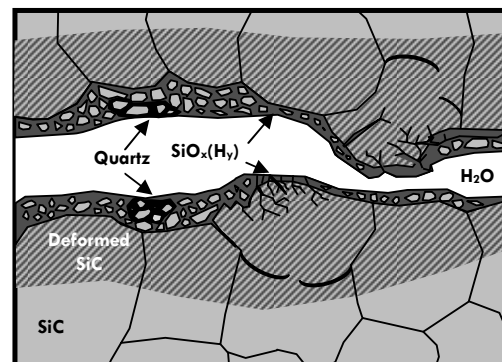
Step 2: Ongoing contact / shear crack formation



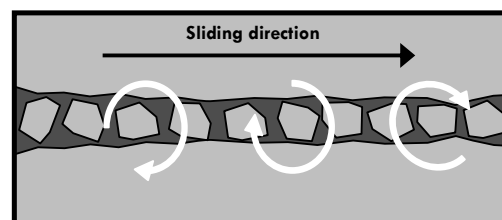
Step 3: Trapped water / hydrothermal reactions



Step 4: Track smoothing / slot filling



Tribo-interface: formation, solution and reprecipitation of silica



Tribo-interface: rounding, deterioration and downsizing of SiC wear particles

Fig. 8. Schematic illustration of our model of wet silicon carbide tribo-corrosion.

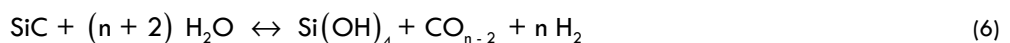
As boundary conditions we assume a sliding contact with water as lubricant for two SiC faces, which have a surface roughness smaller than the average grain size. Otherwise, pronounced grain flaking would result. Both surfaces are “real” surfaces, where mechanical contact is starting as asperity interaction:

- **Step 1:** When in contact without ideal hydrodynamic lubrication, asperity peaks collide, which causes large, but locally extremely restricted rises in pressure and temperature. The collision is not to be viewed as a Hertzian contact but rather as an impact event. Consequently, not only dislocations are inflicted to the ceramic body – SiC will structurally be shattered and disassembled into smaller crystallites and wear debris. Some of these particles will be entirely removed from the tribointerface by water. Other particles derived from erosional wear will accumulate elsewhere on the sliding surface. Strained silicon carbide is more susceptible to chemical attack of hydrothermal water. Hence both reaction gas and silica start to form preferentially on crack surfaces and other highly stressed points.
- **Step 2:** Repeated mechanical contact between asperity peaks now inflicts more severe mechanical deterioration of the SiC grains. Large ruptures and shear cracks enable water to diffuse, to flow or to become pressed into these newly formed open spaces. Also, the SiC single crystals out of which the ceramic body is made locally transform into mosaic crystals due to slip plane gliding. The most important process is that the cracks formed at one event may be sealed off during the next collision event.

The direct mechanical contact of asperity peaks induces only temporarily high pressures and the energy of the impact will be transformed to deformation, cracking and thermal energy. A single event will raise the local temperature only to see a rapid decrease afterwards, because energy is lost to the lubricating water and into the material by heat conduction (SiC has a good thermal conductivity). As the mechanical contact is often repeated, a dynamic interface temperature gradient is established over time. Any measurement of the interface's temperature, for example, by introducing a thermocouple a few millimetres below the actual surface, will thus record temperatures from this gradient and calculations of surface temperatures must involve heat transfer models.

- **Step 3:** Energy of repeated impacts will not be easily modelled, because the material forming a tribolayer changes boundary conditions by the lowering of thermal conductivity with time and the decreasing roughness will also tend lower the energy production with time. Nonetheless, the repetition of contacts will tend to raise the temperature to a dynamic equilibrium value.

The mechanical opening and closing of cracks will be supported by the increased production of further wear debris, which is smeared and pressed into any surface opening. Only now there is a situation, where water is separated and contained from the rest of the lubricating medium. Water trapped this way shows isochoric behaviour upon heating, that is, the dynamic temperature regime causes truly hydrothermal conditions with accordingly induced pressure, which is kept high. Under these conditions we expect hydrothermal reactions to take place, for example:



In a dynamic situation newly formed cracks can also reopen trapped water reservoirs. Then dissolved silica reprecipitates due to pressure relief and, accumulates to build up the oxygen-rich component of the tribolayer, most likely a wet silica-rich phase (SiO_xH_y) with or without oxycarbides ($\text{Si}_x\text{C}_y\text{O}_z$). A minor amount of oxygen and / or hydrogen may be stored in strained / amorphised silicon carbide ³².

- **Step 4:** On the interface where mechanical contact repeatedly takes place, smooth wear tracks will form over time. Wear debris caught between the sliding surfaces will be subject to tribological lapping which inflicts plastic deformation, further reduces the average crystallite size, and makes the grains more roundish. This accounts for the nanometre scale SiC wear particles found in the triboscale. The silica-rich phase out of which a significant part of the tribological layer is composed, originates mainly from reprecipitated silica and only to a minor extent from SiC oxidized directly along the contact zone.

Loose wear debris accumulates on suitable spots on the SiC surface, in particular in any depressions, crevices etc., which are protected from becoming washed out by the counterface of the wear partner. Reprecipitated SiO_x is present in such spots as well, even though these areas comprise a significant (open) pore volume and show poor densification. Nonetheless, when filled up these sites become preferential areas for hydrothermal reactions and spallation.

Due to the dynamic nature of the conditions along the tribo-interface temporarily fluctuating p-T values will be observed. Pressure relief which is related to a drop in temperature causes not only reprecipitation of silica but also dehomogenisation of the fluid. This phenomenon is known from HDAC experiments (Ref. ^{32,34}) and possibly contributes to bulk wear by cavitation further contributing to the fatigue of the already disrupted tribolayer.

In addition to the processes described above a loss of particles to the lubricating medium occurs. A variation in the extent of the individual processes may be the only thing distinguishing severe and mild wear conditions as a tribochemically influenced reaction layer is present even for the mild wear regime. Evidently, the resulting thickness of the individual zones strongly depends on the conditions chosen for tribological exposure (pressure, contact mode, duration, external cooling, etc.).

4. CONCLUSION

The wet tribo-corrosion behaviour of sintered SiC has been discussed in the light of HDAC and tribotests with and without external cooling. While active corrosion is the dominant process under hydrothermal conditions, the formation of a silica-rich phase is always observed during tribological exposure. Such phases have the general composition SiO_xH_y and may locally be of oxycarbide nature. SiO_x is a product of dissolution and reprecipitation under hydrothermal p-T conditions on sliding surfaces with trapped water. The presence of hydrothermal conditions is not limited to extremely short periods of time as evidenced by the formation of crystalline quartz in experiments without external cooling.

For both mild and severe wear conditions we found the presence of this chemically modified triboscale above a layer of mechanically deteriorated silicon carbide. While the latter can reach up to 2 μm bulk thickness the tribochemical layer is much thinner, usually in the range of tens to hundreds of nanometre. Only in areas of severe wear where large wear debris particles (up to hundreds of nanometre in diameter) accumulate in depressions a significantly larger tribolayer thickness can be observed. However, these triboscales are composed of randomly distributed SiC particles loosely connected by SiO_xH_y , comprising a significant amount of partially open pores.

ACKNOWLEDGEMENTS

This work was supported by the Deutsche Forschungsgemeinschaft (DFG) through Ni299/12-1 and Ho 1149/92. We thank Dr. Richard Wirth (Helmholtz-Zentrum Potsdam) for the TEM measurements; Dr. Christoph Berthold, Dipl.-Min. Anselm Loges and Margarete Schloßer are thanked for valuable discussion.

REFERENCES

1. Presser, V., Berthold, C., Wirth, R. & Nickel, K.G. Structural characterisation of tribologically influenced silicon carbide ceramic surfaces. *Current Opinion in Solid State & Materials Science* **submitted**(2009).
2. Kailer, A., Gogotsi, Y.G. & Nickel, K.G. Use of hardness indentation coupled with micro-Raman spectroscopy in high-pressure materials research. *Materials Research Society Symposium Proceedings* **499**, 225 - 230 (1998).
3. Wereszczak, A.A. & Johanns, K.E. Spherical indentation of SiC. *Ceramic Engineering and Science Proceedings* **27**, 43 - 57 (2007).
4. Lankford, J. & Davidson, D.L. Indentation plasticity and microfracture in silicon carbide. *Journal of Materials Science* **14**, 1669 - 1675 (1979).
5. Kitaoka, S., Tsuji, T., Katoh, T., Yamaguchi, Y. & Kashiwagi, K. Tribological Characteristics of SiC Ceramics in High-Temperature and High-Pressure Water. *Journal of the American Ceramic Society* **77**, 1851 - 1856 (1994).
6. Erickson, L.C., Blomberg, A., Hogmark, S. & Brathall, J. Tribological characterization of alumina and silicon carbide under lubricated sliding. *Tribology International* **26**, 83 - 92 (1993).
7. Mussi, A., Rabier, J., Thilly, L. & Demenet, J.L. Plasticity and deformation microstructure of 4H-SiC below the brittle-to-ductile transition. *Physica Status Solidi C* **4**, 2929 - 2933 (2007).
8. Presser, V. & Nickel, K.G. Silica on silicon carbide. *Critical Reviews in Solid State and Material Sciences* **33**, 1 - 99 (2008).
9. Samant, A.V. & Pirouz, P. Activation parameters for dislocation glide in α -SiC. *International Journal of Refractory Metals & Hard Materials* **16**, 277 - 289 (1998).
10. Samant, A.V., Wei, X.L. & Pirouz, P. An optical and transmission electron microscopy study of deformation-induced defects in 6H-SiC. *Philosophical Magazine A* **78**, 737 - 746 (1998).
11. Demenet, J.L., Zhang, M., Hobgood, H.M. & Pirouz, P. Fragile-ductile transition of single crystal 4H-SiC. *Journal de Physique IV* **106**, 53 - 62 (2003).
12. Patten, J., Gao, W. & Yasuto, K. Ductile regime nanomachining of single-crystal silicon carbide. *Journal of manufacturing science and engineering* **127**, 522 - 532 (2005).
13. Hsu, S.M. & Shen, M. Wear prediction of ceramics. *Wear* **256**, 867 - 878 (2004).
14. Lancaster, J.K., Mashal, Y.A.-H. & Atkins, A.G. The role of water in the wear of ceramics. *Journal of Physics D* **25**, A205 - A211 (1992).
15. Kitaoka, S., Yamaguchi, Y. & Takahashi, Y. Tribological characteristics of α -alumina in high-temperature water. *Journal of the American Ceramic Society* **75**, 3075 - 3080 (1992).
16. Sasaki, S. The effects of the surrounding atmosphere on the friction and wear of alumina, zirconia, silicon carbide and silicon nitride. *Wear* **134**, 185 - 200 (1989).
17. Tomizawa, H. & Fischer, T.E. Friction and wear of silicon nitride and silicon carbide in water: hydrodynamic lubrication at low sliding speed obtained by tribochemical wear. *ASLE Transactions* **30**, 41 - 46 (1987).
18. Xu, J. & Kato, K. Formation of tribochemical layer of ceramics sliding in water and its role for low friction. *Wear* **245**, 61 - 75 (2000).
19. Quinn, T.F.J. Oxidational Wear. *Wear* **18**, 413 - 419 (1971).
20. Quinn, T.F.J. Oxidational wear modelling: I. *Wear* **153**, 179 - 200 (1992).
21. Quinn, T.F.J. Oxidational wear modelling: Part II. The general theory of oxidational wear. *Wear* **175**, 199 - 208 (1994).
22. Kitaoka, S., Tsuji, T., Yamaguchi, Y. & Kashiwagi, K. Tribochemical wear theory of non-oxide ceramics in high-temperature and high-pressure water. *Wear* **205**, 40 - 46 (1997).
23. Kraft, T., Nickel, K.G. & Gogotsi, Y.G. Hydrothermal degradation of chemical vapour deposited SiC fibres. *Journal of Materials Science* **33**, 4357 - 4364 (1998).
24. Gogotsi, Y.G. & Yoshimura, M. Degradation of SiC-based fibres in high-temperature, high-pressure water. *Journal of Materials Science Letters* **13**, 395 - 399 (1994).
25. Kraft, T. & Nickel, K.G. Hydrothermal Carbon Coatings of alpha-SiC Crystals. in *Surface Engineering - EUROMAT 99*, Vol. 11 (ed. Dimigen, H.) 306 - 311 (Wiley-VCH, 1999).
26. Gogotsi, Y.G. Hydrothermale Korrosion von SiC - Betrachtung der schädlichen und nützlichen Aspekte. in *Korrosion und Verschleiß von keramischen Werkstoffen* (eds. Telle, R. & Quirnbach, P.) 114 - 122 (Deutsche Keramische Gesellschaft e.V. (DKG), Aachen, 1994).
27. Iler, R.K. *The chemistry of silica*, 896 (John Wiley & Sons, New York, 1979).
28. Perera, G., Doremus, R.H. & Lanford, W. Dissolution Rates of Silicate Glasses in Water at pH 7. *Journal of the American Ceramic Society* **74**, 1269-1274 (1991).
29. Ito, S. & Tomozawa, M. Stress Corrosion of Silica Glass. *Journal of the American Ceramic Society* **64**, C160 (1981).
30. Kennedy, G.C. A portion of the system silica-water. *Economic geology* **45**, 629 - 653 (1950).
31. Andersson, P., Juhanko, J., Nikkila, A.-P. & Lintula, P. Influence of topography on the running-in of water-lubricated silicon carbide journal bearings. *Wear* **201**, 1 - 9 (1995).

32. Presser, V. et al. Tribological and hydrothermal behaviour of silicon carbide under water lubrication. *Wear* (2008).
33. Barringer, E. et al. Corrosion of CVD Silicon Carbide in 500°C Supercritical Water. *Journal of the American Ceramic Society* **90**, 315 - 318 (2007).
34. Presser, V. & Nickel, K.G. Hydrothermal Oxidation of Silicon Carbide Single Crystals Using a Modified Diamond Anvil Cell. in *10th International Conference of the European Ceramic Society* (eds Heinrich, J.G. & Aneziris, C.G.) 191 - 195 (Göller Verlag GmbH, Berlin, 2007).
35. Zimmermann, M. *Experimentelle Untersuchung und numerische Modellierung des Gleitkontaktverhaltens von gesintertem Siliciumcarbid (SSiC)*, 102 (Universität Karlsruhe, Karlsruhe, 1998).
36. Kuhlmann-Wilsdorf, D. Demystifying Flash Temperatures. I. Analytical Expressions based on a simple model. *Materials Science and Engineering* **91**, 107 - 118 (1987).
37. Kuhlmann-Wilsdorf, D. Demystifying Flash Temperatures. II. First-order Approximation for Plastic Contact Spots. *Materials Science and Engineering* **91**, 119 - 133 (1987).
38. Bhushan, B. Contact mechanics of rough surfaces in tribology: multiple asperity contact. *Tribology Letters* **4**, 1 - 35 (1998).
39. Greenwood, J.A. The Area of Contact Between Rough Surfaces and Flats. *Transactions of the ASME* **1**, 81 - 91 (1967).
40. Yoshimura, M., Kase, J.-I. & Somiya, S. Oxidation of SiC powder by high-temperature, high-pressure H₂O. *Journal of Materials Research* **1**, 100 - 103 (1986).
41. Yoshimura, M., Kase, J. & Somiya, S. Oxidation of Si₃N₄ and SiC by High Temperature-High Pressure Water Vapor. in *2nd Int.Symp. Ceramic Materials and Components for Engines* (eds Bunk, W. & Hausner, H.) 529-536 (Germany, 1986).
42. Kim, W.-J., Hwang, H.S., Park, J.Y. & Ryu, W.-S. Corrosion behaviors of sintered and chemically vapor deposited silicon carbide ceramics in water at 360°C. *Journal of Materials Science Letters* **22**, 581-584 (2003).
43. Schwetz, K.A. & Hassler, J. Zur Beständigkeit von Hochleistungskeramiken gegen Flüssigkeitskorrosion. *Ceramic Forum International* **79**, D9 - D19 (2002).
44. Krummhauser, O., Presser, V., Kailer, A. & Nickel, K.G. Comparison of tribological and corrosive behaviour of silicon carbide under water lubrication. in *48. Tribologie Fachtagung. Reibung, Schmierung und Verschleiß. Forschung und praktische Anwendungen. Band 1.*, Vol. 1 13/1 - 13/15 (Gesellschaft für Tribologie, Göttingen, 2007).
45. Bassett, W.A., Shen, A.H., Bucknum, M. & Chou, I.-M. Hydrothermal Studies in a New Diamond Anvil Cell up to 10 GPa and from -190°C to 1200°C. *PAGEOPH* **141**, 487 - 495 (1993).
46. Bassett, W.A., Shen, A.H., Bucknum, M. & Chou, I.-M. A new diamond anvil cell for hydrothermal studies to 2.5 GPa and from -190 to 1200°C. *Review of Scientific Instruments* **64**, 2340 - 2345 (1993).
47. Haselton, H.T., Chou, I.-M., Jr., Shen, A.H. & Bassett, W.A. Techniques for determining pressure in the hydrothermal diamond-anvil cell: Behaviour and identification of ice polymorphs (I, II, V, VI). *American Mineralogist* **80**, 1302 - 1306 (1995).
48. Shen, A.H., Bassett, W.A. & Chou, I.-M. Hydrothermal Studies in a Diamond Anvil Cell: Pressure Determination Using the Equation of State of H₂O. in *High-Pressure Research: Application to Earth and Planetary Sciences* (eds Syono, Y. & Manghnani, M.H.) 61 - 68 (American Geophysical Union, Washington D.C., 1992).
49. Presser, V., Heiß, M. & Nickel, K.G. EOS calculations for hydrothermal diamond anvil cell operation. *Review of Scientific Instruments* **78**, 085104-1 - 085104-9 (2008).
50. Wirth, R. Focused ion beam (FIB): a novel technology for advanced application of micro- and nanoanalysis in geosciences and applied mineralogy. *European Journal of Mineralogy* **16**, 863 - 876 (2004).
51. Lauer, J.L. Wear-Induced Changes in the Raman, Infrared, and Fluorescence Spectra of Silicon Nitride Surfaces. *Applied Spectroscopy* **50**, 1378 - 1388 (1996).
52. Dušek, M., Petříček, V., Wunschel, M., Dinnebier, R.E. & van Smaalen, S. Refinement of modulated structures against X-ray powder diffraction data with JANA2000. *Journal of Applied Crystallography* **34**, 398 - 404 (2001).
53. Byrappa, K., Yoshimura, I. & Yoshimura, M. *Handbook of Hydrothermal Technology: A Technology for Crystal Growth and Materials Processing*, 525 (Noyes Publications, Norwich, 2001).
54. Campbell, A.S. & Fyfe, W.S. Hydroxyl-ion catalysis of the hydrothermal crystallization of amorphous silica; a possible high-temperature pH indicator. *American Mineralogist* **45**, 464 - 468 (1960).
55. Zhu, Y., Yanagisawa, K., Onda, A. & Kajiyoshi, K. The preparation of nano-crystallized cristobalite under hydrothermal conditions. *Journal of Materials Science* **40**, 3829 - 3831 (2005).
56. Yanagisawa, K., Zhu, Y., Onda, A. & Kajiyoshi, K. Hydrothermal synthesis of mono-dispersed quartz powders. *Journal of Materials Science* **39**, 2931 - 2934 (2004).

Chapter 01

Chapter 02

Chapter 03

Chapter 04

Chapter 05

Chapter 06

Chapter 07

Chapter 08

Chapter 09

Chapter 10

Chapter 11

Chapter 12

SUMMARY & OUTLOOK

1. RESULTS

1.1 Analytical results

1.1.1 Dry, thermal oxidation of silicon carbide

Dry, thermal oxidation of silicon carbide, even for single-crystal SiC, is a highly complex issue. Due to SiC's structural anisotropy, we find significant differences in oxidation rates between different faces of single-crystal SiC samples. When the composition and structure of the silica scale is the same for all SiC faces, this cannot be explained in terms of the Deal-and-Grove model where the oxidation rate is only limited by the diffusion of a gas phase – even when there are in fact two gas species diffusing through the up-building SiO₂ scale. One explanation for this phenomenon is supplied by the interlayer model where at the SiC-SiO₂ interface a few nanometers thin oxycarbide layer is formed. Depending on the crystal orientation, this interlayer is formed up to a various thickness and because of the changed chemical composition at the oxidation interface the oxidation rate is changed, too. The literature, however, is not clear about the presence of such an interface (some studies were unable to corroborate its existence) and whether it could contribute to significant oxidation rate anisotropy at temperatures above 1000°C. Another explanation is provided by the simple fact, that different SiC faces (independent from surface reconstruction) show a different surface energy. This is the reason why SiC faces (1) grow with different rates during PVT synthesis, (2) show different etching rates, and in consequence why (3) the oxidation rates are different for various crystallographic faces. However, the latter only applies for reaction limited oxidation kinetics. As SiC oxidation is believed to be diffusion controlled, the different surface energy alone cannot fully explain the pronounced anisotropy of the oxidation rate.

When looking at the temperature-dependency of oxidation rates (Fig. 1) different branches become evident. Below ≈1350°C, there is a great difference of the parabolic oxidation rate between different SiC faces (C- and Si-terminated faces to be more precise). This difference, however, vanishes at approximately 1350°C completely. At higher temperatures, different oxidation rates (“branch 1” vs. “branch 2”) were explained in terms of structural differences, that is, crystalline versus vitreous silica. As oxygen diffusion is believed to be the rate-limiting oxidation process, there must be a relationship between the crystallographic structure of the silica scale and the diffusion coefficient of oxygen.

It is true that for oxidation temperatures above 1200°C and especially above 1350°C, the silica scale undergoes crystallization and radialites appear. AFM/HF-etching experiments show that there is a significant difference between the oxidation rates of silicon carbide covered by either crystalline or vitreous SiO₂. In particular, SiC underneath vitreous silica oxidizes approximately three times faster than when covered by a crystalline oxide scale without considering accelerated oxidation due to grain boundary diffusion and related effects. At higher temperatures, there might also be a change in the main transport mechanism of oxygen through the oxide scale: interstitial oxygen transport instead of molecular permeation. This, however, cannot explain the different branches which show different oxidation rates at the same temperature for different SiC faces / oxide scale characteristics.

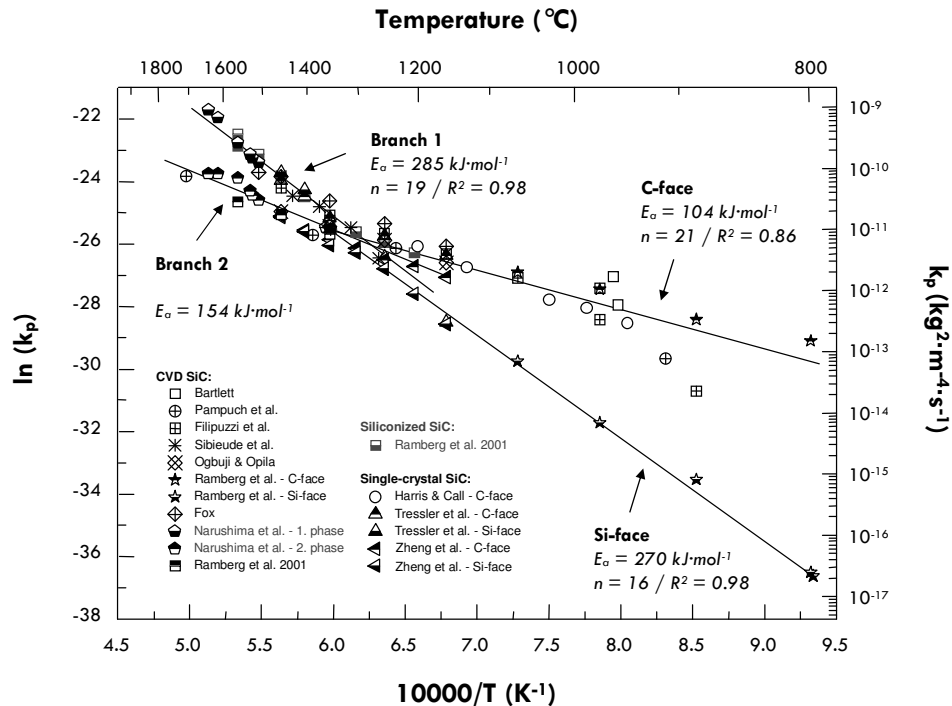


Fig. 1. Arrhenius-plot (Ref. ¹) of various parabolic rate-constants (Bartlett: Ref. ²; Pampuch et al.: Ref. ³; Filipuzzi et al.: Ref. ⁴; Sibieude et al.: Ref. ⁵; Ogbuji & Opila: Ref. ⁶; Ramberg et al.: Ref. ⁷; Fox: Ref. ⁸; Narushima: Ref. ⁹; Ramberg et al. 2001: Ref. ⁷; Harris & Call: Ref. ¹⁰; Tressler et al.: Ref. ¹¹; Zheng et al.: Ref. ^{12,13}).

Besides the anisotropy of oxidation rates of pure SiC single-crystals, impurities – either from the atmosphere or within the carbide itself – greatly influence the structure and formation rate of silica during thermal oxidation. As for SiC ceramic bodies, sintering aids act as intrinsic impurity sources. Boron carbide, for instance, is well-known to cause extensive bubble formation and locally accelerated oxidation rates.

But also contaminations originating from the furnace environment play an important role. Studies on SiC single-crystals in high-purity environments (fused quartz tube) in comparison to experiments conducted in an alumina tube furnace show accelerated oxidation rates for the latter. Also, the morphology of the crystalline scale changes: impurity accumulation (e.g., Na and K) on the surface leads to a recrystallization process which ultimately leads to the formation of small, 1 – 2 μm large crystalline spheres instead of large radialites with tens of micrometer in diameter. In general, SiC covered by crystalline silica would be expected to oxidize slower than when a vitreous scale is present. However, in-between these spheres a significant pore volume, partially filled with impurity-saturated melt, is present acting as pathways for accelerated oxidation.

As for hollow defect types, that is, pipes and voids, no significant influence on the oxidation process was found: neither accelerated oxidation nor forced crystallization was observed. Pipes and voids, however, can act as traps for impurities during sample treatment (polishing etc.) and may, therefore, act as areas of initial devitrification.

1.1.2 Hydrothermal and tribological behavior of silicon carbide

Static hydrothermal treatment of SiC single-crystals in pure water showed an active corrosion mechanism at 500°C and corresponding isostatic pressures (approximately 500 – 800 MPa). Sicilia as present on some samples is a product of dissolution and reprecipitation, for example, after depressurization when the sample chamber is cooled down to room temperature. Also, reprecipitation is possible when the fluid phase is saturated by dissolved silica.

As for tribological exposure, the mechanical component of wear acting on real surfaces (i.e., with asperities) must be considered. Fig. 2 gives an overview over some influencing factors of tribologically induced changes of SiC ceramic surfaces. Chemical reactions in combination with mechanical deterioration, finally, build up a complex tribolayer with (partially) rounded wear debris embedded in a silica-like matrix above a zone in which the SiC grains of the ceramic matrix are structurally shattered. Although being a brittle material, tribologically influenced surfaces of SiC ceramics give evidence of plastic deformation due to the extreme conditions when asperity peaks are in direct physical contact. This phenomenon is well-known from indentation experiments, where it is referred to as “indentation plasticity” and can best be seen in form of “bent” lattice planes of SiC wear debris or glide planes within the ceramic matrix.

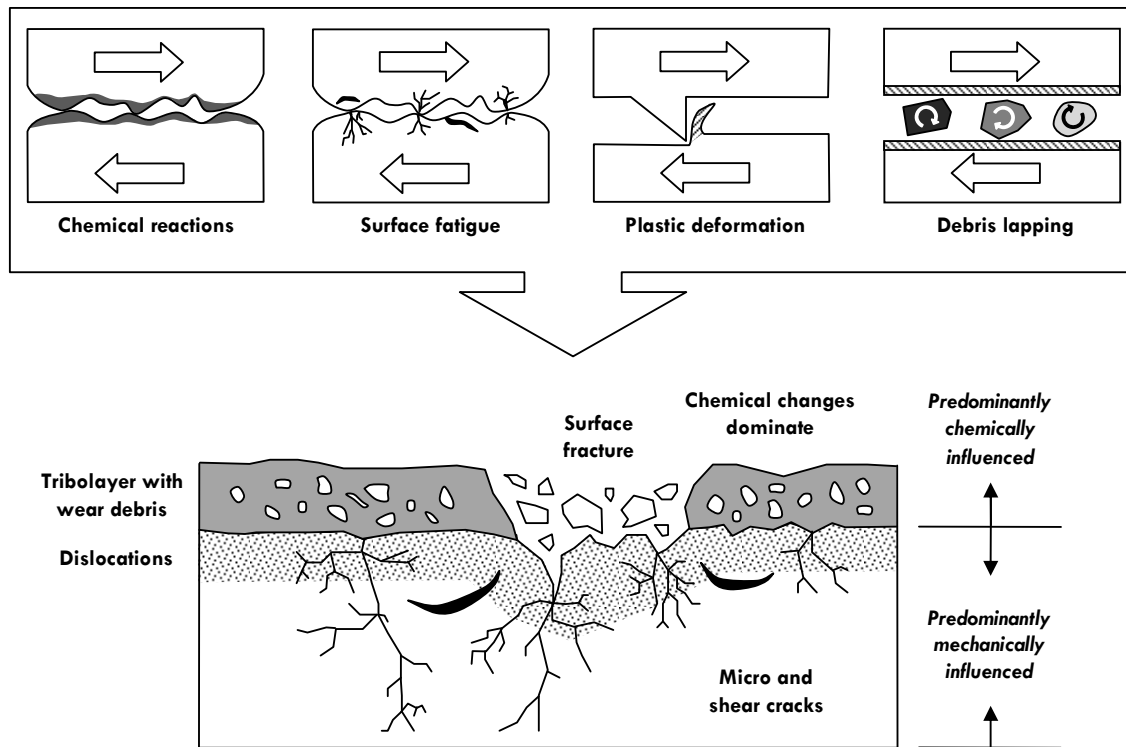


Fig. 2. Major factors for tribologically induced changes on the surface of SiC ceramics.

The underlying mechanisms for tribochemical wear of SiC under water lubrication are considered in a first qualitative model (Fig. 3). Mechanical contact initially leads to debris and crack formation. Inflowing water and hydrothermal fluid trapped at the interface of asperity peaks in sliding contact is then subject to hydrothermal reactions, that is, active corrosion of SiC. Dissolved silica, then, reprecipitates (possibly in form of hydroxycarbides) after depressurization and forms a matrix in which wear particles become embedded. Repeating mechanical contact makes the wear debris more and more round and induces mechanical deformation (bent lattice planes, dislocations etc.). In case that a high contact temperature is maintained for a longer period of time, for example, if the external cooling is turned-off, even crystalline silica was found. The latter evidences the hydrothermal character of the tribochemical wear reactions as far as pressure and temperature are concerned.

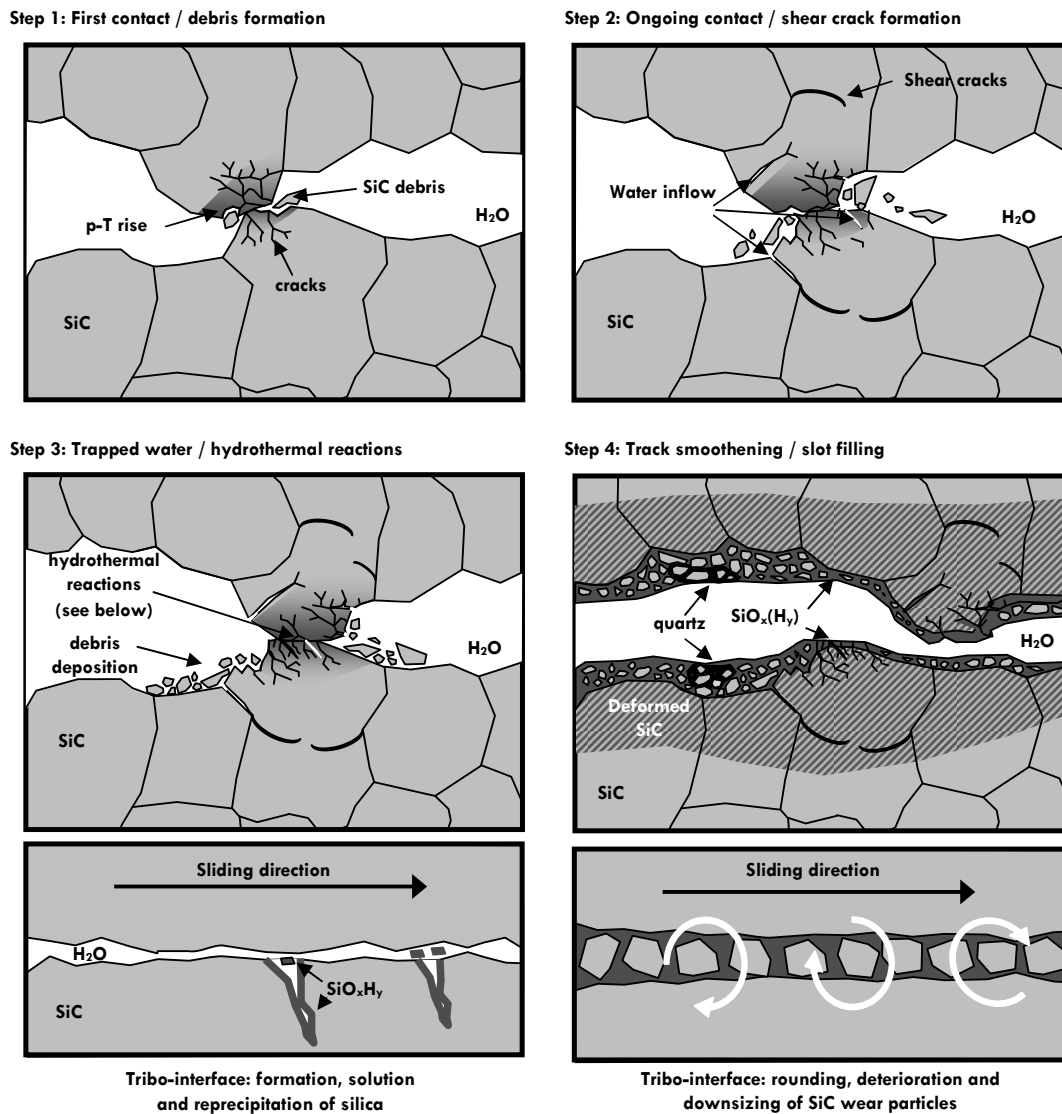


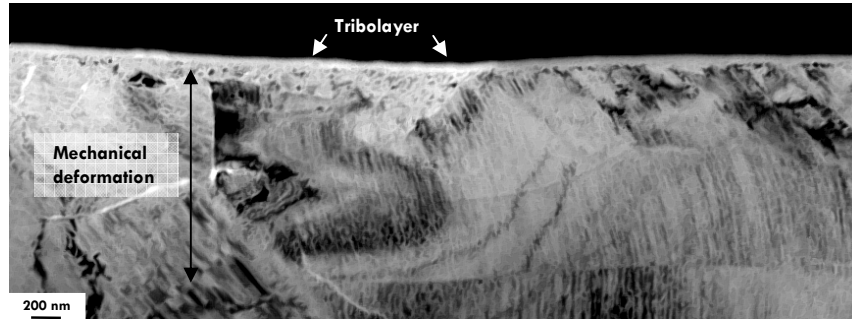
Fig. 3. Schematic illustration of a qualitative wet silicon carbide tribo-corrosion model (Ref. ¹⁴).

The complex interplay of chemical and mechanical mechanisms is highly sensitive to any change of the tribo-system. One such factor is the grain size. As for polycrystalline sintered ceramic bodies, preferential degradation of the grain boundaries and sintering aids must be considered. This is why under otherwise identical parameters samples with a finer grain size have a significantly shorter lifetime expectancy in sliding contact than samples with a more coarse grain size. The most drastic differences, however, can be observed when comparing samples from severe and mild wear regimes, that is, from experiments with and without external cooling. While under external cooling mechanical degradation dominates and only a thin tribochemically influenced layer (tens of nanometer thick) is formed, samples without external cooling show tribolayers with a scale thickness in the range of a few micrometers with partial scale delamination (Fig. 4).

a) With external cooling (TEM dark field)



b) Without external cooling: smooth part (TEM bright field)



c) Without external cooling: rough part (STEM)

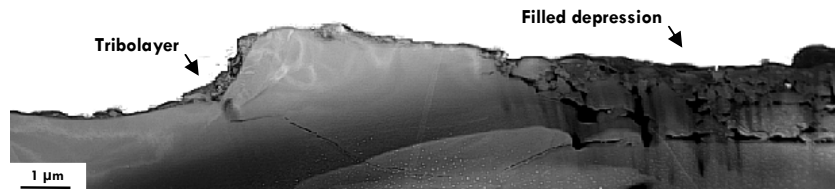


Fig. 4. Electron microphotographs of the superficial area of EKasic® F wear tracks (a) with and (b, c) without external cooling.

White spots in 4c are due to Ga-contamination (Ref. ¹⁴).

1.2 Methodological results

1.2.1 Characterization of defect-types using polarization microscopy

Hollow defects are common phenomena in SiC single-crystals grown by physical vapor transport (PVT). One defect type are so called “voids”. These hollow structures tend to have a parallelepiped outline (hexagonal SiC: hexagonal voids). Within the basal plane, these “hollow crystals” can reach diameters $> 500 \mu\text{m}$ while their vertical expanse is only several micrometers or tens of micrometer large. Another defect type is posed by pipes, that is, hollow tube-like structures with diameters from < 0.1 to $> 5 \mu\text{m}$ and a length that is usually only limited by the single-crystal (i.e., up to several mm). These defects are believed to be hollow-core screw dislocations with, in case of small-period polytypes, a Burger’s vector larger than one unit cell.

Polarization microscopy carried out on hexagonal SiC single-crystals cut perpendicular to the c-axis (= optical axis) should show no interference phenomenon at all: within the basal plane, we can speak of an isotropic cut where the refraction indices are the same just like for a cubic crystal. In the presence of pipes (not voids), however, we see an interference pattern due to the photoelastic effect caused by strain around these hollow-core defects. This effect is well-known to mineralogists as undulatory extinction and becomes clear when inserting an Amici Bertrand lens: strain causes a change of the optical character of SiC and the indicatrix becomes biaxial instead of uniaxial.

Simulation of the interference pattern clearly indicates that for the studied pipes a mixed-character must be present, that is, the pipes cannot be pure screw-dislocations but there must be an edge-component. With such an edge-component, however, the simulated and observed interference patterns converge (Fig. 5).

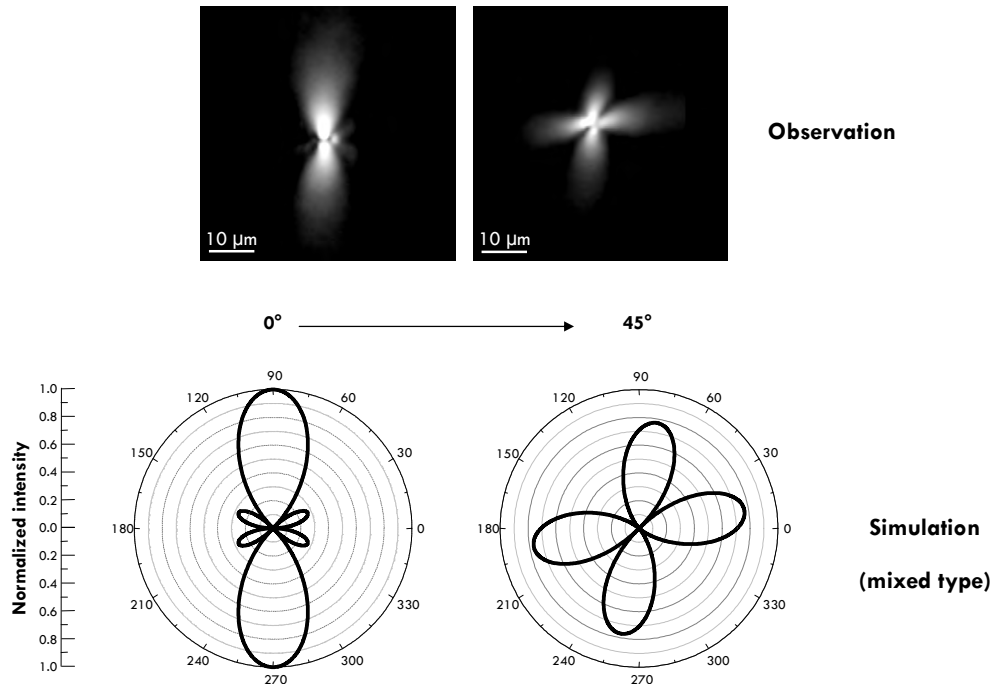


Fig. 5. Comparison between observed and simulated interference pattern (isocontour plot; Ref. 15).

1.2.2 Application of equations of state of water for hydrothermal diamond anvil cell operations

The hydrothermal diamond anvil cell (HDAC) allows gaining *in-situ* visual and analytical information of a sample during hydrothermal treatment. Although being a standard tool in earth sciences, HDAC experiments studying the corrosion behavior is a new approach in materials sciences. While the isochoric sample chamber is externally heated, the isostatic pressure mediated on the sample by the fluid phase is *a priori* unknown. It can, however, be determined by two approaches: (1) direct methods, that actually measure the pressure and (2) indirect methods, that calculate the pressure. As only the chemical reactions between pure water and high-purity silicon carbide were to be studied, it was not possible to introduce a reference material like a ruby chip into the sample chamber for direct pressure determination especially when considering the long periods over which the experiments were conducted (i.e., several hours).

Knowing the density of the fluid phase, for example, by determining the homogenization temperature when an air bubble is present in the sample chamber, the exact pressure corresponding to a measured temperature can be calculated using equations of state of water. Assuming the sample chamber to be constant in volume, the p-T correlation follows an isochoric line arising from the homogenization point (Fig. 6). To avoid nucleation problems, exact homogenization temperatures should only be determined during heating (i.e., disappearing of the air bubble) and not during cooling (i.e., appearing of the air bubble). The assumption of isochoric sample chamber volumes is reasonable at least for the second run as the gasket is known to possibly change its form slightly during the first time that the sample chamber was subject to high p-T conditions for the experiment.

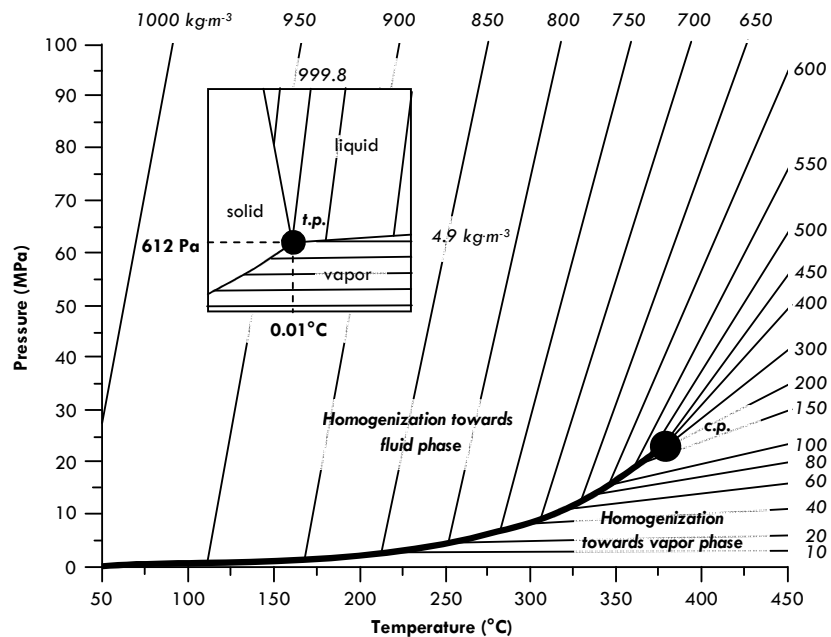


Fig. 6. Phase diagram showing the boiling curve below the critical point (c.p.) and from this phase boundary arise isochors (Ref. ^{16,17}). The small inset illustrates the three phase boundary at the triple point (t.p.).

1.2.3 Raman spectroscopy and profile line deconvolution to characterize amorphization

Raman spectroscopy as a phase- and structure-sensitive characterization method is a suitable tool to characterize strain and amorphization of otherwise crystalline materials. With increased structural damage to the crystal lattice, the shape and position of individual Raman-active modes changes in four ways: (1) the bands become broader, (2) they decrease in total Raman intensity, (3) they shift in their spectral position and (4) they become asymmetric when amorphisation reaches a critical level.¹⁸⁻²⁰ In case of amorphisation due to mechanical contact, Raman-active modes of tribologically influenced SiC will shift towards higher wavenumbers, because mechanical exposure leads to a densification (Fig. 7).²¹ Radiation-induced amorphisation, instead, is known to cause a down-shift of Raman modes.^{19,20}

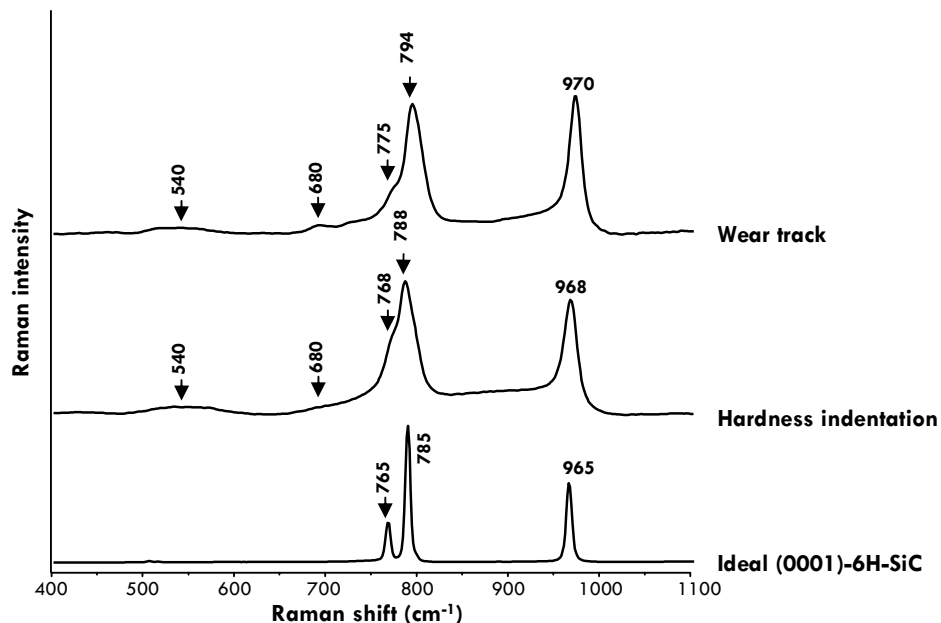


Fig. 7. Raman spectra (Ref. ²²) of a wear track of tribologically influenced SiC, the central part of a Vickers hardness indentation and ideal undistorted undoped (0001)-6H-SiC.

Quantitative characterization of strain- or amorphization-induced Raman profile line broadening requires to separate the bandwidth contribution from (1) the laser source, (2) the instrument (slits etc.), and finally (3) the sample. Using a case in which the form of the Raman modes is maintained (i.e., mild radiation induced amorphization of the natural mineral zircon) the benefits of a Rietveld-based profile line deconvolution approach were demonstrated. In particular, this way also very narrow Raman lines (i.e., small degree of amorphization), which are not accessible via the conventional deconvolution approach using the Irmmer equation, can be analyzed and instrument-independent information are accessible. The basic concept behind this Raman fundamental parameters approach is that every optical device in the instrument contributes to the final band shape in its own way: a slit, for example, contributes a hat function. This way, also the profile form of the laser radiation source can be considered using modular deconvolution. The remaining profile contribution that is not related to the instrument's or laser's profile function, therefore, must originate from the sample and can be used for quantitative analysis.

2. OUTLOOK

This study concentrated on methodological aspects (Raman, μ XRD, FIB / TEM) and chemical & structural aspects of silicon carbide to build up a basis for a more comprehensive understanding for tribologically influenced SiC ceramic surfaces. Applying the described characterization methods, we were able to derive a first qualitative model for the mechanisms underlying tribochemical wear of SiC under water lubrication. In contrast to the literature, we confirmed a chemical component of tribological degradation also for mild wear regimes. Further work will have to concentrate on systematic analysis of different exposure modes and material-related variations (SiC single-crystals vs. SiC ceramics / pre-damaged vs. pristine SiC and so on).

As far as analytical methods are concerned, it was shown that comprehensive understanding cannot be accomplished by applying just one but many complementary methods. Each and every analysis method has its own advantages and limitations. First of all it is imperative to know about instrumental and methodological restrictions, for example, as far the analyzed sample volumina are concerned. Secondly, it is highly desirable to use a true combination of methods, that is, instruments allowing sample characterization by different methods at the same time. This is the only way to ensure that the very same sample position and resolve changes that occur over time. Current developments are on the way to realize the combination, for example, of XRF, XRD and Raman.

As for the sub-micrometer-scale analysis, the FIB technology has proven to be an excellent tool to decrease the excitation volume for EDX analysis and simultaneously allow tomographic imaging. As combination of SEM and Raman-spectroscopy has been realized for a few years, the combination of FIB and Raman is very promising to decrease the large excitation volume that ultimately excludes Raman spectroscopy from being applicable to highly surface sensitive analyses at least for transparent materials and laser radiation that lies in the visible spectrum.

In-situ surface characterization, for example via Raman spectroscopy, will be an important step to gain structural information during tribological exposure. Until now, only the friction coefficient and the temperature a few millimeters below the sliding interface are accessible *in-situ*.

As for wear of SiC under water lubrication, it is highly desirable to derive a quantitative corrosion model – although the prerequisites for that are very difficult to meet. Even for certain choice of material (grain size, polytype distribution, sintering aids) and distinct chemical environment (pure water), the exposure mode in application is highly complex (external cooling? / dynamic or static sliding condition? / SiC-to-water ratio?) and subject to significant changes over time.

REFERENCES

1. Presser, V. & Nickel, K.G. Silica on silicon carbide. *Critical Reviews in Solid State and Material Sciences* **33**, 1 - 99 (2008).
2. Bartlett, R.W. Oxide Films on Beta-Silicon Carbide. *Journal of the Electrochemical Society* **118**, 397 - 399 (1971).
3. Pampuch, R., Ptak, W., Jonas, S. & Stoch, J. Formation of Ternary Si-O-C Phase(s) During Oxidation of SiC. *Materials Science Monographs* **6**, 435 - 448 (1980).
4. Filipuzzi, L., Naslain, R. & Jausaud, C. Oxidation kinetics of SiC deposited from $\text{CH}_3\text{SiCl}_3/\text{H}_2$ under CVI conditions. *Journal of Materials Science* **27**, 3330 - 3334 (1992).
5. Sibieude, F., Rodriguez, J. & Clavaguera-Mora, M.T. Kinetics and crystallization studies by in situ x-ray diffraction of the oxidation of chemically vapour deposited SiC. *Thin Solid Films* **204**, 217 - 227 (1991).
6. Ogbuji, L.U.J.T. & Opila, E.J. A Comparison of the Oxidation Kinetics of SiC and Si_3N_4 . *Journal of the Electrochemical Society* **142**, 925 - 930 (1995).
7. Ramberg, C.E. & Worrell, W.L. Oxygen Transport at High Temperatures: Implications of Oxidation Kinetics. *Journal of the American Ceramic Society* **84**, 2607 - 2616 (2001).
8. Fox, D.S. Oxidation Behavior of Chemically-Vapor-Deposited Silicon Carbide and Silicon Nitride from 1200° to 1600°C. *Journal of the American Ceramic Society* **81**, 945 - 950 (1998).
9. Narushima, T., Goto, T. & Hirai, T. High-Temperature Passive Oxidation of chemically vapor deposited silicon carbide. *Journal of the American Ceramic Society* **72**, 1386 - 1390 (1989).
10. Harris, R.C.A. & Call, R.L. Oxidation of 6H alpha-silicon carbide. *Proceedings of the International conference on silicon carbide 3rd International Conference*, 329 - 336 (1974).
11. Tressler, R.E., Costello, J.A. & Zheng, Z. Oxidation of Silicon Carbide. in *Industrial Heat Exchangers*, Vol. 1 (eds. Hayes, A.J., Liang, W.W., Richlen, S.L. & Tabb, E.S.) 307 - 314 (American Society for Metals, Pittsburgh, 1985).
12. Zheng, Z., Tressler, R.E. & Spear, K.E. Oxidation of Single-Crystal Silicon Carbide. Part I. Experimental Studies. *Journal of the Electrochemical Society* **137**, 854 - 858 (1990).
13. Zheng, Z., Tressler, R.E. & Spear, K.E. Oxidation of Single-Crystal Silicon Carbide. Part II. Kinetic Model. *Journal of the Electrochemical Society* **137**, 2812 - 2816 (1990).
14. Presser, V., Nickel, K.G., Krummhauser, O. & Kailer, A. A Model for Wet Silicon Carbide Tribo-Corrosion. *Wear in press*(2008).
15. Presser, V., Loges, A. & Nickel, K.G. Scanning electron and polarization microscopy study of the variability and character of hollow macro-defects in silicon carbide wafers. *Philosophical Magazine* **88**, 1639 - 1657 (2008).
16. Presser, V., Heiß, M. & Nickel, K.G. EOS calculations for hydrothermal diamond anvil cell operation. *Review of Scientific Instruments* **78**, 085104-1 - 085104-9 (2008).
17. Bassett, W.A., Chou, I.-M., Anderson, A.J. & Mayanovic, R. Aqueous Chemistry in the Diamond Anvil Cell up to and Beyond the Critical Point of Water. in *Chemistry at Extreme Conditions* (ed. Manaa, M.R.) 223 - 240 (Elsevier, Amsterdam, 2005).
18. Kailer, A., Gogotsi, Y.G. & Nickel, K.G. Micro-Raman spectroscopy of indentation-induced phase-transformations. *Materials, Functionality & Design, Proceedings of the European Conference on Advanced Materials and Processes and Applications* **5**, 171 - 174 (1997).
19. Nasdala, L., Irmer, G. & Wolf, D. The degree of metamictization in zircon: a Raman spectroscopic study. *European journal of mineralogy* **7**, 471 - 478 (1995).
20. Nasdala, L. et al. Metamictization of natural zircon: accumulation versus thermal annealing of radioactivity-induced damage. *Contributions to Mineralogy and Petrology* **141**, 125 - 144 (2001).
21. Kailer, A., Nickel, K.G. & Gogotsi, Y.G. Raman microspectroscopy of nanocrystalline and amorphous phases in hardness indentations. *Journal of Raman Spectroscopy* **30**, 939 - 946 (1999).
22. Presser, V., Berthold, C., Wirth, R. & Nickel, K.G. Structural characterisation of tribologically influenced silicon carbide ceramic surfaces. *Current Opinion in Solid State & Materials Science* **submitted**(2009).